The Fourth International Conference

NONLINEAR DYNAMICS

June, 19-22, 2013

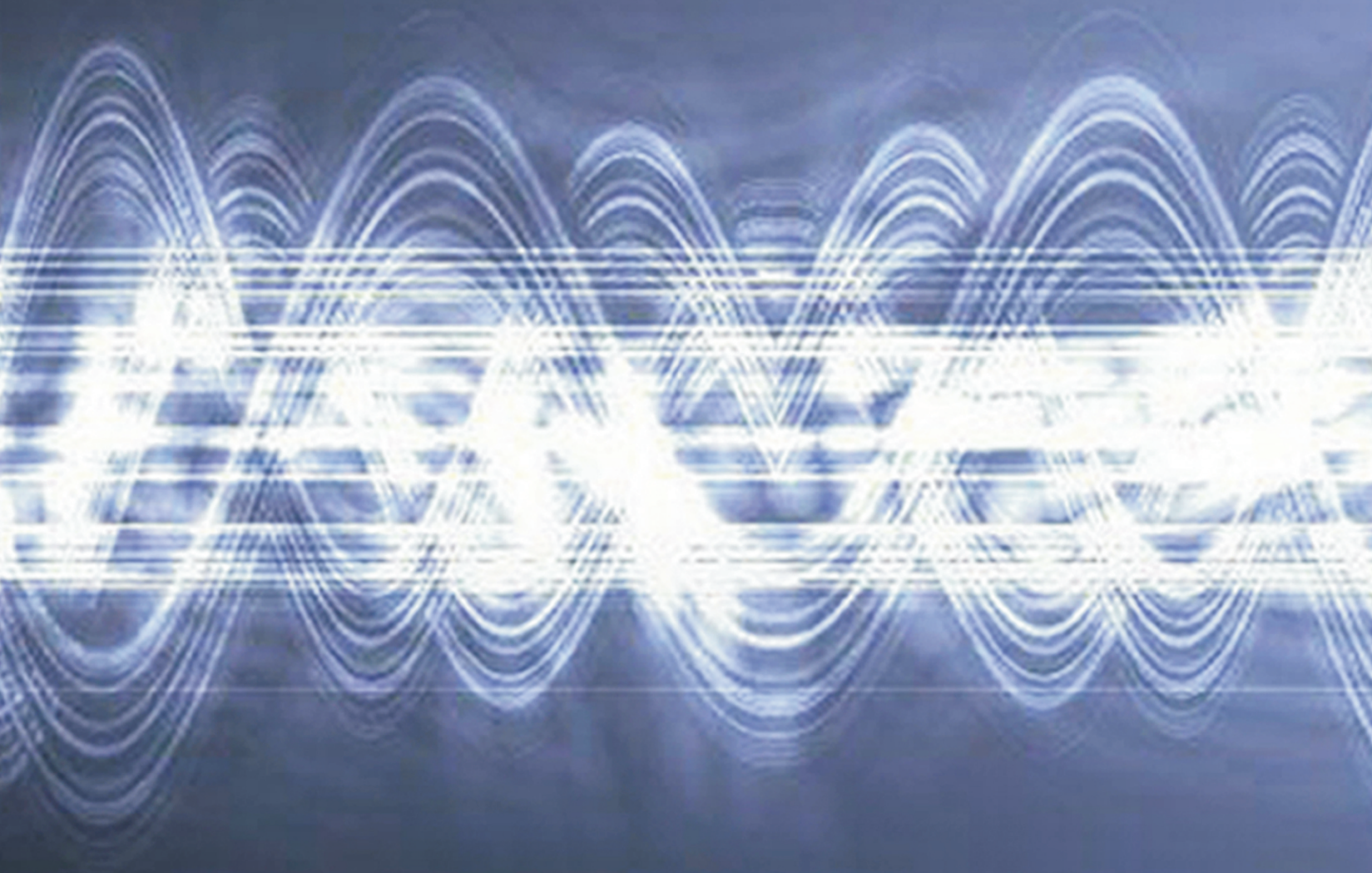

PROCEEDINGS

Ministry of Science and Education of Ukraine
National Technical University "Kharkov Polytechnic Institute"
(Kharkov, UKRAINE)

National Committee of Ukraine on Theoretical and Applied Mechanics

S. Timoshenko Institute of Mechanics NAS of Ukraine

(Kiev, UKRAINE)

McGill University

(Montreal, CANADA)

The Fourth International Conference
"Nonlinear Dynamics – 2013"

Proceedings

June, 19-22, 2013, Sevastopol (Ukraine)

ТОЧКА
ВИДАВНИЦТВО
TOCHKAPRINT.COM.UA

УДК 531; 534; 621
ББК (В) 22.31
М 69

М 69 Ю. В. Міхлін, М. В. Перепелкін Нелінійна динаміка / Тезіси доповідей 4-ої Міжнародної конференції (19-22 червня, 2013 р., Севастополь). – Х.: Вид-во «Точка», 2013. – 444 с.

ISBN 978-617-669-100-6

В сборник включены расширенные тезисы докладов 4-й Международной конференции по нелинейной динамике.

The book of Proceedings includes extended abstracts of presentations on the Fourth International conference on nonlinear dynamics.

ISBN 978-617-669-100-6

Dear Participants of the 4-Fourth International Conference "ND-KhPI-2013",

It is my honor and pleasure to welcome participants of the Fourth International Conference "Nonlinear Dynamic-2013" to be held on June, 19-22, 2013 in Sevastopol, Ukraine.

It can conclude that Nonlinear Dynamics is one of the most important and well-developed theory with an essential contribution in natural history, engineering, technologies and designs, biology, medicine, social sciences etc. An importance of Nonlinear Dynamics is also confirmed by numerous conferences, which are held last years in different countries.

One of them is the Fourth International Conference on Nonlinear Dynamics, which continues a series of preceding First, Second and Third conferences on Nonlinear Dynamics which took place in Kharkov, at the National Technical University "Kharkov Polytechnic Institute" and gathered leading scientists working on Nonlinear Dynamics from around the world. I am pleased that scientists of our university actively continue and develop traditions of known scientists in Mechanics and Mathematics such as V.L.Kirpichov, A.M.Lyapunov, V.A.Steklov, L.D.Landau, I.M.Babakov, A.S.Voljmir, A.P.Filippov, V.L.Rvachov and many others who created a glory of our University, as one of the leading Universities of Ukraine.

I wish to express my sincerely thanks to sponsors of this conference, Prof. Christophe Pierre from Illinois University and Prof. Mathias Legrand from McGill University for their financial support which is very important for the conference organization. I also thank to members of the Scientific and Organizing Committees and other people for their efforts in organization of the conference.

I am sure in a friendly atmosphere for work and discussions, for establishment of new contacts and for exchange of new scientific ideas during the conference. I hope that this meeting will be long remembering, and the conference participants will save good memories on the conference and sights of Sevastopol. I greet you all and wish you a conference crowned by success!

Rector of National Technical University
"Kharkov Polytechnic Institute"
Chairman of Organizing Committee,
Professor *L.L. Tovazhniansky*

Scope of the conference

The objective of the Conference is to bring together scientists and engineers to present and discuss recent developments on the different problems of nonlinear dynamics.

Scientific Committee

Prof. Altenbach H. (Halle, Germany)
Prof. Amabili M. (Montreal, Canada)
Prof. Andrianov I. V. (Aachen, Germany)
Prof. Avramov K.V. (Kharkov, Ukraine)
Prof. Awrejcewicz J. (Lodz, Poland)
Prof. Balthazar J. M. (Sao Paulo, Brasil)
Prof. Breslavsky D.V. (Kharkov, Ukraine)
Prof. van Campen D.H. (Eindhoven, Netherlands)
Prof. Cartmell M. (Glasgow, UK)
Prof. Epureanu B. (Ann Arbor, USA)
Prof. Gendelman O. (Haifa, Israel)
Prof. Gulyayev V.I. (Kiev, Ukraine)
Prof. Hedrih Katica R. (Stevanović) (Belgrade, Serbia)
Academician of the NAS of Ukraine, Prof. Kovalev A.M. (Donetsk, Ukraine)
Prof. Kreuzer E. (Hamburg, Germany)
Academician of the NAS of Ukraine, Prof. Kubenko V.D. (Kiev, Ukraine) – co-Chairman
Prof. Kurpa L.V. (Kharkov, Ukraine)
Prof. Lamarque C.-H. (Lyon, France)
Prof. Lenci S. (Ancona, Italy)
Prof. Manevich A.I. (Dnepropetrovsk, Ukraine)
Prof. Manevitch L.I. (Moscow, Russia)
Academician of the NAS of Ukraine, Prof. Martynyuk A.A. (Kiev, Ukraine)
Prof. Mikhlin Yu.V. (Kharkov, Ukraine) – co-Chairman
Prof. Morachkovsky O.K. (Kharkov, Ukraine)
Prof. Paidoussis M. (Montreal, Canada)
Prof. Pellicano F. (Modena, Italy)
Prof. Petrov Y.P. (Sussex, UK)
Prof. Pierre C. (Montreal, Canada) – co-Chairman
Prof. Pilipchuk V.N. (Detroit, USA)
Prof. Rega G. (Roma, Italy)
Prof. Ribeiro P.L. (Porto, Portugal)
Prof. Shaw S. W. (Lansing, USA)
Prof. Ueda Y. (Waseda, Japan)
Prof. Vakakis A. (Urbana, USA; Athens, Greece)
Prof. Warminski J. (Lublin, Poland)
Prof. Wiercigroch M. (Aberdeen, UK) – co-Chairman
Prof. Zakrzhevsky M.V. (Riga, Latvia)
Academician of the RAS, Prof. Zhuravlev V. Ph. (Moscow, Russia)

Scientific Committee of the mini-symposium «Creep and plasticity at cyclyc loading»

Prof. Altenbach H. (Halle, Germany) – Co-chairman
Prof. Borodiy M. (Kiev, Ukraine)
Prof. Breslavsky D. (Kharkov, Ukraine) – Co-chairman
Prof. Kowalewski Z. (Warsaw, Poland)
Prof. Kruch S. (ONERA, France)
Prof. Morachkovsky O. (Kharkov, Ukraine) – Co-chairman
Prof. K. Naumenko (Halle, Germany)
Prof. Shukayev S. (Kiev, Ukraine)
Prof. Spiliopoulos K. (Athens, Greece)
Prof. Yasniy P. (Ternopil, Ukraine)

Organizing Committee

Prof. Tovazhnyansky, L.L., rector of the NTU "KhPI" – Chairman
Prof. Breslavsky D.V. – vice-Chairman
Prof. Kurpa L.V. – vice-Chairman
Prof. Kravets V.A. – vice-Chairman
Prof. Mikhlin Yu.V. – vice-Chairman
Dr. Larin A.A. – Secretary
Prof. Marchenko A.P.
Prof. Morachkovsky O.K.

CONTENT

NONLINEAR DYNAMICS OF DISCRETE SYSTEMS

Proceedings of the 4th International Conference on Nonlinear Dynamics
ND-KhPI2013
June 19-22, 2013, Sevastopol, Ukraine

Finite Element Approach for Calculations of Nonlinear Forces of Fluid Film and its Application in Rotor Dynamics

Konstantin V. Avramov[1], Oleksii V. Borysiuk[2]

Abstract
The vibrations of asymmetric one disk rotor in arbitrary length journal bearing are simulated. Based on the finite element procedure, the approach for analysis of the journal bearings pressure is suggested. Using this approach, the power series of fluid film forces with respect to the general coordinates and the general velocities of journals are calculated. The harmonic balance method and the continuation technique are used to analyze the rotor vibrations. As a result of bifurcation analysis, it is obtained, that the self- sustained vibrations appear at the frequency of rotor rotation, which is lower, then the frequency of the Hopf bifurcation.

Keywords
Asymmetric rotor, journal bearings, finite element method, harmonic balance method, continuation technique

[1] A.N. Podgorny Institute for Mechanical Engineering Problems, Kharkov, Ukraine
[2] NTU KhPI, Kharkov, Ukraine

* **Corresponding author:** kavramov@ipmach.kharkov.ua

Introduction

The journal bearings are widely used in stationary gas turbine plants. The forces acting on the journals are applied from fluid film. These forces lead to the self-sustained vibrations with significant amplitudes. These forces are nonlinear functions of journals velocities and displacements. Such self-sustained vibrations lead to damage of several rotor systems [1]. At present, modern analytical and numerical methods of nonlinear dynamics [2] are used to study the rotor dynamics. Pozniak [3] is obtained analytical expressions for fluid film pressure in short length journal bearing. The asymptotic solution of the Reynolds' equation, which describes the journal bearing fluid film presure, is reported in [4]. The variational approach is used to obtain this solution. The theoretical basis of the journal bearings calculations is treated in the book [5].

The mathematical model of the self-sustained vibrations of one disk rotors in arbitrary length journal bearings is treated. The finite element solutions of the Reynolds' equation, which are obtained using power series by general coordinates and velocities of journals, are applied to calculate the fluid film nonlinear forces. The harmonic balance method and continuation technique are used to analyze the rotor vibrations.

1. Equations of rotor motions

The rotor, which consists of elastic shaft and rigid disk, in arbitrary length journal bearings is considered. This system is shown on Fig.1. The rotor is asymmetric $\left(l_1 \neq l_2\right)$.

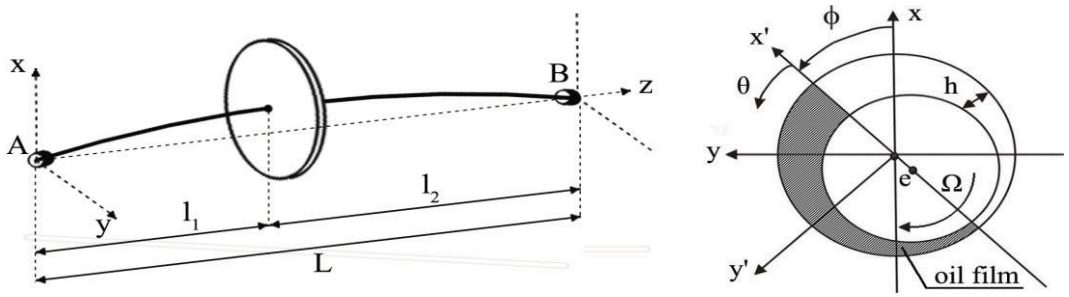

Figure 1. Rotor in arbitrary length journal bearings

The rotor performs precessional rotation with respect to z axis due to asymmetric disk arrangement. Due to the action of the gyroscopic torques, the disk performs compound motions in space. The angles of rotations about the axes x, y are denoted by θ_1, θ_2, respectively. If the rotor vibrates, the journals A and B perform motions, which are described by the general coordinates (x_1, y_1) and (x_2, y_2), respectively. The journals are hold up by the fluid film forces. The projections of these forces on the axes x and y are denoted by $F_x(x_i, y_i), F_y(x_i, y_i), i = 1,2$, respectively. The rotor is moved with angular velocity Ω about z axis. The frequency of the disk rotation takes the following form:

$$\vec{\omega} = \omega_1 \vec{e}_1 + \omega_2 \vec{e}_2 + \omega_3 \vec{e}_3, \tag{1}$$

where $\omega_1 = \dot{\theta}_1 \cos\theta_2 \cos\theta_3 + \dot{\theta}_2 \sin\theta_3$; $\omega_2 = \dot{\theta}_2 \cos\theta_3 - \dot{\theta}_1 \cos\theta_2 \sin\theta_3$; $\omega_3 = \dot{\theta}_3 + \dot{\theta}_1 \sin\theta_2$. Using the equation (1), the angular velocity of the rotor rotation is obtained in the following form: $\Omega = \dot{\theta}_3 + \dot{\theta}_1 \sin\theta_2$. Then the kinetic energy of the disk takes the following form:

$$2T = I_p\left(\dot{\theta}_3 + \dot{\theta}_1 \sin\theta_2\right)^2 + I_e(\dot{\theta}_2^2 + \dot{\theta}_1^2 \cos^2\theta_2) + m\left(\dot{x}^2 + \dot{y}^2\right), \tag{2}$$

where m is mass of the disk; I_e, I_p are diametrical and polar moments of the disk inertia, respectively.

The potential energy of the shaft takes the form:

$$2\Pi = c_{11}\left(x_f^2 + y_f^2\right) + c_{22}\left(\theta_{2,f}^2 + \theta_{1,f}^2\right) + 2c_{12}\left(x_f\theta_{2,f} - y_f\theta_{1,f}\right), \tag{3}$$

where c_{11}, c_{12}, c_{22} are elements of the shaft stiffness matrix; $\varsigma_i = l_i / l$, $i = 1,2$; $x_f = x - \varsigma_1 x_2 - \varsigma_2 x_1$; $y_f = y - \varsigma_2 y_1 - \varsigma_1 y_2$; $\theta_{1,f} = \theta_1 + \dfrac{y_2 - y_1}{l}$; $\theta_{2,f} = \theta_2 - \dfrac{x_2 - x_1}{l}$.

The equations of the rotor motions consist of four equations of two journals equilibrium and four equations of disk motions. The equations of rotor motions are the following:

$$\begin{aligned}
&m\ddot{x} + c_{11}x_f + c_{12}\theta_{2,f} = -m\,g;\\
&m\ddot{y} + c_{11}y_f - c_{12}\theta_{1,f} = 0;\\
&I_e\ddot{\theta}_1 + I_p\Omega\dot{\theta}_2 + c_{22}\theta_{1,f} - c_{12}y_f + \Theta_1(\theta_1,\theta_2) = 0;\\
&I_e\ddot{\theta}_2 - I_p\Omega\dot{\theta}_1 + c_{22}\theta_{2,f} + c_{12}x_f + \Theta_2(\theta_1,\theta_2) = 0,
\end{aligned} \tag{4}$$

where $\Theta_1(\theta_1,\theta_2) = -I_e\ddot{\theta}_1\,\theta_2^2 - \dfrac{1}{2}I_p\Omega\dot{\theta}_2\theta_2^2 - 2I_e\dot{\theta}_1\dot{\theta}_2\theta_2$; $\Theta_2(\theta_1,\theta_2) = I_e\dot{\theta}_1^2\theta_2 + \dfrac{1}{2}I_p\Omega\dot{\theta}_1\theta_2^2$.

The equations of journals equilibrium can be presented in the following form:

$$[\mathrm{K}]\mathrm{z}_f = \mathrm{F}; \tag{5}$$

where $[\mathrm{K}] = \begin{bmatrix} c_{12}l^{-1} - \varsigma_2 c_{11} & 0 & 0 & c_{22}l^{-1} - \varsigma_2 c_{12} \\ 0 & c_{12}l^{-1} - \varsigma_2 c_{11} & \varsigma_2 c_{12} - c_{22}l^{-1} & 0 \\ \varsigma_1 c_{11} + c_{12}l^{-1} & 0 & 0 & c_{22}l^{-1} + \varsigma_1 c_{12} \\ 0 & -\varsigma_1 c_{11} - c_{12}l^{-1} & c_{22}l^{-1} + \varsigma_1 c_{12} & 0 \end{bmatrix}$;

$\mathrm{z}_f = \left[x_f; y_f; \theta_{1,f}; \theta_{2,f}\right]^T$; $\mathrm{F} = \left[F_x(x_1, y_1); F_y(x_1, y_1); -F_x(x_2, y_2); F_y(x_2, y_2)\right]^T$.

The functions $\Theta_i(\theta_1, \theta_2); i = 1,2$ are small and they do not affect on the system dynamics. Therefore, in future analysis these functions are not taken into account. Under the action of gravity, the rotor rotated with constant angular velocity takes up the equilibrium. This equilibrium describes by the following values of the general coordinates: $(\bar{x}, \bar{y}, \bar{\theta}_1, \bar{\theta}_2, \bar{x}_1, \bar{y}_1, \bar{x}_2, \bar{y}_2)$. The rotor motions with respect to this equilibrium are treated. The following change of the variables is used:

$$(x, y, \theta_1, \theta_2, x_1, y_1, x_2, y_2) \to (\bar{x} + x, \bar{y} + y, \bar{\theta}_1 + \theta_1, \bar{\theta}_2 + \theta_2, \bar{x}_1 + x_1, \bar{y}_1 + y_1, \bar{x}_2 + x_2, \bar{y}_2 + y_2). \tag{6}$$

Finally, using the change of the variables (6), the equations of the system motions take the following form:

$$\begin{aligned} m\ddot{x} &= R_X^{(1)}; \quad I_e\ddot{\theta}_2 - I_p\Omega\dot{\theta}_1 + R_X^{(2)} = 0; \\ m\ddot{y} &= R_Y^{(1)}; \quad I_e\ddot{\theta}_1 + I_p\Omega\dot{\theta}_2 - R_Y^{(2)} = 0, \end{aligned} \tag{7}$$

where $R_Y^{(1)} = \widetilde{F}_Y(x_1, y_1) + \widetilde{F}_Y(x_2, y_2)$; $R_X^{(1)} = \widetilde{F}_X(x_2, y_2) + \widetilde{F}_X(x_1, y_1)$;

$R_Y^{(2)} = l_1\widetilde{F}_Y(x_1, y_1) - l_2\widetilde{F}_Y(x_2, y_2)$; $R_X^{(2)} = l_1\widetilde{F}_X(x_1, y_1) - l_2\widetilde{F}_X(x_2, y_2)$.

2. Finite element approach for pressure calculations

The equations of the rotor motions contain the relations for the nonlinear forces of the fluid film. These forces are determined in the following way:

$$\begin{bmatrix} F_x \\ F_y \end{bmatrix} = -\int_0^{L_B}\int_0^{\pi} \begin{bmatrix} \cos(\theta + \phi) \\ \sin(\theta + \phi) \end{bmatrix} p(z_1, \theta) R d\theta dz_1 , \tag{8}$$

where L_B is length of the journal bearing; R is radius of bearing; ϕ is an angle defined by the line of centers (Fig.1); z_1, θ are longitudinal and angular coordinates of the journal bearings; $(z_1 \in [0, L_b])$; $p(z_1, \theta)$ is pressure acting on the journals. It is assumed, that the fluid in bearing takes up the region $\theta \in [0; \pi]$. Bearing A (Fig.1) is considered in order to simplify the future statement. Subscript 1 of the variables indicates that the bearing A is analyzed. The analysis of the bearing B is similar.

The stream of lubrication in bearing is described by the Reynolds' equation [4]:

$$\frac{\partial}{\partial z_1}\left(\frac{h^3}{6\mu}\frac{\partial p}{\partial z_1}\right) + \frac{1}{R^2}\frac{\partial}{\partial \theta}\left(\frac{h^3}{6\mu}\frac{\partial p}{\partial \theta}\right) = \Omega\frac{\partial h}{\partial \theta} + 2\frac{\partial h}{\partial t}, \tag{9}$$

where μ is the fluid viscosity. The value of the clearance between the journal and the bearing surface h is determined as $h = c - x_1(t)\cos(\theta + \phi) - y_1(t)\sin(\theta + \phi)$, where c is nominal value of clearance.

The boundary conditions for the Reynolds' equation are considered. It is assumed, that on the ending of the bearing $z_1 = 0$ and $z_1 = L_b$, the pressure is equal to zero: $p(0,\theta) = p(L_b,\theta) = 0$. Maximum and minimum of the pressure are observed at the ends of the fluid film: $\theta = 0$ and $\theta = \pi$. This describes by the following boundary conditions: $\frac{\partial}{\partial\theta}p(z_1,0) = \frac{\partial}{\partial\theta}p(z_1,\pi) = 0$. The following dimensionless variables are used in future analysis:

$$\widetilde{x}_j = \frac{x_j}{c};\ \widetilde{y}_j = \frac{y_j}{c};\ \widetilde{H} = \frac{h}{c},\ \tau = \Omega t. \tag{10}$$

The Reynolds' equation is rewritten with respect to the dimensionless variables:

$$\begin{aligned}&\frac{\partial}{\partial z_1}\left(\widetilde{H}^3\frac{\partial p}{\partial z_1}\right) + \frac{\partial}{R^2\partial\theta}\left(\widetilde{H}^3\frac{\partial p}{\partial\theta}\right) = \frac{\Omega}{\varsigma}\left[\left(\widetilde{x}_1 + \bar{x}_1\right)\sin(\theta+\phi) - \left(\widetilde{y}_1 + \bar{y}_1\right)\cos(\theta+\phi)\right] - \\ &-\frac{2\Omega}{\varsigma}\left[\widetilde{x}_1'\cos(\theta+\phi) + \widetilde{y}_1'\sin(\theta+\phi)\right],\end{aligned} \tag{11}$$

where $\widetilde{x}_1' = \frac{d\widetilde{x}_1}{d\tau}$; $\varsigma = \frac{c^2}{6\mu}$; $\widetilde{H} = 1 - \widetilde{x}_1\cos(\theta+\phi) - \widetilde{y}_1\sin(\theta+\phi) - \bar{x}_1\cos(\theta+\phi) - \bar{y}_1\sin(\theta+\phi)$.

The combination of the finite element method and the Galerkin approach is used to solve the equations (11). The fluid film is split on M rectangular finite elements with nodes in vertexes. It is considered the finite element E, which occupy the region: $S_E = \left\{(z,\theta)\in R^2 \,\middle|\, z_i < z < z_j;\ \theta_i < \theta < \theta_j\right\}$. The pressure on this finite element $\bar{p}_E(z_1,\theta)$ takes the following form:

$$\bar{p}_E(z_1,\theta) = \sum_{i=1}^{4} p_i u_i(z_1,\theta), \tag{12}$$

where $u_1(z_1,\theta),...,u_4(z_1,\theta)$ are linearly independent trial functions, which satisfy the boundary conditions; $p_1,...,p_4$ are independent parameters.

Following the Galerkin approach, the weak solution for (11) on the finite element E is obtained. Using the integration by parts, the following equations are derived:

$$\begin{aligned}&-\varsigma\iint\limits_{S_E}\widetilde{H}^3\left[\frac{\partial u_j(z_1,\theta)}{\partial z}\frac{\partial\bar{p}_E}{\partial z} + \frac{1}{R^2}\frac{\partial u_j(z_1,\theta)}{\partial\theta}\frac{\partial\bar{p}_E}{\partial\theta}\right]dz_1\,d\theta = \\ &= \Omega\iint\limits_{S_E}\left[\left(\widetilde{x}_1 - 2\widetilde{y}_1' - \bar{x}_1\right)\sin(\theta+\phi) - \left(\widetilde{y}_1 + 2\widetilde{x}_1' + \bar{y}_1\right)\right]u_j(z_1,\theta)\,dz_1\,d\theta;\ j = 1,...,4.\end{aligned} \tag{13}$$

where S_E is the region of the fluid film on the finite element E. The value H^3 takes the form:

$$\widetilde{H}^3 = \sum_{i=1}^{10} a_i(\theta,\phi)F_i(\widetilde{x}_1,\widetilde{y}_1),$$

where $\{F_1,...,F_{10}\} = \{1, x, y, x^2, y^2, xy, x^3, y^3, x^2y, xy^2\}$, $a_i(\theta,\phi)$ are coefficients, which are functions of angles θ,ϕ. These functions are not published here. The equations (13) are transformed into the system of linear algebraic equations with respect to the unknown parameters $[p_1, p_2, p_3, p_4]^T$:

$$\mathrm{A}(\widetilde{x}_1,\widetilde{y}_1)\cdot \mathrm{P}(\widetilde{x}_1,\widetilde{y}_1,\widetilde{x}_1',\widetilde{y}_1')=\mathrm{B}(\widetilde{x}_1,\widetilde{y}_1,\widetilde{x}_1',\widetilde{y}_1'), \tag{14}$$

where the elements of the matrix A and the vector B are determined as:

$$A_{i,j}=-\iint\limits_{S_E}\widetilde{H}^3\left(\frac{\partial u_i}{\partial z}\frac{\partial u_j}{\partial z}+\frac{1}{R^2}\frac{\partial u_i}{\partial \theta}\frac{\partial u_j}{\partial \theta}\right)dz_1 d\theta\,,$$

$$B_i=\frac{\Omega}{\varsigma}\iint\limits_{S_E}\left[(\widetilde{x}_1-2\widetilde{y}_1'-\bar{x}_1)\sin(\theta+\phi)-(\widetilde{y}_1+2\widetilde{x}_1'+\bar{y}_1)\right]u_i\; dz_1\, d\theta\;;\;\; i=1,...,4;\; j=1,...,4\;.$$

The assemblage of all finite elements is carried out. As a result, the system of linear algebraic equations with respect to unknowns p_i for all M finite elements is obtained. In general, this system can be presented in the following form:

$$\left[A_G(\widetilde{x}_1,\widetilde{y}_1)\right]\cdot\left[P_G\right]=\left[B_G(\widetilde{x}_1,\widetilde{y}_1,\widetilde{x}_1',\widetilde{y}_1')\right], \tag{15}$$

where $\left[P_G\right]=\left[P_1,P_2,...\right]$ is global vector of unknowns. We stress, that elements of the matrix and the vector of the right-hand parts of the system (15) are polynomials with respect to the general coordinates $\widetilde{x}_1,\widetilde{y}_1$ and the general velocities $\widetilde{x}_1',\widetilde{y}'$ of the journals. In order to solve the system (15), the elements of the vector $\left[P_G\right]$ are expanded into the truncated series with respect to the displacements and the velocities of the journals $\widetilde{x}_1,\widetilde{y}_1,\widetilde{x}_1',\widetilde{y}_1'$:

$$P_i=\sum_{j=1}^{n}\overline{p}_{i,j}S_j\;, \tag{16}$$

where $\{S_1,S_2,...\}=\left\{1,\widetilde{x}_1,\widetilde{y}_1,\widetilde{x}_1',\widetilde{y}_1',\widetilde{x}_1^2,\widetilde{x}_1\widetilde{y}_1,\widetilde{x}_1\widetilde{x}_1',\widetilde{x}_1\widetilde{y}_1',...\right\}.$

The equations (16) are substituted into the system of linear algebraic equations (15) and the coefficients with the same powers are equated. As a result, the set of linear algebraic equations with respect to coefficients of the expansion (16) $\overline{p}_{i,j}$ is derived. As a result, the global vector of the unknowns $\left[P_G\right]$ is calculated in the form of truncated series with respect to the general coordinates and the general velocities of the journal $\widetilde{x}_1,\widetilde{y}_1,\widetilde{x}_1',\widetilde{y}_1'$. The obtained solution is substituted into the equations of the nonlinear forces of the fluid films (8) and it is obtained:

$$F_x=-\sum_{i=1}^{n}\sum_{j=1}^{m}\int\limits_{z_{i-1}}^{z_i}\int\limits_{\theta_{j-1}}^{\theta_j}\overline{p}_E(z_1,\theta)\cos(\theta+\phi)R\,dz_1 d\theta\;;\; F_y=-\sum_{i=1}^{n}\sum_{j=1}^{m}\int\limits_{z_{i-1}}^{z_i}\int\limits_{\theta_{j-1}}^{\theta_j}\overline{p}_E(z_1,\theta)\sin(\theta+\phi)R\,dz_1 d\theta\,. \tag{17}$$

Performing integration (17), the projections of the forces F_x,F_y are obtained in the form of the power series with respect to the general coordinates and the general velocities of the journal $\widetilde{x}_1,\widetilde{y}_1,\widetilde{x}_1',\widetilde{y}_1'$:

$$\begin{aligned}F_X&=F_{X,0}+F_{X,1}(\widetilde{x}_1,\widetilde{y}_1,\widetilde{x}_1',\widetilde{y}_1')+F_{X,2}(\widetilde{x}_1,\widetilde{y}_1,\widetilde{x}_1',\widetilde{y}_1')+F_{X,3}(\widetilde{x}_1,\widetilde{y}_1,\widetilde{x}_1',\widetilde{y}_1')+\ldots;\\ F_Y&=F_{Y,0}+F_{Y,1}(\widetilde{x}_1,\widetilde{y}_1,\widetilde{x}_1',\widetilde{y}_1')+F_{Y,2}(\widetilde{x}_1,\widetilde{y}_1,\widetilde{x}_1',\widetilde{y}_1')+F_{Y,3}(\widetilde{x}_1,\widetilde{y}_1,\widetilde{x}_1',\widetilde{y}_1')+\ldots\end{aligned} \tag{18}$$

The obtained nonlinear forces (18) are substituted into the dynamical system (7). As a result, the nonlinear dynamical system describing the rotor vibrations is obtained:

$$\ddot{q} + [F]\dot{q} = \widetilde{W}(q, \dot{q}), \tag{19}$$

where $q = [x, \theta_1, y, \theta_2]^T$; $\widetilde{W}(q, \dot{q})$ is nonlinear vector-function.

2. Numerical analysis of vibrations

The harmonic balance method and continuation technique are used to analyze the rotor nonlinear dynamics. The direct numerical integration of the system (7) is carried out to validate the results of the harmonic balance method. Eigenvalues of the linearized system are calculated to estimate the stability of steady rotation. At $\Omega = 715\ rad/s$, steady rotation loses stability and the Hopf bifurcation take place. Then unstable self- sustained vibrations appear. The saddle- node bifurcation takes place in the point S_n and the stable limit cycle appear. The frequency response of the rotor vibrations is shown on Fig.2. Stable and unstable vibrations are shown by solid and dotted lines, respectively.

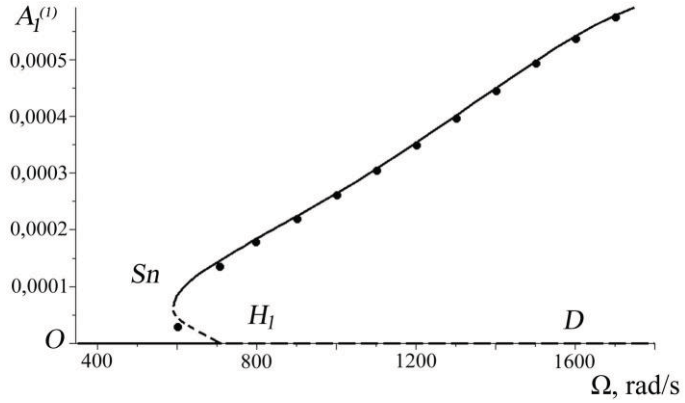

Figure 2. Frequency response

Conclusions

Mathematical model of one disk rotor vibrations in the journal bearings is suggested. The method based on the expansion of the pressure into Taylor series is suggested. The combination of the Galerkin approach and the finite element method is used to obtain the coefficients of this series. The influence of the rotor parameters on the self- sustained vibrations is analyzed.

References

[1] Zhang X. Y. On site testing and analysis of the oil whirl phenomena in national made 200MW stream turbine generator systems *Power Industry*, Vol. 12 (5), pp. 32-37, 1992.

[2] Legrand M., Jiang D., Pierre C., Shaw S.W. Nonlinear normal modes of a rotating shaft based on the Invariant Manifold Method International *Journal of Rotating Machinery*, Vol. 10(4), pp. 319-335, 2004.

[3] Pozniak E.L. Dynamical properties of journal bearing oil film *Izv. Akad. Nauk SSSR, Mechanics and Mechanical Engineering*, pp. 22-29, 1961 (in Russian).

[4] Olimpiev V.I. Eigenfrequencies of rotor-bearing system *Izd. Akad. Nauk SSSR, Mechanics and Mechanical Engineering*, Vol. 3, pp. 24-29, 1960 (in Russian).

[5] Korovchinsky M.V. Theoretical basis of journal bearings analysis *Machinery*, Moscow, 1959.

Proceedings of the 4th International Conference on Nonlinear Dynamics
ND-KhPI2013
June 19-22, 2013, Sevastopol, Ukraine

On Engineering Mechanical Systems, Excited by Small Motors

José Manoel Balthazar [1*]

Abstract
The aim of this study is to describe a large number of phenomena caused by action of vibrations on nonlinear electro-mechanical systems.
We remark that a large number of publications were based on the assumption that the external excitations are produced by an ideal source of power with prescribed time history: prescribed magnitude, phase and frequency, or in random problems with prescribed characteristics.
In reality, the excitations sources are non-ideal, they have always limited power, limited inertia and their frequencies varies according to the instantaneous state of the vibrating system.
We remark that small motors with limited power are used in laboratory test and therefore the investigations of mutual interaction of driven and driving subsystems are very important.
We discuss several contributions on the past, nowadays and perspective futures in engineering that may be modeled by non-ideal systems with many degrees of freedom. Examples of this kind of engineering devices can be presented.

Keywords
Nonlinear electro-mechanical systems, non-ideal sources, limited power

[1] University Estadual Paulista, Rio Claro, SP, Brazil
* **Corresponding author:** jmbaltha@rc.unesp.br

Proceedings of the 4th International Conference on Nonlinear Dynamics
ND-KhPI2013
June 19-22, 2013, Sevastopol, Ukraine

Network of Families of Periodic Solutions of Generalized Hill's Problem

Alexander B. Batkhin[1]*

Abstract
A system of Hamilton with singular perturbation at the origin, which has two corresponding limiting problems, is considered. The generating solutions, obtained from the limiting problems, make it possible to predict properties of corresponding family of periodic solutions of original system as type of symmetry, approximation of initial conditions and period of the solution. An algorithm for studying families of periodic solutions by its generating sequence is proposed. These approach is applied for generalized Hill's problem, and it is shown that all known families of periodic solutions form the common network connecting to each other by both generating sequences and by sharing common orbits with integer multiplicity.

Keywords
generating solution, Hamiltonian system, Hill's problem

[1]Keldysh Institute of Applied Mathematics of RAS, Moscow, Russia
***Corresponding author**: batkhin@gmail.com

Introduction

Consider a system of canonical equations

$$\dot{\mathbf{z}} = J\partial H/\partial \mathbf{z}, \quad \mathbf{z} = (\mathbf{x}, \mathbf{y}), \tag{1}$$

where J is simplectic unit, $\mathbf{x}$ and $\mathbf{y}$ are m-dimensional vectors of canonical coordinates and momenta correspondingly. Let system (1) is defined by Hamiltonian $H(\mathbf{z})$ of the form

$$H(\mathbf{z}) = H_0(\mathbf{z}) + R(\mathbf{x}), \tag{2}$$

where $H_0(\mathbf{z})$ is unperturbed integrable part, $R(\mathbf{x})$ is perturbation function with singularity at the origin.

It is well known that periodic solutions of an autonomous system of ordinary differential equations are not isolated and form families of periodic solutions. In general case these families are one-parametric due to presence of the first integral $H(\mathbf{z}) = h$ of the system (1). Here and further families of periodic solutions which are continuable up to $h \to \infty$ are considered. At the limit $h \to \infty$ the original system (1) can be approximated by its limiting problem, which can be find by Power Geometry algorithms [1, Ch. IV].

1. Limiting Problems

Several assumptions concerning the structure of the Hamiltonian (2) are made. In many cases the Hamiltonian $H_0(\mathbf{z})$ can be written as a quadratic form $H_0(\mathbf{z}) = \langle G\mathbf{z}, \mathbf{z}\rangle$ with symmetric matrix G. Let perturbation function $R(\mathbf{x})$ can be represented as a finite sum $R(\mathbf{x}) = \sum_{k=1}^{n} C_k |\mathbf{x}|^{-k}$, $n \in \mathbb{N}$, and $\lim_{\mathbf{x}\to\infty} R(\mathbf{x}) = 0$.

For each term of the Hamiltonian (1) the 2D vector of power exponents is computed by the rule: $(Q, P) = (\sum_{i=1}^{m} q_i, \sum_{i=1}^{m} p_i)$, where q_i is power exponent of coordinate x_i and p_i is power exponent of corresponding momentum y_i. The set $S(H)$ of all such vectors is called the *support* of the function $H(\mathbf{z})$. According to made above assumptions support $S(H_0)$ consists of three points $(2,0)$, $(1,1)$, $(0,2)$ and support of function $S(R)$ consists of the finite number of points laying in the negative part of abscissa. The convex hull of the support $S(H)$ is called *Newton polygon* in this study it is a triangle $\Gamma(H)$ with three sides Γ_i, $i = 1,2,3$ (see Fig. 1).

One can compute the *truncated Hamiltonian* $\widehat{H}_i$ corresponding to each side of the triangle. There are only two non-trivial truncations. The first truncation corresponding to the side Γ_1 with external normal

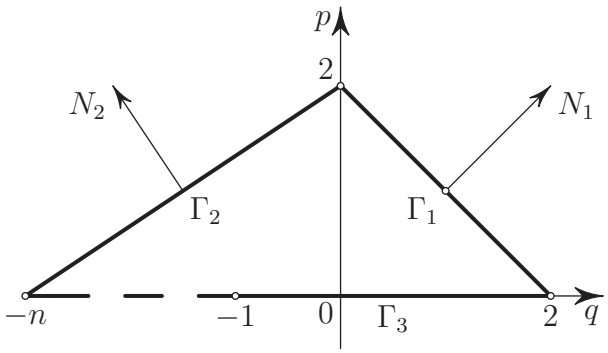

Figure 1. The support $S(H)$ and Newton polygon $\Gamma(H)$ of the Hamiltonian $H(\mathbf{z})$.

$N_1 = (1,1)$ is Hamiltonian $\widehat{H}_1(\mathbf{z}) \equiv H_0(\mathbf{z})$, which describes the motion for large values of the phase coordinates $\mathbf{z}$. The second truncation corresponding to the side Γ_2 with external normal $N_2 = (-2,n)$ is Hamiltonian $\widehat{H}_2 = \sum_{i=1}^{m} a_i y_i^2 + C_n|\mathbf{x}|^{-n}$, which describes the motion near the origin.

The vectors of external normals give canonic transformations of phase coordinates after which the original Hamiltonian (2) can be written in the form

$$\widetilde{H}(\mathbf{Z}) = \widetilde{H}_1(\mathbf{Z}) + \varepsilon \widetilde{H}_2(\mathbf{Z}), \tag{3}$$

where ε is a small parameter, $\widetilde{H}_1$ is Hamiltonian of the limit problem and sign $\widetilde{\ }$ denotes Hamiltonian in new variables $\mathbf{Z}$.

The vector $N_1 = (1,1)$ involves transformation, which shrinks the vicinity of infinite point:

$$\mathbf{z} = \sqrt{|h|}\mathbf{Z}, \quad \widetilde{H}(\mathbf{Z}) = \langle G\mathbf{Z}, \mathbf{Z}\rangle + \sum_{k=1}^{n} \varepsilon_1^k C_k |\mathbf{X}|^{-k} = \pm 1, \text{ where } \varepsilon_1 = |h|^{-1/2}. \tag{4}$$

Thus, at the limit $h \to \pm\infty$ the initial Hamiltonian $H(\mathbf{z})$ coincides with the Hamiltonian of first limiting problem $\widetilde{H}_1 = \langle G\mathbf{Z}, \mathbf{Z}\rangle$, which is integrable.

The vector $N_2 = (-1, n/2)$ involves transformation, which blows up the vicinity of the origin in the coordinate space and shrinks the vicinity of the origin in the momentum space:

$$\begin{aligned} &\mathbf{x} = |h|^{-1}\mathscr{X}, \quad \mathbf{y} = |h|^{n/2}\mathscr{Y}, \quad t = |h|^{n/2+1}s, \\ &\widetilde{\mathscr{H}}(\mathscr{X}, \mathscr{Y}) = C_n|\mathscr{X}|^{-n} + \sum_{i=1}^{m} a_i \mathscr{Y}_i^2 + o(\varepsilon_2), \text{ where } \varepsilon_2 = |h|^{-1}. \end{aligned} \tag{5}$$

The unperturbed part of the Hamiltonian $\widetilde{\mathscr{H}}(\mathscr{X}, \mathscr{Y})$ gives Hamiltonian of the second limiting problem, which describes the motion near the origin in the central field with potential $C_n|\mathscr{X}|^{-n}$. The last problem is integrable, too.

2. Generating Solutions

The idea of generating solution, introduced by Poincare, is used in this study. It was very fruitful in investigation of periodic solutions of restricted three-body problem (see [2, 3]).

Definition 1. Let canonical system defined by function (3) has periodic solution $(\mathbf{x}(t,\varepsilon), \mathbf{y}(t,\varepsilon))$ for $\varepsilon > 0$, which is continuously extendable while $\varepsilon \to 0$. Then its limit (if it exists) is called *generating solution*. Generating solution is called *regular* if it does not pass through the singular points of the (3).

We assume that the system (1) has a periodic solution $\mathbf{z}(t, \mathbf{z}_0)$ with period T: $\mathbf{z}(T, \mathbf{z}_0) = \mathbf{z}_0$ for definite value of Hamiltonian $H(\mathbf{z}_0) = h_0$. Let ρ_h' and ρ_h'' are the minimal and the maximal distance from the origin to orbit $\mathbf{x}(t, \mathbf{z}_0)$. There are three possible ways of continuation of periodic solution $\mathbf{z}(t, \mathbf{z}_0)$ while $h \to \infty$:

1. If $\lim_{h\to\infty}\rho_h' > 0$ then we get generating solution of the first species; such solution is regular and can be find by the normal form method [2, Ch. II, VII].

2. If $\lim_{h\to\infty}\rho_h' = 0$ and $\lim_{h\to\infty}\rho_h'' > 0$ then we get generating solution of the second species.

3. If $\lim_{h\to\infty}\rho_h' = \lim_{h\to\infty}\rho_h'' = 0$ then we get generating solution of the third species.

If generating solution is not regular then it may consist of solutions of special form called *arc-solution*. The arc-solutions start and finish at the singular points of the function (3). In our case generating solutions should be composed from arcs which start and finish at the origin – the only singular point of the perturbation $R(\mathbf{x})$.

According to assumptions made in section 1 the system (1) has two limiting problems with Hamiltonians given by unperturbed parts of (4) and (5) correspondingly.

To obtain the periodic solution of the perturbed system from the generating solution one has to provide matching procedure of arc-solutions near the origin. The matching procedure of the first order matches the velocities of solution of the first limiting problem and velocities of solutions of the second limiting problem at the origin. If matching procedure is successful then we get a periodic solution of a certain family and the whole family can be computed numerically by one of the continuation algorithm (see [4]).

We apply the described above approach to Hill's problem.

3. Generalized Hill's Problem and Its Limiting Cases

Planar *Hill's problem* is a celestial mechanics model being a limit case of the well known restricted three body problem. It has a lot of applications and originally was proposed by G. Hill for the Moon motion theory [5]. A small modification of the original Hill's problem called *generalized Hill's problem* (GHP) is considered in this study. The Hamiltonian of the GHP can be written in the form

$$H(\mathbf{z}) = \langle G\mathbf{z},\mathbf{z}\rangle + \frac{\sigma}{|\mathbf{x}|},\ \text{where } \sigma = \pm 1, \quad G = \begin{pmatrix} -1 & 0 & 0 & -1/2 \\ 0 & 1/2 & 1/2 & 0 \\ 0 & 1/2 & 1/2 & 0 \\ -1/2 & 0 & 0 & 1/2 \end{pmatrix}, \tag{6}$$

where $\mathbf{x} = (x_1, x_2)$, $\mathbf{y} = (y_1, y_2)$, $\mathbf{z} = (\mathbf{x}, \mathbf{y})$.

The canonical equations of Hamiltonian (6) has first integral called Jacobi integral

$$J = 3x_1^2 - \frac{2\sigma}{|\mathbf{x}|} - \dot{x}_1^2 - \dot{x}_2^2 = C,\ C = -2H.$$

If $\sigma = -1$ we get the Newtonian potential of attraction and, therefore, we get the original Hill's problem. If $\sigma = +1$ we get the Newtonian potential of repulsion and we call this case *anti-Hill's problem*.

The essential property of GHP is the presence of two symmetries of extended phase space given by linear transformations

$$\Sigma_1 : (t, x_1, x_2, y_1, y_2) \to (-t, x_1, -x_2, -y_1, y_2) \quad \Sigma_2 : (t, x_1, x_2, y_1, y_2) \to (-t, -x_1, x_2, y_1, -y_2),$$

which involves that all the periodic solutions of the GHP belong to one of the following group:

1. Asymmetric solutions, which change their form under any transformation $\Sigma_{1,2}$.

2. Single symmetric solutions, which are invariant under only one transformation Σ_1 or Σ_2.

3. Double symmetric solutions, which are invariant under any transformation $\Sigma_{1,2}$.

The presence of symmetry of equations considerably simplify the usage of generating solutions defined by corresponding limiting problems.

The first limiting problem is called *Hénon problem* [6] and is obtained by transformation (4). This problem gives two sets of suitable solutions:

1. one-parametric family of regular periodic solutions, which contains the only one generating solution of the first species (see [6]);

2. the countable set of arc-solutions of two types, which are solutions of the second species.

The arc-solutions of the first type were denoted by M. Hénon [7] by symbols $\{\pm j\}$, $j \in \mathbb{N}$. The orbits of the first type arc-solutions are epicycloid (see Fig. 2, left pictures for $j = \pm 1$). The arc-solutions of the second type were denoted by symbols $\{i\}$ and $\{e\}$ and its orbits are ellipses (see Fig. 2, right pictures).

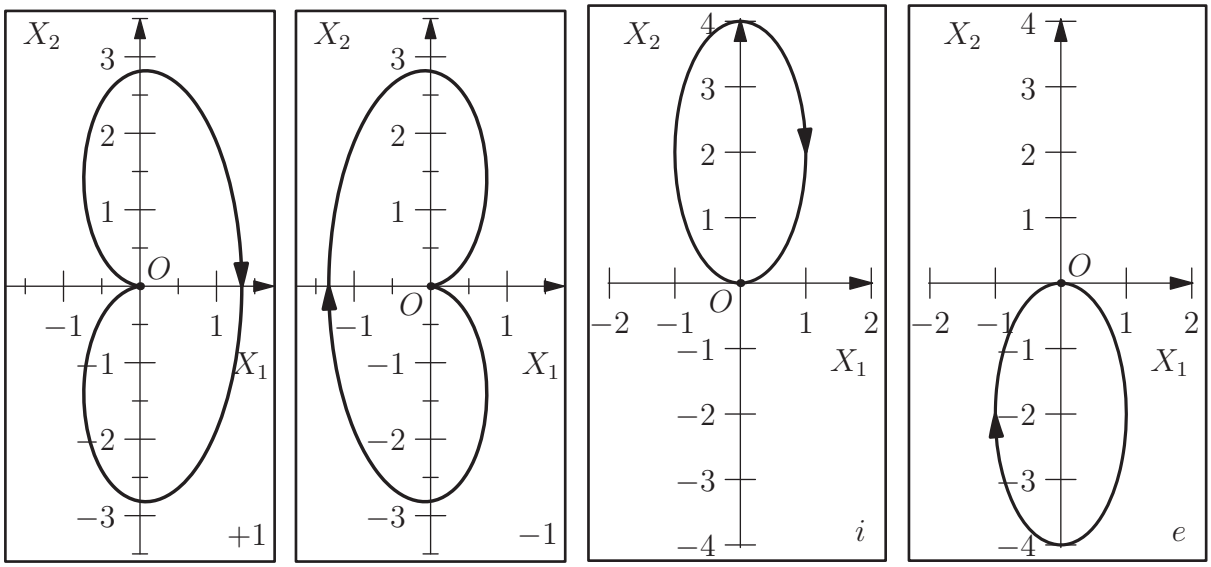

Figure 2. Arc-solutions of the first type $\{+1\}$, $\{-1\}$ and second type $\{i\}$ and $\{e\}$.

The second limiting problem is Kepler problem, which gives solutions in the form of hyperbola with large semi axis equals to 1.

All arc-solutions pass through the origin and it is possible to compose the infinite number of sequences from arc-solutions $\pm j$, $j \in \mathbb{N}$, i, e by matching these arcs with hyperbolas of two types (see [8]). Hyperbolas of the first type have pericenters near OX axis and eccentricity $e \approx 1$, hyperbolas of the second type have pericenters near OY axis and eccentricity $e \gg 1$.

The analysis of the structure of the phase space of the Hill's problem depending on the value of Jacobi integral C was given in [8], and it was shown there that suitable solutions of Hénon problem and Kepler problem can exist simultaneously only for $C < 3^{4/3} \approx 4.34$. Thus, generating solutions can generate only those families of periodic orbits which are continuable up to $C \to -\infty$ (or $h \to +\infty$).

M. Hénon stated that for the Newtonian potential of attraction there are two pairs of arc-solutions, namely, *ii* and *ee*, which can not be matched to each other by hyperbolas described above.

4. Generating Sequences and Families of Periodic Solutions

Statement 1 (M. Hénon [3])**.** A sequence of arc-solutions which does not contain two identical arcs of the second type in succession is a generating solution and it is called *generating sequence* for Hill's problem.

Numerical analysis of all known families of periodic solutions of Hill's problem allows to state the following

Statement 2. Each family of periodic solutions of Hill's problem, which is continuable to solution of the second species, is defined at the limit by generating sequence of Statement 1.

Moreover, numerical explorations of periodic solutions of anti-Hill's problem show that there are no limitations in the structure of generating sequences, i. e.

Statement 3. The sequence composed from the arc-solutions j, $j \in \mathbb{N}$, i, e in arbitrary order, except two sequences consisting of arcs $\{i\}$ and $\{e\}$ only, is a generating solution for an anti-Hill's problem family of periodic solutions.

The generating sequence allows to determine the following properties of corresponding family:

- the type of symmetry of periodic orbits of the family;
- global multiplicity of periodic orbits of the family;
- asymptotics of initial conditions, period and stability index of periodic orbits of the family when $C \to -\infty$.

An algorithm for studying symmetric periodic solutions defined by its corresponding generating sequences was proposed by the author in [6, 9].

1. A generating sequence is composed in according with Statement 1 or Statement 3; the type of symmetry and approximate initial conditions and period of solutions are computed.
2. An orbit of the corresponding family is computed iteratively.
3. The whole family is computed by one of the continuation method.
4. During the computation of the whole family stability of periodic solutions and its bifurcations are detected as well.

More then 20 new families of periodic solutions were found out by this algorithm. Many of them have periodic solutions useful for space flight design [9].

5. Common Network of Families of Generalized Hill's Problem

Some peculiarities of anti-Hill's problem make it easier for prediction the global properties of families defined by generating sequences. Namely,

- the region of allowable motion called the Hill's region is isolated from the origin, therefore, no one family has periodic orbit with collision and global multiplicity of periodic solution is invariant along the family;
- periodic solutions are possible for values $C < 0$ only, as long as configuration space is divided by OY axis for $C \geqslant 0$.

It was shown above that Hénon problem is the limiting problem both for Hill's problem and anti-Hill's problem. Therefore, two families of periodic solutions – one for Hill's problem and the other for anti-Hill's – are called *linked* if they both have the same generating sequence at the limit $C \to -\infty$. Comparing Statement 1 with Statement 3 one can conclude that not every family of periodic solutions of anti-Hill's problem can be continued to a family of Hill's problem. But, on the contrary, all known families defined by generating sequences satisfying the condition of Statement 1 are continuable to families of anti-Hill's problem.

Figure 3 gives the result of computations in the form of schematic drawing of families of periodic solutions of generalized Hill's problem, which form the common network of periodic solutions in the sense that starting from an arbitrary orbit of any family one can continue to any orbit of other family. All families of Hill's problem denoted on Figure 3 (left part of the figure) are described in [5].

Acknowledgments

The work was supported by RFBR, project No 11-01-00023.

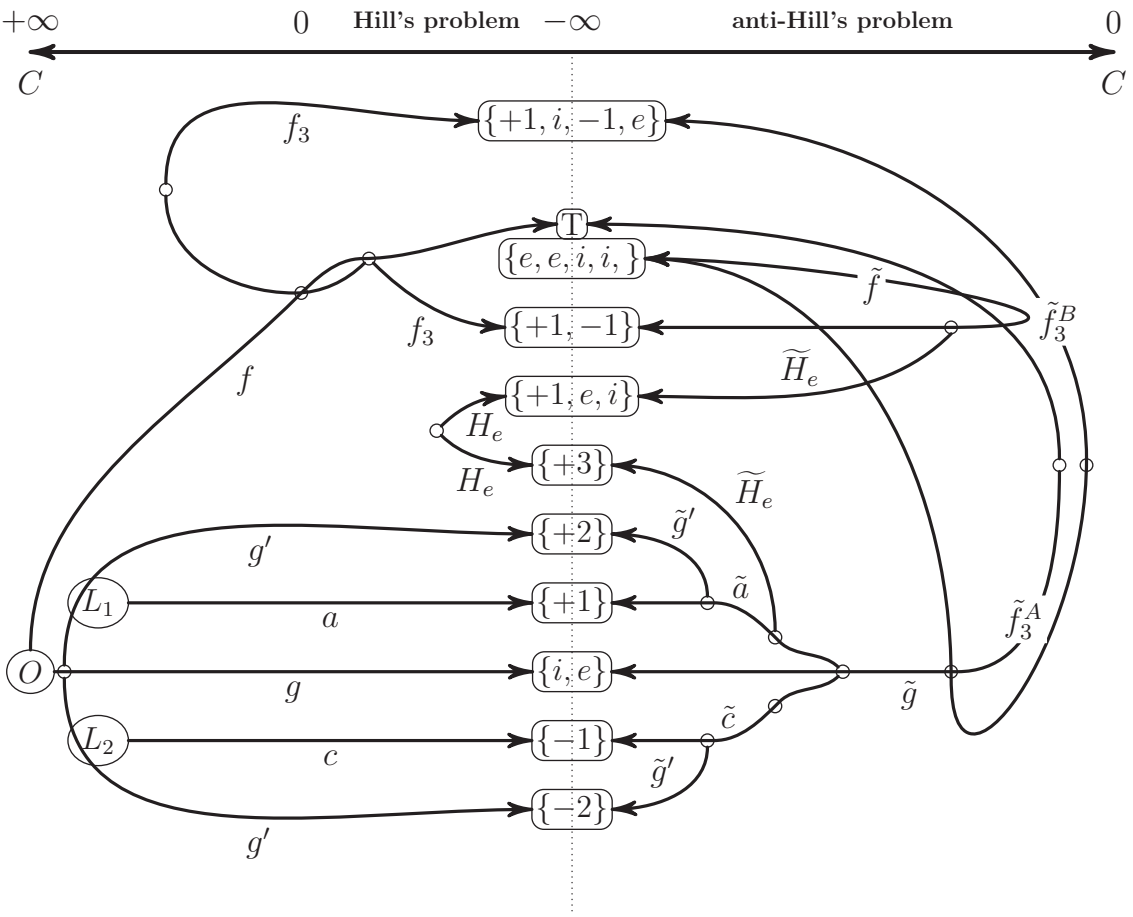

Figure 3. Diagram of families of GHP. The center column is generating sequences of families. $L_{1,2}$ are libration points, O is the origin. The common orbits of two families is circled.

References

[1] Alexander D. Bruno. *Power Geometry in Algebraic and Differential Equations*. Elsevier Science, Amsterdam, 2000.

[2] Alexander D. Bruno. *The Restricted 3–body Problem: Plane Periodic Orbits*. Walter de Gruyter, Berlin, 1994.

[3] Michel Hénon. *Generating Families in the Restricted Three-Body Problem*. Number 52 in Lecture Note in Physics. Monographs. Springer, Berlin, Heidelber, New York, 1997.

[4] Thomas S. Parker and Leon O. Chua. *Practical numerical algorithms for chaotic systems*. Springer-Verlag, 1989.

[5] Alexander. B. Batkhin and Natalia. V. Batkhina. *Hill's Problem*. Volgogradskoe nauchnoe izdatel'stvo, Volgograd, 2009. (in Russian).

[6] Alexander. B. Batkhin. Symmetric periodic solutions of the hill's problem. I. *Cosmic Research*, 51(4), 2013. (to be published).

[7] Michel Hénon. New families of periodic orbits in Hill's problem of three bodies. *Celestial Mechanics and Dynamical Astronomy*, 85:223–246, 2003.

[8] Alexander. B. Batkhin. *Symbolic dynamics and generating planar periodic orbits of the Hill's problem*. Preprint No 34. KIAM, Moscow, Russia, 2011. (in Russian).

[9] Alexander B. Batkhin. *Symmetric periodic solutions of the Hill's problem*. Preprint No 52. KIAM, Moscow, Russia, 2012. (in Russian).

Proceedings of the 4th International Conference on Nonlinear Dynamics
ND-KhPI2013
June 19-22, 2013, Sevastopol, Ukraine

High Symmetry Discrete Breathers in a Three-Dimensional Diatomic Crystal

G.M. Chechin[1*] and P.P. Goncharov[1]

Abstract
We have found a discrete breather with point symmetry group m3m in the model of NaI crystal described by the Morse potential with the appropriate force constants. The Floquet stability analysis of this breather can be simplified by means of the specific group-theoretical method based on the apparatus of irreducible representations of the symmetry group. The method allows us to split the high-dimensional variational system corresponding to the breather into a number of subsystems of sufficiently small dimensions. With the aid of this technique, we have calculated Floquet exponents for each of these subsystems and, therefore, for the infinitesimal perturbations corresponding to the individual irreducible representations of the group m3m.

Keywords
Discrete breathers, group-theoretical methods, stability analysis

[1] Southern Federal University, Rostov-on-Don, Russia
* **Corresponding author:** gchechin@gmail.com

According to the conventional definition, discrete breather represents spatially localized and time-periodic vibration in a nonlinear Hamiltonian lattice (see, e.g., [1], [2]).

We study strong localized discrete breathers in crystal lattice of NaI. This is two-component face-centered cubic crystal with space symmetry group Fm3m. We use the mathematical model of this crystal which was considered in [3]. In this model, the atoms are represented by mass points vibrating near their equilibrium positions (thus, we don't take into account the atomic electron structure of the crystal). It is assumed that atoms interact via the Morse potential. The constants of this potential are different for interactions Na-Na, Na-I and I-I atoms. We use the values of these constants from Ref. [3]. Strong localization of discrete breathers allows one to consider only finite fragment (cluster) of the NaI lattice which contains a sufficiently small number of atoms (N = 33, i.e., four shells around the atom representing the center of the breather).This cluster is shown in Figure 1.

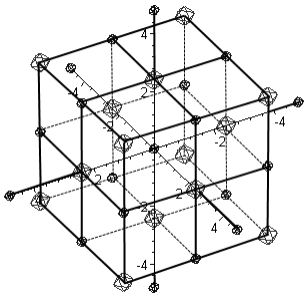

Figure 1. A cluster of the NaI lattice (Na - small circles, I - large circles)

In Ref. [3], the above model was used for constructing low-symmetry breathers which describe vibrations along [1, 1, 1], [1, 1, 0], and [1, 0, 0] directions. As to our understanding, the localized dynamical objects discussed in Ref. [3] are not strictly periodic, because they are generated by initial displacement of one atom in the selected direction. In contrast, we analyze the possibility of existence of discrete breathers with high-symmetry point groups (Oh, Td, etc.). Moreover, we construct discrete

breathers which turn out to be “numerically exact” dynamical objects (besides localization, they must be time-periodic).In Ref. [4], high symmetry discrete breathers in NaI lattice were constructed by the aid of an approximate method, which is a certain generalization of the conventional RWA method (only zero, first and second Fourier harmonics are taken into account).

In Refs. [3, 4], there is no exact stability analysis of the constructed dynamical objects. In contrast to these references, we not only construct numerically exact discrete breathers, but also study their linear stability using the Floquet method. Moreover, we use a specific group-theoretical method for considerable simplification of the stability analysis. This method, based on the apparatus of irreducible representations of symmetry groups, was developed in [5]. It was adapted for studying stability of discrete breathers on square plane lattices in [6].

We have found a discrete breather with point symmetry group Oh in the above model of NaI crystal using the pair synchronization method [6] and steepest descent method in the space of all initial conditions. The time evolution of atom displacements from their equilibrium positions are shown in Figure 2. Light Na atoms are vibrating with greater amplitude than heavy I atoms. These amplitudes decrease from the center of the cluster at different rates for light and heavy atoms.

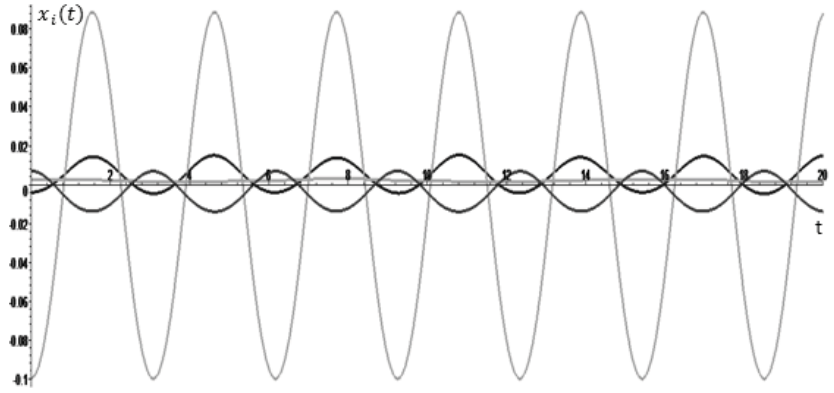

Figure 2. Discrete breather with symmetry point group Oh in NaI lattice

For studying linear stability of this discrete breather we apply the group-theoretical method developed in Ref. [5]. It allows us to decompose the variational system, which is obtained by linearization of original nonlinear equations in a vicinity of the breather, into independent subsystems. As a result, this 99-dimensional variational system is split into 9 subsystems of 1,2,4,5,6, and 10 dimensions. For each of these subsystems, we have applied the Floquet method for studying stability of their zero solutions. This method allows to detect the irreducible representation of the symmetry group Oh to which the generalized degrees of freedom responsible for the breather stability loss, corresponds.

Acknowledgments

The authors are grateful to Russian Foundation for Basic Research (grant No 12-02-31229), Russian Federal Grant Program (grant No P1467), and Southern Federal University (grant program 2013) for financial support.

References

[1] Aubry S. Breathers in nonlinear lattices: existence, linear stability and quantization, *Physica D*, Vol. 103, p. 201, 1997.

[2] Flach S. and Gorbach A. Discrete breathers: advances in theory and applications, *Phys. Rep*., Vol. 467, p. 1, 2007.

[3] Dmitriev S.V., Khadeeva L.Z., Pshenichnyuk A.I., Medvedev N.N. Gap discrete breathers in two-component 3D and 2D crystals with Morse interatomic potentials, *FTT*, Vol. 52, p. 1398, 2010.

[4] Kiselev A.A.and Sievers A.J. Generation of intrinsic vibrational gap modes in three-dimensional ionic crystals, *Phys. Rev. B*, Vol. 55, p. 5755, 1997.

[5] Chechin G.M.and Zhukov K.G. Stability analysis of dynamical regimes in nonlinear systems with discrete symmetries, *Phys. Rev. E*, Vol. 73, p. 036216, 2006.

[6] Bezuglova G.S., Chechin G.M., and Goncharov P.P. Discrete breathers on symmetry-determined invariant manifolds for scalar models on the plane square lattice, *Phys.Rev.E*, Vol.84, p.036606, 2011.

Proceedings of the 4th International Conference on Nonlinear Dynamics
ND-KhPI2013
June 19-22, 2013, Sevastopol, Ukraine

Studying of mobile discrete breathers in monoatomic chains

Chechin George[1], Lobzenko Ivan[1]

Abstract
At present, the problem of exact mobile breathers existence in Hamiltonian nonlinear lattices is not investigated thoroughly. We have found a mobile breather (MDB) in the Fermi-Pasta-Ulam-β chain numerically with high accuracy by means of a descent method. Detailed analysis of different MDB properties is presented. In particular, time evolution of displacement and velocity profiles of this dynamical object, as well as its partial energy in process of site-to-site motion are discussed.
Keywords
discrete breathers, mobile breathers, nonlinear excitations, monoatomic chains

[1] Southern Federal University, Rostov-on-Don, Russian Federation

Discrete breathers (DB) in nonlinear Hamiltonian lattices have captured the significant attention over last two decades. Stationary discrete breathers (SDB) in such systems have been investigated sufficiently well (see, e.g., [1, 2]). SDB is a spatially localized and time-periodic excitation. These dynamical objects were observed in many lattices of different physical nature [2].

In contrast to stationary DB, the mobile discrete breathers (MDB) are much less studied. Exact MDB represents a moving localized excitation which reproduces itself over a number of lattice sites (r) after a certain time interval (period) T:

$$x_i(0) = x_{i+r}(T), v_i(0) = v_{i+r}(T), i = 1..N.$$

Here $x_i(t)$, $v_i(t)$ are displacement and velocity of i^{th} particle of the chain.

Let us note that majority of papers, devoted to studying MDB, actually deal with *approximate* moving objects. Only a few papers discuss *exact* mobile discrete breathers. For example, exact MDB for the Fermi-Pasta-Ulam-β (FPU-β) chain with N=3, N=4 particles have been obtained in [3] and [4], respectively. Nevertheless, the problem of existence of exact MDB in nonlinear Hamiltonian chains with arbitrary N is far from the complete solution [5]. In particular, the role of the small 'tails' which always accompany MDB [6], is not yet understood.

In the present work, we discuss exact mobile discrete breathers existence in the FPU-β chain with N>4 particles. This chain is described by the following dynamical equations

$$\ddot{x}_i = f(x_{i+1} - x_i) - f(x_i - x_{i-1}), \quad i = 1..N, \quad f(\xi) = \xi + \beta\xi^3$$

Periodical boundary conditions are assumed:

$$x_0(t) \equiv x_N(t), x_{N+1}(t) \equiv x_1(t)$$

We apply certain variants of descent methods for constructing MDB, minimizing the following objective function

$$d(\xi, T) = \frac{1}{N}\sum_i (x_i(0) - x_{i+r}(T))^2 + \frac{1}{N}\sum_i (v_i(0) - v_{i+r}(T))^2$$

in the extended phase space of the system. Here, ξ = {xi(0), vi(0) | i=1..N} is the complete set of initial conditions for numerical integration of the dynamical equations. The function d(ξ,T) depends not only on ξ, but also on the unknown period T. The accuracy of MBD construction is determined by the minimal value of d(ξ,T). Exact mobile breather corresponds to the global minimum which must be equal to zero. It is known that the main difficulty of descent methods emerges from the trapping in local minima and, therefore, it needs an enough good initial conditions to reach the global minimum.

With high accuracy, we have obtained exact mobile breathers in FPU-β chains with N=5,7,9,11,13 and β=4 (see Table1). The exact MDB for N particles was used as the initial approximation for (N+2)-particle chain. The corresponding initial displacements and velocities for this breather (N=11) are depicted in Fig.1 and Fig.2, respectively.

It can be seen from Table1 that increasing of N leads to the profile of mobile discrete breather which tends to that corresponding to the case N=∞.

Table 1. Initial conditions corresponding to the numerically exact mobile breathers. The final value of the objective function $d(\xi,T) \sim 10^{-6}$.

	N=5	*N*=7	*N*=9	*N*=11
Displacements				0.001449474
			0.002556741	0.002954408
		-0.008441335	-0.008628172	-0.009417981
	0.048415026	0.077114204	0.077139962	0.07716158
	-0.355554263	-0.332520649	-0.332770085	-0.332794198
	0.470996927	0.479814409	0.480084191	0.48011942
	-0.27231175	-0.253657115	-0.254080245	-0.254284571
	0.019145236	0.050791384	0.052235036	0.050996252
		-0.005295503	-0.005686286	-0.006421704
			0.002741115	0.00257721
				0.000526935
Velocities				1.88E-09
			0.001872348	0.003034375
		-0.015358806	-0.017125342	-0.016170813
	0.082345648	0.080095961	0.081219722	0.081230856
	-0.266283498	-0.255813957	-0.255450654	-0.256018571
	0.267632162	0.254291813	0.2542605	0.254602348
	-0.063312622	-0.064366192	-0.065176544	-0.065242767
	-0.020380774	-0.003614211	-0.002912388	-0.002550606
		0.004781249	0.003210914	0.001759737
			0.000155807	-0.000641832
				-6.44E-05

$T = 13.411911$	$T = 13.518354$	$T = 13.511061$	$T=13.509968$

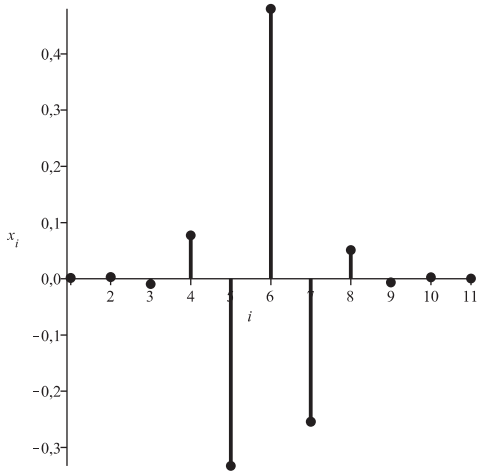

Figure 1. Initial displacements corresponding to the exact MDB in FPU-β chain. N=11

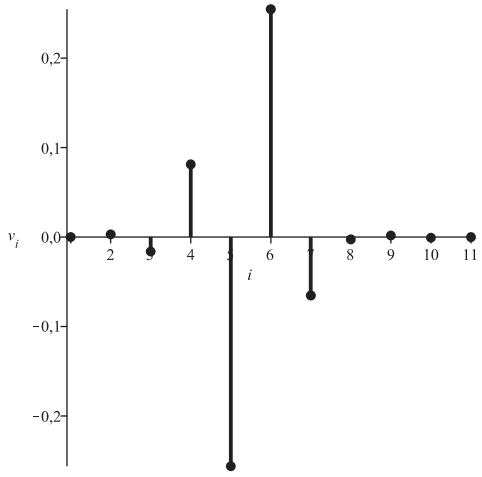

Figure 2. Initial velocities corresponding to the exact MDB in FPU-β chain. N=11

Acknowledgments

The authors are grateful to Russian Foundation for Basic Research (grant No 12-02-31229), Russian Federal Grant Program (grant No P1467), and Southern Federal University (grant program 2013) for financial support.

References

[1] Aubry S. Breathers in nonlinear lattices: existence, linear stability and quantization, *Physica D*, Vol. 103, p. 201, 1997.
[2] Flach S. and Willis C.R. Discrete Breathers, *Physics Reports* Vol. 295, p. 182-264, 1998.
[3] Bao-Feng Feng, Youn-Sha Chan, Intrinsic localized modes in a three particle Fermi-Pasta-Ulam lattice with on-site harmonic potential, *Mathematics and Computers in Simulations* Vol. 74 p. 292-301, 2007.
[4] Yusuke Doi, Kazuyuki Yoshimura, Translational Asymmetry Controlled Lattice and Numerical Method for Moving Discrete Breather in Four Particle System, *Journal of the Physical Society of Japan* Vol. 78, p. 034401 - 034410, 2009.
[5] Flach S. and Gorbach A., Discrete breathers: advances in theory and applications, *Phys. Rep*., Vol. 467, p. 1, 2007.
[6] Yusuke Doi, Kazuyuki Yoshimura, Moving discrete breathers in nonlinear lattice: Resonance and stability, *Wave Motion* Vol. 45, p. 83-99, 2007

Proceedings of the 4th International Conference on Nonlinear Dynamics
ND-KhPI2013
June 19-22, 2013, Sevastopol, Ukraine

Existence and Stability of Symmetry Determined Nonlinear Normal Modes in Electrical Chains

G.M. Chechin[1*], S.A. Shcherbinin[1]

Abstract
We consider an electrical chain of *N* nonlinear capacitors coupled by linear inductors assuming that voltage dependence of capacitors represents an even function. We prove that only *5* symmetry determined nonlinear normal modes (NNMs) can exist in the considered system. The stability of all these dynamical regimes for different *N* is studied with the aid of the group-theoretical method, which allows to simplify radically the variational systems appearing in the stability Floquet analysis. The scaling of the voltage stability threshold in the thermodynamic limit $N \to \infty$ is determined for each NNM.

Keywords
nonlinear dynamics, lattice models, nonlinear normal modes, invariant manifolds, group-theoretical methods

[1] Southern Federal University, Rostov-on-Don, Russia
* **Corresponding author:** gchechin@gmail.com

Introduction

In recent years, a studying of nonlinear vibrations in mesoscopic systems of various physical nature captured the attention (see, e.g., the review [1]). It is essential that in contrast to crystals, where only indirect experiments are possible, in mesoscopic systems one can often observe different dynamical objects directly.

In Ref [2], the existence and linear stability of so-called π-mode in one-dimensional nonlinear electrical lattice was studied. This system constructed on a silicon substrate by CMOS technology, represents a chain of nonlinear (voltage-dependent) capacitors coupled by linear inductors. This chain is shown schematically in Fig.1. Using periodic boundary conditions, one can imagine that the considered circuit represents a ring of *N* cells. For the case *N=4*, such ring is depicted in Fig.1b.

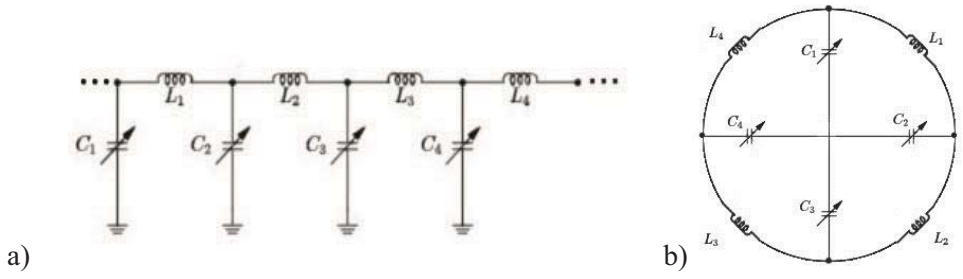

Figure 1. Chain of nonlinear capacitors coupled by linear inductors

The dependence *C(V)* of the capacity *C* on the voltage *V* can be rather complex, but the authors of Ref. [2] used the following simple form of the function *C(V)*:

$$C(V) = C_0(1 - bV^2), \tag{1}$$

where C_0 and b are positive constants.

Applying the Kirchhoff's law for quasi-stationary current to the circuit in Fig.1, one can obtain the following equations:

$$L_0 \frac{dI_j}{dt} = V_j - V_{j+1}, \qquad \frac{dQ(V_j)}{dt} = I_{j-1} - I_j, \qquad j = 1..N.$$

Here $Q(V_j) = Q(V_j(t))$ is a charge on j-th capacitor at instant t (the voltage on this capacitor is equal to $V_j(t)$), while $I_j = I_j(t)$ represents current through the inductor L_j.

Taking into account relations $I_j = \dot{Q}_j$ and $Q_j(t) = \int_0^{V_j} C(V)dV = C_0 V_j(1 - \frac{b}{3}V_j^2)$, one can reduce the above first-order two equations to the system of differential equations of the second order with respect to voltages $V_j(t)$:

$$\ddot{V}_j(1 - bV_j^2) - 2bV_j(\dot{V}_j)^2 = \gamma(V_{j-1} - 2V_j + V_{j+1}), \quad j = 1..N, \gamma = 1/(L_0 C_0) \tag{2}$$

The appropriate scaling of variables in Eq. (2) allows one to suppose $b=1$ and $\gamma = 1$. Taking into account periodic boundary conditions, we obtain the following dynamical model:

$$\ddot{V}_j(1 - V_j^2) - 2V_j(\dot{V}_j)^2 = (V_{j-1} - 2V_j + V_{j+1}), \; j = 1..N, \; V_0(t) \equiv V_N(t), \; V_{N+1}(t) \equiv V_1(t) \tag{3}$$

The so-called π-mode, which was investigated in [2], can be written in the form

$$\boldsymbol{\varphi_1} = \{V(t), -V(t)|V(t), -V(t)|V(t), -V(t)| \ldots\}$$

This means that voltages on every pair of neighboring capacitors are opposite in sign (such dynamical regime can exist only in chains with an even number of cells).

Stability of π-mode depends on the number of chain cells (N). Since this mode represents periodic regime, its stability can be investigated with the aid of the standard Floquet method. However, dimension of the variational system (the system of linearized equations in the vicinity of the considered dynamical regime) and corresponding monodromic matrix is equal to $2N$. Because of this reason, studying of the linear stability of π-mode can be very difficult in the case $N \gg 1$, especially when $N \to \infty$. A special method for studying this problem was developed in [2]. It allows one to decompose the variational Floquet system into independent scalar equations. However, this method is based essentially on the *specific structure* of the dynamical model of the electrical chain, and it seems to be rather difficult.

On the other hand, a general group-theoretical method for splitting variational system into subsystems, whose dimensions can be considerably smaller than that of the original variational system, was developed for dynamical models with discrete symmetry in our paper [3]. This method is based only on symmetry-related arguments and uses the apparatus of irreducible representations of the symmetry group of the model under consideration. In Refs. [4,5], we used this method for analyzing stability of all possible symmetry-determined Rosenberg nonlinear normal modes in FPU-α and FPU-β chains, while in Ref. [6], it was applied for studying stability of discrete breathers and quasi-breathers in 2D scalar dynamical models on the plane square lattices.

Below, we use this group-theoretical method for analyzing stability of the symmetry-determined nonlinear normal modes in the electrical model (3).

1. Symmetry-Determined Nonlinear Normal Modes

The concept of nonlinear normal modes was developed by Rosenberg in [7] (more information on these dynamical objects can be found in [8]). In the dynamical regime corresponding to a given NNM, vibrations of all dynamical variables are described by one and the same time-dependent function $f(t)$. For the case of the electrical model (3), this means that all voltages $V_j(t)$ satisfy the relation:

$$V_j(t) = c_j f(t), j = 1..N,$$

where c_j are constant coefficients.

Rosenberg nonlinear normal modes can exist only in some very specific classes of systems, in particular, in systems whose potential energy is a homogeneous function of all its arguments. However, existence of NNMs in systems with general interactions can be ensured by the presence of some group of discrete symmetry [4, 5, 9, 10]. Hereafter, we call such modes symmetry-determined nonlinear normal modes, or simply NNMs.

There exists only a small number of symmetry determined NNMs in any lattice model. We discussed the cause of such situation in [5]. The matter is that the attempt of construction NNM with large cell in vibrational state leads to appearance of quasiperiodic dynamical regimes which represent *bushes* of NNMs [11-13] (see also the review [14]).

We have found that only five types of symmetry-determined NNMs can exist in the considered electrical chains (this result does not depend on the specific structure of Eqs. (3) – it is a consequence only of the symmetry group of the lattice model):

$$\boldsymbol{\varphi_1} = V(t)\{1,-1|1,-1|1,-1|\dots|1,-1\} \ (\pi\text{-mode}) \tag{4}$$
$$\boldsymbol{\varphi}_2 = \mathrm{V(t)}\{1,1,-1,-1|1,1,-1,-1|\dots\} \tag{5}$$
$$\boldsymbol{\varphi}_3 = \mathrm{V(t)}\{1,0,-1,0|1,0,-1,0|\dots\} \tag{6}$$
$$\boldsymbol{\varphi}_4 = \mathrm{V(t)}\{1,0,-1|1,0,-1|1,0,-1|\dots\} \tag{7}$$
$$\boldsymbol{\varphi}_5 = \mathrm{V(t)}\{-1,0,1,1,0,-1|-1,0,1,1,0,-1|\dots\} \tag{8}$$

Substituting Eqs. (4)-(8) into dynamical equations (3), we obtain only one independent equation with respect to the variable V(t):

$$\ddot{V}(t)[1-V^2(t)] - 2V(t)[\dot{V}(t)]^2 + \mu V(t) = 0, \tag{9}$$

where the following values of the parameter μ correspond to the above NNMs:

$\boldsymbol{\varphi}_1{:}\,\mu = 4,\ \boldsymbol{\varphi}_2{:}\,\mu = 2,\ \boldsymbol{\varphi}_3{:}\,\mu = 2,\ \boldsymbol{\varphi}_4{:}\,\mu = 3,\ \boldsymbol{\varphi}_5{:}\,\mu = 1.$

2. Stability of Nonlinear Normal Modes

The stability of a given NNM can be studied with the aid of the Floquet method. Using this method, we linearize the original system of nonlinear differential equations near this NNM obtaining a variational system. This is the system of *N* second-order differential equations with time-periodic coefficients, whose period *T* is equal to that of the given NNM. Then we reduce this system to the system *F* of *2N* first-order differential equations and construct for it the *monodromic* matrix. The successive *columns* of this matrix can be obtained by integrating *2N* times the system *F* over period *T* using the columns of $2N \times 2N$ identical matrix as the corresponding initial conditions.

The above-mentioned Floquet procedure is very difficult for the case $N \gg 1$. We used a general group-theoretical method [3] for splitting variational systems into subsystems of considerably smaller dimensions than those of the original variational systems. The method is based only on symmetry-related arguments and uses the apparatus of irreducible representations of the symmetry group of the studying dynamical regime. We show that for NNMs (4)-(8) the corresponding variational systems can be split into independent subsystems whose dimensions are equal to 1, 2, 2, 3, 3, respectively.

All these subsystems we write in the matrix form:

$$\hat{A}\ddot{\boldsymbol{\delta}} + \hat{B}\dot{\boldsymbol{\delta}} = \hat{\mathrm{D}}\boldsymbol{\delta}, \tag{10}$$

where matrices $\hat{A}, \hat{B}, \hat{C}$ are constructed from the following elements:

$$c(t) = 1 - V^2$$
$$f(t) = 2(\dot{V}^2 + V\ddot{V} - 1)$$
$$g(t) = -4V\dot{V}$$

Here $V = V(t)$ is the solution of "governing" equation (9) for the corresponding nonlinear normal mode. Below we list the explicit matrix form (10) for each of NNMs (4)-(8).

1) $\boldsymbol{\varphi}_1 = V(t)\{1,-1|1,-1|1,-1|\dots\}$.

All subsystems (10) for this case are one-dimensional with the following 1×1 matrices:

$$\hat{A} = c(t), \hat{B} = g(t), \hat{D} = f(t) - 2\cos \mathrm{k}, \tag{11}$$

where $k = \frac{2\pi}{N} j, \;\; j = 1..N$.

For NNMs $\boldsymbol{\varphi}_2$ and $\boldsymbol{\varphi}_3$, subsystems (10) are two-dimensional:

2) $\boldsymbol{\varphi}_2 = \mathrm{V(t)}\{1,1,-1,-1|1,1,-1,-1|\ldots\}$

$$\hat{\mathrm{A}} = \begin{pmatrix} c & 0 \\ 0 & c \end{pmatrix}; \hat{\mathrm{B}} = \begin{pmatrix} g & 0 \\ 0 & g \end{pmatrix}; \hat{\mathrm{D}} = \begin{pmatrix} f & 1+\gamma \\ 1+\bar{\gamma} & f \end{pmatrix} \tag{12}$$

3) $\boldsymbol{\varphi}_3 = \mathrm{V(t)}\{1,0,-1,0|1,0,-1,0|\ldots\}$

$$\hat{\mathrm{A}} = \begin{pmatrix} c & 0 \\ 0 & 1 \end{pmatrix}; \hat{\mathrm{B}} = \begin{pmatrix} g & 0 \\ 0 & 0 \end{pmatrix}; \hat{\mathrm{D}} = \begin{pmatrix} f & 1+\gamma \\ 1+\bar{\gamma} & -2 \end{pmatrix} \tag{13}$$

In Eqs. (12)-(13) $\gamma = e^{\frac{4\pi}{N} j}, \;\; j = 1..\frac{N}{2}$.

4) For both NNMs $\boldsymbol{\varphi}_4 = \mathrm{V(t)}\{1,0,-1|1,0,-1|1,0,-1|\ldots\}$ and $\boldsymbol{\varphi}_5 = \mathrm{V(t)}\{-1,0,1,1,0,-1|-1,0,1,1,0,-1|\ldots\}$ the three-dimensional subsystems (10) turn out to be *identical* with the following matrices:

$$\hat{A} = \begin{pmatrix} c & 0 & 0 \\ 0 & 1 & 0 \\ 0 & 0 & c \end{pmatrix}; \hat{B} = \begin{pmatrix} g & 0 & 0 \\ 0 & 0 & 0 \\ 0 & 0 & g \end{pmatrix}; \hat{\mathrm{C}} = \begin{pmatrix} f & 1 & \gamma \\ 1 & -2 & 1 \\ \bar{\gamma} & 1 & f \end{pmatrix} \tag{14}$$

where $\gamma = e^{\frac{6\pi i}{N} j}, j = 1..\frac{N}{3}$.

Thus, stability of NNMs in the electrical chain (3) can be investigated by analyzing a set of one-, two- and three-dimensional systems of differential equations with time-periodic coefficients determined by the function *V(t)*.

Zero solutions of the systems (11)-(14) are stable for sufficiently small amplitudes *A* of the time-periodic function *V(t)*, entering coefficients of these systems, that implies the stability of NNMs (4)-(8). Increasing of this amplitudes leads to appearing of parametric resonance in systems (11)-(14) and, as a result, to modulation instability of the corresponding NNM beyond a critical amplitude $A_c(N)$.

In Fig.2, for every nonlinear normal mode we depict $A_c(N)$ as a function of the number (*N*) of chain cells. As can be seen from this figure, the critical amplitudes $A_c(N)$ represent decreasing functions which tend to zero when $N \to \infty$. It is interesting to note that the stability plots for the modes $\boldsymbol{\varphi}_4$ and $\boldsymbol{\varphi}_5$ turn out to be *identical*, despite the different functions *V(t)*, determining the coefficients *c(t), g(t), f(t),* correspond to these modes ($\mu = 3$ for the mode $\boldsymbol{\varphi}_4$ and $\mu = 1$ for the mode $\boldsymbol{\varphi}_5$).

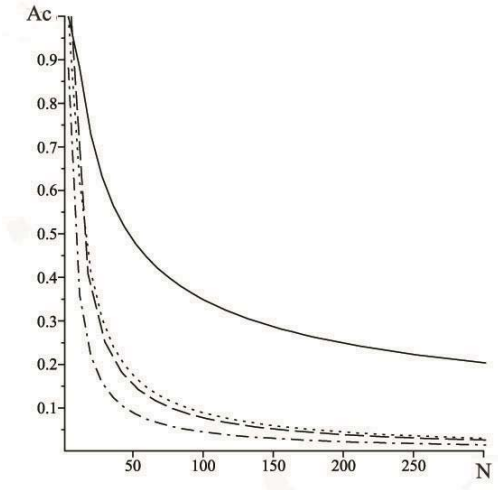

Figure 2. Stability of nonlinear normal modes (4)-(8) for electrical chains with different N. Solid line corresponds to the mode $\boldsymbol{\varphi}_2$ (5), dashed line – to the mode $\boldsymbol{\varphi}_3$ (6), dot-dashed line – to the π-mode $\boldsymbol{\varphi}_1$ (4), dotted line – to the modes $\boldsymbol{\varphi}_4$ (7) and $\boldsymbol{\varphi}_5$ (8).

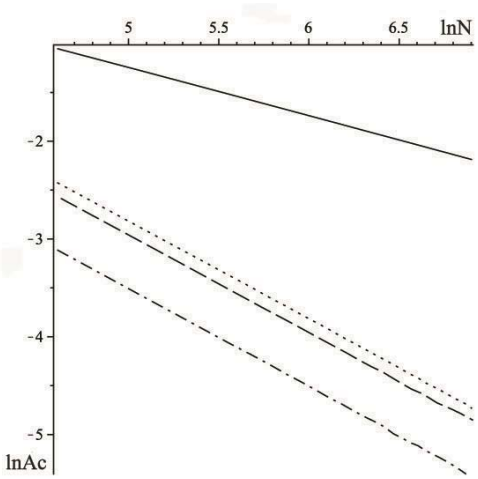

Figure 3. Plots of $A_c(N)$ for nonlinear normal modes (4)-(8) in logarithmic scale. Solid line corresponds to the mode $\boldsymbol{\varphi}_2$ (5), dashed line – to the mode $\boldsymbol{\varphi}_3$ (6), dot-dashed line – to the π-mode $\boldsymbol{\varphi}_1$ (4), dotted line – to the modes $\boldsymbol{\varphi}_4$ (7) and $\boldsymbol{\varphi}_5$ (8).

The functions $A_c(N)$ have been obtained with the aid of the Floquet method applied to the systems (11)-(14) for all possible mode numbers j. For $N \gg 1$, the function $A_c(N)$ for the modes $\boldsymbol{\varphi}_1$ and $\boldsymbol{\varphi}_2$ can be also found in an analytical form. Indeed, in this case one can transform Eqs. (10)-(11) to the Mathieu equation, for which stability properties are well-known, while the two-dimensional system (10),(12) may be decomposed into independent Mathieu equations [actually, this is a consequence of commutation of matrices (12) that allows one to diagonalize them simultaneously]. The corresponding results read:

$$\boldsymbol{\varphi}_1\colon A_c = \frac{2}{\sqrt{3}} tg\left(\frac{\pi}{N} j\right), j = 1..N$$

$$\boldsymbol{\varphi}_2\colon A_c = \sqrt{\frac{4}{3}\frac{\sin\left(\frac{2\pi}{N} j\right)}{1-\sin\left(\frac{2\pi}{N} j\right)}}, j = 1..\frac{N}{2}$$

From these formulae, one can deduce the asymptotic laws for $A_c(N)$ when $N \to \infty$: $A_c(N) \sim N^{-1}$ for the mode $\boldsymbol{\varphi}_1$ and $A_c(N) \sim N^{-0.5}$ for the mode $\boldsymbol{\varphi}_2$.

The similar asymptotic formulas for other NNMs (6)-(8) can be obtained numerically. Indeed, in Fig.3, we present functions $A_c(N)$ in logarithmic scale for large value *N (N>100)*. From this figure, it is obvious that for all NNMs $A_c(N)$ are *power functions* since the dependence of $\ln A_c(N)$ on $\ln N$ represents straight lines. The coefficient β in the formula $A_c(N) = CN^{\beta}$ is determined by inclination of the corresponding straight line to the horizontal axis.

For NNMs (4)-(8) we have obtained the following values of the constants β and *C* entering the law $A_c(N) = CN^{\beta}$:

$\boldsymbol{\varphi}_1$[Eq. (4)]: β_1=0.99, $C_1 = 3.62$.
$\boldsymbol{\varphi}_2$[Eq. (5)]: β_2=0.49, C_2=2.89.
$\boldsymbol{\varphi}_3$[Eq. (6)]: β_3=0.99, C_3=8.57.
$\boldsymbol{\varphi}_4$ and $\boldsymbol{\varphi}_5$[Eqs. (7) and (8)]: β_4=0.99, C_4=7.54. (15)

Relying on the above data, we can assert that for all NNMs, except the mode $\boldsymbol{\varphi}_2$, the constant β determining the rate of decreasing of critical amplitude A_c,with increasing *N*, is equal to unity (β=1), while for $\boldsymbol{\varphi}_2$ it is equal to 0.5. Note that we have obtained the values of the parameter β for modes $\boldsymbol{\varphi}_1$ and $\boldsymbol{\varphi}_2$ analytically, as well as numerically, while for NNMs $\boldsymbol{\varphi}_3$, $\boldsymbol{\varphi}_4$, $\boldsymbol{\varphi}_5$ this parameter was found only numerically. We conjecture that it can be obtained also analytically by the specific asymptotic method developed in [15]. However, this was not done in the present paper, because numerical results (15) seem to be sufficient for hypothesis that the parameter β for NNMs $\boldsymbol{\varphi}_3$, $\boldsymbol{\varphi}_4$ and $\boldsymbol{\varphi}_5$ is equal to unity.

Conclusions

In the present paper, we study periodic vibrations in the chain of nonlinear capacitors coupled by linear inductors, assuming that voltage-dependence of capacitors is described by the function $C(V) = C_0(1 - bV^2)$, as was done in Ref. [2]. These dynamical regimes represent symmetry-determined nonlinear normal modes and we prove that only five types of such modes can exist in the considered electrical chain.

We have studied the stability properties of all these NNMs. For this purpose, we use group-theoretical method that allows one to decompose corresponding variational systems into a number of independent subsystems of considerably less dimensions. This method can be applied not only for periodic dynamical regimes, but also for other regimes. In particular, this is true for bushes of nonlinear normal modes representing quasiperiodic vibrations [11-13].

We also found the asymptotic law of the critical amplitudes $A_c(N)$ beyond which NNMs loose their stability.

Acknowledgments

The authors are grateful to Russian Foundation for Basic Research (grant No 12-02-31507) and to Southern Federal University (grant program 2013) for financial support.

References

[1] Flach S., Gorbach A. Discrete breathers: advances in theory and applications. *Physics Reports,* Vol. 467, p. 1, 2008.
[2] Bhat H. S., Osting B. The zone boundary mode in periodic nonlinear electrical lattices. *Physica D,* Vol. 238. p. 1228, 2009.
[3] Chechin G.M., Zhukov K.G. Stability analysis of dynamical regimes in nonlinear systems with discrete symmetries. *Phys. Rev. E,* Vol. 73, p. 36216, 2006.
[4] Chechin G.M., Novikova N.V., Abramenko A.A. Bushes of vibrational modes for Fermi-Pasta-Ulam chains.*Physica D,* Vol. 166, p. 208, 2002.
[5] Chechin G.M., Ryabov D.S., Zhukov K.G. Stability of low dimensional bushes of vibrational modes in the Fermi-Pasta-Ulam chains. *Physica D,* Vol. 203, p.121, 2005.
[6] Bezuglova G.S., Chechin G.M., Goncharov P.P. Discrete breathers on symmetry-determined invariant manifolds for scalar models on the plane square lattice. *Physical Review E,* Vol. 84, p. 036606, 2011.
[7] Rosenberg R.M. The normal modes of nonlinear n-degree-of-freedom systems. *J. Appl. Mech.,* Vol. 29, p. 7, 1962.
[8] Vakakis A.F., Manevich L.I., Mikhlin Yu.V., Pilipchuk V.N., Zevin A.A. *Normal Modes and Localization in Nonlinear Systems,* Wiley, New York.,1996.
[9] Rink B. Symmetric invariant manifolds in the Fermi-Pasta-Ulam lattice, *Physica D,* Vol. 175, p. 31, 2003.
[10] Chechin G.M., Sakhnenko V.P., Stokes H.T., Smith A.D., Hatch D.M. Non-linear normal modes for systems with discrete symmetry. *Int. J. Non-Linear Mech*., Vol. 35, p. 497, 2000.
[11] Sakhnenko V.P., Chechin G.M. *Dokl. Akad. Nauk,* Vol. 330, p. 308, 1993.
V.P. Sakhnenko, G.M. Chechin.. Symmetry-related selection rules in nonlinear dynamics of autonomous systems. *Phys. Dokl*., Vol. 38, p. 219, 1993.
[12] V.P. Sakhnenko, G.M. Chechin. *Dokl. Akad. Nauk,* Vol. 338, p. 42, 1994.
V.P. Sakhnenko, G.M. Chechin. Bushes of modes and normal vibrations in nonlinear dynamical systems with discrete symmetry. *Phys. Dokl*., Vol. 39, p. 625, 1994.
[13] Chechin G.M., Sakhnenko V.P. Interaction between normal modes in nonlinear dynamical systems with discrete symmetry. Exact results. *Physica D,* Vol. 117, p. 43, 1998.
[14] Bountis T., Chechin C.M., Sakhnenko V.P. Discrete Symmetries and Stability in Hamiltonian Dynamics. *Int. J. of Bifurc. Chaos,* Vol. 21, p. 1539, 2011.
[15] Chechin G.M., Ryabov D.S. Stability of nonlinear normal modes in the FPU-β chain in the thermodynamic limit. *Physical Review E,* Vol. 85, p. 056601, 2012.

Proceedings of the 4th International Conference on Nonlinear Dynamics
ND-KhPI2013
June 19-22, 2013, Sevastopol, Ukraine

Exact Solutions for Discrete Breathers in a Forced – Damped Chain

O.V.Gendelman[1*]

Abstract
Exact solutions for symmetric on-site discrete breathers (DBs) are obtained in a forced–damped linear chain with on-site vibro-impact constraints. The damping in the system is caused by inelastic impacts; the forcing functions should satisfy conditions of periodicity and antisymmetry. Global conditions for existence and stability of the DBs are established by combination of analytic and numeric methods. The DB can lose its stability either by pitchfork, or through Neimark – Sacker bifurcations. The pitchfork bifurcation is related to internal dynamics of each individual oscillator. It is revealed that the coupling can suppress this type of instability. To the contrary, the Neimark – Sacker bifurcation occurs for relatively large values of the coupling, presumably due to closeness of the excitation frequency to a boundary of propagation zone of the chain. Both bifurcation mechanisms seem to be generic for the considered type of forced–damped lattices. Some unusual phenomena, like non-monotonous dependence of the stability boundary on the forcing amplitude, are revealed analytically for the initial system and illustrated numerically for small periodic lattices.

Keywords
Discrete breathers, vibro-impact chains

[1] Faculty of Mechanical Engineering, Technion, Haifa, Israel
* **Corresponding author:** ovgend@tx.technion.ac.il

Introduction

Discrete breathers (DBs) or intrinsic localized modes (ILMs) are well–known in many nonlinear lattices [1,2]. Generally, they are exponentially localized (if a coupling between the neighbors in the lattice has a linear component) and can demonstrate remarkable stability also in two – and three – dimensional lattices [2]. Numerous systems which exhibit the DBs include chains of mechanical oscillators [3], superconducting Josephson junctions [4], nonlinear magnetic metamaterials [5], electrical lattices [6], michromechanical cantilever arrays [7], antiferromagnets [8] and many other physical systems [9].

In the majority of theoretical studies related to the DBs, Hamiltonian models are considered. Still, in many applications the damping cannot be neglected; in order to maintain the DB, one should compensate it by some kind of direct or parametric external forcing [2]. Experimentally, many of the DBs observed in the experiments were in fact created and maintained in the presence of damping and under homogeneous forcing from the external sources.

It is more or less easy to "explain" the nonlinear localization in a chain of forced-damped oscillators on a qualitative level. It is well–known that single forced–damped nonlinear oscillator can exhibit stable steady–state responses with different amplitudes, depending on initial conditions [10]. If one or more oscillators in the lattice are excited at high amplitude, all the others – at low amplitude, and coupling between the oscillators is weak enough to preserve this structure, one obtains an example of strongly localized excitation in conditions of a homogeneous forcing. However, quantitative description of such breathers remains a major challenge. Lack of Hamiltonian structure changes the properties of the DBs. Instead of continuous family of localized solutions, one expects to obtain a discrete set of attractors. Consequently, many of the methods devised for computation and analysis of the Hamiltonian DBs are not applicable in forced-damped systems. Even more important, the DBs in the forced/damped systems can have some qualitative properties absent in their

Hamiltonian counterparts. For instance, one can observe stable moving DBs in forced/damped systems [11]. In Hamiltonian lattices, the existence of such moving stable DBs is generally denied [2], with known exception of the integrable Ablowitz – Ladik model [12]. Also, there exist some special non-integrable Hamiltonian discrete models where the DBs can be computed exactly [13]. To the best of the author's knowledge, no such exact solutions are known in forced-damped discrete lattices. Even in continuous nonlinear models with forcing and damping, some exact solutions for the breathers were obtained only for a handful of special cases [14]. This paper is devoted exactly to this problem and suggests a model, which allows one to derive exact solutions for the forced – damped DBs and to study some of their properties.

We are going to demonstrate that the exact solutions can be derived for the DBs in a vibro-impact (VI) chain. Dynamical systems involving impacts have an important peculiarity – they exhibit extreme (actually, the strongest possible) nonlinearity, but the latter reveals itself only at the moments of impacts; between the impacts the system obeys linear equations of motion, if other sources of nonlinearity are absent. Consequently, the VI models can offer relatively simple description of complicated nonlinear phenomena. Celebrated examples of this sort are problems of bouncing ball [15] and kicked rotor [16], but many other tractable VI models are known and used for description of realistic physical systems, such as Bose – Einstein condensates [17]. One of the few exact solutions for DBs in Hamiltonian systems also uses the VI model [18]; in the current paper, we extend this result for the forced-damped case.

1. Description of the model and analytic solution

The model used here is a homogeneous chain with linear nearest – neighbor interactions; in addition, each particle can move only between inelastic impacts constraints. Such model is topologically equivalent to smooth models with linear interaction and on-site potential, widely used in investigations devoted to the DBs [7]. Sketch of the model system is presented in Fig. 1.

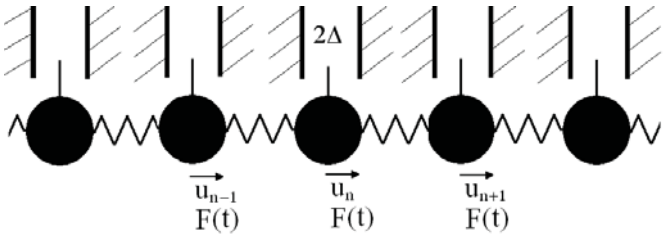

Figure 1. Sketch of the model system.

Each particle is subject to the same external forcing. The forcing function is considered to be 2π-periodic and antisymmetric, as specified below in the equations of motion. Between the impacts, displacement u_n of the n^{th} particle is described as:

$$\ddot{u}_n + \gamma(2u_n - u_{n-1} - u_{n+1}) = F(t), \;\; F(t) = F(t+2\pi), \; F(t+\pi) = -F(t) \tag{1}$$

Without affecting the generality, the clearance Δ and the particle mass are set to unity and the only parameter which characterizes the chain is a coupling coefficient γ. Equations (1) are valid between successive impacts. If the particle with number n impacts the constraint at time instance $t_{i,n}$, the following conditions are satisfied:

$$t = t_{i,n}; \; u_n(t_{i,n}) = \pm 1; \; \dot{u}_n(t_{i,n} + 0) = -k\dot{u}_n(t_{i,n} - 0), \; 0 \le k \le 1 \tag{2}$$

Here k is a restitution coefficient. Notation ± 0 is used to denote the particle's velocities immediately after (+) and before (-) the impact. Values of $k<1$ correspond to inelastic impacts; it is the only source of damping in the model. The model is not solvable in a general form. Therefore, we are going to look for partial solutions for the DBs. In this paper, the simplest on–site symmetric DB is considered. Our motivation for this choice is that namely the DBs of this type are the most explored

ones, both experimentally and numerically. Hence, we adopt that responses of all particles are periodic and symmetric, and only particle with *n=0* impacts each of its constraints symmetrically with period 2π:

$$u_n(t) = u_n(t + 2\pi m) = -u_n(t + \pi(2m+1));\ t_{i,0} = \varphi + \pi m.$$
$$u_0(\varphi) = 1, \dot{u}_0(\varphi + 0) = -k\dot{u}_0(\varphi - 0);\ u_0(\varphi + \pi) = -1, \dot{u}_0(\varphi + \pi + 0) = -k\dot{u}_0(\varphi - 0). \tag{3}$$

Here φ is a "phase lag" of the impacts with respect to the external forcing. Effect of each impact is equivalent to transfer of certain amount of momentum to the impacting particle. For further analysis, the variables are changed as follows:

$$u_n = v_n + f(t), \ddot{f}(t) = F(t). \tag{4}$$

Due to the antisymmetry of *F(t),* it is always possible to find a unique function *f(t)* satisfying Eq. (5) and the antisymmetry condition.

Then, the exact solution for the symmetric one – site DB is expressed as:

$$u_n(t) = f(t) + \frac{4p}{\pi}\left(\frac{-1}{2\gamma}\right)^{|n|} \sum_{l=0}^{\infty} \frac{\left((2l+1)^2 - 2\gamma - \sqrt{(2l+1)^4 - 4\gamma(2l+1)^2}\right)^{|n|} \cos((2l+1)(t-\varphi))}{\sqrt{(2l+1)^4 - 4\gamma(2l+1)^2}}.$$
$$v_0(\varphi) = p\chi(\gamma),\ \chi(\gamma) = \frac{4}{\pi}\sum_{l=0}^{\infty} \frac{1}{\sqrt{(2l+1)^4 - 4\gamma(2l+1)^2}}. \tag{5}$$
$$p\chi(\gamma) + f(\varphi) = 1,\ \dot{f}(\varphi) = p\frac{1-k}{1+k}.$$

Parameters p and φ can be determined from Eq. (5) for each specific choice of *F(t).*

In order to study the DB described by solution (5) in more depth, the case of a simple harmonic forcing is considered. In this case, one can solve Eqs. (5) explicitly:

$$F(t) = -a\cos t \Rightarrow f(t) = a\cos t;\ -a\cos\varphi = p\chi(\gamma) - 1,\ -a\sin\varphi = pq,\ q = \frac{1-k}{1+k},$$
$$p = \frac{\chi(\gamma) \pm \sqrt{\chi^2(\gamma)a^2 - q^2(1-a^2)}}{\chi^2(\gamma) + q^2},\ \varphi = -\arcsin\frac{pq}{a}. \tag{6}$$

Here a is the amplitude of the harmonic forcing. A stable response corresponds to a positive sign in expression (13) for p. It is possible to determine the zone of existence of the DB in the space of parameters. This zone is illustrated in Fig. 2, together with the stability thresholds for the DBs.

2. Stability analysis

The DB solution (5) is 2π-periodic by construction, and thus its stability may be established by analysis of eigenvalues of a monodromy matrix computed on a single time period [19]. Such matrix cannot be computed for an infinite chain; therefore, it is commonly accepted to compute it for a finite chain and to check whether the stability properties depend on the number of particles [11]. In this paper we adopt the same approach and consider the system with N particles and periodic boundary conditions. For systems with smooth nonlinearity, such monodromy matrices are usually computed numerically, by solving complete set of N ODEs for $2N$ independent sets of initial conditions [11, 20]. However, for the vibro-impact chain considered here, in addition to availability of exact solutions, it allows computing the monodromy matrix in a much simpler manner. A state vector of the system is defined as:

$$\mathbf{V} = \begin{bmatrix} u_0 \\ \vdots \\ u_{N-1} \\ w_0 \\ \vdots \\ w_{N-1} \end{bmatrix}. \tag{7}$$

We adopt $w_k = \dot{u}_k$, $k = 0,...,N$. The periodic boundary conditions are imposed as:

$$u_0 = u_N, w_0 = w_N. \tag{8}$$

In the exact solution the impacts occur only at the site $n = 0$ in time instances $t = \varphi, \varphi + \pi$. Consequently, between impacts, the time evolution of the state vector is described by linear equation. With account of (1) and (16), this equation is written as:

$$\dot{\mathbf{V}} = \mathbf{AV} + \mathbf{F}, \mathbf{A} = \begin{pmatrix} 0_{N\times N} & I_{N\times N} \\ \gamma L_{N\times N} & 0_{N\times N} \end{pmatrix}, \mathbf{F} = F(t)\begin{bmatrix} \mathbf{0}_{N\times 1} \\ \mathbf{I}_{N\times 1} \end{bmatrix}$$
$$\varphi < t < \phi + \pi,\ \varphi + \pi < t < \phi + 2\pi. \tag{9}$$

Here

$$\mathbf{L}_{N\times N} = \begin{pmatrix} -2 & 1 & 0 & \cdots & 0 & 1 \\ 1 & -2 & 1 & \ddots & \cdots & 0 \\ 0 & 1 & \ddots & \ddots & 0 & \vdots \\ \vdots & 0 & \ddots & \ddots & 1 & 0 \\ 0 & \vdots & \ddots & 1 & -2 & 1 \\ 1 & 0 & \cdots & 0 & 1 & -2 \end{pmatrix}$$

is the discrete Laplacian adjacency matrix accounting for the linear coupling.

Due to linearity of Eq. (9), evolution of small perturbations of the state vector **V** between the impacts is described by the exponent of matrix **A**. At the moments of impact, the evolution of small perturbations of the state vector is described by so-called "saltation matrix" [21], which takes into account both the perturbation of the state vector at the point of discontinuity and the infinitesimal variation of the impact time instance. For the system under consideration, this matrix at time instance $t = \varphi$ in the lowest-order (linearized) approximation [21] may be written as:

$$\mathbf{S} = \begin{pmatrix} -k & 0 & \cdots & 0 & & & & \\ 0 & 1 & \ddots & \vdots & & & & \\ \vdots & \ddots & \ddots & 0 & & 0_{N\times N} & & \\ 0 & \cdots & 0 & 1 & & & & \\ \dfrac{\omega(1+k)}{w_0(\varphi - 0)} & 0 & \cdots & 0 & -k & 0 & \cdots & 0 \\ 0 & 0 & \ddots & \vdots & 0 & 1 & \ddots & \vdots \\ \vdots & \ddots & \ddots & \vdots & \vdots & \ddots & \ddots & 0 \\ 0 & \cdots & \cdots & 0 & 0 & \cdots & 0 & 1 \end{pmatrix}$$

where $\omega = \ddot{u}_0(\varphi - 0)$. Complete monodromy matrix at the period is thus expressed as:

$$\mathbf{M} = (\mathbf{QS})^2, \mathbf{Q} = \exp(\pi \mathbf{A}). \tag{10}$$

Values of velocity and acceleration of the impacting particle in the moment of impact are taken from the exact solution (5). Expression (10) still requires the numeric computation of the exponent matrix and the multiplication of the matrices, but all of these tasks are much easier from a computational viewpoint than the solution of N second – order ODEs with $2N$ independent sets of the initial conditions.

The loss of stability has been recorded numerically in the space of parameters, when the eigenvalue of the monodromy matrix (or couple of the complex conjugate eigenvalues) with the largest absolute value crossed a threshold of 1.005. For all explored examples, it was found that for $N \geq 400$ the critical parameter values do not depend on N within a relative margin of about 0.1%. Thus, it is possible to suggest that these results on stability of the DBs are also relevant for the infinite chain.

Two generic scenarios of the loss of stability were revealed. The first one corresponds to the transition of two complex conjugate eigenvalues through the unit circle and is related to the Neimark – Sacker bifurcation. The other scenario corresponds to the passage of a single eigenvalue through unity. This scenario corresponds to a pitchfork bifurcation; the latter results in appearance of a pair of stable asymmetric DBs.

Examples for zones of existence and stability for the DBs are presented in Fig. 2.

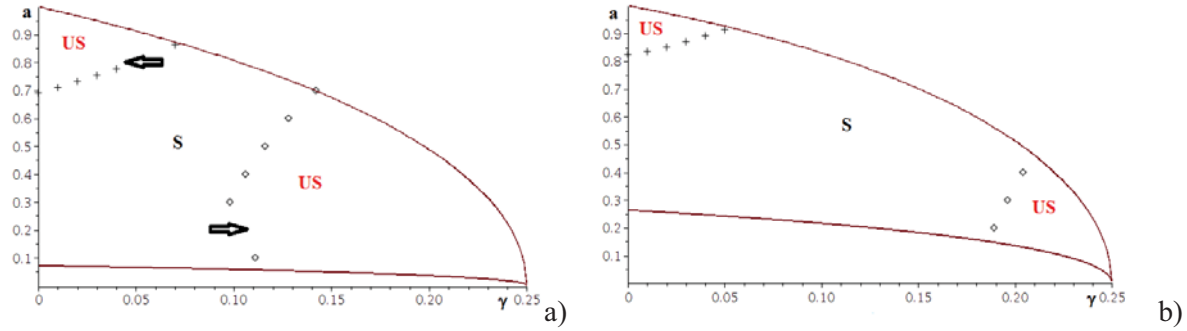

Figure 2. Zones of existence and stability for the symmetric DB on the (γ, a) parameter plane for two different values of the restitution coefficient, a) k=0.8; b) k=0.4. Crosses denote the pitchfork bifurcation line and diamonds denote the line of Neimark – Sacker bifurcation.

One can see that for lower values of the restitution coefficient, the DB exists for a narrower range of amplitudes of the external forcing, but it is stable in a wider range of the coupling coefficients. The pitchfork bifurcation in the upper left corner is similar to the loss of symmetry observed in single vibro–impact oscillator [22]; naturally, this case is equivalent to zero coupling. A similar pitchfork bifurcation, related to a "loss of symmetry", is also known in the regular forced–damped Duffing oscillator [10]. Thus, this scenario of the loss of stability is caused by internal dynamics of each individual oscillator. Our computations reveal interesting and, it seems, previously unknown fact: the coupling between the oscillators can suppress this scenario of the loss of stability and stabilize the symmetric DBs.

It is also possible to conjecture that the Neimark–Sacker bifurcation in the lower right corner is related to four–wave interaction with the boundary of the propagation zone [7]. One can also see that the size of interval of existence of the DBs shrinks and approaches zero as the frequency approaches the boundary of the propagation zone. This observation also correlates with numeric and experimental findings presented in Ref. [7], where the amplitude of the DB was seen to decrease as the forcing frequency gets closer to an optical band. These results allow us to conjecture that both bifurcation mechanisms described above are generic for forced lattices with nonlinear on-site potentials, and not only relevant for the VI chain studied here.

Conclusions

As it was demonstrated above, the vibro-impact model allows derivation of exact analytic solutions for discrete breathers in forced – damped essentially nonlinear chain, without any simplifications or approximations. The zone of existence and stability of the DB solution in the space of parameters has been computed. Two mechanisms of the loss of stability (pitchfork and Neimark–Sacker bifurcations) were revealed. Existence of the asymmetric and quasiperiodic DBs was predicted

analytically and verified numerically. It is interesting to mention that the increase of the coupling can both stabilize and destabilize the symmetric DB in different zones on the plane of parameters and for different bifurcation mechanisms.

References

[1]. Ovchinnikov A.A. *Zh. Exp. Theor. Phys*., **57**, 263, 1969; Flach S., Willis C.R., *Phys. Rep*., **295**, 182, 1998; Aubry S. *Physica D*, **216**, 1, 2006; MacKay R.S., Aubry S. *Nonlinearity*, **7**, 1623, 1994.

[2]. Flach S. ,Gorbach A. *Phys. Rep*., **467**, 1, 2008.

[3]. Cuevas J., English L.G., Kevrekidis P.G., Anderson M. *Phys. Rev. Lett*., **102**, 224101, 2009.

[4]. Trias E., Mazo J.J., Orlando T.P. *Phys. Rev. Lett*. **84**, 741, 2000.

[5]. Lazarides N., Eleftheriou M., Tsironis G.P. *Phys. Rev. Lett*., **97**, 157406, 2006.

[6]. English I.Q., Palmero F., Candiani P., Cuevas J., Carretero-Gonzalez R., Keverkidis P.G., Sievers A.J. *Phys. Rev. Lett*. **108**, 084101, 2012.

[7]. Sato M., Hubbard B.R, Sievers A.J. *Rev. Mod. Phys*. **78**, 137, 2006; Sato M., Imai S., Fujita N., Nishimura S., Takao Y., Sada Y., Hubbard B.E., Ilic B., Sievers A.J., *Phys. Rev. Lett*., **107**, 234101, 2011.

[8]. Schwarz U.T., English L.Q., Sievers A.J. *Phys. Rev. Lett*. **83**, 223, 1999.

[9]. Sievers A.J., Takeno S. *Phys. Rev. Lett*., **61**, 970, 1988; Takeno S., Sievers A.J. *Solid State Commun*., **67**, 1023, 1988, Kenig E., Malomed B.E., Cross M.C., Lifshitz R. *Phys. Rev. E,* **80**, 046202, 2009.

[10]. Nayfeh A.H., Mook D.T. *Nonlinear Oscillations,* Wiley, New York, 1996.

[11]. Marin J.L., Falo F., Martinez P.J., Floria L.M. *Phys. Rev. E*, **63**, 066603, 2001.

[12]. Ablowitz M.J., Ladik J.F. *J. Math. Phys*., **17**, 1011, 1976.

[13]. OvchinnikovA.A., Flach S., *Phys. Rev. Lett*., **83**, 248, 1999.

[14]. Barashenkov I.V., Smirnov Yu.S. *Phys. Rev. E*. **54**, 5707, 1996; Barashenkov I.V., Bogdan M.M., Korobov V.I. *Europhys. Lett*. **15**, 113, 1991.

[15]. Tufillaro N.B., Abbott T., Reilly J. *An Experimental Approach to Nonlinear Dynamics and Chaos,* Addison-Wesley, 2002.

[16]. Casati G., Chirikov B.V., Izrailev F.M., Ford J., in *Stochastic Behaviour in Classical and Quantum Hamiltonian Systems*, *Vol. 93 of Lecture Notes in Physics*, edited by Casati G. and Ford J., Springer, New York,.1979.

[17]. Shaw S.W., Holmes P. *ASME J. of Appl. Mech*., **50**, 849, 1983; Page J.B., *Phys. Rev. B*, **41**, 7835, 1990; Sandusky K.W., Page J.B., Schmidt K.E. *Phys. Rev. B*, **46**, 6161, 1992; Casati G., Ford J., Vivaldi F., Visscher W.M. *Phys. Rev. Lett*. **52** 1861, 1984; Gendelman O.V., Savin A.V. *Phys. Rev. Lett*., **92**, 074301, 2004; Savin A.V., Tsironis G.P., Zolotaryuk A.V. *Phys. Rev. Lett*., **88**, 154301, 2002; Rom-Kedar V., Turaev D. *Chaos*, **22**, 026102, 2012.

[18]. Gendelman O.V.and L.I.Manevitch L.I. *Phys. Rev. E*, **78**, 026609, 2008.

[19]. Landau L.D., Lifshitz E.M. *Mechanics,* Pergamon Press, 1960.

[20]. Seydel R. *Practical Bifurcation and Stability Analysis*, Springer, 2010

[21]. Fredriksson M.H., Nordmark A.B. *Proc. R. Soc. Lond. A*, **456**, 315, 2000; di Bernardo M., Budd C.J., Champneys A.R., Kowalczyk P. *Piecewise-smooth Dynamical Systems. Theory and Applications,* Springer, 2008.

[22]. Shaw S.W., Holmes P. Phys. Rev .Lett. **51**, 623, 1983.

[23]. Gendelman O.V. *Chaos, Solitons and Fractals,* **28** , 522, 2006.

[24]. Abramowitz M., Stegun I.A. *Handbook of Mathematical Functions,* Dover, New York, 1965.

Proceedings of the 4th International Conference on Nonlinear Dynamics
ND-KhPI2013
June 19-22, 2013, Sevastopol, Ukraine

Effective Analytical Approach to an Approximate Solution of Dynamic Problems of Structures with Significant Nonlinearities

Victor Gristchak[1], Yu. Fatejeva[2]

Abstract
In this paper an effective asymptotic approach for actual dynamic problems of structures with significant nonlinearities and variable parameters is presented. Special attention is paid conceptually to hybrid asymptotic approach which combines the WKBJ and Galerkin methods and perturbation technique. Some problems for father investigations are discussed.

Keywords
Asymptotic approach, dynamic problems, structures with significant nonlinearities, variable parameters, WKBJ method, Galerkin method, perturbation technique.

[1] Zaporizhzhye National University, Zaporizhzhye, Ukraine
[2] Zaporizhzhye National University, Zaporizhzhye, Ukraine
***Corresponding author:** grk@znu.edu.ua

Introduction

Along with development of computer engineering, applications of asymptotic methods to the set of problems are developed too. A number of complex mechanical problems can be significantly simplified due to application of hybrid asymptotic approaches [1]. Such solutions can be used as an approximation for the further numerical calculations.

A wide variety of deformable structures with variable geometry and time dependent parameters, reduced to singular differential equations with variable coefficients and boundary problems, can be solved analytically only in exceptional cases. Since the field of the most known asymptotic solutions application is limited, hybrid asymptotic methods [3] are in the stage of developing. There are a number of hybrid approaches which are based on approximate solution improvement. Phase integral – Galerkin (or WKB-G) technique proposed in 1993 [2] and widely published during the last 15 years has already shown its advantages in different branches of modern aerospace, machinery and structural mechanics, heat transfer [4, 5], and in systems with significant nonlinearities such as satellite vibrations in the plane of elliptical orbit [6] and etc.

In this paper new results on the hybrid WKB-G method application for solution of non homogeneous differential equations with variable coefficients and significant nonlinearities, with respect to dynamic problems are discussed. The obtained solutions possess a high accuracy and can be useful in a wide variety of applications.

1. Formulation of Problem

To introduce the method we consider following non homogeneous nonlinear singular differential equation with variable coefficients

$$\varepsilon^2 T''(x) + a(x,\varepsilon)T' + c(x,\varepsilon)T(x) - \beta b(x,\varepsilon)G(T) = \Phi(x) \qquad (1)$$

where ε, β – scalar parameters, $a(x,\varepsilon), c(x,\varepsilon), b(x,\varepsilon)$ – some differentiable functions, $G(T)$ – nonlinear function, $\Phi(x)$ – given function and initial or boundary conditions are given.

In the first step a perturbation solution $T(x)$ is developed with β [3] as an

$$T = T_0 + \beta T_1 + \beta^2 T + \ldots \tag{2}$$

Substituted (2) into the initial equation (1), the differentiation is distributed onto various terms [1], the left hand side is expressed in the form of a power series in β and the coefficient of each power of β is set zero:

$$\beta^0 : \ \varepsilon^2 T_0''(x) + a(x,\varepsilon) T_0' + c(x,\varepsilon) T_0 = \Phi(x) \tag{3}$$

$$\beta^1 : \ \varepsilon^2 T_1''(x) + a(x,\varepsilon) T_1' + c(x,\varepsilon) T_1 = b(x) G(T_0) \tag{4}$$

The equation (3) we rewrite in form

$$T_0''(x) + \bar{a}(x,\varepsilon) T_0' + \bar{c}(x,\varepsilon) T_0 = \bar{\Phi}(x) \tag{5}$$

where

$$\frac{a}{\varepsilon^2} = \bar{a} \quad \frac{b}{\varepsilon^2} = \bar{b} \quad \frac{\Phi}{\varepsilon^2} = \bar{\Phi} \tag{6}$$

In order to simplify homogeneous differential equation (5)

$$T_0''(x) + \bar{a}(x,\varepsilon) T_0' + \bar{c}(x,\varepsilon) T_0 = 0 \tag{7}$$

with respect T_0', new variable is

$$T_0 = u_0 \exp \int -\frac{\bar{a}}{2} dt \tag{8}$$

Corresponding derivatives from (8) will be

$$T_0' = u_0' \exp \int -\frac{\bar{a}}{2} dt + u_0 \exp \int -\frac{\bar{a}}{2} dt \left(-\frac{\bar{a}}{2} \right) = \exp \int -\frac{\bar{a}}{2} dt \left(u_0' - u_0 \frac{\bar{a}}{2} \right) \tag{9}$$

$$T_0'' = \exp \int -\frac{\bar{a}}{2} dt \left(u_0'' - u_0' \bar{a} - u_0 \frac{\bar{a}'}{2} + u_0 \frac{\bar{a}^2}{4} \right) \tag{10}$$

Finally we obtain initial homogeneous equation in form

$$u_0'' + \bar{Q} u_0 = 0 \tag{11}$$

where

$$\left(-\frac{\bar{a}^2}{4}-\frac{\bar{a}'}{2}+\bar{c}\right)=\bar{Q} \tag{12}$$

or
$$\varepsilon^2 u_0'' + Q u_0 = 0. \tag{13}$$

2. WKBJ Procedure

In the second step using WKBJ (or phase-integral) method in standard procedure

$$u_0 = \exp\int \varepsilon^{-1}\varphi_0 dx \tag{14}$$

were $\varphi_i(x)$ – unknown functions

$$u_0' = \exp\int \varepsilon^{-1}\varphi_0 dt\left(\varepsilon^{-1}\varphi_0\right) \tag{15}$$

$$u_0'' = \exp\int \varepsilon^{-1}\varphi_0 dt\left(\left(\varepsilon^{-1}\varphi_0\right)^2 + \varepsilon^{-1}\varphi'_0\right) \tag{16}$$

WKB-approximation of initial linear homogeneous equation with using (15-16) for function u_0 becomes

$$u_0^{WKB} = c_1 \sin I(x) + c_2 \cos I(x) \tag{17}$$

where

$$I(x) = \int \varepsilon^{-1} i Q(x)^{\frac{1}{2}} dx$$

General solution of initial non homogeneous nonlinear equation is

$$T^{WKB} = T_0^0(x) + T_0^p(x) + \beta\left[T_1^0(x) + T_1^p(x)\right] \tag{19}$$

Final result of calculations is

$$\begin{aligned} T^{WKB}(x) = E(x)\{&\sin I(x)\left[c_1 + \bar{c}_1\left(\Phi(x), b(x)G(T_0)\right)\right] + \\ &+ \cos I(x)\left[c_2 + \bar{c}_2\left(\Phi(x), b(x)G(T_0)\right)\right]\} \end{aligned} \tag{20}$$

where

$$I(x) = \int \varepsilon^{-1} i Q(x)^{\frac{1}{2}} dx \quad \frac{a}{\varepsilon^2} = \bar{a} \quad \frac{b}{\varepsilon^2} = \bar{b} \quad \frac{\Phi}{\varepsilon^2} = \bar{\Phi} \tag{21}$$

$$\bar{c}_1(x) = -\int \frac{\cos I(x)\Phi(x)}{\exp\int -\frac{\bar{a}}{2} dx I'(x)} dx - \beta\int \frac{\cos I(x) b(x) G(T_0)}{\exp\int -\frac{\bar{a}}{2} dx I'(x)} dx$$

$$\bar{c}_2(x) = \int \frac{\sin I(x)\Phi(x)}{\exp\int -\frac{\bar{a}}{2} dx I'(x)} dx + \beta\int \frac{\sin I(x) b(x) G(T_0)}{\exp\int -\frac{\bar{a}}{2} dx I'(x)} dx$$

$$E(x) = \exp \int -\frac{\overline{a}}{2} dx$$

3. Hybrid Asymptotic Solution

In the third step we will keep the perturbation functions but replaced the gauge functions by new amplitudes which depend on ε [1, 2]. In the Bubnov-Galerkin orthogonality principle one seeks an approximate solution in the form of a linear combination of specified (known) coordinate functions with unknown amplitudes δ_0 which are function of ε :

$$u_H(x,\varepsilon) = \exp \int \delta_0 \varphi_0 dx \tag{22}$$

$$u'_H(x,\varepsilon) = \exp \int \delta_0 \varphi_0 dx (\delta_0 \varphi_0) \tag{23}$$

$$u''_H(x,\varepsilon) = \exp \int \delta_0 \varphi_0 dx \left((\delta_0 \varphi_0)^2 + \delta_0 \varphi'_0\right) \tag{24}$$

$$R = \varepsilon^2 \left((\delta_0 \varphi_0)^2 + \delta_0 \varphi'_0\right) + Q(x) \tag{25}$$

$$\delta_0^2 \varepsilon^2 I_1 + \delta_0 \varepsilon^2 \frac{Q(b) - Q(a)}{2} + I_1 = 0 \tag{26}$$

where

$$\int \left(\pm iQ(x)^{\frac{3}{2}} \right) dx = I_1 \tag{27}$$

For amplitudes δ_0 we obtain following sequences:

$$\delta_{01,2} = -\frac{Q(b) - Q(a)}{\pm 4 \int_a^b \left(iQ(x)^{\frac{3}{2}} \right) dx} \pm \sqrt{\left(\frac{Q(b) - Q(a)}{4 \int_a^b \pm \left(iQ(x)^{\frac{3}{2}} \right) dx} \right)^2 - \frac{1}{\varepsilon^2}} \tag{28}$$

The result of three-step hybrid asymptotic solution of initial non homogeneous nonlinear differential equation with variable coefficients for function $T^H(x)$ is given in form

$$\begin{aligned} T^H(x) = E(x) \{ & \sin I^H(x, \delta_{0_1}) [c_1 + \overline{c}_1(\Phi(x), b(x) G(T_0))] + \\ & + cos I^H(x, \delta_{0_2}) [c_2 + \overline{c}_2(\Phi(x), b(x) G(T_0))] \} \end{aligned} \tag{29}$$

where

$$I^H(x) = \pm \int \delta_{0_{1,2}} iQ(x)^{1/2} dx \tag{30}$$

4. Numerical Results

To obtain an approximate analytical solution of nonlinear equation:

$$\varepsilon^2 y'' + y + \beta y^5 = x \tag{31}$$

where ε and β – are parameters.

Using solution (20) with initial conditions

$$\begin{aligned} y(0) &= 1 \\ y'(0) &= 0 \end{aligned} \tag{32}$$

we obtain the result in form

$$y^{WKB}(x) = \left(\cos\frac{x}{\varepsilon} + x\right) + \beta\left[e_1 \sin\frac{x}{\varepsilon} + e_2 \cos\frac{x}{\varepsilon} - \left(\cos\frac{x}{\varepsilon} + x\right)^5\right] \tag{33}$$

at $\varepsilon = 0.1$ and $\beta = 0.1$ solution (33) becomes

$$y^{WKB}(x) = \left(\cos\frac{x}{0.1} - x\right) + 0{,}1\left[-0{,}8\sin\frac{x}{0.1} + \cos\frac{x}{0.1} - \left(\cos\frac{x}{0.1} + x\right)^5\right] \tag{34}$$

Comparison of numerical results using approximate analytical solution and direct numerical calculations of initial equation (31) are given in Figure 1.

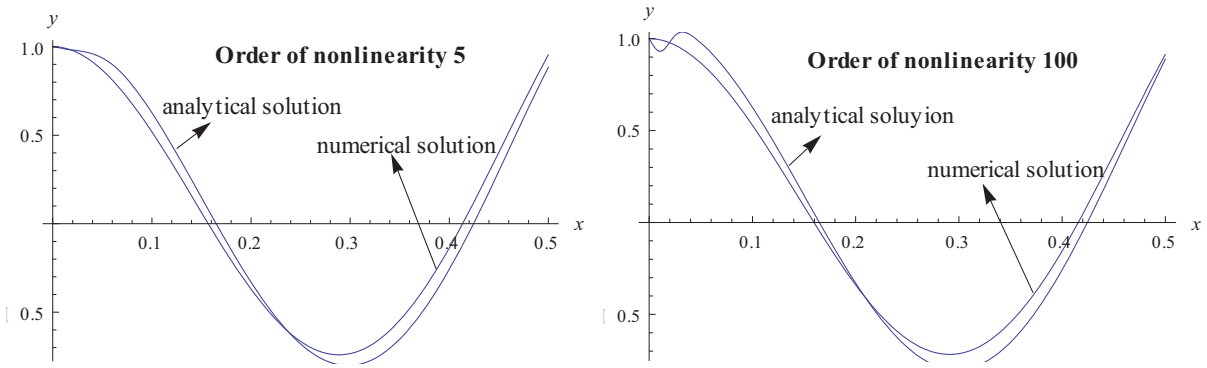

Figure 1.Comparison of analytical and numerical solutions

Conclusions

In this study we have discussed three-term hybrid asymptotic method for an approximate analytical solution of dynamic problems of structures with significant nonlinearities and with variable parameters. A hybrid WKBJ-Galerkin method on the basis of obtained analytical solution will be effective for «small» values of scalar (perturbation) parameters and for «large» values as well.

An example shows that in some type of nonlinear differential equations in the fixed initial interval of variable *x* proposed analytical solution is not sensitive to order of nonlinearities.

References

[1] Geer J.F., Andersen C.M. A Hybrid Perturbation-Galerkin Method for Differential Equations Containing a Parameter*, Pan American Congress on Appl. Mech*., pp. 460-463, 1991.

[2] Gristchak V.Z., Dmitrieva Ye. A Hybrid WKB-Galerkin Method and its Application, *Technische Mechanik*, №15, pp. 281-294, 1995.

[3] Gristchak V.Z., Kabak V.N. Double Asymptotic Method for Nonlinear Forced Jscillations Problems of Mechanical Systems with Time Dependent Parameters, *Technische Mechanik*, Band 16, Heft 4, pp. 285-296, 1996.

[4] Gristchak V.Z., Ganilova O.A. Application of a Hybrid WKB-Galerkin Method in Control of the Dynamic Instability of a Piezolaminated Imperfect Column, *Technische Mechanik*, №26(2), pp. 106-116, 2006.

[5] Gristchak V.Z., Pogrebitskaja A.M. On Approximate Analytical Solutions of Nonlinear Thermal Emission Problems, *Technische Mechanik*, №31(2), pp. 112-120, 2011.

[6] Gristchak V.Z., Gristchak D.D. Refined Analytical Solution for Satellite Nonlinear Vibration Problem in the Plane of Elliptical Orbit, *Proc. of the 4-th International Conference «Nonlinear Dynamics», Sevastopol,* 19-22 June 2013 (to be published).

Proceedings of the 4th International Conference on Nonlinear Dynamics
ND-KhPI2013
June 19-22, 2013, Sevastopol, Ukraine

Refined Analytical Solution for Satellite Nonlinear Vibration Problem in the Plane of Elliptical Orbit

V.Z. Gristchak[1*], D.D. Gristchak[2]

Abstract
A three-step hybrid perturbation-WKB-Galerkin method is presented for a solution of the satellite nonlinear vibration problem in the plane of elliptical orbit. This analytical approach is effective for the solution of a variety of singular nonlinear differential equations which involve scalar parameters. The resulting (approximate) solution has a form of a sum where each term consists of the product of three functions according to perturbation (on parameter at nonlinear term) and WKB-Galerkin method. As a result it is obtained analytical solution of the problem as a function of orbit parameters. This approach gives a possibility to obtain more refined approximate analytical solution which is effective as well for small and as for large scalar parameters. Comparison of results by using of the proposed solution and direct numerical calculations are given.

Keywords
Perturbation-WKB-Galerkin method, satellite nonlinear vibration problem, singular nonlinear differential equations, refined approximate analytical solution.

[1] Zaporizhzhye National University, Zaporizhzhye, Ukraine
[2] National Aviation University, Kiev, Ukraine
* **Corresponding author:** grk@znu.edu.ua.

Introduction

Satellite vibration problem in the plane of elliptical orbit was investigated in some publications [1-6]. Paper [1] is devoted to calculation of satellite periodic vibrations on the basis of the equation proposed in [2]. The local method of analysis of significant nonlinear dynamic problems is given in [3] and the usage of this method for the singular perturbations was discussed in [4].

An effective approximate analytical approach on the basis of hybrid asymptotic methods with respect to vibrations of systems with significant nonlinearities and variable parameters which is described by non homogeneous nonlinear differential equations with variable coefficients is discussed in [10]. This approach, as shown in [8, 9], gives a possibility to obtain more refined an approximate analytical solutions of a variety nonlinear problems.

1. Formulation of problem

In the spirit of [2] it is supposed that satellite moves in central gravitation field so that its mass center moves on elliptical orbit. It is investigated plane satellite movement with respect to its mass center.

Differential equation of this problem proposed by V.V. Belecky [3] in the form:

$$(1+e\cos\nu)\frac{d^2\delta}{d\nu^2}-2e\sin\nu\frac{d\delta}{d\nu}+\mu\sin\delta=4e\sin\nu \qquad (1.1)$$

where δ – double angle between radius-vector of mass center and axis of inertia with respect in which inertia moment is equal C; $\mu = 3(A-C)/B$; e – orbit eccentricity; ν – angle distance of radius-vector from orbit perigee (real anomaly); B – moment of inertia with respect to main inertia axis of satellite which is perpendicular to plane of orbit; A – inertia moment with respect to third main axis of inertia.

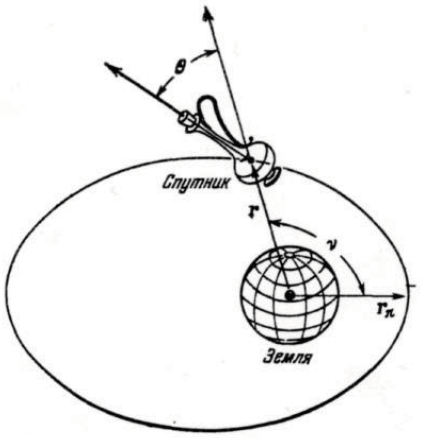

Figure 1. Scheme of satellite on orbit [2]

After some simplifications the initial equation (1.1) will be considered in the form:

$$\varepsilon^2 \frac{d^2\delta}{d\nu^2} - a(\nu)\frac{d\delta}{d\nu} + b(\nu)\left(\delta - \frac{\delta^3}{6}\right) = F(\nu) \tag{1.2}$$

where

$$a(\nu) = \frac{1}{\mu^2}\frac{2e\sin\nu}{1+e\cos\nu} \qquad b(\nu) = \frac{1}{1+e\cos\nu}\cdot\frac{1}{\mu} \qquad F(\nu) = \frac{1}{\mu^2}\frac{4e}{1+e\cos\nu}\sin\nu$$

$$\delta = 2\theta \quad \mu = \frac{A-C}{B} \quad \varepsilon^2 = \frac{1}{\mu^2} \tag{1.3}$$

$$\sin\delta = \delta - \frac{\delta^3}{6} + \frac{\delta^5}{120} + \ldots \text{ [12]} \qquad -3 \le \mu \le 3 \quad 0 \le e \le 1$$

For an approximate analytical solution of singular nonlinear differential equation with variable coefficients (1.2) is used a hybrid asymptotic method [8]. In step one the solution is determined by forming a perturbation expansion [11] in λ.

For an approximate analytical solution of singular nonlinear differential equation with variable coefficients (1.2) is used the hybrid asymptotic method [8].

In step one the solution of equation (1.2) is determined by forming a perturbation expansion in λ as a scalar parameter as the following:

$$\delta = \delta_0 + \lambda\delta_1 + \ldots = \sum_{i=0}^{\infty} \lambda^i \delta_i \tag{1.4}$$

for the equation

$$\varepsilon^2 \frac{d^2\delta}{d\nu^2} - a(\nu)\frac{d\delta}{d\nu} + b(\nu)\delta - \lambda\bar{b}(\nu)\delta^3 = F(\nu) \tag{1.5}$$

where

$$\lambda = \frac{1}{6\mu} \quad \bar{b}(\nu) = \mu b(\nu) \quad \lambda = \frac{\varepsilon}{6} \tag{1.6}$$

Introducing (1.4) into (1.5) and saving two first terms of expansion, we obtain the system of two linear differential equations

$$\lambda^0: \quad \varepsilon^2 \frac{d^2\delta_0}{d\nu^2} - a(\nu)\frac{d\delta_0}{d\nu} + b(\nu)\delta_0 = F(\nu) \tag{1.7}$$

$$\lambda^1: \quad \varepsilon^2 \frac{d^2\delta_1}{d\nu^2} - a(\nu)\frac{d\delta_1}{d\nu} + b(\nu)\delta_1 = \bar{b}(\nu)\delta_0^3 \tag{1.8}$$

with resulting solution of initial equation (1.2) which is determined through WKB method [9]:

$$\delta(\nu) = E(\nu)\left\{\sin I(\nu)\left[a_1 + \int \frac{F(\nu)\cos I(\nu)}{E(\nu)I'(\nu)}d\nu + \lambda\int \frac{\bar{b}(\nu)\delta_0^3\cos I(\nu)}{E(\nu)I'(\nu)}d\nu\right] - \right.$$
$$\left. - \cos I(\nu)\left[a_2 + \int \frac{F(\nu)\sin I(\nu)}{E(\nu)I'(\nu)}d\nu + \lambda\int \frac{\bar{b}(\nu)\delta_0^3\sin I(\nu)}{E(\nu)I'(\nu)}d\nu\right]\right\} \tag{1.9}$$

where a_1, a_2 – are constants; $\delta_0(\nu)$ – general solution of linear equation (first approximation) at given initial conditions; $E(\nu) = \exp\int^{\xi} \frac{a(\nu)}{2}d\xi$; $I(\nu) = \int^{\xi} \varepsilon^{-1}Q(\nu)^{1/2}\,d\xi$; $Q(\nu) = \left[\frac{a^1(\nu)}{2} - \frac{a^2(\nu)}{\varepsilon^2\cdot 4} + b(\nu)\right]$; $\bar{a}(\nu) = \frac{a(\nu)}{\varepsilon^2}$; $\tilde{b}(\nu) = \frac{b(\nu)}{\varepsilon^2}$; $(\,)' = \frac{d}{d\nu}$.

2. Hybrid WKB-Galerkin method in nonlinear satellite vibration problem in plane of elliptical orbit

In correspondence with [7] solution of initial equation (1.2) is presented in form

$$U_{0H}(\nu) = \exp\int \Delta_0\varphi_0(\nu)d\nu \tag{2.1}$$

where

$$\Delta_0 \text{ – unknown parameter and } \varphi_0 = Q(\nu)^{1/2} \tag{2.2}$$

Galerkin's orthogonality criteria,

$$\int_a^b R\left(\varphi_0,...,\varphi_n,\frac{d\varphi_0}{d\nu},...,\Delta_0,...,\Delta_n,\nu,\varepsilon\right)\cdot\varphi_i d\nu = 0 \tag{2.3}$$

leads to the expressions for Δ_0:

$$\Delta_{0_{1,2}} = \pm\frac{Q(b)-Q(a)}{4\int_a^b Q^{3/2}(\nu)d\nu} + \sqrt{\frac{1}{\varepsilon^2} + \left[\frac{Q(b)-Q(a)}{4\int_a^b Q^{3/2}(\nu)d\nu}\right]^2} \tag{2.4}$$

For the case $Q(\nu) > 0$, the hybrid solution of nonlinear problem is given by

$$\delta(\nu)=\widetilde{E}(\nu)\left\{\sin\widetilde{I}(\nu)\left[a_1+\int\frac{F(\nu)\cos\widetilde{I}(\nu)}{\widetilde{E}(\nu)\widetilde{I}'(\nu)}d\nu+\lambda\int\frac{\bar{b}(\nu)\delta_0^3\cos\widetilde{I}(\nu)}{\widetilde{E}(\nu)\widetilde{I}'(\nu)}d\nu\right]-\right.$$
$$\left.-\cos\widetilde{I}(\nu)\left[a_2+\int\frac{F(\nu)\sin\widetilde{I}(\nu)}{\widetilde{E}(\nu)\widetilde{I}'(\nu)}d\nu+\lambda\int\frac{\bar{b}(\nu)\delta_0^3\sin\widetilde{I}(\nu)}{\widetilde{E}(\nu)\widetilde{I}'(\nu)}d\nu\right]\right\} \tag{2.5}$$

where

$$\widetilde{E}(\nu)=\phi(\nu)\exp\int\frac{a(\nu)}{2}d\nu,\phi(\nu)=\exp\int\frac{Q(a)-Q(b)}{4\int_a^b Q^{3/2}(\nu)d\nu}\cdot\sqrt{Q(\nu)}\,d\nu,$$
$$\widetilde{I}(\nu)=\int_a^\nu\sqrt{\frac{1}{\varepsilon^2}-\left[\frac{Q(a)-Q(b)}{4\int_a^b Q^{3/2}(\nu)d\nu}\right]^2}\cdot\sqrt{Q(\nu)}\,d\nu,\lambda=\frac{1}{6\mu},\quad\bar{b}=b(\nu)\cdot\mu. \tag{2.6}$$

Results of numerical calculations and comparison of the analytical approach with direct numerical results using system «Mathematica» [13] at $e=0{,}8;\ \mu=3$ and initial conditions

$$\delta_0(0)=1$$
$$\delta_0'(0)=0 \tag{2.7}$$

with visualization of vibration processes are given in Fig. 2-4.

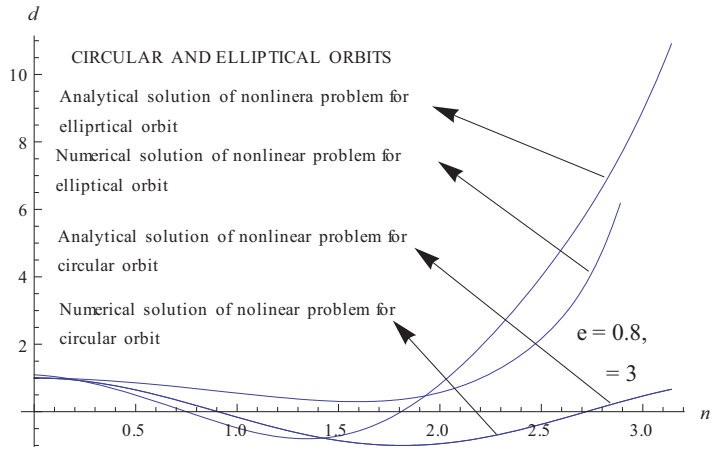

Figure 2. Analytical and numerical solutions for satellite nonlinear vibration problem in planes of circular and elliptical orbits

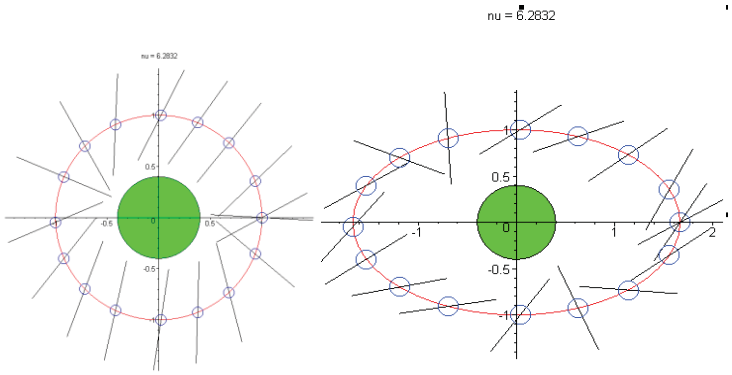

Figure 3. Satellite vibration in plane of circular **(e = 0)** and elliptical **(e = 0.8)** orbits

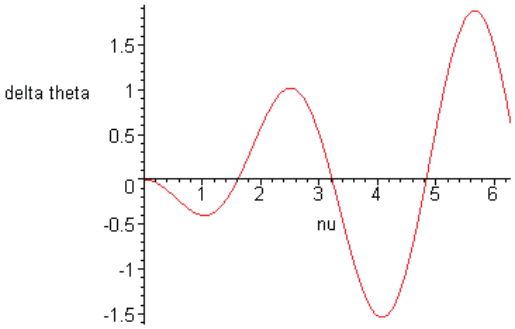

Figure 4. Difference in angles of satellite axes in cases of circular and elliptical orbits

Conclusion

Nonlinear satellite vibration problem in plane of elliptical orbit leads to singular nonlinear non-homogeneous differential equation with variable coefficients. Proposed solution on the basis of three-step hybrid asymptotic method valid as well for «small» as for «large» scalar parameters and it is more refined in comparison with known analytical approaches.

References

[1] Bruno A.D,, Petrovich V.Yu. Determination of periodic oscillations of the satellite, *Math. Modeling*, V 9 (6), pp. 82-94, 1997 (in Russian).

[2] Bruno A.D, *Local Method of Nonlinear Analysis of Differential Equations*, Nauka, Moscow, 1979.

[3] Beletsky V.V. *Motion of Satellite with Respect to the Mass Center in Gravity Field,* Published by MSU, Moscow, 1975.

[4] Sarychev V.A., Sazonov V.V., Zlatoustov V.A. Periodic oscillations of the satellite in a plane of the elliptic orbit, *Space Researches*, V. 15 (6), pp. 809-834, 1977 (in Russian).

[5] Bruno A.D., Varin V.P. Limit problems for the equation of oscillation of a satellite, *Celestial Mechanics*, V. 66, № 1, pp. 17-68, 1977.

[6] Sadov S.Yu. Normal form of equations of the satellite oscillations in singular case, *Mathematical Notices*, V. 58 (5), pp. 785-789, 1995 (in Russian).

[7] Gristchak V.Z. Hybrid asymptotic methods and technics of their application, published by *Zaporizhzhye National University*, Zaporizhzhye, 2009 (in Ukrainian).

[8] Gristchak V.Z.. Dmitriyeva O.M. Use of the hybrid VKB-Galerkin method to solve some boundary problems of mechanics, *Notices of the NAS of Ukraine*, 4, pp. 63-67, 1999 (in Ukrainian).

[9] Gristchak D.V. New approximate analytical solution of the problem on fundamental vibrations of the multilayer plate with variable by time mass and coefficient of damping, *New Materials in Metallurgy and Machine-Building*, 1, pp. 114-117, 2005 (in Ukrainian).

[10] Gristchak V.Z., Fatejeva Yu. An effective analytical approach to approximate solution of dynamic problems of structures with significant nonlinearities, *Proc. of 4-th International Conference «Nonlinear Dynamics»*, Sevastopol,19-22 June 2013 (to be published).

[11] Nayfeh A.H. *Introduction to Perturbation Technics*, Wiley, New York, 1981.

[12] G.A. Korn, T.M. Korn *Mathematical Handbook for scientists and engineers*, cMGRAW Hill Book Company, New York, 1961.

[13] Wolfram Stephen *«Mathematica». A System for Doing Mathematics by Computer*, Second Edition, Addison-Wesley Publishing Co., Redwood City, California, 1991.

Proceedings of the 4th International Conference on Nonlinear Dynamics
ND-KhPI2013
June 19-22, 2013, Sevastopol, Ukraine

On the decay rate of solutions of nonlinear systems in critical cases

Victoria Grushkovskaya[1], Alexander Zuyev[1*]

Abstract
This paper is devoted to the investigation of the behavior of solutions of nonlinear systems in the critical case of q pairs of purely imaginary roots. The reduction principle and the normal form method are used for studying this problem. The main result suggests an explicit estimate of the decay rate of solutions of nonlinear mechanical system with two purely imaginary eigenvalues. The result obtained is illustrated by means of the numerical integration.

Keywords
Asymptotic estimate, critical case, stability

[1] Institute of Applied Mathematics and Mechanics, National Academy of Sciences of Ukraine, Donetsk, Ukraine
* **Corresponding author:** al_zv@mail.ru

Introduction

The study of the asymptotic behavior of solutions remains a challenging problem for general classes of nonlinear ordinary differential equations. For example, a power estimate for the solutions of systems defined by homogeneous vector fields was proved by N.N. Krasovskii [1] and V.I. Zubov [2]. K. Peiffer and A.Ya. Savchenko [3] considered a system in the critical case of a couple of purely imaginary eigenvalues. Estimates for the norm of solutions of the reduced system in the critical case of q pairs of purely imaginary roots were analyzed in [4].

In recent paper [5], we proposed an approach for the construction of such estimates for systems with neutral and critical components.

Consider a system of differential equations:

$$\dot{x} = Ax + R(x), \tag{1}$$

where $x = (x_1, x_2, ..., x_n)^T \in R^n$ is the phase vector, A is a real $[n \times n]$ matrix with constant coefficients, and $R(x)$ is a real function, analytic in some neighborhood of the origin, such that its Maclaurin series expansion starts with terms of at least second order.

Assume that the characteristic equation of matrix A has q pairs of purely imaginary roots $(\pm i\omega_1, ..., \pm i\omega_q)$ and $p = n - 2q$ roots with negative real parts. Assume also that there are no multiple roots among the purely imaginary ones.

Theorem 1 [5] Le*t the stability of the trivial solution of system (1) is ensured by terms of up to the third order. Then there exists an* $\varepsilon > 0$ *such that the estimate*

$$|x(t)| \le \left(\alpha_1 (t - t_0) + \alpha_2 |x_0|^{-2}\right)^{-1/2}, \ t \ge t_0, \ x(t_0) = x_0, \tag{2}$$

holds for any solution $x(t)$ *of system* (*1*) *with initial conditions* $|x_0| < \varepsilon$, *where* α_1, α_2 *are positive constants.*

In this paper, we apply Theorem 1 for studying the decay rate of oscillations of a pendulum system with partial dissipation. For this system, coefficients in (2) are computed in terms of mechanical parameters. As a part of the investigation, a Lyapunov function is constructed explicitly as the sum of Lyapunov functions for neutral and stable subsystems. The result obtained is illustrated by means of the numerical integration of equations of the perturbed motion for different values of damping coefficient.

1. Model description

Consider a double pendulum consisting of two weightless rods of length l suspended by hinges (Fig. 1). The rods can oscillate in the vertical plane. The friction in the hinges and the air resistance are neglected. We assume that the mass m is suspended by a spring to the second rod and moves along the rod with damping.

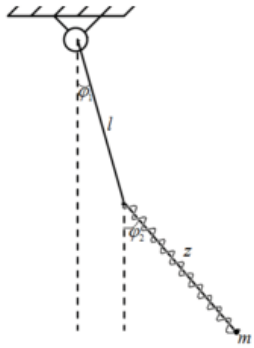

Figure 1. Double pendulum with partial dissipation

Let κ be the stiffness coefficient of the spring, ν be the damping coefficient for the translational motion of the mass m along the rod, φ_1 and φ_2 be angles formed by rods and the vertical line, and z be the length of the spring.

In our notation, the kinetic energy (T) and the potential energy (V) of the system are

$$T = ml^2\dot{\varphi}_1^2 + \frac{m}{2}z^2\dot{\varphi}_2^2 + \frac{m}{2}\dot{z}^2 + ml\dot{\varphi}_1\dot{z}\sin(\varphi_2 - \varphi_1) + mlz\dot{\varphi}_1\dot{\varphi}_2\cos(\varphi_2 - \varphi_1),$$
$$V = -2mgl\cos\varphi_1 - mgz\cos\varphi_2 + \frac{\kappa}{2}z^2,$$

where g is the gravity constant. Then the Lagrange equations take the form:

$$\begin{aligned}
&2ml^2\ddot{\varphi}_1 + ml\ddot{\varphi}_2 z\cos(\varphi_2 - \varphi_1) + ml\ddot{z}\sin(\varphi_2 - \varphi_1) - ml\dot{\varphi}_2^2 z\sin(\varphi_2 - \varphi_1) + 2ml\dot{\varphi}_2\dot{z}\cos(\varphi_2 - \varphi_1) + \\
&+2mgl\sin\varphi_1 = 0, \\
&ml\ddot{\varphi}_1 z\cos(\varphi_2 - \varphi_1) + mz^2\ddot{\varphi}_2 + ml\dot{\varphi}_1^2 z\sin(\varphi_2 - \varphi_1) + 2m\dot{\varphi}_2\dot{z}z + mgz\sin\varphi_2 = 0, \\
&ml\ddot{\varphi}_1\sin(\varphi_2 - \varphi_1) + m\ddot{z} - ml\dot{\varphi}_1^2\cos(\varphi_2 - \varphi_1) - mg\cos\varphi_2 - m\dot{\varphi}_2{}^2 z + \kappa z = -\nu\dot{z}.
\end{aligned} \tag{3}$$

It is easy to show that the considered system has four equilibria. We consider only the lower equilibrium: $\varphi_1 = 0, \varphi_2 = 0, z = z_0$. From the third equation in (3), it follows that $z_0 = mg/\kappa$.

Substituting $z = \tilde{z} + mg/\kappa$, we obtain equations of the perturbed motion. Let expand them into the Maclaurin series with respect to $\varphi_1, \varphi_2, \tilde{z}, \dot{\varphi}_1, \dot{\varphi}_2, \dot{\tilde{z}}$ up to third order terms. Then substituting $\varphi_1 = x_1, \varphi_2 = x_2, \tilde{z} = x_3, \dot{\varphi}_1 = x_4, \dot{\varphi}_2 = x_5, \dot{\tilde{z}} = x_6,$ we get

$$
\begin{aligned}
&\dot{x}_1 = x_4, \dot{x}_2 = x_5, \dot{x}_3 = x_6,\\
&\dot{x}_4 = -\frac{2g}{l}x_1 + \frac{g}{l}x_2 - \frac{\kappa}{ml}x_1x_3 - \frac{\nu}{ml}x_1x_6 + \frac{\kappa}{ml}x_2x_3 + \frac{\nu}{ml}x_2x_6 + \frac{g}{3l}x_1^3 - \frac{g}{2l}x_1^2x_2 + \frac{g}{2l}x_1x_2^2 - \frac{g}{6l}x_2^3,\\
&\dot{x}_5 = \frac{2\kappa}{m}x_1 - \frac{2\kappa}{m}x_2 - \frac{\kappa^2}{m^2g}x_1x_3 + \frac{\nu\kappa}{m^2g}x_1x_6 + \frac{\kappa^2}{m^2g}x_2x_3 - \frac{\nu\kappa}{m^2g}x_2x_6 - \frac{2\kappa}{mg}x_5x_6 - \frac{4\kappa}{3m}x_1^3 + \frac{3\kappa}{m}x_1^2x_3 -\\
&-\frac{5\kappa}{2m}x_1x_2^2 + \frac{\kappa^3}{m^3g^2}x_1x_3^2 - \frac{\kappa^2\nu}{m^3g^2}x_1x_3x_6 + \frac{l\kappa}{mg}x_1x_4^2 + \frac{5\kappa}{6m}x_2^3 - \frac{\kappa^3}{m^3g^2}x_2x_3^2 + \frac{\kappa^2\nu}{m^3g^2}x_2x_3x_6 -\\
&-\frac{l\kappa}{mg}x_2x_4^2 + \frac{2\kappa^2}{g^2m^2}x_3x_5x_6,\\
&\dot{x}_6 = -\frac{\kappa}{m}x_3 - \frac{\nu}{m}x_6 - 2gx_1^2 + 3gx_1x_2 - \frac{3}{2}gx_2^2 + lx_4^2 + \frac{mg}{\kappa}x_5^2 - \frac{\kappa}{m}x_1^2x_3 - \frac{\nu}{m}x_1^2x_6 + \frac{2\kappa}{m}x_1x_2x_3 +\\
&+\frac{2\nu}{m}x_1x_2x_6 - \frac{\kappa}{m}x_2^2x_3 - \frac{\nu}{m}x_2^2x_6 + x_3x_5^2.
\end{aligned}
\tag{4}
$$

The matrix of the linear approximation of system (4) has two eigenvalues with negative real parts and two pairs of purely imaginary eigenvalues:

$$
\lambda_{1,2} = \frac{-\nu \pm \sqrt{\nu^2 - 4\kappa m}}{2m}, \lambda_{3,4} = \pm i\omega_1, \lambda_{5,6} = \pm i\omega_2,
$$

where $\omega_1 = \sqrt{\dfrac{mg + \kappa l + \sqrt{m^2g^2 + \kappa^2 l^2}}{ml}}, \omega_2 = \sqrt{\dfrac{mg + \kappa l - \sqrt{m^2g^2 + \kappa^2 l^2}}{ml}}.$

2. The decay rate of oscillations

By the reduction principle system (4) can be reduced to the following form [5,6]:

$$
\begin{aligned}
&\dot{z}_s = i\omega_s z_s + Y_s^{(0)}(z,\bar{z}) + \sum_{|k|=3} P_s^{(k)}(\zeta) z_1^{k_1} z_2^{k_2} \bar{z}_1^{k_3} \bar{z}_2^{k_4} + H_s(z,\bar{z},\zeta), \quad s = 1,2,\\
&\dot{\zeta}_1 = \zeta_2 + \sum_{|k|=2} Q_1^{(k)}(\zeta) z_1^{k_1} z_2^{k_2} \bar{z}_1^{k_3} \bar{z}_2^{k_4} + E_1(z,\bar{z},\zeta),\\
&\dot{\zeta}_2 = -\frac{\kappa}{m}\zeta_1 - \frac{\nu}{m}\zeta_2 + \sum_{|k|=2} Q_2^{(k)}(\zeta) z_1^{k_1} z_2^{k_2} \bar{z}_1^{k_3} \bar{z}_2^{k_4} + E_2(z,\bar{z},\zeta),
\end{aligned}
\tag{5}
$$

where $Y_s^{(0)}(\xi,\eta)$ are forms of third order with respect to variables $z, \bar{z}$, P_s and Q_j are linear forms of ζ, H_s and E_j are equal to zero as $\zeta_1 = \zeta_2 = 0$ and do not contain linear terms of these variables. Consider then a pair of systems

$$
\dot{z}_s = i\omega_s z_s + Y_s^{(0)}(z,\bar{z}), \quad s = 1,2, \tag{6}
$$

and

$$\begin{aligned}\dot{\zeta}_1 &= \zeta_2,\\ \dot{\zeta}_2 &= -\frac{\kappa}{m}\zeta_1 - \frac{\nu}{m}\zeta_2.\end{aligned} \tag{7}$$

Let $V_1(z,\bar{z})$ be a positive definite Lyapunov function with negative definite derivative $V_1^{'}$ along the trajectories of system (6). Suppose that the sign of this derivative is independent of terms of higher than third order in the right-hand side of respective equations. A Lyapunov function $V_2(\zeta)$ for system (7) can be taken in the form

$$V_2(\zeta) = \frac{\kappa^2+\nu^2+\kappa m}{m}\zeta_1^2 + (\kappa+m)\zeta_2^2 + 2\nu\zeta_1\zeta_2\,. \tag{8}$$

The derivative of function (8) along the trajectories of system (7) is: $V_2^{'} = -\dfrac{2\nu\kappa}{m}\left(\zeta_1^2+\zeta_2^2\right)$.

A Lyapunov function for system (5) has the following form:

$$V = V_1(z) + V_2(\zeta).$$

It is a positive definite function with respect to all its variables. Denote the derivatives of functions V_1, V_2 along the trajectories of systems (6), (7) by $V_1^{'}, V_2^{'}$, respectively. Then the following estimate holds for sufficiently small z_s, ζ_j [5, 6]:

$$\dot{V} \le -(1-\delta_1)\left(\left|V_1^{'}\right| + \left|V_2^{'}\right|\right).$$

To find the function V_1, we simplify system (6) using normalization transformations described in [7, 8]. As a result, we obtain the system

$$\dot{r}_s = r_s\left(a_{s1}r_1^2 + a_{s2}r_2^2\right) + R_s(r,\theta), \quad s = 1,2\,, \tag{9}$$

where $|R_s| \le \Delta_s |r|^4$ with some constants Δ_s. For the mechanical system considered, coefficients a_{sj} are given by the following expressions:

$$a_{11} = -\frac{10\left(558227+48252\sqrt{101}\right)\nu}{101\left(80\nu^2+3371+319\sqrt{101}\right)}, \quad a_{22} = -\frac{10\left(558227-48252\sqrt{101}\right)\nu}{101\left(80\nu^2+3371-319\sqrt{101}\right)},$$

$$a_{12} = -\frac{1000\left(51+5\sqrt{101}\right)\left(838\nu^2+39087+1612\sqrt{101}\right)\nu}{1919\left(130321+404\nu^4+16204\nu^2\right)},$$

$$a_{21} = -\frac{1000\left(51-5\sqrt{101}\right)\left(838\nu^2+39087-1612\sqrt{101}\right)\nu}{1919\left(130321+404\nu^4+16204\nu^2\right)}.$$

These coefficients correspond to the following choice of mechanical parameters:

$$l=1, m=1, \kappa=1, g=10. \tag{10}$$

Asymptotic stability of the trivial solution of system (9) is ensured by the third-order forms with all values of parameter ν. The Lyapunov function for system (9) can be taken in the form $V_1 = r_1^2 + r_2^2$. Then

$$\begin{aligned} &\dot{V}_1 = 2a_{11}r_1^4 + 2\left(a_{12}+a_{21}\right)r_1^2r_2^2 + 2a_{22}r_2^4 + 2\left(r_1R_1\left(r,\theta\right) + r_2R_2\left(r,\theta\right)\right) \\ &\le -a_{\min}\left(r_1^2+r_2^2\right)^2 + 2\sqrt{\Delta_1^2+\Delta_2^2}\,|r|^5, \end{aligned} \tag{11}$$

where $a_{\min}$ is the minimal eigenvalue of the matrix $N = \begin{pmatrix} -a_{11} & -\left(a_{12}+a_{21}\right)/2 \\ -\left(a_{12}+a_{21}\right)/2 & -a_{22} \end{pmatrix}$:

$$a_{\min} = \nu\left(0.006\nu^4 + 0.539\nu^2 + 1.086\right)^{-1}\left(4.422\nu^2 + 32.391 - \left(0.004\nu^4 + 0.162\nu^2 + 1.303\right)\left(2.891\nu^{12} + \right.\right.$$
$$\left.\left. + 2.632\cdot 10^2\nu^{10} + 9.428\cdot 10^3\nu^8 + 1.428\cdot 10^5\nu^6 + 8.708\cdot 10^5\nu^4 + 1.888\cdot 10^6\nu^2 + 6.651\cdot 10^6\right)^{1/2}\right).$$

For any positive δ_2, there exists an $\varepsilon_2 > 0$ such that estimate (11) implies

$$\dot{V}_1 \le -a_{\min}\left(1-\delta_2\right)\left(r_1^2+r_2^2\right)^2 = -a_{\min}\left(1-\delta_2\right)V_1^2 \text{ as } |r| \le \varepsilon_2. \tag{12}$$

Exploiting fact that V is the sum of Lyapunov functions for systems (6), (7) and returning to variables x_s, we obtain a Lyapunov function for system (4) corresponding to the choice of mechanical parameters (10):

$$V\left(x\right) = \frac{91}{10100}x_1^2 + \frac{1}{202}x_2^2 + \left(2+\nu^2\right)x_3^2 + \frac{23}{50500}x_4^2 + \frac{11}{4040}x_5^2 + 2x_6^2 - \frac{9}{1010}x_1x_2 + \frac{1}{10100}x_4x_5 +$$
$$+2\nu x_3x_6 + R\left(x\right), \text{ where } \left|\ R\left(x\right)\right| \le \tilde{\delta}|x|^2.$$

It can be shown that

$$V \le \left(\frac{a_{\min}}{2}\left(1-\delta_1\right)\left(1-\delta_2\right)\left(t-t_0\right) + V_0^{-1}\right)^{-1}, \forall t \ge t_0. \tag{13}$$

Moreover, since $\left(Gx,x\right)$ is positive definite quadratic form, we have the following estimate:

$$\lambda_{\min}|x|^2 \le \left(Gx,x\right) \le \lambda_{\max}|x|^2, \tag{14}$$

where $\lambda_{\min}, \lambda_{\max}$ are the minimal and maximal eigenvalue of the matrix G, $\lambda_{\min} = \frac{321-\sqrt{52541}}{202000}$, $\lambda_{\max} = 2 + \frac{\nu^2}{2} + \frac{\sqrt{\nu^2+4\nu^2}}{2}$, for all ν. Therefore,

$$V(x) \geq \left(\frac{321-\sqrt{52541}}{202000} - \tilde{\delta} \right) |x|^2, \; V_0 = V(x_0) \leq \left(2 + \frac{\nu^2}{2} + \frac{\sqrt{\nu^4+4\nu^2}}{2} + \tilde{\delta} \right) |x_0|^2 . \qquad (15)$$

Combining inequalities (15) and (13), we get estimate (2) for solution $x(t)$ of system (4) in the some ε -neighborhood of the origin with the following coefficients:

$$\alpha_1 = \frac{321-\sqrt{52541}}{404000}(1-\delta)a_{\min}, \; \alpha_2 = \left(\frac{321-\sqrt{52541}}{202000} - \tilde{\delta} \right) \frac{2}{4+\nu^2+\sqrt{\nu^4+4\nu^2}+2\tilde{\delta}},$$

$$\delta = 1-(1-\delta_1)(1-\delta_2)\left(1 - \frac{202000\tilde{\delta}}{321-\sqrt{52541}}\right).$$

The result obtained is illustrated by means of the numerical integration of system (4) for different values of the damping coefficient ($\nu = 0.1, \nu = 1$) and the following initial conditions at $t_0 = 0$: $x_1(0) = 1$, $x_2(0) = x_3(0) = x_4(0) = x_5(0) = x_6(0) = 0$. Simulation results confirm that theoretical estimate (2) holds for large values of t:

$$\overline{\lim_{t\to+\infty}} \left(|x(t)|\sqrt{t} \right) \approx 21 \leq \frac{1}{\sqrt{\alpha_1}} \approx 61, \text{ for } \nu = 0.1; \; \overline{\lim_{t\to+\infty}} \left(|x(t)|\sqrt{t} \right) \approx 8 \leq \frac{1}{\sqrt{\alpha_1}} \approx 21, \text{ for } \nu = 1.$$

Conclusions

In this paper, the double pendulum with partial dissipation has been studied. Using the center manifolds theory and normal form method we have obtained the rate of decay for oscillations of such system in terms of its mechanical parameters. An explicit construction of a Lyapunov function is also proposed. Estimate obtained are confirmed by simulation results.

References

[1] Krasovskii N.N. *Stability of Motion*: *Applications of Lyapunov's Second Method to Differential Systems and Equations with Delay*, Stanford University Press, Stanford, 1963.
[2] Zubov V.I. *Methods of A.M. Lyapunov and their application*, Noordhoff, Groningen, 1964.
[3] Peiffer K., Savchenko A.Ya. On the asymptotic behavior of a passively stabilized system with one critical variable *Rend. Accad. Sci. Fis. Mat. Napoli*, Vol. 67 (4), pp. 157-168, 2000.
[4] Jakubczyk B., Zuyev A. Stabilizability conditions in terms of critical hamiltonians and symbols *Systems and Control Letters*, Vol. 54, pp. 597-606, 2005.
[5] Grushkovskaya V., Zuyev A. Asymptotic behavior of solutions of a nonlinear system in the critical case of q pairs of purely imaginary eigenvalues *Nonlinear Analysis: Theory, Methods & Applications,* Vol. 80, pp.156-178, 2013.
[6] Kamenkov G.V. *Stability and oscillations of nonlinear systems*, Nauka, Moscow, 1972 (in Russian).
[7] Molchanov A.M. Separation of motions and asymptotic methods in the theory of nonlinear oscillations *Soviet Math. Dokl.*, Vol. 2, pp.162-165, 1961.
[8] Molchanov A.M. Stability in the case of a neutral linear approximation, *Soviet Dokl. Akad. Nauk SSSR*, Vol. 141, pp.24-27, 1961 (in Russian).

Proceedings of the 4th International Conference on Nonlinear Dynamics
ND-KhPi2013
June 19-22, 2013, Sevastopol, Ukraine

Bifurcation Phenomena in Relaxation Auto-oscillation of Waveguiding Systems

Valery Gulyayev *, Olga Glushakova, Sergey Glazunov

Abstract
In this paper, based on a non-linear wave model, the problem about generation of self-induced vibrations in waveguiding systems is stated. The techniques for solution of the formulated non-linear differential equations are proposed. The cases of stationary and non-stationary variations of a perturbation parameter are considered. It is found that diapasons of its varying exist, where auto-oscillations of the system are generated. The stated problem is shown to be singularly perturbed, so, the auto-oscillations are of relaxation type with fast and slow motions, and nearly discontinuous velocities. It is found that the bifurcation states of the waveguiding system does not practically depend on its length but it is determined primarily by positions of extremum points in the diagram of friction function change. Typical regimes of non-stationary variations of the perturbation parameter are the possibility to obviate the states of self-induced vibrations by choosing special rates of its varying.
In practice, such phenomena might appear, for example, in towing a transport facility on a water or solid surface. Similar processes also occur in the devices of deep drilling.
These devices should be simulated by distributed systems transmitting longitudinal extension-compression or torsion waves.

Keywords
Waveguide1, relaxation autovibrations2, bifurcation birth3, bifurcation loss4, slow motion5, fast motion6

National Transport University, Kiev, Ukraine
***Corresponding author:** valery@gulyayev.com.ua

Introduction

Self-excitation of periodic vibrations in dynamical systems is one of the most widespread self-organization phenomena in nature. The simplest and clearest model, illustrating the process of mechanical autovibration generating, is the 1 DOF oscillator including a conveyor belt with a load on it and restrained by elastic weightless spring. Between the belt and load, the conditions of nonlinear frictional interaction are realized, which at certain constant values of the belt velocity v cause self-excitation of periodic reciprocating motions of the weight. But the considered model undergoes qualitative alterations if the spring is long (Fig. 1).

Figure 1. Model of an elastic waveguiding system

Then, its mass may be comparable or even larger than the body mass, it cases to be a simple elastic element, and becomes an elastic waveguide for transmitting longitudinal extension-compression waves. Such device should be simulated by distributed systems with vibrations possessing modes arranged in an ordered (wave) fashion. In practice, such phenomena may appear, for example, in towing a transport facility on a water or solid surface. Similar processes also occur in

devices of deep drilling. At the drill string extraction from the bore-hole cavity, the drill bit grates with its surface and the string begins to play the role of a waveguide. However, apparently the most distinctive auto-oscillations wave processes are generated in drilling the deep vertical bore-holes [1 - 6].

Then, as a result of non-linear frictional interaction between the rotating bit and the near bottom surface of the well, the bit begins to commit torsional vibrations and torsional waves begin to propagate along the drill string (Fig. 2). Analysis of these vibrations was performed on the basis of the non-linear model of torsional wave pendulum in [7 - 9]. As established, the auto-oscillations constitute non-damping periodic motions of a non-linear dissipative system which are sustained by external non-vibrational source of energy [10]. The major factor adding complexity to the problem is tat the equation describing this process belongs to the singularly perturbed type [11, 12] and has relaxation solutions [13].

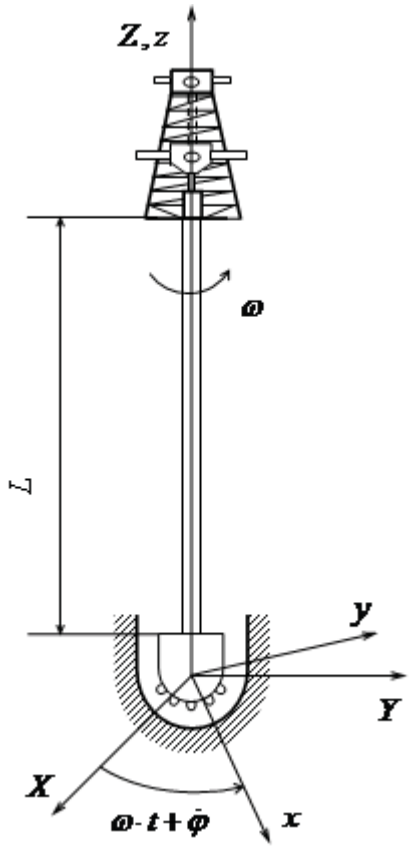

Figure 2. Model of a torsional waveguiding system

It can be concluded that analogous effects take place also in other self-vibrating systems. So, in this paper, the questions of analysis of stationary and transient self-oscillating processes in homogeneous and heterogeneous waveguides are considered. It is established that owing to the absence of the wave dispersion in the considered dynamic models, the transfer from study of a wave equation throughout the whole length of the waveguide to analysis of one non-linear differential equation with a delay argument can be fulfilled. It is shown that the auto-oscillations include segments of fat and slow motions inside every period. The self-excited oscillations proceed in the manner of quantized time.

The question of energy dissipation influence on the vibration modes is analyzed.

1. Equations of the Drill String Vibration

For the purpose of theoretically simulating the phenomenon of self-excitation of a waveguide vibration, the wave model of a dragging device with elastic cable of length L (Fig. 1) is used. By treating the elastic cable as an elastic waveguide and neglecting dissipative effects, its axial vibrations can be described by the wave equation

$$\rho A\frac{\partial^2 u}{\partial t^2}-EA\frac{\partial^2 u}{\partial x^2}=0 \tag{1}$$

where A is the cross-section area of the cable, ρ is its material density, and E is its elasticity modulus. Then the velocity of the longitudinal wave is equal to $\alpha=\sqrt{E/\rho}$.

Eq. (1) has the d'Alembert solution

$$u(x,t)=f(x-\alpha t)+g(x+\alpha t) \tag{2}$$

Here, $f(x-\alpha t)$, $g(x+\alpha t)$ are the arbitrary continuous functions.

Since the end $x=L$ is moving with constant velocity v, it can be considered as clamped one for the elastic displacement. Then

$$u(L,t)=0 \text{ or } f(L-\alpha t)+g(L+\alpha t)=0 \tag{3}$$

To deduce the boundary condition at the left end $x=0$, consider the dynamic equilibrium of the forces applied to it. So, one has

$$F^{in}+F^{fr}+F^{el}=0, \tag{4}$$

where $F^{in}=-m\ddot{u}$ is the inertia force acting on the body, $F^{fr}=F^{fr}(v+\dot{u})$ is the friction force formed between the body and horizontal surface, it will be defined later. Here, the dot over a symbol denotes derivative with respect to time.

After performing some substitutions and transformations, Eq. (4) will look like to the following non-linear relationship

$$m\left[\ddot{f}(-\alpha t)-\ddot{f}(-\alpha t+2L)\right]+\frac{EA}{\alpha}\left[\dot{f}(-\alpha t)-\dot{f}(-\alpha t+2L)\right]-F^{fr}(v+\dot{u})=0. \tag{5}$$

Here, $f=f(0,t),\ u=u(0,t)$.

A distinctive characteristic of this equation is the small value of coefficient J before the second derivative $\ddot{f}(-\alpha t)$ in comparison with the coefficients before the other unknown variables. Because of this, the formulated problem belongs to the class of singularly perturbed and that is why its periodic solutions are relaxation or have the shapes of saw tooth curves.

The foregoing example of vibration self-excitation in the elongated system, permitting the passage of elastic longitudinal waves, is rather a multi-purpose formal problem which can be easily rearranged for analysis of similar processes in mechanical or electric (electronic) waveguiding systems. Indeed, inasmuch as only several parameters characterize the treated waveguide system, it does not present a real challenge to perform corresponding replacements of their values for other mechanical or electric system. Among them are the mass m, wave velocity α, elasticity modulus E, acoustic stiffness $n=\alpha\rho A$ and friction function $F^{fr}(v+\dot{u})$. So, one might expect that auto-oscillations processes in different mechanical and physical waveguide systems exhibit the properties of similarity and the regularities of their manifestation, established for one of them, are typical for others.

2. Results of Computer Simulation

If the problem on torsional auto-vibration of a waveguide represented by a drill string is considered, then longitudinal velocity α should be substituted by transversal velocity $\beta=\sqrt{G/\rho}$ and displacement $u(x,t)$ by torsion angle $\varphi(x,t)$

The analysis of the bit dynamics was performed by integrating appropriate equation by the Runge-Kutta method with the initial conditions $\varphi(0)=0$, $\dot{\varphi}(0)=0$ for different values of ω. The integration step was selected to be $\Delta t = 7.769\cdot 10^{-6}\ s$.

Firstly, consider the homogeneous drill string 1000 m in length. The characteristic parameters used for its analysis are selected as follows: $G=8.077\cdot 10^{10}\ Pa$, $\rho=7.8\cdot 10^{3}\ kg/m^3$. External and internal radii of the tube cross-section are $r_1=0.0841m$ and $r_2=0.0741m$, so $I=3.12\cdot 10^{-5}\ m^4$.

One of the main features, influencing on the process of the bit torsion vibration, is the law of the friction moment M^{fr} dependence on the total velocity $\omega+\dot{\varphi}$ of its rotation. The shape of function $M^{fr}(\omega+\dot{\varphi})$ is determined by many factors what is more, the values of their parameters vary during the drilling process. So, it is conceivable that no universal functions of this kind can be chosen for analysis of the system dynamics. The most commonly encountered relationships between M^{fr} and $\omega+\dot{\varphi}$ are represented by the Coulomb friction law shown in [5,9]. It is used in our investigation for analysis of general regularities of auto-oscillations proceedings.

The calculation results permit us to formulate some regularities. On the one hand, in the process of functioning, the drill string can be either in the states of stationary rotation or of torsional self-induced elastic oscillation, depending on the chosen regime of drilling. As this takes place, the value ω_b of the angular velocity ω corresponding to the bifurcation state of the limit cycle birth equals the value $\omega=2.85\ rad/s$, which conforms to the minimum point of the $M^{fr}(\omega+\dot{\varphi})$ diagram. The regimes of motion with $\omega<\omega_b$ are characterized by the stationary rotation without any oscillation when the system changes from its initial state $\varphi(0)=0$, $\dot{\varphi}(0)=0$ to some quasi-static equilibrium state $\varphi(t)=\varphi_{st}$, $\dot{\varphi}(t)=0$ and self-induced vibrations do not take place. But during the system transition from outside to inside this diapason through the value $\omega=\omega_b$, the Hopf bifurcation occurs and limit cycles appear together with the unstable stationary solutions $\varphi(t)=const$, $\dot{\varphi}(t)=0$.

Figs 3 and 4 present φ and $\dot{\varphi}$ as functions of t for the value $L=2000m$ at $\omega_b=0.71\,rad/s$ in the time segment $0\le t\le 400s$. The motion process begins from the state $\varphi(0)=0$, $\dot{\varphi}(0)=0$ and steeply rearranges to periodic oscillations, which acquire relaxation character.

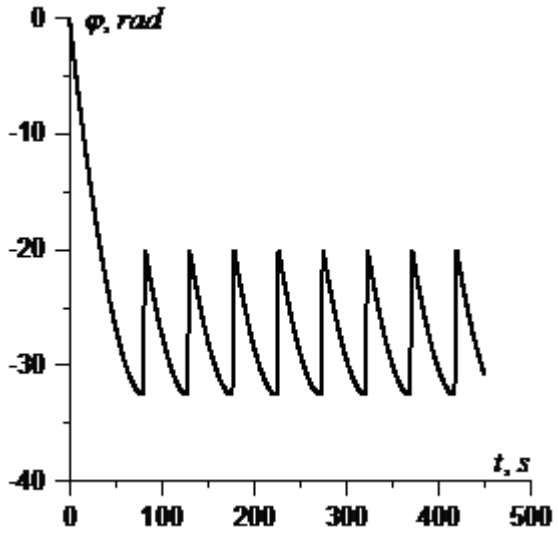

Figure 3. The diagram of relaxation change of the $\varphi(t)$ function at the torsion waveguide

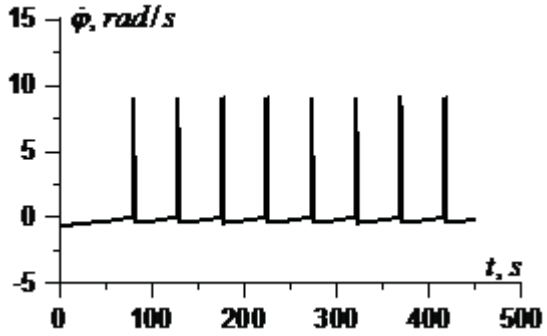

Figure 4. The $\dot{\varphi}(t)$ function diagram for the torsion waveguide

The diagrams testify that use of the torsion waveguide model for investigation of drill string vibration self-excitation permitted not only to reflect general regularities of limit cycle birth bifurcations, but also to find radically new, subtler feature, unique only to wave systems. The feature derives from delay of the elastic moment action on the bit and it is associated with formation of the so-called quantized time with the resulting effect of constant angular velocity staying during time segment $\Delta\tau$ [8]. It is equal to the time duration of the torsion wave passing the path from the bit to the upper end and backward

$$\Delta\tau = 2L/\beta . \tag{6}$$

As a consequence of this the $\dot{\varphi}(t)$ function acquires additional small-sized quasi-discontinuities with small steps in time $\Delta\tau = 2L/\beta$ [7 - 9]. They are not distinguishable in the chosen scale.

The phenomenon found is analogous to the phenomenon of space-time quantization in physics, where some fundamental (minimal) length l and time quantum $\Delta\tau = l/c$ are introduced. Here c is the relativistic velocity. In our case the "fundamental length" is $l = 2L$ and the "relativistic velocity c" equals β.

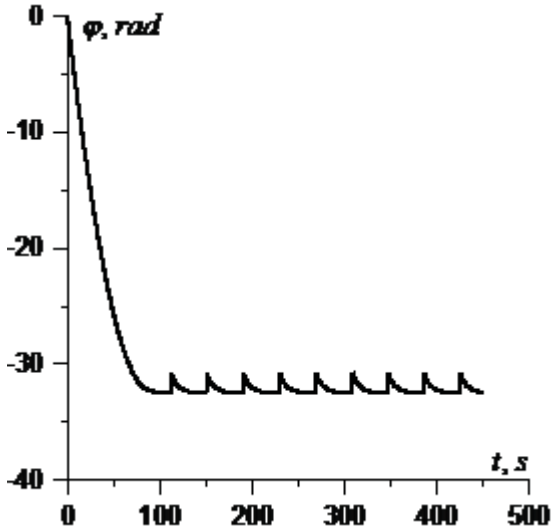

Figure 5. Auto-oscillations n of elastic torsion pendulum in dissipative medium

It should be pointed out the established effects of auto-oscillations generation are typical for waveguide systems transmitting non-dispersive waves. They are described by equations of type (1). However, in practice, these equations are not met in pure form because in real systems there always is the energy dissipation at the expense of the friction forces existence. For example, in the bore-hole the drill string is immersed in washing liquid, so its torsion vibrations are described by equation

$$\rho I_z \frac{\partial^2 \varphi}{\partial t^2} + k \frac{\partial \varphi}{\partial t} - GI_z \frac{\partial^2 \varphi}{\partial z^2} = 0, \tag{7}$$

where k is the dissipation coefficient.

The k coefficient depends on the viscosity of the washing liquid, its temperature and the clearance between the DS and bore-hole surfaces.

In this event, the foregoing techniques are not valid and the constitutive equations should be numerically integrated by numerical methods. In Fig.5 the diagram of a bit vibration is shown for the value $k = 50\, N \cdot s$.

As the calculations testify, in the cases of small k, the auto-oscillations properties of the system and modes of its torsions retain, though their quantized character is lost. But with the enlargement of k, the motion separation into slow and fast ones becomes more discernible. As this takes place, the amplitudes of the auto-oscillations become smaller.

References

[1] Brett J.F. The genesis of torsional drill string vibrations *SPE Drill. Eng.,* Vol. 7, pp. 168-174, 1992.

[2] Challamel N. Rock destruction effect on the stability of a drilling structure *J. Sound Vibr*., Vol. 233 (2), pp. 235-254, 2000.

[3] Leine R.I., Campen D.H. and Keultjes W.J.G. Stick-slip whirl interaction in drill string dynamics *J. Vibr. Acoust*., Vol. 124, pp. 209-220, 2002.

[4] Mihajlovic N., van de Wouw N., Hendriks M. P. M. and Nijmeijer H. Friction-induced limit cycling in flexible rotor systems: An experimental drill-string set-up *Nonlin. Dyn*., Vol. 46 (3), pp. 273-291, 2006.

[5] Tucker R.W. and Wang C. On the effective control of torsional vibrations in drilling systems *J. Sound Vibr.*, Vol. 224 (1), pp. 101-122, 1999.

[6] Zamanian M., Khadem S.E. and Ghazavi M.R. Stick-slip oscillations of drag bits by considering damping of drilling mud and active damping system *J. Petrol. Sci. Eng.*, Vol. 59, pp. 289-299, 2007.

[7] Gulyayev V.I., Glushakova O.V. Large-scale and small-scale self-excited torsion vibrations of homogeneous and sectional drill strings *Interact. Multiscale. Mec*., Vol. 4 (4), pp. 291 – 311, 2011.

[8] Gulyaev V.I., Glushakova O.V. and Hudoliy S.N. Quantized attractors in wave models of torsion vibrations of deep-hole drill strings *Mechanics of Solids*, Vol. 45 (2), pp. 264-274, 2010.

[9] Gulyayev V.I., Hudoliy S.N., Glushakova O.V. Simulation of torsion relaxation auto-oscillations of drill string bit with viscous and Coulombic friction moment models *J. Multi-body Dyn.*, Vol. 225, pp. 139 – 152, 2011.

[10] Hassard B.D., Kazarinoff N.D. and Wan Y.-H. Theory and Applications of Hopf Bifurcation. Cambridge University Press, Cambridge, London, New York, New Rochelle, Melbourne, Sydney, p. 367, 1981.

[11] Chang K.W. and Howes F.A. Nonlinear Singular Perturbation Phenomena *Springer-Verlag*, New York, Berlin, Heidelberg, Tokyo, p. 245, 1984.

[12] Shishkin G.I. and Shishkina L.P. Difference Methods for Singular Perturbation Problems Russian Academy of Science, Ekaterinburg, CRC Press Taylor & Francis Group Boca Raton, USA, 408 p., 2009.

[13] Mishchenko E.F. and Rozov N.H. Differential Equations with Small Parameter and Relaxation Vibrations Nauka, Moscow, 247 p. (in Russian), 1975.

Proceedings of the 4th International Conference on Nonlinear Dynamics
ND-KhPI2013
June 19-22, 2013, Sevastopol, Ukraine

Double Triggers of the Coupled Singularities in Rheonomic System Nonlinear Dynamics

Katica R. (Stevanović) Hedrih[1]

Abstract
Properties and phenomena in nonlinear dynamics of the rheonomic systems with no ideal constraints of the **Amontons-Coulomb's friction** type are considered. Starting from differential equation of a known rheonomic system nonlinear dynamics with ideal constraints and trigger of coupled singularities, corresponding double differential equations of the corresponding rheonomic systems with no ideal constraints of the **Amontons-Coulomb's friction** type are derived. For this no ideal rheonomic system nonlinear dynamics, triggers of coupled one side singularities as well as **double trigger of coupled singularities and coupled one side singularities in phase portraits** are identified. By use linearization of double differential equation around one side singularities, properties of local dynamics of considered no ideal rheonomic system are investigated.

Keywords
rheonomic, nonlinear, friction, trigger, one side singular point

[1] Mathematical Institute SANU, Belgrade and Faculty of Mechanical Engineering University of Niš, Serbia
*** Corresponding author:** khedrih@eunet.rs,khedrih@sbb.rs

Introduction

We start with one of possible definitions of a trigger of coupled singularities (see Ref. [5]), which contain coupled, two stable centre type and one unstable saddle type singularities. Also, in phase portrait which contain trigger of coupled singularities exists a homoclinic orbit in the form of number "eight". These singularities can be corresponding to stable or unstable equilibrium positions or to relative, dynamic, equilibrium position on the system nonlinear dynamics with nonlinear properties different type. Also, change of a bifurcation parameter (see Ref. [2]), of the nonlinear system can be source for existence, or no, of a trigger of coupled singularities. In source is a bifurcation phenomenon.

In the systems with the changes of some kinetic parameters of the system dynamics, especially oscillations, the process of losing stability of one static equilibrium position or relative dynamic equilibrium position is followed with appearance of two close stable statically or relative dynamical equilibrium positions (see Refs. [1-11] and [14]). Also, these two newly appeared singularities with the previous stable equilibrium position, which lost its stability, make a trigger of coupled singularities (see Refs. [5] and [7-8]). Also, a trigger of coupled singularities, with corresponding choice of kinetic parameters of system dynamics, can be degenerate into one threefold (triple) singular point, corresponds to stable equilibrium position or stable relative dynamic equilibrium position.

Our attention, now is focused to the selected group of special type of triggers of coupled singularities caused by discontinuities of kinetic parameter properties and identified in the rheonomic system with no ideal constraints and contact with friction. These discontinuities are caused by Amontons-Coulomb's type friction appearing between coupled elements of the mechanical system with relative motion in relation one to other.

By using examples of the heavy mass particle motion along rotating rough curvilinear circle lines about eccentrically positioned axis, corresponding differential double equation is derived and also, corresponding trigger of coupled singularities of the phase portraits are considered.

1. Description of the first rheonomic system nonlinear dynamics with friction

Starting from basic and very known rheonomic system: A heavy mass particle moving with ideal contact along rotating circle about vertical central axis with constant angular velocity, presented in very known book [1], as well as corresponding models in Refs. [7, 9], a double differential equation of like sane rheonomic system, but with no ideal constraint of **Amontons-Coulomb's friction** type (see Figure 1.a*) is derived in the following form:

$$\ddot{\varphi} \pm \mu\dot{\varphi}^2 + \Omega^2\left[\left\langle \lambda - \cos\varphi \right\rangle \sin\varphi - \varepsilon\cos\varphi \pm \mu\lambda\cos\varphi \pm \mu\left\langle \varepsilon + \sin\varphi \right\rangle \sin\varphi\right] \pm \mu_1 2\dot{\varphi}\Omega\cos\varphi = 0 \quad \begin{cases} \dot{\varphi} > 0 \\ \dot{\varphi} < 0 \end{cases} \quad (1)$$

where φ is generalized independent coordinate of relative position of mass particle on circle line, $\lambda = \frac{g}{R\Omega^2}$, $\mu = tg\alpha$ coefficient of the friction between mass particle and cylindrical circle line surface in real constructions, $\mu_1 = tg\alpha_1$ coefficient of the friction between mass particle and circle line surface in real constructions, $\varepsilon = \frac{e}{R}$ axis eccentricity, $\theta = \Omega t$, rheonomic coordinate of circle rotation, Ω angular velocity of the vertical eccentrically positioned axis of circle rotation. For detailed explanations of contacts rough surfaces between mass particle and circle line in real construction of considered model and corresponding friction forces see Refs. [12]. [13] and [11].

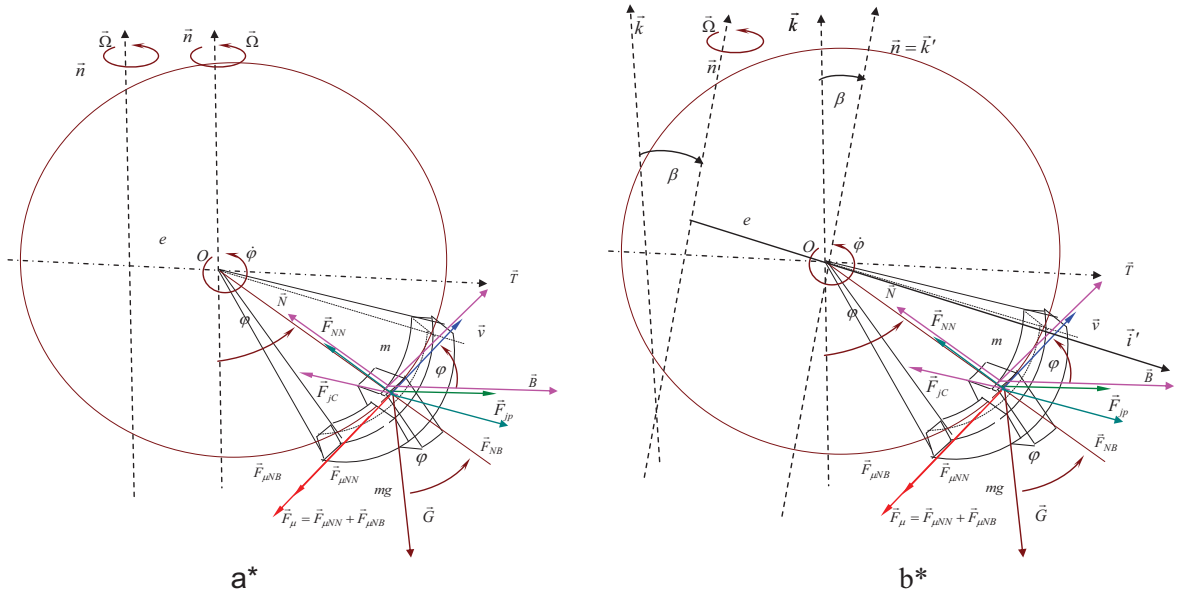

Figure 1. Two models of the rheonmic system with no ideal constraint of Amontons-Coulomb's friction type: a* - vertical eccentrically positioned axis of circle rotation and b* - skew eccentrically positioned axis of circle rotation

For the model presented in Figure 1.a* normal reactions $\vec{F}_N$ in radial direction on the circle and binorla reaction $\vec{F}_B$ in binormal direction orthogonal to the circle surface are:

$$\vec{F}_N = \left\langle -mR\left[\dot{\varphi}^2 - \dot{\theta}^2\sin\varphi\left(e + R\sin\varphi\right)\right] + mg\cos\varphi \right\rangle \vec{N} \quad (2)$$

$$\vec{F}_B = \left[-2mR\dot{\varphi}\dot{\theta}\cos\varphi + m\left(e + R\sin\varphi\right)\ddot{\theta}\right]\vec{j}' \quad (3)$$

Amontons0Coulomb's friction type friction force $\vec{F}_\mu = \left(-\mu F_N - \mu_1 F_B\right)\vec{T}sign\vec{v}_r$ (see Figure 1. a*) is in the following form:

$$\vec{F}_{\mu}=-\Big\langle \mu\Big|-mR\left[\dot{\varphi}^2-\dot{\theta}^2\sin\varphi\left(e+R\sin\varphi\right)\right]+mg\cos\varphi\Big|+\mu_1\Big|-2mR\dot{\varphi}\dot{\theta}\cos\varphi+m\left(e+R\sin\varphi\right)\ddot{\theta}\Big|\Big\rangle\vec{T}\,sign\vec{v}_r \quad (4)$$

2. Description of the second rheonomic system nonlinear dynamics with friction

Second no ideal rheornomic system is presented in Figure 1.b*. This system is with rotating circle about eccentrically and skew positioned axis of rotation, for angle β with respect to the vertical and contact between circle and heavy mass particle is no ideal, with **Amontons-Coulomb's friction** type. For this model, presented in Figure 1.b*, normal reactions $\vec{F}_N$ in radial direction on the circle and binorla reaction $\vec{F}_B$ in binormal direction orthogonal to the circle surface are in the form:

$$\vec{F}_N=\Big\langle -mR\left[\dot{\varphi}^2-\dot{\theta}^2\sin(\varphi+\beta)\left\langle\varepsilon+\sin(\varphi+\beta)\right\rangle\right]+mg\left[\cos\beta\cos(\varphi+\beta)+\cos\theta\sin\beta\sin(\varphi+\beta)\right]\Big\rangle\vec{N} \quad (5)$$

$$\vec{F}_B=\Big[-2mR\dot{\varphi}\dot{\theta}\cos(\varphi+\beta)+m\left\langle e+R\sin(\varphi+\beta)\right\rangle\ddot{\theta}-mg\sin\theta\sin\beta\Big]\vec{j}' \quad (6)$$

Amontons-Coulomb's friction type $\vec{F}_{\mu}=\left(-\mu F_N-\mu_1F_B\right)\vec{T}sign\vec{v}_r$ (see Figure 1. b*) is in the form

$$\begin{aligned}\vec{F}_{\mu}=&-\Big\langle \mu\Big|-mR\left[\dot{\varphi}^2-\dot{\theta}^2\sin(\varphi+\beta)\left\langle\varepsilon+\sin(\varphi+\beta)\right\rangle\right]+mg\left[\cos\beta\cos(\varphi+\beta)+\cos\theta\sin\beta\sin(\varphi+\beta)\right]\Big\rangle\vec{T}\,sign\vec{v}_r\\&-\Big\langle \mu_1\Big|-2mR\dot{\varphi}\dot{\theta}\cos(\varphi+\beta)+m\left\langle e+R\sin(\varphi+\beta)\right\rangle\ddot{\theta}-mg\sin\theta\sin\beta\Big|\Big\rangle\vec{T}\,sign\vec{v}_r\end{aligned} \quad (7)$$

For this second rheonomic system dynamics, with skew positioned axis of circle rotation by angle β to the vertical, presented in Figure 1.b*, and with no ideal constraint of **Amontons-Coulomb's friction** type, double differential equation is derived in the following form:

$$\begin{aligned}&\ddot{\varphi}\pm\mu\dot{\varphi}^2+\Omega^2\left\langle\frac{g}{\Omega^2R}\cos\beta-\cos(\varphi+\beta)\right\rangle\sin(\varphi+\beta)-\varepsilon\Omega^2\cos(\varphi+\beta)\pm\mu\frac{g}{R}\cos\beta\cos(\varphi+\beta)\pm\\&\pm\mu\Omega^2\left\langle\varepsilon+\sin(\varphi+\beta)\right\rangle\sin(\varphi+\beta)\pm\mu_1 2\dot{\varphi}\Omega\cos(\varphi+\beta)=\\&=\frac{g}{R}\left[\cos(\varphi+\beta)\mp\mu\sin(\varphi+\beta)\right]\sin\beta\cos\Omega t\mp\mu_1\frac{g}{R}\sin\Omega t\sin\beta\quad\begin{cases}\dot{\varphi}>0\\\dot{\varphi}<0\end{cases}\end{aligned} \quad (8)$$

3. One side singular points and trigger of coupled singularities

For beginning, let introduce that $\mu=tg\alpha$ and $\mu_1=0$, then previous double differential equations (1) and (8) is possible rewrite in the following forms:

$$\begin{aligned}&\frac{d\varphi}{dt}=v\\&\frac{dv}{dt}=\mp\frac{1}{\cos\alpha}\sin\alpha v^2-\frac{1}{\cos\alpha}\Omega^2\lambda\sin(\varphi\pm\alpha)+\frac{1}{\cos\alpha}\varepsilon\Omega^2\cos(\varphi\pm\alpha)+\frac{1}{\cos\alpha}\Omega^2\cos(\varphi\pm\alpha)\sin\varphi\quad\begin{cases}\dot{\varphi}>0\\\dot{\varphi}<0\end{cases}\end{aligned} \quad (9)$$

and

$$\begin{aligned}&\frac{d\varphi}{dt}=v\\&\frac{dv}{dt}=\mp\frac{1}{\cos\alpha}\sin\alpha v^2-\frac{1}{\cos\alpha}\Omega^2\lambda\cos\beta\sin(\varphi+\beta\pm\alpha)+\frac{1}{\cos\alpha}\varepsilon\Omega^2\cos(\varphi+\beta\pm\alpha)+\\&\quad+\frac{1}{\cos\alpha}\Omega^2\cos(\varphi+\beta\pm\alpha)\sin(\varphi+\beta)+\frac{1}{\cos\alpha}\Omega^2\lambda\cos(\varphi+\beta\mp\alpha)\sin\beta\cos\Omega t\quad\begin{cases}\dot{\varphi}>0\\\dot{\varphi}<0\end{cases}\end{aligned} \quad (10)$$

suitable for analysis and comparing singularities and triggers of coupled singularities as well as triggers of coupled one side singularities.

3. 1. Singular points and trigger of coupled singularities in ideal system

For first, let to made a list of singular points of corresponding ideal rheonomic system by introducing in previous systems, (9) and (10), that is $\mu = tg\alpha = 0$ and central axis of circle rotation, $\varepsilon = 0$, which are known in listed Refs. [1], [11] and [7-8]. For $\alpha = 0$ singylar points denoted by φ_{0s} are $(\varphi_{0s}, v = 0)$ where:

$$tg\varphi_{0s} - \lambda \sin\varphi_{0s} = 0 \;\Rightarrow\; \sin\varphi = 0 \;\Rightarrow\; \varphi_{0s} = s\pi,\ s = 1,2,3,4,... \tag{11}$$

$$1 - \lambda\cos\varphi_{0s} = 0 \;\Rightarrow\; \varphi_{0s} = \arccos\lambda \pm 2s\pi,\ s = 1,2,3,4,... \Rightarrow \text{ for the case that } |\lambda| \le 1 \tag{12}$$

For the case that $|\lambda| \le 1$ in the phase portrait of this ideal rheonomic system dynamics a trigged of coupled singularities with homoclinic orbit in the form of number "eight" exists.

If axis of the circle rotation is eccentrically positioned, $\varepsilon \neq 0$, then singular points $(\varphi_{\varepsilon 0s}, v = 0)$ of ideal rheonomic system nonlinear dynamics are defined as roots of the following characteristic nonlinear transcendent equation:

$$v = 0, \quad -\lambda tg\varphi_{\varepsilon 0s} + \varepsilon + \sin\varphi_{\varepsilon 0s} = 0 \tag{13}$$

For this model presented in Figyre 1.a*, corresponding phase portrait of nonlinear dynamics is presented in Figure 2. a*. From this phase portrait singular points and trigger of coupled singularities are presented. Also, homoclinic orbits in the form of number "eight" are visible.

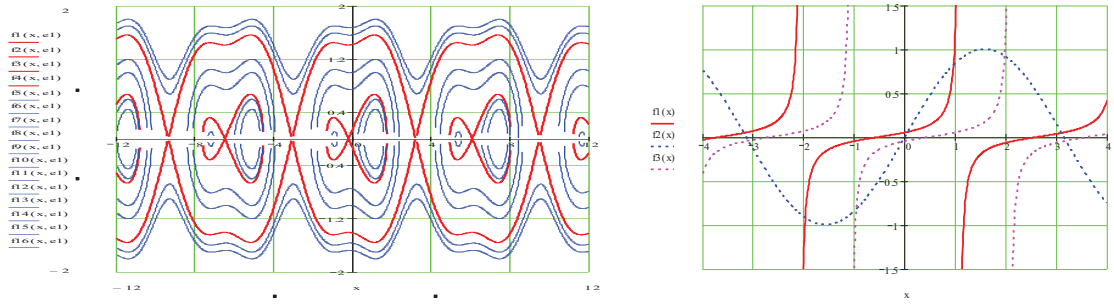

a* b*

Figure 2. a* Phase portrait of a model of the rheonmic system dynamics with ideal constraints and vertical eccentrically positioned axis of circle rotation and b* Graphical presentation of roots of characteristic equation for obtaining singular point of nonlinear dynamics of no ideal system correspond to ideal system with phase portrait in a*.

3. 2. One side singular points and trigger of coupled singularities in rheonomic system with vertical axis of circle rotation and Amontons-Coulomb's friction

For the rheonomic system with no ideal constraint of **Amontons-Coulomb's friction** type (see Figure 1. a*) and vertical axis of circle rotation, conditions for obtaining singular points are:

$$v_s = 0$$

$$-\lambda\sin(\varphi_s \pm \alpha) + \cos(\varphi_s \pm \alpha)\sin\varphi_s + \varepsilon\cos(\varphi_s \pm \alpha) = 0 \quad \begin{cases} \dot{\varphi} > 0 \\ \dot{\varphi} < 0 \end{cases} \tag{14}$$

For the case that eccentricity of the axis of circle rotation is $\varepsilon = 0$, previous conditions are: $\lambda tg(\varphi_s \pm \alpha) - \sin\varphi_s = 0 \quad \begin{cases} \dot{\varphi} > 0 \\ \dot{\varphi} < 0 \end{cases}$. Roots of this characteristic equation are one side singular points of nonlinear dynamics of no ideal system correspond to ideal system with phase portraits in Figure 2.a*

for $\varepsilon = 0$ graphically is presented in Figure 2. b*. From this figure it is visible that exists two sections between curves $f(\varphi_s) = \lambda tg(\varphi_s \pm \alpha)$ $\begin{cases} \dot{\varphi} > 0 \\ \dot{\varphi} < 0 \end{cases}$ and $f(\varphi_s) = \sin\varphi_s$ depending on direction of velocity of mass particle motion.

Taking into account that angle of the friction α is small, and that form Figure 2.b* it is visible that there are small distance between cross sections of previous listed functions for ideal and no ideal cases of the system nonlinear dynamics, we can use the following approximation: By use development of the previous functions in Taylor series around $\varphi_{\varepsilon 0s}$ and kipping only linear parts, taking denotation $\varphi_s \approx \varphi_{\varepsilon 0s} + s$

$$f(\varphi_s) = \lambda tg(\varphi_{\varepsilon 0s} + s \pm \alpha_0) \approx \lambda tg\varphi_{\varepsilon 0s} + \lambda \frac{1}{\cos^2 \varphi_{\varepsilon 0s}} (s \pm \alpha_0) \quad \begin{cases} \dot{\varphi} > 0 \\ \dot{\varphi} < 0 \end{cases}$$

$$f(\varphi_s) = \sin(\varphi_{\varepsilon 0s} + s) + \varepsilon \approx \sin\varphi_{\varepsilon 0s} + \varepsilon + s\cos\varphi_{\varepsilon 0s} \quad \begin{cases} \dot{\varphi} > 0 \\ \dot{\varphi} < 0 \end{cases} \tag{15}$$

and taking into account condition (13) previous characteristic equation rewritten in linear approximation give a double relation-expression of difference-distance between position of singular point of ideal and two one side singular points of no ideal system dynamics in the following form:

$$s \approx \frac{\mp \alpha\lambda\cos\varphi_{\varepsilon 0s}}{\left\langle \lambda - \cos^3 \varphi_{\varepsilon 0s} \right\rangle} \quad \begin{cases} \dot{\varphi} > 0 \\ \dot{\varphi} < 0 \end{cases} \tag{16}$$

For one side syngular points of rheonomic system dynamics with friction and vertical eccentric axis of circle rotation, around singular point $\varphi_{\varepsilon 0s}$ of system nonlinear dynamics with ideal contact of mass particle and circle, for $\lambda > \cos^3 \varphi_{\varepsilon 0s}$ difference between singular points in the first approximation of considered ideal and no ideal system dynamics is $s \approx \frac{\mp \alpha\lambda\cos\varphi_{\varepsilon 0s}}{\left\langle \lambda - \cos^3 \varphi_{\varepsilon 0s} \right\rangle}$ $\begin{cases} \dot{\varphi} > 0 \\ \dot{\varphi} < 0 \end{cases}$ and for $\lambda < \cos^3 \varphi_{\varepsilon 0s}$ this difference is $s \approx \frac{\pm \alpha\lambda\cos\varphi_{\varepsilon 0s}}{\left\langle \cos^3 \varphi_{\varepsilon 0s} - \lambda \right\rangle}$ $\begin{cases} \dot{\varphi} > 0 \\ \dot{\varphi} < 0 \end{cases}$. This result is approximate.

For one side syngular points of rheonomic system dynamics with friction, around zero singular point of system nonlinear dynamics with ideal contact of mass particle nad circle for $\lambda > 1$ difference between singular points in the first approximation of considered ideal and no ideal system dynamics is $s \approx \frac{\pm \lambda\alpha}{(\lambda - 1)}$ and for $\lambda < 1$ this difference is $s \approx -\frac{\pm \lambda\alpha}{(1 - \lambda)}$.

Then it is visible, that singular points presented be expression in first approximation:

$$\varphi_s \approx \varphi_{\varepsilon 0s} + \frac{\pm \alpha\lambda\cos\varphi_{\varepsilon 0s}}{\left\langle \cos^3 \varphi_{\varepsilon 0s} - \lambda \right\rangle} \quad \begin{cases} \dot{\varphi} > 0 \\ \dot{\varphi} < 0 \end{cases} \tag{17}$$

Existence of one side singular point depending of direction of mass particle velocity during the motion and also existence of "half singular points" – "one side " singular points around singular point of corresponding system with ideal contact between mass particle and circle is identified. Then, these two "stable or unstable one side singular points" of the rheonomic system with Amontons-Coulomb's type friction around corresponding singular point of corresponding rheonomic system dynamics with ideal contacts present a trigger of coupled singularities. This trigger of coupled "stable or unstable one side singular points" is caused by Amontons-Coulomb's type friction in the system dynamics.

In the case that singular point of the ideal system is unstable saddle type singular point, then this trigger of the coupled "one side singularities" is unstable. In the case that singular point of the ideal system is stable centre type singular point, then this trigger of the coupled "one side singularities" is stable. In the case that a trigger of coupled singularities exists in nonliner dynamics of ideal system, then around each of the singular points of this trigger exists corresponding number of stable or unstable trigger of the coupled "one side singularities".

Conclusions

For this no ideal rheonomic system nonlinear dynamics, trigger of coupled "one side singularities" as well as **double trigger of coupled singularities and coupled "one side singularities" in phase portraits** are identified and conditions for their existence or appearance are investigated. By use linearization of double differential equation around one side singularities, properties of local dynamics of considered no ideal rheonomic system are investigated, but no pages to present these results. Next step of investigation was focused to the motion of a heavy mass particle moving, with no ideal contact, along rotating rough circle, with constant angular velocity, about axis skew positioned to the vertical for the case of the central axis as well as eccentric axis. Double nonlinear noautonomous differential equations are obtained for describing rheononlinear dynamics of this defined rheonomic system, but no pages to present these results.

Influence of the no ideal constraint of **Amontons-Coulomb's friction** type to the nonlinear dynamics of the rheonomic system and corresponding three geometric-parametric analysis of the existence of double triggers of coupled "one side singularities" are investigated, but no pages to present these results.

Acknowledgments

Parts of this research were supported by the Ministry of Sciences and Technology of Republic of Serbia through Mathematical Institute SANU Belgrade Grant ON174001 "Dynamics of hybrid systems with complex structures, Mechanics of materials" and Faculty of Mechanical Engineering University of Niš.

References

[1] Andronov A.A., Vitt A.A., Haykin S.E. *Teoriya Kolebaniy,* Nauka, Moscow, 1981 (in Russian).
[2] Guckenheimer J., Holmes Ph. Nonlinear Oscillations, Dynamical Systems, and Bifurcations of Fields, Springer-Verlag, 1983.
[3] Hedrih (Stevanović) K. *The Vector Method of the Heavy Rotor Kinetic Parameter Analysis and Nonlinear Dynamics*, University of Niš, 2001.
[4] Hedrih (Stevanović) K. Nonlinear Dynamics of a Heavy Material Particle Along Circle which Rotates and Optimal Control**,** in *Chaotic Dynamics and Control of Systems and Processes in Mechanics* (Eds: G. Rega, and F. Vestroni), pp. 37-45. IUTAM Book, Series *Solid Mechanics and Its Applications* (Ed. by G.M.L. Gladwell), Springer**,** XXVI, 2005.
[5] Hedrih (Stevanović) K. A trigger of coupled singularities, *Meccanica***,** Vol.39, No. 3, pp. 295-314, 2004.
[6] Hedrih (Stevanović K. Dynamics of coupled systems, *Nonlinear Analysis: Hybrid Systems,* Vol. 2, Issue 2,June 2008, pp. 310-334.
[7] Hedrih (Stevanović) K. On rheonomic systems with equaivalent holonomic conservative system, *Proc. of the Int. Conf. ICNM-IV. Nonlinear Dynamics* (Ed. by W. Chien and all), Shanghai,. pp. 1046-1054, 2002.
[8] Hedrih (Stevanović) K. On rheonomic systems with equivalent holonomic conservative systems applied to the nonlinear dynamics of the Watt's regulator, *Proc. of the Eleventh World Congress in Mechanism and Machine Sciences, IFToMM*, Vol. 2, China Machine Press, Tianjin, China, pp. 1475-1479, 2004.
[9] Hedrih (Stevanović) K. Free and forced vibration of the heavy material particle along line with friction: Direct and inverse task of the theory of vibrorheology, *Proc. of the 7th EUROMECH Solid Mechanics Conference* (Ed. By J. Ambrósio et.al.), Lisbon, Portugal, pp.1-20, 2009.

[10] Hedrih (Stevanović) K**.** Vibrations of a heavy mass particle moving along a rough line with friction of coulomb type, Int. J. of Nonlinear Sciences & Numerical Simulation 10(11), pp. 1705-1712, 2009.
[11] Hedrih (Stevanović) K. Discontinuity of kinetic parameter properties in nonlinear dynamics of mechanical systems, Keynote Invited Lecture *Proc. of the 9th Brazilian Conference on Dynamics Control and their Applications*, Serra Negra, Brasil, 2010, pp. 8-40, 2010.
[12] Rašković D. *Teorija Oscilacija (Theory of Oscillations)*, Naučna Knjiga, 1952.
[13] Rašković P. D., Analitička Mehanika (Analytical Mechanics), Mašinski fakultet Kragujevac, 1974.
[14] Stoker, J. J. *Nonlinear Vibrations,* Interscience Publishers, New York, 1950.

Proceedings of the 4th International Conference on Nonlinear Dynamics
ND-KhPI2013
June 19-22, 2013, Sevastopol, Ukraine

Nonlinear Normal Modes In Systems with Pendulum Absorbers

Anna A. Klimenko[1], Yuri V. Mikhlin[1*]

Abstract
Dynamics of the 2-DOF system containing the pendulum absorber and the 3-DOF non-ideal system with the pendulum absorber is considered by using the nonlinear normal modes theory and the asymptotic-numerical procedures. The localized and non-localized vibration modes are constructed. The vibration modes stability is analyzed by different methods. The nonlinear normal modes approach and the modified Rauscher method are used to construct forced vibration modes in the 2-DOF system with the pendulum absorber.

Keywords
pendulum systems, nonlinear normal modes

[1]*Dept. of Applied Mathematics, National Technical University "KPI", Kharkov, Ukraine*
*** Corresponding author:** muv@kpi.kharkov.ua

Introduction

Pendulum systems are classical models on nonlinear dynamics. Numerous applications of such systems are known in engineering, in particular, in vibro-absorption problems [1,2]. Here the Kauderer-Rosenberg concept of nonlinear normal modes (NNMs)[3-7] is used to construct the NNMs and analyze their stability for two-DOF system containing the pendulum absorber. The NNMs approach and the modified Rauscher method [5-7,8] are used too to construct forced vibrations modes of this system under external periodic excitation.

The dynamics of a structure excited by a non-ideal excitation device with limited power capacity is considered. In such system the influence of the structure to the excitation device must be taken into account. In the non-ideal systems a jump to large amplitude vibrations in the resonance domain, that is the Sommerfeld effect [9], can be observed. Analytical description of this effect was first made by V.O.Kononenko[10]. Then investigations of the non-ideal systems where continued by A.Aliphov, J.Balthazar et al. Here NNMs in the non-ideal system with the pendulum absorber are considered. Both a construction of the NNMs and analysis of the regimes stability are made. It is selected the most appropriate for absorption localized vibration mode, when large vibrations of the absorber combine with small vibration of the main elastic structure.

1. Nonlinear Normal Modes In Mechanical System Having the Pendulum Absorber

One considers free vibrations of the two-DOF system which is shown in Fig. 1. It is necessary to reduce vibrations of the linear subsystem with the point mass m_1; the anchor spring is linear. The linear oscillator is connected with a pendulum absorber, having the mass m_2. The system motions are determined by two generalized coordinates x and θ. Equations of motion are the following:

$$\begin{cases} (m_1+m_2)\ddot{x}+m_2 l\ddot{\theta}\cos\theta-m_2 l\dot{\theta}^2\sin\theta+kx=0; \\ \ddot{x}\cos\theta+l\ddot{\theta}+g\sin\theta=0. \end{cases} \tag{1}$$

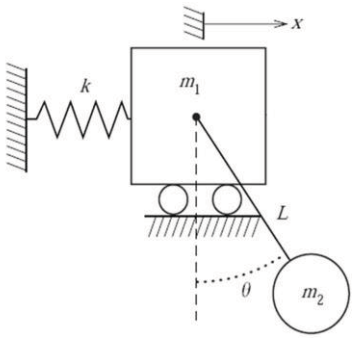

Figure 1. The mechanical system having the pendulum absorber.

The Maclaurin series are introduced for the functions $\cos\theta$ and $\sin\theta$. The terms up to the third order are saved in these series. It is assumed that the absorber mass is essentially smaller than one of the linear subsystem. One uses the following transformation, $m_2 \to \varepsilon m_2$, where ε is the small parameter. Two nonlinear vibration modes can be selected in this system: a) the coupled vibrations mode (non-localized mode), $x=x(t)$, $\theta=\theta(t)$, when amplitudes of two generalized coordinates have the same order; b) the localized vibration mode, when amplitudes of $\theta=\theta(t)$ are essentially larger than ones of $x=x(t)$, this mode is the most appropriate for absorption of linear subsystem vibrations.

The Kauderer-Rosenberg concept of nonlinear normal modes is based on construction of the NNM trajectories (modal lines) in the system configuration space. The NNM modal line for the n-DOF system in the system configuration space can be presented as

$$x_i = p_i(x);\ (i=2,3,...,n). \tag{2}$$

In general, the NNM modal lines in a configuration space are curvilinear. For the conservative system having the energy integral of the form

$$\frac{1}{2}\sum_{k=1}^{n}\dot{x}_k^2+\Pi(x_1,x_2,...,x_n)=h, \tag{3}$$

where*h* is a value of the system energy, equations to obtain trajectories in configuration space are the following:

$$2x_i''\frac{h-\Pi}{1+\sum_{k=2}^{n}x_k'^2}-\Pi_x x_i'=-\Pi_{x_i}\ (i=2,3,...,n), \tag{4}$$

where prime means a derivation by the new independent variable $x_1 \equiv x$.

An analytical continuation of these trajectories to the maximum equipotential surface $\Pi(x_1,...,x_n)=h$ is possible if the following boundary conditions are satisfied [3-5]:

$$x_i'(X)[-\Pi_x(X,x_2(X)...,x_n(X))]=-\Pi_{x_i}(X,x_2(X)...,x_n(X));\ (i=2,3,...,n), \tag{5}$$

where X is the vibration amplitude. The modal line (2) can be obtained from the equations (4) and the boundary conditions (5) in the form of power series [4,5]. One has here the next equation to obtain the trajectory $\theta = \theta(x)$ of the coupled vibration mode for the system (1):

$$\begin{aligned}
&(h-V)\varepsilon m_2 l\left(\theta'^2\left(\theta-\frac{\theta^3}{6}\right)-\theta''\left(1-\frac{\theta^2}{2}\right)\right)\left(l\theta'+1-\frac{\theta^2}{2}\right)+\\
&+(h-V)l\theta''\left(m_1+\varepsilon m_2+\varepsilon m_2 l\theta'\left(1-\frac{\theta^2}{2}\right)\right)+\\
&+\tilde{K}\left(-kx\left(l\theta'+1-\frac{\theta^2}{2}\right)+g\left(\theta-\frac{\theta^3}{6}\right)\left(m_1+\varepsilon m_2+\varepsilon m_2 l\theta'\left(1-\frac{\theta^2}{2}\right)\right)\right)=0.
\end{aligned} \tag{6}$$

Analytical continuation of the solution to the maximal equipotential surface $h-V=0$, where all velocities vanish, is possible under the following boundary conditions at the surface:

$$\tilde{K}\left(-kx\left(l\theta'+1-\frac{\theta^2}{2}\right)+g\left(\theta-\frac{\theta^3}{6}\right)\left(m_1+\varepsilon m_2+\varepsilon m_2 l\theta'\left(1-\frac{\theta^2}{2}\right)\right)\right)=0. \tag{7}$$

The NNM is presented in the form of the power series by the small parameter, $\theta=\theta(x)=\theta_0+\varepsilon\theta_1+\ldots$, where θ_0, θ_1, **…,** are presented as power series by x. Substituting the series to the equations (6) and (7), then selecting terms of the different order by ε and x, one obtains algebraic equations to determine coefficients of these series. Trajectory of the NNM in two approximations by ε is shown in Fig. 2. Here the next values of the system parameters and initial values, corresponding to obtained analytical solution, are chosen: $m_1=1$ (kg), $m_2=0.1$ (kg), $l=1$ (m), $k=5$ (kg/s^2), $\varepsilon=0.1$; $x(0)=0.1$, $\dot{x}(0)=0$, $\theta(0)=-1.3$, $\dot{\theta}(0)=0$.

Trajectory of the localized vibration mode is determined of the form: $x=x(\theta)$. This trajectory is presented of the form of the power series by the small parameter, $x=x(\theta)=\varepsilon x_1+\varepsilon^2 x_2+\ldots$, where x_1 and x_2, are also presented as power series by θ. By analogy with a construction of the non-localized vibration mode one determines coefficients of these series. The near rectilinear trajectory of the localized mode is presented in Fig. 3. Here $l=1, m_1=1, m_2=0.1, k=3, \varepsilon=0.1, \theta(0)=0.5$ **.**Checking numerical simulation shows a very good exactness of both analytical solutions.

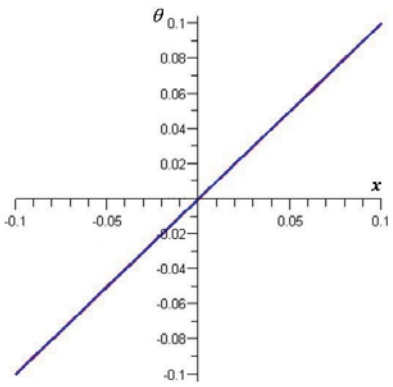

Figure 2. Trajectory of coupled vibration mode in configuration space

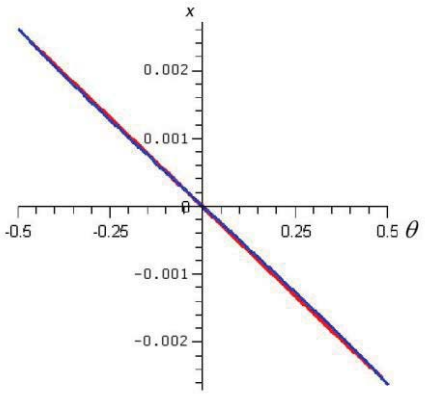

Figure 3. Trajectory of localized vibration mode in configuration space

A trajectory of the non-localized vibration mode is near rectilinear. Stability of the mode will be determined by variations, which are orthogonal to the trajectory. So, only a single variation equation can be analyzed in the stability problem. Using a harmonic approximation of the solution, it is possible to rewrite the variation equation as the well-known Mathieu equation. The more exact method of the stability analysis is based on the Hill equation. Results of the stability analysis are shown in Fig. 4. The next values of the system parameters are used: $l=1, m_1=1, m_2=0.1, k=3, \varepsilon=0.1$. Here the Mathieu equation gives us boundaries of narrow region, and the Hill equation gives us more exact results with large region of instability. In the inner region there is a transfer from the unstable coupled NNM to other non-localized NNMs as a result of bifurcation.

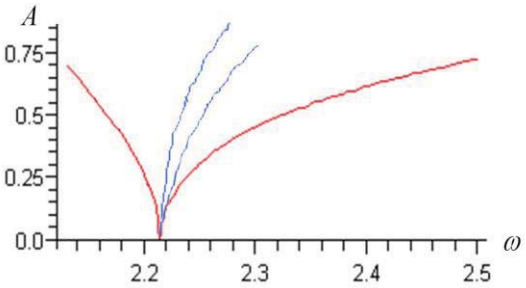

Figure 4. Boundaries of the stability/instability regions for the non-localized vibration mode.

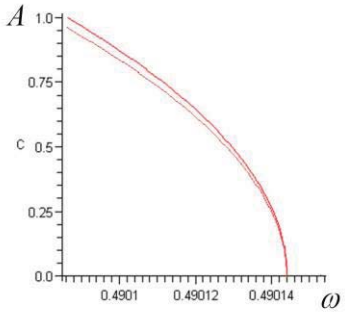

Figure 5. Boundaries of the stability/instability regions for the localized vibration mode.

Stability of the localized NNM is analyzed by using the Hill equation too. Boundaries of the stability/ instability of the localized NNM, are shown in Fig. 5. In the Figs. 4 and 5 $\omega=\omega_1/\omega_2$, where $\omega_1=\sqrt{k/m_1}, \omega_2=\sqrt{g/l}$. Note that the region of instability is very narrow. So, the localized vibration mode is very effective for absorption of elastic vibrations.

2. Forced Nonlinear Normal Modes in Mechanical System Having the Pendulum Absorber

Forced vibration modes can be obtained by the NNMs approach, and by the Rauscher method, modified for n-DOF systems. The Rauscher method is first proposed for the single-DOF system [11]. Generalization of the method to general n-DOF non-autonomous systems to construct NNMs in such systems is proposed in [8, 5]. One considers the system presented earlier under the external periodical excitation which stresses to the linear subsystem. The steady-state resonance vibration mode is analyzed. First of all, the corresponding autonomous system is considered. One uses a representation of generalized coordinates in regime of the NNM of autonomous system as Fourier series, namely,

$$\begin{aligned} x &= A_1\cos(\Omega t)+A_2\cos(2\Omega t)+A_3\cos(3\Omega t)+..., \\ \theta &= B_1\cos(\Omega t)+B_2\cos(2\Omega t)+B_3\cos(3\Omega t)+... \end{aligned} \tag{8}$$

One has from here, using some trigonometric transformations, that

$$\cos(\Omega t)=\alpha_1 x+\alpha_2\theta+\alpha_3 x^2+\alpha_4\theta^2+... \tag{9}$$

When coefficients of the expansions (9) are determined from corresponding algebraic equations, then the two-DOF “pseudo-autonomous” system is obtained, namely,

$$
\begin{aligned}
&(m_1+\varepsilon m_2)\ddot{x}+\varepsilon m_2 l\ddot{\theta}(1-\theta^2/2)-\varepsilon m_2 l\dot{\theta}^2(\theta-\theta^3/6)+kx=\\
&\varepsilon F(\alpha_1 x+\alpha_2\theta+\alpha_3 x^2+\alpha_4\theta_2+\ldots);\\
&\ddot{x}(1-\theta^2/2)+i\ddot{\theta}+g(\theta-\theta^3/6)=0.
\end{aligned}
\tag{10}
$$

It corresponds to principal idea of the Rauscher method. In the autonomous system (10) the NNMs are constructed by using the procedure presented in preceding Section. Then two generalized position coordinates can be obtained as new Fourier series which are more precise than series (8). So, the recurrent process is constructed, and the pointed out series of operations can be repeated several times to reach a necessary exactness. As a result, the steady-state resonance regime is constructed. Numerical simulation confirms a good exactness of the proposed approach. The non-localized forced vibration mode and the localized forced mode are shown in Fig.6 and 7, respectively; here the variable θ and x are presented on vertical and horizontal axes, respectively. Here $m_1=1, m_2=0.1, l=1, k=5, \varepsilon=0.1, f=0.1$.

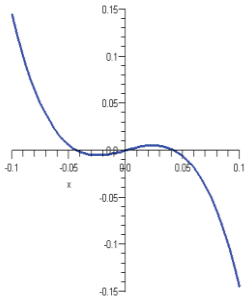

Figure 6. Trajectory of the non-localized forced vibration mode.

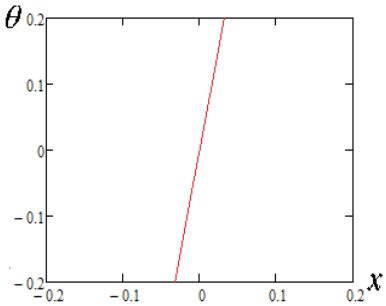

Figure 7. Trajectory of the localizedforced vibration mode.

Frequency response for the non-localized mode is shown in Fig. 8 while the frequency response for the localized mode is shown in Fig. 9. Calculations are made for the following values of the system parameters: $m_1=m_2=1, \varepsilon=0.01, l=0.5, F=3$. One can see that in the regime of the localized forced mode amplitudes of the linear oscillator are essentially smaller than ones of the pendulum. So, the localized forced mode is effective for absorption of vibrations of the linear subsystem.

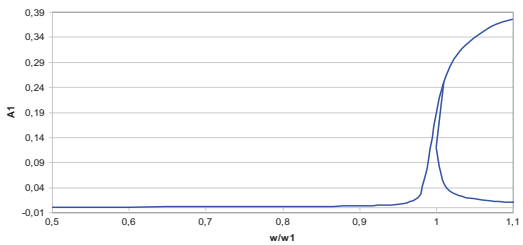

Figure 8a.

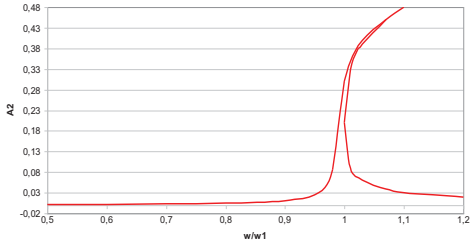

Figure 8b.

Figure 8. The frequency response of the non-localized forced vibration mode. Figure 8a. Frequency response of the variable x. Figure 8b. Frequency response of the variable θ.

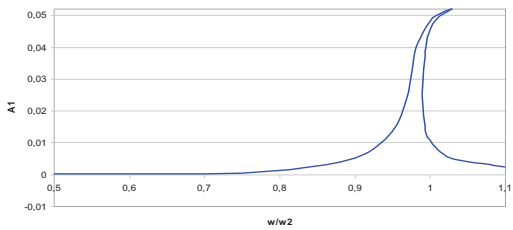

Figure 9a.

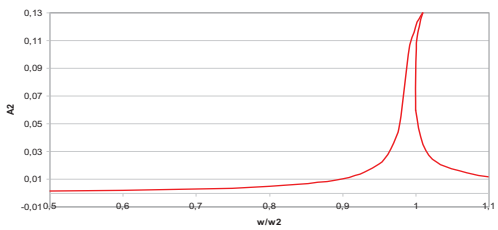

Figure 9b.

Figure 9. The frequency response of the localized forced mode. Figure 9a. Frequency response of the variable x. Figure 9b. Frequency response of the variable θ.

3. Nonlinear Normal Modes in the Non-ideal System with the Pendulum Absorber

One considers the non-ideal system, containing the elastic linear substructure under the engine D excitation. Simultaneously this substructure influences to the engine. The system contains too the pendulum absorber having the mass m_2. The model under consideration is presented in Fig. 10.

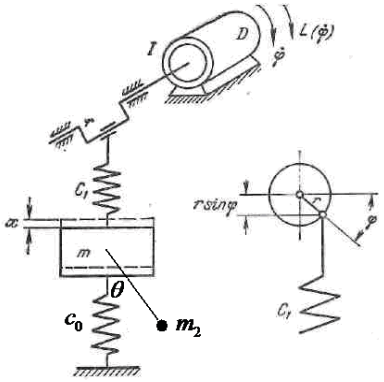

Figure 10. The non-ideal system with the pendulum absorber.

Equations of motion of the system are the following:

$$\begin{cases} \left(M+\varepsilon m_2\right)\ddot{x}+\left(c_0+c_1\right)x=c_1 r\sin\varphi-\varepsilon m_2 l\left(\ddot{\theta}\cos\theta-\dot{\theta}^2\sin\theta\right); \\ I\ddot{\varphi}=\varepsilon\left(a-b\dot{\varphi}+c_1 r\left(x-r\sin\varphi\right)\cos\varphi\right); \\ l\ddot{\theta}+g\sin\theta+\ddot{x}\cos\theta=0. \end{cases} \tag{11}$$

Here ε is a small parameter.

Two nonlinear vibration modes can be selected in this non-ideal system: a) the coupled non-localized vibrations mode, when vibration amplitudes of all generalized coordinates are of the same order; b) the localized vibration mode, when amplitudes of θ are essentially larger than ones of linear elastic subsystem; this mode is the most appropriate for absorption.

Trajectories of the NNMs by Kauderer-Rosenberg are determined as $x=x(\varphi)$, $\theta=\theta(\varphi)$. The solution is obtained in series by the small parameter ε, and by the new independent variable φ by analogy with the procedure described in the Section 1.

Trajectory of the mode of coupled vibrations for the parameters $M=10$, $m_2=0.1$, $\varepsilon=0.1$, $c_0=50$, $c_1=50$, $a=1$, $b=1$, $r=0.1$, $I=1$ and $l=1$, are presented in Fig. 11;

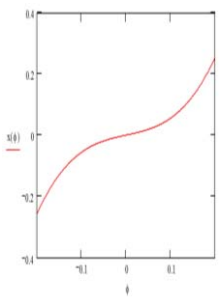

Figure 11a.

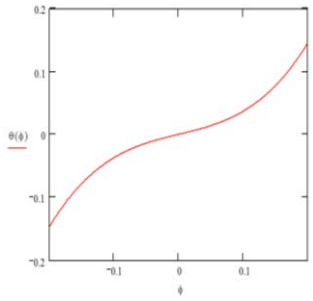

Figure 11b.

Figure 11. Trajectory of the coupled vibrations in the non-ideal system configuration space. In the Figure 11a the trajectory is shown on the place of variables x and φ; in the Figure 11b – on the place of the variables θ and φ.

Trajectory of the localized vibration mode is determined by the functions $x=x(\varphi)$, $\theta=\theta(\varphi)$ too.

A method of power series is used. A trajectory, which was constructed for the parameters $M=1$, $m_2=0.1$, $\varepsilon=0.1$, $c_0=5$, $c_1=5$, $a=1$, $b=1$, $r=0.1$, $I=1$ и $l=0.1$, are presented in Fig. 12.

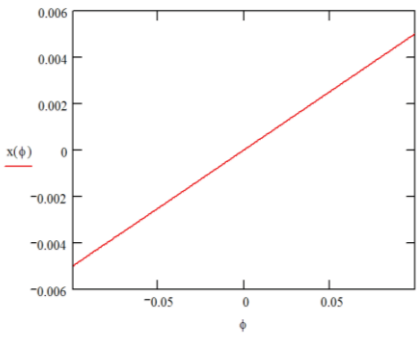

Figure 12a.

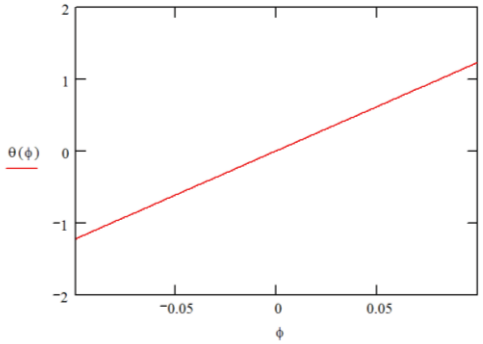

Figure 12b.

Figure 12. Trajectory of the localized vibrations in the non-ideal system configuration space. In Figure 12a this trajectory is shown on the place of the variables x and φ; in Figure 12b - on the place of the variables θ and φ.

Analysis of the obtained NNMs stability is made, and the stability/ instability regions for both modes are obtained. It is resulted that a region of instability of the localized mode is very narrow.

Conclusions

Nonlinear normal vibration modes (NNMs) of the mechanical systems containing the pendulum absorbers are considered. The NNMs approach permits to construct coupled and localized vibration modes of the systems. The localized vibration mode is the most appropriate for absorption of the elastic substructure vibrations. Forced resonance vibration modes are constructed by using a composition of the nonlinear normal modes approach and the modified Rauscher method. The same approach allows to analyze NNMs in the non-ideal system containing a pendulum absorber.

References

[1] *Vibrations in Engineering* (Frolov K.V., editor),Mashinostroenie, Moscow, 1995 (in Russian).
[2] Cuvalci O., Ertas A. Pendulum as vibration absorber for flexible structures: experiments and theory,*Trans. ASME. Journal of Vibrations and Acoustics,* Vol.118, pp. 558-566, 1996.
[3] Rosenberg R. Nonlinear vibrations of systems with many degrees of freedom, *Advances of Applied Mechanics,* 9, Academic Press, New York, pp. 156–243, 1966.
[4] Mikhlin Yu. Normal vibrations of a general class of conservative oscillators, *Nonlinear Dynamics,* Vol.11, pp. 1–16, 1996.
[5] Vakakis A.F., Manevitch L.I., MikhlinYu.V., Pilipchuk V.N, Zevin, A.A. *Normal Modes and Localization in Nonlinear Systems,* Wiley Interscience, New York, 1996.
[6] Avramov, K.V., Mikhlin, Yu.V. *Nonlinear Dynamics of Elastic Systems,*Regular and Chaotic Dynamics, Moscow-Izhevsk, 2010 (in Russian).
[7] Avramov K.V., MikhlinYu.V. Nonlinear normal modes for vibrating mechanical systems. Review of theoretical developments. *Applied Mechanics Review*, Vol. 63 (6), 21 pages, 2010.
[8] Mikhlin Yu Resonance modes of near-conservative nonlinear systems, *Prikladnaja Matematica I Mekhanica (PMM USSR),* Vol. 38, pp. 425–429, 1974.
[9] Sommerfeld A. Beiträge Zum Dynamischen Ausbau Der Festigkeitslehe, *Physikal Zeitschr*, Vol. 3, pp. 266-286, 1902.
[10] Kononenko V. *Vibrating systems with limited power supply,* Illife Books, London, 1969..
[11] Rauscher M. Steady oscillations of systems with nonlinear and unsymmetric elasticity, *Journal of Applied Mechanics,* Vol. 5, pp. 169-177, 1938.

Proceedings of the 4th International Conference on Nonlinear Dynamics
ND-KhPI2013
June 19-22, 2013, Sevastopol, Ukraine

Synchronization of New Type in the Chain of Weakly Coupled Active Oscillators

Margarita Kovaleva [1*], Leonid Manevitch[1]

Abstract

We have shown earlier that the strongly modulated vibrations with complete energy exchange between two weakly coupled active oscillators (generators) can exist under certain conditions revealed by a symmetry analysis. These vibrations are adequately described by Limiting Phase Trajectories (LPTs) which were initially introduced for conservative systems. From mathematical viewpoint, their existence in active systems means that LPT can be attractor. On the other side, it was also shown that it is possible to extent the LPT concept to the conservative system with many degrees of freedom. Then, the LPT describes the complete energy exchange between different parts of the system. In terms of LPT the transition to energy localization on excited initially part of the system is also predicted. Therefore, the natural question arises: whether the LPT can be attractor in the systems with many degrees of freedom? Such extension of our previous results to this case turns out to be very complicated problem. We used the mentioned results related to conservative system with many degrees of freedom and two weakly coupled generators as a starting point. It is meant the concept of the effective particles alongside with introducing the LPTs as well as with the symmetry analysis revealing the conditions for existence of the integral of motion. It is shown that under these conditions the principally new types of the non-conventional synchronization in the multi- particle system of weakly coupled generators can be realized.

Keywords
active oscillator, chain of weakly coupled generators, synchronisation, limiting phase trajectory, effective particle, symmetry.

[1] Semenov Institute of Chemical Physics Russian Academy of Sciences, Moscow, Russia

* **Corresponding author:** margo.kovaleva@gmail.com

Introduction

The problem of synchronization is a fundamental problem which is being discussed by the generations of scientists. In our previous paper we have revealed the new aspect of the phenomenon: it was shown for the first time that synchronization with almost complete periodical energy exchange between two generators can exist. This new regime manifests as highly modulated oscillations whose period is that of the energy exchange [1]. Here we faced the question: whether some similar regime can be observed in n-DoF system with $n>2$? Because even the study of 2-DoF system turned out to be a very complicated problem, its extension to the chain of active oscillators (generators) seemed very unlikely to be achieved.

The adequate technique for our research was developed in a series of papers [2]. There is a new concept of *effective particles* and *limiting phase trajectories* which was used to describe the energy

exchange and localization in the chains of nonlinear conservative oscillators. It is very important that the main asymptotic approximation in the framework of multiple scale procedure admits the "occupation number" integral. This is a consequence of the *symmetry* which can be revealed by *group theory analysis*. Such symmetry was also found under certain conditions in the system of two weakly coupled dissipative oscillators. We have noted that in the whole class of the active systems with *n>2* one can also distinguish a sub-class with the symmetry providing the existence of the "occupation number" integral. However, contrary to the system of two weakly coupled auto-generators, the existence of a single integral in the case *n>2* is insufficient for prediction of non-conventional synchronization. It becomes sufficient only in the framework of the concept of the effective particles and limiting phase trajectories,

1. Initial System and Its Reduction

We consider the chain of nonlinear generators with periodic boundary conditions. Omitting the symmetry analysis revealing the conditions which provide the existence of the "occupation number" integral, let us present the final equations describing the dynamics of such system:

$$\frac{d^2u_j}{dt^2}+u_j+8\alpha u_1^{\,3}+2\beta(2u_j-u_{j-1}-u_{j+1})+$$
$$+2\gamma\left(\left(u_j^{\,2}+v_j^{\,2}-\left(u_{j-1}^{\,2}+v_{j-1}^{\,2}\right)\right)\left(u_{j-1}^{\,2}+v_{j-1}^{\,2}\right)-\left(u_j^{\,2}+v_j^{\,2}-\left(u_{j+1}^{\,2}+v_{j+1}^{\,2}\right)\right)\left(u_{j-1}^{\,2}+v_{j+1}^{\,2}\right)\right)v_j=0 \tag{1}$$

where $\frac{du_j}{dt}=v_j$, β is coupling parameter.

The *occupation number integral* takes a conventional view after transition to complex variables:

$$\dot{\varphi}_j=i\beta\left(\varphi_{j-1}-2\varphi_j+\varphi_{j+1}\right)+i\alpha\left|\varphi_j\right|^2\varphi_j+\gamma\left(\left(\left|\varphi_j\right|^2-\left|\varphi_{j-1}\right|^2\right)\varphi_{j-1}-\left(\left|\varphi_{j+1}\right|^2-\left|\varphi_j\right|^2\right)\varphi_{j+1}\right)\varphi_j,$$
$$j=1,2...n \tag{2}$$

where $\varphi_j=v_j+iu_j$

By a direct check one can prove that the system (2) has integral:

$$N=\sum_{j=1}^{n}\left|\varphi_j\right|^2 \quad , \tag{3}$$

n – number of oscillators.

System (1) in the particular case $\alpha=0$ was presented in [3] as a phenomenological model of dissipative system, at that the existence of the integral has been discussed for the case *n=2* only.

The linearized system corresponding to (1) has the normal modes which can be conserved also if the nonlinearity is taken into account (then they are Nonlinear Normal Modes, NNMs).

We consider further the case *n=4 for concreteness.* Then the four NNMs are defined by vectors:*(1,1,1,1)-in-phase mode*, *(1,-1,-1,1)* – out-of-phase mode , *(-1,-1,1,1* and *(1,-1,1,-1) – two modes corresponding to formation of the synchronous pairs.* The *frequency* spectrum of the linear normal vibrations looks as follows:

$$\varpi=\varpi_0\sin^2\frac{\pi k}{N} \tag{4}$$

and contains two equal frequencies. They correspond to the modes with synchronous pairs as the frequency does not depend on the choice of the pairs.

A significant point for application of the effective particles concept to the n-DoF systems is the frequency spectrum densification with the growth of n or decrease the coupling parameter. The high frequencies of the NNMs become closest, and the resonant NNMs can interact strongly. We consider only the interaction of three upper by frequency modes.

To take into account a collective character of the process under consideration we deal further with a projection of the equations of motion on the modal basis ($\varphi_j \to \xi_j$). Then we perform a transition to effective particles which are formed by a combination of the resonant NNMs, (I,II and III). The corresponding variables represent the groups (clusters) of the generators [2] which move as wholes:

$$\begin{aligned} \psi_1 &= \xi_2 - \left(\sqrt{1-c^2}\,\xi_1 + c\xi_3\right) \\ \psi_2 &= \xi_2 + \left(\sqrt{1-c^2}\,\xi_1 + c\xi_3\right) \\ \phi &= \left(c\xi_1 - \sqrt{1-c^2}\,\xi_3\right) \end{aligned} \tag{5}$$

We suppose that the modes with same frequency have similar amplitudes, and using the N-integral, transform the variables and the system as follows:

$$\begin{aligned} \psi_1 &= \sqrt{N}\,\cos\theta\, e^{i\delta_1} \\ \psi_2 &= \sqrt{N}\,\sin\theta\, e^{i\delta_2} \\ \Delta &= \delta_2 - \delta_1 \end{aligned} \tag{6}$$

$$\begin{aligned} &\frac{d\theta}{d\tau_2} = \frac{1}{2}\sin\Delta + \frac{k}{4}\left(\sin 2\theta \sin 2\Delta - 2\sin\Delta\right) - \\ &2\lambda\left(\sin 4\theta(1-\cos 2\Delta) + 8\cos 2\theta\cos\Delta\right), \\ &\sin 2\theta\,\frac{d\Delta}{d\tau_2} = \cos 2\theta\cos\Delta + 2k\left(\sin 4\theta\cos^2\Delta - 2\cos 2\theta\cos\Delta - 4\sin 4\theta\right) - \\ &-2\lambda\left(\sin 2\theta\sin 2\Delta - 4\left(\cos^4\theta + \sin^4\theta\right)\sin\Delta\right), \end{aligned} \tag{7}$$

where $\tau_1 = 2\beta\tau_2, k = \frac{\alpha X}{16\beta}$, $\lambda = \frac{\gamma X^2}{64\beta} > 0$.

2. Phase Plane Analysis

This system was studied in both conservative ($\gamma = 0$) and dissipative cases. The phase planes for different parameters are presented in Fig. 1. Initially, we can see two stationary points ($\theta = \pi/4, \Delta = 0$) and ($\theta = \pi/4, \Delta = \pi$). In the 2-DOF system they correspond to in-phase and out-of-phase NNMs correspondingly. If ($k \le -\frac{1}{2}$), the in-phase mode is unstable; if ($k \ge \frac{1}{2}\left(\sqrt{1+64\lambda^2}\right)$ or $k \le -\frac{1}{2}\left(\sqrt{1+64\lambda^2}\right)$) the out-of-phase mode loses its stability. For some range of dissipation parameter a stable limiting cycle attracts phase trajectories from a wide range of initial conditions. The attractor of this type corresponds to the stationary energy exchange between the two parts of the initial system, i.e., – the clusters of oscillators (effective particles). This limiting cycle can be described by the LPT.

When the limiting cycle loses its stability, two stable focuses become global attractors. They correspond to the situation when almost all energy is concentrated on one effective particle (cluster of oscillators) which is a bright example of energy localization.

Conclusions

We have studied a system of coupled nonlinear active oscillators and have found for the first time the principally new types of synchronization in a chain of nonlinear generators. In certain range of the parameters an intensive energy exchange between two parts of the chain corresponds to attracting phase trajectories for a wide range of initial conditions. When the motion of this type loses

its stability another significant phenomenon can be observed: synchronization of the chain of identical generators in which almost all energy is concentrated only on one part of the chain.

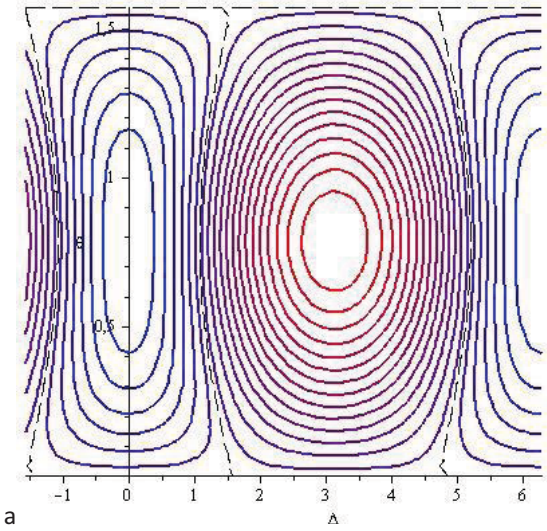

a

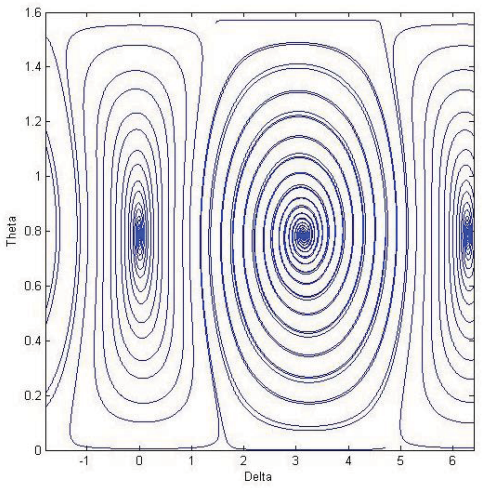

b

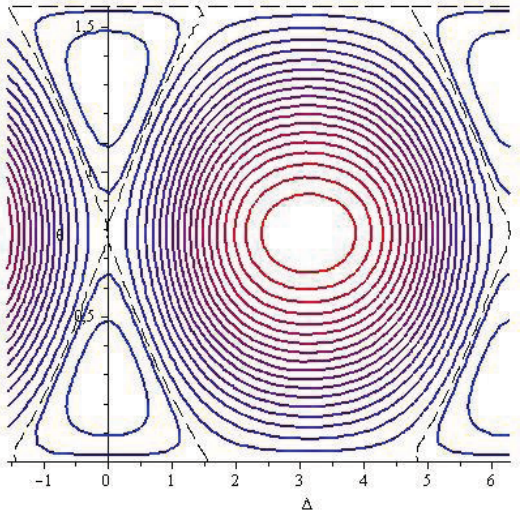

c

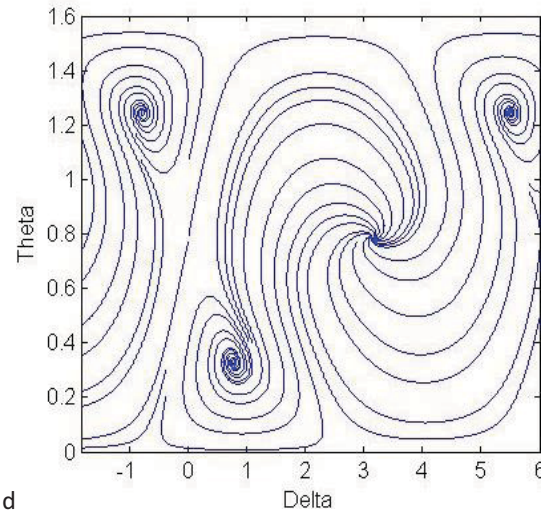

d

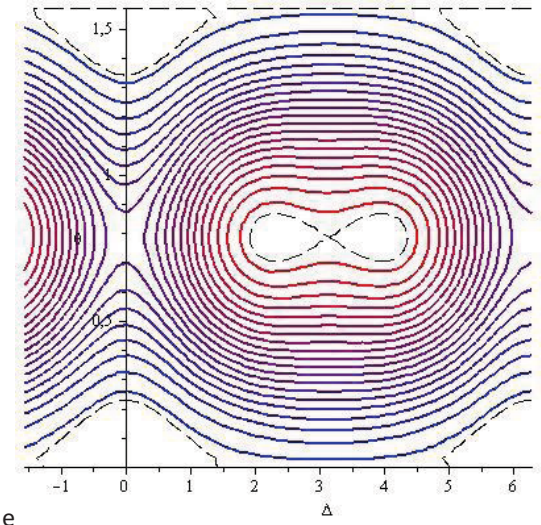

e

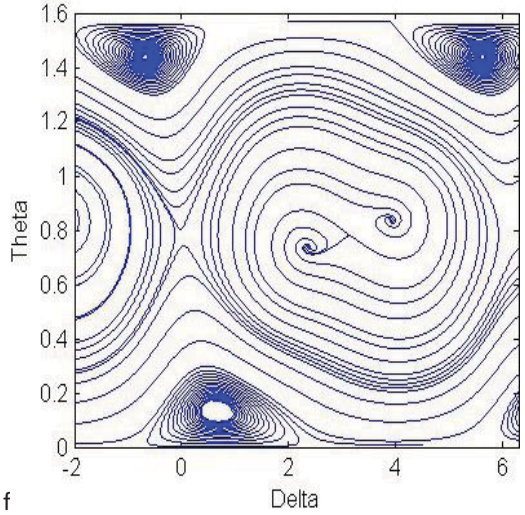

f

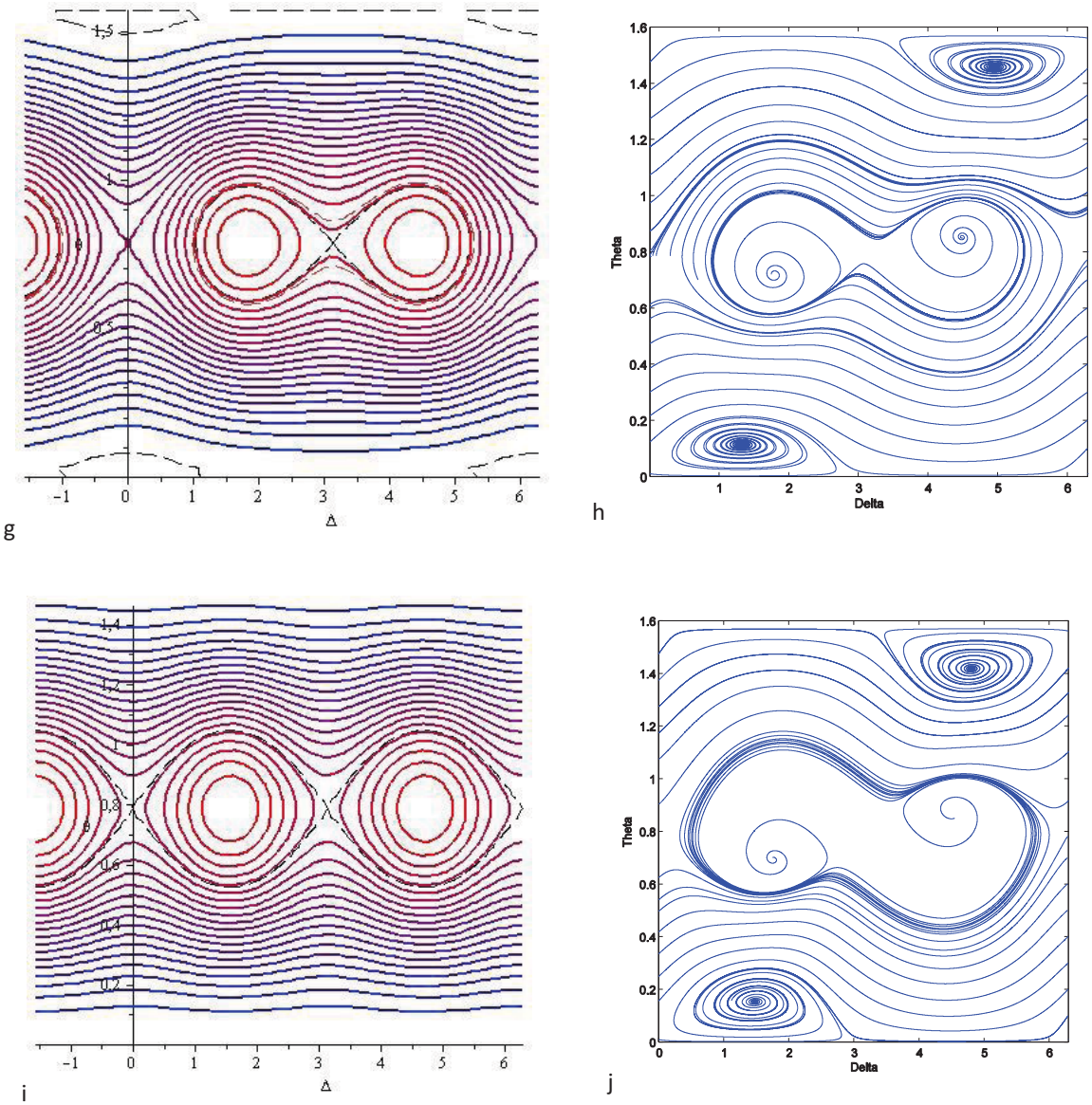

Figure 1. Phase planes for system (θ, Δ) with different parameters: (a) $k = 0.2, \lambda = 0$: conservative system, stationary points $(0, \pi/4)$ and $(\pi, \pi/4)$; (b) $k = 0.2, \lambda = 0.01$; due to dissipation stationary points become focuses: $(0, \pi/4)$ - unstable focus, $(\pi, \pi/4)$ - stable focus; (c) $k = 0.4, \lambda = 0$: the point $(0, \pi/4)$ transforms into a knot; (d) $k = 0.4, \lambda = 0.1$: two new unstable focuses appear; (e) $k = 0.6, \lambda = 0$: the stable point $(\pi, \pi/4)$ loses stability; two new stable points appear;(f) $k = 0.6, \lambda = 0.05$:unstable focuses become stable, two new stable focuses appear; (g) $k = 0.8, \lambda = 0$; (h) $k = 0.8, \lambda = 0.0185$ the focuses loose stability and an unusual stable limiting cycle encircling 3 stationary points) attracts phase trajectories from a wide range of initial conditions;(j) $k = 0.8, \lambda = 0.02$ limiting cycle loses stability, two stable focuses become global attractors;(i) , $k = 1, \lambda = 0$,at the high nonlinearity level the phase plane of new symmetry appears

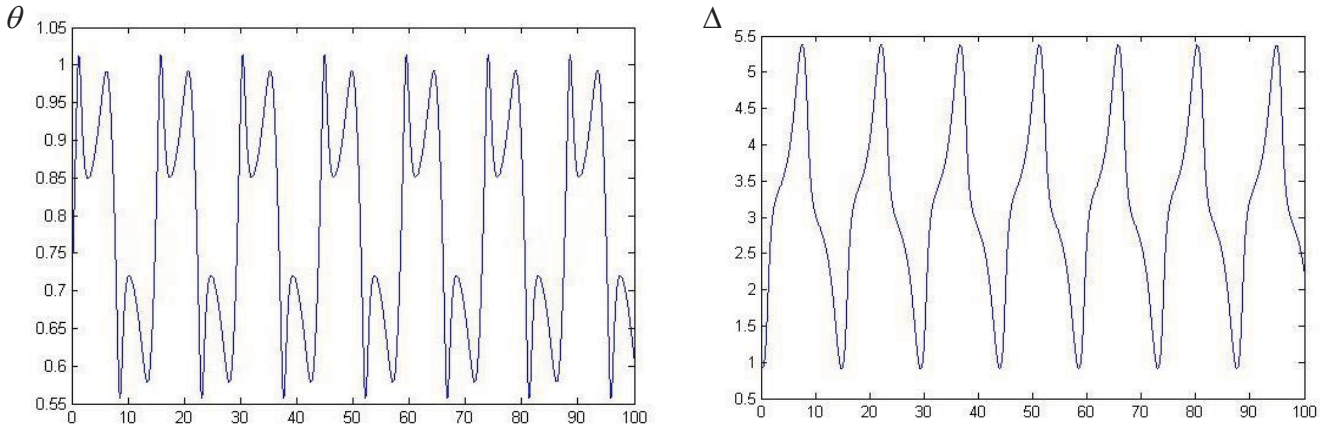

Figure 2. (a),(b) - Temporal evolution of variables θ, Δ, correspondingly

References

[1] Manevitch L.I., Kovaleva M.A., Pilipchuk V.V. Non-conventional synchronization of weakly coupled active oscillators *Europh. Lett.,* Vol. 101, 50002, 2013.

[2] Manevitch L.I., Smirnov V.V. Limiting phase trajectories and the origin of energy localization in nonlinear oscillatory chains *Phys. Rev. E* 82, 036602.

[3] Pilipchuk V. N., in *Problems of Nonlinear Mechanics and Physics of Materials*, edited by Manevitch A. I. ,RIK NGA, Dnepropetrovsk, 1999 ISBN: 966-7476-10-3.

Proceedings of the 4th International Conference on Nonlinear Dynamics
ND-KhPI2013
June 19-22, 2013, Sevastopol, Ukraine

Subharmonic Modes in Vibroimpact Systems

Yuri Kostenko[1*], Mykola M.Tkachuk[1, 2*], Andrey Grabovsky[1*], Mykola A.Tkachuk[1*].

Abstract
The investigation of subharmonic modes in vibroimpact systems is presented in the paper. New approach with sets of phase variables is proposed. Results for variation of phase variables were obtained. Functional that describes the character of oscillation process was built.

Keywords
Subharmonic modes, phase variables, character of oscillation process

[1] NTU "KhPI", Kharkiv, Ukraine.
[2] Stanford University, Stanford, California, U.S.
* **Corresponding author:** kostenko.yuriy@gmail.com

Introduction

In papers [1-7] it was found that in the large heavily loaded vibroimpact machines subharmonic modes can be established. In this case the period of steady-state vibrations for one of the bodies T_2 (due to periodic colliding of bodies) can be a multiple with respect to the period of oscillation for another body T_1 caused, first of all, by influence of periodic disturbing force.

The purpose of this paper is to study the steady movement modes in vibroimpact system with two degrees of freedom (Figure. 1).

1. Description of the problem

The sustained modes of motion in vibroimpact system with two degrees of freedom are researched. The equations of motion is presented below.

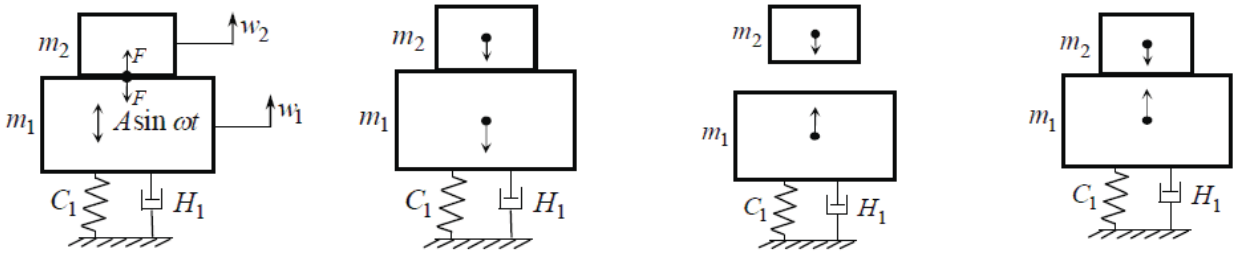

Figure 1. Two-mass vibroimpact system

Equations of motion:

$$\begin{cases} m_1\ddot{w}_1 + C_1 w_1 + H_1\dot{w}_1 + A\sin\omega t + m_1 g + F = 0; \\ m_2\ddot{w}_2 + m_2 g - F = 0. \end{cases} \quad (1)$$

Here w_1 and w_2 are displacements of the bodies 1 and 2 that have masses m_1, m_2; C_1, H_1 are coefficients of stiffness and damping for the body 1; A, ω are the amplitude and frequency of the harmonic excitation force; g is an acceleration of gravity[1].

1.1. Proposed approach.

The main idea is the new representation of nonnegative force of impact interaction F as the relative approach function $\zeta = (w_1 - w_2)$ of displacements of the mass 1 and 2 and their velocity:

$$F^{\wedge} = \begin{cases} F^{\wedge} \geq 0\,,\ \zeta \geq 0; \\ F^{\wedge} = 0\,,\ \zeta < 0. \end{cases} \tag{2}$$

In this case in the first quadrant $(\zeta > 0, \dot{\zeta} > 0)$ the function F coincides with its representation in form of power series or other functional series, for example, Taylor series:

$$F^{\wedge}(\zeta, \dot{\zeta}) = \alpha_1 \zeta + \alpha_2 \dot{\zeta} + \alpha_3 \zeta \dot{\zeta} + \ldots \tag{3}$$

The task is to identify sustained modes in this system with coefficients α_i. Let's use the following designation: $Z(t) = \{z_1, z_2, z_3, z_4\}^T$ - set of phases variables $w_1, \dot{w}_1, w_2, \dot{w}_2$; operator of numerical integration $L_\tau : Z(t+\tau) = L(Z(t))$. Operator L_τ does the conversion of the initial phase state to the state after specified time interval τ. It can be done by the using of numerical integration method. If denote Z_1 - values of phases variables in some time θ, then $Z_2 = L_{kT}(Z_1)$, where $T = 2\pi\omega$ - period of the stir up force, $k = 1,2...$ - integer. Equations $Z_2 - Z_1 = 0$ are nonlinear equations with respect to Z_1. Solution that obtained with different values of k gives a possibility to determine different periodical modes. If $k > 1$, they are subharmonic ones

2. The implementation of introduced approach to specific example.

For a test example it was used 2-mass system that has parameters: $m_1 = 15960kg$, $m_2 = 0{,}5m_1$, $C = 5280kN/m$, $H = 127680N \cdot s/m$, $A = 293kN$, $\nu = 16Hz$.

The integration is performed by the Runge-Kutta method. Time period 1/16 s, which corresponds to the period of one complete oscillation of the system is considered. This time interval in case of the numerical integration is equal to 5000 iteration steps.

To assess the changes in the character of the oscillatory process in the system is carried out varying the phase variables $Z(t) = \{z_1, z_2, z_3, z_4\}^T$ within the limits of $\Delta_{i\max} = 0.1\, A_{i\max}$, where $A_{i\max}$ is the maximum value of the variable in the steady state. Four parameters were taken as varied ones: the displacements of the 1st and 2nd bodies, as well as their velocities. The range of variation is equal to five steps to reduce variable and 5 ones in the direction of increasing. Thus, the base point corresponds to zero increment $\Delta_1 = 0, \Delta_2 = 0, \Delta_3 = 0, \Delta_4 = 0$ is central point of this range. According to the results of calculations for a set of variables Z it were obtained their values $Z_2 = L_{kT}(Z_1)$, when $k = 1$, $T = 1/16s$. These values correspond to the values of state variables for the considered two-mass system, which has made one complete oscillation. As stated earlier, the condition $Z_2 - Z_1 = 0$ should be accomplished for periodical solution. It is necessary to consider the fact that search of Z_2 is performed by numerical integration, which in due of its implementation on the PC has some inaccuracy. A consequence of this seems appropriate conversion from $Z_2 - Z_1 = 0$ to expression $Z_2 - Z_1 \to 0$. Thus, the solution will be periodic in the minimum of the functional I, that is represented in form

$$I = \frac{(Z_1 - Z_2)^2}{A_{\max}{}^2} \tag{4}$$

Accordingly, having the values Z_1 and Z_2 for every set of Δ, is proposed to build a functional I, that describes the changes in the oscillation process due the variation of phase variables $Z(t) = \{z_1, z_2, z_3, z_4\}^T$, allows to assess visually its character.

Figure 2-5 shows sections of the functional (4) with the variation of different state variables.

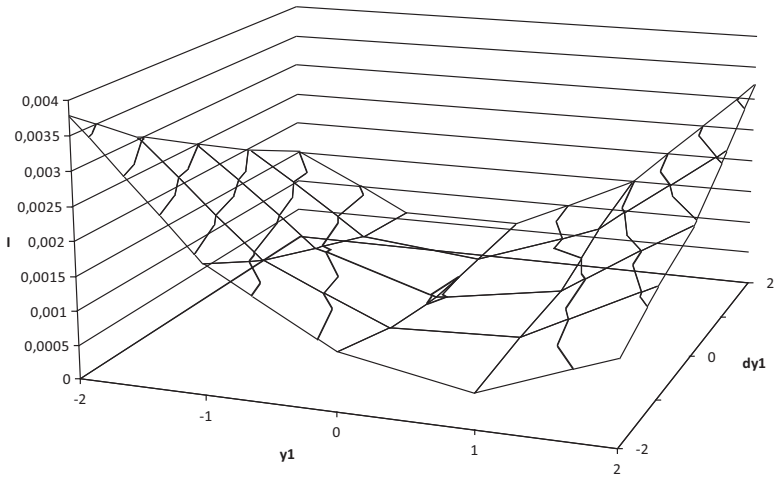

Figure 2. Functional I at varying displacement and velocity of the 1-st body

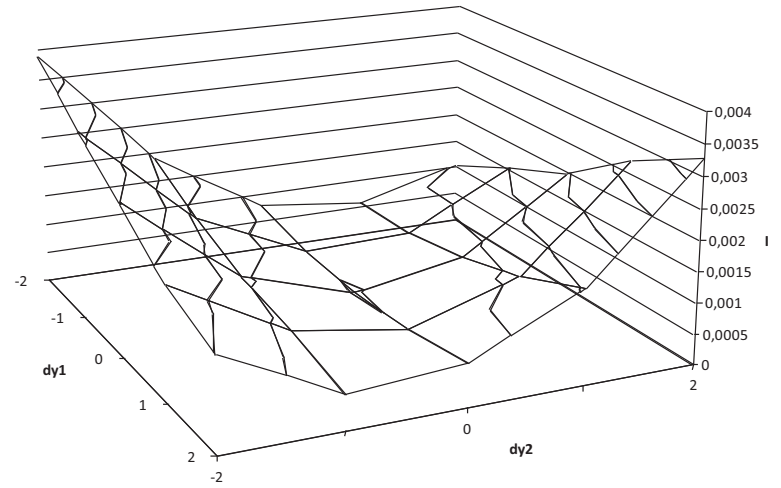

Figure 3. Functional I at varying velocities of the 1-st and 2-nd bodies

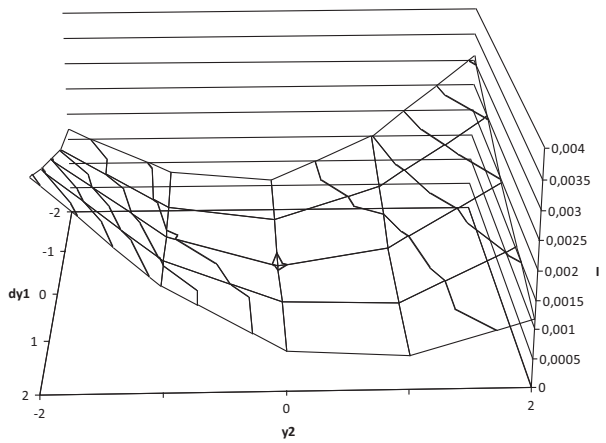

Figure 4. Functional I by varying the velocity of the 1-st body and displacement for 2-nd one

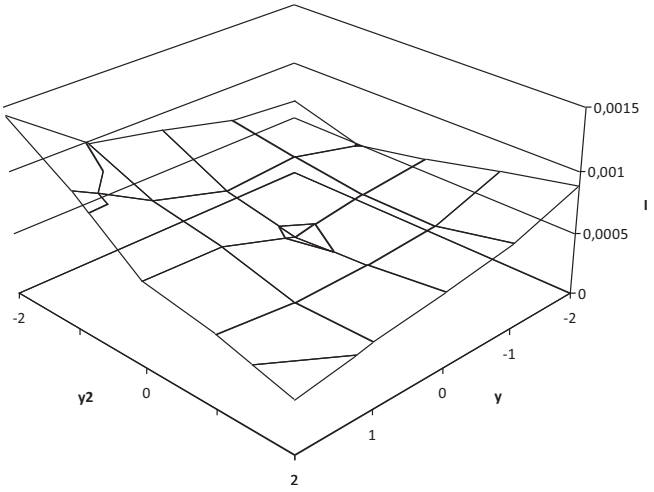

Figure 5. Functional I at varying displacements of the 1-st and 2-nd bodies

Conclusions

We can conclude by using the presented results that the minimum of the functional I in different sections locates near the base point ($\Delta_1 = 0, \Delta_2 = 0, \Delta_3 = 0, \Delta_4 = 0$), that correspond to a steady state in a real system when condition $Z_2 - Z_1 = 0$ is true. It corresponds to the previously presented assumptions when $Z_2 - Z_1 \to 0$ that was done for the numerical search of functional I. This allows to conclude that this approach could be applied to search of the harmonic and subharmonic modes in vibro-impact systems. Analysis and studying of modes at $k > 1$ will be an object of further studies.

References

[1] Barchan E.N., Experimental exploration of dynamical processes in shock machine with unbalanced drive *Mashinoznavstvo ta SAPR,* Vol. 3, pp. 17, 2007. (in Russian)
[2] Barchan E.N., Shkoda A. V., Prosyanok V. V. Experimental exploration of dynamical processes in modernized shock machine *Mashinoznavstvo ta SAPR,* Vol. 23, pp. 26-32, 2007. (in Russian)
[3] Barchan E.N., Tkachyk N.A., Grabovskiy A.V. The modeling of the dynamic of shock machine with unbalanced drive *8-th international symposium of engineer-mechanics in Lviv,* Vol. 1, pp. 79, 2007 (in Ukrainian).
[4] Barchan E.N., Grabovskiy A.V, Martynenko A.V. Computer modeling of dynamic and stress-strained state of spatial constructions *Actual Problems of Solid Medium Mechanic and Strength of Constructions,* pp. 236-38, 2007.
[5] Tkachuk M.A., Grabovsky A.V. ,Tkachuk M.M.. An approach to identification of impact interaction model for a vibroimpact system *Proc. of the 3d International Conference on Nonlinear Dynamics*. Khrakov, NTU "KhPi", pp. 207-212, 2010.
[6] Grabovsky A.V., Methods and algorithms for verification of shock interaction in vibroimpact systems *East-European Journal of Advanced Technologies*. Vol. 3/9(45), pp. 42-46, 2010. (in Ukrainian).
[7] Kostenko Y.V., Tkachyk N.A., Grabovsky A.V., Tkachyk N.N. Numerical determination of the effect for form of impact interaction influence on the character of dynamical processes in vibro-impact systems *XXV International Science Conference "Mathematical Methods in Technics and Science"*, pp. 94-98, 2012 (in Russian).

Proceedings of the 4th International Conference on Nonlinear Dynamics
ND-KhPI2013
June 19-22, 2013, Sevastopol, Ukraine

Discrete model of geysers

Kovriguine Dmitry Anatolyevich

Abstract
A discrete mathematical model describing all essential dynamical patterns which probably accompany a geyser recharge cycle is proposed. A growth of Taylor babbles, naturally observed at the start of geyser activity, is treated as a dynamical instability of nonlinear oscillations in the low-quality damped forced cavity resonator governed sensitively by small changes in the viscosity of subsoil caused by the temperature growth. Time series generated by the discrete model are close to those provided by real-time data obtained from dynamical tests.
Keywords
Resonance, cavity resonator; nonlinear oscillations'

Mechanical Engineering Institute of the Russian Academy of Sciences, Nizhny Novgorod, Russia,
Corresponding author: kovriguineda@gmail.com

Introduction

Geysers are rare natural phenomena and several conditions must meet together for the geyser recharge. These are a water supply, a heat source and a reservoir connected with a plumbing system [1]–[7]. There are known about six basic types of geysers classified in general by the physical portraits and the individual geometry of their reservoirs [6]. Geysers are essentially hot springs that exhibit unstable thermodynamical and hydrodynamic patterns. Though, there can be many other contributing factors supporting the dynamical activity. An adequate geyser modeling presents a permanent challenge for theoretical and experimental researchers. The multiphase flows of more than one phase are natural when modeling geysers. These flows are extremely complex because of large deformations and fast transformations in temporally evolving interfaces between the vapor and liquid phases. A complication of these flows is that the phases can be dispersed unevenly both in cross-sections of the plumbing system, with some unknown geometry, and axially. Nowadays the theoretical investigations, based on the complete set of hydrodynamic equations including that of mass conservation, momentum, angular momentum and the energy, provided by appropriate constitutive equations, seem to be not so fruitful, as desirable, from the physical viewpoint and because of a high computational complexity [8], [9]. In order to understand anything and overcome pragmatically such complexities, the different empirical distributions of flows are usually gathered into groups called flow pattern. This approach is useful for modeling when identifying the occurrence of individual flow patterns provided by simplified models related to various flow patterns. In particular, the correlations between the pressure drop and flow rates of the phases relationships which are central for in practice. There are many flow patterns intensively investigated for vertical up- and down-flow, horizontal flow and flow at other inclinations, though namely the vertical flow patterns seem to be of key interest in the context of geyser activity. They include a *bubble* flow within the liquid; a *slug* or *plug* flow of larger bubbles approaching diameters of the plumbing system; a *churn* flow characterized by chaotic vibrations; an *annular* flow, where the liquid flows on the wall downwards as a film together with the upward gas flow in the core; *wispy annular* flow with a great concentration of droplets in the gas core [10].

The first section of the present paper proposes, based on the analysis of the enhancement and suppression factors, an *ad hoc* discrete dynamical model describing the geyser activity in accordance with some popular empirical maps related to various vertical flow patterns [11]–[18]. This simplest model is motivated by discrete nature features in the evolution of slugs, and has no contradictions

with known experimental data [19]. A competition between the resonance and the energy dissipation in the vertical slug flow is considered as a feasible initial stage in the geyser activation, since the flow development of co-current gas-liquid vertical slug flow showed that void fraction, Taylor bubble and liquid slug lengths, and slug frequency are parameters essential to any description of the dynamical instability [20], [21]. From a physical viewpoint, it is obvious that the activity of geyser always causes a decrease in the viscosity of the subsoil fluid filling the plumbing system and because of the increase in dynamical lengths of vapor slugs. Hence, the amplitude of thermo-mechanical oscillations may rapidly increase with a rise of the temperature. It is assumed that the rate of energy dissipation depends upon the ambient temperature, and a simple temperature dependence of the energy dissipation versus the temperature may be selected as a linear function with a small slope, which should enter both into the heat balance equation and that describing mechanical vibrations [22]. A physical picture of dynamic processes in almost active geysers seams to be quite simple. A drop in the viscosity leads to some increase in the amplitude, which contributes to some additional heat portion. This heat causes some decrease in the viscosity, so that the heat injection should be reduced. It is clear that such processes should be saturated and would approach some stationary state. However, the system under consideration, being nonlinear one, can possess hysteretic steady-state regimes of motion, which can lead to dangerous oscillation regimes even being far from the resonant frequency.

1. ENHANCEMENT AND SUPPRESSION FACTORS ACCOMPANYING THE GEYSER ACTIVITY

Display equations should be set apart from the body of the text and centered. Use 1 line spaces to separate equations from text. Numbered consecutively, using Arabic numerals enclosed in parentheses and positioned flush right along the final baseline of the equation. Although systems under consideration are highly complex and exhibit unique patterns for every given geyser, nonetheless, we can trace some their common features using simple tools of the nonlinear dynamics. Mathematical modeling of the geyser activity is ranged from simplest physical descriptions based on the Bernoulli principle for ideal fluids, through the analytical studies over the theory of nonlinear dynamical systems [23], up to numerous numerical simulations of multiphase fluid and heat transport, predominantly through the porous media [24]. Experimental studies are focused on the monitoring of natural geysers [3] together with laboratory investigations [19].

Multiphase flows frequently occur in space technologies. To predict the local flow pattern, a flow pattern map is used that displays the transition boundaries between the flow patterns, typically plotted on logarithmic scales, using representative parameters describing the liquid and gas phases [11]–[17]. Figures 1 and 2 illustrate widely quoted flow pattern maps for vertical flow proposed by Fair [11] and then by Hewitt and Roberts [12]. Arrows show a typical geyser activity cycle.

For instance, let the internal diameter of a vertical pipe be $2.54\times10^{-2}\,[m]$. Let the concrete fluid properties be the liquid density and vapor density: $\rho_l = 961\,[kg/m^3]$, $\rho_l = 32\,[kg/m^3]$, correspondingly, and the liquid viscosity and vapor viscosity, $\mu_l = 0.4\,[kg\ m^{-1}s^{-1}]$, $\mu_g = 0.01\,[kg\ m^{-1}s^{-1}]$, as well. Suppose that the vapor quality is $x = 0.56$ and let the total flow rate of liquid and vapor be $0.454\,[kg/s]$. The mass velocity is defined a ratio between the mass flow rate and the internal cross-sectional area of the tube: $\dot{m} = 895.2\,[kg/m^2 s]$. The parameter on the horizontal axis to the Fair map is calculated as follows: $\left(x/(1-x)\right)^{0.9}\left(\rho_l \mu_g \rho_g^{-1} \mu_l^{-1}\right)^{0.5} = 1.07$. Thus, the pair of values, 895.2 and 1.07, on the Fair map identifies the flow regime to be annular flow (marked by the diamond symbol in Fig. 1). To use the map for vertical up flow shown, for example in Fig. 2, where v_{gs} denotes the superficial gas velocity; v_{ls} is that of a liquid; ρ_g and ρ_l stand for the gas and liquid densities, correspondingly. The momentum flux of the liquid and gas are calculated using the local vapor quality. Then the values of the vertical and horizontal coordinates are determined and the intersection of these two values on the map identifies the flow pattern predicted to exist at these flow conditions. Transition curves on these maps marks approximately transition zones analogous to that between laminar and turbulent flows. For a more comprehensive and fundamental treatment of two-phase flow transitions, refer to the paper [15]. The most widely quoted flow pattern maps for predicting the transition between two-phase regimes for adiabatic motion in horizontal tubes are proposed by Baker [16]. Then Taitel and Dukler [17], based on the analytical and empirical analysis of the flow transition mechanisms, have constructed the

unified map determined by the dimensionless characteristic numbers, namely the Martinelli parameter, the gas Froude number, the liquid-phase and vapor-phase Reynolds numbers and one more parameter, as a ratio between the gravity force and the related gradient. Point out that vertical patterns seem to be more complicated compared with the horizontal ones, since their description in terms of characteristic numbers is absent.

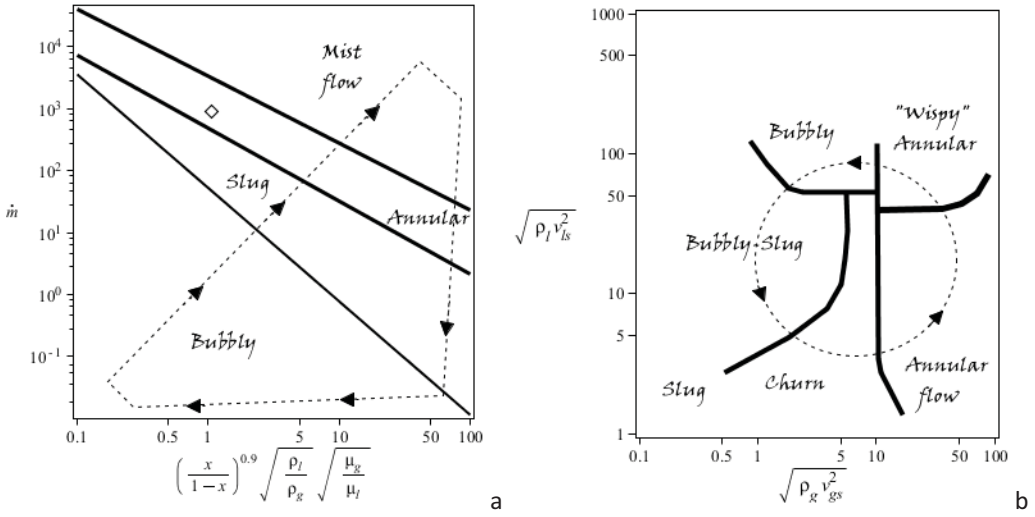

Figure 2. a – Two-phase flow pattern map of Fair [11] for vertical tubes; b – Gas momentum flux versus liquid momentum flux for vertical two-phase co-current upwards flow in a vertical tube [12]

Basic patterns of the flow boiling in vertical pipes can be the following: bubbles appear at the heated surface and then are lifted in a saturated liquid upward turning into larger bubbles, approaching widths of standpipe diameters. Then bubbles grow and create a slug flow at a high vapor concentration. These Stokes bubbles break down in wide tubes to produce turbulent churn flow, since the liquid travels to and fro in a chaotic oscillatory motion while the vapor flows upwards. In narrow tubes an annular flow may occur. The vapor flows in the core of the plumbing system with a high pressure, while the liquid falls downward on the walls as a liquid film under the gravity. At high vapor quality, this film can dry out and the remaining liquid, as small droplets, is flowing jointly with the vapor phase. Finally all droplets are vaporized and the gas phase is superheated [25], [26]. Then the thermal system experiences an adiabatic cooling and the recharge process can be repeated again. The onset of churn flow, illustrated in Fig. 3, is accompanied by a sharp increase in pressure gradient [13], [27] at the fixed fluid pressure and the fixed fluid rate flow. This may be associated with a coherent interaction between the upward gas and downward flows. This cooperative effect can turn into the resonant excitation, if consider a vapor instead the air. As the gas velocity is increased after

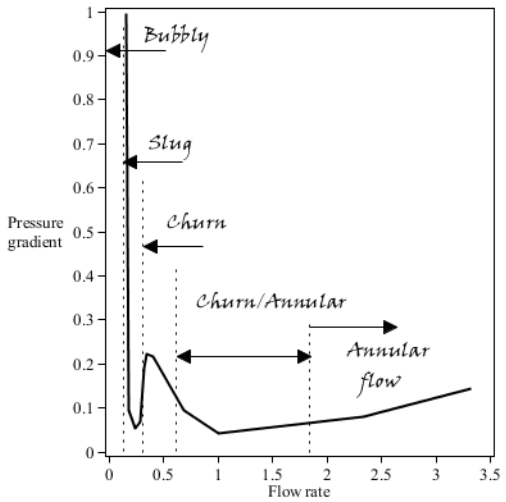

Figure 3. Dimensionless data for pressure gradient in fully developed air-water flux in a vertical tube [13]

the churn flow regime has been entered, the pressure gradient initially decreases and the passes through a minimum.

Then again the pressure gradient increases as the gas flow rate increases up to that of the annular flow. In a saturated flow, the boiling heat is usually transferred by two different mechanisms, convective evaporation and nucleate boiling. Experimental correlations are usually evaluated by combining the contribution of these two mechanisms, including the so-called *enhancement factor* of the convective boiling, E, associated with the presence of bubbles, and also, the *suppression factor* of the nucleate boiling, S, since the liquid flow might suppress bubble nucleation [27]. Let us introduce an operator T defined by the mapping [28]: $x_{n+1} = E(x_n)$ as $x_n \le x_c$, otherwise $x_{n+1} = S(x_n)$ at $x_n > x_c$. Here E and S are continuous functions defined by the present state of the dynamical system, x_n, which is developed up to the new state x_{n+1}, accordingly to the so-called Poincaré mapping T. A jump at the critical point x_c describes the shock phenomenon associated with the collapse of long Taylor bubbles because of condensation at upper parts of the standpipe. The distance between two neighborhood points n and $n+1$ can be defined, in the context of geyser dynamics, as a characteristic lifetime of an individual slug in the standpipe, while the variable x_n may be interpreted as any measured physical parameter, for instance, as the dimensionless energy. The enhancement factor E dominates as the value of x_n exceeds no the critical point x_c. Otherwise, the suppression factor S takes place. Due to the simplicity, we assume the branches $E(x_n) = a_{11} + a_{12}x_n$ and $S(x_n) = a_{21} + a_{22}x_n$ to be linear functions. In spite of simplicity, the study of this dynamical system is also complicated enough. Although, one would declare *a priory* that the parameters a_{11}, a_{12} and a_{21} should be non-negative constants, moreover $a_{12} \ge 1$ and $a_{21} \le 0$, if we consider the geyser dynamics (Fig. 4). A piecewise-linear Poincaré mapping characterized by the critical threshold $x_c = 2/3$ at the parameters: $a_{11} = 3/2$; $a_{12} = 0$; $a_{21} = 2$; $a_{22} = -2$, is depicted in Fig. 4a, starting from the initial point $x_0 = 1/10$. The explicit mapping which exhibits a typical chaotic behavior is shown in Fig. 4b.

Point out that the analogous piecewise linear Poincaré maps can generate, at small values of the parameter a_{21}, almost periodic time series, close to the real-time data represented in the work [19]. Similar structures are also inherent in air bubble formation [29]. As one may conclude the geyser dynamics can by extremely sensitive to small changes in the system parameters and the initial conditions. So that, no one contributing factor can be neglected when developing an adequate mathematical model in the ideal case.

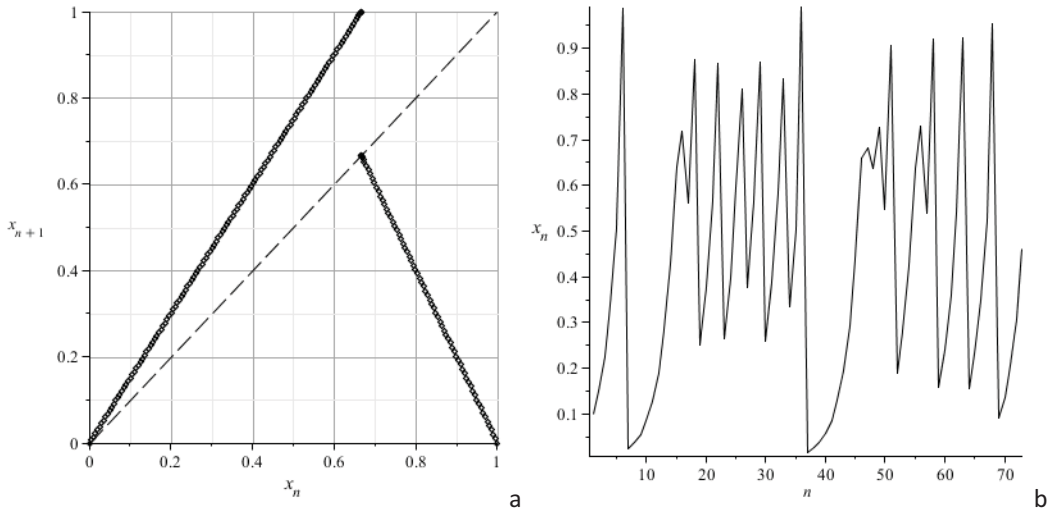

Figure 4. Competition between the enhancement and suppression factors: a –Lamerey diagram; b – symbolic mapping

Conclusions

A discrete dynamical model describing the geyser activity cycle is proposes, based on the analysis of the relevant enhancement and suppression factors, and in accordance with some popular empirical maps related to various vertical two-phase flow patterns [11]–[18], as well. This simplest model is motivated by discrete features in the evolution of slug flow, and has no essential contradictions with known experimental data [19]. Possibly, this can help to confirm or refute some hypotheses in geyser activity observed in the nature [30], [31].

References

[1] E. T. Allen and A. L. Day, *Hot Springs of the Yellowstone National Park*, Publ. 466. Carnegie Institute of Washington: Washington, D.C., 1935.

[2] T. F. W. Barth, *Volcanic Geology: Hot Springs and Geysers of Iceland*, Publ. 587. Carnegie Institute of Washington: Washington, D.C., 1950.

[3] T. S. Bryan, *The Geysers of Yellowstone*, Third Edition. Uni. Press of Colorado, 1995.

[4] J. S. Rhinehart, "Fluctuations in geyser activity caused by variations in earth tidal forces, barometric pressure, and tectonic stresses," *Jour. Geophys. Res.*, vol. 77, pp. 342–350, 1972.

[5] J. S. Rhinehart, "18.6-year tide regulates geyser activity," *Science*, vol.177, pp. 346–347, 1972.

[6] J. S. Rhinehart, *Geysers and Geothermal Energy*, Springer-Verlag, 1980.

[7] D.E. White, "Some principles of geyser activity mainly from Steamboat Springs," *Nevada. Amer. Jour. Sci.*, vol. 265, pp. 641–684, 1967.

[8] D. Jamet, D. Torres and J. U. Brackbill, "On the theory and computation of surface tension: The elimination of parasitic currents through energy conservation in the second-gradient method," *Journal of Computational Physics*, vol. 182, pp. 262–276, 2002.

[9] R. . Nourgaliev, T. N. Dinh, T. G. Theofanous, D. Joseph, "The lattice Boltzmann equation method: theoretical interpretation, numerics and implications," *Int. J. Multiphase Flow*, vol. 29(1), pp. 117–169, 2003.

[10] D. Barnea, "A unified model for predicting flow-pattern transitions for the whole range of pipe inclinations," *Int. J. Multiphase Flow*, vol. 13, pp. 1–12, 1987.

[11] J. R. Fair, "What You Need to Design Thermosyphon Reboilers," *Petroleum Refiner*, Vol. 39(2), pp. 105–124, 1960.

[12] G. F. Hewitt and D.N. Roberts, Studies of two-phase patterns by simultaneous x-ray and flash photography, *UKAEA Report AERE M2159*, 1969.

[13] D. G. Owen and G. F. Hewitt, An improved annular two-phase flow model, *Proc. Third International Conference on Multiphase Flow*, The Hague, Netherlands, paper C1, 1986

[14] A. W. Bennett, G. F. Hewitt, H. A. Kearsey, R. K. F. Keeys and P. M. C. Lacey, *Flow visualisation studies of flow boiling at high pressures. Proceedings of the Institution of Mechanical Engineers*, 180, Paper no 5. 1965.

[15] D. Barnea, O. Shoham and Y. Taitel, "Flow pattern transition for downward inclined two-phase flow: Horizontal to vertical," *Chemical Engineering Science*, vol. 37, pp. 735–740, 1982.

[16] O. Baker, "Simultaneous flow of oil and gas," *Oil and Gas Journal*, vol. 53, pp 185–195, 1954.

[17] Y. Taitel and A. E. Dukler, "A model for predicting flow regime transitions in horizontal and near-horizontal gas-liquid flow," *American Institute of Chemical Engineers Journal*, vol. 22, pp 47–55, 1976.

[18] A. Kawahara, P. M.-Y. Chung, M. Kawaji, "Investigation of two-phase flow pattern, void fraction and pressure drop in a microchannel," *Int. J. Multiphase Flow*, vol. 28(9), pp. 1411–1435, 2002.

[19] S. Lasic, "Geyser model with real-time data collection," *European Jour. of Physics*, vol. 27(4), pp. 995–1005, 2006.

[20] R. Kaji, B. J. Azzopardi, D. Lucas, "Investigation of flow development of co-current gas-liquid vertical slug flow," *Int. J. Multiphase Flow*, vol. 35(4), pp. 335–348, 2009.

[21] U. Kadri, M. L. Zoeteweij, R. F. Mudde and R. V. A. Oliemans, "A growth model for dynamic slugs in gas-liquid horizontal pipes," *Int. J. Multiphase Flow*, vol. 35(5), pp. 439–449, 2009.

[22] R. L. Fogelson and E. P. Likhachev, Temperature dependence of viscosity. *Tech. Physics*, vol. 71(8), pp. 128–131, 2001.

[23] P. S. Landa and D.A. Vlasov, "Geyser as a self-oscillatory system," *Doklady Mathematics*, vol. 76(1): pp. 623–628, 2007.

[24] S. E. Ingebritsen, and S. A. Rojstaczer, "Geyser periodicity and the response of geysers to deformation," *J. Geophys. Res*., vol. 101(B10), 21, pp. 891–921, 1996.

[25] W. Owhaib, C. Martín-Callizo and B. Palm, "Evaporative heat transfer in vertical circular microchannels," *Appl. Thermal Eng. J*., vol. 24, pp. 1241–125, 2004.

[26] S. S. Kutateladze and A. I. Leontiev, *Heat Transfer, Mass Transfer, and Friction in Turbulent Boundary Layers*, Hemisphere Publishing Corp., 1989.

[27] S. Jayanti and G. F. Hewitt, "Prediction of the slug-to-churn flow transition in vertical two-phase flow," *Int. J. Multiphase Flow*, vol. 18, pp. 847–860, 1992.

[28] Ju. I. Neimark, *Mathematical Models in Natural Science and Engineering: An Example-Based Approach (Foundations of Engineering Mechanics)*, Springer, 2003.

[29] A. Tufaile and J. C. Sartorelli, "Hénon-like attractor in air bubble formation," *Physics Letters A*, vol. 275(3), pp. 211–217, 2000.

[30] T. H. Brikowski, "Deep fluid circulation and isotopic alteration in the geysers geothermal system: Prole models," *Geothermics*, vol. 30, pp. 333–347, 2001.

[31] S. Hurwitz, A. Kumar, R. Taylor, H. Heasler, "Climate-induced variations of geyser periodicity in Yellowstone National Park," *Geology*, vol. 36(6), pp. 451–454, 2008.

Proceedings of the 4th International Conference on Nonlinear Dynamics
ND-KhPI2013
June 19-22, 2013, Sevastopol, Ukraine

Motion of a Rod on a Surface

Alexander S. Kuleshov[1*], Sergey V. Ifraimov[2]

Abstract
Motion of the rigid infinitely thin rod on a fixed convex surface is investigated. Equations of motion of the rod on an arbitrary convex surface under the action of gravity are derived. The condition when the obtained equations possess an invariant measure is found; the possible cases, when this condition is valid are described. All equilibria of the rod on the surface are found and discussed.

Keywords
Nonholonomic system, Rigid rod, Equilibria

[1] Department of Mechanics and Mathematics, Moscow State University, Moscow, Russia
[2] Dorodnicyn Computing Centre of the Russian Academy of Sciences, Moscow, Russia
* **Corresponding author:** kuleshov@mech.math.msu.su

1. Necessary facts from Differential Geometry

To derive equations of motion of the rod on the surface we need some facts from Differential Geometry. Below we briefly discuss these facts.

We shall assume that the coordinate grid on the surface

$$\mathbf{r} = \mathbf{r}(q_1, q_2) \tag{1}$$

consists on the lines of curvature and directions of these lines are defined at every point of the surface by unit vectors

$$\mathbf{u}_1 = \frac{1}{h_1}\frac{\partial \mathbf{r}}{\partial q_1}, \qquad \mathbf{u}_2 = \frac{1}{h_2}\frac{\partial \mathbf{r}}{\partial q_2}, \qquad (\mathbf{u}_i \cdot \mathbf{u}_j) = \delta_{ij} \tag{2}$$

Here h_1 and h_2 are the Lame's coefficients

$$h_i(q_1, q_2) = \left|\frac{\partial \mathbf{r}}{\partial q_i}\right|, \qquad i = 1,2$$

The vector

$$\mathbf{e}(q_1, q_2) = [\mathbf{u}_1 \times \mathbf{u}_2]$$

is the normal vector to the surface (1) at the point (q_1, q_2).

Let us denote by $k_i(q_1, q_2), i = 1,2$ the principal curvatures of the surface (1), then we get

$$\frac{\partial \mathbf{e}}{\partial q_1} = -h_1 k_1 \mathbf{u}_1, \qquad \frac{\partial \mathbf{e}}{\partial q_2} = -h_2 k_2 \mathbf{u}_2 \tag{3}$$

Equations (3) follow from the Rodrigues's theorem [1]. Furthermore, using (2) and (3) it is possible to derive the following equations

$$\frac{\partial \mathbf{u}_1}{\partial q_1} = -\frac{1}{h_2}\frac{\partial h_1}{\partial q_2}\mathbf{u}_2 + h_1 k_1 \mathbf{e}, \qquad \frac{\partial \mathbf{u}_1}{\partial q_2} = \frac{1}{h_1}\frac{\partial h_2}{\partial q_1}\mathbf{u}_2,$$
$$\frac{\partial \mathbf{u}_2}{\partial q_1} = \frac{1}{h_2}\frac{\partial h_1}{\partial q_2}\mathbf{u}_1, \qquad \frac{\partial \mathbf{u}_1}{\partial q_1} = -\frac{1}{h_1}\frac{\partial h_2}{\partial q_1}\mathbf{u}_2 + h_2 k_2 \mathbf{e} \tag{4}$$

2. Kinematic equations

Let the rigid infinitely thin rod moves without sliding on the convex surface defined by the equation (1). Suppose that the rod touches the surface at a single point P. Let us introduce the moving coordinate system $Px_1x_2x_3$ that is rigidly connected with the rod. We denote by $\mathbf{e}_1$, $\mathbf{e}_2$ and $\mathbf{e}$ the unit vectors of this system. The unit vector $\mathbf{e}_1$ is directed such that the radius-vector $\overrightarrow{PG}$ of the center of mass G of the rod has a form: $\overrightarrow{PG} = s\mathbf{e}_1$. The unit vector $\mathbf{e}$ is a normal vector to the supporting surface at the point P. The unit vector $\mathbf{e}_2$ is chosen such that the vectors $\mathbf{e}_1$, $\mathbf{e}_2$ and $\mathbf{e}$ form the right handed set of vectors.

We shall define the position of the rod on the surface by the previously introduced variable s and by the angle φ defined as follows:

$$\mathbf{e}_1 = \mathbf{u}_1\cos\varphi + \mathbf{u}_2\sin\varphi, \qquad \mathbf{e}_2 = -\mathbf{u}_1\sin\varphi + \mathbf{u}_2\cos\varphi \tag{5}$$

Since the rod moves on the surface without sliding the velocity of the point P of the rod equals to zero. This condition can be described by two nonholonomic constraints:

$$h_1\dot{q}_1 + \dot{s}\cos\varphi = 0, \qquad h_2\dot{q}_2 + \dot{s}\sin\varphi = 0$$

If we denote $\dot{s} = u$ the corresponding nonholonomic constraints can be rewritten as follows:

$$\dot{q}_1 = -\frac{u}{h_1}\cos\varphi, \qquad \dot{q}_2 = -\frac{u}{h_2}\sin\varphi \tag{6}$$

Using (5) and taking into account (3), (4) and (6) we get

$$\dot{\mathbf{e}}_1 = \left(\dot{\varphi} + \left(\frac{\partial h_1}{\partial q_2}\cos\varphi - \frac{\partial h_2}{\partial q_1}\sin\varphi\right)\frac{u}{h_1 h_2}\right)\mathbf{e}_2 - \left(k_1\cos^2\varphi + k_2\sin^2\varphi\right)u\mathbf{e},$$
$$\dot{\mathbf{e}} = \left(k_1\cos^2\varphi + k_2\sin^2\varphi\right)u\mathbf{e}_1 + \left(k_2 - k_1\right)u\sin\varphi\cos\varphi\mathbf{e}_2$$

Let us define the vector $\boldsymbol{\omega} = \omega_1\mathbf{e}_1 + \omega_2\mathbf{e}_2 + \omega\mathbf{e}$ such that $\dot{\mathbf{e}}_1 = [\boldsymbol{\omega}\times\mathbf{e}_1]$, $\dot{\mathbf{e}} = [\boldsymbol{\omega}\times\mathbf{e}]$. Then the vector $\boldsymbol{\omega}$ is the absolute angular velocity vector of the system $Px_1x_2x_3$. Its components on the axes of the system $Px_1x_2x_3$ have the following form:

$$\omega_1 = \left(k_1 - k_2\right)u\sin\varphi\cos\varphi, \qquad \omega_2 = \left(k_1\cos^2\varphi + k_2\sin^2\varphi\right)u,$$
$$\omega = \dot{\varphi} + \left(\frac{\partial h_1}{\partial q_2}\cos\varphi - \frac{\partial h_2}{\partial q_1}\sin\varphi\right)\frac{u}{h_1 h_2} \tag{7}$$

3. Dynamical equations

In order to derive equations of motion of the rod on the surface we shall use the Gibbs –Appell method. First of all let us find the expression for the energy of accelerations of the system. We shall

use the variables u and ω as quasivelocities in this problem. The energy of accelerations can be found using the formula:

$$S = \frac{M}{2}\mathbf{a}_G^2 + \frac{1}{2}\left(\boldsymbol{\varepsilon}\cdot\Theta_G\boldsymbol{\varepsilon}\right) + \left(\left[\boldsymbol{\omega}\times\Theta_G\boldsymbol{\omega}\right]\cdot\boldsymbol{\varepsilon}\right) \tag{8}$$

Here M is the mass of the rod, $\mathbf{a}_G$ is the acceleration of the rod's center of mass, $\boldsymbol{\varepsilon} = \dot{\boldsymbol{\omega}}$ is the angular acceleration of the rod, Θ_G is the central inertia tensor of the rod. We shall assume that the vectors $\mathbf{e}_1$, $\mathbf{e}_2$ and $\mathbf{e}$ are directed along the principal axes of inertia of the rod. Then Θ_G has the following form:

$$\Theta_G = \begin{pmatrix} 0 & 0 & 0 \\ 0 & J & 0 \\ 0 & 0 & J \end{pmatrix}$$

In the explicit form expression (8) can be written as follows:

$$S = J_P\left(k_1 - k_2\right)\left(u\dot{\omega} - 3\omega\dot{u} - 2\left(\frac{\partial h_2}{\partial q_1}\sin\varphi - \frac{\partial h_1}{\partial q_2}\cos\varphi\right)\frac{u\dot{u}}{h_1h_2}\right)uk_\varphi\sin\varphi\cos\varphi -$$
$$-J_P\left(\left(\frac{\partial k_1}{\partial q_1}\cos^2\varphi + \frac{\partial k_2}{\partial q_1}\sin^2\varphi\right)\frac{\cos\varphi}{h_1} + \left(\frac{\partial k_1}{\partial q_2}\cos^2\varphi + \frac{\partial k_2}{\partial q_2}\sin^2\varphi\right)\frac{\sin\varphi}{h_2}\right)k_\varphi u^2\dot{u} +$$
$$+\frac{J_Pk_\varphi^2}{2}\dot{u}^2 + \frac{J_P}{2}\dot{\omega}^2 + Msu\omega\dot{\omega} + Mk_\varphi^2su^2\dot{u}$$

Here $J_P = J + Ms^2$ are the moments of inertia of the rod about the axes Px_2 and Px_3 and $k_\varphi = k_1\cos^2\varphi + k_2\sin^2\varphi$ is the normal section in the direction $\mathbf{e}_1$.

If the rod moves under the action of the forces with the potential $V\left(q_1, q_2, s, \varphi\right)$ then its equations of motion written in the form of the Gibbs – Appell equations have the form

$$\frac{\partial S}{\partial\dot{u}} = -\frac{\partial V}{\partial s} + \frac{\cos\varphi}{h_1}\frac{\partial V}{\partial q_1} + \frac{\sin\varphi}{h_2}\frac{\partial V}{\partial q_2} - \left(\frac{\partial h_2}{\partial q_1}\sin\varphi - \frac{\partial h_1}{\partial q_2}\cos\varphi\right)\frac{1}{h_1h_2}\frac{\partial V}{\partial\varphi}, \qquad \frac{\partial S}{\partial\dot{\omega}} = -\frac{\partial V}{\partial\varphi} \tag{9}$$

Equations (9) together with the (6) and with the equations

$$\dot{s} = u, \qquad \dot{\varphi} = \omega + \left(\frac{\partial h_2}{\partial q_1}\sin\varphi - \frac{\partial h_1}{\partial q_2}\cos\varphi\right)\frac{u}{h_1h_2} \tag{10}$$

form the complete system of equations of motion of the rod on the surface.

4. Motion of the Rod on the Surface of Revolution

Suppose that the supporting surface is the surface of revolution. It is defined with respect to the fixed cartesian frame by the equation

$$\mathbf{r} = \begin{pmatrix} \rho\left(q_1\right)\cos q_2 \\ \rho\left(q_1\right)\sin q_2 \\ \zeta\left(q_1\right) \end{pmatrix} \tag{11}$$

In this case the Lame's coefficients h_1 and h_2 take the form:

$$h_1 = h_1(q_1) = \sqrt{\left(\frac{d\rho}{dq_1}\right)^2 + \left(\frac{d\zeta}{dq_1}\right)^2}, \qquad h_2 = h_2(q_1) = \rho(q_1) \tag{12}$$

and the principal curvatures k_1 and k_2 may be written as follows:

$$k_1 = k_1(q_1) = \frac{\frac{d^2\zeta}{dq_1^2}\frac{d\rho}{dq_1} - \frac{d^2\rho}{dq_1^2}\frac{d\zeta}{dq_1}}{\left(\left(\frac{d\rho}{dq_1}\right)^2 + \left(\frac{d\zeta}{dq_1}\right)^2\right)^{\frac{3}{2}}}, \qquad k_2 = k_2(q_1) = \frac{\frac{d\zeta}{dq_1}}{\rho\sqrt{\left(\frac{d\rho}{dq_1}\right)^2 + \left(\frac{d\zeta}{dq_1}\right)^2}} \tag{13}$$

We shall assume that the rod moves on the surface under the action of gravity. Suppose that the direction of gravity is defined with respect to the fixed cartesian frame by the following formula:

$$\mathbf{F} = -Mg\left(\mathbf{e}_x \cos\alpha + \mathbf{e}_z \sin\alpha\right)$$

i.e. the direction of gravity forms the angle $\pi/2 - \alpha$ with the axis of symmetry of the surface. Then the potential energy of the rod has the following form

$$V = Mg\left[\left(\rho\cos q_2 + \frac{s\cos\cos q_2}{h_1}\frac{d\rho}{dq_1} - s\sin\varphi\sin q_2\right)\cos\alpha + \left(\zeta + \frac{s\cos\varphi}{h_1}\frac{d\zeta}{dq_1}\right)\sin\alpha\right] \tag{14}$$

Equations of motion of the rod on the surface of revolution have the form (6), (9) and (10) where we should substitute h_1 and h_2 by the corresponding expressions (12) and k_1 and k_2 by the corresponding expressions (13). We should use also the expression (14) for the potential energy of the system.

5. Equilibria of the Rod on the Supporting Surface

Equations of motion of the rod on the supporting surface have a particular solution $s = s_0$, $\varphi = \varphi_0$, $q_1 = q_{10}$, $q_2 = q_{20}$ where s_0, φ_0, q_{10}, q_{20} are constants. This solution corresponds to the equilibrium of the rod on the supporting surface. Conditions of existence of equilibria have the form:

$$\frac{\partial V}{\partial s} = \frac{\cos\varphi}{\sqrt{\left(\frac{d\rho}{dq_1}\right)^2 + \left(\frac{d\zeta}{dq_1}\right)^2}}\frac{\partial V}{\partial q_1} + \frac{\sin\varphi}{\rho}\frac{\partial V}{\partial q_2}, \qquad \frac{\partial V}{\partial \varphi} = 0 \tag{15}$$

In order to clarify the physical meaning of these conditions we represent the potential energy of the rod in the form:

$$V(q_1, q_2, s, \varphi) = \left(M\mathbf{g}\cdot\left(\mathbf{r} + s\mathbf{e}_1\right)\right)$$

Substituting this expression to the conditions (15) and taking into account (2)-(5) we can re-write the conditions (15) as follows:

$$\left(M\mathbf{g}\cdot s\mathbf{e}_2\right) = 0, \qquad \left(M\mathbf{g}\cdot\left(-k_\varphi s\mathbf{e}\right)\right) = 0 \tag{16}$$

Let us discuss the possible solutions of the system (16). Obviously the system has a solution $s = 0$. In this case the rod touches the surface by its center of mass and it will be in equilibrium independently on the values of the other coordinates φ, q_1 and q_2. Therefore equilibria of this type form

the manifold $\left\{(q_1,q_2,s,\varphi)\big|_{s=0}\right\}$ and they are not isolated. The investigation of stability of these equilibria is a sufficiently difficult problem [2]. We shall not study this problem here.

When $s\neq 0$ equations (16) take the form:

$$\left(M\mathbf{g}\cdot\mathbf{e}_2\right)=0,\qquad k_\varphi\left(M\mathbf{g}\cdot\mathbf{e}\right)=0$$

These conditions are valid when the rod is directed along the gravitational vertical. The center of mass G of the rod will be below (stable equilibrium) or above (unstable equilibrium) of the point P. These conditions are valid also when the normal section curvature $k_\varphi=0$. In this case the normal section of the supporting surface through the direction of the rod is a straight line. In equilibrium position the rod touches the surface along this straight line. In this case we have the multipoint contact of the rod with the surface.

6. Existence of an invariant measure

Equations of motion of the rod on the surface of revolution resolved with respect to the derivative have a form:

$$\dot u=-\frac{Msu^2}{J_P}+\left(3\omega+2\frac{d\rho}{dq_1}\frac{u\sin\varphi}{\rho h_1}\right)\frac{(k_1-k_2)u\sin\varphi\cos\varphi}{k_\varphi}+$$
$$+\left(\frac{dk_1}{dq_1}\cos^2\varphi+\frac{dk_2}{dq_1}\sin^2\varphi\right)\frac{u^2\cos\varphi}{h_1k_\varphi}+\frac{Mgs}{J_Ph_1k_\varphi}\left(\frac{d\rho}{dq_1}\sin\alpha-\frac{d\zeta}{dq_1}\cos q_2\cos\alpha\right),$$
$$\dot\omega=-\frac{Msu\omega}{J_P}-(k_1-k_2)k_\varphi u^2\sin\varphi\cos\varphi+\frac{Mgs\cos\varphi\sin q_2\cos\alpha}{J_P}+$$
$$+\frac{Mgs}{J_Ph_1}\left(\frac{d\rho}{dq_1}\cos q_2\cos\alpha+\frac{d\zeta}{dq_1}\sin\alpha\right)\sin\varphi,$$
$$\dot\varphi=\omega+\frac{d\rho}{dq_1}\frac{u\sin\varphi}{h_1\rho},\qquad \dot s=u,\qquad \dot q_1=-\frac{u\cos\varphi}{h_1},\qquad \dot q_2=-\frac{u\sin\varphi}{\rho}$$

It is known (see e.g. [3]) that the smooth function $\mu(\mathbf{x})$ is a density of the invariant measure for the equation $\dot{\mathbf{x}}=\mathbf{v}(\mathbf{x})$ if and only if $\operatorname{div}(\mu\mathbf{v})=0$, where

$$\operatorname{div}(\mu\mathbf{v})=\sum_k\frac{\partial(\mu v_k)}{\partial x_k}\tag{17}$$

Equation (17) can be represented in the form

$$-\frac{d}{dt}(\ln\mu)=\sum_k\frac{\partial v_k}{\partial x_k}$$

Applying the corresponding formula to the equations of motion of the rod we found that these equations possess the invariant measure when the condition

$$\rho k_2\frac{dk_1}{dq_1}-\rho k_1\frac{dk_2}{dq_1}+2k_1k_2\frac{d\rho}{dq_1}-2k_1^2\frac{d\rho}{dq_1}=0\tag{18}$$

is valid. The corresponding density of the invariant measure has the form

$$\mu=\left(J_Pk_\varphi\right)^{\frac{3}{2}}\rho h_1\sqrt{k_1}$$

(for $k_1\neq 0$) or the form

$$\mu = \left(J_P \sin^2 \varphi\right)^{\frac{3}{2}} k_2^2 h_1$$

(for $k_1 = 0$). The existence of the invariant measure facilitates the process of integration of equations of motion of the rod on the surface of revolution. Moreover the existence of an integral invariant with a positive density is interesting also for the possible application of ergodic theory to this problem.

Note that the condition (18) is valid for many convex surfaces. Indeed it is valid in the case when the supporting surface is a cylinder, a cone, a paraboloid, a sphere, an ellipsoid etc.

Equations of motion of the rod on the surface of revolution form the system of six first-order autonomous differential equations. We shall continue the study of this problem by various methods.

Acknowledgments

For the first author (Alexander S. Kuleshov) this work was supported financially by the Russian Foundation for Basic Research (grant no. 11-01-00322).

References

[1]. Do Carmo M. P. *Differential geometry of curves and surfaces,* Prentice-Hall. Englewood Cliffs. New Jersey, 1976.

[2]. Tatarinov Ya.V. Consequences of non-integrable perturbation of integrable constraints: Non-linear effects of motion near the equilibrium manifold *Journal of Applied Mathematics and Mechanics,* Vol. 56, N. 4, pp. 507-517, 1992.

[3]. Bolotin S.V., Karapetyan A.V., Kugushev E.I., Treshev D.V. *Theoretical Mechanics,* Academiya, Moscow, 2010 (in Russian).

Proceedings of the 4th International Conference on Nonlinear Dynamics
ND-KhPI2013
June 19-22, 2013, Sevastopol, Ukraine

Interaction of Frame Type Constructions with Tuned Mass Dampers and the Damping Devices Having Nonlinear Elastic and Dissipative Characteristics

V.V. Kulyabko[1*], D.S. Yaroshenko[1]

Abstract
In this paper it is considered a modeling of the static-dynamic interaction of buildings and structures with special damping devices, including the Tuned Mass Dampers. Ways of extinguishing of oscillations and positions of location of devices with nonlinear-elastic and nonlinear-dissipative elements are discussed. Corresponding solutions are connected with modes of natural vibrations. Classification of tasks by four types of complexity is offered for frame structures.

Keywords
Tuned Mass Damper, nonlinearly elastic element, model

1 SHEE "Prydniprovs'k State Academy of Civil Engineering and Architecture", Dnipropetrovs'k, Ukraine
* **Corresponding author:** kulyabko-vv@mail.ru

Introduction

The Damping Devices (DD) and the Tuned Mass Dampers (TMD) are widespread in mechanical engineering. However, in the second half of the XX century they also find very wide application in modern construction. And, such devices are used not only in buildings under construction, but also at reconstruction of the already existing. More than 10 thousand structures worldwide (more than 30 countries) are protected by Seismic Isolation devices, Energy Dissipation systems, devices of protection against dynamics loads (Japan, China, Russia, the USA, Iran, Italy, etc.).

It is connected with growth of heights and spans of buildings and structures. Therefore, dynamic loadings and the levels of vibration of such objects grow. It is dangerous for durability of constructions (it is necessary to supervise in them dynamic tension), for vibration resistance work of the equipment (a sad example – accident on Fukushima-2011) and for comfortable stay and activity of people (therefore speeds and accelerations of crossovers are studied).

Dynamic impacts in structural models are considered as force loads (a wind, a tsunami, operation of a machine and the equipment), and kinematic loads (seismicity, transport) – see works of authors at the previous ND conferences. Generally in building science there are four groups of nonlinearities [1, 2]:

a) geometrical nonlinearity: a work of torsion fibers and some constructions of ultimate flexural rigidity;

b) physical: nonlinear internal friction in materials of constructions, forces (constant on the module, position, etc.) dry friction in knots, joints, DD, TMD;

c) constructional: change of the design scheme of a construction in the course of loading and vibrations, work of adaptive systems (gaps, "switching off" or "inclusion" of elements, connections), work of semi-rigid joints in seismic constructions, etc.;

d) genetic: the accounting of all history of loading with accumulation of residual tension in use, etc.

Authors conclude that for stabilization of building constructions by means of DD and TMD the most perspective is a use of groups of nonlinearities b and c.

Designs of linear and nonlinear DD (TMD, absorbers, dampers with viscous friction and with dry friction, energy dissipators etc.) are known. Application and selection of parameters of such devices were considered in works of Den Gartog (linear TMD), B. G. Korenev, L.M.Reznikov (nonlinear TMD), A.L.Zakora and M.I.Kazakevich (anti-hunting of guys and bridge designs). It is a lot of interesting constructive decisions and analytical calculations on anti-hunting it is published by KhPI works (Y.V. Mikhlin's and K.V.Avramov's schools).

In many cases object of protection is simulated as a single-mass system without friction. Sometimes nonlinear systems were investigated with application of linearization of characteristics. Problem is that the modern domestic bundled software (BS) on the basis of FEM yet don't allow to model complex challenges of nonlinear dynamics of branched constructions. Therefore designers of dynamic protection of constructions needs in available engineering techniques: from creation of individual dynamic models of interaction of a construction from DD and drawing up rational systems of the nonlinear differential equations and their decision – before design receptions (it is desirable, - patented and proved) and trial tests.

Main material

Let's divide discussed construction tasks and their models of nonlinear damping of complexity level into four types (are discussed: task, constructive decisions, extent of specification of static-dynamic models, type of systems of the differential equations of the linear and nonlinear, free and forced oscillations).

The first type of tasks. It is the simplest type on complexity. Here it is possible to mean, for example, ways of vibrations decrease of the object given to model of an oscillator well described in works [3,4] with additional elements (if TMD, as though the second oscillator) join. If to consider classical TMD, in the works stated above the bigger attention was paid to option with linear forces of viscous resistance.

Unfortunately, in literature of researches on (more convenient in exploitation) dampers of dry friction have much less. The reason of such phenomenon – not only in complexity of settlement justifications (bundled software don't solve this nonlinear problem), but also in some advantages (besides "settlement character") on the party of dampers of viscous friction. However application, for example, easy-to-work frictional dampers on railway transport by their quantity exceeds much dampers of viscous friction. It allows to predict the same broad use of powers of dry friction for stabilization and protection of building objects.

Some comparison of ways of anti-hunting of the construction modeled by an oscillator, is carried out in work [5] where results of calculation of dynamic coefficients for TMD, absorbers, dampers with viscous and dry friction are shown. It is shown that it is under certain conditions better indicators at dampers and TMD, is worse – at absorbers.

The second type of tasks. Separate rod bent designs, subsystems of flat rather simple frames are considered. They are accepted in the form of discrete and continual models with finite number of degrees of freedom and the concentrated masses (fig. 1, a,c) between which there can be generally communications, DD, TMD, etc. with nonlinear power characteristics (fig. 1, b). Designs of a construction and additional elements can be modeled as in the form of absolutely rigid, and bent elements.

Separate characteristics of a set (see explanations to fig. 1, b) linear and nonlinear bearing elements of construction designs, vibration insulation, guy systems, the guy lines and switching off communication in anti-seismic construction, interaction between subsystems, internal friction in a material of elements of a design (it can have linear or nonlinear and sedate dependence) can be modeled.

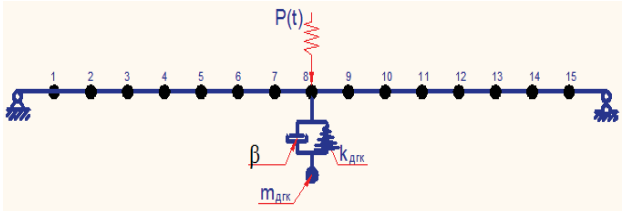

a)

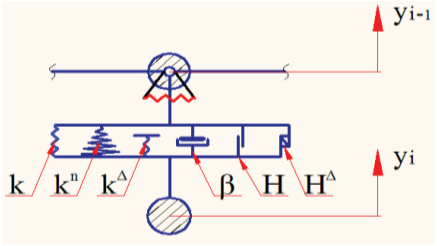

b)

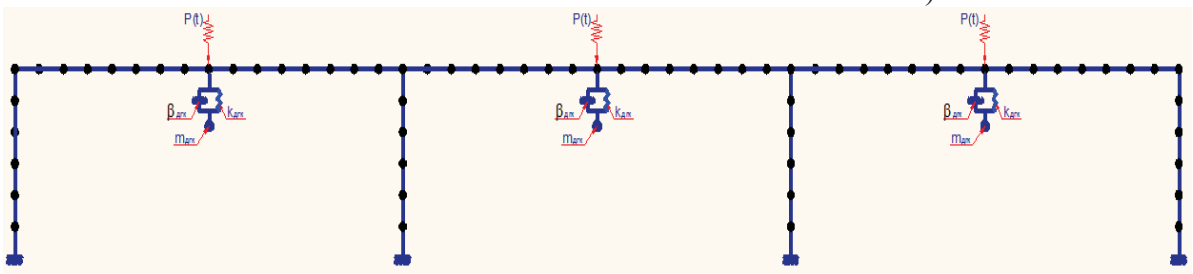

c)

Figure 1. Examples of objects (a,c) and set of modeling of linear k, β and nonlinear characteristics (b): k^n - a conic spring; k^Δ - a spring with a gap; H, H^Δ - dry constant and variable friction on the module

Combinations composed this set with parallel and consecutive schemes it is possible to model elements with nonlinear and elastic elements (like rubber, rubber-metal vibro-insulators, etc.), difficult nonlinear properties of elements of construction designs (gaps, jumps, chaos, and also other nonlinear dependences of deformation on the applied force, entry conditions, plasticity, etc.).

On a fragment (fig. 1, b) subsystems are connected through the described set. Let's accept, for example, that nonlinear elastic and dissipative forces in elements of a set work all six (from left to right) devices. Then the part of system of the differential equations, describing movement of a fragment of model, will assume the following air:

$$\begin{cases} \dots \\ m\ddot{y}_i + \left[k(y_i - y_{i-1})\right] + \left[c_1(y_i - y_{i-1}) + c_2(y_i - y_{i-1})^3\right] + \left[\begin{cases} y_i - y_{i-1} \geq \Delta, k(y_i - y_{i-1}) \\ y_i - y_{i-1} < \Delta, 0 \end{cases}\right] + \\ + \left[\beta(\dot{y}_i - \dot{y}_{i-1})\right] + \left[H sign(\dot{y}_i - \dot{y}_{i-1})\right] + \left[H \frac{(y_i - y_{i-1})}{(y_i - y_{i-1})_{st}} sign(\dot{y}_i - \dot{y}_{i-1})\right] = P(t); \\ \dots \end{cases} \quad (1)$$

The purposes of studying of tasks and frames of the second type – the following. At first it is necessary to find regularities of a range of own frequencies, and then - places of possible demonstration of the main antinode in the most important for object stabilization own forms. At this stage linear models and calculations by means of the bundled software can be used. It is necessary for decrease further amplitudes of the compelled fluctuations on resonant forms by means of concrete DD and TMD with significantly nonlinear characteristics in the specified models.

Let's analyze, generally flexural forms of flat regular frames for check of demonstration of original properties of own oscillations like zones of a condensation of frequencies. On this analogy of properties of "not movable" frames to properties of very widespread not cutting beams (bridges, pipelines, platforms, crane beams) great Ukrainian the mechanic S. P. Tymoshenko paid attention still.

Let's try to find zones of a condensation of own frequencies on ranges, for example, a two-story frame with immovable knots (Fig. 2, a). Profile of cores of a frame is the double-T-iron №45 (a wall of the double-T-iron – in the frame plane). Span and heights of floors are equal 8 m.

Let's accept the following numbering of models:

- model №1 is according to the settlement scheme №1 (to Fig. 2, b) the size of evenly distributed loading (weight) of all elements of a frame of 2.5 kN/m;
- model №2 is similar to the model №1, but load of 5 kN/m;
- model №3 is according to the settlement scheme №2 (to Fig. 2, c), load of 5 kN/m and the size of rigidity of horizontal communications are equal to the doubled longitudinal rigidity of elements of a frame;
- model №4 is similar to the model №3, but rigidity of horizontal communications are equal to zero ("free across a frame");
- model №5 is similar to the model №4, but rigidity of horizontal and vertical connection on marks of bridgings are equal to zero ("free across and verticals frame").

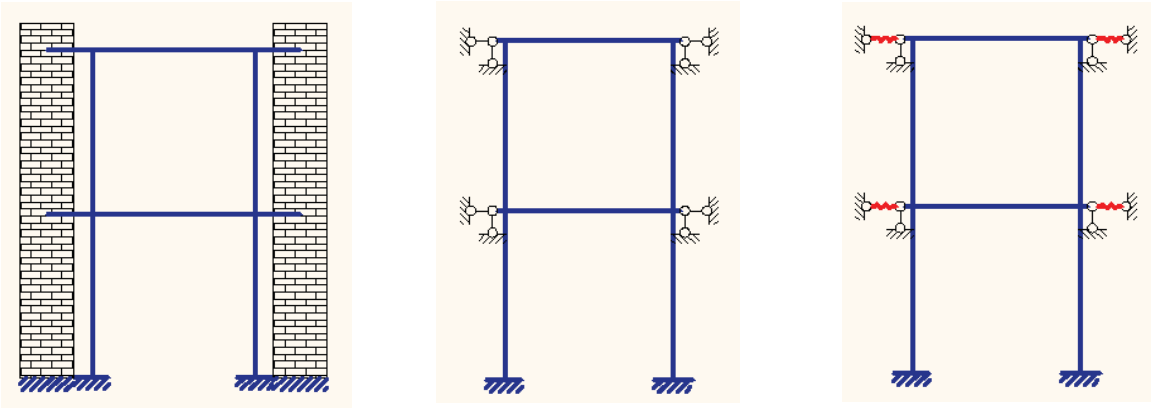

a) the frame scheme with not movable junctions

b) the design scheme №1 (all junctions - not movable)

c) the design scheme № 2 (overlapping with elastic horizontal junctions)

Figure 2. Schemes of a two-storied frame

In the design scheme №1 horizontal and vertical external junctions in level of crossbars of overlapping are accepted absolutely rigid, and in the design scheme №2 horizontal basic cores – elastic, ultimate rigidity. Types and frequencies of the first six forms of natural modes of a frame only for model №1 and frequency ranges for all five models are given in table 1.

It appeared that in case of a frame with not movable knots the quantity of forms of natural modes is equal in each zone of a condensation to quantity of elements of a frame (it is strictly similar to continuous beams). In these zones frequencies of all forms of natural modes of a frame with conditionally linearly - not movable knots of crossing of columns and crossbars lie. And, with a small mass of cores some forms (in connection with symmetry of a frame) "are as though duplicated", having and identical frequencies. At increase of weight of cores there is their small "bifurcation" on a frequency axis. The rigidity of horizontal communications there is less, the similar " separation " are more noticeable.

In the absence of horizontal communications in level of crossbars to the first place with the lowest frequencies there are the forms connected with general and flexural fluctuations of a frame as a two-storied console core (for model №4 it is the 1st and 2nd forms). These forms have lower frequencies, than all forms from a condensation zone. In the absence of all communications in level of crossbars are shown gradually and other type of forms, - the cores connected with longitudinal fluctuations (the 9th and 10th forms for model №5).

The third type of tasks. In this type we will bring certain «installation+TMD» systems with complications, for example, the damper. Constructive decisions and calculations of TMD with two inertial elements are provided, for example in [6]. In [7] the device and the principle of work of a polyfrequency vibro-extinguish by means of work of system of automatic control changes of rigid and dissipative characteristics of various circles of the cascade of the quencher depending on frequency and intensity of dynamic impact on object of clearing of vibrations are possible is described.

Table 1. Forms and frequency spectrum of a frame with stationary knots

№ form	**1**	**2**	**3**	**4**	**5**	**6**
Type of a form	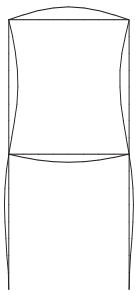	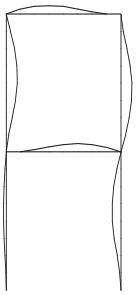	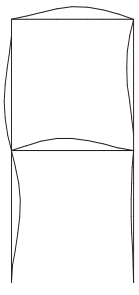	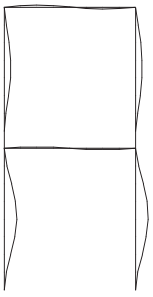	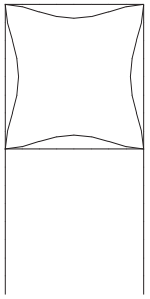	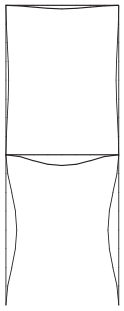
Frequency Hz	9	12.8	12.8	17.4	18.6	18.6
Frequency ranges of frames on different models						

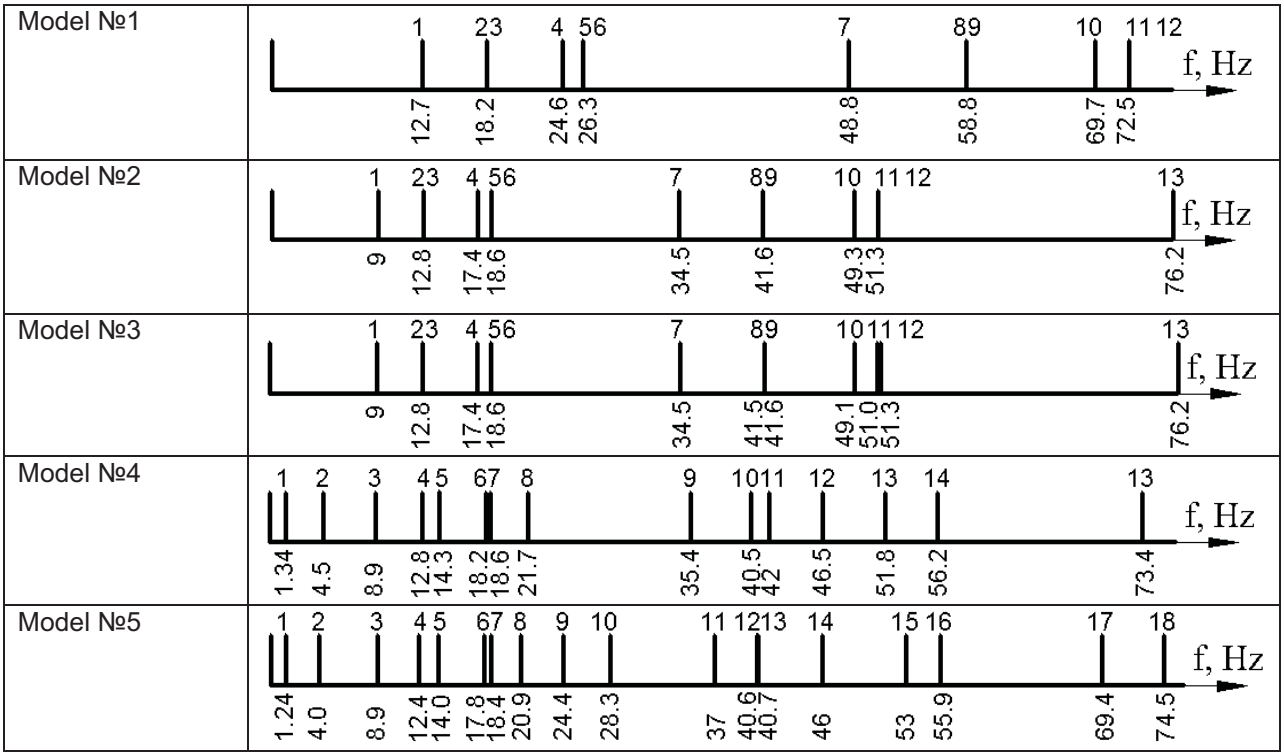

The fourth type of tasks. At last, the most difficult systems are collected in the fourth type of tasks. Here we will carry spatial one - or multy-storied frames with irregular constructive solutions of branched designs. For example, an office building of the former Ministry of highways Georgian the Soviet Socialist Republic (today belongs to Bank of Georgia) in Tbilisi (fig. 3, a), complex skyscrapers the Moscow City (fig. 3, b - the «City of the Capitals» complex).

a) b)

Figure 3. Modern branched spatial frames

Conclusions

In summary we will notice that many unresolved problems of increase of safety, durability and comfort of buildings and constructions can be investigated and solved by adequate modeling of static-dynamic interaction of construction designs with damping devices. It is for this purpose expedient to develop, synthesize and in every possible way to check, compare and test the device with straight-line and nonlinear characteristics. In work the way of modeling of systems with gaps and dry friction which are the main components of semi-fixed knots with rather mobile elements, seismic-isolating belts and other means of damping and protection of buildings and constructions from external vibrations, blows and other dynamic influences is shown.

Besides, the way of search of the most effective arrangement of damping devices in difficult regular and irregular frames – taking into account the analysis of the main forms of natural vibrations from zones of a condensation of frequencies is recommended.

References

[1] Perelmuter A.V., Slivker V.I. *Design models of constructions and possibility of their analysis,* «Steel», Kyiv, 2002. (in Russian)

[2] Kulyabko V.V.,Yaroshenko D.S. About discretization of dynamic models (on examples of beams and frames), in need to take into account different types of nonlinearities. *Space Structures of Buildings*, Moscow, issue 13, pp. 130-139, 2012. (in Russian)

[3] Den Hartog J.P. *Mechanical Vibrations,* Fizmatgis, Moscow, 1960. (in Russian)

[4] Korenev B. G. Dynamic Vibration Absorbers. *Theory and Technical Applications* / Korenev B. G., Reznikov L. M. - Chichester : J. Wiley and Sons, 304 p., 1993.

[5] Kulyabko V.V.,Yaroshenko D.S. An efficient way dampening of vibration of structures. *Collected papers (Branch engineering and construction),* Poltava, issue 2, Vol. 2, pp. 204-213, 2012. (in Russian)

[6] Belokobilsky S.V., Eliseev S.V. and Kashuba V.B. The Tuned Mass Dampers representing a chain with two inertia elements. *Collected papers (Branch engineering and construction),* Poltava, issue 2, Vol. 2, pp. 172-179, 2012. (in Russian)

[7] V.V. Kulyabko, V.M. Gene, and A.F. Shevchenko, SU Patent No. 3281070/25-28, Polyfrequency vibration damper. Izobret., No. 40, 1982.

Proceedings of the 4th International Conference on Nonlinear Dynamics
ND-KhPI2013
June 19-22, 2013, Sevastopol, Ukraine

Localization of the Vibratory Energy of a System With Time-Dependant Mass Into a Nonsmooth Energy Sink

C.-H. Lamarque[1], A. Ture Savadkoohi[1]*

Abstract
Vibratory energy transfer from a main system with deterministic and constant mass to a nonlinear energy sink (NES) with smooth or nonsmooth potential has been already developed. Here, we will deal with the energy transfer problem of a main linear system but with time-dependant mass to a nonsmooth NES at different time scales. Invariant manifold of the system at fast time scale will be detected and then reduced system at first slow time scale by tracing its fixed points and fold singularities will be studied. This study will let us predict different scenarios and behaviors of the system. The system can finally present periodic responses with low or high energy levels and/or strongly modulated responses by repeatedly bifurcations between its stable zones. This study will let us design a NES system according to the aim of its usage (passive control and/or energy harvesting).

Keywords
Time-Dependant Mass, Energy Exchange, NES, Non-Smooth, Multi-Scale, Passive Control

[1]ENTPE, Université de Lyon, LGCB & LTDS UMR CNRS 5513, Vaulx-en-Velin, France
***Corresponding author**: alireza.turesavadkoohi@entpe.fr

Introduction

Efficiency of NES systems in passively controlling structures has been proved theoretically and experimentally [1–3]. Most of the past studies dealt with the passive control process of a linear system with "constant mass" by a NES with "essential cubic nonlinearity". In this paper we would like to study the energy exchange process between a main linear system with "time-dependant" mass by a NES with piece-wise linear potential. Organization of the paper is as it follows: Mathematical model of the system and its analytical treatments at different scales of time are presented in Section 1. A numerical example by showing detailed dynamics of the system during the energy exchange is given in Section 2. Application of the developed techniques in the passive control of time-dependant systems is discussed in Section 3 by giving an example. Finally conclusions are collected in Section 4.

1. Mathematical Representation of the System and Its Analytical Treatments

Let us consider a 2dof system that is consists of a main structure with time-dependant mass, damping and elastic stiffness as $\widetilde{M}(t)$, C and k_1 which is coupled to a non-smooth NES with the mass m. The mass m can move freely in a distance equal to 2δ until it reaches to elastic springs, k_2, at two sides. The overall damping of the NES system is supposed to be $\tilde{\lambda}$. Governing equations of the system can be summarized as:

$$\begin{cases} \widetilde{M}(t)\ddot{x}_1 + C\dot{x}_1 + k_1 x_1 + \tilde{F}(x_1 - x_2) + \tilde{\lambda}(\dot{x}_1 - \dot{x}_2) = \Gamma \sin(\Omega t) \\ m\ddot{x}_2 + \tilde{F}(x_2 - x_1) + \tilde{\lambda}(\dot{x}_2 - \dot{x}_1) = 0 \end{cases} \tag{1}$$

where $\widetilde{M}(t) = M_0(1 + \varepsilon M(t))$ and the non-smooth potential $\tilde{F}$ of the NES is defined as:

$$\tilde{F}(z)=-\frac{\partial V(z)}{\partial z}=-\tilde{F}(-z)=\begin{cases} 0 & -\delta\leq z\leq\delta \\ k_2(z-\delta) & z\geq\delta \\ k_2(z+\delta) & z\leq-\delta \end{cases} \tag{2}$$

ε is a small parameter which corresponds to ratio of the mass of NES and initial mass of the main system, i.e. $0<\varepsilon=\dfrac{m}{M_0}<<1$. We assume that $(1+\varepsilon M(t))\geq 0$ for a time long enough.

We would like to re-scale the system on the basis of the new time domain T where $T=t\sqrt{\dfrac{k_1}{M_0}}=t\vartheta$. Equation (1) reads $(x_i(t)\rightarrow y_i(T))$:

$$\begin{cases} \ddot{y}_1+(1+\varepsilon M(T))^{-1}\varepsilon\zeta\dot{y}_1+(1+\varepsilon M(T))^{-1}y_1+(1+\varepsilon M(T))^{-1}\varepsilon\hat{F}(y_1-y_2) \\ +(1+\varepsilon M(T))^{-1}\varepsilon\lambda(\dot{y}_1-\dot{y}_2)=(1+\varepsilon M(T))^{-1}\varepsilon f_0\sin(\omega T) \\ \varepsilon\ddot{y}_2+\varepsilon\lambda(\dot{y}_2-\dot{y}_1)+\varepsilon\hat{F}(y_2-y_1)=0 \end{cases} \tag{3}$$

Considering that $(1+\varepsilon M(T))^{-1}\simeq(1-\varepsilon M(T))+o(\varepsilon^2)$, we will have:

$$\begin{cases} \ddot{y}_1+(1-\varepsilon M(T))\varepsilon\zeta\dot{y}_1+(1-\varepsilon M(T))y_1+(1-\varepsilon M(T))\varepsilon\hat{F}(y_1-y_2) \\ +(1-\varepsilon M(T))\varepsilon\lambda(\dot{y}_1-\dot{y}_2)=(1-\varepsilon M(T))\varepsilon f_0\sin(\omega T) \\ \varepsilon\ddot{y}_2+\varepsilon\lambda(\dot{y}_2-\dot{y}_1)+\varepsilon\hat{F}(y_2-y_1)=0 \end{cases} \tag{4}$$

where $\dfrac{C}{\sqrt{M_0k_1}}=\varepsilon\zeta$, $\dfrac{1}{k_1}\tilde{F}=\varepsilon\hat{F}$, $k=\dfrac{1}{\varepsilon}\dfrac{k_2}{k_1}$, $\dfrac{\tilde{\lambda}}{\sqrt{M_0k_1}}=\varepsilon\lambda$, $\dfrac{1}{k_1}\Gamma=\varepsilon f_0$ and $\dfrac{\Omega}{\vartheta}=\omega$. We assume that $k=o(\varepsilon^0)$ and scaled potential of the NES reads as:

$$\hat{F}(z)=\begin{cases} 0 & -\delta\leq z\leq\delta \\ k(z-\delta) & z\geq\delta \\ k(z+\delta) & z\leq-\delta \end{cases} \tag{5}$$

First, we transfer the system to $v=y_1+\varepsilon y_2$ and $w=y_1-y_2$. Then we apply complex variables of Manevitch [4] to the system i.e. ($\varphi_1e^{i\omega T}=\dot{v}+i\omega v$ and $\varphi_2e^{i\omega T}=\dot{w}+i\omega w$ with $i=\sqrt{-1}$). We can present the functions $\hat{F}(w)$ and $M(T)$ in the form of Fourier series:

$$\hat{F}(w)=\hat{F}\Big(-\frac{i}{2\omega}(\varphi_2e^{i\omega T}-\varphi_2^*e^{-i\omega T})\Big)=\sum_{j=-\infty}^{+\infty}f_j(\varphi_2,\varphi_2^*)e^{i\omega jT} \tag{6}$$

$$M(T)=\sum_{j=-\infty}^{+\infty} m_j e^{i\omega jT} \tag{7}$$

where the $.^*$ represents the complex conjugate of the function under consideration and $\sum_{j=-\infty}^{+\infty}|m_j|<+\infty$. We would like to analyze the averaged form of equation (4) around the $1:1$ resonance, i.e. $\omega=1+\sigma\varepsilon$ by studying its detailed components at different scales of the ε. By ignoring some obvious higher order terms of ε in system (4) we will have:

$$\begin{cases} \dot{\varphi}_1+\dfrac{i}{2}(1+\sigma\varepsilon)\varphi_1+\dfrac{\varepsilon}{2(1+\varepsilon)}\zeta\varphi_1-\dfrac{i}{2(1+\varepsilon)(1+\sigma\varepsilon)}(\varphi_1+\varepsilon\varphi_2)+ \\ \dfrac{i}{2(1+\varepsilon)(1+\sigma\varepsilon)}(\varepsilon m_0\varphi_1-\varepsilon m_2\varphi_1^*)=-\dfrac{i\varepsilon f_0}{2} \\ \\ \dot{\varphi}_2+\dfrac{i}{2}(1+\sigma\varepsilon)\varphi_2+\dfrac{\varepsilon}{2(1+\varepsilon)}\zeta\varphi_1-\dfrac{i}{2(1+\varepsilon)(1+\sigma\varepsilon)}(\varphi_1+\varepsilon\varphi_2)+ \\ \dfrac{i}{2(1+\varepsilon)(1+\sigma\varepsilon)}(\varepsilon m_0\varphi_1-\varepsilon m_2\varphi_1^*)-\dfrac{i}{2}(1+\varepsilon)\varphi_2 G(|\varphi_2|^2)+\dfrac{1+\varepsilon}{2}\lambda\varphi_2= \\ -\dfrac{i\varepsilon f_0}{2} \end{cases} \tag{8}$$

where the function $G(\chi)$ is defined as [5]:

$$G(\chi)=\begin{cases} 0 & \text{if} \quad \dfrac{\sqrt{\chi}}{\omega}<\delta \\ \\ \dfrac{k}{\pi\omega}\left(-\dfrac{2\delta\omega}{\chi}\sqrt{\chi-(\delta\omega)^2}+2\arccos\left(\dfrac{\delta\omega}{\sqrt{\chi}}\right)\right) & \text{if} \quad \dfrac{\sqrt{\chi}}{\omega}\geq\delta \end{cases} \tag{9}$$

We introduce fast ($T=\tau_0$) and slow ($\tau_1=\varepsilon\tau_0$, ...) time scales to the system and then we will consider its behavior at different scales of ε [6].

1.1 ε^0 and ε^1 orders

ε^0 order of the (8) is equivalent to:

$$\begin{cases} \dfrac{\partial\varphi_1}{\partial\tau_0}=0\Rightarrow\varphi_1=\varphi_1(\tau_1) \\ \\ \dfrac{\partial\varphi_2}{\partial\tau_0}+\dfrac{i\Big(1-G\big(|\varphi_2|^2\big)\Big)+\lambda}{2}\varphi_2=\dfrac{i}{2}\varphi_1 \end{cases} \tag{10}$$

fixed points of the system i.e. $\Phi(\tau_1)$ ($\tau_0 \to \infty, \frac{\partial \varphi_2}{\partial \tau_0} = 0$) can be defined as:

$$\frac{i\Big(1-G\big(|\Phi|^2\big)\Big)+\lambda}{2}\Phi = \frac{i}{2}\varphi_1 \tag{11}$$

By considering $\varphi_1 = N_1 e^{i\delta_1}$ and $\Phi = N_2 e^{i\delta_2}$ following invariant manifold of the system at τ_0 time scale can be obtained:

$$N_1 = N_2\sqrt{\lambda^2+\big(1-G(N_2^2)\big)^2} \tag{12}$$

The stability borders of the invariant manifold is defined as ($H(N_2^2) = 2N_2G'(N_2^2)$) [5]:

$$\lambda^2+\big(1-G(N_2^2)\big)\big(1-H(N_2^2)N_2-G(N_2^2)\big) > 0 \tag{13}$$

Let us study the system at the ε^1 order; the first equation of the system (8) reads:

$$\frac{\partial \varphi_1}{\partial \tau_1}+\frac{i}{2}(2\sigma+1+m_0-i\zeta)\varphi_1-\frac{i}{2}m_2\varphi_1^*-\frac{i}{2}\varphi_2 = -\frac{i}{2}f_0 \tag{14}$$

We would like to analyze the behavior at the slow time scale τ_1 around its invariant manifold in τ_0 time scale. This means that we should consider obtained relationship in (11) in the equation (14):

$$\begin{aligned}&\frac{\partial}{\partial \tau_1}\big(\Phi-i\lambda\Phi-\Phi G(|\Phi|^2)\big)\\&=-\frac{i}{2}f_0-\frac{i}{2}(2\sigma+1+m_0-i\zeta)\big(\Phi-i\lambda\Phi-\Phi G(|\Phi|^2)\big)+\frac{i}{2}m_2\big(\Phi-i\lambda\Phi-\Phi G(|\Phi|^2)\big)^*+\frac{i}{2}\Phi\end{aligned} \tag{15}$$

Let us assume that $m_2 = m_{2r}+im_{2i}$, where m_{2r} and m_{2i} are real and imaginary parts of the m_2, respectively. After some mathematical manipulation, the reduced form of system in the compact form can be summarized as:

$$\begin{cases}\dfrac{\partial N_2}{\partial \tau_1} = \dfrac{\Sigma_1(N_2,\delta_2)}{E(N_2)}\\ \\ \dfrac{\partial \delta_2}{\partial \tau_1} = \dfrac{\Sigma_2(N_2,\delta_2)}{E(N_2)}\end{cases} \tag{16}$$

Ordinary fixed points of the system are those who satisfy $E(N_2) \neq 0$ and $\Sigma_1(N_2,\delta_2) = \Sigma_2(N_2,\delta_2) = 0$. In addition to ordinary fixed point, the system may posses fold singularities that satisfy $E(N_2) =$

$\Sigma_1(N_2,\delta_2)=\Sigma_2(N_2,\delta_2)=0$. It is worthwhile to mention that the criterion $E(N_2)=0$ which provides some lines namely "fold lines" of the system is the same as the stability border which already defined in equation (13).

2. A Numerical Example

We choose a special profile for periodically change of the mass and we will analyze the behavior of the forced system taking into account the chosen pattern of time-dependant mass. The general view of the mass profile is depicted in Figure 1. Let us assume a general definition for the periodically change of mass as it follows:

$$M(T)=\alpha+\beta T \qquad T\in[0,\frac{2\pi}{\omega}] \tag{17}$$

Fourier coefficients of the function $M(T)$ are obtained as:

$$c_n=\frac{\omega}{2\pi}\int_0^{\frac{2\pi}{\omega}} M(T)e^{-i\omega nT}\,\mathrm{d}T \tag{18}$$

It can be proved that for the mass protocol of Figure 1 ($\alpha=0$) we have $c_0=m_0=\frac{\beta\pi}{\omega}$, $c_n=\frac{-\beta}{in\omega}$; so $m_{2r}=0$ and $m_{2i}=\frac{\beta}{2\omega}$. If in analytical developments one chooses m_0 and M_2, then the function of $M(T)$ is defined as:

$$\begin{aligned} M(T)=\sum_{n=-\infty}^{\infty} c_n e^{in\omega T} &\approx c_0+c_2e^{2i\omega T}+\overline{c_2}e^{-2i\omega T}=\underbrace{c_0}_{m_0}+2\Re(\underbrace{c_2}_{m_2}e^{2i\omega T}) \\ &= m_0-2m_{2i}\sin(2\omega T) \end{aligned} \tag{19}$$

where $\Re(...)$ stands for the real part of a complex variable.

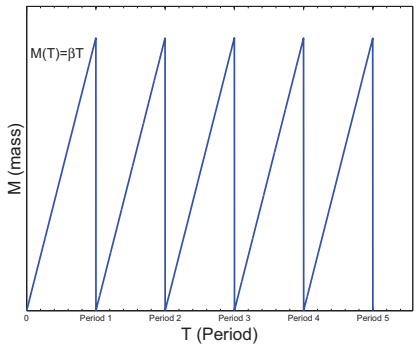

Figure 1. The profile of the periodically varying mass of the main system.

2.1 $\beta=0.5$, $f_0=3.624$

Here we would like to analyze system behavior under forcing term $f_0=3.624$. The full dynamics of system at τ_1 time scales are depicted in Figure 2a. Since points no. 1, 2 and 3 are very close to each

other, we also plotted a zoomed area which covers mentioned points at the same figure. The invariant manifold of the system and obtained numerical results (assumed initial conditions: $y_1(0) = 1.5$ and $y_2(0) = y_1'(0) = y_2'(0) = 0$) are illustrated in Figure 2b. This figure shows that the system repeatedly faces bifurcations between its stable zones. This behavior is named strongly modulated response and is the result of existence of fold singularities ($E(N_2) = \Sigma_1(N_2, \delta_2) = \Sigma_2(N_2, \delta_2) = 0$). The overall time histories of system amplitudes until $T = 10^4$ and also during a narrow time window $9.2 \times 10^4 \leq T \leq 9.6 \times 10^4$ are depicted in Figure 3 showing a beating response due to the strongly modulated behavior of the system at the given time span during the τ_1 time scale. As an example, phase portraits of the reduced system of (16) around fold singular point ($E(N_2) = \Sigma_1(N_2, \delta_2) = \Sigma_2(N_2, \delta_2) = 0$) no. 1 (see Figure 2a) which is saddle/unstable and around fixed point no. 2 (see Figure 2a) which is stable are presented in Figure 4. Other points namely, no. 3 and 4 are unstable and finally no. 5 which is slightly above the second fold line is unstable as well. It can be seen that flows of the system change their directions by aiming at the first line when the system reaches to its singular point i.e. point no. 1 in Figure 2a (see Figure 4a). This means that the system is ready to experience a reverse jump from the first fold line to the second fold via bifurcation. This repeatedly bifurcations of the system and energy exchange between two oscillators will continue until the system get attracted by other stable/unstable fixed points of the system after very long time.

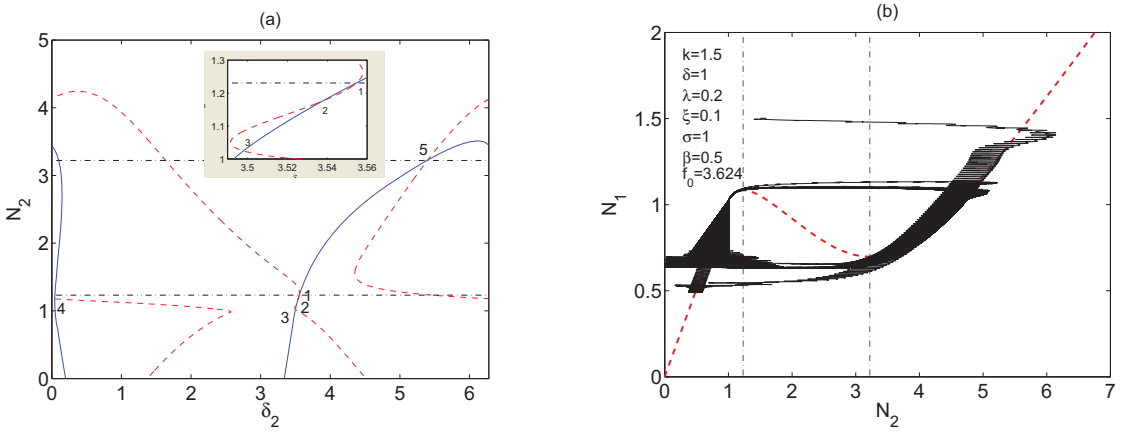

Figure 2. Dynamics of the system with $\beta = 0.5$, $f_0 = 3.624$: a) fold singularities and fixed points-$\Sigma_1 = 0$ (—), $\Sigma_2 = 0$ ($- - -$), $E = 0$($-\cdot-\cdot-$); b) Invariant manifold ($- - -$), stability borders ($-\cdot-\cdot-$) and numerical results (—).

3. Application to the Passive Control: an Example

In order to show the capability of the proposed NES in controlling systems with time-dependant mass under external periodic excitations, we first show numerical results for following single dof system:

$$\ddot{y}_1 + (1 + \varepsilon M(T))^{-1} \varepsilon \zeta \dot{y}_1 + (1 + \varepsilon M(T))^{-1} y_1 = (1 + \varepsilon M(T))^{-1} \varepsilon f_0 \sin(\omega T) \tag{20}$$

which is Eq. 3 without coupled NES. We suppose that $M(T) = \gamma \cos(2\omega T)$ which makes the linear system to be similar to the Mathieu Equation [6]. We consider the same initial conditions as in Section 2 for the system with $\gamma = 0.2$ and $\sigma = 0$. Displacement history of the linear single dof system (Eq. (20)) and linear system with coupled NES (Eq. (3)) are depicted in Figure 5 showing capability of the NES not only in preventing the diverging response of the system but also in decreasing its amplitude in a considerable amount.

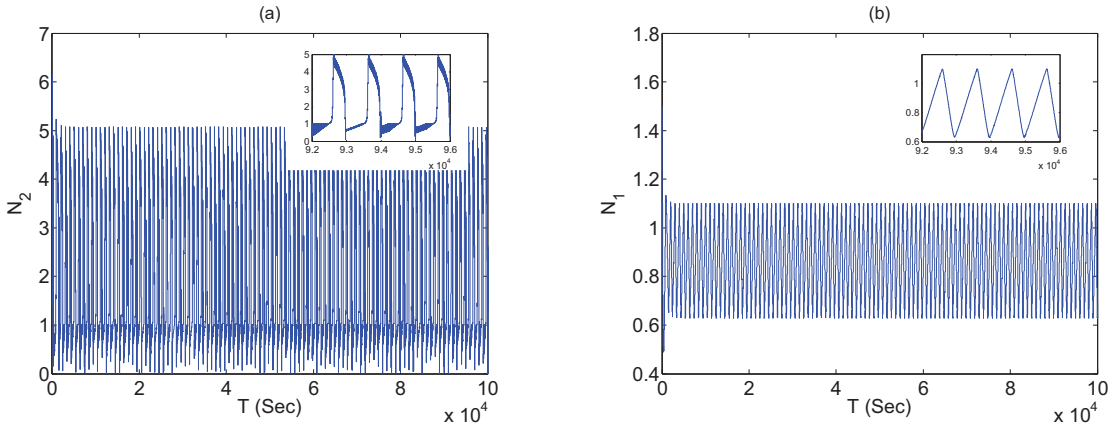

Figure 3. History of the change of system amplitudes under $f_0 = 3.624$ for $0 \leq T \leq 10^5$ (global) and $9.2 \times 10^4 \leq T \leq 9.6 \times 10^4$ (narrow time window): a)N_2 ; b)N_1

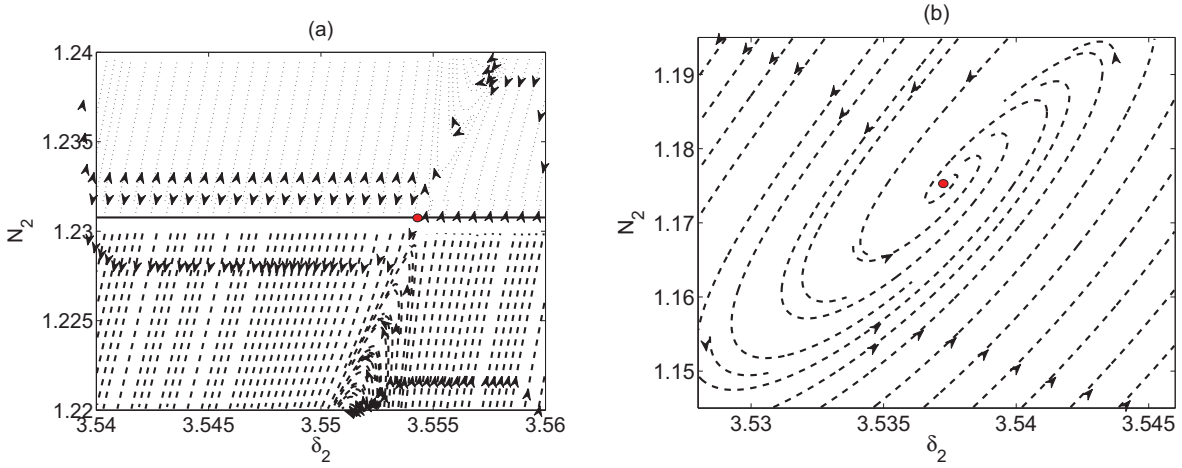

Figure 4. Phase portrait of the system with $\beta = 0.5$ and $f_0 = 3.624$ around point: a) no. 1; b) no. 2

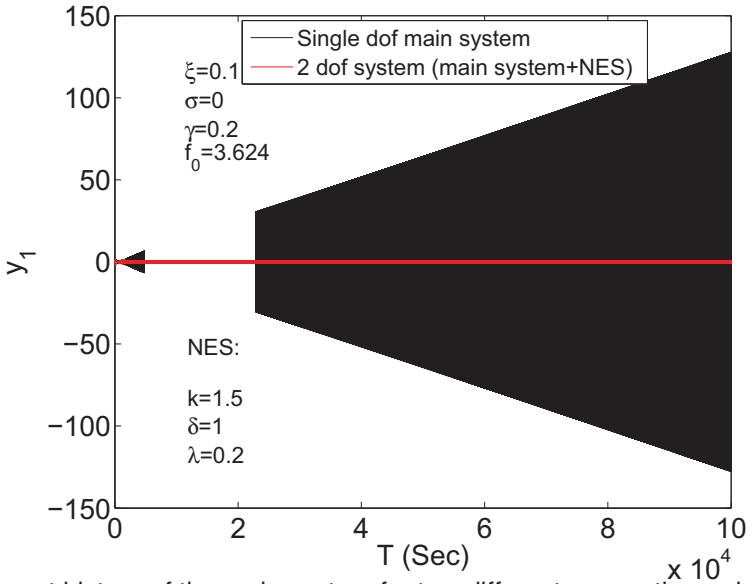

Figure 5. Displacement history of the main system for two different cases: the main system without and with coupled NES.

Conclusions

Developed techniques in the paper will let us design a nonlinear passive control system for structures where their masses are time dependant, e.g. in cables due to different weights of ice during day and night or in vehicles due to the change of the weight of fuel in their tanks. The system can present strongly modulated response and/or periodic one according to existence of fixed and fold singularities.

Acknowledgments

This work is supported by the "Peugeot Citroën Automobiles".

References

[1] Vakakis A. F. Inducing passive nonlinear energy sinks in vibrating systems, *ASME Journal of Vibration and Acoustics*, **123**, pp. 324-332, 2001.

[2] Gendelman O. V. and Lamarque C.-H. Dynamics of linear oscillator coupled to strongly nonlinear attachment with multiple states of equilibrium, *Chaos, Solitons & Fractals*, **24**, pp. 501-509, 2005.

[3] Gourdon E., Alexander, N. A., Taylor, C. A., Lamarque, C.-H. and Pernot, S. Nonlinear energy pumping under transient forcing with strongly nonlinear coupling: theoretical and experimental results, *Journal of Sound and Vibration*, **300**, pp. 522-551, 2007.

[4] Manevitch L. I. The description of localized normal modes in a chain of nonlinear coupled oscillators using complex variables, *Nonlinear Dynamics*, **25**, pp. 95-109, 2001.

[5] Ture Savadkoohi A., Lamarque C.-H. and Dimitrijevic Z. Vibratory energy exchange between a linear and a non-smooth system in the presence of the gravity, *Nonlinear Dynamics*, **70**, pp. 1473-1483, 2012.

[6] Nayfeh A. H. and Mook D. T. *Nonlinear oscillations*, John Wiley and Sons, New York, 1979.

Proceedings of the 4th International Conference on Nonlinear Dynamics
ND-KhPI2013
June 19-22, 2013, Sevastopol, Ukraine

Envelope Rotational Waves in Molecular Chain

Victor A. Lykah[1*], Eugene S. Syrkin[2]

Abstract
Molecular chain with rotational degrees of freedom and quadrupolar interaction between linear molecules is investigated theoretically. Rotation of the molecules is placed in the plane of an adsorbing surface only. The envelope waves in molecular chains are considered. On the base of the linear solutions for the waves, the continual nonlinear equations are derived for slow evolution of the wave amplitudes. Hamilton dynamics for the envelope amplitudes is considered in the phase space. It describes the energy transfer between the degrees of freedom.

Keywords
Molecular chain, envelope waves, Hamilton dynamics

[1] NTU "Kharkiv Polytechnic Institute", Kharkiv, Ukraine
[2] Institute for Low Temperature Physics and Engineering, Kharkiv, Ukraine
* **Corresponding author**: lykahva@yahoo.com; syrkin@ilt.kharkov.ua

Introduction

Molecular crystals are investigated extensively; it is caused by their structural properties, unusual electric and thermal conductivity [1, 2]. Molecular cryocrystals [2] are interesting due to applications in low temperature technique. They also have the simplest molecules with well known interactions. A considerable simplification of description with keeping of the basic physical features is an application of chain models to the linear lattice dynamics and thermodynamics of molecular cryocrystals. Low dimensional systems are very important either as models or as objects for applications. Chain models are necessary stage of investigation of dynamics and thermodynamics of more complex systems: crystals [3], nonlinear dynamics of atomic and molecular lattices [4], and their thermal conductivity [5].

In the present paper we investigate the rotational nonlinear envelope waves of the ordered molecular chain. It was naturally to begin the investigation of this complex problem starting from more simple cases as the linear rotational oscillations [6, 7] or long-wave limit for arbitrary amplitudes and nonlinearity [8,9].

The soliton dynamics of nonlinear systems have been investigated essentially in the framework of simple models of the homogeneous medium [10].The propagation of a nonlinear wave in a periodic medium initiates a gap or gaps in the dispersion law of linear excitations. When the width of the gap is small, the excitations from these two branches interact with each other strongly. Solitons exist with the parameters lying near the gap. The examples are nonlinear optical medium with the modulation of the refractive index [11] and the one-dimensional anharmonic diatomic chain [12].

Here we use the same model approximations as in works [2, 6-9]: one degree of freedom for each molecule, and very hard translational potential. Thus the translational modes are frozen and can be neglected. The molecular chain consists of the linear molecules with quadrupolar interaction [2] between the nearest neighbors.

The molecular chain energy was found to have minimum value for the molecules' alternating ordering: $(\phi_{2n} = \pi/2 + \pi j; \phi_{2n+1} = \pi j)$ *or* $(\phi_{2n} = \pi j; \phi_{2n+1} = \pi/2 + \pi j)$. Here $i, j, n = 0, \pm 1, \pm 2, .,$ an angle ϕ_i is between the principal axis of a molecule and direction of radius-vector which connects centers of inertia of the *i*-th and $(i+1)$-th molecules. Therefore, the molecular system splits onto

two sublattices, index $i = 2n$ $(i = 2n+1)$ defines even (odd) site.

The Lagrangian of the system is $L = K - U$. Here U and $K = \frac{1}{2}\sum J_i \dot{\phi}_i^2$ are potential and kinetic energies of the chain, the *i*-th molecule has moment of inertia $J_i = J_0$ and angle velocity $\dot{\phi}_i$. Then the Lagrangian variation yields system of equations for the chain motion in even (ϕ_{2m}) and odd (ψ_{2m+1}) sites [6-8]. Previously we found integral of motion and the effective potential. We show that the rotational excitations demonstrate a strong anisotropy in the angle space: directions of easy excitation or "valleys" on the effective potential exist.

Discrete equation of linear waves

In the limit case of small oscillations of molecules around the equilibrium positions [6, 7] are brand new and more convenient variables. They are introduced by relations: $\phi_{2m} = v_{2m}$; $\phi_{2m+1} = \pi/2 + u_{2m+1}$. Here v_{2m}, u_{2m+1} are small deviations of the angles from the equilibrium positions. After expansion of terms as power series in small perturbations, the set of equations of the motion can be transformed into the linear system. For harmonic wave excitations the substitution of coordinates in sites $x = jR$ where $j = 0, \pm 1, \pm 2, ...$ transforms into $v_j = v(jR,t) = v(t)exp(-ikjR), u_j = u(jR,t) = u(t)exp(-ikjR)$. The set of equations of the motion can be transformed into a linear system of differential-difference equations for the small oscillations [6, 7]:

$$\begin{cases} -\ddot{v}_{2m} = b_v v_{2m} + d(u_{2m-1} + u_{2m+1}); \\ -\ddot{u}_{2m+1} = b_u u_{2m+1} + d(v_{2m} + u_{2m+2}). \end{cases} \quad (1)$$

Here the basic parameters are $b_v = 4(-a+b+c) = 14, b_u = 4(a+b+c) = 24, d = 2(c-b) = 8$, the parameters of quadrupolar-quadrupolar interaction are $a = 5/4; b = 3/8; c = 35/8$. The dimensionless time is introduced: $t \to \tau = t\omega_0$ where $\omega_0^2 = \Gamma / J_0$ is characteristic frequency. The interaction parameters is $\Gamma = 3Q^2 / 4R_0^5$, a quadrupolar moment of a molecule *Q*, the distance between the centers of inertia of the molecules R_0.

The system of equations for amplitudes of Fourier presentation has solution if its main determinant is equal to zero. That leads to dispersion relations [6, 7]. The dispersion relations are transformed near the edges of the band gap:

$$\omega_{12}^2 \simeq \frac{\omega_0}{2}[b_u + b_v \pm \sqrt{(b_u - b_v)^2 + 16d^2\kappa^2}\ ]; \quad (2)$$
$$\omega_2^2 \simeq \omega_0 b_u;\ \ \omega_1^2 \simeq \omega_0 b_v;\ \ \kappa \to 0;$$

where $\kappa = kR - \pi/2$ is introduced. Indexes 2 and 1 correspond to above and below branches of dispersion relation correspondingly. They describe the gap in the spectrum. At $k = \pm\pi/2R$ the group velocity of the linear waves equals zero: $\partial\omega/\partial k = 0$. In this case the real solutions of the linearized system (1) can be written as standing waves:

$$\begin{cases} v_n(t) = v_0 \cos(\frac{\pi n}{2})\sin(\omega t);\ \ n = 2m; \\ u_n(t) = u_0 \sin(\frac{\pi n}{2})\sin(\omega t);\ \ n = 2m+1. \end{cases} \quad (3)$$

Here *n* ,*m* are integer and *n* is the lattice site number. Now we account the cubic contributions in this expansion.

Envelope nonlinear waves

Let us find expansion of the variables v and u around values in i-th and i+1-th sites. Then we introduce dimensionless space coordinate: $\xi = x / R_0$. Note that deviations are $\Delta x = 2R_0$ and $\Delta\xi = 2$. Then expansions can be written as $v_{i+2} = v_i + 2v_{i'} + 2v_{i''}; u_{i-1} = u_{i+1} - 2u_{i+1'} + 2u_{i+1''}$. Here derivations are $v' = \partial v / \partial\xi$ and $v'' = \partial^2 v / \partial\xi^2$, the same formulae we have for u, u', u''. After substitution of expansions in the system equations [6-8] we obtain system of continual dynamical nonlinear differential equations for the variables $v \equiv v_{2m}$ and $u \equiv u_{2m+1}$. We use expansion to cubic terms and account inequalities $v >> v' >> v''$ and $u >> u' >> u''$. In nonlinear terms space derivations can be neglected.

For investigation of the envelope waves, amplitude and phase are supposed to be varied as functions of coordinate and time [10]. However, we can built simpler solution (3) following to [12]. These solutions do not contain k, κ. The nonlinear equations take the following form for the waves' amplitudes:

$$\begin{cases} -\omega^2 v + \omega_1^2 v + 2du - 2du' - 8[-av^3 + b(v-u)^3 + c(v+u)^3] = 0; \\ -\omega^2 u + \omega_2^2 u + 2dv + 2dv' - 8[+au^3 + b(u-v)^3 + c(u+v)^3] = 0. \end{cases} \quad (4)$$

Here for shortening we denote $v_0 \to v; u_0 \to u$. Let us introduce small parameter of the problem. In [12] for a diatomic chains the parameter has the meaning of the relative atomic mass difference: $\epsilon^2 = \dfrac{M-m}{M+m}$ and can be made very small by isotopes choose. In our problem the parameter has the meaning of relative difference of the frequencies squares

$$\epsilon^2 = \frac{\omega_2^2 - \omega_1^2}{\omega_2^2 + \omega_1^2}. \quad (5)$$

Then the continual dynamic equations for the envelope short length waves are

$$\begin{cases} \dfrac{(\omega_1 - \omega)}{(\omega_2 - \omega_1)}\epsilon^2(\omega_2^2 + \omega_1^2)v + 2du - 8[-av^3 + b(v-u)^3 + c(v+u)^3] = 2du'; \\ \dfrac{(\omega_2 - \omega)}{(\omega_2 - \omega_1)}\epsilon^2(\omega_2^2 + \omega_1^2)u + 2dv - 8[+au^3 + b(u-v)^3 + c(u+v)^3] = -2dv'. \end{cases} \quad (6)$$

Hamiltonian can be presented with small parameter.

The Hamilton equations for envelope waves

A comparison with canonical equations $\dot{q}_i = \partial H / \partial p_i; \dot{p}_i = -\partial H / \partial q_i$ [13] gives analogy

$$t \to \xi; \dot{q}_i \to u'; \dot{p}_i \to v'.$$

Then for the system under investigation we obtain the canonical system of equations

$$\begin{cases} u' = \dfrac{\partial H(u,v)}{\partial v}; \\ v' = -\dfrac{\partial H(u,v)}{\partial u}; \end{cases} \quad (7)$$

where Hamiltonian in the variables $u - v$ is

$$H(u,v) = \frac{1}{2d}\{[-\frac{\omega^2}{2}(v^2+u^2) + \frac{1}{2}(\omega_1^2 v^2 + \omega_2^2 u^2)] + 2duv - 2[a(u^4 - v^4) + b(v-u)^4 + c(v+u)^4]\}. \quad (8)$$

Then the Hamiltonian can be presented with a small parameter for the envelope short length waves as:

$$H(u,v)=\frac{1}{2d}\{\frac{(\omega_2^2+\omega_1^2)}{2(\omega_2-\omega_1)}\epsilon^2[(\omega_1-\omega)v^2+(\omega_2-\omega)u^2] \\ +2duv-2[a(u^4-v^4)+b(v-u)^4+c(v+u)^4]\}; \quad (9)$$

The solutions describe the system evolution along a level curve of the Hamiltonian. For the graphic presentation let us introduce new more convenient variables $\mu=v-u;\pi=v+u$. The level curves are shown in the phase plane $\mu-\pi$ in fig.1.

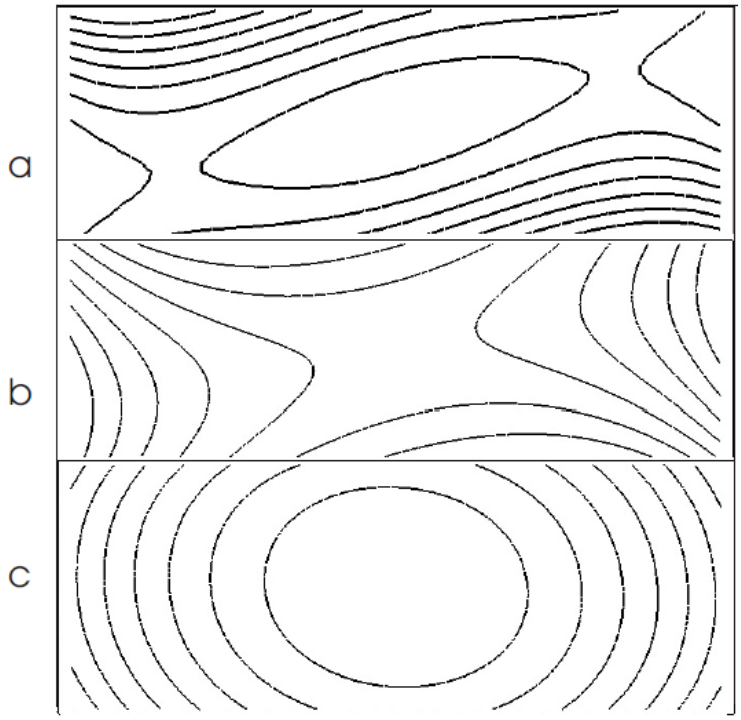

Figure 1. Change of topology of the potential relief of the Hamiltonian (8, 9) on the phase plane of the angles $\mu-\pi$. a) $\omega<\omega_1$; b) $\omega_1<\omega<\omega_2$; c) $\omega_2<\omega$. In the case b the system has infinite solutions only. Horizontal axis shows μ in ranges [-1.51;1.51], vertical axis shows π in ranges [-0.3;0.3].

If $\omega<\omega_1$, then two saddle points exist and one focus (minimum) is between them. The system has finite and infinite solutions; they are divided by the soliton solutions (separatrixes). The finite solutions have oscillating behavior; they are shown by closed curves in fig.1a and oscillating curves in fig.2a. The soliton solutions are shown in fig.2b.

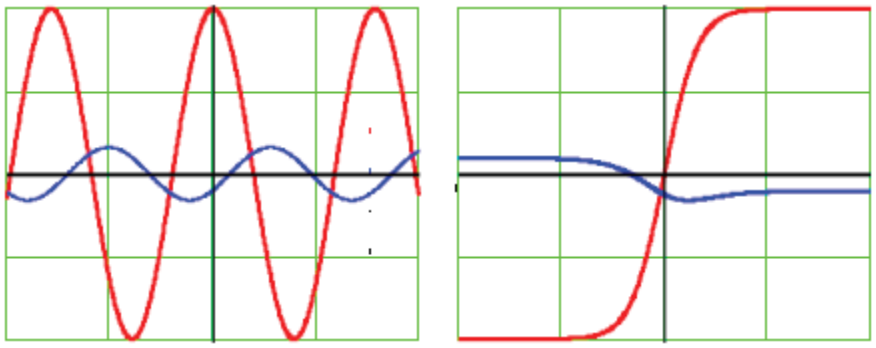

Figure 2. The space change of variables μ (large amplitude curves) and π (small amplitude curves) in the envelope waves follow the Hamiltonian (8, 9). Images are normalized on the maximum value. Left panel: finite small amplitude solutions. Right panel: soliton solution.

If $\omega_1<\omega<\omega_2$, then one saddle point exists. The system has infinite solutions only, fig.1b.

If $\omega_2 < \omega$, then one unstable focus exists. The system has finite solutions only (see fig.1c).

Conclusions

The following results were obtained for the diatomic molecular chain with quadrupole interaction. The discrete and continuous dynamic nonlinear equations were derived. The linear solutions that correspond to the short wave limit give rise to the envelop waves and solitons in the nonlinear case. The small parameter is introduced to describe the chain dynamics near the gap. The small parameter of the problem has the meaning of the relative difference of the proper frequencies. The system of equations is transformed to the Hamilton's equations. The Hamiltonian of the system is found. Qualitative analysis of the solutions is done in the phase plane. Changing of topology is shown in dependence on the wave frequencies.

References

[1] *Semiconducting Polymers: Chemistry,Pphysics and Engineerings*. Eds G. Hadziioannou, P.F. van Hutten. Willey-VCH Verlag, Weinheim, 2000.
[2] Freiman Yu.A and Manzhelii V.G. *Physics of Cryocrystals*, ed A.A.Maradudin, Woodbury, New York, 1996.
[3] Born M., Kun Huang. *Dynamical Theory of Crystal Lattices*, Claridon Press, Oxford, 1954.
[4] Toda M. *Theory of Nonlinear Lattices*, Springer, Berlin, 1981.
[5] Lepri S., Livi R and Politi A. Thermal conduction in classical low-dimensional lattices, *Physical Report*, Vol. 377, pp. 1–80, 2003.
[6] Lykah V.A. and Syrkin E.S. Rotational oscillations of molecular chain with quadrupolar interaction, *Phys. Status Solidi* (c) Vol. 1., pp 3052-3056, 2004.
[7] Lykah V.A. and Syrkin E.S. Small rotational oscillations of molecular chain with duadrupolar interaction. *Phys. Low-dimension Structures* N 7/8, 103, 2004.
[8] Lykah V.A., Syrkin E.S. Phase transitions in the adsorbed molecular chains, *Central European Science Journals,* Vol. 3, pp 61-68, 2005.
[9] Lykakh V. A., Syrkin E. S. Nonlinear orientation dynamics of a molecular chain. *Theor. and Math. Phys*., Vol. 168, N 2, pp 1048-1063, 2011.
[10] Karpman V. I. *Nonlinear waves in dispersive media*. Pergamon, Oxford (1975).
[11] a) Mills D., Trullinger J. Gap solitons in nonlinear periodic structures, *Phys. Rev*. B 36, Vol. 36, N 2 pp.947-952, 1987. b) Coste J., Peyraud J. Stationary waves in a nonlinear periodic medium: Strong resonances and localized structures. II. The continuous model, *Phys. Rev.* B 39, N 18, pp.13096-13105, 1989. c) Coste J., Peyraud J. Dynamics of gap solitons, *Phys. Rev*. B Vol. 40, N 18,, pp.12201-12208, 1989.
[12] a) Chubykalo O. A., Kovalev A. S., Usatenko O. V. Dynamical solitons in a one-dimensional nonlinear diatomic chain. *Phys. Rev.* B, Vol. 47, N 6, pp.3153-3160, 1993. b) Kovalev A. S., Usatenko O. V., Gorbatch A. V. Bifurcation picture for gap solitons in nonlinear modulated systems. *Phys. Rev*. E, Vol. 60, N 2, pp.2309-2316, 1999.
[13] Landau L.D. and Lifshits E.M. *Mechanics*, Nauka, Moscow, 1971.

Proceedings of the 4th International Conference on Nonlinear Dynamics
ND-KhPI2013
June 19-22, 2013, Sevastopol, Ukraine

Synchronic Regimes in Oscillator-Rotator System (Rotation in Vertical Plane)

Arkadiy Manevich[1*], Catherine Sayko[1]

Abstract
An analytical and numerical investigation of steady-state regimes in an oscillator - rotator system (in vertical plane) under harmonic excitation is presented. Periodic motions with synchronous oscillation and rotation are studied. It is shown that such motions exist and are stable in certain domain of the system parameters. Bounds of this domain are determined analytically. All theoretical results are confirmed by numerical simulation.
Keywords
Oscillator-rotator system, nonlinear oscillation, synchronous regime

[1] Dniepropetrovsk National University, Dniepropetrovsk, Ukraine
* **Corresponding author:** armanevich@yandex.ru

Introduction

Mechanical systems displaying interaction of oscillating and rotating elements were investigated in connection with various technical applications in numerous works, see, e. g., [1], [2]. In these works various problems related to synchronous oscillation – rotation regimes were considered, but the task of detailed analytical description of the non-uniform rotation and its reciprocal influence on the body oscillation, apparently, was not posed.

In the presented report the stationary dynamics of a basic oscillator – rotator system under external harmonic excitation is studied. In distinction on papers [3, 4] we consider here the case of oscillation and rotation in vertical plane, i. e. in the gravity field. We constrict ourselves by description of synchronous oscillation-rotation regimes (when the average angular velocity is equal to the cyclic frequency of the oscillation). It is shown that an adequate solution for these regimes can be obtained by a straightforward analytical procedure. The additional parameter connected with the gravity results in essential complication of the system dynamics. All theoretical results are verified in comprehensive numerical simulation.

1. The Model and Governing Equations

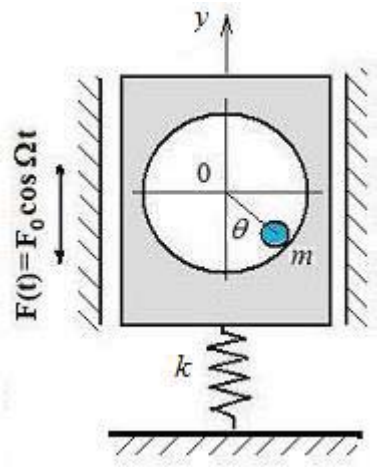

Figure 1. The oscillator-rotator system

The considered system consists of an oscillator ("primary mass", or "object") of mass M with a spring k, and connected with it rotator (point mass m, or ball) which is mounted on the vertical plane of the oscillating body and may move along a circle of radius R. The primary body is excited by the harmonic force $F(t)=F_0\cos\Omega t$ and can move along the vertical axis y (Fig. 1).

Equations of motion of the system with respect to generalized coordinates – vertical deflection of the object y and the rotation angle θ – which take into account the viscous damping in both degrees of freedom through dissipative Rayleigh functions $\Phi_1=0.5\beta_1\dot{y}^2$, $\Phi_2=0.5R^2\beta_2\dot{\theta}^2$, in dimensionless form are as follows:

$$\overline{\Omega}^2 \ddot{u} + \overline{\Omega}^2 \bar{\beta}_1 \dot{u} + u + \mu \cdot \overline{\Omega}^2 \frac{d^2}{d\tau^2}(\cos\theta) = f\cos\tau \qquad (1)$$

$$\ddot{\theta} + \bar{\beta}_2 \dot{\theta} + p \cdot \sin\theta - \ddot{u} \cdot \sin\theta = 0 \qquad (2)$$

where

$$u = \frac{y}{R},\ \ \tau = \Omega t,\ \ \bar{\Omega} = \frac{\Omega}{\omega_0},\ \ \omega_0 = \sqrt{\frac{k}{M+m}},\ \ \mu = \frac{m}{m+M},\ \ f = \frac{F_0}{(M+m)R\omega_0^2},\ \ p = \frac{g}{R\Omega^2}\ , \qquad (3)$$

$$\bar{\beta}_1 = \frac{\beta_1}{(M+m)\Omega},\quad \bar{\beta}_2 = \frac{\beta_2}{m\Omega}$$

(upper dots denote differentiation with respect to dimensional time τ).

2. Rotation of the Mass at Harmonic Oscillation of the Object

2.1. An analytical solution

At the first stage we seek stationary synchronic rotation regimes at harmonic oscillation of the primary body with certain amplitude (which is specified on the second stage), i. e. only the equation for angle θ (2) is solved for given kinematical excitation of the body $u = a\cos\tau$. Equation (2) takes the form:

$$\ddot{\theta} + \bar{\beta}_2 \dot{\theta} + (a\cos\tau + p)\sin\theta = 0 \qquad (4)$$

Synchronous rotational regimes are sought as a superposition of the uniform rotation and a periodic perturbation:

$$\theta = \tau + j\pi + \psi(\tau) \qquad (j = 0;1) \qquad (5)$$

where $\psi(\tau)$ is a periodic function (of period $2\pi/m$, m is an integer) which further assumed to be small comparing to 1. Value $j = 0$ relates to rotation close to in-phase with the body oscillation, $j = 1$ - to rotation close to anti-phase one with the body. Then equation (4) after some algebra is reduced to the following equation with respect to $\psi(\tau)$:

$$\ddot{\psi} + \bar{\beta}_2 \dot{\psi} + (-1)^j p\sin(\tau + \psi) + (-1)^j \frac{a}{2}\sin\psi = -\bar{\beta}_2 - (-1)^j \frac{a}{2}\sin(2\tau + \psi) \qquad (j = 0;1) \qquad (6)$$

Replacement of $j = 0$ by $j = 1$ is equivalent to simultaneous change of sign for a and p. Further we drop $(-1)^j$, but admit both positive and negative a and p values. Along with equation (6) we consider the linearized equation obtained in assumption of smallness of ψ compared to 1:

$$\ddot{\psi} + \bar{\beta}_2 \dot{\psi} + \left(p\cos\tau + \frac{a}{2}(1 + \cos 2\tau) \right)\psi = -\bar{\beta}_2 - \frac{a}{2}\sin 2\tau - p\sin\tau \qquad (7)$$

We seek solution of this non-homogeneous equation with periodic coefficients by expanding ψ in Fourier series

$$\psi = \sum_{n=0}^{\infty} [\psi_n^{(1)} \cos n\tau + \psi_n^{(2)} \sin n\tau] \qquad (8)$$

After some algebra we come to an infinite set of equations with respect to $\psi_n^{(1)}$, $\psi_n^{(2)}$. The numerical analysis showed that it is sufficient to take into account only the first five equations with respect to $\psi_0^{(1)}$, $\psi_1^{(1)}$, $\psi_1^{(2)}$, $\psi_2^{(1)}$, $\psi_2^{(2)}$ (neglecting with $\psi_3^{(1)}$, $\psi_3^{(2)}$, $\psi_4^{(1)}$, $\psi_4^{(2)}$). Thus the approximate solution for the synchronous regimes includes the zero-, first and second harmonics:

$$\theta = \tau + j\pi + \psi_1^{(0)} + \psi_1^{(1)} \cos\tau + \psi_1^{(2)} \sin\tau + \psi_2^{(1)} \cos 2\tau + \psi_2^{(2)} \sin 2\tau \quad (j = 0;1) \qquad (9)$$

In the limit case of undamped system without gravity ($\bar{\beta}_2 = 0$ and $p = 0$) the roots of determinant Δ of the set of equations for $\psi_k^{(s)}$ ($k = 0-2$, $s = 1,2$) are equal to 0; 4/3, 4; 8; -16. The first nonzero root $a = 4/3$ corresponds to the lower bound of the first instability zone on the Ince-Strutt diagram for the Hill equation (the homogeneous equation corresponding to equation (7)).

It is apparent that values of amplitude a in the interval from 0 till the first positive root are of main interest (in case of rotation close to in-phase with oscillation). For damped systems with gravity the first root depends upon values of parameters p and $\bar{\beta}_2$.

2.2. Domain of existence and stability of the synchronous oscillation-rotation regimes

The obtained in the paper analytical solution exists and is stable in certain domain E in plane (p, a) (for a given damping parameter $\bar{\beta}_2$). Boundaries of this domain are determined by following conditions.

- The loss of energy for a cycle due to dissipation can be compensated by input of energy from the object to the rotator (this condition specifies the lower bound for the amplitude a).
- Condition of vanishing determinant Δ determines the upper bound for a.
- Condition of smallness of coefficients $\psi_k^{(s)}$ ($k = 0-2$, $s = 1,2$) comparing to 1 determines the right (upper) bound for parameter p (at given a).

In the work equations and formulas for these boundaries are obtained. The *lower bound* for oscillation amplitudes a_* (for given p and $\bar{\beta}_2$) in the first approximation is specified by formula

$$a_* = (2 - \bar{\beta}_2) - \sqrt{(2 - 3\bar{\beta}_2)^2 + 4\,p^2} \tag{10}$$

In particular case $p = 0$ expression (10) is reduced to $a_* = 2\bar{\beta}_2$, which was obtained earlier (in another notations) in works [1, 3]. The *upper bound* of the domain E (by a) is approximately determined by expression for the zero point of determinant Δ:

$$a^* = \frac{4}{3} + p^2 + 2\bar{\beta}_2^2 + \ldots \tag{11}$$

The *right bound* (by p) is obtained from equation

$$p^3 + \left(2\bar{\beta}_2^2 + a(1 - \frac{3a}{4})\right)p = \left[p^2(1 - \frac{a}{4}) + a(1 - \frac{3a}{4})(1 - \frac{a}{4}) + a\bar{\beta}_2^2\right]\psi_{\max} \tag{12}$$

where $\psi_{\max}$ is the maximal admitted value of the coefficients $\psi_k^{(s)}$ (a value less than 1)). In Fig. 2, *a*, *b*, domains of existence of synchronous regimes are constructed at $\bar{\beta}_2 = 0.2$, for $\psi_{\max} = 0.5$ and $\psi_{\max} = 0.75$, respectively. Here curves 1, 2 and 3 are the lower, upper and right bounds of the domain, respectively.

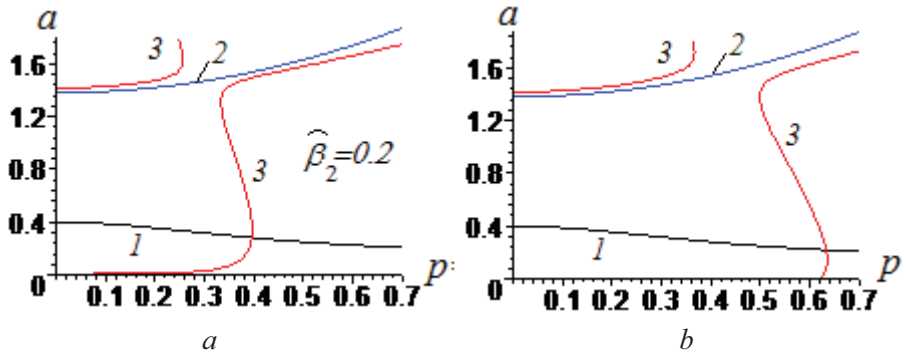

a *b*

Figure. 2. Domain of existence of synchronous regimes ($\bar{\beta}_2 = 0.2$); а) $\psi_{\max} = 0.5$; б) $\psi_{\max} = 0.75$

The synchronous oscillation-rotation regimes do not exist at sufficiently large p values, approximately greater than $0.4 – 0.6$.

3. Results of Numerical Simulation. Comparison with the Analytical Solution

Numerical experiments were conducted for nonlinear and linear equations (2), (7) and (6) with initial conditions yielding from the analytical solution (9): $\theta(0) = j\pi + \psi_0^{(1)} + \psi_1^{(1)} + \psi_2^{(1)}$, $\dot{\theta}(0) = 1 + \psi_1^{(2)} + 2\psi_2^{(2)}$. There were changed amplitude of the body oscillation a and parameter p (for given $\bar{\beta}_2$). Values of p and a were chosen in the central part of the domain E and in vicinity of its boundaries.

In Fig. 3, *a* - *c*, results for $p = 0.2$, $a = 1.0$ are presented (it was assumed $\bar{\beta}_2 = 0.2$, and this point is *close to the center* of E). Fig. 3, *a*, *b,* show the times series for $\psi(\tau)$ and angle $\theta(\tau)$, obtained in the analytical solution (9), and results of numerical simulation of linear equation (7) and nonlinear equation (6). The analytical and numerical solutions for the linear equation nearly coincide (curves in Fig. 3, *a, b*) and are very close to numerical solution of the nonlinear equation.

Fig. 3, *b,* shows that the rotation is close to the uniform one. The last plot (Fig. 3, *c*) presents the phase curve in coordinates ($u = a\cos\tau$, $\cos\theta$), obtained in the numerical simulation.

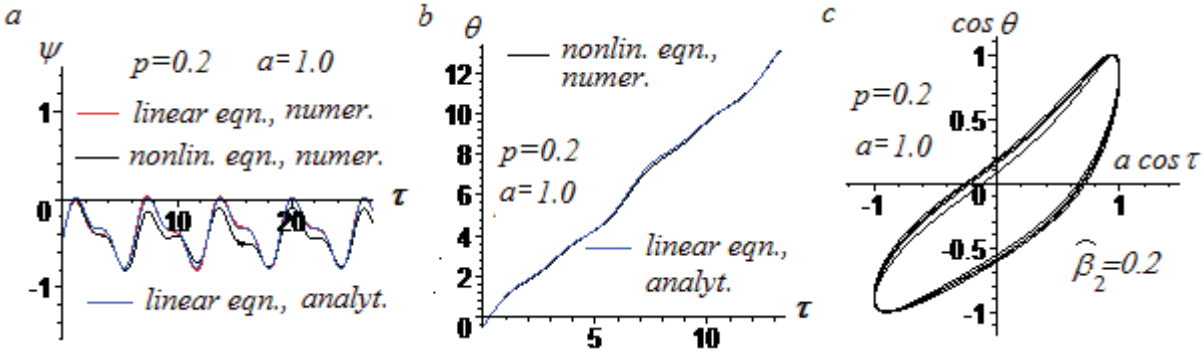

Figure 3. Comparison of the analytical and numerical solutions for $p = 0.2$, $a = 1.0$ ($\bar{\beta}_2 = 0.2$); (*a*) - (*b*) – times series for $\psi(\tau)$ and $\theta(\tau)$; (*c*) –phase curve ($a\cos\tau$, $\cos\theta$)

Phase curves enable us to separate visually synchronous rotational regimes from asynchronous ones. At synchronous oscillation - rotation the phase curve is a closed loop which superimposes on itself on each new cycle. Here the phase curve testifies synchronous rotation and oscillation.

When the parameters were chosen *in a vicinity of the boundary* of domain E, then the synchronous rotation became unstable. Near the *right bound* of the domain E the angular perturbation ψ begins to oscillate with increasing amplitude due to parametrical resonance, which leads to the loss of stability of synchronous regimes (Fig. 4 for $p = 0.38$, $a = 1.0$, $\bar{\beta}_2 = 0.2$).

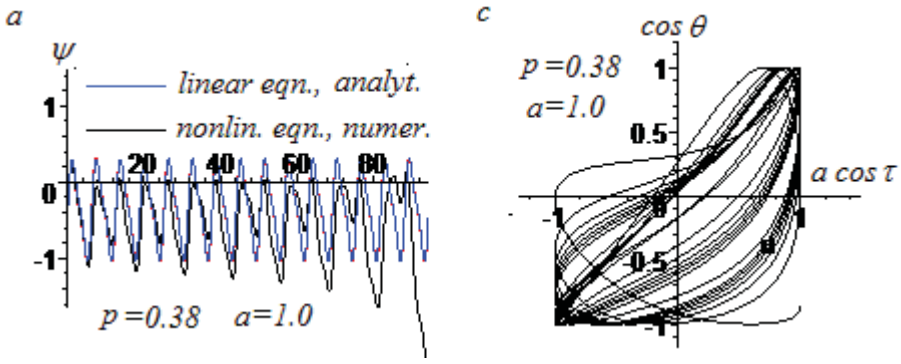

Figure 4. Comparison of the analytical solution and numerical simulation for system $p = 0.38$, $a = 1.0$ ($\bar{\beta}_2 = 0.2$); (*a*) – times series for $\psi(\tau)$, (*c*) – phase curve ($a\cos\tau$, $\cos\theta$)

Similar behavior was observed near the *upper* bound of domain E. Near the *lower bound* (e.g., at $p=0.2$, $a=0.36$, $\beta_2=0.2$) in the numerical simulation of nonlinear equation (6) value of ψ increases monotonously by modulus, and rotation terminates after several cycles of oscillation.

Summarizing we can conclude that the obtained analytical solution well correlate with the results of numerical simulation for values p and amplitude a lying inside the domain E and in a vicinity of its boundaries.

4. Synchronous Oscillation-Rotation Regimes in the 2DoF System

At the second stage equation (1) has been solved with using the obtained solution for non-uniform rotation of the ball (9) in order to account for reciprocal effect of the rotator on the body oscillation. This solution can be also obtained in the straightforward analytical approach. As the solution (9) has been derived under zero initial phase for the body oscillation $u=a\cos\tau$ and in view of a possible phase shift between the oscillation and the external force we assume a certain initial phase ϕ_0 for the force. For synchronous oscillation-rotation regimes the following solution has been obtained:

$$u=a\cos\tau+b_2\cos 2\tau+c_2\sin 2\tau+b_3\cos 3\tau+c_3\sin 3\tau \tag{13}$$

Expressions for a, b_s, c_s (s=2, 3) and phase ϕ_0 depend upon coefficients $\psi_s^{(1)}$, $\psi_s^{(2)}$, which in turn depend upon oscillation amplitude a. Finally we come to equation with respect to a of form $F(a)=0$, where

$$F(a)=\left[(1-\bar\Omega^2)a-(-1)^j\mu\bar\Omega^2(1-0.5\psi_2^{(2)})\right]^2+\left[\beta_1\bar\Omega^2 a+(-1)^j\mu\bar\Omega^2(0.5\psi_2^{(1)}-\psi_0^{(1)})\right]^2-f^2 \tag{14}$$

Equation $F(a)=0$ determines frequency response curves (FRCs). With account of the set (9) it is an algebraic equation with respect to a. Each root specifies a synchronic oscillation-rotation regime (if a falls within the domain E). Computations showed that, as a rule, only one real root for in-phase rotation exists which falls into this domain.

In Fig. 5 there are presented FRCs for in-phase rotation ($j=0$) computed for parameters $p=0.2$, mass ratio $\mu=0.1$, damping factors $\beta_1=\beta_2=0.2$ at two amplitudes of the external excitation ($f=0.6$ and 0.3, plots *a, b*, respectively, black lines 1). Lower and upper bounds for the oscillation amplitude a at given p are shown by horizontal lines. The FRCs for the oscillator without the attached rotator are depicted by red lines 2.

The lower and upper bounds cut a certain portions of the FRCs; they can relate to separate parts of the pre-resonance ($\bar\Omega<1$) and post-resonance ($\bar\Omega>1$) ranges in cases of "strong" excitation (plot *a*), or to one interval including the resonance peak at "moderate" excitation (plot *b*). For very weak

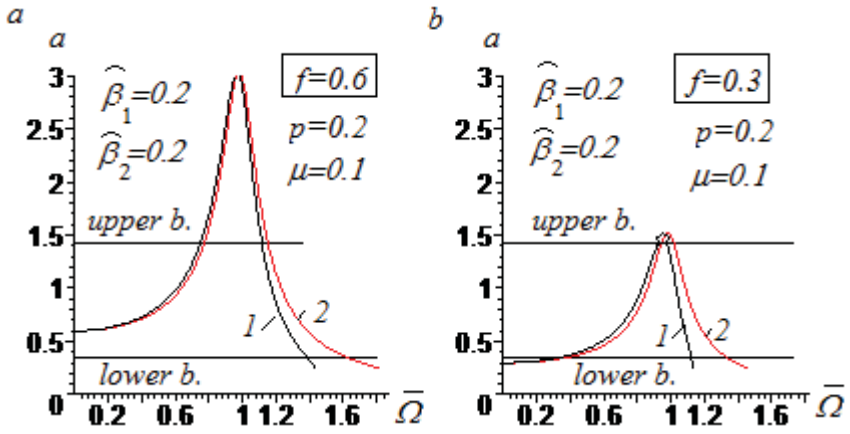

Figure 5. Frequency-response curves for synchronous in-phase oscillation-rotation regimes ($\mu=0.1$, $\beta_1=\beta_2=0.2$, $j=0$) at different amplitudes of external excitation; *a*) $f=0.6$; *b*) $f=0.3$. Curves 1 and 2 relate to the oscillator with and without rotator, respectively

excitation the FRCs lie beneath the lower bound, so synchronous regimes are absent. Post-resonance parts of ranges of the synchronous regimes, as a rule, correspond to rather narrow intervals of $\bar{\Omega}$-values; so synchronous regimes do not exist at sufficiently large $\bar{\Omega}$ (the amplitudes a are too small).

Comparing the FRCs for the oscillator-rotator systems (curves 1) with those for individual oscillators (curves 2) we see that distinctions are relatively small (at assumed here mass ratio $\mu = 0.1$); the differences are noticeable only in narrow resonance and post-resonance ranges.

The obtained analytical solution of the set (1), (2) has been compared with results of numerical simulations of this set. We took the system with parameters: $\mu = 0.1$, $\bar{\beta}_1 = \bar{\beta}_2 = 0.2$, $f = 0.6$. Putting $j = 0$ we singled out the regime close to *in-phase* rotation with respect to the body oscillation (not necessarily with respect to the external force).

We considered the entire $\bar{\Omega}$-range allotted by the lower and upper bounds, and a vicinity of this range. Some results of comparison for $\bar{\Omega} = 0.5$ are presented in Fig. 6, where analytical and numerical times series are given for the body oscillation u and angular velocity ω (plots *a, b*, respectively).

Two curves for the body oscillation u practically coincide, discrepancies between analytical and numerical curves are larger for the angular velocity ω, but synchronism persists. In this case coefficients b_s and c_s in analytical solution (14) are rather small (of order 0.01), and the higher harmonics do not affect noticeably the main harmonics.

Similar results were obtained for another $\bar{\Omega}$ values when amplitudes of oscillation were got into the domain E. Numerical simulation with various initial conditions showed also that the synchronous regime (close to sin-phase one) is an attractor in rather wide region of initial conditions.

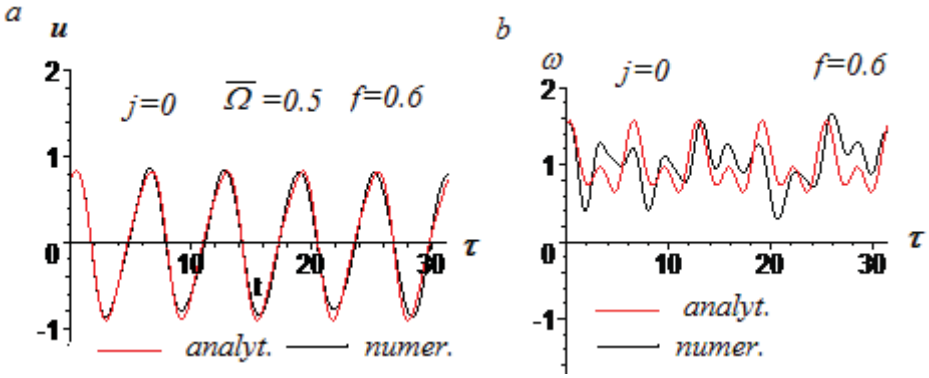

Figure 6. Comparison of the analytical and numerical solutions of set (1),(2) for in-phase rotation ($\mu = 0.1$, $\bar{\beta}_1 = \bar{\beta}_2 = 0.2$, $f = 0.5$, $j = 0$) at $\bar{\Omega} = 0.5$; (*a*) body oscillation u, (*b*) angular velocity ω

Conclusions

An analytical description for synchronous rotation-oscillation regimes in the oscillator –rotator system in the vertical plane under the harmonic excitation is obtained. These regimes exist and are stable in certain field of parameters (p, f, $\bar{\Omega}$) (3) when the point (p, a) (a is the oscillation amplitude) falls into the domain E found above. Non-uniformity of rotation is periodical with prevailing second harmonics (of period π in dimensionless time), along with a constant phase shift (with respect to oscillation). In certain vicinity of the bound non-uniform component of rotation includes the first harmonics with period 2π (gradually increasing parametric oscillation of the angle component) which results in instability of the synchronous rotational regime outside of the domain E.

The analytical solutions are confirmed by the numerical simulation with high accuracy. The obtained results can be used for the choice of parameters of various mechanical systems, in particular, of ball- and bowl absorbers of oscillations, and estimation of their efficiency.

References

[1] Blekhman I. I. *Vibrational mechanics*. *Nonlinear Dynamic Effects, General Approach, Applications.* World Scientific, 2000.

[2] Babitsky V. I. Principles of Dynamic Suppression of Vibrations, *Vibrations in Science and Technology*, v. 6, *Protection from Vibrations and Impacts*, K.V. Frolov, ed., Moscow, Mashinostroenie, 1981, p. 326-365 (in Russian).

[3] Gendelman O. V., Sigalov G., Manevitch L. I., Mane M., Vakakis A. F., Bergman L. A. Dynamics of an eccentric rotational nonlinear energy sink, *ASME J. Appl. Mech*., **79** , 2012.

[4] . Sigalov G., Gendelman O.V., AL-Shudeifat M. A., Manevitch L. I., Vakakis A.F., Bergman L.A. Resonance captures and targeted energy transfers in an inertially-coupled rotational nonlinear energy sink, *Nonlinear Dynamics*, **6a**, issue 4, 2012.

Proceedings of the 4th International Conference on Nonlinear Dynamics
ND-KhPI2013
June 19-22, 2013, Sevastopol, Ukraine

Limiting Phase Trajectories as an Alternative to Nonlinear Normal Modes

Leonid Manevitch[1*]

Abstract
We present a new concept of limiting phase trajectories (LPTs) which allows to understand and describe adequately a wide class of highly non-stationary processes in both classical and quantum mechanics. Such processes are characterized by strong modulation and intense energy exchange between different parts of the system. The LPT-concept turns out to be alternative to the concept of nonlinear normal modes (NNMs) which describe naturally the stationary and weakly modulated processes.. While the latter deals with instabilities and bifurcations leading to appearance of additional NNMs, the former allows to predict a transition from intense energy exchange to energy localization and formation of breather-like excitations.. Besides, it predicts existence of qualitatively new type of synchronization in the system of weakly coupled generators which can be attributed as LPT-synchronization in contrast to conventional NNM-synchronization.

The specific mathematical techniques for description of LPTs deals with non-smooth temporal transformations that leads to simple presentation of strongly modulated vibrations. A series of applications to the significant vibration problems are presented.

We present a recently developed concept of limiting phase trajectories (LPTs) providing a unified description of highly non-stationary processes which are rather ubiquitous in a wide class of dynamical systems of classical and quantum mechanics. Such processes are characterized by strong modulation and intense energy transfer between different parts of the system. In fact, this new concept paves a way for a systematic study and classification of highly non-stationary as well as transient regimes and their local and global bifurcations. Such processes occurring in a variety of physical models are actually quite off the well-studied paradigm based on the concept of nonlinear normal modes (NNMs) which can be efficient only for description of nearly stationary processes. Thus, when the latter deals with instabilities and bifurcations leading to appearance of additional NNMs, the LPT concept allows to predict a transition from intense energy exchange to complete energy transport and formation of strongly localized (e.g.. breather-like) excitations. Moreover, the same concept of limiting phase trajectories can predict the formation of the all new type of synchronization in the system of weakly coupled generators, named as LPT-synchronization, and this in contrast to conventional NNM-synchronization.

Alongside with well-known asymptotic method we use some special mathematical technique based on non-smooth temporal transformations that leads to an efficient description of strongly modulated as well as transient regimes. Several applications of the aforementioned methodology to some significant problems of nonlinear dynamics as well as quantum mechanics are presented.

Keywords
Nonlinear Normal Modes, Limiting Phase Trajectory, effective particles, synchronization, energy exchange and localization

[1] Semenov Institute of Chemical Physics Russian Academy of Sciences, Moscow, Russia
* **Corresponding author:** manevitchleonid3@gmail.com

Introduction

The *linear and nonlinear normal vibrations* are synchronous single frequency motions of the linear and nonlinear Hamiltonian systems. The corresponding spatial distributions of the displacements are described by *linear or nonlinear normal modes* (LNMs or NNMs) [1,2]. They describe also the *stationary* forced and self-sustained oscillations in non-conservative systems. It was shown recently that in the systems of weakly coupled oscillators the alternative class of regular

solutions can be introduced which includes the strongly *modulated* and *non-stationary* processes [3-6]. These solutions were denoted as *limiting phase trajectories* (LPTs), and a special technique applicable for their study is based on non-smooth temporal transformations [7].Contrary to LNMs and NNMs, they describe the maximum possible energy exchange between the clusters of the oscillators (effective particles). The conditions of the *transition from intensive energy exchange to energy localization* can be also formulated in terms of LPTs [4-6].

1. LPTs vs NNMs

The concept of LPT is valid in the case when the resonance conditions between different NNMs arise, and therefore the phenomenon of a coherence takes place. Because of this phenomenon, the resonant NNMs cease to be appropriate tool for dynamical analysis, and transition to *effective particles* (in 2DoF systems – *to real particles*) has to be performed. Then, from physical viewpoint one can observe the beats between effective particles each of which is a cluster of the real particles. The beats are described adequately in *slow time* scale by LPTs, and corresponding temporal behavior – by non-smooth functions in appropriate variables. From mathematical viewpoint, the principal difference between NNM and LPT manifests in the different basic number systems which are the most suitable in these cases. They are well-known *complex (elliptic)* numbers and less known *hyperbolic numbers,* respectively.

When the excitation intensity grows both NNMs and LPTs undergo a series of transformations.

For NNMs, they are bifurcations of stationary points in slow timescale that means the instability of NNM and formation of new stationary points (NNMs) and corresponding separatrix. As for LPT, its coincidence with separatrix leads to impossibility of complete energy exchange between the effective particles and, as consequence, to the energy localization on the initially excited effective particle.

The applications of LPT concept involve a number of important problems of both mechanics and physics. In particular, they are:

1) Transient vibrations of the forced nonlinear oscillator (in this case LPT describes the most intense process in which the oscillator takes periodically the maximum possible energy from its source). If a damping is taken into account, the LPT concept predicts also the existence of a limit cycle when the excitation includes two harmonic forces with closely situated frequencies.
2) Nonlinear beats in conservative 2DoF systems corresponding to complete energy exchange in a slow time scale between two weakly coupled oscillators while NNMs are the stationary states. In terms of the LPTs one can predict the transition from complete energy exchange to energy localization on the excited oscillator. In these terms the conditions of efficient targeted energy transfer in the presence of damping are also formulated.
3) Intensive energy exchange between effective particles and transition to energy localization on excited effective particle in the oscillatory chains with many degrees of freedom.
4) Self-sustained oscillations of new type providing synchronization on the LPT contrary to conventional synchronization on NNM. .
5) Energy exchange and localization in carbon nanotubes.

We discuss briefly these problems, opposing in all cases the LPTs and NNMs concepts.

Conclusions

Due to its importance, the notion of effective particle should be clarified once more. The discussion of the mechanism of the intensive energy exchange and the transition to the energy localization requires first of all identifying the elementary excitations in the considered system. In the

gaseous media they are almost *free motions of weakly interacting particles* (atoms or molecules), which are involved in the almost free motion. In the oscillatory chain, as in all crystalline solids, the particles interact strongly. In this case the *weakly interacting NNMs of the oscillatory chain as a whole* can be considered as elementary excitations. However, with an increase in the number of the particles the resonance relations between the certain frequencies arise. Under strongly asymmetric initial conditions, corresponding to a combination of the resonating normal modes, this leads to the appearance of the *coherence* that entails (in the nonlinear case) *essential intermodal interaction*. As a result, the resonating normal modes cannot be considered as the elementary excitations. In a system of two weakly coupled oscillators with strongly asymmetric initial conditions the elementary excitations are the motions of the particles themselves, similarly to the case of the gaseous medium. Their bias can be represented as the sum and the difference of the modal variables; corresponding motion is beating. When the number of the particles increases, in the presence of resonant modes *a motion of the effective particle,* which includes a certain number of the real particles, can be considered as the elementary excitation. Its bias (similar to that for two weakly coupled oscillators) is constructed as combination of modal variables. The coupling between the introduced effective particles is weak, although the original equations of motion may not contain a small parameter. Thus, the concept of the beats can be extended to multidimensional systems. In addition, the introduction of the effective particles and LPTs allows an adequate description of the transition from the intense energy exchange to the energy localization with increasing the excitation intensity. Thus, it is possible to trace a connection of discrete models with continuous systems, having localized, soliton-like solutions (breathers). We note that an increase in the number of the resonant modes means that the spatial extent of effective particle is reduced, and it approaches to the profile, typical for the breather in the infinite chain. An increase in the number of such particles occurs when the resonant mode nearest to the boundary of the spectrum is "uninhabited." Of course, outside the intermodal resonance and the coherence manifestation, the wave language is quite adequate.

In the terms of the effective particles and LPTs, a simple analytic description of the intense energy exchange with the use of non-smooth functions can be obtained.

Acknowledgments

The author is grateful to Dr. A.S. Kovaleva, Dr. V.V. Smirnov, M.A. Kovaleva, Dr. D.S. Shepelev for fruitful collaboration.

References

[1] Manevitch L.I., Mikhlin Yu.V, Pilipchuk V.N. *Method of Normal Vibrations for Essentially Nonlinear Systems* (in Russian), Nauka, Moscow, 1989.

[2] Vakakis A.F., Manevitch L.I., Mikhlin, Pilipchuk, Zevin A.A. *Normal Modes and Localization in Nonlinear Systems*, Wiley, New York,1996.

[3] Manevitch L.I. New Approach to Beating Phenomenon in Coupling Nonlinear Oscillatory Chains, *Arch.Appl.Mech.*,77, pp.201-212, 2007.

[4] Manevitch L.I., Smirnov V.V. Limiting phase trajectories and the origin of energy localization in nonlinear oscillatory chains *Phys. Rev. E* 82, 036602.

[5] Manevitch L.I., Gendelman O.V. *Tractable Models of Solid Mechanics,* Springer, London-New York, 2011.

[6] Manevitch L.I., Kovaleva M.A., Pilipchuk V.N. Non-conventional Synchronization of Weakly Coupled Active Oscillators, *Europh.Lett.*, 101, 50002, 2013.

[7] Pilipchuk V.N., *Nonlinear Dynamics: Between Linear and Impact Limits*, Springer, Berlin, 2010.

Proceedings of the 4th International Conference on Nonlinear Dynamics
ND-KhPI2013
June 19-22, 2013, Sevastopol, Ukraine

Two Qquasi-Time-Optimal Controls for Wheeled Robot

Morozov Yury[1]*

Abstract
A quasi-time-optimal control design problem for planar motion of a mobile robot with constrained control is considered. The control objective is to place a target point on robot's platform to a given curvilinear path and to stabilize motion along this path. The path is assumed to be feasible, i.e. is smooth and has bounded curvature. In the mathematical model under consideration, the current curvature of the trajectory of the target point is taken as control. Because time-optimal controllers are sensitive to disturbances, parameter variations and unmodeled dynamics truly time-optimal control systems are not practical. Proximate time-optimal controllers or quasi-time-optimal controllers are more robust and give near time-optimal responses. In this paper two quasi-time-optimal controls are proposed. The first control is an extension of an earlier derived quasi-time-optimal control designed for a straight target path to the case of general curvilinear path. The second control is designed specifically for the curvilinear path following problem. Both are signum controls but use different switching curves. In addition, the second control uses current curvature of the target path, whereas the first control does not rely on this information. For the proposed control laws, attraction domains in the space "distance to the trajectory - angle deviation" are constructed. If an initial point belongs to the attraction domain, the control goal is attained in a finite time. The discussion is illustrated by numerical examples demonstrating advantages of the proposed control laws.

Keywords
quasi-time-optimal control, wheeled robot, finite time

[1]ICC RAS, Moscow, Russia
*__Corresponding author__: tot1983@inbox.com

Introduction

The kinetic model of a mobile robot is very popular model for demonstration of various controllers. There are many different control laws that place a target point on robot's platform to a given curvilinear path and stabilize motion along this path. Usually, authors propose controls without restrictions. Unfortunately, those controls cannot be used to solve our problem. At the end of the last century Pao [1] synthesized proximate time-optimal controllers for the mechanical systems. The main feature of her approach is to use the functions of saturation in the control law with small adjustable parameters. It is known that the function of saturation has linear part and it is not smooth. It is often approximated by smooth functions and usually, the accuracy of the approximation depends on a single parameter. The fewer this parameter the better approximation. In this paper we will use the signum functions in control. This function will be defined later. We will not approximate signum function, but we will approximate switching curve, which is used in our control laws. Both our controls have only one adjustable parameter. We use the idea, which is similar an idea from [2]. Balluchi *et al.* proposed variable structure control, which can be use only in an open neighborhood of the path in the reduced state space. Constructed attraction domain is small and the control is not A quasi-time-optimal control. These problems are related to a failed the change of coordinates. In this paper we use the change of coordinates from [3]. A quasi-time-optimal control design problem is a problem of finding of the control law, which is time-optimal control if a custom parameter is zero. The solution of time-optimal problem is very hard for the arbitrary nonlinear system, but sometimes you can find a proximate solution of this problem, that arbitrarily close to the optimal solution.

1. Problem Statement

Consider a planar motion of a mobile robot. The kinematics of mobile robot can be described as

$$\dot{x} = y, \dot{y} = \psi(y)u + \phi(y)^2 c(\xi)/(1 - c(\xi)x)), \psi(y) = \phi(y)^3, \phi(y) = (1+y^2)^{\frac{1}{2}}, \tag{1}$$

where dot denotes derivation with respect to the independent variable ξ, $x \in R$ is a distance to the given curvilinear path, $y \in R$ is a angle deviation from the given path, $c(\xi) < C$ is a curvature of the given path, u denotes a control.

Problem 1 The goal of this paper is to determine control inputs $u(x,y,C)$ subject to $|u(x,y,C)| < U$ for a mobile robot to place a target point on robot's platform to a given curvilinear path in finite-time and to stabilize motion along this path.

1.1 Quasi-time-optimal control designed for a straight target path

Suppose that the curvature of the given path is negligible, i.e. $C << 1$. In this assumption, we will consider $\delta_c(y,x) = \phi(y)^2 c(\xi)/(1 - c(\xi)x))$ as a parametric perturbation.

To solve Problem 1, we apply quasi-time-optimal control designed for a straight target path (see, e.g., [4])

$$u = -U\text{sign}(S), S = U_\lambda x + \left(1 - \phi(y)^{-1}\right)\text{sign}(y), U_\lambda = \frac{U}{1+\lambda} \tag{2}$$

where

$$\lambda > \frac{\delta_c}{U - \delta_c} > 0, \delta_c < U \tag{3}$$

where δ_c a boundary of the parametric perturbation. Here and below,

$$\text{sign}(s) = \begin{cases} 1 & , \quad s > 0 \\ -1 & , \quad s < 0 \\ [-1 \ 1] & , \quad s = 0. \end{cases} \tag{4}$$

We have stable sliding mode along curve $S(x,y) = 0$ if the parameter λ satisfies the inequality $\lambda > \lambda^*$ where

$$\lambda^* = \delta/(U - \delta), \delta = \max_y(\delta_c(y)) = \delta_c(0), \delta_c(y) = C/(1 - Cx^*)/\phi(y), \tag{5}$$

or

$$\lambda^* = \frac{C}{U - C - UCx^*}, \tag{6}$$

where x^* is a given boundary of variable x.

Let us choose the $\delta_c(y,x)$ as $-C\text{sign}(u)/(1 - C|x|)\psi(y)$. Substituting $\delta_c(y,x)$ into (1), we have

$$\dot{x} = y, \dot{y} = \psi(y)(u - C\text{sign}(u)/(1 - C|x|)), \tag{7}$$

Let us find the critical points of the system (7) is closed by (2). It is easy to prove that $x_c^{\pm} = \pm(\frac{1}{C} - \frac{1}{U})$ are unstable saddles of the system (7). Than (8) can be rewrite as

$$x^* = x_c^+ - \frac{1}{U\lambda^*}, \lambda^* > \frac{C}{U - C} + \varepsilon, \varepsilon > 0. \tag{8}$$

Lemma 1 Let the system (7) be closed by (2) and the enquality (8) be hold, than system (7) is local stabilized in finite time by the state-feedback control (2) and there is sliding mode [5] along curve $s(x,y) = \{(x,y)^{\text{T}} : S(x,y) = 0, |x| \le x^*\}$.

Unfortunately, the attraction domain of the system (7), (2) is smaller the attraction domain of system of system (1), (2). To construct the attraction domain for the system (7), (2) we build a separatrix passing through the saddle points, integrating the system (7), (2) forward and backward in time [6].

So, we have the separatrix

$$\begin{array}{l} S > 0: \ Ux + \ln(|1 - c|x||)\text{sign}(x) = +\phi(y)^{-1} + s0^+, \\ S < 0: \ Ux + \ln(|1 - c|x||)\text{sign}(x) = -\phi(y)^{-1} + s0^-, \end{array} \tag{9}$$

where $s0^{\pm}(x_c^{\pm},0) = \pm(2-u/c-\ln(u/c))$. We find four points (in spesial case 2) of intersection of the separatrix (9) and the swiching curve (2), solving following systems

$$\begin{cases} x = -1/U_\lambda \left(1-\phi(y)^{-1}\right)\text{sign}(y), S>0, \\ xU+\ln(|1-c|x||)\text{sign}(x) = +\phi(y)^{-1}+2-u/c-\ln(u/c), \end{cases} \tag{10}$$

$$\begin{cases} x = -1/U_\lambda \left(1-\phi(y)^{-1}\right)\text{sign}(y), S<0, \\ xU+\ln(|1-c|x||)\text{sign}(x) = -\phi(y)^{-1}-2+u/c+\ln(u/c). \end{cases} \tag{11}$$

Let us the point x_0^* be calculated as $x_0^* = \arg_{x<0}(U|x|+\ln(|1-c|x||)\text{sign}(x)-1-s0^+=0)$. Now, we can construct the attraction domain, which contains sliding mode's curve segment. Example of the attraction domain is shown on Figure 1.

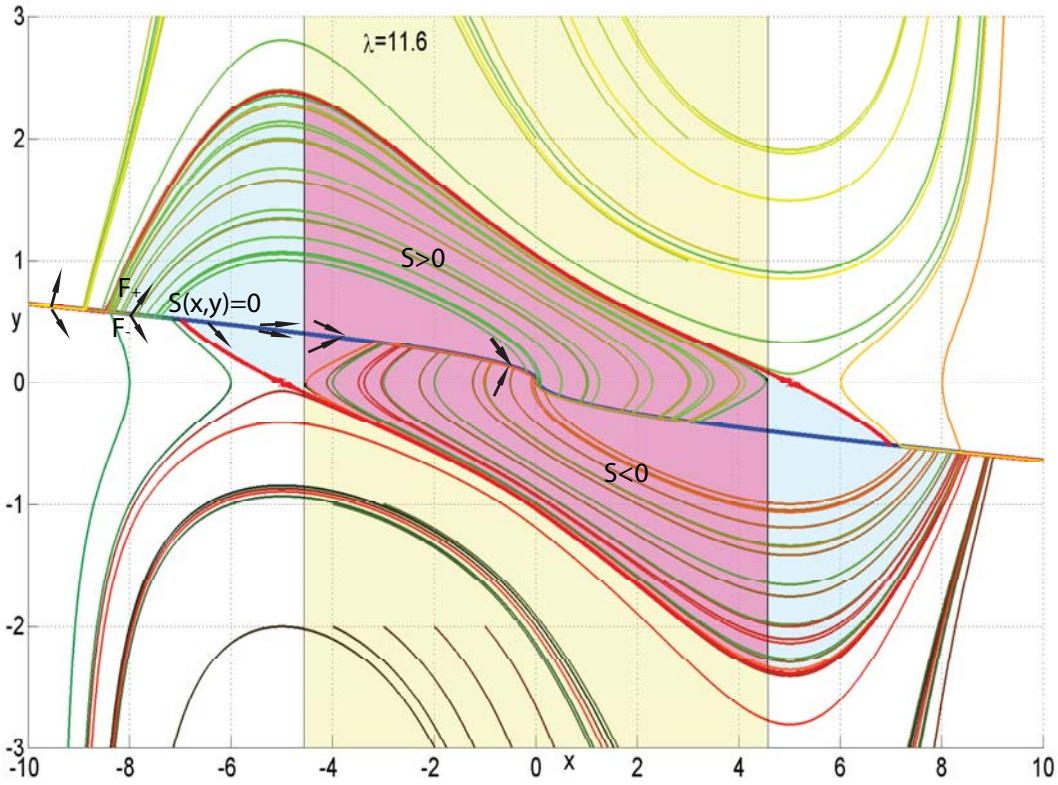

Figure 1. Attraction domain,switching curve and phase pathes by $c = U/2$, $U = 0.2$

The the attraction domain, which assures the attraction sliding mode, is the darkest domain on Figure 1. It's boundary consists of four curves: two parallel lines and the upper curve touches the right edge of the domain and crosses the left border, the lower curve touches the left edge of the area and crosses the right boundary. It is worth noting that the separatrices of the saddles does not touch the boundary area, they create the bondary of the attraction domain for the system (7). It can be seen that all trajectories that began outside the domain of attraction go to infinity. It can be shown that the increase in the value of the parameter causes the expansion of the domain of attraction. Unfortunately the linear dimension of the region of attraction for the x-coordinate is limited, i.e. $\lim\limits_{\lambda\to\infty} x^* = x_c^+$. On the other hand, the domain of attraction can be increased by decreasing the value of the parameter c. This is due to the fact that the saddle points go to infinity in decreasing the value of the parameter c. In the limiting case when $c = 0$ the system (7) has no saddle points. This means that the parameter c is the bifurcation parameter of the system (7), because the topology of the phase portrait changes.

1.2 Quasi-time-optimal control designed for a curvilinear target path

Using separatrix (9) we construct new switching curve and control

$$\begin{cases} S_C = xU_\lambda + \ln(|1-C|x||)\text{sign}(x) + \left(1-\phi(y)^{-1}\right)\text{sign}(y), \\ u = -\text{sign}(S_C(x,y)) \end{cases} \tag{12}$$

Let us the parameter λ^* be calculated as $\lambda^* = \arg_{x<0}\{S_C(-x_c,0)=0\} = Ux_c/\ln(1-Cx_c)-1$.

it can be shown, that the system (7) be closed by (12) with $\lambda >= 1$ is unstable.

Compare the attraction domain for he system (7) is closed by (12) with the attraction domain for the system (7) is closed by (2), if in controls are set $\lambda = \lambda^*$(for example, if $U = 0.2$, $C = 0.1$ then $\lambda^* \simeq 0.0438$). Unfortunally, both domains do not contain sliding mode's curve segment with this parameter λ, but there is limit unstable cycle in the closed system (7), (2). This cycle vanish from the system if $\lambda = 1$.

Note, the limit unstable cycle has unsmooth boundary and the switching curve passes through those points. There is likely flowing solutions through these points, which was not investigated.

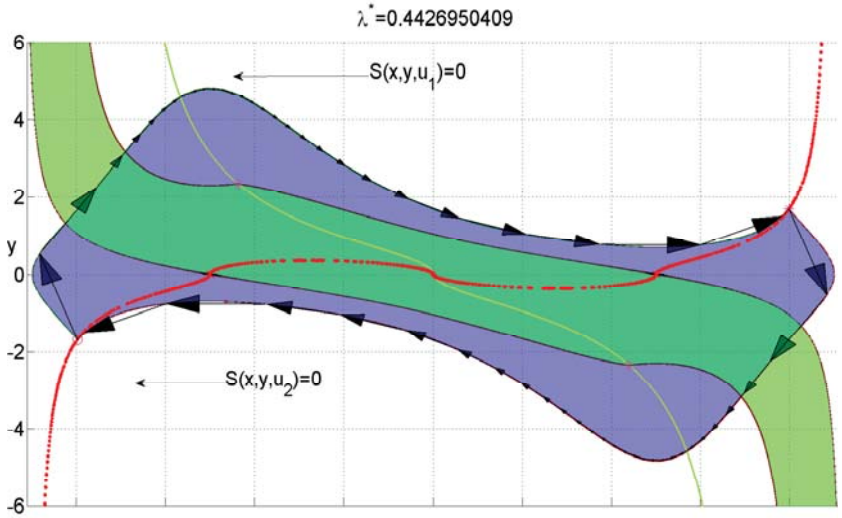

Figure 2. Attraction domains and switching curves

The cases when $0 < \lambda < \lambda^*$, $\lambda^* < \lambda < 1$ is more complicate.

2. Results and Discussion

In this work we considered two quasi-time-optimal controls (12), (2) for the system (7) and constructed attraction domain's for case when $C = 0.5U$. In case small λ sliding mode doesn't exist in our system and phase paths pierce the switching curves (see Figure 2). We can get sliding mode if we take a sufficiently large value λ (see Figure 1), but for the control (12) it cannot be large than λ^*. Unfortunally, because of a space of a paper is limited, a large part of the computation and the statement are omitted.

In spite of the attraction domain for the closed system (7), (2) (the boundary of this domain is shown arrows on Figure 1) is bigger then the attraction domain for the control (2), but the control (2) is better then the control (12), because of it is more robust.

Acknowledgments

This work was supported by the Russian Foundation for Basic Research (RFBR) grant No. 13-01-00347.

References

[1] L. Y. Pao and G. F. Franklin. Proximate time-optimal control of third-order servomechanisms. *IEEE Tran. Automatic Control*, 38(4):560–579, 1993.

[2] A. Balluchi et al. Path tracking control for dubin's cars. *Proc. IEEE International Conference Robotics and Automation*, pages 3123–3128, 1996.

[3] A. V. Pesterev. Synthesis of a stabilizing control for a wheeled robot following a curvilinear path. *Automat. Rem. Contr.*, 73(7):1134–1144, 2012.

[4] Yu. V. Morozov. Quazi-time-optimal control of wheeled vehicle. *Proc. International Conference "Modelling, control and stability" (MCS-2012, Sevastopol)*, pages 73–74, 2012.

[5] A. F. Philippov. *Differential equations with discontinuous right-hand side.* Nauka, 1985 (in Russian).

[6] V. G. Boltyanskiy. *Mathematical methods of optimal control. Second edition, revised and enlarged.* Nauka, 1969 (in Russian).

Proceedings of the 4th International Conference on Nonlinear Dynamics
ND-KhPI2013
June 19-22, 2013, Sevastopol, Ukraine

Nonlinear Aeroelasticity of Insect like Flapping Wing Structure

Indrajit Mukherjee[1]*, S.N. Omkar [2]

Abstract
Studies have revealed that Insect like flapping flight can serve as a benchmark in designing Micro Aero Vehicles owing to its power efficiency and high maneuverability. The development of these next generation vehicles demands careful considerations of various factors of which aerodynamic wing design, stability and control have central importance. Because of their small size and speed, the flight control of these vehicles in gusty environments poses tremendous challenges on their design. The wing structure of FMAV in general is flexible in nature after being inspired by insects, which are known to flex their wing quite significantly. However detailed analytical studies on aero-elastic response of a wing structure, aimed at designing these vehicles are rare. In this article we take up the study of the response of a flapping wing structure modeled as a flexible beam under gust loading with a revised quasi-steady aerodynamic model. The details of the coupled structural and aerodynamic modeling are reported and the responses of the system are outlined.

Keywords
Micro Aerial Vehicle, Insect Flight, Aeroelasticity, Gust load

[1],Graduate Student, Indian Instituite of Science, Bangalore, India
[2],Principal Research Scientist, Indian Instituite of Science, Bangalore, India
***Corresponding author**: inder@aero.iisc.ernet.in

Introduction

In the past decade, the study of Micro Air Vehicle (MAV) and its design has emerged as one of the major thrust areas of research in Aerospace Engineering. A MAV essentially is a flight vehicle with a small wing span envisioned of performing military operations such as reconnaissance, surveillance or even operations like fire rescue [1]. They can also be deployed for missions like aerial surveys for agriculture, traffic monitoring and pollution control, meteorological data collection and a whole host of other applications.

This miniaturization of flight vehicle having similar size and weight as that of natural fliers has motivated researchers to study of the mechanism of flying in insects and birds. In nature there exists two different forms of flight namely bird and insect flight [2]. While both these forms are based on flapping wings, there are important differences in wing kinematics among them. Insect flight, the more efficient of the two modes of flight is capable of hover as insects flap their wings in a nearly horizontal plane by large changes in wing pitch angle to produce lift even in the absence of any forward velocity. The class of MAV, whose design is influenced by the flapping flight of insect, is variously known as Flapping Wing Micro Air Vehicles (FMAV) or entomopter. The drive for the design and development of such a vehicle has triggered interests among researchers to take up the detailed study of the mechanism of flying in insects in recent times though it has received considerable attention from bio-fluid dynamics community since long owing to the challenges it offers.

The aerodynamics and mechanisms of insect flight have posed formidable challenge to the research community, which until recent times were unresolved. Initially researchers adopted quasi-steady models to explain the mechanism of insect flight. Early efforts came from Osborne [3], Weigh Fog [4] and later by Pringle [5]. The premise of quasi steady modeling in general is based on the assumption that the instantaneous forces on the flapping wing motion are equivalent to force generated for steady motion by a fixed wing at the same instantaneous velocity and angle of attack. However Ellington in his seminal work [6] demonstrated that the quasi steady modeling approach under predicts the lift generated by in-

sects, especially in hover. In fact it has been shown that insects cannot sustain their weight by adopting this lift generating mechanism alone. Ellington concluded that the underlying mechanisms of insect flight are essentially unsteady in nature; however the nature of unsteadiness was not clear. This has been possible to address only recently due to the developments in experimental studies and computational tools. Different mechanisms have been reported in literature, which can explain the enhanced lift generation by insects to keep them afloat. These are namely, rotational circulation or Kramer effect, delayed stall phenomenon associated with leading-edge vortices, and wake-capturing for aerodynamics enhancement. Succinct accounts on the historical perspectives of insect flight can be found in reviews [2, 7].

Owing to the flexible nature of insect wings, studies on the aero-elastic coupling in flapping flight have also been carried out. Singh and Chopra [8] examined the aero-elastic response of insect-based, biomimetic, flapping wings in hover. Banerjee and Patil [9] investigated three dimensional aeroelastic analysis of membrane wings and concluded that the flexibility of the wing has a significant effect on the thrust. In spite of the existing volume of work in aero elasticity of insect flight, the requirement for a multi parameter analytical model describing the aeroelastic interaction involved to aid the designer during the preliminary design stage of entomopter cannot be ignored. Such models would immensely help the designers to explore the feasible design space of FMAV. Since FMAVs will be deployed for a diverse nature of operations ranging from military missions to urban civil applications, it is imperative that in order to successfully engage them in these missions, their design should be robust with stable hover capability. However owing to the miniaturization, and low speed of operation, FMAV would be highly sensitive to ambient conditions like gust loading. The aerodynamic response of FMAV would severely be affected by the unsteadiness of gust load which in turn would significantly influence the controllability of the vehicles. As a result our ability in successfully controlling the flight performances of these vehicles in gusty environment would in turn dictate the viability of FMAV as a potential candidate for the above mentioned applications. The need for mitigating adverse effects of gust loading is of primal importance. Golubev aptly underscores the importance of the study of gust load in [10]. He gives a thorough review of unsteady gusty urban environment and proposes three canonical forms of flow disturbances. He then goes on to obtain high accuracy 2D-Navier stokes simulations of SD 7003 airfoil interacting with the canonical form of proposed flow disturbances however. The work though very much relevant with our present concern, does not address the issue of gust-vehicle interaction where the vehicle's wing surface is flexible and hence ignores the complex aero elastic interaction. As FMAV having flexible wing is a plausible design option, importance of such studies cannot be undermined. Such requirements trigger the need for the development of a comprehensive analytical model which can serve as a ready-to-use framework for obtaining flight performance of FMAV under different operating flight conditions. The model should be adequate to account for the complex interaction of the flexible wing structure with the surrounding fluid motion generated by the flapping of wings. In the next section we enumerate the essential modeling details considered by us for the present study.

1. Problem Formulation

In this section the structural and aerodynamic methods adopted for modeling the aero elastic behavior of flapping flight are presented. In the present study we only consider the interaction of a single wing with the surrounding flow structure thereby neglecting the effect induced by one wing on the other. In the present study the wing structure of FMAV is considered to be flexible and we model the wing from first principle using Euler Bernoulli beam theory with inertially coupled bending and twisting motions. We prescribe rigid translation and rotations to the wing structure such that the kinematics of the wing is properly represented. The structural model is coupled with a revised quasi steady aerodynamic model of insect flight in hover. Although such methods have their limitations in accuracy, they offer insights and can aid the designers due to their conciseness. The model used here is proposed by Dickinson and Sane [11] is widely used for its modularity and usability. We begin our study by representing the essential details of the kinematics of flapping flight in hover, which we outline in the next section.

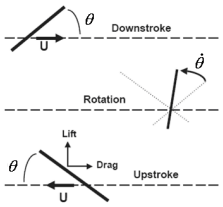

Figure 1. Schematics of idealized wing rotation [**?**]

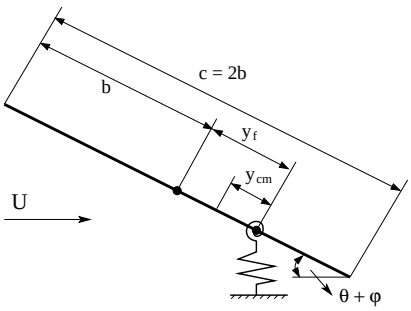

Figure 2. Schematic of a typical cross section of the wing structure

1.1 Wing Kinematics

An accurate quantitative description of wing kinematics holds the key for aerodynamics and hence aeroelastic analysis of insect flight. Insects fly [2, 12] by oscillating (plunging) and rotating (pitching) their wings through large angles while sweeping them forward and backward. The wing beat cycle has a typical frequency range of 5-200 Hz. The wing stroke of an insect is divided into two phases namely the translational phase and rotational phase. The wing motion of an insect is approximately confined to a plane known as the stroke plane which passes through their wing bases. The stroke plane could be inclined at an angle called the stroke plane angle with respect to the horizontal. The wings flap back and forth about the stoke plane. For the present study we focus our attention only on the hover, for which we idealize the wing tip trajectory as a straight line with stroke plane being parallel to the horizontal reference. Figure 1 gives a schematic representation of different phases of the wing movement. The translational velocity and the pitch angle constitute the parameters for the wing kinematics and can be represented as

$$\begin{aligned} U &= U_0 sin(\omega t) \\ \theta &= \theta_0 + \theta_1 \sin(\omega t) \end{aligned} \tag{1}$$

where U is the translation, θ is the rigid rotation of the wing, ω is frequency of the pitching motion, U_0, θ_0 and θ_1 are constants. Once the kinematics of the prescribed motion is specified we focus on addressing issues related to structural and aerodynamic modeling of the insect flight which are addressed in the subsequent sections.

1.2 Structural Modeling

The wing is modeled as a cantilevered Euler Bernoulli beam with the cross section being a symmetric aerofoil, i.e. without having any camber. The elastic and centroidal axes of the beam are not coincident and hence the bending and twisting motions of the beam get coupled. We recall that for a structural member with non-circular cross section, torsion is associated with warping action which is essentially an axial displacement of the cross section of the member. However for the present problem the effect of warping is ignored. The derivation is not produced here, refer [13] for further details. The governing equation of motion without the aerodynamic loading are given by

$$\begin{aligned} \rho A\ddot{w} - \rho A y_{cm}\ddot{\phi} - \rho A\dot{\theta}^2 w + \rho A y_{cm}\dot{\theta}^2\phi + \frac{\partial^2}{\partial x^2}(EI_{yy}w'') \\ = \rho A\ddot{U} sin(\theta) - \rho A y_{cm}\ddot{\theta} \end{aligned} \tag{2}$$

$$\begin{aligned}\rho J\ddot{\phi} - \rho J\dot{\theta}^2\phi - \rho A y_{cm}\ddot{w} + \rho A y_{cm}\dot{\theta}^2 w - \frac{\partial}{\partial x}(GJ\phi') \\ = \rho J\ddot{\theta} - \rho A y_{cm}\ddot{U}sin(\theta)\end{aligned} \tag{3}$$

where w, ϕ are the transverse displacement and twist of the wing structure. ρ is the material density, A is the cross-section area of the wing structure. I_{yy}, J are the 2nd moment and polar moment of area. E, G are elastic and shear modulii of the wing structure respectively.

1.3 Aerodynamic modeling

Aerodynamic model provides a mathematical framework capable of describing the main flow phenomena by capturing the essential flow physics and avoiding details which are intractably complex. The flow associated with insect flapping flight is incompressible, laminar, unsteady and occurs at low Reynolds numbers. While representing any aerodynamic phenomenon quasi steady approach of modeling turns out to be the natural choice as initial candidate for consideration because of its modularity and ready to use frame work that it offers. It has been proved to be highly useful in the aero-elastic pre-design calculations aiding the designer with the insights on the nature of loads. However it has been observed quasi steady approach of modeling insect flight turns out to be inaccurate as they fail to predict the aerodynamic loads and moments generated by the wings during an flapping cycle correctly [6]. A possible remedy is to introduce some form of empirical 'correction' to improve the accuracy of predictions of forces from quasi steady models. These are described as semi empirical methods. Such 'corrections' are incorporated based on experimental data generated. The semi empirical approach has a great appeal owing to its simple representation, usability and the fact that allows the user. However on the downside the semi empirical approach does not reflect properly the relevant flow physics involved and relies instead on data points for its derivation. Walker and Westneat [14] introduced a semi empirical model for insect-like flapping which they described as unsteady due to the inclusion of Wagner's function and apparent mass effect. For the present study we adopt a quasi steady framework which is influenced by the quasi-steady model introduced by Dickinson et al. [11]. The revised quasi steady model proposed by Dickinson et al. happens to be one of the most widely used models and forms the basis of studies like that of by I. Faruque et al. [15]. The model was developed to account for the forces and moments data obtained from their earlier experiments on Robofly. The lift force predicted by the aerodynamic model has different components as shown below

$$L_{qs} = L_t + L_r + L_a \tag{4}$$

where L_t, L_r and L_a are components of lift due to translational, rotational and added mass effects respectively. The model does not provide any functional relation of wake capture in terms of kinematic variables of flapping and hence will also not be considered for the present study. For details refer [13]. The expression of the lift force becomes

$$\begin{aligned}L_{qs} = \frac{1}{6}\rho_a\dot{U}^2 lc\Big(0.225 + 1.58sin(\frac{2.13\pi}{180}(\theta+\phi) - 7.2)\Big) \\ \frac{1}{4}\pi\rho_a lc^2\Big(\ddot{w} - (y_f - \frac{c}{2})(\ddot{\theta}+\ddot{\phi})\Big) + \frac{1}{4}\pi\rho_a lc^2\frac{d}{dt}\Big(\dot{U}sin(\theta+\phi)\Big) \\ +\pi\rho_a lc^2(\frac{3c}{4} - y_f)\dot{U}(\dot{\theta}+\dot{\phi})\end{aligned} \tag{5}$$

The expression for moment becomes

$$\begin{aligned}M_{qs} = \frac{1}{6}\rho_a\dot{U}^2 lc(\frac{c}{4}+y_f)\Big(0.225 + 1.58sin(\frac{2.13\pi}{180}(\theta+\phi) - 7.2)\Big) \\ +\frac{1}{4}\pi\rho_a lc^2 y_f\Big(\ddot{w} - (y_f - \frac{c}{2})(\ddot{\theta}+\ddot{\phi})\Big) - \frac{1}{4}\pi\rho_a lc^2(\frac{3c}{4} - y_f)\frac{d}{dt}\Big(\dot{U}sin(\theta+\phi)\Big) \\ +\pi\rho_a\dot{U}lc^2(\frac{c}{4}+y_f)(\frac{3c}{4} - y_f)(\dot{\theta}+\dot{\phi}) - \frac{1}{128}\pi\rho_a lc^4(\ddot{\theta}+\ddot{\phi}),\end{aligned} \tag{6}$$

where ρ_a is the density of air, U is the wing translation, S is the wing planform area, $\hat{r}(S)$ is the non-dimensional second moment of area. The second moment of area is defined [16] in terms of the normalized chord $\hat{c}$ and normalized radius $\hat{r}$. For the present problem the wing is modeled as a thin Euler

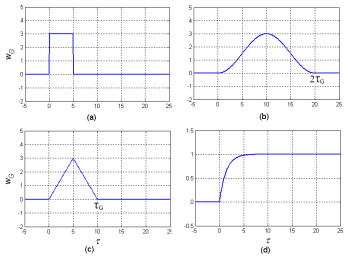

Figure 3. Gust velocity distributions

Bernoulli beam having rectangular planform. The beam has a span length of l and width or chord length of $c = 2b$. So the expression for the second moment of area can be evaluated accordingly. The pitch axis of the wing coincides with its elastic center. Here in this problem, it is located at a distance of y_f from the center of the cross-section, refer figure 2.

1.4 Gust Loads

The response of FMAV due to gust is one of the critical factors, the design of FMAV would depend on. As a result gust needs to be accurately modeled to get the wing response such that it is acceptable within the limitations of modeling. For obtaining the wing response due to gust load, the gust is first specified in terms of gust velocity having a suitable distribution and the lift force generated due to the penetration of wing into the velocity profile is obtained thereafter. For the present problem we assume that the gust is unaffected by the penetration of the wing and the magnitude of gust velocity remains same along the wing span. Some of the standard gust signatures are as follows:

(a) Sharp Edged Gust:

$$w_G(\tau) = w_0(H(\tau) - H(\tau - \tau_G)) \tag{7}$$

(b) 1-Cosine Gust:

$$w_G(\tau) = \frac{1}{2} w_0(H(\tau) - H(\tau - 2\tau_G))(1 - cos(\frac{\pi\tau}{\tau_G})) \tag{8}$$

(c) Triangular Gust:

$$\begin{aligned} w_G(\tau) = w_0\Big(2(\frac{\tau}{\tau_G})H(\tau) + 2(1 - 2(\frac{\tau}{\tau_G}))H(\tau - \frac{\tau_G}{2}) \\ -2(1 - \frac{\tau}{\tau_G})H(\tau - \tau_G)\Big) \end{aligned} \tag{9}$$

(d) Graded Gust:

$$w_G(\tau) = w_0 H(\tau)(1 - e^{-0.75\tau}) \tag{10}$$

Here τ is the dimensionless time defined as

$$\tau = \frac{1}{b}\int_0^t \dot{U} dt, \tag{11}$$

where b is the semi-chord length of the wing and U is the displacement of the wing as stated before. $H(\tau)$ denotes the Heaviside function, w_0 is the magnitude of gust velocity and τ_G is the gust intensity. The different gust profiles are plotted in fig 3. For the present study, we will focus only on the response of the wing structure in the presence of sharp edged gust. The lift force generated by a wing due to the penetration into a gust can be expressed as

$$\begin{aligned} L_G(\tau) &= C_L b \hat{r}_2^2(S)\rho\dot{U}\left(w_G(0)\psi(\tau) + \int_0^\tau \frac{\partial w_G(\tau_0)}{\partial \tau_0}\psi(\tau - \tau_0)d\tau_0\right) \\ &= C_L b \hat{r}_2^2(S)\rho\dot{U}\int_0^\tau w_G(\tau_0)\frac{\partial \psi(\tau - \tau_0)}{\partial \tau}d\tau_0 \end{aligned} \tag{12}$$

where $L_G(\tau)$ is the gust load $\psi(\tau)$ is the Kussner's function which is, in general, expressed in terms of Bessel's functions. However, for practical purposes the approximate expression as obtained by Von Karman and Sears [17] for elliptic wings in an incompressible flow is used. This form can be expressed as

$$\psi(\tau) = 1 - A_3 e^{-b_3\tau} - A_4 e^{-b_4\tau} \tag{13}$$

The constants are $A_3 = A_4 = 0.5$, $b_3 = 0.130$ and $b_4 = 1$. In their seminal work, Von Karman and Sears [17] had proved that gust load always acts at quarter chords point, even when the nature of the load is not completely circulatory. As a result, the aerodynamic moment about the flapping axis due to gust is given by

$$M_G(\tau) = \frac{1}{2} b L_G(\tau) \tag{14}$$

2. Aeroelastic Responses of Bending-Torsion based wing model

The governing equations of motion describing the aero-elastic interactions of the flapping wing structure in hover are given by

$$\begin{aligned} \rho A\ddot{w} - \rho A y_{cm}\ddot{\phi} - \rho A\dot{\theta}^2 w + \rho A y_{cm}\dot{\theta}^2\phi + \frac{\partial^2}{\partial x^2}(EI_{yy}w'') \\ = \rho A\ddot{U}sin(\theta) - \rho A y_{cm}\ddot{\theta} + Lcos(2\theta+\phi) \end{aligned} \tag{15}$$

$$\begin{aligned} \rho J\ddot{\phi} - \rho J\dot{\theta}^2\phi - \rho A y_{cm}\ddot{w} + \rho A y_{cm}\dot{\theta}^2 w - \frac{\partial}{\partial x}(GJ\phi') \\ = \rho J\ddot{\theta} - \rho A y_{cm}\ddot{U}sin(\theta) + Mcos(2\theta+\phi) \end{aligned} \tag{16}$$

where L and M denote the total Lift and Moment due to various forces acting on the wing. In the presence of the gust L and M takes the form

$$\begin{aligned} L &= L_{qs} + L_G \\ M &= M_{qs} + M_G, \end{aligned} \tag{17}$$

where L_{qs} and L_G are expressions for quasi steady aerodynamic loading and Gust loading respectively. Similarly M_{qs} and M_G respectively are moment due to quasi steady and gust loading. It can be seen that in the absence of gust load the expressions L and M become $L = L_{qs}$ and $M = M_{qs}$ respectively.
The given system is a set of coupled partial differential equations in $w(x,t)$ and $\phi(x,t)$ having time varying co-efficients and does not have closed form solutions. The system of equations obtained are first non-dimensionalized. Galerkin projection based method is then invoked which reduces the system into a set of coupled non-linear ordinary differential equations. The resulting system can be written as

$$\mathbf{a}(w,\dot{w},\ddot{w},\phi,\dot{\phi},\ddot{\phi},t) + \mathbf{b}(w,\dot{w},\phi,\dot{\phi},\ddot{w},\ddot{\phi},t) = 0 \tag{18}$$

The entries of the vector **a** and **b** are long expressions and not shown here. The presence of strongly nonlinear terms involving multiplicative coupling does not make the system amenable for analytical techniques like perturbation methods. Rearranging the entries of **a** and **b** and defining state vector $X = \{x_1, x_2, x_3, x_4\}$ such that $x_1 = w$, $x_2 = \dot{w}$, $x_3 = \phi$ and $x_4 = \dot{\phi}$, we arrive at the system of nonlinear dynamical equation.

$$\mathbf{F}(\mathbf{X}, \dot{\mathbf{X}}, \mathbf{t}) = \mathbf{0} \tag{19}$$

We resort to a suitable numerical scheme to find the response of the system. For a typical wing data set, refer Table (1), the system responses i.e., the wing twist and plunge are obtained. The results are plotted in Figure 4. It is noted that the wing twist is the dominant of the two responses. However the wing plunge is more sensitive to the gust as compared to the twist i.e., the percentage change in plunge is more of the two responses. This is mainly owing to the fact that the gust velocity, the way its modeled here, is along the direction of the wing plunge.

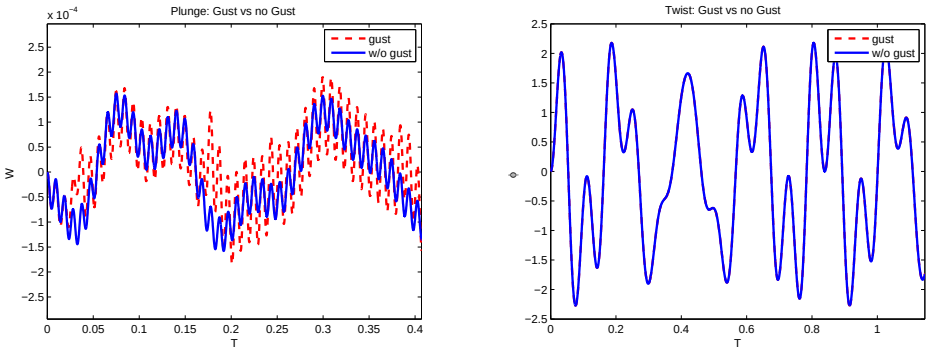

(a) (b)

Figure 4. Typical Aeroelastic responses, with and without gust for (a) Wing plunge; and (b) Wing twist.

Table 1. Wing Data

$l = .08m$	$c = .01m$	$\rho = 1300kg/m^3$	$\mu = 0.33$	$A = 0.12$
$EI_{yy} = 10e4$	$GJ = 3e4$	$y_f = 0.005m$	$y_{cm} = 0.3$	

3. Summary and Conclusions

The present article outlines the development of a quasi steady aeroelastic model for a flexible wing structure, executing insect like flapping motion. For this purpose a structural model is developed from the first principle by idealizing the wing structure as a bending torsion coupled Euler Bernoulli beam. A revised quasi-steady aerodynamic model with features of capturing the necessary aerodynamic forces that an insect wing experiences is then invoked. The coupling between the wing-structure with the fluid medium is established and pitching and plunging responses of the wing-structure are obtained to demonstrate the utility of the present model for studies related to obtaining aero elastic responses and stability of flapping wing. The model developed can also be readily used in obtaining wing responses under gust load and thus can serve as an essential tool in the preliminary design of Flapping wing based Micro Air Vehicles.

Acknowledgments

The authors thank Dr. Sangamesh R., Mechanical Engineering, IISc and Dr. S. Sane, NCBS for relevant technical inputs and insights. The first author acknowledges the efforts of Dr. V. H. Gupta, Department of Computer Science and Automation, Mr. P. Mondal and Mr. A. K. Patra, Aerospace Engineering, IISc, in preparing the manuscript. The authors record their special thanks for Professor Y.V. Mikhlin for extending all the support.

References

[1] T. J. Mueller. *Fixed and Flapping Wing Aerodynamics for Micro Air Vehicle Applications.* AIAA, Reston, VA, 2001.

[2] S. A. Ansari, R. Zbikowski, and K. Knowles. Aerodynamic modeling of insect-like flapping flight for micro air vehicles. *Progress in Aerospace Sciences*, 42(2):129–172, 2006.

[3] M.F. M. Osborne. Aerodynamics of flapping flight with application to insects. *Journal of Experimental Biology*, 28:221–245, 1951.

[4] T. Weis-Fogh. Quick estimate of flight fitness in hovering animals, including novel mechanisms for lift production. *Journal of Experimental Biology*, 59:169–230, 1973.

[5] J.W. S. Pringle. *Insect Flight.* Oxford University Press, 1957.

[6] C. P. Ellington. The aerodynamics of hovering insect flight 1: The quasi-steady analysis. *Philosophical Transactions of the Royal Society of London, Series B*, 305:1–15, 1984.

[7] S. P. Sane. The aerodynamics of insect flight. *Journal of Experimental Biology*, 206:4191–4208, 2003.

[8] B. Singh and I. Chopra. Insect-based hover-capable flapping wings for micro air vehicles: experiments and analysis. *AIAA Journal*, 46(9):2115–2135, 2008.

[9] S. P. Banerjee and M. J. Patil. Aeroelastic analysis of membrane wings. In *Proc. 49th AIAA/ASME/ASCE/AHS/ASC Structures, Structural Dynamics, and Materials Conference*, Schaumberg, IL, April, 2008.

[10] Vladimir V. Golubev. On unsteady response of mav wing in gusty urban environment. In *Proc. 37th National and 4th International Conference on Fluid Mechanics and Fluid Power*, IIT Madras, Chennai, India, December, 2010.

[11] S. P. Sane and M. H. Dickinson. Wing rotation and the aerodynamic basis of insect flight. *Journal of Experimental Biology*, 205:1087–1096, 2002.

[12] M. H. Dickinson, F. O. Lehmann, and S. P. Sane. Wing rotation and the aerodynamic basis of insect flight. *Science*, 284:1954–1960, 1999.

[13] I. Mukherjee and S. N. Omkar. Aeroelastic response of an insect like flapping wing structure using a revised quasi-steady approach. In *Proc. 54th AIAA/ASME/ASCE/AHS/ASC Structures, Structural Dynamics, and Materials Conference*, Boston, Massachusetts, April, 2013.

[14] J. A. Walker and M. W. Westneat. Mechanical performance of aquatic rowing and flying. *Proceedings of Royal Society London Ser B*, 267:1875–1881, 2000.

[15] I. Faruque and J. S. Humbert. Dipteran insect flight dynamics part 1: Longitudinal motion about hover. *Journal of Theoretical Biology*, 264:538–554, 2010.

[16] C. P. Ellington. The aerodynamics of hovering insect flight ii. morphological parameters. *Philosophical Transactions of the Royal Society of London, Series B*, 305:17–40, 1984.

[17] T. Von Karman and W. R. Sears. Airfoil theory for non-uniform motion. *Journal of Aeronautical Science*, 5(10):379–390, 1938.

Proceedings of the 4th International Conference on Nonlinear Dynamics
ND-KhPI2013
June 19-22, 2013, Sevastopol, Ukraine

A Non-linear Mathematical Model of HIV/AIDS with Vertical Transmission

Sandip Omar[1*], Balram Ji Omar [2]

Abstract
In this paper, a nonlinear deterministic mathematical model for the problem is proposed and analyzed qualitatively using stability theory of differential equation. In writing the model we have divided the population under consideration into three subclasses i.e. susceptible, infective and that of AIDS patients. The result shows that the disease free equilibrium is locally stable at threshold parameter less than unity and unstable at threshold parameter greater than unity. It is shown that the positive non-trivial equilibrium is always locally stable under certain condition showing that the disease becomes endemic due to constant migration of the population into the community.

Keywords
AIDS epidemic, Stability Analysis, Vertical Transmission

[1] Vivekananda Gramodyog P. G. College, Dibiyapur, Auraiya, India
[2] All India Institute of Medical Sciences, Rishikes, India
* **Corresponding author:** sandipomar@yahoo.com

Introduction

Vertical transmission is a factor in many important diseases, including AIDS, Chagas's disease, Hepatitis B and Rinderpest in Cattle. However, the mathematical Modeling of vertical transmission is of very recent origin having begun with the model of Fine and LcDuc (1978) for keystone virus. HIV, the human immunodeficiency virus is the etiological agent for AIDS (Acquired Immune-deficiency Syndrome) .It is a fatal disease, which breaks down the body's immune system, leaving the victim vulnerable to a host of life threatening opportunistic infections, neurological disorders or unusual malignancies. It causes mortality of millions of people and expenditure of enormous amount of money in healthcare and disease control. Thus, the most urgent public health problem today is to device effective strategies to minimize the destruction caused by the AIDS epidemic.

In view of the above, in this paper we propose a model with AIDS in a population with variable size structure including demographic and epidemiological considerations. The total population is divided into three subclasses of susceptible, infectives and that of AIDS patients. It is assumed that a fraction of infectives moves to join AIDS class. In this consideration, a model is formulated using nonlinear interaction of standard mass action type, migration, natural mortality process and AIDS related deaths.

1. Mathematical Model

We consider the total human population of size N (t) at time t with constant immigration of susceptible at a rate Q_0. An individual in the population may be in one of the distinct epidemiological subclasses; Susceptible S (t), Infective I (t) (also assumed to be infectious) and AIDS population A (t) with natural mortality rate d in all the classes. It is assumed that the susceptible become infected via sexual contact with infective and then some of babies born are also infected at birth and hence directly recruited into infective class with a rate θ .The interaction of susceptible and infective is of standard mass action type with a contact rate β_1.It is also assumed that infective move to AIDS class with a rate δ.

With these assumptions and considerations, the spread of disease is assumed to be governed by the following system of nonlinear ordinary differential equations:

$$\begin{cases} \dfrac{dS}{dt} = Q_0 - \dfrac{\beta_1 S(I+A)}{N} - dS & S(0) = S_0 \\ \dfrac{dI}{dt} = \dfrac{\beta_1 S(I+A)}{N} - (\delta + d)I + \theta(I+A) & I(0) = I_0 \\ \dfrac{dA}{dt} = \delta I - (\alpha + d)A & A(0) = A_0 \\ S(0)=S_0>0,\ I(0)=I_0>0 \text{ and } A(0)=A_0>0 \end{cases} \quad (1)$$

where Q_0 is the constant immigration rate to the class of susceptibles, d is natural mortality rate constant, δ is the rate of movement from infectious class, so that (1/δ) denotes the average incubation period, α is the disease-induced death rate constant and β_1 is the transmission coefficient.

To simplify the model, It is reasonable to assumed that the AIDS patients are isolated and sexually inactive and hence they are not capable of producing children, i.e. θA =0 and they also do not contribute to viral transmission horizontally i.e. $\frac{\beta_1 SI}{N}$ negligible. In view of the above assumptions, the system reduces to model (1) modified as-

$$\begin{cases} \dfrac{dS}{dt} = Q_0 - \dfrac{\beta_1 SI}{N} - dS & S(0) = S_0 \\ \dfrac{dI}{dt} = \dfrac{\beta_1 SI}{N} - (\delta + d)I + \theta I & I(0) = I_0 \\ \dfrac{dA}{dt} = \delta I - (\alpha + d)A & A(0) = A_0 \\ N(0)=N_0>0,\ I(0)=I_0>0 \text{ and } A(0)=A_0>0 \end{cases} \quad (2)$$

The above equations can now be written as using N=S+I +A,

$$\begin{cases} \dfrac{dN}{dt} = Q_0 - dN - \alpha A + \theta I & N(0) = N_0 \\ \dfrac{dI}{dt} = \dfrac{\beta_1 (N-I-A)I}{N} - (\delta + d)I + \theta I & I(0) = I_0 \\ \dfrac{dA}{dt} = \delta I - (\alpha + d)A & A(0) = A_0 \end{cases} \quad (3)$$

From the model, it is noted that in the absence of infection, the population size approaches the steady state value Q_0/d. It may be assumed that usually θ is quite small as there have been very few HIV positive babies born. We shall also assumed that θ<d<α .During the early stages of the epidemic, if it is assumed that $S \cong N \cong Q_0/d$ then the growth of infectious people I(t) can be approximately governed by the following equation

$$\frac{dI}{dt} = [\beta_1 + \theta - (\delta + d)]I \qquad I(0) = I_0 \quad (4)$$

This gives

$$I(t) = I_0 \exp((R_0 - 1)/T)t \quad (5)$$

where $R_0 = \dfrac{\beta_1 + \theta}{\delta + d}$ and $T = \dfrac{1}{(\delta + d)}$, the time during which people remain infective and I_0 is the initial infective population at t = 0. The doubling time t_d of the epidemic is given by

$$t_d = \frac{(\ln 2)T}{R_0 - 1} \quad (6)$$

Thus, as before, if $R_0>1$, the infection triggers an epidemic otherwise for $R_0<1$, the epidemic prevalence is zero.

2. **Stability Analysis**

Now we analyze the model given by equations (7-9). The model has two non-negative equilibria namely E_0 (Q_0/d, 0, 0), the disease free, and E*(N*, I*, A*) the endemic equilibrium, where (N*, I*, A*) are positive solutions of the equations and are obtained as

$$N^* = \beta_1 \gamma I^*, \qquad I^* = \frac{Q_0}{[\beta_1 d\gamma + \frac{\alpha\delta}{(\alpha+d)} - \theta]}, \qquad A^* = \frac{\delta I^*}{(\alpha+d)},$$

where $\gamma>0$ is defined as

$$\gamma = \frac{1+\frac{\delta}{(\alpha+d)}}{[\beta_1+\theta-(\delta+d)]}$$, γ is positive only when $(\beta_1+\theta)>(\delta+d)$,

It is noted that E* is positive only when

$$\beta_1 d\gamma + \frac{\alpha\delta}{(\alpha+d)} > \theta$$

It is found that equilibrium level of infectives I* increases as Q_0 increases or γ decreases leading to increases A*. Further the equilibrium level of AIDS patients A* decreases as α increases. It is also noted that when the disease remain endemic, the disease induced deaths reduce the equilibrium population size from Q_0/d to N*.

To determine the local stability of E_0 and E*, the following variational matrices are computed around E_0 and E*,

$$M(E_0) = \begin{bmatrix} -d & \theta & -\alpha \\ 0 & [\beta_1-(\delta+d)+\theta] & 0 \\ 0 & \delta & -(\alpha+d) \end{bmatrix}$$

$$M(E^*) = \begin{bmatrix} -d & \theta & -\alpha \\ [\beta_1-(\delta+d)+\theta]\frac{I^*}{N^*} & -\frac{\beta_1 I^*}{N^*} & -\frac{\beta_1 I^*}{N^*} \\ 0 & \delta & -(\alpha+d) \end{bmatrix}$$

From M (E_0), it can be seen that E_0 is locally asymptotically stable (LAS) provided

$$(\beta_1+\theta) < (\delta+d) \tag{7}$$

i.e. for $R_0<1$ and under this condition the equilibrium E* does not exist. However, if $R_0>1$ the equilibrium E_0 is a saddle point which is stable in N-P-A manifold and unstable in I-direction. In such a case E* exists and the infection is maintained in the population.

The characteristic equation corresponding to M (E*) is given by

$$f(\lambda) = \lambda^3 + a_1\lambda^2 + a_2\lambda + a_3 = 0 \tag{8}$$

where

$$a_1 = 2d + \alpha + \frac{\beta_1 I^*}{N^*}$$

$$a_2 = \frac{\beta_1 I^*}{N^*}\{\alpha+2d+\delta\} + d(d+\alpha) - \theta[\beta_1-(\delta+d)+\theta]\frac{I^*}{N^*}$$

$$a_3 = \frac{\beta_1 I^*}{N^*}(\alpha d + d^2 + \delta d) - (\alpha + d)\theta[\beta_1 - (\delta + d) + \theta]\frac{I^*}{N^*}$$

Thus by Routh-Hurwitz criteria, E* is locally asymptotically stable as it can be seen for

$a_1>0$, $a_2>0$, $a_3>0$, and $a_1a_2-a_3>0$

Now to show that E* is globally asymptotically stable, we first establish a lemma.

***3.* Lemma**: The region

$$\Omega = \left\{(N, I, A); 0 \le N(t) \le \frac{Q_0}{d}; 0 \le I(t) \le I_{\max} \;;\; 0 \le A(t) \le \frac{\delta I_{\max}}{(\delta + d)}\right\}$$

is a region of attraction for $(\beta_1+\theta)>(\delta+d)$, where

$$I_{\max} = \frac{Q_0}{d}\left\{1 + \frac{\theta}{\beta_1} - \frac{(\delta + d)}{\beta_1}\right\}$$

Theorem: *If the endemic equilibrium E* exists, then it is globally asymptotically stable provided the following conditions are satisfied in* Ω,

$$\alpha^2 < \frac{d}{\delta}(\alpha + d)\left\{\left(\frac{d}{2} - \theta\right) + \sqrt{\frac{d}{2}\left(\frac{d}{2} - 2\theta\right)}\right\} \tag{9}$$

Proof: Consider the following positive definite function about E*,

$$V = \frac{1}{2}(N - N^*)^2 + k_1\left\{I - I^* - I^* \ln\left(\frac{I}{I^*}\right)\right\} + \frac{1}{2}k_2(A - A^*)^2 \tag{10}$$

where the constants k_1 and k_2 can be chosen suitably.

The derivative of V along the solution of the system (3) can be written as

$$\frac{dV}{dt} = (N - N^*)[Q_0 - dN - \alpha A + \theta I] + k_1(I - I^*)\left[\frac{\beta_1(N - I - A)}{N} - (\delta + d) + \theta\right] + k_2(A - A^*)[\delta I - (\alpha + d)A] \tag{11}$$

where

$$a_{11} = d,\;\; a_{22} = \frac{\beta_1 k_1}{N^*},\;\; a_{33} = (\alpha + d)k_2,$$

$$a_{12} = \frac{\beta_1 k_1}{NN^*}(I + A) + \theta,\;\; a_{13} = -\alpha,\;\; a_{23} = k_2\delta - \frac{\beta_1 k_1}{N^*},$$

Thus a sufficient condition for $\frac{dV}{dt}$ to be negative definite is that,

$$\begin{cases} a_{12}^2 - a_{11}a_{22} < 0 \\ a_{13}^2 - a_{11}a_{33} < 0 \\ a_{23}^2 - a_{22}a_{33} < 0 \end{cases} \tag{12}$$

Now choosing $k_2 = \frac{k_1\beta_1}{\delta N^*}$ and $k_1 = \frac{N^*}{\beta_1}\left[\left(\frac{d}{2} - \theta\right) + \sqrt{\frac{d}{2}\left(\frac{d}{2} - 2\theta\right)}\right]$, the conditions (12) give

$$\alpha^2 < \frac{d}{\delta}(\alpha + d)\left\{\left(\frac{d}{2} - \theta\right) + \sqrt{\frac{d}{2}\left(\frac{d}{2} - 2\theta\right)}\right\}$$

Hence V is a Liapunov function with respect to E* whose domain contains Ω, proving the theorem.

Conclusions

In this paper, a mathematical model is proposed and analyzed to study the effect of vertical transmission in a population of variable size with constant recruitment into susceptible population under the assumption that due to sexual interaction of susceptibles with infectives, the infected babies are born to increase the growth of infective population directly. It is also assumed that persons in AIDS class are isolated and incapable of producing children. It is shown that for the system (2), as usual, there exists a threshold parameter R_0. If $R_0<1$ the disease dies out and when $R_0>1$ the disease becomes endemic. The model has two non-negative equilibria namely E0 (Q_0/d, 0, 0), the disease free equilibrium and E*(N*, I*, A*), the endemic equilibrium for $R_0>1$. It is found that the equilibrium state E0, corresponding to the disappearance of disease, is locally asymptotically stable if $R_0<1$ and for $R_0>1$ it is unstable and the infection is maintained in the population. Further the endemic equilibrium E* which exists only when $R_0>1$ and is always locally asymptotically stable. For this endemic equilibrium we have found a Liapunov function and shown that this equilibrium is globally asymptotically stable, if the conditions (9) are satisfied. It is noted that when disease remain endemic, the disease induced deaths reduce the equilibrium population size from Q_0/d to N*. It is shown that I* increases as Q_0 or β_1 increases or as δ decreases leading to A*.It is further noted that increase in the rate of infected babies born, leads to increase in the population of infectives and that of AIDS patients. The above analysis also suggests that if unsafe sexual interaction is restricted, the spread of the disease could be slowed down. Also the infected people may be educated and advised not to indulge in sexual activities, even at the early stage of infection to avoid the birth of infected offspring.

References

[1] Fine P. and Leduc J. Towards a quantitative understanding of the epidemiology of keystone virus in the eastern united states *Am. J. Trop. Med. Hyg*. Vol.27, pp.322-388, 1978.

[2] Anderson R.M., May R.M. The invasion, persistence and spread of infectious diseases within animal and plant communities *Phil. Trans. R. Soc. London B,* Vol.134, pp.533-570, 1986.

[3] Anderson R.M. The role of mathematical models in the study of HIV transmission and the epidemiology of AIDS *J. AIDS* Vol.1, pp.241-256, 1988.

[4] Greenhalgh D., Doyle M., Lewis F. A mathematical treatment of AIDS and condom use *IMA J. Math. Appl. Med. Biol.* Vol. 18, pp.225-262, 2001.

[5] Hsieh Y.H., Chen C.H. Modeling the social dynamics of a sex industry: Its implications for spread of HIV/AIDS. *Bull. Math. Biol.* Vol.66, pp.143-166, 2004.

[6] Mukandavire, Z., Garira W., Chiyaka C. Asymptotic properties of an HIV/AIDS model with a time delay *J. Math. Anal. Appl*. V.330 , pp.916-933, 2007.

[7] Naresh R., Tripathi A. and Sharma D. Modelling the effect of screening of unaware infectives on the spread of HIV infection, *Appl. Math. Comp*.Vol.184, pp.1053-1068, 2007.

[8] Naresh R., Tripathi A., Omar S. Modelling the spread of AIDS epidemic with vertical transmission, *Appl. Math. Comp.* Vol. 178, pp.262-272, 2006.

[9] Medley G.F.,Anderson R.M.,Cox D. R., Billard L. Incubation period of AIDS in patients infected by blood transfusions, *Nature*, Vol. 328, 719-721, 1987.

[10] Moss A.R., Osmond D., Baccheeti P. et. al. Risk Factors for AIDS & HIV seropositivity in homosexual men , *Amer. J. Epidemiol*., Vol.135, pp.1035-1047, 1987.

[11] Waziri A.S., Massave E.S., Makinde O.D. Mathematical modelling of HIV/AIDS dynamics with treatment and vertical transmission, Vol.2(3), pp.77-89, 2012.

Proceedings of the 4th International Conference on Nonlinear Dynamics
ND-KhPI2013
June 19-22, 2013, Sevastopol, Ukraine

Chaos in a Cardiorespiratory Model

Evgeniy Pechuk[1*], Tatyana Krasnopolskaya[1]

Abstract
A new modified cardiorespiratory model based on the well-known DeBoer beat-to-beat model and the Zaslavsky map, which describes dynamics of the respiratory system as a generator of central type, is studied in details. The respiratory tract was firstly modeled by the self-oscillating system under the impulsive influence of heartbeats. The steady-state regimes of the modified model are investigated by methods of the dynamical system theory. The regular (periodic and quasi-periodic) and chaotic regimes typical for functioning of the cardio system, are found and studied.

Keywords
Cardiorespiratory System, DeBoer Model, Chaos

[1] Institute of Hydromechanics NAS of Ukraine, Kiev, Ukraine
* **Corresponding author:** uzuzun@i.ua

Introduction

The human cardiovascular system closely interacts with different organs and systems of organism. Realized self-oscillations in a cardiovascular system are under an activity of practically entire organism (see [2-5, 9-11]). Physiological rhythms are not isolated processes. There are numerous interactions of rhythms between itself and with an internal and external environment. Cardiac and respiratory rhythms form up during embryo development, and even the brief break of these rhythms after a birth results in death.

Existence of breathing and heart rhythm synchronization effect, found experimentally in the cardiovascular system both for healthy people and with pathologies, is well-proven in work Toledo [10] in 2002. It is well known, the dynamic process of mutual synchronization can be realized only in a case of presence of a subsystem mechanical interaction. Therefore, the indicated effect display testifies the presence of both direct and feedback interactions between the cardiovascular and respiratory systems.

A heart system and organism of man in general have one of major descriptions of activity, such as a blood pressure dynamics. His time-history, along with electrocardiogram (ECG), is an important information generator for research and diagnostics of laws and pathologies of the cardiovascular system. The task of mathematical model construction, describing the dynamics of arterial blood pressure, is far from completion. Complications of such design are related to the necessity of taking into account of influence on the cardiac rhythms not only the cardiovascular system but also other organs and systems of organism, in particular a respiratory system.

1. The Mathematical Model of a Direct and Reverse Interactions

The DeBoer model describes the cardiovascular system which is under direct action of respiratory systems (it corresponds to the experimental data) [3]. This model was substantially developed later. The sinus node responsiveness (and other detailed factors) is taking into account in the work of Seidel and Herzel [9] (the so-called SH-model). In this model chaotic dynamics was found in dynamics of the cardiosystem.

Both DeBoer and SH models consider only direct respiratory influence on heartbeats. The SH-model was further developed in [5], where an effect of heartbeat and the resultant changes in the baroreceptor afferent activity to the SH-model are added and the cardiorespiratory synchronization

found due to this modification. Interaction of blood pressure and amplitudes of breathing oscillations revealed in accordance with principles of optimum control in the DeBoer model is investigated in the Grinchenko-Rudnitsky model [2]. This model explains, in particular, an appearance of a peak on the Meyer frequency in the spectrums of pressure oscillations and synchronization of cardiac and respirator rhythms.

However, this model does not consider the reverse mechanical influence effect of the heartbeat changes on a breathing phase (frequency). In the present study, we add to the DeBoer model the self-oscillating system describing dynamics of the respiratory system as a generator of central type [4], which is under impulsive influence of heartbeat.

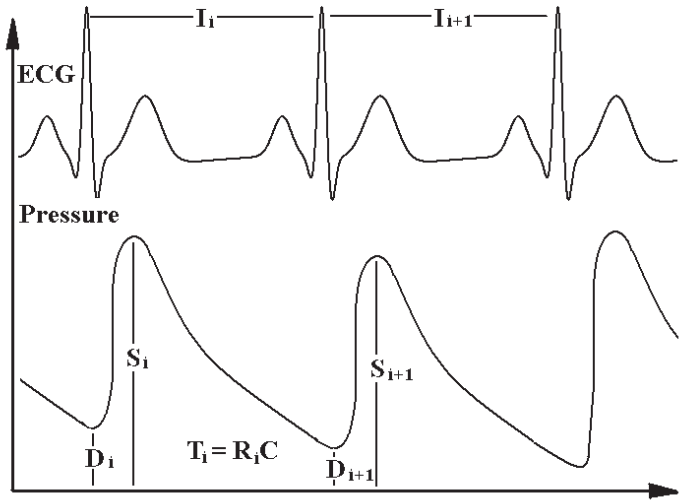

Figure 1. Characteristics of the heartbeat in DeBoer model

The DeBoer model describes the followings main characteristics of the heartbeat (see Figure 1) system: systolic pressure S , diastolic pressure D, R-R interval I and arterial time constant T (in a state of rest for a healthy man S=120 mmHg, D=80 mmHg, I=800 ms, T=1500 ms). This mathematical model is a system of five discrete nonlinear maps. This model contains only a direct mechanical influence of the respirator system on the cardiosystem and can be written in the form:

$$
\begin{aligned}
D'_i &= S'_{i-1}\exp\left(-\frac{2}{3}\frac{I'_{i-1}}{T'_{i-1}}\right)\\
S'_i &= D'_i + \gamma\frac{T_0}{S_0}I'_{i-1} + \frac{A}{S_0}\sin\left(2\pi f T_0 t_i\right) + \frac{c_2}{S_0}\\
I'_i &= G_v\frac{S_0}{T_0}\hat{S}'_{i-\tau_v} + G_\beta\frac{S_0}{T_0}F(\hat{S}',\tau_\beta) + \frac{c_3}{T_0}\\
T'_i &= 1 + G_\alpha\frac{S_0}{T_0} - G_\alpha\frac{S_0}{T_0}F(\hat{S}',\tau_\alpha)\\
\hat{S}'_i &= 1 + \frac{18}{S_0}\arctan\frac{S_0(S'_i-1)}{18}
\end{aligned}
\qquad (1)
$$

where $i \geq 1$, $D' = D/S_0$, $S' = S/S_0$, $\hat{S}' = \hat{S}/S_0$, $I' = I/T_0$, $T' = T/T_0$, $F(\hat{S},\tau) = 1/9(\hat{S}_{i-\tau-2} + 2\hat{S}_{i-\tau-1} + 3\hat{S}_{i-\tau} + 2\hat{S}_{i-\tau+1} + \hat{S}_{i-\tau+2})$, $t_i = \sum_{k=0}^{i-1} I'_k$ is a real time, A=3 mmHg is a breathing amplitude, f=0.25 Hz is a breathing frequency, $c_2 = S_0 - D_0 - \gamma I_0$, $c_3 = I_0 - S_0(G_v + G_\beta)$,

$\gamma = 0.016$ mmHg, $G_\alpha = 18$ ms/mmHg, $G_\beta = 9$ ms/mmHg, $G_v = 9$ ms/mmHg, $\tau_\alpha = \tau_\beta = 4$, $\tau_v = 0$, is equal to 0 if frequency of heartbeat is less then 75 beat/min, and τ_v is equal to 1, if frequency is more then 75 beat/min.

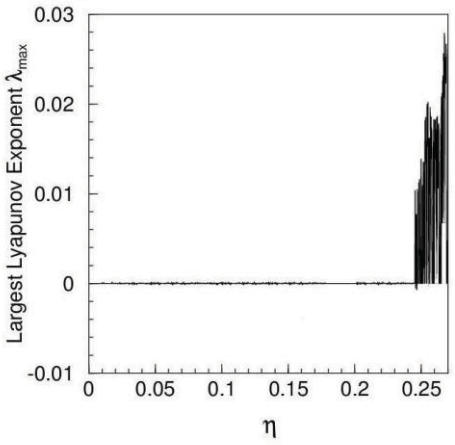

Figure 2. Largest Lyapunov exponent of the modified system

We suppose that a healthy man at rest breathes periodically with a permanent frequency and an amplitude of motions of thorax. In that case a breathing process can be described as the self-oscillating system [4], which has a steady limit cicle. Thus for the mathematical modeling of a such system equations of the Zaslavskiy map could be used. Famous Zaslavsky map is the system of equations [8, 12] which describes the dynamics of an amplitude r_n and a phase φ_n of the system (in which periodic self-oscillations with a frequency ω are realized) which is under T-periodic impulsive action of constant intensity η. Te system has the following form:

$$r_{n+1} = \left(r_n + \eta \sin \varphi_n\right) \exp\{-\kappa T\} \tag{2}$$

$$\varphi_{n+1} = \varphi_n + \omega T + \nu \left(r_n + \eta \sin \varphi_n\right) \frac{1 - \exp\{-\kappa T\}}{\kappa} \tag{3}$$

where κ, ν are constant parameters.

In our approach these equations are used to describe changes of an amplitude and phase of a respiratory system effect for every R-R interval with intensity, which is proportional to systolic pressure: $\tilde{\eta} = -\eta(S_n - S_0)$:

$$r_{n+1} = \left(r_n - \eta(S_n - S_0) \sin \varphi_n\right) \exp\{-\kappa I_n\} \tag{4}$$

$$\varphi_{n+1} = \varphi_n + 2\pi f I_n + \nu \left(r_n - \eta(S_n - S_0) \sin \varphi_n\right) \frac{1 - \exp\{-\kappa I_n\}}{\kappa} \tag{5}$$

where I is R-R interval, $\eta > 0$, κ, ν are constant parameters of interaction.

Thus, we study the dynamics of the modified model of cardiorespiratory system, which consists of the DeBoer model with direct respiratory influence $(A + r_i)\sin\varphi_i$, and with reverse influence modeled by the Zaslavskiy map system.

2. Numerical Simulations Results

In accordance with physiology of healthy man, the followings values of variables and constants are used in our numerical simulations: $I'[0] = 0.53$, $S'[-j] = 1.08$, $j = 0,...,6$, $r'[0] = 0$, $\varphi'[0] = 0$, $\kappa = 0.001$ 1/ms, $\nu = 0.001$ 1/msmmHg. In order to study steady-state regimes first of all the largest

Lyapunov exponent [1, 6, 7] was found. The dependence of the largest Lyapunov exponent of the modified system on values of the bifurcation parameter η is shown in Figure 2. The dynamics of the system changes with increasing of this parameter. There is the region where Lyapunov exponent positive ($\eta > 0.245$) that means transition to chaos occurs. We emphasize that η describes intensity of heart influence on a respiratory system. The next Figure 3 illustrates a behavior of systolic pressure data in the modified model. Power spectra computed from these data are shown in Figure 4. The spectrum in Figure 4.a and in Figure 4.b has discrete peaks which are situated equidistantly with a frequency difference. So that, graphs indicate that there are regular regimes in the modified system.

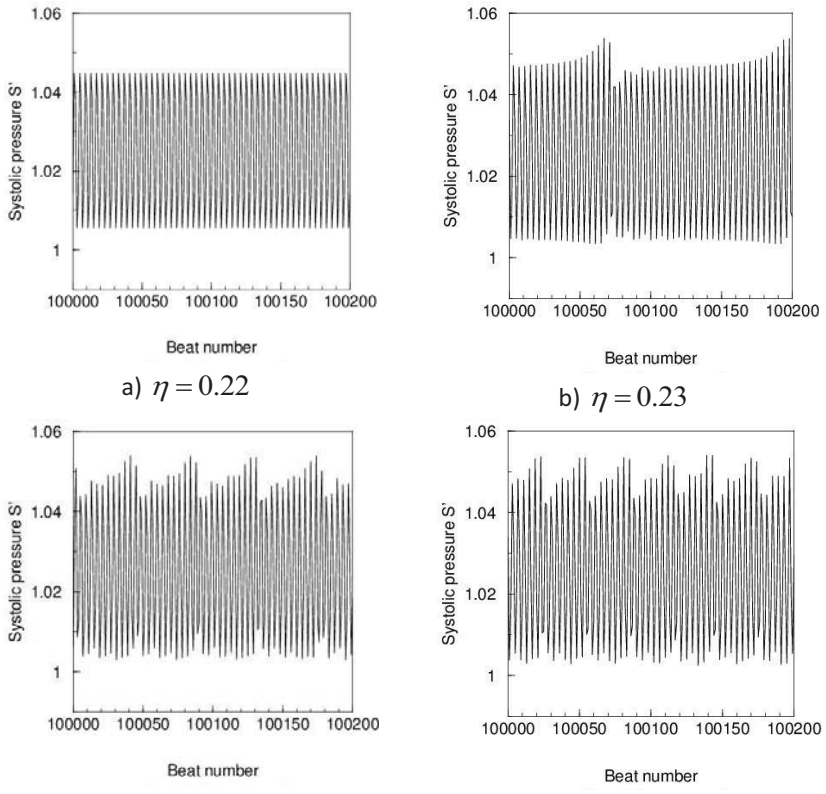

Figure 3. Simulated systolic pressure data (cases a, b, c and d)

Finally, for the steady-state regimes, when the largest Lyapunov exponent is positive and the chaotic regime is realized, the power spectrum is continuous (Figure 4.c).

Phase portrait projections on the plane of the simulated systolic pressure and R-R interval data are presented in Figure 5. The phase portrait in the Figure 5.a represents a singular solid curve and corresponds to quasiperiodic regime. There are only several points in the phase portrait in Figure 5.b which means that at $\eta = 0.24$ the modified system has regular periodic regime. And in Figure 5.c when $\eta = 0.25$ the phase portrait has numerous lines (the number of which increases in time) and corresponds to chaotic steady-state regime. So we have found such steady-state basic regimes as:

1. at $\eta = 0.22$, periodic regime (Figure 3.a);
2. at $\eta = 0.23$, quasiperiodic regime (Figure 3.b, Figure 4.a, Figure 5.a);
3. at $\eta = 0.24$, periodic regime (Figure 3.c, Figure 4.b, Figure 5.b);
4. at $\eta = 0.25$, chaotic regime (Figure 3.d, Figure 4.c, Figure 5.c).

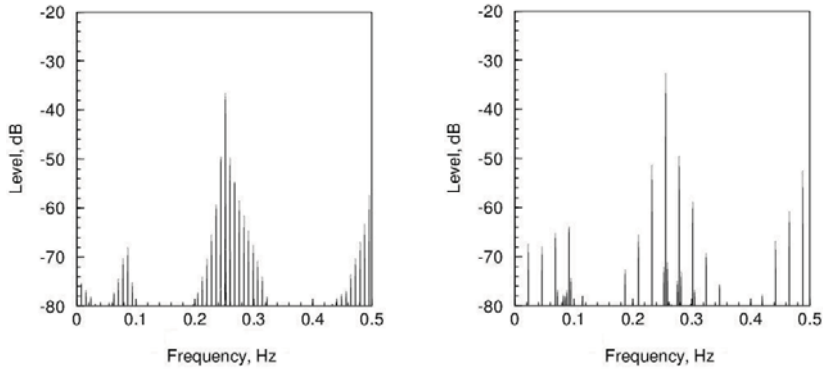

a) $\eta = 0.23$ b) $\eta = 0.24$

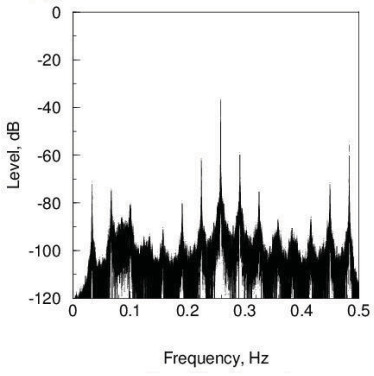

c) $\eta = 0.25$

Figure 4. Power spectra computed from systolic pressure data (cases a, b and c)

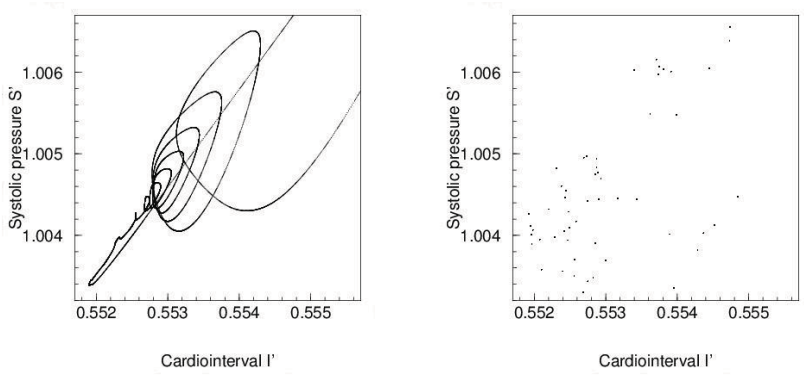

a) $\eta = 0.23$ b) $\eta = 0.24$

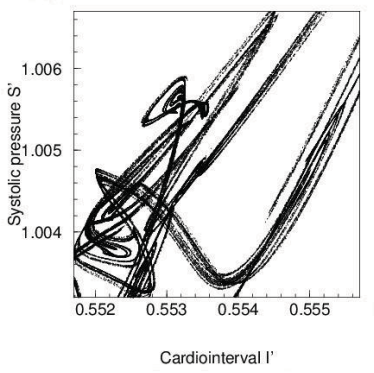

c) $\eta = 0.25$

Figure 5. The parts of phase portraits simulated systolic pressure and R-R interval data (cases a, b and c)

Conclusions

On the basis of the DeBoer model an interaction of the heartbeat and the respiratory system as dissipative Zaslavskiy map is studied and the modified model of cardiosystem is constructed. In this model both direct and reverse influence of subsystems – cardiovascular and respiratory ones, are taken into account.

The methods of modern theory of the dynamical systems are used to study laws of the steady-state regimes of the modified model. Firstly the chaotic regimes were found out. Analysis of bifurcation curves of the largest Lyapunov exponent, projections of phase portraits, temporal realizations and power spectrums allowed to investigate the basic laws of dynamics of the model. The dynamics of heartbeat and respiratory systems are in good correspondence with experimental information of healthy man. It is found irregularities of phase trajectories of the modified model depending on intensity of heart rhythm influence on breathing, what is well known characteristic for the dynamics of the cardiovascular system of healthy man.

References

[1] Anishshenko V. S. *Acquaintance with nonlinear dynamic,* Institute of Computer Science, Moscow-Izhevsk, 2002 (in Russian).

[2] Grinchenko V. T., Rudnitskiy A. G. A model of interaction of the cardiovascular and respiratory systems, *Acoustic Journal*, Vol. 9, N. 3, pp. 16-26, 2006.

[3] DeBoer R. W., Karemaker J. M., Strakee J. Hemodynamic fluctuations and baroreflex sensitivity in humans: A beat-to-beat model *Amer. J. Physiol*., Vol. 253, pp. H680-H689, 1987.

[4] Glass L., Mackey M. C. *From Clocks to Chaos. The Rhythms of Life,* Princeton University Press, Princeton, 1988.

[5] Kotani K. et al. Model for cardiorespiratory synchronization in humans *Physical Review E.*, Vol. 65, pp. 051923-051932, 2002.

[6] Kouznetsov S. P. *Dynamic chaos*, Physmatlit, Moscow, 2001 (in Russian).

[7] Krasnopolskaya T. S., Shvets A. Yu. *Regular and chaotic dynamics of the systems with limited excitation,* Institute of Computer Science, Moscow-Izhevsk, 2008 (in Russian).

[8] Sagdeev R. Z., Usikov D. A. and Zaslavsky G. M. *Nonlinear Physics: From the Pendulum to Turbulence and Chaos*, Harwood Academic Publishers, New-York, 1988.

[9] Seidel H., Herzel H. Bifurcations in a nonlinear model of the baroreceptor-cardiac reflex *Acoustic Journal*, Vol. 115D, pp. 145-160, 1998.

[10] Toledo E. [et al.]. Does synchronisation reflect a true interaction in the cardiorespiratory system *Med. Engng Phys.*, Vol. 24, pp. 45-52, 2002.

[11] Yang T., Jacobstein M. D., Levy M. N. Synchronization of automatic cells in S-A node during vagal stimulation in dogs *Am. J. Physiol.*, N. 246, pp. H585-H591, 1984.

[12] Zaslavsky G. M. The simplest case of a strange attractor *Phys. Lett. A*, Vol. 69, pp. 145-147, 1978.

Proceedings of the 4th International Conference on Nonlinear Dynamics
ND-KhPI2013
June 19-22, 2013, Sevastopol, Ukraine

Nonlinear Normal Modes in the Rotor Dynamics

N.V.Perepelkin[1], Yu.V.Mikhlin[1]*, C.Pierre[2], E.Harutyunyan[3]

Abstract
A new approach combining both the nonlinear normal vibration modes approach and the modified Rauscher method is proposed and used to construct forced resonance vibrations in non-autonomous systems with the internal resonance. Corresponding iterative process is described. Forced vibrations of the one-disk unbalanced rotor with the linearly isotropic elastic shaft and nonlinear elastic bearings of Duffing type are considered. Gyroscopic effects, inertial forces in supports, an asymmetrical disposition of the disk in the shaft and internal resonance are taken into account.

Keywords
Nonlinear vibration modes, Rauscher method, one-disk rotor.

[1] National Technical University, Kharkov, Ukraine
[2] Illinois University, Urbana, USA
[3] National Academy of Sciences of Armenia, Yerevan, Armenia
* **Corresponding author:** muv@kpi.kharkov.ua

Introduction

Nonlinear normal vibrations modes (NNMs) are a generalization of the normal vibrations in linear systems. The Kauderer-Rosenberg concept of NNMs [1-3] is based on determination of trajectories in the configuration space of the dynamical system. Shaw and Pierre reformulated the concept of NNMs for nonlinear dissipative systems [4, 5]. Their analysis is based on computation of invariant manifolds of motion on which the NNMs take place. One chooses a couple of independent phase variables (u, v) of the nonlinear dynamical system, so-called "master coordinates" (or active coordinates), where u is some dominant generalized coordinate, and v is the corresponding generalized velocity. By the Shaw-Pierre approach, the NNM is such regime when all generalized coordinates and velocities are univalent functions of the selected couple of master variables. The master coordinates can be chosen as new independent ones instead of time. In a case of internal resonance it can observe that *four phase coordinates are active*, and all of them must be chosen as new independent variables. In this case all other phase coordinates are determined as univalent functions of the selected four master coordinates.

The Rauscher method is first proposed for the single-DOF system [6]. General procedures of the Rauscher method utilization to construct NNMs in n-DOF non-autonomous systems are described in [7,8]. If we have both external and internal resonances, the Shaw-Pierre approach in combination with the modified Rauscher method permits to reduce the n-DOF non-autonomous dynamical system to two-DOF nonlinear system for each nonlinear normal mode of forced vibrations.

It is well known that rotor systems display a complicated nonlinear behavior. Moreover, internal resonances in the rotor systems must be taken into account. Asymptotic method to analyze the nonlinear dynamics of rotating shaft is first suggested in [9]. Bolotin [10] took into account a nonlinear inertia in a model of the one disk rotor. Different nonlinear effects in the rotor dynamics are

discussed in [11]. Dynamic behavior of a rigid rotor with nonlinear elastic restoring forces is analyzed in [12]. It is shown that, in addition to synchronous solutions, relatively small damping forces made possible the onset of the rotor precession motions which are periodic or quasi-periodic. An experimental confirmation of the theoretical data is sought. Different problems of the rotor dynamics are considered in [13]. Numerical simulation is used to analyze the symmetrical single-disc flexible rotor–bearing system in [14]. The 4-DOF nonlinear model of the rotor dynamics is considered in [15] by using the multiple scales method. In many publications mostly the simplest models, such as the Jeffcott rotor, are considered due to a complexity of the rotor system dynamics. It seems that the NNMs approach is appropriate to analyze the rotor steady-state dynamics. The NNMs are constructed here for the rotor system with internal resonance which is realized in the rotor dynamics with the isotropic-elastic shaft and supports. Gyroscopic effects, asymmetrical disposition of the disk in the shaft, nonlinear restoring forces and inertial forces in supports are taken into account. The NNM approach and the modified Rauscher method is used in analysis of the rotor forced vibration modes.

1. Iterative procedure to construct forced nonlinear normal vibration modes in a case of internal resonance

One considers the nonlinear dynamical system under an external periodical excitation, reduced to principal coordinates and written in the following canonical form:

$$\begin{cases} \dot{q}_1 = s_1 \\ \dot{s}_1 = -\nu_1^2 q_1 - f_1(\mathbf{q},\mathbf{s}) + F_1 \cos(\Omega t) \\ \dot{q}_2 = s_2 \\ \dot{s}_2 = -\nu_2^2 q_2 - f_2(\mathbf{q},\mathbf{s}) + F_2 \cos(\Omega t) \\ \ldots \\ \dot{q}_k = s_k \\ \dot{s}_k = -\nu_k^2 q_k - f_k(\mathbf{q},\mathbf{s}) + F_k \cos(\Omega t) \\ \ldots \qquad\qquad (k = \overline{3,N}) \end{cases} \tag{1}$$

Here $\mathbf{q} = \{q_1, q_2, ..., q_N\}^T$ and $\mathbf{s} = \{s_1, s_2, ..., s_N\}^T$ are general coordinates and corresponding velocities. It is assumed that two eigenfrequencies, ν_1 and ν_2, are close to the excitation frequency, Ω, that is $\Omega \approx \nu_1 \approx \nu_2$. In this case two master (active) coordinates, $q_{1,2}$, and two corresponding velocities, $s_{1,2}$, may be taken as independent ones to construct forced NNMs. It is presupposed that there is some approximate representation of the master coordinates in the form of the Fourier series:

$$\begin{aligned} q_1 &= A_1 \cos(\Omega t) + B_1 \sin(\Omega t) + A_2 \cos(2\Omega t) + B_2 \sin(2\Omega t) + A_3 \cos(3\Omega t) + B_3 \sin(3\Omega t) + .., \\ s_1 &= \Omega\left(B_1 \cos(\Omega t) - A_1 \sin(\Omega t) + 2B_2 \cos(2\Omega t) - 2A_2 \sin(2\Omega t) + 3B_3 \cos(3\Omega t) - 3A_3 \sin(3\Omega t)\right) + .., \\ q_2 &= .., \quad s_2 = ... \end{aligned} \tag{2}$$

After some transformations relations (2) can be inverted in the following form:

$$\cos(\Omega t) = \alpha_1 q_1 + \alpha_2 s_1 + \alpha_2 q_2 + \alpha_3 s_2 + \alpha_5 q_1^2 + \alpha_6 s_1^2 + ... \tag{3}$$

A similar relation can be obtained for the function $\sin(\Omega t)$ too. By using the relation (3), the next *N*-DOF "pseudo-autonomous" system is obtained instead of the system (1):

$$\begin{cases} \dot{q}_k = s_k & \left(k = \overline{1,N}\right) \\ \dot{s}_k = -\nu_k^2 q_k - f_k\left(\mathbf{q},\mathbf{s}\right) + F_k\left(\alpha_1 q_1 + \alpha_2 s_1 + \alpha_2 q_2 + \alpha_3 s_2 + \alpha_5 q_1^2 + \alpha_6 s_1^2 + ...\right) \end{cases} \tag{4}$$

Transformations above correspond to principal idea of the Rauscher method. In the obtained autonomous system the NNMs can be constructed as functions of four new independent variables, q_1, s_1, q_2, s_2, as $q_i = q_i(q_1, s_1, q_2, s_2)$, $s_i = s_i(q_1, s_1, q_2, s_2)$, $\left(i = 3,4,...,N\right)$.

Passing on to the new independent variables, one presents the differentiation in time t of the form of the linear differential operator in partial derivatives: $\dfrac{\mathrm{d}}{\mathrm{d}t} = \mathrm{L} = \dot{q}_1 \dfrac{\partial}{\partial q_1} + \dot{s}_1 \dfrac{\partial}{\partial s_1} + \dot{q}_2 \dfrac{\partial}{\partial q_2} + \dot{s}_2 \dfrac{\partial}{\partial s_2}$

After applying the operator L to (4) one obtains,

$$\begin{cases} \dot{q}_1 = s_1, \;\; \dot{s}_1 + \nu_1^2 q_1 + f_{01}\left(\mathbf{q},\mathbf{s}\right) = 0, \\ \dot{q}_2 = s_2, \;\; \dot{s}_2 + \nu_2^2 q_2 + f_{02}\left(\mathbf{q},\mathbf{s}\right) = 0, \\ \left.\begin{array}{l} \dot{q}_1 \dfrac{\partial q_i}{\partial q_1} + \dot{s}_1 \dfrac{\partial q_i}{\partial s_1} + \dot{q}_2 \dfrac{\partial q_i}{\partial q_2} + \dot{s}_2 \dfrac{\partial q_i}{\partial s_2} = s_i \\ \dot{q}_1 \dfrac{\partial s_i}{\partial q_1} + \dot{s}_1 \dfrac{\partial s_i}{\partial s_1} + \dot{q}_2 \dfrac{\partial s_i}{\partial q_2} + \dot{s}_2 \dfrac{\partial s_i}{\partial s_2} + \nu_i^2 q_i + f_{0i}\left(\mathbf{q},\mathbf{s}\right) = 0 \end{array}\right\}, \;\; i = \overline{3,N} \end{cases} \tag{5}$$

After eliminating the time t by using the first four equations of the system (5), the partial differential equations are obtained from the other 2N-4 equations. Then the relations (6) can be determined as solutions of this system of PDEs, for example, in power series:

$$\begin{aligned} q_n &= a_1^{(n)} q_1 + a_2^{(n)} s_1 + a_3^{(n)} q_2 + a_4^{(n)} s_2 + a_5^{(n)} q_1^2 + ..., \\ s_n &= b_1^{(n)} q_1 + b_2^{(n)} s_1 + b_3^{(n)} q_2 + b_4^{(n)} s_2 + b_5^{(n)} q_1^2 + ...; \quad n = \overline{3,N}. \end{aligned} \tag{6}$$

Substituting the series (6) to the PDEs system and equating terms of the same powers on q_1, s_1, q_2, s_2, one obtains algebraic equations with respect to unknown coefficients of these series. The relations (6) determine the Shaw-Pierre NNMs of the autonomous system (4) in a case of the internal resonance. They allow reducing the n-DOF system (1) to the two-DOF one for each resonance NNM. Four master phase coordinates can be obtained from this reduced system in a form of the more precise Fourier series instead of the representation (2). So, the iterative process can be constructed, and the pointed out series of operations can be repeated some times to reach a necessary exactness. Numerical simulation confirms a good exactness of the proposed approach.

2. Forced vibration modes of the one-disk rotor

A model of the rotor dynamics with an asymmetrical disposition of the disk on the shaft is considered (Fig. 1). Gyroscopic effects, nonlinearity and inertial forces in supports are taken into account. The fixed and moving coordinate systems and positional angles of the disk are shown in the Fig. 2. Mathematical model of the rotor has the following parameters: l is the shaft length; l_1, l_2 are distances of the disk up to left and right supports, respectively; $h_1 = l_1 / l; h_2 = l / l_2$; $c_x^{(1)}$, $c_y^{(1)}$ are coefficients characterizing linear terms in the left support restoring force; $k_x^{(1)}$, $k_y^{(1)}$ are similar ones for the right support; $c_x^{(2)}, c_y^{(2)}$ are coefficients characterizing cubic terms in the left support restoring

force; $k_x^{(2)}$, $k_y^{(2)}$ are ones for the right support; c_{11}, c_{12}, c_{22} are the stiffness coefficients of the shaft ; β is a coefficient of damping in supports; ρ_1, ρ_2 are coefficients of damping during the disk motion; m is the disk mass; ε is an eccentricity of the disk mass center.

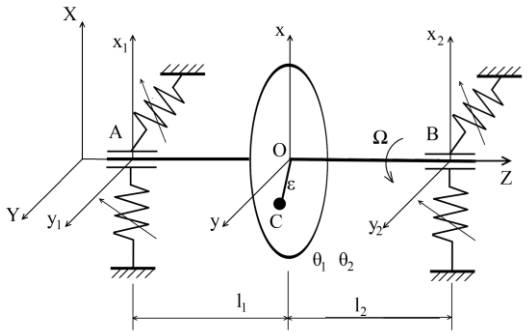

Fig.1. Principal model of the rotor system with massive bearings.

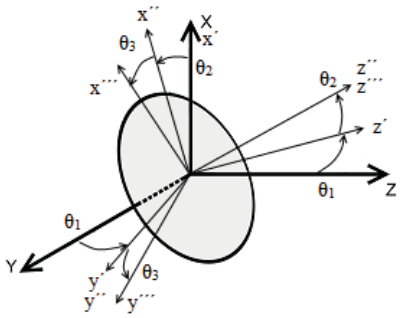

Fig. 2. Fixed and moving coordinate systems. Disk positional angles.

Equations of the rotor motion are the following:

$$
\begin{cases}
m\ddot{x} + \rho_1\dot{x} + c_{11}\left(x - h_1x_2 - h_2x_1\right) + c_{12}\left(\theta_2 - \left(x_2 - x_1\right)/l\right) = \varepsilon\Omega^2 m\cos\Omega t \\
m\ddot{y} + \rho_1\dot{y} + c_{11}\left(y - h_1y_2 - h_2y_1\right) + c_{12}\left(-\theta_1 - \left(y_2 - y_1\right)/l\right) = \varepsilon\Omega^2 m\sin\Omega t \\
I_e\ddot{\theta}_1 + \rho_2\dot{\theta}_1 + I_p\Omega\dot{\theta}_2 - c_{21}\left(y - h_1y_2 - h_2y_1\right) - c_{22}\left(-\theta_1 - \left(y_2 - y_1\right)/l\right) = 0 \\
I_e\ddot{\theta}_2 + \rho_2\dot{\theta}_2 - I_p\Omega\dot{\theta}_1 + c_{21}\left(x - h_1x_2 - h_2x_1\right) + c_{22}\left(\theta_2 - \left(x_2 - x_1\right)/l\right) = 0 \\
m_1\ddot{x}_1 + \beta\dot{x}_1 + s_1\left(x - h_1x_2 - h_2x_1\right) + s_2\left(\theta_2 - \left(x_2 - x_1\right)/l\right) + c_x^{(1)}x_1 + c_x^{(2)}x_1^3 = 0 \\
m_1\ddot{y}_1 + \beta\dot{y}_1 + s_1\left(y - h_1y_2 - h_2y_1\right) + s_2\left(-\theta_1 - \left(y_2 - y_1\right)/l\right) + c_y^{(1)}y_1 + c_y^{(2)}y_1^3 = 0 \\
m_2\ddot{x}_2 + \beta\dot{x}_2 + s_3\left(x - h_1x_2 - h_2x_1\right) + s_4\left(\theta_2 - \left(x_2 - x_1\right)/l\right) + k_x^{(1)}x_2 + k_x^{(2)}x_2^3 = 0 \\
m_2\ddot{y}_2 + \beta\dot{y}_2 + s_3\left(y - h_1y_2 - h_2y_1\right) + s_4\left(-\theta_1 - \left(y_2 - y_1\right)/l\right) + k_y^{(1)}y_2 + k_y^{(2)}y_2^3 = 0
\end{cases}
\tag{7}
$$

Note that the cubic nonlinearity can be considered as an acceptable approximation for different types of the support restoring forces [9,12-15].

3. Construction of the forced vibration modes in the one-disk rotor model

One considers the 8-DOF model (7). The generalized coordinates q_1, s_1, q_2, s_2 are chosen as master coordinates in regime of the resonance NNM. The proposed previously procedure which joints the NNMs approach and the modified Rauscher method are used [16,17]. Results of numerical calculation presented below are obtained for the next system parameters:

$m = 18\,\text{kg}$, $m_1 = m_2 = 1.8\,\text{kg}$, $I_p = 0.36\,\text{kg m}^2$, $I_e = 0.195\,\text{kg m}^2$, $l = 1\,\text{m}$, $l_1 = 0.3\,\text{m}$, $h_1 = 0.3$, $h_2 = 0.7$,

$c_x^{(1)} = c_y^{(1)} = k_x^{(1)} = k_y^{(1)} = 7\cdot10^5\,\text{N/m}$, $c_x^{(2)} = c_y^{(2)} = k_x^{(2)} = k_y^{(2)} = 8\cdot10^{10}\,\text{N/m}^3$, $\rho_1 = 10\,\text{N s m}^{-1}$, $\rho_2 = 5\,\text{N s}$,

$\beta = 60\,\text{N s m}^{-1}$, $\varepsilon = 5\cdot10^{-5}\,\text{m}$, Young modulus, E = 2.1·1011 Pa, and a radius of the shaft cross-section is equal to 0.015 m. The first fundamental dimensionless frequency is equal here to 144.27. Frequency responses of principal coordinates near the first resonance are presented in Fig.3. Trajectories of the resonance vibrations in the system configuration space are presented in Fig. 4. Here points and circles denote results obtained analytically (by using the HBM and NNM approach

respectively), and lines correspond to numerical simulation. A ratio of the external excitation frequency to the first fundamental frequency is equal to $\omega = \Omega / \nu_1 = 1.0298$.

	First harmonic	Third harmonic
q_1	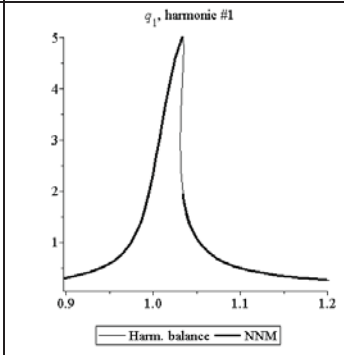	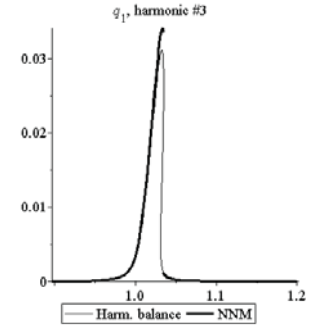
q_3	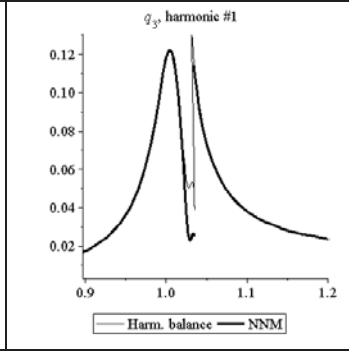	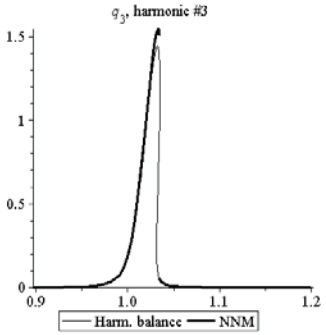

Fig. 3. Frequency responses near the first resonance. Bold curves correspond to the NNM approach, and thin curves correspond to calculations by the HBM. Frequencies on the horizontal axis are dimensionless; all amplitudes are multiplied by the scaling coefficient 1000.

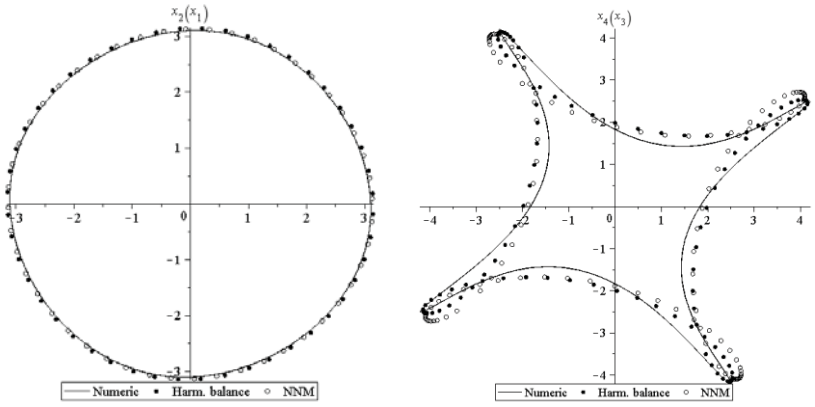

Fig.4, a Fig.4, b

Fig. 4. Trajectories of the forced resonance nonlinear normal mode in the system configuration space: 4,a – trajectory on x_1, x_2 plane, 4,b – trajectory on x_3, x_4 plane. Here displacement values are multiplied by the scaling coefficient 1000.

4. Stability and bifurcations of the forced vibration modes

Analysis of the forced NNMs stability shows [17] that in some frequency range the obtained before forced NNMs may become unstable at certain values of system's parameters. In this region a pair of new solutions bifurcates. The results below are obtained for the next parameters of the system:

$\rho_1 = 5\ \mathrm{N\,s\,m^{-1}}$, $\rho_2 = 5\,\mathrm{N\,s}$, $m = 12\,\mathrm{kg}$, $m_1 = m_2 = 2\,\mathrm{kg}$, $I_p = 0.24\,\mathrm{kg\,m^2}$, $I_e = 0.1225\,\mathrm{kg\,m^2}$, $l = 0.8\,\mathrm{m}$, $l_1 = 0.24\,\mathrm{m}$, $\varepsilon = 0.00003m$, $c_x^{(1)} = c_y^{(1)} = k_x^{(1)} = k_y^{(1)} = 7\cdot 10^5\ \mathrm{N/m}$, $c_x^{(2)} = c_y^{(2)} = k_x^{(2)} = k_y^{(2)} = 8\cdot 10^{10}\ \mathrm{N/m^3}$, $\beta = 60\,\mathrm{N\,s\,m^{-1}}$, $E = 2.1\cdot 10^{11}\,\mathrm{Pa}$, $J = 3.976\cdot 10^{-8}\,\mathrm{m^4}$.

The frequency response for the first harmonic of the disk displacement x is shown in Fig. 5a. The new solutions stability is shown in Fig. 5b. One chooses some value of the frequencies ratio, namely, $\omega = \Omega / \nu_1 = 1.02$. Regimes, denoted as A, B and C (Fig. 5,b), correspond to the chosen frequency value. Space representation of the rotor precession, corresponding to the regimes A and B, are shown in Fig. 6. Trajectories, which describe a motion of the disk center (the point marked with number 1) and motion of the left and right supports (points 2 and 3 respectively), are cyclic symmetric lines in the regime A (Fig. 6a). But for the chosen rotation frequency the regime A is unstable.

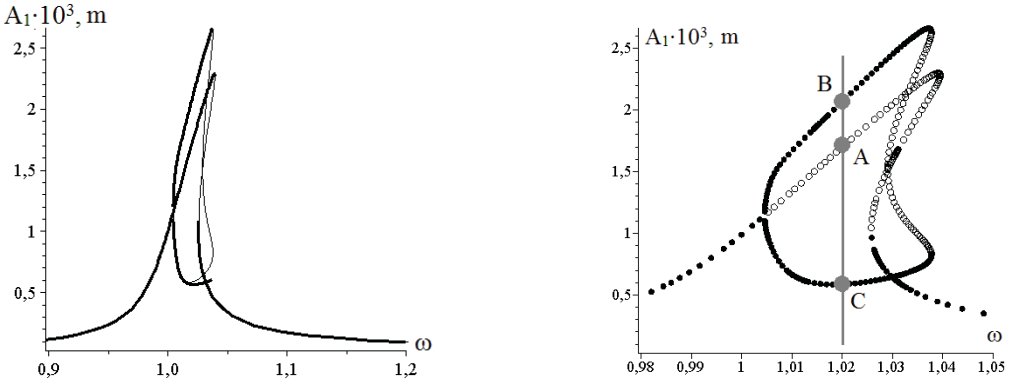

(a) (b)

Fig. 5. Frequency response for the first harmonic of the disk displacement x. Fig.5a represents solutions obtained by the HBM (bold) and by the NNMs method (thin lines); Fig.5b represents results of the stability analysis (points correspond to stable solutions and circles correspond to unstable ones).

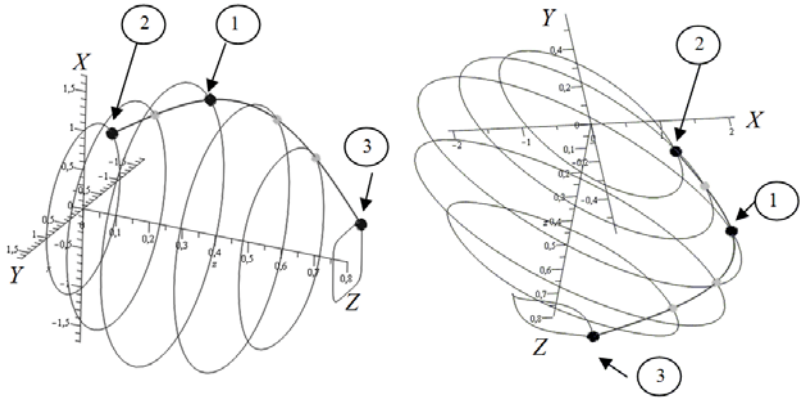

(a) (b)

Fig.6. Space representation of the rotor precession (regime A - Fig.6a, regime B - Fig.6b,). Trajectories describe a motion of the disk center, left and right supports (points 1,2,3 respectively). Points correspond to the analytical solution; lines correspond to checking numerical calculations. All displacements are measured in mm.

Trajectories corresponding to regimes B and C are center symmetric. Space representation of trajectories B is trajectories describing a motion of the disk center, left and right supports (points 1, 2, 3 respectively presented in Fig. 6b, where) are shown. The disk center circumscribes a trajectory close to the ellipse. In the regime B the vibration amplitudes on direction of the axis OX are essentially

more than amplitudes of motion on direction OY; for the regime C everything is inverse. These regimes are stable.

Conclusions

The approach which combines both the nonlinear normal modes and the modified iteration Rauscher methods is proposed and used to construct forced resonance vibrations in non-autonomous systems having the internal resonance. The NNMs method permits to reduce the n-DOF non-autonomous problem to the 2-DOF nonlinear system for each NNM. Forced vibrations of the 8-DOF system describing a dynamics of the one-disk unbalanced rotor with the linearly isotropic elastic shaft and nonlinear elastic bearings are considered. Gyroscopic effects, inertial forces in supports, an asymmetrical disposition of the disk in the shaft and internal resonance are taken into account. The forced NNMs of the system are obtained and frequency responses of the system are constructed. A stability analysis gives regions where regimes of synchronous rotor precession with cyclic symmetric trajectories are unstable, and regimes with center symmetric trajectories appear.

References

[1] Vakakis A., Manevitch L., Mikhlin Yu., Pilipchuk V., Zevin A. *Normal Modes and Localization in Nonlinear Systems,* Wiley, New York, 1996.
[2] Mikhlin Yu.V., Avramov K.V. Nonlinear normal modes for vibrating mechanical systems. Review of theoretical developments *Appl. Mech. Review*, Vol. 63, pp.4-20, 2010.
[3] Rosenberg R. Nonlinear vibrations of systems with many degrees of freedom *Advances of Appl. Mech.*, Vol. 9, pp.156–243, 1966.
[4] Shaw S., Pierre C. Nonlinear normal modes and invariant manifolds *J. of Sound and Vibration*, Vol. 150, pp.170–173, 1991.
[5] Shaw S., Pierre C. Normal modes for nonlinear vibratory systems *J. of Sound and Vibration*, Vol. 164, pp.85–124, 1993.
[6] Rauscher M. Steady oscillations of system with nonlinear and unsymmetrical elasticity *J. of Appl. Mech.*, Vol. 5, A-169, 1938.
[7] Mikhlin Yu.V. Resonance modes of near-conservative nonlinear systems. *Appl. Math. and Mech. (PMM USSR)*, Vol. 38 (3), pp.425-429, 1974.
[8] Avramov K.V., Mikhlin Yu.V. *Nonlinear Dynamics of Elastic Systems,* Regular and Chaotic Dynamics, Moscow-Izhevsk, 2010 (in Russian).
[9] Grobov V.A. *Asymptotic Methods for Calculations of Bending Vibrations of Turbo Machines Shafts*, USSR Academy of Science, Moscow, 1961 (in Russian).
[10] Bolotin V.V. *Nonconservative Problems of the Theory of Elastic Stability*, Pergamon Press, New York, 1963.
[11] Adams M.L. Nonlinear dynamics of flexible multi-bearing rotors *J. of Sound and Vibration*, Vol. 71, pp.129-144, 1980.
[12] Guido A.R., Adiletta G. Dynamics of a Rigid Unbalanced Rotor with Nonlinear Elastic Restoring Forces. Part I: Theoretical Analysis *Nonlinear Dynamics*, Vol. 19, pp.359–385; Part II: Experimental Analysis *Ibid,* pp. 387–397, 1999
[13] Genta G. *Dynamics of Rotating Systems,* Springer, Berlin, 2005.
[14] Lu Y.L., Dai R., Hei1 D., Zhang Y.F., Liu H., Yu L. Stability and bifurcation of a non-linear bearing-flexible rotor coupling dynamic system *Proc. of the Institution of Mech. Engineering. Part C: J. of Mech. Engineering Sci.*, Vol. 223(4), pp. 835-849, 2009
[15] Avramov K.V. Asymptotic analysis of forced vibrations of a one-disc rotor on a non-linear flexible base *Proc. of the Institution of Mech. Engineering. Part C: J. of Mech. Engineering Sci.*, Vol. 224(8), pp.1593-1604, 2010.
[16] Mikhlin Yu.V., Perepelkin N.V. Non-linear normal modes and their applications in mechanical systems *Proc. of the Institution of Mech. Engineering. Part C: J. of Mech. Engineering Sci.*, Vol. 225 (10), pp. 2369-2384, 2011.
[17] Perepelkin N.V., Mikhlin Yu.V. Construction and stability analysis of resonance motions of the single-disk rotor with the nonlinear elastic bearings *Dynamical Systems*, Vol.1(29), №2, pp.269-280, 2011 (in Russian).

Proceedings of the 4th International Conference on Nonlinear Dynamics
ND-KhPI2013
June 19-22, 2013, Sevastopol, Ukraine

Classical Resonance Interactions and Tunneling in Macroscopic Quantum Dynamics

Valery Pilipchuk[1*]

Abstract
Non-stationary effects of the resonance energy exchange between two nonlinear oscillators of different physical nature are analyzed in terms of new descriptive variables namely energy partition and coherency (phase shift) indexes. In particular, it is shown that such a couple represents conjugate variables of an effective Hamiltonian system whose phase plane captures all major specifics of the modal interaction. Furthermore, the presence of damping still preserves the Hamiltonian structure of equations affecting however their temporal scales and parameters. Formulated in general terms of coupled oscillators, the approach seems to have a wide area of applicability dealing with non-stationary resonance interactions and beating effects in physics and classical mechanics. Nonlinear liquid sloshing in square base tank and the dynamics of two coupled elastic oscillators are considered for illustrating purposes. Some analogies with interactions of quantum states in macroscopic quantum dynamics are discussed.

Keywords
Resonance interaction, nonlinear oscillator, effective Hamiltonian

[1] Wayne State University, Detroit, MI
* **Corresponding author:** valery.pilipchuk@yahoo.com

Introduction

Resonance interactions of oscillators are responsible for fundamental effects in different areas of physics and classical mechanics. The resonance between any two oscillators/modes destroys their individuality by generating a new effective oscillator of energy flow between the two parent oscillators, which is known as beating. In particular, the fundamental character of such energy exchange oscillators is revealed by the fact of their exact integrability in many physically reasonable cases. The present work illustrates such a standpoint, first of all, on a liquid sloshing model [1], which includes all the typical phases of continual dynamic analyses. It is shown that 1:1 resonance interactions of two nonlinear oscillators are described by a specific one-degree-of freedom Hamiltonian system whose conjugate coordinates are the energy partitioning and phase difference of oscillations. Besides, it is shown that such approach bridges the gap between the notion of Nonlinear Normal Modes [2] of elastic vibrating systems and the Liquid Sloshing Modes. In the case of elastic oscillations, a strongly nonlinear conservative oscillator describing the dynamics of energy partition between two identical linearly coupled oscillators with polynomial restoring force characteristics is introduced and analyzed. Temporal shapes of such oscillator are close to harmonic when the initial energy disbalance between the interacting oscillators is relatively small. However, the effective oscillator becomes strongly nonlinear as the amplitude of energy exchange increases. It is shown nevertheless that the oscillator is exactly solvable for the entire range of energy swing and, as a result, the original first-order averaging system, describing the dynamics of coupled oscillators, admits exact analytical solution. Despite of very different physical contents and analytical approaches to system' reduction, the final form of effective Hamiltonian appears to have surprisingly similar mathematical structure, which is known as Boson Josephson Junction in macroscopic quantum dynamics [3]. Such

observation allows us to track interesting physical analogies while revealing a common geometrical nature of resonance modal interactions.

1. Describing States of Two Identical Oscillators, 1:1 resonance

Let us consider an assembly of two identical harmonic oscillators as shown in Fig. 1. Further, different types of physical coupling are introduced. The present section, however, does not require any details on the nature of coupling. Moreover, no coupling at all can be assumed.

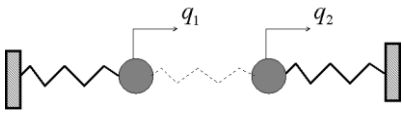

Figure 1. Two identical unit-mass oscillators of the same frequency Ω.

The dynamic states of such assembly are characterized by new descriptive variables whose definitions and physical meaning are discussed below.

1.1 Descriptive variables

Let assume no damping for a while and consider the quantities, all of which are measured in energy units,

$$E_k = \frac{1}{2}(\dot{q}_k^2 + \Omega^2 q_k^2); \quad k = 1,2 \tag{1}$$

$$E_{12} = \frac{1}{2}(\dot{q}_1\dot{q}_2 + \Omega^2 q_1 q_2) \tag{2}$$

Since the fast phase of oscillations is associated with a single frequency Ω, the dynamic states of the assembly can be fully characterized by the following three types of variables [4]:

Total energy excluding coupling:

$$E_1 + E_2 = E_0 \tag{3}$$

Energy distribution (partition):

$$\frac{E_1 - E_2}{E_1 + E_2} = P = -\sin\theta, \quad -1 \le P \le 1 \tag{4}$$

Coherency of vibrations:

$$\frac{E_{12}}{\sqrt{E_1 E_2}} = Q = -\cos\Delta, \quad -1 \le Q \le 1 \tag{5}$$

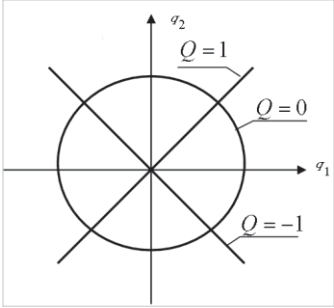

Figure 2. Interpretation for the coherency index in case *P = 0*.

The number $P=0$ indicates equipartition of the energy, $E_1=E_2$, whereas at $P=1$ or $P=-1$ all the energy belongs to the first or to the second oscillator, respectively. The coherency index Q is interpreted as follows

$$Q=\begin{cases} -1: & q_2=-\left(\dfrac{1-P}{1+P}\right)^{1/2}q_1, \quad out\text{-}of\text{-}phase \\ 0: & \dfrac{q_1^2}{1+P}+\dfrac{q_2^2}{1-P}=\dfrac{E_0}{\Omega^2}, \quad elliptic\ mode \\ 1: & q_2=\left(\dfrac{1-P}{1+P}\right)^{1/2}q_1, \quad in\text{-}phase \end{cases} \tag{6}$$

These relationships, as well as definitions (3) through (5) are obtained by using the transformation of state variables as introduced below. Generally speaking, there is an alternative of using either the indexes $\{P(t),Q(t)\}$ or the angles $\{\theta(t),\Delta(t)\}$. We show, however, that the mixed combination $\{P(t),\Delta(t)\}$ represents a set of conjugate Hamiltonian variables.

1.2 Transformation of states

These relationships, as well as definitions (3) through (5) are obtained by using the transformation of state variables [4], $\{q_1,\dot q_1,q_2,\dot q_2\}\to\{E_0(t),P(t),\Delta(t),\delta(t)\}$:

$$\begin{aligned} &q_1=\Omega^{-1}\sqrt{E_0(1+P)}\cos\delta, \quad \dot q_1=-\sqrt{E_0(1+P)}\sin\delta \\ &q_2=-\Omega^{-1}\sqrt{E_0(1-P)}\cos(\delta+\Delta), \quad \dot q_2=\sqrt{E_0(1-P)}\sin(\delta+\Delta) \end{aligned} \tag{7}$$

In particular, the variables $\{E_0(t),P(t),\Delta(t)\}$ in (7) and (3) through (5) are the same as can be verified by the direct substitution of (7) in (3) through (5).

2. Illustrating Models and Analogies

Transformation (7) is applied now to a coupled set of two free oscillators

$$\begin{cases} \ddot q_1+2\zeta\Omega\dot q_1+\Omega^2q_1+H_1(q_1,q_2,\dot q_1,\dot q_2)=0 \\ \ddot q_2+2\zeta\Omega\dot q_2+\Omega^2q_2+H_2(q_1,q_2,\dot q_1,\dot q_2)=0 \end{cases} \tag{8}$$

where H_1 and H_2 are polynomials, ζ is a damping ratio.

Expressions (7) are substituted in (8) under compatibility conditions $\dot{q}_k = dq_k / dt$, then the new equations are solved with respect to the first derivatives of new variables. Finally, the standard one-step averaging with respect to that fast phase δ is applied. The following two subsections illustrates the outcome by specifying the polynomials H_1 and H_2.

2.1 Liquid sloshing model

It was shown in [1] that equations (8) describe a two-mode model for liquid sloshing in a square tank, when the polynomials are given by

$$\begin{aligned} H_1(q_1,q_2,\dot{q}_1,\dot{q}_2) &\equiv S_3 q_1\dot{q}_1^2 + S_4 q_1\dot{q}_2^2 + S_5 q_2\dot{q}_1\dot{q}_2 + S_8 q_1^3 + S_9 q_1 q_2^2 \\ H_2(q_1,q_2,\dot{q}_1,\dot{q}_2) &\equiv S_3 q_2\dot{q}_2^2 + S_4 q_2\dot{q}_1^2 + S_5 q_1\dot{q}_2\dot{q}_1 + S_8 q_2^3 + S_9 q_2 q_1^2 \end{aligned} \tag{9}$$

where the constant coefficients S_k depend upon the fluid level *h*.

Following the suggested methodology and introducing a variable temporal scale *s* associated with the energy decay, gives the effective Hamiltonian system in terms of the new variables

$$\begin{aligned} &\frac{dP}{ds} = -\frac{\partial H}{\partial \Delta}, \quad \frac{d\Delta}{ds} = \frac{\partial H}{\partial P} \\ &H = H(P,\Delta) = \frac{1}{2}\kappa P^2 + \frac{1}{2}(1-P^2)\cos 2\Delta \end{aligned} \tag{10}$$

where

$$s = \frac{\Omega^2(S_4 - S_5) - S_9}{4\Omega^3}\int_0^t E_0(t)dt\,, \quad E_0(t) = E_0(0)\exp(-2\zeta\Omega t)\,, \tag{11}$$

and $\kappa = -4 + \dfrac{17 + \coth^2(\pi h) + 4\,\mathrm{sech}(2\pi h)}{6 - 2\sqrt{2}\,\tanh(\pi h)\tanh(\sqrt{2}\pi h)}$ is the only parameter of Hamiltonian system (10).

System (10) is exactly solvable in terms of the elliptic functions, however, drawing the level lines $H(P,\Delta) = const.$ allows for a complete characterization of possible sloshing modes as well as non-stationary dynamics near them.

2.2 Coupled elastic oscillators with polynomial restoring force characteristics

Consider the case of linearly coupled elastic oscillators, for which

$$\begin{aligned} H_1(q_1,q_2) &\equiv -\beta q_2 + \alpha_3 q_1^3 + \alpha_5 q_1^5 \\ H_2(q_1,q_2) &\equiv -\beta q_1 + \alpha_3 q_2^3 + \alpha_5 q_2^5 \end{aligned} \tag{12}$$

Following the same procedure and introducing the new constant temporal scale associated with the strength of coupling, $s = \beta t / \Omega$, leads to the Hamiltonian

$$H = -\frac{1}{2}\kappa P^2 - \sqrt{1-P^2}\cos\Delta \tag{13}$$

where $\kappa = \kappa(t) = \dfrac{3\alpha_3 E_0(t)}{4\beta\Omega^2} + \dfrac{5\alpha_5 E_0^2(t)}{4\beta\Omega^4}$, and $E_0(t)$ is defined in (11).

The conservative case, $\zeta = 0$, is exactly solvable in terms of the elliptic functions. For small nonzero damping ratios, different types of asymptotic and qualitative analyses of the Hamiltonian are still applicable; see also Conclusion.

2.3 Boson Josephson Junction

Bose-Einstein condensate in a double well symmetric potential is characterized by the effective classical Hamiltonian [3] $H_{eff} = \Lambda z^2/2 - \sqrt{1-z^2}\cos\phi$, which can be obtained from (13) by replacing the variables as $\Delta \to \pi - \phi, \quad P \to z, \quad \kappa \to \Lambda$, and $s = 2Kt/\hbar$. Here $\phi = \theta_2 - \theta_1$ is the phase difference of time dependent amplitudes of the wave function that obeys the so-called nonlinear Schrődinger equation, $z = (N_1 - N_2)/(N_1 + N_2)$ is the population disbalance in terms of the numbers of particles associated with each of the two traps. Therefore, $N_k \leftrightarrow E_k$.

Conclusions

Resonance interactions of two identical nonlinear oscillators are described by the effective Hamiltonian system whose conjugate coordinates are the energy partitioning and phase difference of oscillations. Furthermore, using the angular coordinate θ instead of P in (4), gives a single conservative oscillator, which is close to that solvable exactly in terms of elementary functions [4,5]. Classification of nonlinear sloshing modes in a square tank is given in terms of phase plane diagrams. It is shown that, above some critical fluid level, both in-phase and out-of-phase (diagonal) sloshing modes disappear. Instead either a running phase oscillation or two, clock-wise and counter-clock-wise, sloshing modes may occur. Moreover, the effective Hamiltonian does exist in this case even under the presence of damping. The influence of damping is captured by appropriate re-scaling the time variable. Section 2.3 points to a complete analogy between the interaction of classical oscillators and interaction of quantum states of Bose-Einstein condensates in terms of macro- and micro-level physical parameters. Although transformation (7) can always be applied to (8), the resultant system may generally appear to be non-Hamiltonian. In such cases, local analyses near stationary points complemented by the idea of limiting phase trajectories (LPT) [6] can be used for asymptotic integration of the resultant equations. For that reason, the mathematical tools of non-smooth temporal transformations [5] can be effectively applied; see [7] for a recent example and references.

Acknowledgments

The author greatly appreciates Prof. Takashi Ikeda of Hiroshima University for analytical details of his model described in [1].

References

[1] Ikeda T., Ibrahim R. A., Harata Y., and Kuriyama T. Nonlinear liquid sloshing in a square tank subjected to obliquely horizontal excitation *Journal of Fluid Mechanics*, 700, pp. 304-328, 2012.

[2] Manevich L. I., Mikhlin Yu. V., and Pilipchuk V. N. *Metod normalnykh kolebanii dlya sushchestvenno nelineinykh system*, Nauka, Moscow, 1989.

[3] Raghavan S., Smerzi A., Fantoni S., and Shenoy S. R. Coherent oscillations between two weakly coupled bose-einstein condensates: Josephson effects, π-oscillations, and macroscopic quantum self-trapping *Phys. Rev. A*, 59, pp. 620-633, 1999.

[4] Pilipchuk V.N. Classical resonance interactions and Josephson junction in macroscopic quantum dynamics. *arXiv:1205.4842v1*, 2012.

[5] Pilipchuk V.N. *Nonlinear Dynamics: between linear and impact limits,* Springer-Verlag, Berlin Heidelberg, 2010.

[6] Manevich L.I. New approach to beating phenomenon in coupled nonlinear oscillatory chains *Archive of Applied Mechanics*, 77, 301-312, 2007.

[7] Manevitch L. I., Kovaleva M. A., and Pilipchuk V. N. Non-conventional synchronization of weakly coupled active oscillators *EPL (Europhysics Letters)*, 101(5), p. 50002, 2013.

Proceedings of the 4th International Conference on Nonlinear Dynamics
ND-KhPI2013
June 19-22, 2013, Sevastopol, Ukraine

Dynamics of Nonlinear Dissipative Systems in Vicinity of Internal Resonance

Kateryna Y. Plaksiy [1*], Yuri V. Mikhlin [1]

Abstract
A behavior of nonlinear dissipative systems in vicinity of internal resonance is considered. Two-DOF mechanical systems, namely, the spring-mass system and the spring-mall-pendulum system, are considered. A reduced system with respect to the system energy, an arctangent of the vibration amplitudes ratio, and the phase difference, is analyzed. A concept of nonlinear normal modes is used in this analysis.

Keywords
Internal resonance, nonlinear normal modes, localization of energy

[1] *National Technical University "KPI", Kharkov, Ukraine*
* **Corresponding author:** plaksiyYA@rambler.ru

Introduction

Investigation of behavior of nonlinear systems near internal resonance is an important step to solve some theoretical and applied problems. It means, in particular, problems of transfer and localization of the vibration energy [1-4]. The internal resonance can lead to a loss of stability of vibration modes, and to appearance of new vibration regimes as a result of bifurcation [1-4]. Dissipation in nonlinear system and corresponding variation of vibration frequencies can lead the system under consideration to the internal resonance, or to output the system from the resonance region.

In this paper two 2-DOF nonlinear dissipative elastic systems (Figs. 1 and 2) are considered in a vicinity of internal resonance. An analysis is made by using so-called *reduced system* [5] which is written with respect to the system total energy, an arctangent of the ratio of amplitudes and a difference of phases. Simultaneously an investigation of stability and bifurcation of vibration modes similar to nonlinear normal modes by Kauderer and Rosenberg [1,2,6] is made. In dissipative systems such regimes will contain an exponential decrease of the vibration amplitudes. Analytical results are compared with numerical and numerical-analytical simulation by using programs on C++ and the MATLAB package.

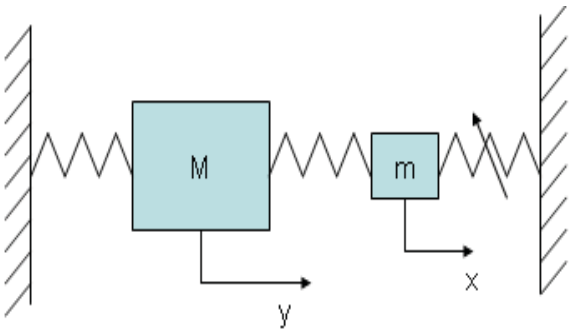

Figure. 1. The spring-mass system

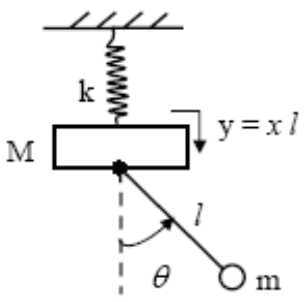

Figure. 2. The spring-mass-pendulum system

1. Resonance behavior of the nonlinear spring-mass system

Equations of motion of the spring-mass system (Fig.1) can be written of the following form:

$$\begin{cases} \varepsilon\ddot{x} + \varepsilon k_x x + \varepsilon^2 q x^3 + \varepsilon \cdot 2\eta_x \dot{x} = \varepsilon\gamma_1 y \\ \ddot{y} + \omega_y^2 y + \varepsilon k_y y + \varepsilon \cdot 2\eta_y \dot{y} = \varepsilon k_y x \end{cases} \tag{1}$$

where the small parameter ε is introduced in assumption that some parameters of the system are small.

There are two nonlinear normal modes in system (1) without dissipation: the non-localized mode of the coupled vibrations, when amplitudes of both masses are compared, and the localized mode, when amplitude of the small mass vibrations is essentially larger than ones of the big mass.

The multiple scales method [7] is applied to the system (1). Introducing a detuning parameter, $\omega_x^2 - \omega_y^2 = \varepsilon\Delta$ and the next asymptotic series, $x = x_0 + \varepsilon x_1 + \ldots$, $y = y_0 + \varepsilon y_1 + \ldots$, $T = T_0 + T_1 + \ldots = t + \varepsilon t + \ldots$ one has a systems of partial differential equations in the first and second approximations by the small parameter, respectively:

$$\begin{cases} \dfrac{\partial^2 y_0}{\partial T_0^2} + \omega_y^2 y_0 = 0 \\ \dfrac{\partial^2 x_0}{\partial T_0^2} + 2\eta_x \dfrac{\partial x_0}{\partial T_0} + (\eta_x^2 + \omega_y^2) x_0 = \gamma_1 y_0 \end{cases} \tag{3}$$

$$\begin{cases} \dfrac{\partial^2 y_1}{\partial T_0^2} + \omega_y^2 y_1 = -2\dfrac{\partial^2 y_0}{\partial T_1 \partial T_0} - 2\eta_y \dfrac{\partial y_0}{\partial T_0} + k_y (x_0 - y_0) \\ \dfrac{\partial^2 x_1}{\partial T_0^2} + 2\eta_x \dfrac{\partial x_1}{\partial T_0} + (\eta_x^2 + \omega_y^2) x_1 = -2\dfrac{\partial^2 x_0}{\partial T_0 \partial T_1} - 2\eta_x \dfrac{\partial x_0}{\partial T_1} - q x_0^3 + \gamma_1 y_1 - \Delta x_0 \end{cases} \tag{4}$$

A solution of system (3) can be presented as:

$$\begin{cases} y_0 = A_0(T_1) e^{i\omega_y T_0} + \overline{A}_0(T_1) e^{-i\omega_y T_0} \\ x_0 = e^{-\eta_x T_0}(B_0(T_1) e^{i\omega_y T_0} + \overline{B}_0(T_1) e^{-i\omega_y T_0}) + C_1(T_1) e^{i\omega_y T_0} + \overline{C}_1(T_1) e^{-i\omega_y T_0} \end{cases} \tag{5}$$

where $C_1(T_1) = \dfrac{\gamma_1 A_0(T_1)(\eta_x^2 + \varepsilon\Delta - 2i\eta_x\omega_y)}{(\eta_x^2 + \varepsilon\Delta)^2 + 4\eta_x^2\omega_y^2}$.

One substitutes the relations (5) to the system of the second approximation (4) and eliminates then secular terms. The following change of variables, $A_0 = a_y e^{ib_y}$, $B_0 = a_x e^{ib_x}$ leads to a system of the equations concerning amplitudes and phases of the solution:

$$\begin{cases} a_y'(T_1) = -\dfrac{L}{R} a_y \\ b_y'(T_1) = -\dfrac{S}{R} \\ a_x'(T_1) = \dfrac{D}{F} a_x - a_x a_y^2 \left(\dfrac{I}{F}\sin(2\varphi) - \dfrac{E}{F}\cos(2\varphi)\right) \\ b_y'(T_1) = -\dfrac{P}{F} + a_y^2 \left(\dfrac{Q}{F} + \dfrac{I}{F}\cos(2\varphi) + \dfrac{E}{F}\sin(2\varphi)\right) \end{cases} \tag{6}$$

where $\varphi = b_y - b_x$, $R = 2\omega_y N$, $L = 2(\eta_y \omega_y N + k_y \gamma_1 \eta_x \omega_y)$, $S = k_y(\gamma_1(\eta_x^2 + \varepsilon\Delta) - N)$, $N = (\eta_x^2 + \varepsilon\Delta)^2 + 4\eta_x^2\omega_y^2$, $F = 2\omega_x N^2 W$, $Q = 6q\gamma_1^2 NW$, $P = N^2(k_y\gamma_1\eta_x^2 - \Delta W)$, $D = 2\omega_y\eta_x\gamma_1 k_y N^2$, $I = 3q\gamma_1^2 W((\eta_x^2 + \varepsilon\Delta)^2 - 4\eta_x^2\omega_y^2)$, $E = 12q\gamma_1^2 W\eta_x\omega_y(\eta_x^2 + \varepsilon\Delta)$, $W = \eta_x^4 + 4\omega_y^2\eta_x^2$.

The *reduced system* [5] with respect to the system total energy, an arctangent of the ratio of amplitudes and a difference of phases, can be obtained from the system (6) of the next form:

$$\begin{cases} K' = (-\dfrac{L}{R}\cos^2\psi + \dfrac{D}{F}\sin^2\psi)K - K^3\cos^2\psi\sin^2\psi[\dfrac{I}{F}\sin(2\varphi) - \dfrac{E}{F}\cos(2\varphi)] \\ \psi' = (\dfrac{L}{R} + \dfrac{D}{F})\cos\psi\sin\psi - K^2\sin\psi\cos^3\psi[\dfrac{I}{F}\sin(2\varphi) - \dfrac{E}{F}\cos(2\varphi)] \\ \varphi' = -\dfrac{S}{R} + \dfrac{P}{F} - K^2\cos^2\psi[\dfrac{Q}{F} + \dfrac{I}{F}\cos(2\varphi) + \dfrac{E}{F}\sin(2\varphi)] \end{cases} \quad (8)$$

where $D = 2\omega_x\eta_x\gamma_1 k_y N$, $Q = 6q\gamma_1^2 C_{ay}^2 W$, $S = k_y(\gamma_1(k_x - \omega_y^2) - N)$, $P = k_y\gamma_1 N(\eta_x^2 - \omega_x^2 + \omega_y^2)$, $R = 2\omega_y N$, $F = 2\omega_x NW$, $L = 2(\eta_y\omega_y N + k_y\gamma_1\eta_x\omega_y)$, $I = 3q\gamma_1^2 W((\eta_x^2 + \varepsilon\Delta)^2 - 4\eta_x^2\omega_y^2)$.

Analysis of the reduced system (8) equilibrium points shows that the coupled vibration mode loses stability in a vicinity of resonance, and the localized mode remains stable irrespectively to a choice of initial conditions and the system parameters. It is obtained that in a vicinity of resonance there is a transition from the non-localized mode to localized one at $t \to \infty$. New vibration modes do not appear.

In Figure 3 the dependence $\varphi(\psi)$ is represented. The straight line $\psi = 0$ corresponds to the non-localized mode of connected vibrations, and the straight line $\psi = \pi/2$ corresponds to the mode when the vibration energy is localized on coordinate x.

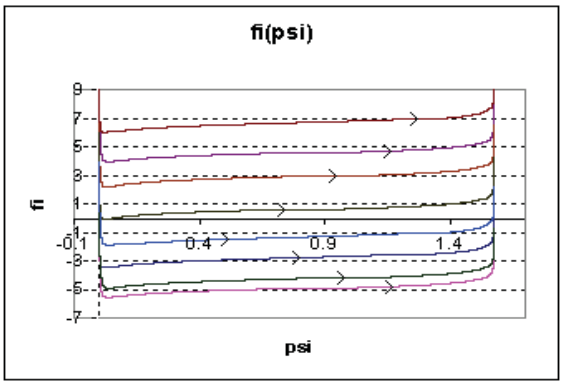

Figure. 3. Dependence $\varphi(\psi)$

In Figures 4 trajectories of non-localized and localized motions are shown. Note that the non-localized mode of the coupled vibrations is unstable, and the localized mode is stable in a vicinity of internal resonance.

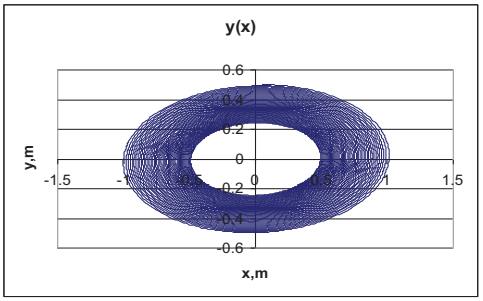

a) trajectory of connected motions

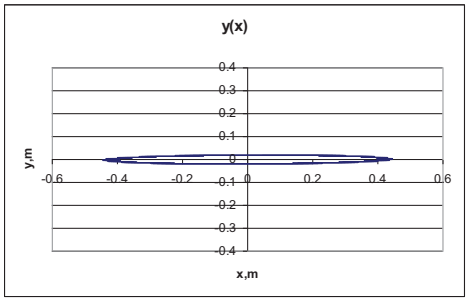

b) trajectory of localized motions

Figure.4. Trajectories in the system (1) configuration space

2. Resonance behavior of the spring-mass-pendulum system

Equations of the spring-mass-pendulum system motion are the following:

$$\begin{cases} \ddot{x} + p^2 x + 2\varepsilon\eta_x \dot{x} - \alpha(\ddot{\theta}\sin\theta + \dot{\theta}^2\cos\theta) = 0 \\ \ddot{\theta} + 2\varepsilon\eta_\theta\dot{\theta} + \sin\theta - \ddot{x}\sin\theta = 0 \end{cases} \tag{2}$$

where $\omega_1 = \sqrt{\dfrac{k}{M+m}}$, $\omega_2 = \sqrt{\dfrac{g}{l}}$, $p = \dfrac{\omega_1}{\omega_2}$, $\alpha = m/(m+M)$, $\tau = \omega_2 t$.

There are two nonlinear normal modes in system (2) without dissipation: the x-mode of vertical vibrations ($x = x(t)$, $\theta = 0$) which is localized, and the non-localized pendulum mode ($x = x(t)$, $\theta = \theta(t)$) when both vibration amplitudes are of the same order.

Application to the system (2) of the multiple scales method together with the following scaling of coordinates $x \to \varepsilon x$, $\theta \to \varepsilon\theta$ and the decomposition of coordinates and time in asymptotic series as $\varepsilon x = \varepsilon x_0 + \varepsilon^2 x_1$, $\varepsilon\theta = \varepsilon\theta_0 + \varepsilon^2\theta_1$ and $T = T_0 + T_1 + T_2 = \tau + \varepsilon\tau + \varepsilon^2\tau$, leads to systems of the equations for the first and second approximation by the small parameter:

$$\begin{cases} \dfrac{\partial^2 x_0}{\partial T_0^2} + 4x_0 = 0 \\ \dfrac{\partial^2\theta_0}{\partial T_0^2} + \theta_0 = 0 \end{cases} \tag{9}$$

$$\begin{cases} \dfrac{\partial^2 x_1}{\partial T_0^2} + 4x_1 = -2\dfrac{\partial^2 x_0}{\partial T_1 \partial T_0} + \alpha\left(\dfrac{\partial^2\theta_0}{\partial T_0^2}\right)\theta_0 + \alpha\left(\dfrac{\partial\theta_0}{\partial T_0}\right)^2 - 2\eta_x\dfrac{\partial x_0}{\partial T_0} - x_0\Delta \\ \dfrac{\partial^2\theta_1}{\partial T_0^2} + \theta_1 = -2\dfrac{\partial^2\theta_0}{\partial T_1\partial T_0} + \left(\dfrac{\partial^2 x_0}{\partial T_0^2}\right)\theta_0 - 2\eta_\theta\dfrac{\partial\theta_0}{\partial T_0} \end{cases} \tag{10}$$

The solution of system (9) is presented of the form:

$$\begin{cases} x_0 = A_x(T_1)e^{2iT_0} + \overline{A}_x(T_1)e^{-2iT_0} \\ \theta_0 = A_\theta(T_1)e^{iT_0} + \overline{A}_\theta(T_1)e^{-iT_0} \end{cases} \tag{11}$$

The solution (11) is substituted to the system of the second approximation (10), and secular terms are eliminated. The next change of variables $A_x = a_x e^{i\beta_x}$, $A_\theta = a_\theta e^{i\beta_\theta}$ leads to a system of the equations concerning amplitudes and phases of solutions:

$$\begin{cases} a_x' = \dfrac{\alpha}{2}a_\theta^2\sin\varphi - \eta_x a_x \\ a_\theta' = -2a_x a_\theta\sin\varphi - \eta_\theta a_\theta \\ \beta_x' = \dfrac{\alpha}{2}\dfrac{a_\theta^2}{a_x}\cos\varphi + \dfrac{\Delta}{4} \\ \beta_\theta' = 2a_x\cos\varphi \end{cases} \tag{12}$$

where $\varphi = \beta_x - 2\beta_\theta$.

Transfer to the reduced system, proposed in [5], is used here. The reduced system is written with respect to the next new variables: total energy R, an arctangent of the ratio of amplitudes ψ and difference of phases φ. This transfer leads to the following system:

$$\begin{cases} R' = -R(\eta_x \cos^2\psi + \eta_\theta \sin^2\psi) \\ \psi' = R\sin\psi(-\sqrt{\alpha}\sin\varphi + (\eta_x - \eta_\theta)\cos\psi) \\ \varphi' = (\sqrt{\alpha}R\dfrac{\sin^2\psi}{\cos\psi} - 2\sqrt{\alpha}R\cos\psi)\cos\varphi + \dfrac{\Delta}{4} \end{cases} \tag{13}$$

Analysis of the reduced system (13) on equilibrium points shows that depending on energy level of the system it can obtain a region where vertical vibrations lose stability as a result of bifurcation. A transition to two modes of the coupled vibrations is realized. Then, when the energy decreases, there is an outcome from this region, the bifurcation disappears, and the vertical vibration mode again becomes stable.

In Figures 6,7 a dependence $\varphi(\psi)$ for a case when the system is in region of existence of bifurcation, and for a case when the system is not in this region, respectively, are presented. The straight line $\psi = 0$ corresponds to the localized vibrations.

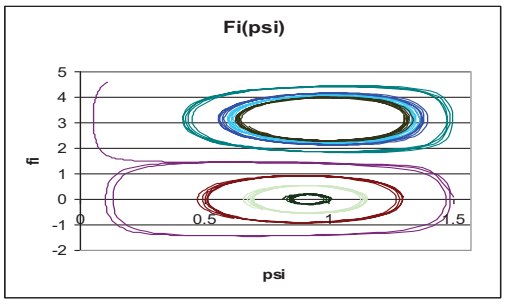

Figure. 6. Dependence $\varphi(\psi)$. The bifurcation of the vertical vibrations exist

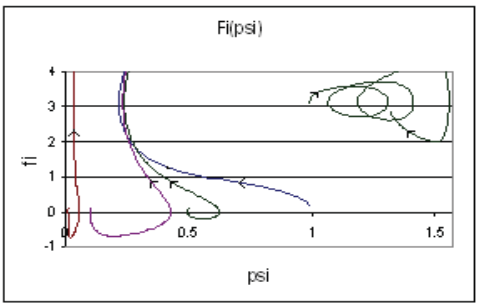

Figure. 7. Dependence $\varphi(\psi)$. The bifurcation of the vertical vibrations does not exist

In Figures 8,9 trajectories in the system configuration space for the localized mode in a case of existence of bifurcation and in a case when bifurcation doesn't happen, respectively, are presented. Obviously, we can see that if the bifurcation exists, vertical vibrations lose stability (Fig. 8), otherwise, vertical vibrations remain stable (Fig. 9).

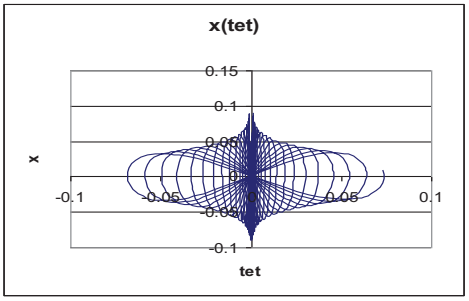

Figure. 8. Dependence $x(\theta)$

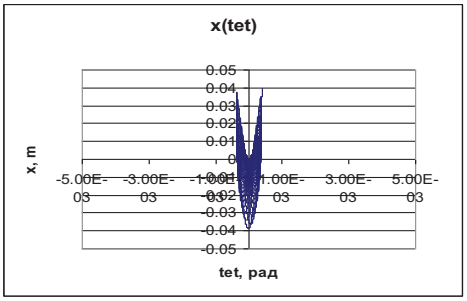

Figure. 9. Dependence $x(\theta)$

For the system (2) additional analysis of stability of vertical vibrations on the basis of the linearized equations in variations ($x = \widetilde{x} + u$, $\theta = \widetilde{\theta} + v$)

$$\begin{cases} \ddot{u} + p^2 u + 2\varepsilon\eta_x \dot{u} - \alpha(\ddot{\widetilde{\theta}}v + 2\dot{\widetilde{\theta}}\dot{v} + \ddot{v}\widetilde{\theta}) = 0 \\ \ddot{v} + v + 2\varepsilon\eta_\theta \dot{v} - \ddot{\widetilde{x}}\cdot v - \ddot{u}\widetilde{\theta} = 0 \end{cases} \tag{14}$$

and next reduction of the equations (14) to the Mathieu's equation is conducted. One has after some simplification the following equations:

$$\ddot{v}+v+2\varepsilon\eta_\theta\dot{v}-v(-\omega_x^2Ae^{-\varepsilon\eta_x\tau}\cos\omega_x\tau+2\varepsilon\eta_x\omega_xAe^{-\varepsilon\eta_x\tau}\sin\omega_x\tau+\varepsilon^2\eta_x^2Ae^{-\varepsilon\eta_x\tau}\cos\omega_x\tau)=0 \qquad (15)$$

Separation of the time scales $T_0=\tau$ and $T_1=\varepsilon\tau$, introduction of new variables $r=\frac{\omega_xT_0}{2}$ at designations $a=\frac{4}{\omega_x^2}$, $\mu=4Ae^{-\eta_xT_1}$, $v'=\frac{dv}{d\tau}$, $v''=\frac{d^2v}{dr^2}$ leads to the following equations:

$$\varepsilon^0: \qquad v_0''+v_0(a+\mu\cos2r)=0 \qquad (16)$$

$$\varepsilon^1: \qquad v_1''+v_1(a+\mu\cos2r)=-\frac{4\eta_\theta}{\omega_x}v_0'-\frac{4}{\omega_x}\frac{\partial v_0'}{\partial T_1}+\frac{\eta_x}{2\omega_x}\mu v_0\sin2r \qquad (17)$$

Equation (16) is the well-known Mathieu's equation.

It is obtained that the vertical vibrations stability depends on time that confirms results of previous analysis of the reduced system.

In Figures 10, 11 boundaries of regions of stability/instability for vertical vibrations of the system (2) are shown for two values of time. We can see that a region of instability located in the middle of the boundary lines, are narrowed over time, that is, vertical vibrations which are unstable at the beginning of the process become eventually stable.

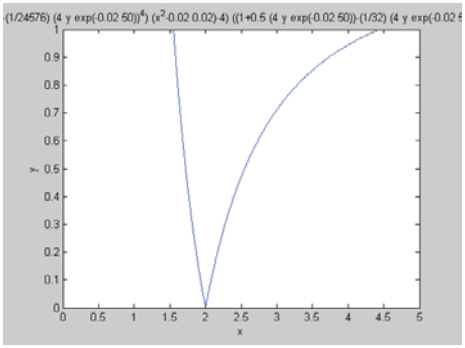

Figure. 10. Boundaries of the instability region at $\tau=50$

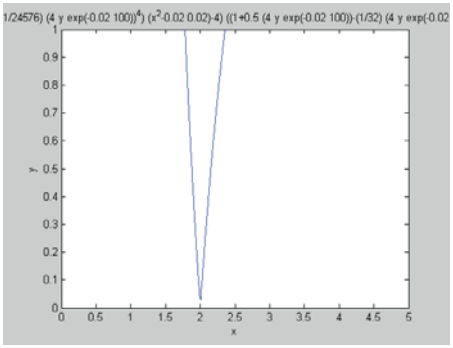

Figure. 11. Boundaries of the instability region at $\tau=100$

The presented above approach can be applied in analysis of dynamics of the dissipative system with limited power supply (so-called non-ideal system) which contains the nonlinear absorber. Resonance dynamics of this 3-DOF system is investigated.

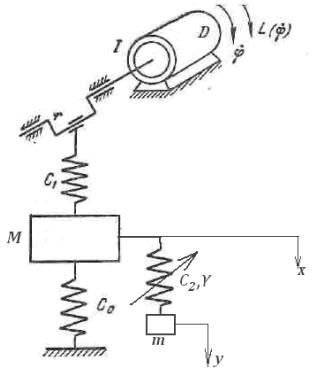

Figure.12. The non-ideal system which contains the nonlinear absorber

Conclusions

Behavior of two nonlinear dissipative systems in vicinity of the internal resonance is investigated. So-called reduced system is used in the corresponding analysis. The reduced system is

written with respect to the system total energy, an arctangent of the vibration amplitudes ratio, and the phase difference. In 2-DOF mass-spring and mass-spring-pendulum systems an analysis of stability and bifurcation of the localized and coupled vibrations is made. It is obtained new results on existence nonlinear vibration modes in the resonance region, and on evolution of equilibrium points under dissipation. Reliability of obtain analytical results is confirmed by numerical and numerical-analytical simulation.

References

[1] Avramov K.V., Mikhlin Yu.V. *Nonlinear Dynamics of Elastic Systems*. Regular and Chaotic Dynamics, Moscow-Izhevsk, 2010.
[2] Vakakis A.F., Manevitch L.I., Mikhlin Yu.V., Pilipchuk V.N, and Zevin A.A. *Normal Modes and Localization in Nonlinear Systems*. Wiley Interscience, New York, 1996.
[3] V.M. Starzhinskii, *Applied Methods of Nonlinear Vibrations*, Nauka, Moscow, 1977 (in Russian).
[4] A.F. Vakakis, O.V. Gendelman, L.A. Bergman, D.M. McFarland, G. Kerschen, Y.S. Lee, *Nonlinear Targeted Energy Transfer in Mechanical and Structural Systems*, Springer Science, 2008.
[5] Wang, F., Bajaj, A., Kamiya, K. *Nonlinear Normal Modes and Their Bifurcations for an Inertially-Coupled Nonlinear Conservative System*. Purdue University, 2005.
[6] R.M. Rosenberg, On nonlinear vibrations of systems with many degrees of freedom, *Advances of Appl. Mech.*, № 9, pp. 156- 243, 1966.
[7] Nayfeh A.H. *Perturbation Methods*. Wiley, New York, 1973.

Proceedings of the 4th International Conference on Nonlinear Dynamics
ND-KhPI2013
June 19-22, 2013, Sevastopol, Ukraine

High-Speed Impact Action on Rotable Body

S. Polukoshko[1], V. Gonca[2]

Abstract
In this paper the action of high-speed impact on the target, which could rotate, is discussed. Target is designed for using as conduct-of-fire trainer; its screen is fired by light bullet from pistol. Target material is high-strength steel, material of bullets –lead and steel. Target is mounted on the shaft by means of sleeve-type journal bearing in such way that it is in equilibrium in the vertical position. When the bullet is colliding with target, last rotates at some angle depending on a friction in bearing and impact force. The purpose of this work is target parts designing in respect to the strength and rigidity under impact action of bullet. Estimation of the dynamic deflection of axial rod was carried out with Plaxis 2D-v8 dynamic modules program (Delft, the Netherlands). The field test of designed target – measurement of shaft deflection - confirmed the absence of the permanent residual deformation.

Keywords
high-speed impact, Hertz contact, functional equation of Timoshenko, dynamics reaction

[1] Engineering Research Institute "VSRC", Ventspils University College, Ventspils, Latvia
[2] Riga Technical University, Institute of Mechanics, Riga, Latvia
*** Corresponding author:** pol.svet@inbox.lv

Introduction

Problem of definition of elements dimensions subject to action of impacts often arise in designing of machine or engineering constructions. In spite of great importance of problem, until now there is no universal approach to the calculation of impulsive reaction and impact duration definition, since the amplitude of impact force and impact duration depend on the large number of factors. In practice the range of impact duration is 10^{-3} – 10^{-12} s and forces in the contact points reach very large values. In view of this impact can lead to large deformation or even to destruction of bodies, to the appearance of impact wave, elements vibrations, heating of bodies etc. [2], [6], [8].

Many problems of collision with small velocities (less than 250m/s) fall into the interests of structural dynamics. Formation of dents and penetrations is closely related to the overall deformation of structure, and characteristic time of loading and reaction is milliseconds. With the impact velocity increasing to 500-2000 m/s general deformation of structure becomes secondary, and a primary value acquires the behavior of material in a small zone (2-3 diameters of projectile) near-by the place of collision; time of loading and reaction is microseconds. At the velocity up to 2000 -3000 m/s local pressure becomes by an order of magnitude greater than ultimate strength and material behaves as a liquid. At ultra-high speeds (more than 12000 m/s) a material undergo to explosive evaporation. The boundary of speed rate is relative and depends on a set of parameters: velocity of impact, geometrical and strength characteristics of a target and a projectile, the angle of impact.

The problem of collision of bullet moving with velocity 430 m/s and mobile target, considered in given work, belongs to the class of intermediate problems in which it is necessary to consider both local deformations in the point of collision, and the overall deformation of a structure. For it solving the contact theory of Hertz in a combination with a dynamic problem of impact of bodies taking into account flexibility of a target is used. For the elements strength examination the dynamic module of program Plaxis-8v (Delft, the Netherlands) is applied.

1. Statement of Problem

The design model of trainer target is presented in Fig.1; target consists of screen, mounted shaft. The screen of a target with dimensions: length 400 mm, height 140 mm and a thickness 10mm from a high-strength steel librates vertically. The screen fastens on two posts with cross-section section 15 x60 mm and height 50 cm and 28 cm, posts are kept on a shaft of 16 mm diameter due to the friction in bearings. When the bullet hit to the screen, screen rotates round fixed axis, then it is return to starting position. The shot at a target is made from a pistol with calibre of 9.0 mm; speed of a bullet at the face of gun is equal 430 m/s, distance – 20m. The mass of a bullet m_1=6.1g, diameter d=9 mm, a bullet is shell-type lead with steel core, a thickness of a cover-1mm, cylindrical part of bullet is of length 9 mm, a head part (point of bullet is round headed) is hemispherical in radius 4.5 mm, a tail end is flat. Specific energy of a bullet (indicator of penetrative action) e = 4.2 J/mm^2, an impulse S = 2.2 Ns. Mass of rotation part of target m_2=9.844 kg, geometrical characteristics: centre of gravity position regarding to the axes passing through the middle of an axis of rotation: Xc=5mm, Yc=52mm, Zc=30mm, moment of inertia Jz=0.18kgm^2, Jzx=0, Jyz = - 0.062 kgm^2.

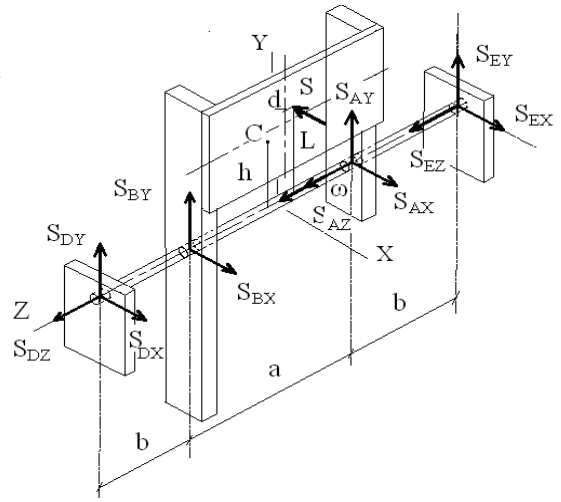

Figure 1. Design model of the shooting training device: b=100мм, a=400 mm

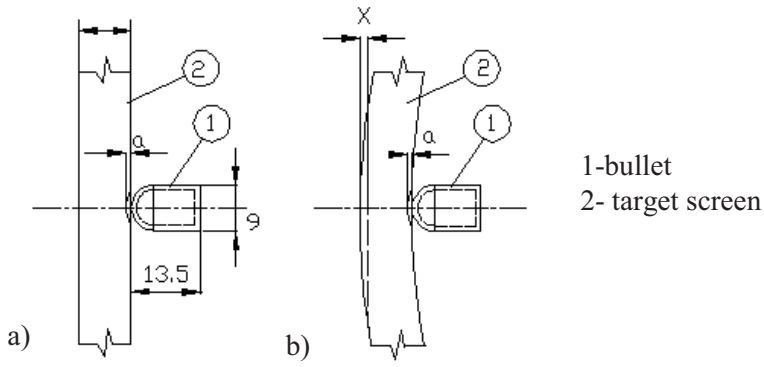

Figure 2. The scheme of bullet impact: a) the first stage of impact, b) the second stage

In Fig. 2 the scheme of impact is presented. The impact direction is considered perpendicular to the screen. A purpose of this study is target parts strength and rigidity examination under impact of bullet action. Target screen is considered as simply supported beam, posts are considered as cantilever beam.

2. Analytical Models and Numerical Solutions

In solving the formulated problem impact parameters - contact force and duration of the contact interaction - are determined in accordance with existing impact theory, the duration of contact

interaction is compared to the natural period of the target, strength of items is checked for the most disadvantageous option for the design.

2.1 Parametrs of impact in accordance with quasistatic Hertz's model

Contact force expressed through the approach of mass centres in accordance with quasistatic Hertz's model is $F_e = k\alpha^n$, where *n*- index of power, for the spherical body $n = 3/2$; α – relative approach or indentation between the surfaces of sphere and plane plate; k – proportionality factor, depending on curvature of surfaces in the point of contact and properties of materials.

Duration of contact interaction *t*, maximal contact force F_{max} and maximal approach a_{max}, expressed through the pre-impact velocity [1], [2], [5], [8], are equals:

$$t = 2.9432 \cdot \left(\frac{5}{4}\frac{m_1}{k}\right)^{\frac{2}{5}} v_0^{-\frac{1}{5}},\ F_{max} = k^{\frac{2}{5}}\left(\frac{5}{4}m_1 v_0^{\ 2}\right)^{\frac{3}{5}},\ \alpha_{max} = \left(\frac{5}{4}\frac{m_1 v_0^{\ 2}}{k}\right)^{\frac{2}{5}}. \quad (1)$$

For the collision a sphere with plane plate taking into account properties of colliding bodies (for lead and steel respectively elasticity modulus E_1=16000 MPa, E_2=200000 MPa, Poisson ratio μ_1=0.42, μ_2=0.3, density ρ_1= 11340 кг/м^3, ρ_2=7800 кг/м^3), factor k=1.596·10^9 N/m$^{3/2}$. Pre-impact velosity v_0=0.9·430=387 m/s, (velocity before target 10% less than velocity in shot), then maximal force F_{max}=327 kN, maximal approach α_{max}=3.482 mm and duration of impact t=2.65 · 10^{-5} s.

2.2 Parameters of impact in accordance with small arms designing rules

Contact force in accordance with small arms designing rules is taken as resistance force in [3]:

$$F = 0.25\pi d^2 \lambda a(1 + Bv^2), \quad (2)$$

where *d* – bullet gage, λ – the factor taking into account the influence of bullet form, *a* and *B* – factors, characterized the properties of medium: *a* – factor, taking into account strength of medium and effecting on resistance regardless of velocity, *B*–factor, taking into account density and viscosity of the medium, which influence on resistance depending on velocity.

$B = 5.5 \cdot 10^{-7}\ s^2/m^2$, $a = 3.426 \cdot 10^9\ N/m^2$, for light bullet λ=1.0, then :

$$F = 2.179 \cdot 10^5 (1 + 5.5 \cdot 10^{-7} v^2)$$

under v_0=387 m/s F= 236 kN, *for* v_0=0 F= 218 kN.

Having written down the equations of motion and separating the variables, having integrated it within velocities from v_0 to *0* and ways from *0* to *s*, we find the depth of bullet penetration *s*.

$$m_1\ddot{x} = -F \text{ and } s = ln(1 + Bv_0^2)m_1 / \lambda C d^2, \quad (3)$$

where for the steel (hard and soft mild) with HB 444 $C = 2960 Ns^2/m^4$; if λ=1, s=2.145mm.

Duration of impact action is $t = s/v_{av}$, where v_{av} is the average bullet velocity, v_{av}=0.9v_0; for λ=1 t=1.109 · 10^{-5} s.

2.3 Parameters of impact in accordance with Timoshenko theory of the impact on beam

First, the possibility of using Timoshenko theory of the impact on beam is examined [7], [8]. Velocity of the longitudinal waves propagation in media C_v (compression stress waves) and natural period of the bullet τ are:

$$C_v = \sqrt{\frac{E_1}{\rho_1}}, \quad \tau = \frac{2l}{C_v}, \quad (4)$$

where l – bullet length, l = 13, 5 mm, for lead C_v = 1188 m/s, τ=2.273 · 10^{-5} s.

Let present the target screen by the beam model. Natural frequency of the first mode of the simply supported beam ω_1, excluding transversal shear and rotational effect. and period T, respectively, are:

$$\omega_1 = \frac{\pi^2 1^2}{L^2}\sqrt{\frac{E}{\rho}\frac{J}{A}} = \frac{3.14^2 \cdot 1^2}{0.39^2}\sqrt{\frac{2\cdot 10^{11}}{7800}\frac{0.14\cdot 0.1^3}{12\cdot 0.14\cdot 0.01}} = 948.52\ \ s^{-1}, \tag{5}$$

$$T = \frac{2\pi}{\omega_1} = \frac{2\cdot 3.142}{948.52} = 6.624\cdot 10^{-3} s.$$

Because the duration of impact in accordance with Hertz's theory is less than natural frequency of beam and comparable with bullet period we can conditionally use Timoshenko theory of impact on beam which take into account the vibration of flexible beam. Functional equation Timoshenko theory of impact:

$$\alpha = \left(\frac{P}{k}\right)^{2/3} = s - x = v_0 t - \frac{1}{m_1}\int_0^t dt\int_0^t P(t)dt - \sum_{i=1,3,5,\ldots}\frac{1}{\omega_i}\frac{2}{m_2}\int_0^t P(t_1)\sin\omega_i(t-t_1)dt_1, \tag{6}$$

where: α - local deformation, s- full displacement of the bullet from the beginning of impact, x - beam deflection under impact force $P(t)$ action in the middle of beam.

The solution of Eq. (6) was fulfilled by means of small increment method where the contact force is regarded as constant during any time increment Δτ. For approximate solution of this equation we divided natural period of beam into 3600 intervals $\Delta\tau = T/n = T/3600$ and received impact force $F=F(t)$, s, $x=x(t)$, $\alpha=\alpha(t)$ and time of impact t=14.5$n\Delta\tau$=2.50 · 10^{-5}s.

Solution was fulfilled in MathCAD program and graphical results are presented in Fig. 3-6.

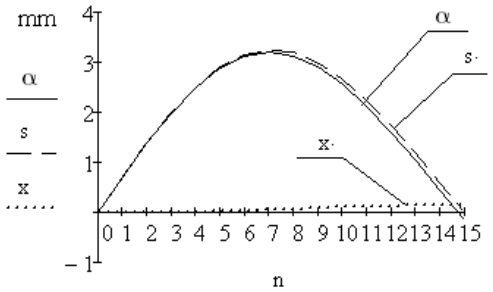

Figure 3. Plot of deformation during impact

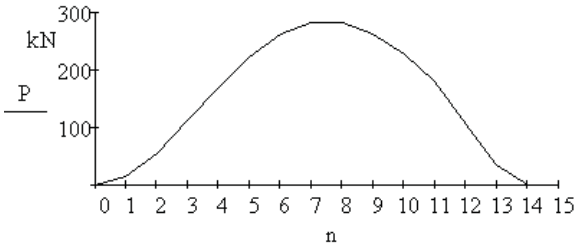

Figure 4. Plot of impact force

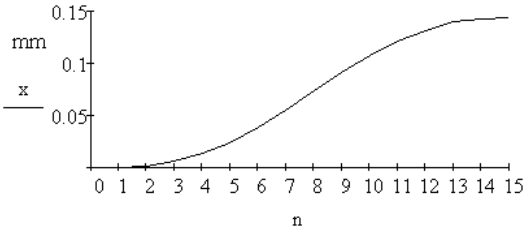

Figure 5. Plot of beam deflection during impact

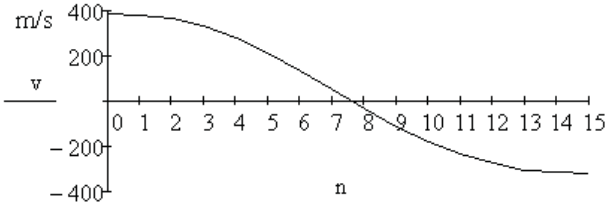

Figure 6. Plot of bullet velocity

2.4 Strength analysis of target elements

Accepting the duration of impact t =2.5 · 10^{-5} s, we received that deformation wave can spread on *0.125 m*, which is less than distance to the supports. In the view of this, boundary conditions are not influence on the beam vibration and beam may be considered as infinite beam on the elastic base. This solution was executed with help of dynamic module of program Plaxis-8v (Delft, the Netherlands) [4]. Elastic base was taken with vanishingly small spring factor, sinusoidal form of impact impulse is assumed, and then the maximum value of impact force is equal 148 kN.

Some results are presented bellow. In Fig. 7, 8 beam deflection and bending moment in by the end of impact are given; maximal bending moment and stress M_{max} =0. 59 kNm, σ_{max}=252 MPa. In Fig. 9 the vibration motion of the points in the middle and in the end of screen are presented.

Maximal bending moment in the post M_{max}=1.27 kNm, σ_{max}=132 MPa is observed when bullet hits its upper end.

Shaft receive maximal loading when bullet hits the lower corner of screen and post. Maximal bending moment in shaft M_{max}=0.06 kNm, σ_{max}=146 MPa, maximal share force in post which create bending moment in shaft Q_{max}= 7.0 kN. In Fig. 10 the vibration motion of the points in the middle of the shaft and under the bearing are presented.

Designed size of elements is enough for dynamical load acceptance.

Using principle of moment of angular momentum for the system as rigid body we can calculated the post-impact angular velocity

$$\omega = (S \cdot L - M_f)/J_Z ,$$

where M_f is friction moment in bearing, it may be neglected during impact. The target receive maximal angular velosity when bullet hits the upper screen edge – ω_{0max}=2.86 s^{-1}, minimal angular velosity when the lower edge ω_{0min}=1.05 s^{-1}. Further motion of target screen with this initial condition is shown in Fig.11-12.

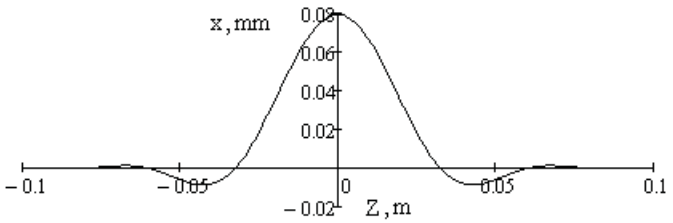

Figure 7. Beam defection after impact

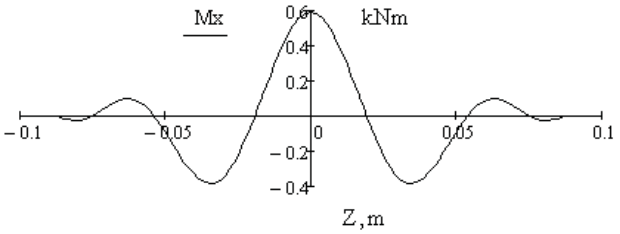

Figure 8. Bending moment in beam after **impact**

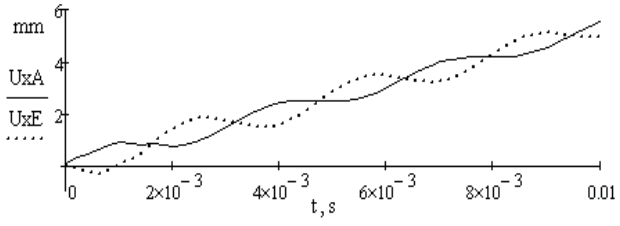

Figure 9. Point A (middle of target beam) and [illegible]

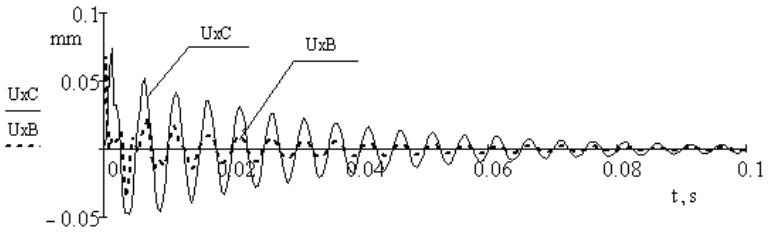

Figure 10. Vibration of shaft: point C- middle of shaft, point B-under bearing

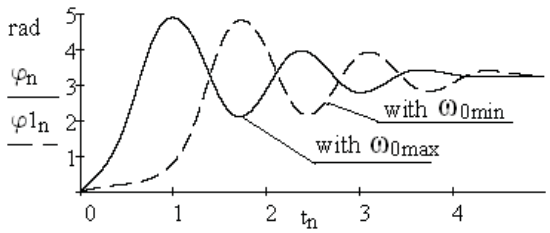

Figure 11. Target screen rotation angle dependence on time φ=φ(t)

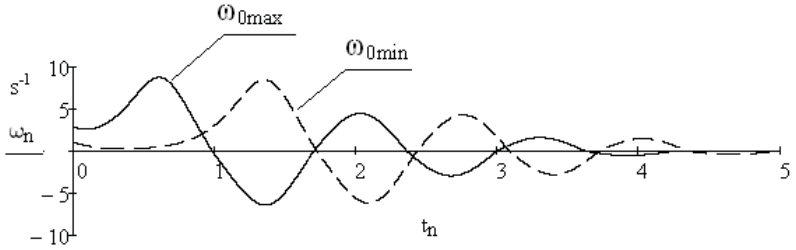

Figure 12. Target screen angular velocity dependence on time ω=ω(t)

Conclusions

Above cited research shows that the duration of impact is very important for all design calculations. In order to allow free rotation of the target screen on shaft, its deflections and residual deformations under action of the dynamic impulses are inadmissibles.

Executed tests field test of designed target confirmed the correctness of details dimensions: measurements of shaft deflection confirmed the absence of the permanent residual deformation, appearance test showed the absence of damage. Local deformations in a place of bullet impact on the screen is also not find out.

Acknowledgments

Acknowledgments could be skipped in the paper. Put Acknowledgments here. Put Acknowledgments here. This study has been supported by the ERDF's grant, within the project "SATTEH", No 2010/0189/2DP/2.1.1.2.0/10/APIA/VIAA/019, being implemented in Engineering Research Institute "Ventspils International Radio Astronomy Centre" of Ventspils University College (VIRAC).

References

[1] ESDU-78035 *Tribology Series, Contact Phenomena I: stress, deflections and contact dimensions for normally loaded unlubricated elastic components*; Engineering Science Data Unit, London, 1978.
[2] Kilchevsky N.A. *Theory of Solid Bodies Collisions.* Academy of Sciences of Ukraine, Institute of Mechanics, Kiev,1969. (in Russian)
[3] Kirillov V.M. *Principles of Designing Concept of Small Arms. Properties, Ballistic Solution, Ammunition, Guns.* Penza, Russia, 1963. (in Russian)
[4] Plaxis 2D-v8, Plaxis b.v. Delft, Netherland, 2007.
[5] Polukoshko S., Sokolova S., Kononova O. Contact Forces in Vibro-Impact Systems, *RTU Scientific Papers, 6.ser. Engineering and Transport.* Vol.28, pp. 78-87, 2008.
[6] Stronge W. J. *Impact Mechanics*. Cambridge, 2000.
[7] Timoshenko S.P. *Strenth and Vibration of Constructions Elements.* Nauka, Moscow, 1975. (in Russian)
[8] Zukas J. A., Nicholas T, H.F.Smitt and others. *Impact Dynamics,* Wiley Interscience, New-York, 1980.

Proceedings of the 4th International Conference on Nonlinear Dynamics
ND-KhPI2013
June 19-22, 2013, Sevastopol, Ukraine

Quasi-Satellite Orbits: A Perturbative Treatment

V. Sidorenko[1*]

Abstract
Quasi-satellite orbits (QS-orbits) are studied in the framework of restricted spatial circular three-body problem. By use of double numerical averaging evolutionary equations the long-term behavior of asteroid's orbital elements is described. Special attention is paid to possible transitions between the motion in QS-orbit and another types of orbits existing at 1:1 resonance. As an example of the motion in QS-orbit the dynamics of near-Earth asteroid 2004GU9 is considered.

Keywords
Three-body problem, mean-motion resonance

[1] Keldysh Institute of Applied Mathematics, Moscow, Russia
* **Corresponding author:** vvsidorenko@list.ru

Introduction

The investigations on long-term evolution of asteroid's orbits are crucial to understanding the route through which the present configuration of the Solar System came to be. In this connection the so-called co-orbiting asteroids (which share their orbits with major planets) attract the special attention: are they the primordial remnants of the building blocks of the corresponding major planet or migrants from the other parts of the Solar System?

The most well known examples of co-orbits in natural objects are provided by Trojan groups of asteroids and by asteroids moving in horseshoe orbits. These asteroids are precluded from having relatively close encounters with their host planets. However, there exists another class of co-orbiting objects in which the opposite is true: they remain very near to the host planet eternally or, at least, for long enough time. Since typically they never enter the planet's Hill sphere, they cannot be considered as satellites in the usual sense of the word. In order to emphasize this specific they are called quasi-satellites (QS). The motion of asteroid in QS-regime corresponds to 1:1 mean motion resonance with resonance argument $\varphi = \lambda - \lambda'$ librating around 0 (λ and λ' are the mean longitudes of the asteroid and the planet respectively).

For the first time the existence of QS-orbits was discussed probably by J.Jackson at the beginning of twentieth century [2]. The recent increase of interest to QS-orbits is inspired by the discovery of the real Earth's quasi-satellites (e.g., [1]).

Since outside the Hill sphere the gravity field of the planet is weak enough, the QS orbit can be treated as a slightly perturbed heliocentric Keplerian orbit. This offers great opportunities for analytical consideration of the motion in QS orbit. Different examples of perturbation technique application can be found in [4],[5],[6].

1. Double Averaged Equations Describing the Dynamics at 1:1 Mean-Motion Resonance

In the case of mean-motion resonance three dynamical processes can be distinguished: "fast" process corresponds to planet and asteroid motions in orbit, "semi-fast" process is a variation of the resonance argument (which describes the relative position of the planet and the asteroid in their orbital

motions), and, finally, "slow" process is the secular evolution of the orbit shape (characterized by the eccentricity) and orientation (it depends on the ascending node longitude, inclination and argument of pericenter).

To study the "slow" process we constructed the evolutionary equations by means of numerical averaging over the "fast" and "semi-fast" motions. As a specific feature of these evolutionary equations we should mention that their right hand sides are not uniquely defined by values of the "slow" variables in some domains of these variables. The ambiguity appears since the averaging can be done over "semi-fast" processes with different qualitative properties - in other words, it can be done over QS-orbit, HS(horseshoe)-orbit, etc. The consideration of this ambiguity provides us an opportunity to predict whether the motions in QS- or HS-orbits are permanent or not; for non-permanent motions in QS-orbits the conditions of capture into this regime and escape from it can be established. More details can be found in our forthcoming paper [7].

2. Example: Dynamics Of Near-Earth Asteroid 2004GU9

Asteroid 2004GU9 moves currently in a QS-orbit (Fig. 1); its osculating elements are presented in Table 1. We chose this asteroid among the other quasi-satellites of the Earth due to the absence of close encounters with Venus and Mars - it justifies to some extent the consideration of the secular effects in its motion on the base of evolutionary equations obtained under the scope of RC3BP (we realize that this model is insufficient for investigation of real asteroid dynamics; we want only to provide better understanding of the time scales and to illustrate some other quantitative characteristics of QS-mode of orbital motion).

Table 1. Osculating orbital elements of asteroid 2004GU9.
Epoch: March 14, 2012 (JD2456000.5)

Element	Value
a (AU)	1.001056350821795
e	.1362904920360489
i (°)	13.64944749947083
Ω (°)	38.74489028357296
ω(°)	280.625598836612
M(°)	217.2153150061352

Note. Orbital elements were taken from JPL Small-Body Database

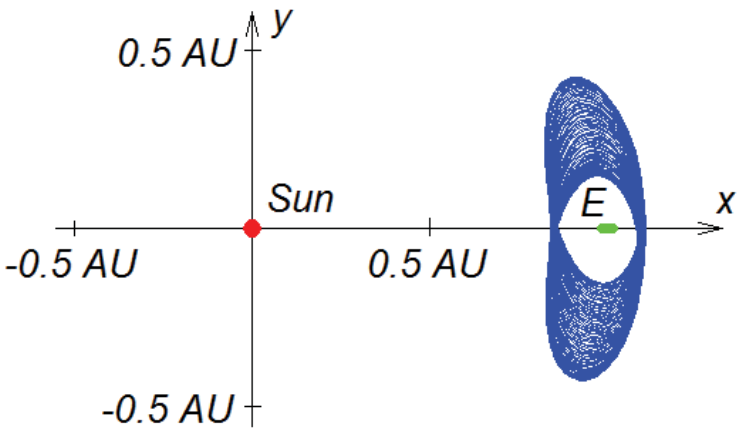

Figure 1. The projection of the asteroid 2004GU9 trajectory (from March 14, 2012 to March 14, 2112) on the plane of the Earth (E) osculating orbit in the reference frame corotating with the Earth.

Fig. 2 demonstrates the behavior of the resonance phase φ according to the results of direct numerical integration of the equations of motion corresponding to RC3BP with the initial values

provided by the elements in Table 1 and the mass parameter $\mu = 3.04 \cdot 10^{-6}$ (we added the mass of the Moon to the mass of the Earth). As one can see, the motion in a QS-orbit will last for approximately 500 years, with a subsequent transition to an HS-orbit.

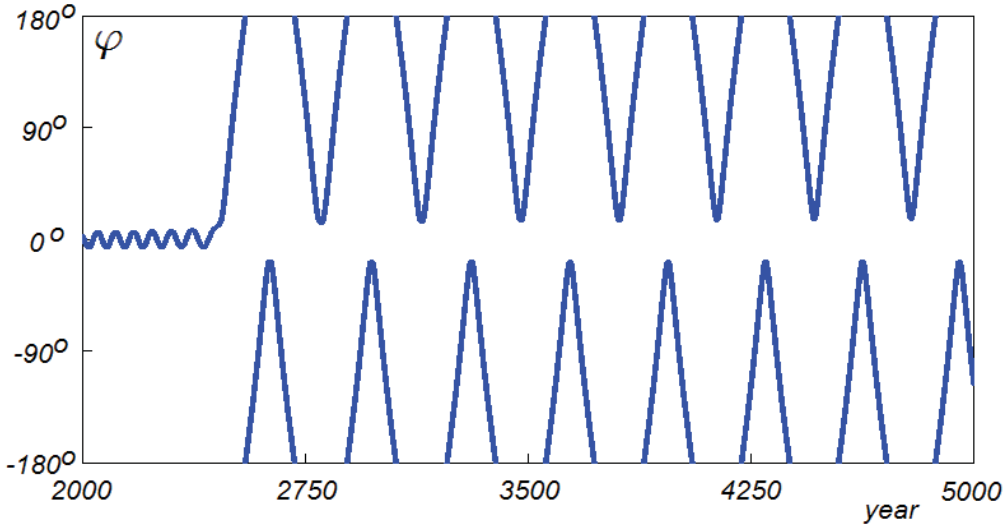

Figure 2. The behavior of the resonance phase φ of 2004GU9

The graphs in Fig. 3 demonstrate that our evolutionary equations provide an accurate description of secular evolution.

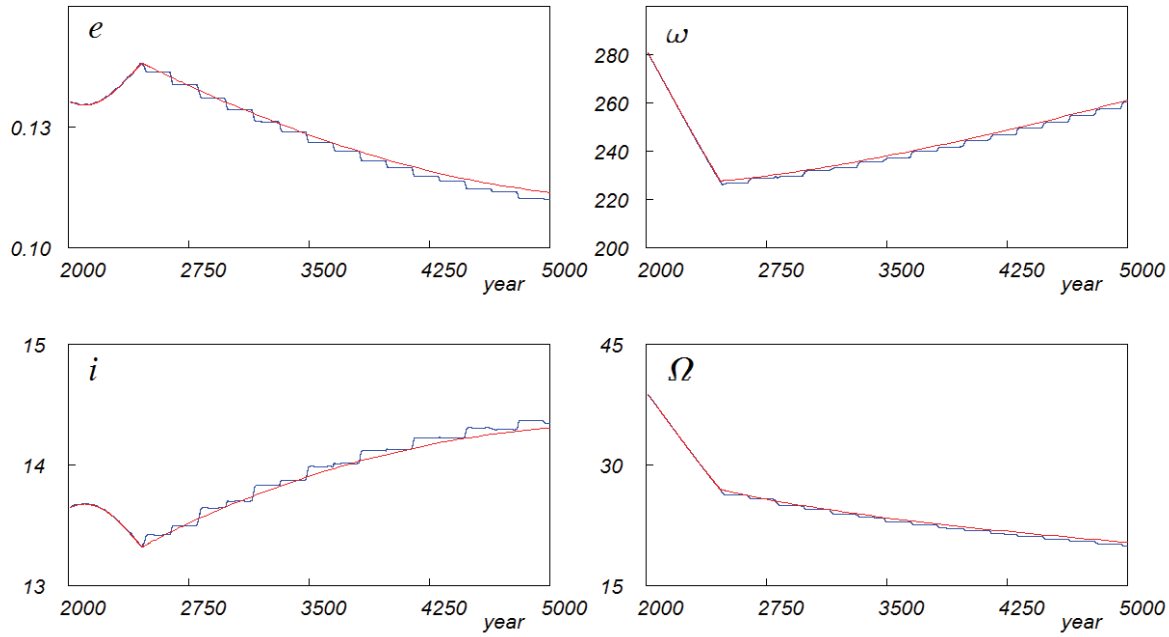

Figure 3. Evolution of 2004GU9 orbital elements. The stair-step lines correspond to the result of the direct integration of the motion equations, smooth lines characterize the secular behavior according to evolutionary equations

Acknowledgments

The work was supported in part by the Russian Foundation for Basic Research (project 13-01-00251) and by the Presidium of the Russian Academy of Sciences under the scope of the Program 22 “Fundamental problems of Solar system investigations”.

References

[1] Connors M., Veillet C., Brasser R., Wiegert P., Chodas P., Mikkola S., and Innanen K. Discovery of Earth's quasi-satellite, *Meteorit. Planet. Sci.*, Vol. 39, pp. 1251-1255, 2004.

[2] Jackson J. Retrograde satellite orbit, *Mon. Not. R. Astron. Soc.*, Vol. 74, pp. 62-82, 1913.

[3] Lidov M.L., and Vashkovyak M.A. On quasi-satellite orbits for experiments on refinement of the gravitation constant, *Pis'ma v Astronomicheskii Zhurnal*, Vol. 20, pp. 229-240, 1994 (in Russian. English trans.: *Astronomy Letters*, Vol. 20, pp. 188-198, 1994)

[4] Mikkola S., Innanen K., Wiegert P., Connors M., and Brasser R. Stability limits for the quasi-satellite orbit*, Mon. Not. R. Astron. Soc.*, Vol. 369, pp. 25-24, 2006.

[5] Namouni F. Secular interactions of coorbiting objects, *Icarus*, Vol. 137, pp. 293-314, 1999.

[6] Nesvorny D., Thomas F., Ferraz-Mello S., and Morbidelli A. A perturbative treatment of the co-orbital motion, *Celest. Mech. Dyn. Astron.*, Vol. 82, pp. 323-361, 2002.

[7] Sidorenko V.V., Neishtadt A.I., Artemyev A.V., and Zelenyi L.M. Quasi-satellite motion of small celestial bodies: setting of and extinction, *Dokl. Akad. Nauk RAN*, Vol. 450, 2013 (in print)

Proceedings of the 4th International Conference on Nonlinear Dynamics
ND-KhPI2013
June 19-22, 2013, Sevastopol, Ukraine

A Model Containing Coupled Subsystems. Main Oscillations Mode

Valentin Tkhai[1], Ivan Barabanov[2*]

Abstract
The paper represents an approach to investigate the dynamics of the model containing coupled systems which assumes the classification of subsystems according to their dynamical behavior and analyzing typical combinations of subsystems. This approach is implemented to investigate the existence of oscillations and their stability, stabilization problems, bifurcations, and resonance. The results concerning the main oscillations mode are presented.

Keywords
Coupled systems, Oscillations, Stabilization

[1]Trapeznikov Institute of Control Sciences, Moscow, Russia
[2]Trapeznikov Institute of Control Sciences, Moscow, Russia and Lomonosov Moscow State University, Moscow, Russia
*__Corresponding author__: ivbar@ipu.ru

Introduction

Considered is a model containing coupled systems (MCCS) described by the system of ordinary differential equations (ODE) which contains autonomous subsystems. The subsystems in the systems are coupled, the intensity of coupling being determined by a real parameter ε: the coupling vanishes as $\varepsilon = 0$ such that subsystemes become independent. Parameter ε can be either scalar or vector; it represents in the vector case the hierarchical structure of subsystems constituting the system. The subsystems, either linear or nonlinear, can be of any order. When ε is small we have a model with weakly coupled subsystems (MWCS).

The Solar system can serve as a natural example of the MWCS. Its mathematical description represents an N-planet problem, which considers the motion of $N+1$ gravitating bodies with one of them largely superior in mass (the "Sun" and the "planets"). When the interaction between planets is neglected the problem decomposes to N independent sun-planet problems, and the influense of other planets in a particular sun-planet problem can be described in the frame of theory of perturbations. The sun-planets-satellites system is an example of a two-level MWCS.

Another example of the MWCS is the translational-rotational motion of the artificial earth satellite. Since the size of the satellite is much less than the distance to Earth, translational and rotational motions weakly influence each other. Here the ratio between the size of the satellite and the satellite-earth distance can be taken as parameter ε. Some other examples of MWCS: a system of interacting moving objects (such as robots, aircrafts, etc.), chains of oscillators, Sommerfeld's sympathetic pendulum, spring systems, resonance shaker screen, and so on.

A natural approach to investigate dynamics of the MWCS was proposed in [1]. This paper is devoted to the problems of oscillations existance and bifurcations, of stability and stabilization for the main oscillations mode.

1. An Approach to Study the MWCS Dynamics

It is clear that the dynamics of a subsystem affects the dynamics of the whole system. When the behaviour of all but one subsystems is completely described, we need to describe the dynamics of a subsystem under a given influence. However, forces not taken into account can result in qualitative dynamic effects. For

example, the restricted 3-body problem (introduced in 1764 by L. Euler) does not regard the influence of the small mass point onto the other points, and therfore, does not comply with Newton's 3rd law [2]. The nonrestricted problem statement yields [2] the abrupt instability when the parameters tend to resonance ones. Thus, it is logically justified to decouple the subsystems of the whole system, to study them separately and then to transfer obtained results to the initial system. This approach is widely used in stability theory and control [3–8]. In the vector Lyapunov function method, which was implemented to obtain conditions of asymptotic stabilty by Matrosov and his disciples [3–5], absolute values of interactions between subsustems were estimated. Merkin and Zubov [6, 7] used decoupling in order to split up precession and nutation systems in the gyroscopic system. Pyatnitsky, Chernousko, as well as their disciples, obtained decoupling through control [8, 9].

An MWCS splits up as $\varepsilon = 0$, in other words, subsystems, which constitute an MWCS, decouple naturally. As for interactions between subsystems, they are taken into account according to Newton's 3rd law, i.e. to an action there is an equal reaction. The last approach, compared to that of [3–8], allows to study dynamical properties in greater details.

Examples above illustrate that MWCSs really exist, regardless of which way to study them we choose. Paper [1] proposes a natural approach that reflects the essence of the MWCS: subsystems are categorized according to their dynamical properties, and different links of categories are analyzed. Let us clarify this by using an example of the simple stability problem.

Suppose that an MWCS contains subsystems categorized according to stability by linearization. Then, in order to analyse stability of the whole MWCS we need to consider only two links: 1) all subsystems are stable; 2) at least one subsystem is unstable.

2. Oscillations, Bifurcation, Stability, Stabilization, and Resonance in MWCS

Let us implement our approach to study oscillations, bifurcation, stability, stabilization, and resonance.

We consider single-frequency oscillations of subsystems. Subsystems are supposed to be autonomous. While a linear subsystem admits isochronous single-frequency oscillations, for a nonlinear system we have either a cycle, or a family of oscillations with the period T depending on a single parameter [10, 11].

Definition 1. [12, 13]. *A point of the family of single-frequency oscillations is called* ordinary point (o-point) *if* $dT \neq 0$ *for this point; otherwise (*$dT = 0$*) it is called* critical point (c-point).

Remark. *A c-point can degenerate into an equiliprium (e-point).*

Note that the period behaviour in the case of symmetrical periodic motions was studied in [14] for initial points in the interior and on the boundary of a connected domain.

Interactions between subsystems of MWCS are cosidered in the frame of theory of perturbations. When connections don't depend explicitely on time, we have an autonomous MWCS. Otherwise, we have a special type of quasiautonomous system.

Oscillations, stability, bifurcations, and stabilizations in quasiautonomous periodic systems of general form

$$\frac{dx}{dt} = X(x) + \mu X_1(\mu, x, t), \quad x \in R^n$$

(μ is a small parameter) were studied in [12, 13, 15–18]. It was established that the oscillation of the generating autonomous system in an o-point differ from those of perturbed quasiautonomous system by $O(\mu)$ [12]. As for c-point, resonant oscillations can occur [17]. The same holds for equilibrium [16].

Definition 2. *Oscillations mode in the perturbed quasiautonomous system is called o-mode, c-mode, and e-mode, according to the type of the point of oscillations family in the generating autonomous system (definition 1).*

We will later omit the term "mode" when it does not result in misunderstanding.

Consider a periodic MWCS that is supposed to contain m subsystems that become independent as $\varepsilon = 0$. Each subsystem has its own mode, according to definition 2. Then the oscillations mode in the whole system depends on the modes in the subsystems. Hence, we have the following qualitatively different combinations of modes: o-o, o-c, o-e, c-c, c-e, e-e, o-o-c, o-c-c, o-e-e, c-c-e, c-e-e. Several modes of the same type may occur in each combination.

The genral statement of the problem of oscillations, bifurcations, stability, and stabilization for MWCS is as follows: to find existence conditions for oscillations, describe bifurcation scenario, obtain stability conditions for oscillations in NWCS and stabilization conditions in terms of linking controls, analyze resonance effects.

Each autonomous subsystem may contain its own small parameter, the coupling of subsystems in the MWCS being described by the parameter ε. This approach allows a subsystem to be quasiautonomous.

However combinations of modes are numerous, there are only two or three main ones. This is due to the fact that, o-point is a rule for an autonomous system (see Law in [10, 11]). Hence, the combination of o-modes is worth being studied first. We call this combination the main mode of oscillations in MWCS.

3. Main Oscillations Mode

Let's outline the approach to study the main MWCS oscillations mode. We need to solve the following problems: a) describe an MWCS containing two subsystems of the second order; b) find necessary and sufficient conditions for the oscillations of that system; c) describe bifurcation scenario; d) construct oscillations of the system; e) find stability conditions for the oscillations; f) find conditions of the stabilization by small controls; g) generalize the results to the case of arbitrary number of subsystems of any order.

Cinsider a sufficiently smooth 2π-periodic MWCS in state space R^4 containing two nonlinear subsystems of the second order (ε is a small parameter).

$$\begin{aligned} \frac{dx_s^*}{dt} &= X_{0s}^*(x_s^*, y_s^*) + \varepsilon X_{1s}^*(\varepsilon, x_1^*, y_1^*, x_2^*, y_2^*, t), \\ \frac{dy_s^*}{dt} &= Y_{0s}^*(x_s^*, y_s^*) + \varepsilon Y_{1s}^*(\varepsilon, x_1^*, y_1^*, x_2^*, y_2^*, t) \\ s &= 1, 2 \end{aligned} \tag{1}$$

Both subsystems are supposed to allow 2π-periodic motions as $\varepsilon = 0$. An autonomous system have an alternative: a periodic motion is either a cycle or a member of a family. We consider the second case. Denote $T_s(h_s)$, $s = 1, 2$ the period of a subsystem, which depend on its own parameter h_s, members of oscillations family being divided into two sets of o-points and c-points [12, 13]. Since $dT_s(h_s) = 0$ for a c-point, we can conclude that almost all members of the oscillations family are o-points. Note that isochronous oscillations are realized in linear subsystems.

Each subsystem (1) permits a family of periodic motions as $\varepsilon = 0$ (γ_s is the shift along the trajectory).

$$x_s^* = \varphi_s^0(h_s, t + \gamma_s), \quad y_s^* = \psi_s^0(h_s, t + \gamma_s), \quad s = 1, 2 \tag{2}$$

Functions (2) represent a conditionaly periodic solution of MWCS. They include 2π-periodic solutions as $h = h^*, h^* = (h_1^*, h_2^*)$. We find a 2π-periodic solution of MWCS at $\varepsilon \neq 0$ that tends to the 2π-periodic solution with $h = h^*$ as $\varepsilon \to 0$. Actually, we find the set of γ_1, γ_2 that guarantees the property above.

Reduce the linear part of the generating system to a system with constant right-hand side [12]. An o-point implies a Jordan box, so we have the system (X_s, Y_s are nonlinear with respect to x_s, y_s).

$$\begin{aligned} \frac{dx_s}{dt} &= X_s(x_s, y_s, t + \gamma_s) + \varepsilon X_{1s}(\varepsilon, \gamma_1, \gamma_2, x_1, y_1, x_2, y_2, t), \\ \frac{dy_s}{dt} &= x_s + Y_s(x_s, y_s, t + \gamma_s) + \varepsilon Y_{1s}(\varepsilon, \gamma_1, \gamma_2, x_1, y_1, x_2, y_2, t) \\ s &= 1, 2 \end{aligned} \tag{3}$$

3.1 Oscillations Existance and Bifurcation

With the aid of (2) and (3) introduce functions

$$C_{xs}(\gamma_1, \gamma_2) = \int_0^{2\pi} X_{1s}(0, \varphi_1(h^*, t + \gamma_1), \psi_1(h^*, t + \gamma_1), \varphi_2(h^*, t + \gamma_2), \psi_2(h^*, t + \gamma_2), t)dt$$
$$s = 1, 2$$

and write the system of equations.

$$C_{xs}(\gamma_1, \gamma_2) = 0, \quad s = 1,2 \tag{4}$$

Equations (4) are called amplitude equations. They represent necessary conditions for a periodic solution of MWCS to exist. In the case of simple root of (4), these equations become sufficient conditions. The following theorem holds.

Theorem 1. *Let MWCS* (1) *be in the main mode. Consistency of equations* (4) *is necessary condition of oscillations of* (1)*. If there exists a simple root of* (4)*, then there exists an isolated periodic solution of* (1) *(sufficient condition) that differs from the periodic solution of the generating system by the perturbation magnitude. In addition, if the sufiitient condition is satisfied, there exist at least two periodic solutions of* (1)*, i.e. the bifurcation of the periodic solution of the generating system occurs.*

Theorem 1 is proved with the aid of the implicit function theorem.

3.2 Stability of Oscillations

Given a simple root (γ_1^*, γ_2^*) of (4), we construct a periodic solution of MWCS. Then write variational equations of (1) for this periodic solution. The zero characteristic exponent λ splits up as an isolated periodic solution appears. We can write the following.

$$\lambda = \alpha_1 \varepsilon^{1/2} + \alpha_2 \varepsilon + o(\varepsilon) \tag{5}$$

Appropriate calculations are given in [12]. Numbers α_1 and α_2 for λ_s can be efficiently calculated [12] in terms of coefficients of (4), α_1 being roots of a biquadratic equation.

Theorem 2. *Consider MWCS in the main mode. If*

$$\alpha_{1s}^2 \le 0, \quad \alpha_{2s} < 0; \quad s = 1,2$$

then the periodic solution of MWCS is asymptotically stable. If either

$$\alpha_{1s}^2 \le 0, \quad \alpha_{2s} > 0$$

or $\alpha_{1s}^2 > 0$ *for at least one subsystem s, then the periodic solution is unstable.*

3.3 Stabilization

We can solve two stabilization problems basing on Theorem 2. The first problem concerns the stabilization of a periodic motion of the generating system, the second one deals with the periodic motion of MWCS. Both problems are solved with the aid of small periodic in t controls, which are linear in state coordinates.

3.4 Example

Theory above can be illustrated by the example of two coupled conservative one degree of freedom mechanical systems. For example, we can consider coupled pendula under perturbations. Let conservative systems have potential wells, such that each of them permits oscillations in the o-mode. So we have the main mode of MWCS, which can be studied using the above methods.

4. Conclusion

Introduction of the concept of model with weakly coupled subsystems (MWCS) was inspired by a number of applications. The study of MWCS is based on the natural approach: subsystems are categorized according their dynamical properties, then different links and combinations of subsystems are analyzed. This approach allows to solve problems of existance of oscillations, their bifurcations, and stability and stabilization. Corresponding results for a single subsystem were obtained earlier.

Acknowledgments

This work is financially supported by the Russian Foundation for Basic Researches (project Nos. 13-01-00376 and 13-01-00347) and by the Program 14 of the Branch of Energetics, Engineering, Mechanics and Control Problems of the Russian Academy of Sciences.

References

[1] Tkhai V.N. A model containing coupled subsystems. *Autom. Remote Control*, in print, 2013.

[2] Tkhai V.N. On stability of the constant Laplace solutions in the unrestricted three body problem *Appl. Math. Mech.*, Vol. 42, Iss. 6, pp. 1026-1032, 1978.

[3] Matrosov V.M. Vector lyapunov functions method to analyse complex systems with distributed parameters *Autom. Remote Control*, Vol. 34, No. 1, pp. 5-22, 1973.

[4] Matrosov V.M. and Voronov A.A., Eds. *Vector Lyapunov Functions Method in Theory of Stability,* Nauka, Moscow, 1987.

[5] Matrosov V.M. *Vector Lyapunov Functions Method: Analysis of Dynamics of Nonlinear Systems,* Fizmatlit, Moscow, 2001.

[6] Merkin D.R. *Gyroscopic Systems,* Nauka, Moscow, 2001.

[7] Zubov V.I. *Analytical Dynamics of a Set of Bodies,* Leningrad State University, Saint-Petersburg, 1983.

[8] Pyatnitsky E.S. Decoupling principle in control of mechanical systems *Soviet Mathematics. Doklady*, Vol. 300, No. 2, pp. 300-303, 1988.

[9] Chernousko F.L., Ananievskiy I.M. and Reshmin S.A. *Methods of Control of Nonlinear Mechanical Systems,* Fizmatlit, Moscow, 2006.

[10] Tkhai V.N. Period of oscillations over a family of nonlinear oscillations and periodic motions of perturbed system in the critical point *Appl. Math. Mech.*, Vol. 74, Iss. 6, pp. 812-823, 2010.

[11] Tkhai V.N. The law of one variable dependence for the period of nonlinear oscillations *Appl. Math. Mech.*, Vol. 75, Iss. 3, pp. 430-434, 2011.

[12] Tkhai V.N. Oscillations and stability in quasiautonomous systems. I. Simple point of the one-parameter family of periodic motions *Autom. Remote Control*, Vol. 67, No. 9, pp. 1436-1444, 2006.

[13] Barabanov I.N. and Tkhai V.N. Stabilization of oscillations from a monoparametric family of autonomous system *Autom. Remote Control*, Vol. 70, No. 2, pp. 203-208, 2009.

[14] Tkhai V.N. On the behaviour of the period for symmetrical periodic motions *Appl. Math. Mech.*, Vol. 76, Iss. 4, pp. 616-622, 2012.

[15] Makarenkov O.Yu. The Poincaré index and periodic motions of perturbed autonomous systems *Proc. Moscow Math. Soc.*, Vol. 69, Iss. 70, pp. 4-45, 2009.

[16] Tkhai V.N. Forced resonant oscillations of nonlinear autonomous system in equilibrium neighborhood *Autom. Remote Control*, Vol. 71, No. 11, pp. 2360-2366, 2010.

[17] Tkhai V.N. Oscillations and stability in quasiautonomous system. II. Critical point of the one-parameter family of periodic motions *Autom. Remote Control*, Vol. 72, No. 7, pp. 1450-1457, 2012.

[18] Tkhai V.N. Quasiautonomous mechanical system: Oscillations, stability, bifurcation, and resonance *Proceedings of the 10th International Chetaev Conference, Kazan*, Vol. 2, pp. 522-532, 2012.

Proceedings of the 4th International Conference on Nonlinear Dynamics
ND-KhPI2013
June 19-22, 2013, Sevastopol, Ukraine

Some Problems of the Theory of Parametric Oscillations

Alexandr Zevin[1*]

Abstract
In the first part of the paper, the definition and mathematical models of parametric oscillations are discussed. It is shown that the universally adopted definition of such oscillations is not quite correct. It is found that that a limit cycle of a self-oscillating system coincides with a periodic solution of some parametric system, which may lead to a wrong choice of the mathematical model (as an example, the parametric model of a swing is discussed).
In the second part, some general properties of the stability regions in parametrically excited Hamiltonian systems are established: unlike the known results, the excitation is not supposed to be small. The classical Rayleigh theorem on the behavior of natural frequencies of a conservative system is extended on the critical frequencies of a parametric excitation.

Keywords
parametric oscillations, mathematical models, Hamiltonian systems, stability regions

[1] Institute of Transport Systems and Technologies NAS of Ukraine, Dnepropetrovsk, Ukraine
[*] **Corresponding author:**zevin@westa-inter.com

Introduction

Parametric oscillations occur in problems of mechanics, control and other fields of science and technology. There is a great number of publications, devoted to analytical and numerical study of stability of specific parametrically excited systems; at the same time, qualitative theory is developed to a much lesser extent. The known general results on stability regions are obtained by asymptotic methods and, therefore, are applicable only to systems with small parametric excitation.

Below the definitions of parametric oscillations in linear and nonlinear systems and the correctness of some parametric mathematical models are discussed; for parametric Hamiltonian systems, some general properties of stability regions are indicated.

1. On the definition of parametric oscillations

Various systems in mechanics, dynamic stability of elastic systems and control theory are described by the linear differential equation with periodic coefficients

$$\dot{x} = A(\omega t)x, \tag{1}$$

$$x \in \mathrm{R}^n, \ A(\omega t) = A(\omega t + 2\pi) = \left[a_{ik}(\omega t)\right]_{i,k=1}^{n}.$$

Often, the coefficients of (1) are some varying parameters of the system, so, oscillations in such system are called parametric (defining them as caused by periodic fluctuations of the system parameters).

This definition is not quite accurate. First, the coefficients of (1) may not be the parameters of the system, for example, in parametric models of bridges in wind flow, the periodicity of the

coefficients is due to the Karman vortices shedding. [1]. Second, the periodic fluctuations of the parameters do not necessarily lead to an equation with periodic coefficients. Thus, small oscillations of a pendulum with the suspension point, vibrating in the vertical direction, is described by the equation

$$\ddot{x} + (\omega_0^2 + p(\omega, \omega t)x = 0,$$

where x is an angle coordinate and $p(\omega, \omega t) = p(\omega, \omega t + 2\pi)$ is a reduced acceleration of the suspension point. If the latter is regarded as a parameter, then the oscillations of the system comply with the above definition. But then horizontal acceleration of the suspension point should also be regarded as a parameter, yet, in this case the oscillations are described by an equation with a constant coefficient

Similarly, the vibrations of an elastic rod, compressed by a longitudinal periodic force, is described by equation of the form (1) , while the same force applied perpendicular to the axis of the rod, results in forced oscillations. On the other hand, the vibrations of a circular rod under a distributed periodic radial loads are described by an equation with periodic coefficients, etc.

Given these considerations, it would be more accurate to simply call (1) by an equation with periodic coefficients, without introducing any special term. As soon, however, the term «parametric oscillations» became generally accepted, it is appropriate to understand by it oscillations in any homogeneous linear system with periodic coefficients, regardless of their physical sense.

Consider now the nonlinear system

$$\dot{x} = f(x, \omega t), \tag{2}$$

$$x \in \mathrm{R}^n, \quad f(x, \omega t) = f(x, \omega t + 2\pi), \quad f(0, t) = 0.$$

Because of the last condition, $x = 0$ is an equilibrium point. Therefore, the corresponding linearized equation is of the form (1). For this reason, it is natural to term the families of periodic solutions, emanating from this point, by parametric oscillations.

2. Parametric models of dynamic systems.

Consider the self-oscillating system

$$\dot{x} = f(x), \tag{3}$$

$$x \in R^n, \ f(0) = 0.$$

It can be written as

$$\dot{x} = C(x)x, \qquad C(x) = \int_0^1 f_x(sx)ds.$$

Assume that (3) has a periodic solution. $x(t) = x(t + T)$. Obviously, it is also a solution of the equation

$$\dot{x} = A(t)x, \quad A(t) = A(t + T) = C(x(t)). \tag{4}$$

Thus, any periodic solution of an autonomous system, having an equilibrium position, coincides with a solution of a linear system with periodic coefficients. In this connection, it may seem that the stability of this solution can be investigated with the help of equation (4), using the results of the theory of linear parametric oscillations.

This approach, however, is incorrect. The coincidence of a solution in systems (3) and (4) does not mean that it is simultaneously stable or unstable in the both systems. Indeed, the stability of $x(t)$ in (3) depends on the corresponding variational equation

$$\dot{y} = A_0(t)y\,, \qquad A_0(t) = f_x(x(t))\,,$$

which is different from (4).

The coincidence of a solution of a self-oscillating and a parametric system can lead to an error when constructing the mathematical model for a physical system. The parametric model of a swing (often presented as an evident example of parametric oscillations) may serve as an example of such an error.

When riding on a swing, one squats and raises while going down and up, respectively. In steady motion, the angular coordinate and reduced length of the swung, $x(t)$ and $L(t)$, are periodic functions with $L(t)$ taking its maximum and the minimum values at. $x_p(t) \approx 0$ and $\left|x_p(t)\right| \approx \max\left|x_p(t)\right|$. Clearly, the equation of a pendulum with the periodic length $L(t)$,

$$\frac{d}{dt}\left[L^2(t)\frac{dx}{dt}\right] + \varepsilon\frac{dx}{dt} + gL(t)\sin x = 0\,, \tag{5}$$

admits the same solution $x_p(t)$, what, at the first sight, proves the parametric model of a swing. Meanwhile, this model is wrong.

It turns out [2,3] that, contrary to the apparent stability of oscillations of a sing, the solution $x_p(t)$ in (5) is unstable. This discrepancy is explained as follows. In a swing, the function $L(t)$ does not set a priori, but is determined by the current position of the swing. Under an external perturbation, $L(t)$ becomes non-periodic along with the swing for as long as the initial motion is restored. On the contrary, in (5) the function $L(t)$ remains periodic regardless of any disturbances.

Thus, the swing is a self-oscillating system (a more detailed justification of self-oscillatory nature of the swing can be found in [3]). Note that while these considerations are obvious enough, proponents of the parametric model still exist [4].

The above considerations show that for any physical system, the use of a parametric model is justified only when the exciting forces are independent on the phase coordinates, being solely the functions of time

3. Parametric oscillations in Hamiltonian systems

Consider the equation

$$J\dot{x} = H(\omega t, \mu)x\,, \tag{6}$$
$$x \in \mathrm{R}^{2n}, \quad H(\omega t, \mu) = H(\omega t + 2\pi, \mu) > 0\,, \qquad H(\omega t, 0) = H_0$$

Here $\omega = 2\pi / T$ is the frequency of the parametric excitation, the parameter μ describes its intensity, J is a nonsingular skew-symmetric matrix, $H(\omega t, \mu)$ is a symmetric positive definite matrix. Note that the vector Hill equation

$$\frac{d}{dt}\left[M(\omega t, \mu)\frac{dy}{dt}\right] + C(\omega t, \mu)y = 0\,, \tag{7}$$
$$M(\tau, \mu) = M(\tau + 2\pi, \mu) > 0\,, \quad C(\tau, \omega, \mu) = C(\tau + 2\pi, \omega, \mu) > 0\,,$$

which is often found in applications, can be reduced to (6).

Fundamentals of the stability theory for equation (6) were laid by Lyapunov and Poincare, and the further development is in the works by Krein, Gel'fand, Lidskii, Yakubovich and other researchers [1]. In [5] the proofs of main theorems of the theory were significantly simplified and some new facts were established.

In applications, the most interesting are the stability regions in the plane μ, ω. The known general results of such kind are obtained via asymptotic methods and are applicable only to systems with small parametric excitation. So, popular ideas on the stability of these systems are based on the results of numerical studies of specific systems, primarily with one degree of freedom

The following are non-local results on the stability regions (some of which can be found in [6,7])

As is known, the instability regions in the plane μ, ω adjacent to the points

$$\mu = 0, \ \ \omega = \omega_q = \frac{\omega_p^0 + \omega_k^0}{r}, \ p, k = 1,...,n,$$

where ω_p^0 are the natural frequency of system (6) at $\mu = 0$.

Let C_k be a region of stability. We call it convex in ω when any vertical segment K_1K_2 lies in this region, provided that $K_1, K_2 \in C_k$.

Theorem 1. The regions C_k are convex in ω.

Thus, for any μ, all the points between the boundaries of neighboring instability regions, belong to a stability region C_k (Figure 1). Clearly, Theorem 1 greatly facilitates stability analysis in system (6). Indeed, instead of checking stability at every point of the plane μ, ω, it is sufficient to calculate the boundaries $\omega_k^{\pm}(\mu)$

As is known [1], for small μ, the converse is true, i.e., at any point between $\omega_+^-(\mu)$ and $\omega_k^+(\mu)$, the system is unstable. It appears, however [5], that this may not hold as μ increases, namely, at some points of the boundaries $\omega_k^{\pm}(\mu)$, new stability regions, going inside the instability ones, may arise (see point K in Figure 1). Note that such an effect exists only in systems with $n \geq 3$.

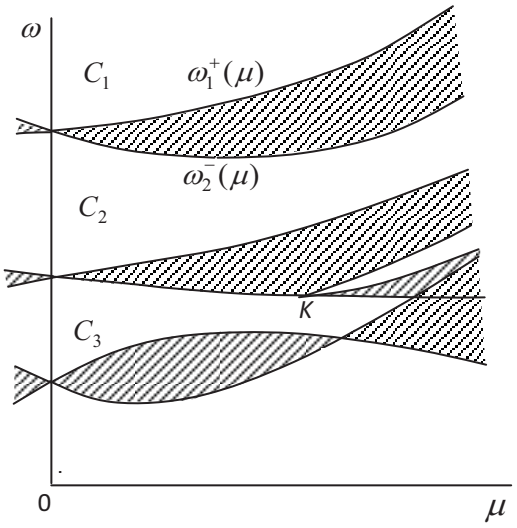

Figure 1. Stability regions in Hamiltonian systems

Now assume that $H = H(\omega t, \varepsilon)$, and $H(\omega t, \varepsilon)$ increases with ε (in the sense of the quadratic form).

Theorem 2. The functions $\omega_i^{\pm}(\mu)$ increase with an increase in the Hamiltonian.

For system (7), this theorem implies the following

Corollary. In (7), $\omega_i^{\pm}(\mu)$ increase with $C(\omega t, \mu)$ and decrease with $M(\omega t, \mu)$.

Note that, in accordance with the classical Rayleigh theorem, in an autonomous system, the natural frequencies ω_i^0 increase when C increases or M decreases. Thus, the above corollary extends the Rayleigh theorem to the critical frequencies $\omega_i^{\pm}(\mu)$ of the parametric resonance.

This conclusion holds for the system

$$M\ddot{y} + K\dot{y} + C(\omega t)y = 0,$$

$$y \in \mathrm{R}^n,\ M > 0,\quad C(\omega t) > 0,$$

where K is a skew-symmetric matrix of gyroscopic forces (note that for the natural frequencies of the corresponding autonomous system, such result is set in [8])

Conclusions

1. It is shown that the existing definition for parametric oscillations is not quite correct, and some modifications for linear and nonlinear systems are proposed.
2. It is found that the coincidence of a periodic solution of autonomous and parametrically excited systems may lead to a wrong choice of the mathematical models for some systems.
3. Some general non-local results on the stability regions of parametric Hamiltonian systems are indicated.

References

[1] Yakubovich V.A. and Starzhinsky V.M. *Linear Differential Equations with Periodic Coefficients and their Applications*. Nauka, Moscow, 1972 (in Russian).
[2] Pinsky M. and Zevin A. Oscillations of a pendulum with a periodically varying length and a model of swing. *Int. J. Non-Linear Mech*., Vol.34, pp.105-109, 1999.
[3] Zevin A.A. and Filonenko L.A. Qualitative study of oscillations of a pendulum with periodically varying length and the mathematical model of swing. *Prikl. Mat. Mekh*, Vol.71, pp. 989-1003, 2007 (in Russian).
[4] Belyakov A.O., Seyranian A.P. and Luongo A. Dynamics of the pendulum with periodically varying length. *Physica D*, Vol. 238, pp. 1589-1597, 2009.
[5] Zevin A.A. New approach to the stability theory of linear canonical systems of differential equations with periodic coefficients. *J. Appl. Maths. Mechs.,* Vol.68, pp. 183-198, 2004.
[6] Zevin A.A.. Generalization of the Rayleigh theorem to nonlinear and parametrically excited systems. *J. Sound Vibr*., Vol. 171, pp.473-482, 1994.
[7] Zevin A.A. Analysis of stability and instability regions in parametrically excited Hamiltonian systems. *Nonlinear Dynamics*, Vol.12, pp.327-341, 1997.
[8] Zhuravlev V.F. Generalization of the Rayleigh theorem on gyroscopic systems. *Prikl. Mat. Mekh*, Vol. 40, pp.606-610, 1976 (in Russian).

Proceedings of the 4th International Conference on Nonlinear Dynamics

ND-KhPI2013

June 19-22, 2013, Sevastopol, Ukraine

Aircraft Landing Gear Shock Absorbers with Rectangular Load Characteristics

Aleksey N. Zotov[1], Anvar R. Valeev[2], Aleksey A. Kudreyko[3*], Natalia S. Golovkina[4]

Abstract
A numerical study of motion of landing gear shock absorber in vibro-impact system is carried out. The assembly consists of vibration absorbers with rectangular load characteristics induced by dry friction forces. The theoretical results confirm the absence of bounce on landing.

Keywords
Flight safety, aircraft bouncing, vibro-impact system, quasi-zero stiffness.

[1]Department of Mechanics and Design of Machines
[2]Department of Design and Operation of Oil and Gas Pipelines and Storages
[3]Department of Physics
[4]Faculty of Architecture and Construction

Ufa State Petroleum and Technological University
Kosmonavtov St. 1, 450062 Ufa, Russia
[*]**Corresponding author:** akudreyko@rusoil.net

Introduction

The problem with bouncing on landing in some aircrafts presents a difficulty for aviation. The loss of contact between the aircraft landing gear and the ground is potentially dangerous for aviation.

In this article we suggest to use the landing gear vibro-impact resistant systems as vibration absorbers with rectangular load characteristics (hysteresis loops) induced by dry friction forces [1]. The configuration of our system is presented in Fig. 1 by analytic functions. We aimed to reduce the bounce of aircraft after landing with the vertical velocity V_0. The solution of this problem is possible if after landing we put conditions on the coordinate of aircraft.

Concept and research design

Aircraft landing dynamic analysis is presented by the load characteristics given in Fig. 1 and differential equation (1), where the lift force is neglected

$$\begin{aligned} m\ddot{x} = mg - (((mg + F_*)/2)\tanh[k(x + x_*)] + (mg + F_*)/2 + \\ + q(F_*/2)\tanh[k(x + x_*)] + F_*/2)\mathrm{sgn}[\dot{x}]) - \\ - (P_* \tanh[k_2(-x[t])] + P_* - q_2(P_* \tanh[k_2(-x[t])] + P_*)\ \mathrm{sgn}(\dot{x})) \end{aligned} \quad (1)$$

with initial conditions

$$x_0(0) = 0, \dot{x}_0(0) = V_0$$

where x_0 is the coordinate of the aircraft, g is the gravitational acceleration, m is a mass of the aircraft, F_*, P_* are forces acting upon the fuselage (the friction forces are neglected). Coefficients $q, q_2 < 1$ relate to the height of the hysteresis loop, x_* is the coordinate of the hysteresis loop for $x > 0$, k, k_2 are dimensionless coefficients that determine the shape of the hysteresis loop, $R = qF_*, R_2 = q_2 P_*$ are dry friction forces.

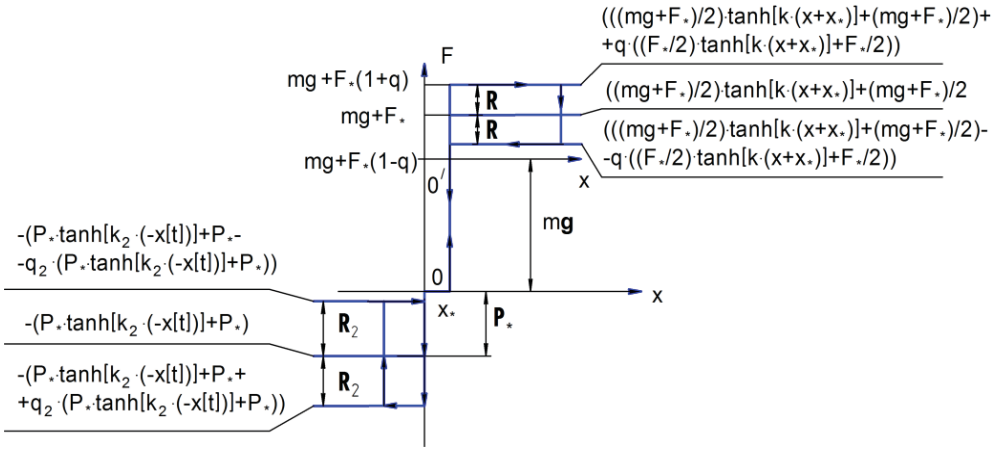

Figure 1. Load characteristics of the shock absorber.

Suppose that during halting, the overload cofficient s for the given load characteristics $F_* > P_*$ is given by

$$s = \frac{mg + F_*(1+q)}{mg} \tag{2}$$

In order to get quantitative results, determine the constants in (1). Let $m = 28500\,kg$, $= 7$ $k = k_2 = 10^4$. Plots in Fig. 2 are obtained from the numerical solution of (1) and represent the coordinate of the aircraft versus time after landing for $V_0 = 6\,m/s$.

Data analysis and evaluation

The analysis of the solutions of equation (1) allows us to propose that the application of shock absorbers with load characteristics given in Fig. 1 prevents aircraft bouncing (see Figs. 2 e, f). For any value of coefficient q, we can always set such x_*, that the condition $x > 0$ holds during the whole decay time.

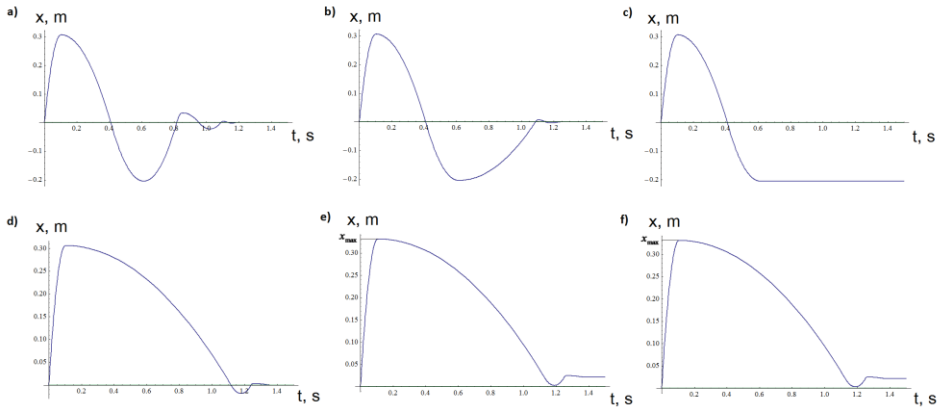

Figure 2. Coordinate of the fuselage versus time (a, d, e: $\boldsymbol{x_* = 0, P_* = 0}$). $\boldsymbol{s = 7, m = 2850\,kg, k = k_2 = 10^4, V_0 = 6\,m/s}$, a) $\boldsymbol{q = 0,80,\ F_* = 931\,kN, q_2 = 0, P_* = 0, x_* = 0}$ b) $\boldsymbol{q = 0,80,\ F_* = 931\,kN,\ q_2 = 0,99, P_* = 57\,N, x_* = 0}$, c) $\boldsymbol{q = 0,80, F_* = 931\,kN, q_2 = 0,99,\ P_* = 85\,N, x_* = 0}$, d) $\boldsymbol{q = 0,98, F_* = 846,36\,kN, q_2 = 0,\ P_* = 0, x_* = 0}$, e) $\boldsymbol{q_2 = 0,98, F_* = 846,36\,kN,\ q_2 = 0, P_* = 0, |x_*| = 0,02\,m}$, f) $\boldsymbol{q_2 = 0,98,}$
$\boldsymbol{F_* = 846,36\,kN, q_2 = 0,98, P_* = 846,36\,kN, |x_*| = 0,02\,m}$.

The value of q for the maximum deviation $x_{\max}$ is minimally determined when it ranges between 0,98 and 0,99 (Figs. 2 e, f). In our example, if $|x_*| = 0{,}02\ m, q_2 = 0$, then for $q = 0{,}98$, $x_{\max} \approx 0{,}33$ m (Fig. 2 e). To avoid the bounce for $q = 0{,}8$, the condition of $x_0 \approx 0{,}23\ m$ must hold. The value of the maximum deviation is $x_{\max} \approx 0{,}61\ m$. The presence of hysteresis in load characteristics for $x < 0$ is derermined by P_*, q_2 and has no impact on $x(t)$ (see Figs. 2 e, f).

Consider the effect of the tire elasticity of the landing gear. To do this, it is necessary to consider a two-dimensional model as shown in Figs. 3 a, b, where all wheels are replaced by a single wheel. The elasticity of such wheel is defined by the function $c_1 x_1^2 + c_1 x_1^2 \mathrm{sgn}[x_1]$, where c_1 is the constant characterizing the shape of the load characteristics (Fig. 3 c). In general, such shape of the restoration force corresponds to reality [2]. However, in our case we employed a simpler model. Besides the tire elasticity, the wheel is acted on by the damper force, which is proportional to the velocity of the center of the wheel $\dot{x}_1$, where μ is the conversion factor. The load characteristics of the landing gear shock absorber are shown in Fig. 3 d.

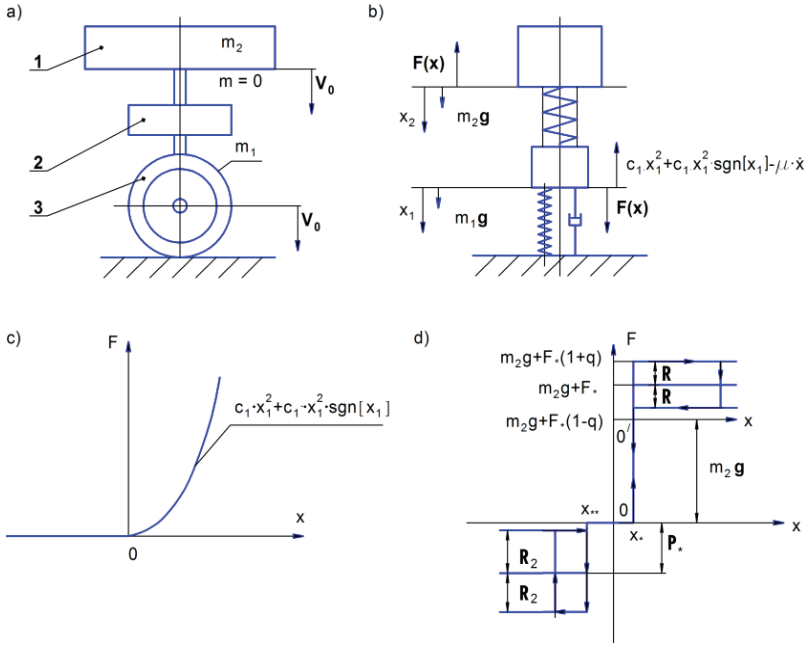

Figure 3. Landing simulation with vertical velocity V_0
$\boldsymbol{x_1}$- fuselage displacemen, $\boldsymbol{x_2}$- displacement of the center of the gear wheel,
$\boldsymbol{x_*, x_{**}}$- coordinates of the hysteresis loops

a) 1 – aircraft fuselage of mass m_2, 2 – landing gear shock absorber (mass is neglected), 3 – wheel of mass m_1
b) forces acted on by each body of the system with two degrees of freedom during landing
c) load characteristics of the gear wheel
d) load characteristics of the landing gear shock absorber resistant system.

The motion of the airframe for the load characteristics given in Fig. 3 b is represented by the following differential equations

$$m_1\ddot{x}_1 = m_1 g - (c_1 x_1^2 + c_1 x_1^2\ \mathrm{sgn}(x_1) - \mu\dot{x}_1) + \left(\frac{(m_2 g + F_*)\tanh(k\cdot(x_2 - x_1 - x_*))}{2} + \frac{m_2 g + F_*}{2} + \right.$$
$$+ \frac{q\cdot(F_*\tanh(k(x_2 - x_1 + x_*)) + F_*)\,\mathrm{sgn}(\dot{x}_2 - \dot{x}_1)}{2} - \left(\frac{P_*\tanh(k_2(-(x_2 - x_1) - x_{**}))}{2} + \right. \qquad (3)$$
$$\left. \left. + \frac{P_*}{2} + \frac{q_2(P_*\tanh(k_2(-(x_2 - x_1) - x_{**})) + P_*)\,\mathrm{sgn}(\dot{x}_2 - \dot{x}_1)}{2} \right) \right)$$
$$m_2\ddot{x}_2 = m_2 g - \left(\frac{(m_2 g + F_*)\tanh(k\cdot(x_2 - x_1 - x_*))}{2} + \frac{m_2 g + F_*}{2} + \frac{q\,(F_*\tanh(k\cdot(x_2 - x_1 + x_*)) + F_*)\,\mathrm{sgn}(\dot{x}_2 - \dot{x}_1)}{2} - \right.$$
$$\left. - \left(\frac{P_*\tanh(k_2(-(x_2 - x_1) - x_{**}))}{2} + \frac{P_*}{2} + \frac{q_2\,(P_*\tanh(k_2(-(x_2 - x_1) - x_{**})) + P_*)\,\mathrm{sgn}(\dot{x}_2 - \dot{x}_1)}{2} \right) \right)$$

where the lift force is neglected. Constants $k = k_2 = 10^4$ in system (3) determine the shape of the hysteresis loops, $\dot{x}_1$, $\dot{x}_2$ represent velocities of the fuselage and the center of mass of the landing gear, $c_1 = \frac{m_1+m_2}{0{,}05^2}\ N/m$ is an arbitrarily given value of the static displacement of the center of the wheel. The initial conditions for system (3) take the form $x_1 = x_2 = 0, \dot{x}_1 = \dot{x}_2 = V_0$. The solution of (3) shows that the bounce during landing can be avoided when $P_* = 0$ and $R_2 = 0$ as well as $P_* \neq 0$ and $R_2 \neq 0$. The presence of the hysteresis loop in load characteristics for $(x_2 - x_1) < 0$ does not yield any advantages with respect to the case when the loop is absent, i.e. $P_* = 0, q_2 = 0, x_2 - x_1 < 0$. Thus, in the following, we will consider only resistant systems without hysteresis loop.

The solution of system (3) is shown in Figs. 4. Regarding Figs. 4 c, d, the bounce does not occur because $x_1 > 0$ during the time decay after landing. To achieve the condition $x_1 > 0$, the coefficient μ must be greater than a boundary value. In this example, $\mu_* \approx 10^4$ N · s/m. The 9,45-g load acting on the fuselage (Fig. 4) is determined by $s = \left(m_2 g + F_*(1+q)\right)/m_2 g$.

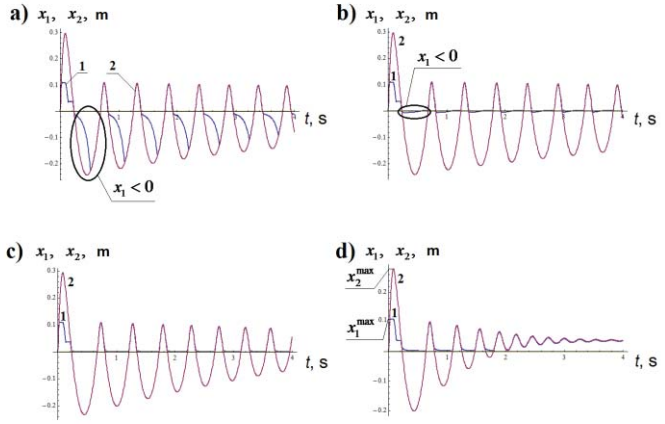

Figure 4. Time history diagram of the center of the wheel and fuselage x_1, x_2 for the load characteristics given in Fig. 3 d ($P_* = 0, R_2 = 0$).
$q = 0{,}98$, $c_1 = 1{,}12 \cdot 10^8\ N/m$, $x_* = 0{,}002\ m$, $V_0 = 6\ m/s$, $F_* = 1{,}2 \cdot 10^6\ N$,
$P_* = 0, R_2 = 0, m_1 = 50\ kg, m_2 = 28500\ kg$
a) $\mu = 5000\ N \cdot s/m$, b) $\mu = 8000\ N \cdot s/m$, c) $\mu = 20000\ N \cdot s/m$, d) $\mu = 80000\ N \cdot s/m$.

The maximum displacement of the fuselage for such load factor is $x_2^{\max} \approx 0{,}28$ m (Fig. 4 d) and the maximum displacement of the center of the wheel is $x_1^{\max} \approx 0{,}12$ m. The calculated displacements can be technically achieved.

References

[1] Zotov A.N. Systems with quasi-zero-stiffness characteristic. Proc. of the 6th EUROMECH Nonlinear Dynamics Conference, ENOC 2008.
[2] Jankowski L., Mikulowski G. Adaptive landing gear: optimum control strategy and improvement potential, Proc. ISMA 2006, Leuven, Belgium, 2006.

Proceedings of the 4th International Conference on Nonlinear Dynamics
ND-KhPI2013
June 19-22, 2013, Sevastopol, Ukraine

Behavior of the Van der Pol and Duffing Oscillators under Varying System Parameters

Vaibhav Bajaj[1*], Nihit Prakash[1], Naik Raghavendra Datta[1]

Abstract
The paper involves thorough study of non-linear vibratory oscillators and numerical methodology to analyze and resolute the non-linear dynamical behavior. The study involves an analysis of the *Van der Pol oscillator* and the *Duffing oscillator* with third and fifth degrees of nonlinearity. The equilibrium and stability analysis of the oscillators with graphical representation of solutions in time and phase trajectories is simulated through *XPP-AUT* and *MATLAB*.
It is observed by analysis of the Van der Pol oscillator that a variation of parameters, in particular, an increase of damping, leads to loss of sinusoidal character of the oscillator periodic motion. The frequency and phase place of the oscillator also change with varying parameters simultaneously.
For the Duffing oscillator, the phase trajectories were found consistent with equations proving the stability and equilibrium at the observed locations. Number and character of the equilibrium states are analyzed depending on values of the system parameters. Saddle points and centers are obtained and presented in the phase plot.

Keywords
Oscillator, pacemaker, equilibrium

[1] BITS Pilani K.K Birla Goa Campus, Goa, India
*** Corresponding author:** vaibhav.bajaj393@gmail.com

NONLINEAR DYNAMICS OF DISTRIBUTED SYSTEMS

Proceedings of the 4th International Conference on Nonlinear Dynamics
ND-KhPI2013
June 19-22, 2013, Sevastopol, Ukraine

Aeroelastic Vibrations of Plates Iinteracting with Incompressible Potential Stream

Konstantin V. Avramov[1], Christophe Pierre[2]

Abstract

Cantilever plates with geometrical nonlinearities interacting with potential flows are considered. A solution of the singular integral equations with respect to the aerodynamic derivatives of the plate pressure drop is the basis of the proposed method of aeroelastic vibrations analysis. The Von Karman equations with respect to transversal displacements and the stress function are used to describe the plate vibrations with geometrical nonlinearity. Using the Galerkin method, the nonlinear dynamical system with respect to generalized coordinates is derived to describe the system aeroelastic vibrations. The shooting technique and the continuation algorithm are used to analyze bifurcations and stability of the plate self-sustained vibrations.

Keywords

Singular integral equations with respect to aeroelastic derivatives of the plate, Von Kaman equations, shooting technique and continuation algorithm

[1] A.N. Podgorny Institute for Mechanical Engineering Problems, Kharkov, Ukraine
[2] University of Illinois, USA

* **Corresponding author:** kavramov@ipmach.kharkov.ua

Introduction

The singular integral equations with respect to a circulation density are used basically to analyze the aeroelasticity of the plates in three-dimensional potential flow. The vorticity shed from the trailing edge of the plate and a wake formation are taken into account. This wake effects on the plate vibrations. This leads to long transients, which are analyzed numerically. Then it is impossible to analyze in constructive way the stability and the bifurcations of the steady vibrations.

In this paper the singular integral equations with respect to the plate pressure drop is suggested. The drop of the pressure outside the plate is equal to zero and the wake is not analyzed. Then the system steady-state vibrations can be analyzed using the single harmonic approximation in time of the plate drop of a pressure. Moreover, the methods for stability and bifurcations analysis, such as the harmonic balance, the continuation technique, nonlinear normal modes, will be used to analyze flutter.

The approach for stability and bifurcations analysis of the plate vibrations is developed in this paper. Assuming, that the gas is three-dimensional, potential, inviscid and incompressible, the system of the singular integral equations with respect to the plate drop of the pressure is derived.

The singular integral equation with respect to the pressure acting on the plate was derived by Albano, Rodden [1]. The series of spatial functions were used to approximate the pressure. Katz [2] analyzed the aerodynamics of wings by using the vortex method. Morino, Chen, Suciu [3] suggested the method to predict the flowing of finite thickness curved surfaces. Djojodihardjo, Widnall [4] suggested the numerical procedure to solve the singular integral equation with respect to a circulation density. Hess [5] considered the method to determine the circulation density of three dimensional bodies. Strganac and Mook [6] analyzed the wings flowing at arbitrary angle of attack. The vortex method was used to solve the aerodynamic problem.

1. Problem formulation

Cantilever plate interacting with gas flow is considered. If the plate is turned out in flutter, it performs geometrically nonlinear vibrations. Note, that the boundary conditions on the plate free sides are nonlinear functions of the plate displacements. In this paper the plate vibrations in potential gas flow accounting above-mentioned factors are analyzed.

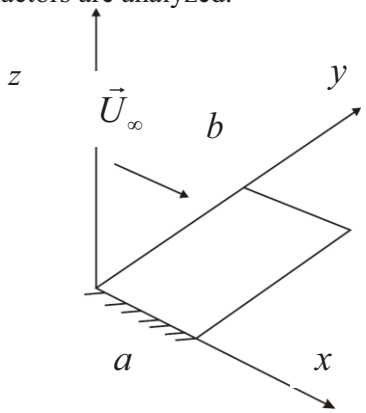

Figure 1. Sketch of the mechanical system

Transversal displacements $w(x,y,t)$ and the stress function $\Phi(x,y,t)$ are used to describe the plate vibrations with geometrical nonlinearities. Then the plate vibrations are described by two Von Karman partial differential equations:

$$D\nabla^4 w + ch\dot{w} + \rho h\ddot{w} + \Delta p = \frac{\partial^2\Phi}{\partial y^2}\frac{\partial^2 w}{\partial x^2} - 2\frac{\partial^2\Phi}{\partial y\partial x}\frac{\partial^2 w}{\partial x\partial y} + \frac{\partial^2\Phi}{\partial x^2}\frac{\partial^2 w}{\partial y^2}; \tag{1}$$

$$\frac{1}{Eh}\nabla^4\Phi = \left(\frac{\partial^2 w}{\partial x\partial y}\right)^2 - \frac{\partial^2 w}{\partial x^2}\frac{\partial^2 w}{\partial y^2}, \tag{2}$$

where $D = \frac{Eh^3}{12\left(1-\nu^2\right)}$; E,ν are the Young's modulus and the Poisson's ratio, respectively; ρ is the density of the plate material; h is the plate thickness; c is the coefficient of linear damping; Δp is the pressure drop acting on the plate. The pressure drop is determined from the solution of the aerodynamic problem, which is treated below.

In this paper, the bending vibrations of the plate $w(x,y,t)$ in the gas flow are described by nonlinear finite-degree-of-freedom dynamical system. Therefore, the bending vibrations of the plate are expanded using the plate eigenmodes $\psi_j(x,y)$ as:

$$w(x,y,t) = \sum_{j=1}^{N_1} q_j(t)\psi_j(x,y), \tag{3}$$

where $q_j(t)$ are the generalized coordinates. The stress function Φ takes the following form:

$$\Phi = \sum_{j=1}^{N_2}\sum_{\nu=1}^{N_3}\theta_{j\nu}(t)F_{j\nu}(x,y). \tag{4}$$

It is assumed, that the plate vibrations are harmonic:

$$q_j(t) \approx \gamma_j\cos(\omega t) + \delta_j\sin(\omega t);\ j = 1,...,N_1. \tag{5}$$

The plate is streamed by three-dimensional, potential, inviscid and incompressible gas. On the significant distance from the plate the flow has constant velocity U_∞, which is parallel to x axis

(Fig.1). The projections of the flow velocities on x, y, z axes are denoted by $\widetilde{u}(x,y,z,t); \widetilde{v}(x,y,z,t); \widetilde{w}(x,y,z,t)$, respectively. The velocity potential $\varphi(x,y,x,t)$ and the pressure $p(x,y,z,t)$ meet the Laplace equation:

$$\nabla^2\varphi = 0; \nabla^2 p = 0; \ \nabla^2\varphi = \frac{\partial^2\varphi}{\partial x^2} + \frac{\partial^2\varphi}{\partial y^2} + \frac{\partial^2\varphi}{\partial z^2}. \tag{6}$$

Now the boundary conditions for the Laplace equations (6) are considered. The velocity potential meets the Sommerfeld radiation condition: $\lim_{x^2+y^2+z^2\to\infty} \text{grad}\varphi = 0$. The nopenetration boundary condition is true on the plate surface:

$$\left.\frac{\partial\varphi}{\partial z}\right|_{z=0} = \frac{\partial w}{\partial t} + U_\infty \frac{\partial w}{\partial x}. \tag{7}$$

The pressure drop

$$\Delta p(x,y,t) = p(x,y,z)\big|_{z=0^+} - p(x,y,z)\big|_{z=0^-};$$

is equal to zero on the plane $z = 0$ outside the plate. Thus, the pressure drop is equal to zero on the plate boundary ∂S:

$$\Delta p\big|_{\partial S} = 0. \tag{8}$$

2. Singular integral equations with respect to aerodynamic derivatives of pressure drop

The aerodynamic derivatives [7] are used to obtain the perturbations of the flow induced by the plate vibrations:

$$\varphi(x,y,z,t) = \sum_{j=1}^{N_1}\left[\varphi_j^{(0)}(x,y,z)q_j(t) + \varphi_j^{(1)}(x,y,z)\dot{q}_j(t)\right]; \tag{9}$$

$$p(x,y,z,t) = \sum_{j=1}^{N_1}\left[p_j^{(0)}(x,y,z)q_j(t) + p_j^{(1)}(x,y,z)\dot{q}_j(t)\right]. \tag{10}$$

Following Belotserkovskii, Skripach [8], the functions $\varphi_j^{(0)}(x,y,z)$, $\varphi_j^{(1)}(x,y,z)$, $p_j^{(0)}(x,y,z)$, $p_j^{(1)}(x,y,z)$ satisfy the Laplace equation:

$$\nabla^2\varphi_j^{(k)} = 0; \quad \nabla^2 p_j^{(k)} = 0; k = 0,1; \ j = 1,...,N_1. \tag{11}$$

The index j indicates the number of eigenmodes, which induced the pressure drop.

The solution of the second equation (11) takes the following form [9]:

$$p_j^{(k)}(x,y,z) = \frac{1}{4\pi}\iint_S \Delta p_j^{(k)}(x_1,y_1)\left[\frac{\partial}{\partial z_1}\left(\frac{1}{r}\right)\right]_{z_1=0} \mathrm{d}x_1\mathrm{d}y_1, \tag{12}$$

where $r = \sqrt{(x-x_1)^2 + (y-y_1)^2 + (z-z_1)^2}$; S is region of the plate middle plane; $\Delta p_j^{(k)}(x_1,y_1) = p_j^{(k)}(x_1,y_1,z_1)\big|_{Z_1=0^+} - p_j^{(k)}(x_1,y_1,z_1)\big|_{Z_1=0^-}$ are aerodynamic derivatives of the plate pressure drop; x_1, y_1 are integration variables.

The Bernoulli equation is used in the following form:

$$p(x,y,z)=-\rho_\infty\left(\frac{\partial\varphi(x,y,z,t)}{\partial t}+U_\infty\frac{\partial\varphi(x,y,z,t)}{\partial x}\right), \tag{13}$$

where ρ_∞ is the gas density. The equations (9, 10) are substituted into the equation (13) and the equation (5) is used. As a result, the following system of the partial differential equations is obtained:

$$U_\infty\frac{\partial\varphi_j^{(0)}}{\partial x}-\omega^2\varphi_j^{(1)}=-\frac{p_j^{(0)}}{\rho_\infty};\ U_\infty\frac{\partial\varphi_j^{(1)}}{\partial x}+\varphi_j^{(0)}=-\frac{p_j^{(1)}}{\rho_\infty}. \tag{14}$$

The method of constants variation is used to solve the equations (14). The solution of this system takes the form:

$$\begin{aligned}\varphi_j^{(0)}(x,y,z)&=B_j^{(1)}(x,y,z)\exp\left(\mathrm{i}\frac{\omega}{U_\infty}x\right)+B_j^{(2)}(x,y,z)\exp\left(-\mathrm{i}\frac{\omega}{U_\infty}x\right);\\ \varphi_j^{(1)}(x,y,z)&=\frac{\mathrm{i}}{\omega}B_j^{(1)}(x,y,z)\exp\left(\mathrm{i}\frac{\omega}{U_\infty}x\right)-\frac{\mathrm{i}}{\omega}B_j^{(2)}(x,y,z)\exp\left(-\mathrm{i}\frac{\omega}{U_\infty}x\right),\end{aligned} \tag{15}$$

where i is the imaginary unit. The solution of the equation (14) takes the form:

$$\begin{aligned}\varphi_j^{(1)}(x,y,z)&=-\frac{1}{U_\infty\rho_\infty\omega}\int\limits_{-\infty}^{x}\left[\omega\,p_j^{(1)}(\xi,y,z)\cos\left(\frac{\omega}{U_\infty}(\xi-x)\right)+p_j^{(0)}(\xi,y,z)\sin\left(\frac{\omega}{U_\infty}(\xi-x)\right)\right]\mathrm{d}\xi;\\ \varphi_j^{(0)}(x,y,z)&=\frac{1}{U_\infty\rho_\infty}\int\limits_{-\infty}^{x}\left[-p_j^{(0)}(\xi,y,z)\cos\left(\frac{\omega}{U_\infty}(\xi-x)\right)+\omega\,p_j^{(1)}(\xi,y,z)\sin\left(\frac{\omega}{U_\infty}(\xi-x)\right)\right]\mathrm{d}\xi.\end{aligned} \tag{16}$$

The expansions (9, 10) are substituted into the boundary condition (7). As a result, the time independent boundary conditions are obtained:

$$\left.\frac{\partial\varphi_j^{(0)}}{\partial z}\right|_{z=0}=U_\infty\frac{\partial\psi_j}{\partial x};\ \left.\frac{\partial\varphi_j^{(1)}}{\partial z}\right|_{z=0}=\psi_j. \tag{17}$$

The solution (12) is substituted into the equation (17) and the result is substituted into (17). As a result, the following system of singular integral equations is obtained:

$$\begin{aligned}&4\pi U_\infty^2\rho_\infty\frac{\partial\psi_j(x,y)}{\partial x}=\\ &-\omega\iint\limits_S\Delta p_j^{(1)}(x_1,y_1)K_S(x-x_1,y-y_1)\mathrm{d}x_1\mathrm{d}y_1+\iint\limits_S\Delta p_j^{(0)}(x_1,y_1)K_C(x-x_1,y-y_1)\mathrm{d}x_1\mathrm{d}y_1;\\ &4\pi U_\infty\rho_\infty\omega\psi_j(x,y)=\\ &\omega\iint\limits_S\Delta p_j^{(1)}(x_1,y_1)K_C(x-x_1,y-y_1)\mathrm{d}x_1\mathrm{d}y_1+\iint\limits_S\Delta p_j^{(0)}(x_1,y_1)K_S(x-x_1,y-y_1)\mathrm{d}x_1\mathrm{d}y_1,\end{aligned} \tag{18}$$

where

$$K_C(x-x_1,y-y_1)=-\int\limits_{-\infty}^{x-x_1}\frac{\cos\dfrac{\omega(\lambda+x_1-x)}{U_\infty}}{\left[\lambda^2+(y-y_1)^2\right]^{3/2}}\mathrm{d}\lambda;\ \ K_S(x-x_1,y-y_1)=-\int\limits_{-\infty}^{x-x_1}\frac{\sin\dfrac{\omega(\lambda+x_1-x)}{U_\infty}}{\left[\lambda^2+(y-y_1)^2\right]^{3/2}}\mathrm{d}\lambda.$$

The kernels $K_C(\tilde{x},\tilde{y})$ and $K_S(\tilde{x},\tilde{y})$ satisfy the following relations: $\lim\limits_{\substack{\tilde{x}\to 0\\ \tilde{y}\to 0}} K_C(\tilde{x},\tilde{y})=\infty$; $\lim\limits_{\substack{\tilde{x}\to 0\\ \tilde{y}\to 0}} K_S(\tilde{x},\tilde{y})=-\infty$.

The following dimensionless variables and the parameters are used:

$$\chi=\frac{\omega\, a}{U_\infty};\ \bar{\lambda}=\frac{\lambda}{a};\ \bar{x}_1=\frac{x_1}{a};\ \bar{y}_1=\frac{y_1}{b};\ \bar{x}=\frac{x}{a};\ \bar{y}=\frac{y}{b};\ r=\frac{a}{b};\ \tau=\omega\, t;\vartheta_i=\frac{q_i}{h};$$
$$K_S=\frac{a\,\bar{K}_S}{b^3};K_C=\frac{a\bar{K}_C}{b^3};\ \Delta\,\bar{p}_j^{(1)}=\frac{\omega\, a\Delta p_j^{(1)}}{\rho_\infty U_\infty^2};\ \Delta\,\bar{p}_j^{(0)}=\frac{a\Delta p_j^{(0)}}{\rho_\infty U_\infty^2},\tag{19}$$

where χ is the Strouhal number. The system of the singular integral equations (18) with respect to dimensionless variables and parameters takes the following form:

$$\iint\limits_{\bar{S}}\left[\Delta\,\bar{p}_j^{(1)}(\bar{x}_1,\bar{y}_1)\bar{K}_C(\bar{x}-\bar{x}_1,\bar{y}-\bar{y}_1)+\Delta\bar{p}_j^{(0)}(\bar{x}_1,\bar{y}_1)\bar{K}_S(\bar{x}-\bar{x}_1,\bar{y}-\bar{y}_1)\right]\mathrm{d}\bar{x}_1\mathrm{d}\bar{y}_1=\psi_j(\bar{x},\bar{y})\frac{4\pi\chi}{r^2};\tag{20}$$

$$\iint\limits_{\bar{S}}\left[-\Delta\,\bar{p}_j^{(1)}(\bar{x}_1,\bar{y}_1)\bar{K}_S(\bar{x}-\bar{x}_1,\bar{y}-\bar{y}_1)+\Delta\bar{p}_j^{(0)}(\bar{x}_1,\bar{y}_1)\bar{K}_C(\bar{x}-\bar{x}_1,\bar{y}-\bar{y}_1)\right]\mathrm{d}\bar{x}_1\mathrm{d}\bar{y}_1=\frac{\partial\psi_j(\bar{x},\bar{y})}{\partial\bar{x}}\frac{4\pi}{r^2};\tag{21}$$

$$\bar{K}_S=-\int\limits_{-\infty}^{\bar{x}-\bar{x}_1}\frac{\sin\chi\left(\bar{\lambda}+\bar{x}_1-\bar{x}\right)}{\left[r^2\bar{\lambda}^2+(\bar{y}-\bar{y}_1)^2\right]^{3/2}}\mathrm{d}\bar{\lambda};\ \bar{K}_C=-\int\limits_{-\infty}^{\bar{x}-\bar{x}_1}\frac{\cos\chi\left(\bar{\lambda}+\bar{x}_1-\bar{x}\right)}{\left[r^2\bar{\lambda}^2+(\bar{y}-\bar{y}_1)^2\right]^{3/2}}\mathrm{d}\bar{\lambda},$$

where $\bar{S}$ is the region of the plate middle plane with respect to the dimensionless coordinates.

The equation (20) is differentiated with respect to $\bar{x}$ and the result is substituted into the equation (21). Then the following singular integral equation is derived:

$$\iint\limits_{\bar{S}}\frac{\Delta\bar{p}_j^{(1)}(\bar{x}_1,\bar{y}_1)\mathrm{d}\bar{x}_1\mathrm{d}\bar{y}_1}{\left[r^2(\bar{x}-\bar{x}_1)^2+(\bar{y}-\bar{y}_1)^2\right]^{3/2}}=-\frac{8\pi\chi}{r^2}\frac{\partial\psi_j(\bar{x},\bar{y})}{\partial\bar{x}}.\tag{22}$$

The index j indicates on the number of eigenmode, which induced the pressure. The equation (21) is differentiated and the result is substituted into (20). Then the following singular integral equation is derived:

$$\iint\limits_{\bar{S}}\frac{\Delta\bar{p}_j^{(0)}(\bar{x}_1,\bar{y}_1)\mathrm{d}\bar{x}_1\mathrm{d}\bar{y}_1}{\left[r^2(\bar{x}-\bar{x}_1)^2+(\bar{y}-\bar{y}_1)^2\right]^{3/2}}=\frac{4\pi}{r^2}\left[\chi^2\psi_j(\bar{x},\bar{y})-\frac{\partial^2\psi_j(\bar{x},\bar{y})}{\partial\bar{x}^2}\right].\tag{23}$$

Numerical vortex method [7] is used to solve the system of singular integral equations (22, 23).

3. Finite – degree-of-freedom model of system vibrations

In order to study aeroelastic vibrations, the Galerkin method is applied to every equation of the system (1, 2), separately. The solution (3, 5) is substituted into the equation (2) and the Galerkin method is applied. The system of linear algebraic equations with respect to the generalized coordinates $\theta_{j\nu}(t)$ is derived:

$$\sum_{j=1}^{N_2}\sum_{\nu=1}^{N_3}A_{rl\,j\nu}\theta_{j\nu}=\sum_{i_1,i_2=1}^{N_1}B_{rl\,i_1\,i_2}q_{i_1}q_{i_2};\ r=1,...,N_2;\ l=1,...,N_3,\tag{24}$$

where

$$A_{rlj\nu}=\int_S\left(\frac{\partial^2 F_{rl}}{\partial x^2}\frac{\partial^2 F_{j\nu}}{\partial x^2}+2\frac{\partial^2 F_{rl}}{\partial x^2}\frac{\partial^2 F_{j\nu}}{\partial y^2}+\frac{\partial^2 F_{rl}}{\partial y^2}\frac{\partial^2 F_{j\nu}}{\partial y^2}\right);$$

$$B_{rli_1i_2}=Eh\int_S\left(\psi_{i_1,xy}\psi_{i_2,xy}-\psi_{i_1,xx}\psi_{i_2,yy}\right)F_{rl}dxdy.$$

The solution of the system (24) takes the form:

$$\theta_{j\nu}=\sum_{i_1,i_2=1}^{N_1}c_{j\nu,i_1i_2}q_{i_1}q_{i_2}. \tag{25}$$

The stress function (4) is substituted into the equation (1) and the Galerkin method is applied. As a result, the nonlinear dynamical system with respect to the generalized coordinates is derived in the following form:

$$\sum_{i=1}^{N_1}\rho h I_{ji}\left(\ddot{q}_i+\frac{c}{\rho}\dot{q}_i+\omega_i^2 q_i\right)+\sum_{i=1}^{N_1}\left(P_{ji}^{(0)}q_i+P_{ji}^{(1)}\dot{q}_i\right)+\sum_{i,i_1,i_2=1}^{N_1}\chi_{jii_1i_2}q_iq_{i_1}q_{i_2}=0, \tag{26}$$

where

$$I_{ji}=\int_S\psi_i\psi_j dxdy;\;\; P_{ji}^{(0)}=\int_S\Delta p_i^{(0)}(x,y)\psi_j dxdy;\; P_{ji}^{(1)}=\int_S\Delta p_i^{(1)}(x,y)\psi_j dxdy;$$

$$\chi_{jii_1i_2}=\int_S\left\{2G_{i_1i_2,xy}\psi_{i,xy}-G_{i_1i_2,yy}\psi_{i,xx}-G_{i_1i_2,xx}\psi_{i,yy}\right\}\psi_j d\,x\,dy;$$

here ω_i are eigenfrequencies of the plate linear vibrations. The dynamical system (26) with respect to dimensionless variables and parameters takes the form:

$$\sum_{i=1}^{N_1}R_{ji}\left(\chi^2\vartheta_i''+\alpha\chi^2\vartheta_i'+\chi_1^2\Omega_i^2\vartheta_i\right)+\varepsilon\sum_{i=1}^{N_1}\left(\chi^2\pi_{1,ji}\vartheta_i+\pi_{2,ji}\vartheta_i+\chi\pi_{3,ji}\vartheta_i'\right)+\chi_1^2\sum_{i,i_1,i_2=1}^{N_1}\alpha_{jii_1i_2}\vartheta_i\vartheta_{i_1}\vartheta_{i_2}=0. \tag{27}$$

4. The results of the numerical analysis

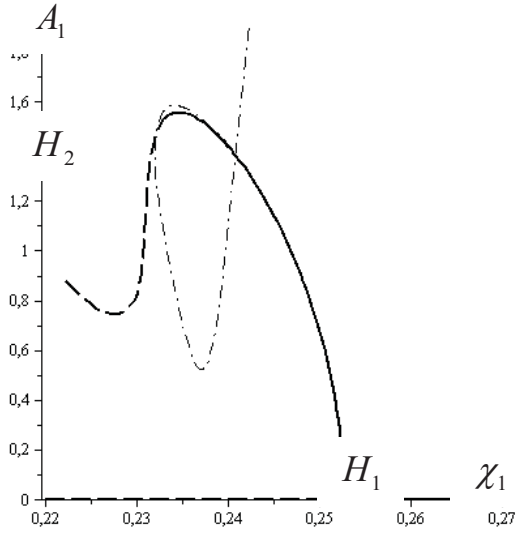

Figure 2. Bifurcation diagram of self-sustained vibrations

The numerical analysis of the dynamical system (26) is carried out using the combination of the shooting method and continuation technique. The results are shown on the bifurcation diagram (Fig.2). If χ_1 is decreased, the equilibrium of the plate loses stability and the Hopf bifurcation takes place. Thus, the plate self- sustained vibrations occur. The Naimark- Sacker bifurcation is observed in the point H_2. As a result of this bifurcation, the almost periodic and chaotic motions are observed.

References

[1] Albano E., Rodden W. P. A doublet-Lattice method for calculating lift distributions on oscillating surfaces in subsonic flows *AIAA Journal*, Vol. 7**,** pp. 279- 285, 1969.

[2] Katz J. Calculation of the aerodynamic forces on automotive lifting surfaces. *ASME Journal of Fluids Engineering,* Vol. 107, pp. 438-443, 1985.

[3] Morino L., Chen L. T., Suciu, E. O. Steady and oscillatory subsonic and supersonic aerodynamics around complex configuration *AIAA Journal*, Vol. 13, pp. 368-374, 1975.

[4] Djojodihardjo R. H., Widnall S. E. A numerical method for the calculation of nonlinear, unsteady lifting potential flow problems *AIAA Journal*, Vol. 7, pp. 2001-2009, 1969.

[5] Hess J. L. Review of integral-equation techniques for solving potential-flow problems with emphasis of the surface-source method *Computer Methods in Applied Mechanics and Engineering*, Vol. 5, pp. 145-196, 1975.

[6] Strganac T. W., Mook D. T. Numerical model of unsteady subsonic aeroelastic behavior. *AIAA Journal*, Vol. 28, pp. 903-909, 1990.

[7] Belotserkovskii S. M., Lifanov I. K. *Method of Discrete Vortices*. CRC Press, New York, 1993.

[8] Belotserkovskii S. M., Skripach B. K. *Aerodynamic Derivatives of Aircrafts and Wings at Subsonic Flows*. Nauka, Moscow (in Russian), 1975

[9] Dowell E. H., Curtiss H. C., Scanlan R. H., Sisto F. *A Modern Course in Aeroelasticity.* Kluwer Academic Publishers, New York. 1995

Proceedings of the 4th International Conference on Nonlinear Dynamics
ND-KhPI2013
June 19-22, 2013, Sevastopol, Ukraine

Dynamics of Structures in the Canonical Parabolic Problem

E. P. Belan[1]*, S. P. Plyshevskaya[2]

Abstract
The scalar parabolic equation at a segment with the Neumann's condition is considered . The dynamics of its stationary structures is investigated when the coefficient of diffusion approaches zero. It is proved that the original problem possesses the orbitally exponentially stable one-parameter family of solutions of the type of internal shock layer for sufficiently small coefficient of diffusion.

Keywords
parabolic problem, bifurcation, stability, Galerkin method, orbitally stability, internal shock layer, stationary structures.

Taurida V. I. Vernadsky National University, , Simferopol, Ukraine
***Corresponding author**: belan@crimea.edu

Introduction

Consider an equation

$$\frac{\partial u}{\partial t} = \mu \frac{\partial^2 u}{\partial x^2} + u - u^3, \quad 0 < x < \pi, \quad t > 0 \tag{1}$$

with boundary conditions of the second kind

$$u_x(0,t) = 0, \quad u_x(\pi,t) = 0 \tag{2}$$

and initial conditions

$$u(x,0) = u_0(x), \tag{3}$$

where is a μ positive parameter. In the space $\overset{0}{H}{}^1(0,\pi)$, this equation generates a dynamical system. Each solution of this equation approaches, as $t \to \infty$, one of its stationary solutions.

The original system of equations belongs to the class of trigger systems with diffusion: -1 and 1 are exponentially stable spatially homogeneous stationary points for any $\mu > 0$ and 0 is an unstable point whose instability index is equal to 1 for $\mu > 1$. The transition of the parameter μ through 1 increases the instability index of the trivial solution by an order of magnitude. As a result, two branches $\pm\varphi_1(x,\mu)$ of spatially inhomogeneous stationary points with instability index 1 continuous in μ bifurcate at the origin.

By using the method of central manifolds, we arrive at the following equality:

$$\varphi_1^{\pm}(x,\mu) = \pm\frac{2}{\sqrt{3}}\sqrt{1-\mu}\cos x + O(1-\mu).$$

As the parameter μ decreases and passes through k^{-2}, $k = 2,\ldots$, the instability index of zero increases (each time) by an order of magnitude. As a result, a pair of stationary points $\pm\varphi_k(x,\mu)$ with instability index k separates from zero. The following inequality is true:

$$\varphi_k^{\pm}(x,\mu) = \pm\frac{2}{\sqrt{3}}\sqrt{1-k^2\mu}\cos kx + O(1-k^2\mu).$$

To study the behavior of the indicated points as the parameter μ deviates from the corresponding bifurcation value, we construct a hierarchy of simplified models of the original problem.

1. Galerkin Approximation

We set

$$u = z_0 + \sum_{k=1}^{N} z_k \cos kx \tag{4}$$

and substitute this representation in (1). Further, equating the coefficients of $\cos kx$, $k = 0,...,N$, we arrive at the gradient system of equations

$$\dot{z}_k = -\frac{\partial G_N(z,\mu)}{\partial z_k}, \quad k = 0,...,N. \tag{5}$$

In system (5), the trivial solution is unstable with instability index 1 for $\mu > 1$. As the parameter μ passes through 1, the instability index of zero increases by an order of magnitude. As a result, two branches of fixed points $\pm z^1(\mu,N)$ defined on $[0,1)$ separate from zero. The zero and all even components of $z^1(\mu,N)$ are equal to zero. The odd components $z^1_{2k+1}(\mu,N)$, $k = 0,1\ldots$, are not equal to zero and, in addition, $(-1)^k z^1_{2k+1} > 0$, $z^1_1 > -z^1_3 > z^1_5 > \ldots$.

Hence, we arrive at the following approximate equality:

$$\varphi_1(x,\mu) \approx \sum_{k=0}^{m} z^1_{2k+1}(\mu,N)\cos(2k+1)x, \tag{6}$$

where $2m+1 = N$ if N is odd and $2m = N$ if N is even.

The presented analysis of Eqs. (6) enables us to make the following conclusions: In the vicinity of 1, the function $\varphi_1(x,\mu)$ has a quasiharmonic form with low amplitude. The amplitude of $\varphi_1(x,\mu)$ increases as μ decreases. The maximum values of $|\,\varphi_1(x,\mu)\,|$ are attained at the points 0 and π. The growth of amplitude of the function $\varphi_1(x,\mu)$ terminates as soon as it becomes equal to 1. The subsequent decrease in μ is accompanied by the growth of intervals adjacent to 0 and π in which $\varphi_1(x,\mu)$ takes constant values 1 and –1, respectively. As soon as μ attains a certain value depending on N according to (6), we observe the development of the Gibbs phenomenon: $\varphi_1(x,\mu)$ begins to oscillate. As N increases, the amplitude of oscillations decreases and their frequency increases. Thus, for small μ, $\varphi_1(x,\mu)$ is a solution of the internal shock (transient) layer.

In Figure 1, we present the plot of the function $\varphi_1^+(x,\mu)$ for various values of the parameter μ.

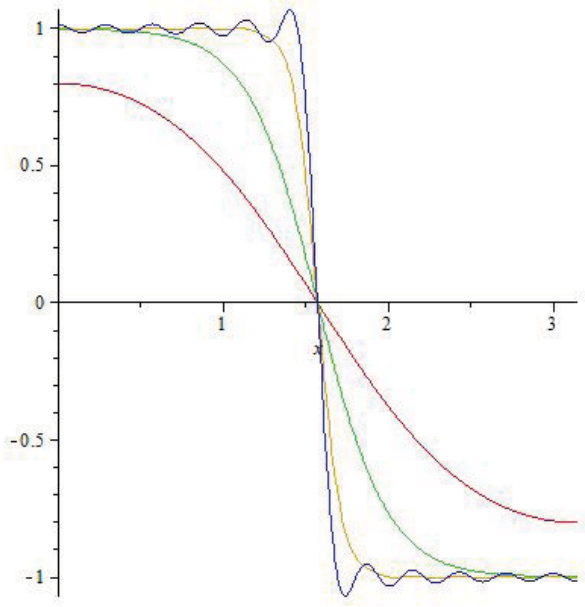

Figure 1. Plot of the function $\varphi_1^+(x,\mu)$ for $\mu = 0.5$, $\mu = 0.09$, $\mu = 0.01$, $\mu = 0.001$

We now pass to the problem of stability of φ_1. As already indicated, $\pm\varphi_1(x,\mu)$ are born unstable with instability index 1. The stationary points $\pm z^1(\mu,N)$ are also unstable with instability index 1. The spectrum of the stability matrix $z^1(\mu,N)$

$$-\frac{\partial^2 G_N(z,\mu))}{\partial z^2}\,|_{z=z^1(\mu,N)} \tag{7}$$

lies on the real axis and its maximal point $\lambda_1(\mu,N)$ belongs to the positive semiaxis. The other points of the spectrum $z^1(\mu,N)$ lie on the negative semiaxis. The value of $\lambda_1(\mu,N)$ decreases as μ decreases from 1. In this case, the points of the spectrum become closer. The minimal point of the spectrum increases and its maximal negative point decreases. The indicated dynamics of the spectrum takes place within the interval $(0.11,1)$ of changes in the parameter μ. Beyond this interval, the dynamics of $\lambda_1(\mu,N)$ depends on N. We now describe the behavior of $\lambda_1(\mu,N)$ for N greater or equal to $N=5$. The function $\lambda_1(\mu,5)$ is monotonically increasing on $[0,1)$, $\lambda_1(0,5)\approx -0.19$, and $\lambda_1(0.209,5)=0$. The function $\lambda_1(\mu,6)$ is monotonically decreasing on $[0,0.11)$ and $\lambda_1(0,6)=0.16$. We now note that $\lambda_1(\mu,2k+1)$ is a monotonically increasing function in the interval $(0,\mu_1^*(2k+1))$ and $\lambda_1(\mu,2k)$ is a monotonically decreasing function in the interval $(0,\mu_1^*(2k))$. The following inequalities are true:

$$\lambda_1(0,2k-1)<\lambda_1(0,2k+1) \quad \text{and} \quad \lambda_1(0,2(k-1))>\lambda_1(0,2k).$$

These inequalities are obtained as a result of numerical calculations performed for the values of N from 5 to 30. There are serious reasons to believe that these inequalities remain valid for $N>30$.

According to the numerical results, for $N\geq 10$, we get the following principal feature of the function $\lambda_1(\mu,N)$: $\lambda_1(\mu,N)=0$ in the interval $(\mu^1(N),\mu^2(N))$. We can present the following examples: $\mu^1(22)=0.04$, $\mu^2(22)=0.07$; $\mu^1(23)=0.03$, $\mu^2(23)=0.076$; $\lambda_1(0.08,22)=0.000014$, and $\lambda_1(0.03,22)=0.000032$.

The results presented above enable us to make the following conclusion: For small μ, the spectrum of the stationary point $\varphi_1(\cdot,\mu)$ of the original problem contains 0.

We now justify this assertion.

By using the equality

$$\varphi_1(x,\mu)=\sum_{k=1}^{\infty}\varphi_{1,k}(\mu)\cos(2k+1)x,$$

we continue the function $\varphi_1(x,\mu)$ onto the real axis by periodicity.

The function continued in this way to $\mathbb{R}$ is denoted by $\varphi_1(x,\mu)$. It is clear that $\varphi_1(x,\mu)$ satisfies Eq. (1) on $\mathbb{R}$. Hence, $\varphi_1(x+\alpha,\mu)$ also satisfies this equation for any $\alpha\in(-\frac{\pi}{2},\frac{\pi}{2})$. If μ is located near the critical value, then, for any small $\alpha\neq 0$, the function $\varphi_1(x+\alpha,\mu)$ does not satisfy the boundary conditions (2).

By using the results based on the asymptotic methods [2],[3], we conclude that, for small $\mu>0$ and any $|\alpha|<\delta$, $\delta=\delta(\mu)$, the function $\varphi_1(x+\alpha,\mu)$ is an approximate solution of (1). This means that, for small μ, $\varphi_1(\cdot,\mu)$ is a point of an orbitally exponentially stable one-parameter family of stationary points.

This family is a one-parameter family of solutions of the type of internal shock layer [2],[3]. Each element of this family of solutions is determined by the transition point. Thus, the original problem has the following specific feature: If the parameter μ is located near the critical value 1, then there exists an isolated stationary solution $\varphi_1(x,\mu)$ monotonically decreasing in the interval $[0,\pi]$ and such that $\varphi_1(\frac{\pi}{2},\mu)=0$ and $\varphi_1(\pi-x,\mu)=-\varphi_1(x,\mu)$. As the parameter μ decreases and passes through the value specified by the condition $\varphi_1(0,\mu)=1$, the function $\varphi_1(x,\mu)$ turns into a solution of the type of internal shock layer with transition point $\frac{\pi}{2}$. In this case, we observe the loss of the isolated character of the stationary solution $\varphi_1(x,\mu)$. For small $\mu>0$, the original problem possesses a one-parameter family of solutions of the shock-layer type, i.e., a solution of the shock-layer type passes through every point of $(0,\pi)$. The problem of the character of bifurcation connected with the transition from the isolated

solution to a one-parameter family of solutions of the shock type is of significant interest. To solve this problem, we consider simplified models (5) of the original problem.

In the gradient systems (5), as the parameter μ decreases, we observe the realization of a great variety of saddle-node bifurcations. The bifurcations leading, by virtue of (4), to the solutions of the shock-layer type with one transition point are characterized by the following specific features: For fixed N, the bifurcation values of the parameter μ are close. The branches of stationary points born stable or unstable are defined for all positive values of the parameter μ lower than the corresponding bifurcation value. The character of stability of the analyzed branches of stationary points within the indicated range of the parameter μ is preserved. The spectra of stationary points of the indicated type almost coincide. As the parameter μ decreases, the highest points points of these spectra slowly move from zero. The stationary points in the branch slowly vary as the parameter μ decreases.

2. Numerical Analysis

To illustrate these observations, we now present examples of saddle-node bifurcations for $N = 22$. Thus,

$$\mu = 0.03, \quad (\,0.309,\ 1.098, -0.477, -0.038,\ 0.205, -0.111, \dots),$$

$$\{-2.000, -1.499, -0.000035\};$$

$$\mu = 0.0297, \quad (\,0.408,\ 0.995, -0.554,\ 0.119,\ 0.120, -0.146, \dots),$$

$$\{-2.000, -1.497, -0.000016\};$$

$$\mu = 0.031, \quad (\,0.046,\ 1.238, -0.083, -0.332,\ 0.062,\ 0.134, \dots),$$

$$\{-2.000, -1.500,\ 0.000048\};$$

$$\mu = 0.0285, \quad (\,0.044,\ 1.240, -0.080, -0.339,\ 0.061,\ 0.141, \dots),$$

$$\{-2.000, -1.500, -0.000044\};$$

$$\mu = 0.0275, \quad (\,0.399,\ 1.007,\ -0.553,\ 0.107,\ 0.133, 0.152, \dots),$$

$$\{-2.000, -1.498, -0.00006\};$$

$$\mu = 0.0273, \quad (\,0.132,\ 1.218,\ -0.235, -0.283,\ 0.168,\ 0.077, \dots),$$

$$\{-2.000, -1.500, -0.000059\}.$$

It is clear that the next point of the spectrum after the maximal point along the negative semiaxis is located near -1.500.

The solutions of the shock type with different transition points are presented in Figure 2. These approximate solutions correspond to the bifurcation values of the parameter μ obtained for system (5) in which $N = 22$.

We emphasize that the dependence of stationary points born as a result of saddle-node bifurcations on the parameter μ is weak. We now present an example illustrating this observation. For $\mu = 0.000001$, the stable wave of stationary points born at $\mu \approx 0.0285$ corresponds to the point

$$(\,0.044,\ 1.268, -0.088, -0.411,\ 0.086,\ 0.233, \dots).$$

Hence, the changes in the spectrum are also insignificant. The indicated point corresponds to the following three maximal points of the spectrum: $\{-1.807, -1.542, -0.052\}$. A similar behavior is also demonstrated by the unstable branches of stationary points with instability index 1.

The saddle-node bifurcations corresponding, for the original problem, to the solutions of the shock-layer type with one transition point are realized for systems (5) with different N. We observe the following regularity: As N increases, the corresponding bifurcation value of the parameter decreases. Thus, the

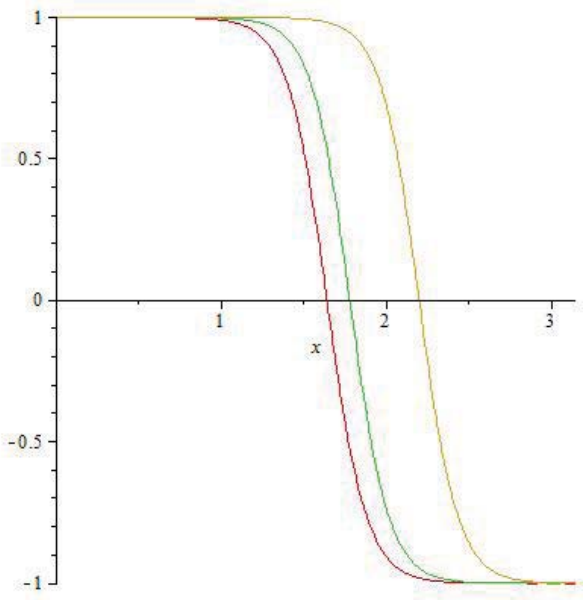

Figure 2. $\mu_1^* = 0.0285 \quad \{-2.0000, -1.5001, -0.00004\}$, $\mu_2^* = 0.0273 \quad \{-2.0000, -1.5000, -0.00005\}$, $\mu_3^* = 0.0275 \quad \{-2.0000, -1.4982, -0.00006\}$

bifurcation value ≈ 0.0275 of the parameter μ for $N = 21$ corresponds to the bifurcation value ≈ 0.0252 for $N = 22$. In this case, the following point is born stable:

$$(\ 0.497,\ 0.886, -0.587,\ 0.247,\ 0.0042, -0.112, \dots), \quad \{-2.000, -1.499, -0.00003\}.$$

The bifurcation value $\mu = 0.025$ for $N = 21$ corresponds to the bifurcation value $\mu = 0.02$ for $N = 22$.

We study the behavior of the function $\varphi_2(x,\mu)$ as μ decreases from the critical value 2^{-2}. In view of the equality

$$\varphi_2(x,\mu) = \varphi_1(2x, 4\mu)$$

and the already discussed behavior of the function $\varphi_1(x,\mu)$ as μ decreases, the behavior of the function $\varphi_2(x,\mu)$ becomes clear. In this connection, we emphasize that, for small μ, the function $\varphi_2(x,\mu)$ is a solution of Eq. (1) of the shock-layer type with transition points $(\frac{\pi}{4}, \frac{3\pi}{4})$.

We now pass to the problem of stability of $\varphi_2(x,\mu)$. To this end, we again consider system (5). For any N, the instability index of zero in system (5) increases by 1 as the parameter μ decreases and passes through the value 2^{-2}. As a result of this bifurcation, two continuous branches of fixed points $\pm z^2(\mu,N)$ determined on $[0,\ 2^{-2})$ separate from the origin. The following components of $z^2(\mu,N)$ are nonzero: $z_2^2,\ z_6^2, \dots$. The points $\pm z^2(\mu,N)$ are born unstable with instability index 2. For the two points of the spectra of the fixed point $z^2(\mu,N)$, we have $\lambda_1^2(\mu,N) > \lambda_2^2(\mu,N) > 0$, and the other points belong to the negative semiaxis. The functions $\lambda_k^2(\mu,N), k = 1,2$, decrease as the parameter μ decreases. In this case, the minimal point of the spectrum increases and the maximal negative point decreases. If $N = 2(2k+1)$, then $\lambda_k^2(\mu,N), k = 1,2$, are nonnegative functions in $[0,\ 2^{-2})$ and, in addition, $\lambda_k^2(0,N) < 0$. Thus, in this case, $\lambda_k^2(\mu,N), k = 1,2$, move from the positive semiaxis to the negative semiaxis. We emphasize that the values of the parameter μ for which this transition is realized are sufficiently close. As an illustration of this type of behavior of the spectrum, we present some examples restricting ourselves to the case $N = 22$. Thus, we indicate the four highest points of the spectrum:

$$\mu = 0.030, \quad \{-1.498, -1.480,\ 0.00021,\ 0.00007\};$$
$$\mu = 0.029, \quad \{-1.498, -1.482,\ 0.00015,\ 0.00003\};$$
$$\mu = 0.027, \quad \{-1.499, -1.486,\ 0.00004, -0.00003\};$$
$$\mu = 0.025, \quad \{-1.499, -1.489, -0.00012, -0.00005\};$$

$$\mu = 0.023, \quad \{-1.500, -1.492, -0.00023, -0.00017\};$$
$$\mu = 0.020, \quad \{-1.501, -1.495, -0.00050, -0.00042\};$$
$$\mu = 0.010, \quad \{-1.522, -1,512, -0.00656, -0.00602\};$$
$$\mu = 0.001, \quad \{-1.742, -1.644, -0.08016, -0.07943\}.$$

In addition, if $N \neq 2(2k+1)$, then two positive points of the spectrum also become lower as the parameter μ decreases. However, we do not observe their transition through 0. Starting from a certain value of the parameter μ depending on N, the positive points of the spectrum slowly increase. If $N = 21$, then this value of the parameter $\mu \approx 0.021$. The value $\mu = 0.021$ is associated with the following four points of the spectrum of the stationary point z^2: $\{-1.501, -1.497,\ 0.00089,\ 0.00081\}$. As the parameter μ decreases further, the growth of the maximal points is slow. In the case where $N = 21$ and $\mu = 0.01$, we have the following maximal points of the spectrum of the point z^2: $\{-1.532, -1.5168,\ 0.0103,\ 0.0098\}$. The facts presented above enable us to make the following conclusion: There exists a value of the parameter μ_2^s such that, for $\mu < \mu_2^s$, the spectrum of stability of $\varphi_2(x, \mu)$ contains 0 with geometric multiplicity 2 and the remaining spectrum lies on the negative semiaxis. The appearance of the outlined structure of the spectrum of stationary structure $\varphi_2(x, \mu)$ is explained by the fact that, for $\mu < \mu^s{}_2$, the point $\varphi_2(\cdot, \mu)$ is a point of the two-parameter family of solutions of the shock-wave type. The indicated family of stationary points is orbitally exponentially stable. Each point of this family is determined by two parameters (transition points).

Note that the approximate solutions of the shock-layer type with two transition points correspond to the stationary points of system (5) appearing as a result of saddle-node bifurcations. These saddle-node bifurcations have the following specific features:

We present an example of bifurcation of this sort for system (5) in which $N = 21$. In this case, a saddle-node bifurcation is realized for $\mu \approx 0.0135$. For $\mu = 0.0135$, this system has two close points:

$$(-0.088, -0.307,\ 1.143,\ 0.196,\ 0.117,\ 0.256, \dots),$$

$\{-2.002, -1.5097, -1.4994, -0.0049,\ 0.00026\}$ and

$$(-0.044, -0.392,\ 1.105,\ 0.291,\ 0.048,\ 0.281, \dots),$$

$\{-2.001, -1.501, -1.4870, -0.0018, -0.0016\}$.

Here, together with the stationary points, we present the corresponding five maximal points of the spectrum.

Conclusions

Existence of an orbital asymptotically stable family of stationary solutions of the considered problem for sufficiently small coefficient of diffusion is shown in this article. Points of the family are stationary solutions of internal transition layer, which are constructed using the Galerkin method.

References

[1] Henry D. *Geometric theory of semilinear parabolic equations*, Lect. Notes Math., Berlin–Heidelberg–New York: Springer, 1981.

[2] Vasil'eva A.B., Butuzov V.F. *Asymptotic methods in a singular perturbation theory*, Vyssh. Shkola, Moscow, 1990.

[3] Chang K.W., Howes F.A. *Nonlinear singular perturbation phenomenon*, New York–Berlin–Heidelberg–Tokyo, 1984.

Proceedings of the 4th International Conference on Nonlinear Dynamics
ND-KhPI2013
June 19-22, 2013, Sevastopol, Ukraine

Dynamic Analysis of a Slender Microbeam by Means of the Homotopy Analysis Method

Pierpaolo Belardinelli[1]*, Stefano Lenci[1]

Abstract
This paper employs the strain-gradient elasticity theory to derive the non linear mechanical equation for a slender microbeam with an electrical actuation. The microbeam is fixed at both edges and a geometric nonlinearity is also present accounting for the axial stretch. A reduced-order model for the governing equation of motion is obtained and the single-degree-of-freedom problem is studied. Particular attention is paid to investigate the influence of the high-order length scale parameters, introduced by the non-classical theory, that progressively modifies the oscillating behaviour. Adopting the homotopy analysis method (HAM), the free vibrations of the beam are investigated and the effects of several parameters, such an applied axial load, are analyzed. The results on the nonlinear phenomena reveal both an hardening and a softening behaviour, in competition between them. As a benchmark for the analytical results, a numerical solution is also proposed.

Keywords
MEMS, microbeam, HAM, strain-gradient elasticity theory

[1]DICEA, Polytechnic University of Marche, 60131 Ancona, Italy
*__Corresponding author__: p.belardinelli@univpm.it

Introduction

Control and design of Micro-electro-mechanical systems (MEMS) is, nowadays, a fundamental step in widely different engineering fields. Other than mechanical applications, as micro switches, micro-electromechanical silicon resonators [1], biological and biomedical applications have become field of particular interest with widespread use in a variety of activities.

The approaches on an electrically actuated microbeam problem depend on the assumptions on the mechanical and electrical features, developing more or less complex and easy-to-use models. Furthermore, to perform a better characterization and in order to advance in the MEMS dynamic knowledge [2], new techniques and models are developed and applied to microbeam problems. The mechanical modeling of an electrically-actuated microbeams, is, often, based on the classical mechanics [3]. Recently, the modeling in microstructures is moving towards the non-classical continuum theories [4]. The deformation, when the characteristic length is on the micro scale order, has been shown to be size dependent [5], and high-order elastic theories can catch this phenomena. The non-classical approach increments the order of the governing differential equations introducing high-order length scale material parameters [6; 7]. This work wants to apply the modified strain-gradient elasticity proposed by [8] at an electrically-actuated clamped-clamped microbeam. An electric actuation, caused by an applied voltage difference, introduces into the model a nonlinear electric term. The model includes also the effect of the axial stretch, that generates a nonlinear integro-differential term.

In this work the analytical approximation, performed by means of the homotopy analysis method (HAM) [9], is used to investigates the beam dynamics. The homotopic approach is often a valid alternative to the perturbation techniques avoiding any type of small/large physical parameters and providing an efficient approximations [10]. The method has already been applied to a microbeam problem [11], but with a different model derived from the classical theory. Moreover, contrary to the numerical solution, an analytical approximation is a lightweight method to perform a parametric analysis.

1. Problem Formulation

We consider the system in Figure 1, composed by an upper moving electrode and a stationary lower substrate, separated by a dielectric medium. An electric force acts on the upper microbeam due to the applied electric voltage difference between the two electrodes, provoking a deformation. A dielectric medium, having a relative permittivity ε_r, refereed to the vacuum permittivity ε_0, separates the microbeam from the electric ground.

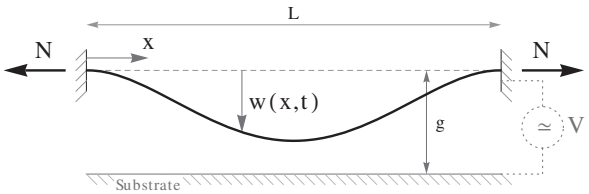

Figure 1. The 1-D model for the electrically actuated microbeam with the main geometrical dimensions

The equation governing the transverse deflection of an electrically actuated slender microbeam, modelled within the framework of the modified strain-gradient elasticity theory, reads [12]:

$$\ddot{w} + c\dot{w} + w^{iv} - \alpha_3 w^{vi} - \left(N + \alpha_1 \int_0^1 \left(w'\right)^2 dx\right) w'' = \frac{\alpha_2 V^2}{\left(1-w\right)^2} \tag{1}$$

The right-hand side of the equation represents the nonlinear electric actuation generated by the applied potential difference V. We remark that the integro-differential term is due to considering a second-order axial stretch in the beam-model formulation. For a device clamped at both edges, the associated dimensionless boundary conditions are:

$$w = w' = w'' = 0 \quad \text{at} \quad x = 0, 1 \tag{2}$$

All the variables in the problem (1-2) are dimensionless: the transverse deflection w and the dimensionless longitudinal coordinate x are normalized, respectively, with respect to the initial gap g and the beam length L, while the dimensionless time is normalized by means of the term: $\sqrt{\left(\rho S L^4\right)/D_1}$. The nondimensional constants and parameters in Eq. (1) are given as follows:

$$\alpha_1 = \frac{ESg^2}{2D_1},\ \alpha_3 = \frac{D_2}{D_1 L^2},\ c = \frac{\hat{c}L^4}{\sqrt{\rho S L^4 D_1}},\ N = \frac{ESN_0L^2}{D_1},\ \alpha_2 V^2 = \frac{bL^4\varepsilon_0\varepsilon_r}{2D_1 g^3}V^2 \tag{3}$$

$\hat{c}$ is the mechanical damping, ρ and S indicate the density and the beam cross section, respectevely, while with N_0 we take into account for an axial load generated by fabrication defects. Consequently the use of the strain-gradient elasticity theory, the equations of motion are enriched with further material parameters, namely $l_n (n = 0; 1; 2)$:

$$D_1 = EI + \mu S\left(2l_0^2 + \frac{8}{15}l_1^2 + l_2^2\right), \quad D_2 = \mu I\left(2l_0^2 + \frac{4}{5}l_1^2\right) \tag{4}$$

where μ is the Lamé's second parameter and EI represents the bending stiffness (E is the Young's modulus and I is the moment of inertia). Contrary to the classical theory, the formulation presented in Eqs. (1, 2) is characterized by: i) the appearance in Eq. (1) of the sixth-order differential term; ii) the non-classical boundary conditions ($w''(0) = w''(L) = 0$ for a fully clamped beam) in Eq. (2).
We write the beam deflection as the sum of a static (w_s) and a dynamic (w_d) response of the system, obtaining:

$$w_s^{iv} + w_d^{iv} - \alpha_3 w_s^{vi} - \alpha_3 w_d^{vi} + c\dot{w}_d + \ddot{w}_d = \left[N + \alpha_1 \int_0^1 \left(w_s'^2 + 2w_s'w_d' + w_d'^2\right) dx\right]\left(w_s'' + w_d''\right) + \\ + \frac{\alpha_2 V^2}{\left(1-w_s\right)^2\left(1 - w_d/\left(1-w_s\right)\right)^2} \tag{5}$$

and

$$w_s + w_d = 0, \quad w_s' + w_d' = 0, \quad w_s'' + w_d'' = 0, \quad \text{at} \quad x = 0,1 \tag{6}$$

Preliminarly the static problem must be solved [13], using the static solution w_s in Eqs. (5, 8) we have:

$$w_d^{iv} - \alpha_3 w_d^{vi} + c\dot{w}_d + \ddot{w}_d - N w_d'' - \alpha_1 \int_0^1 \left(2w_s' w_d' + {w_d'}^2\right) dx\, w_s'' + \\ - \alpha_1 \int_0^1 \left({w_s'}^2 + 2w_s' w_d' + {w_d'}^2\right) dx\, w_d'' = \alpha_2 \left(2V_{dc}V_{ac} + V_{ac}^2\right)\eta_0 + \alpha_2 V^2 \sum_{k=1}^{n} w_d^k \frac{c_i}{(1-w_s)^{i+2}} \tag{7}$$

and

$$w_d = w_d' = w_d'' = 0 \tag{8}$$

The constants c_i in Eq. (7) are the coefficients of an optimal polynomial series approximation (truncated at the order n) for the nonlinear electric term [12; 14]. This is a crucial task to get a reliable and analytical-solvable single-degree-of-freedom problem.

1.1 Reduced-order model

Using the Galerkin decomposition method we discretize the continuous problem ruling out the spatial dependence in Eq. (7). We assume:

$$w_d(x,t) = \sum_{i=1}^{\infty} \phi_i(x) u_i(t) \tag{9}$$

Substituting Eq. (9) into Eq. (7), multiplying for the function ϕ_i and integrating from 0 to 1, for the $i-th$ degree of freedom we have:

$$\ddot{u}_i + c\dot{u}_i + K_i u_i + \sum_j C_{ij} u_i u_j + \sum_{j,k} E_{ijk} u_i u_j u_k = F_{0i} + \\ + F_{1i} u_i + \sum_j F_{2ij} u_i u_j + \sum_{j,k} F_{3ijk} u_i u_j u_k + \sum_{j,k,m} F_{4ijkm} u_i u_j u_k u_m + \ldots + \sum_{j,k,m,..,n} F_{nijkm\ldots n} u_i u_j u_k u_m \ldots u_n \tag{10}$$

To save space the expressions of the coefficients are here not reported but can be easily calculated as previously described. The coefficients F are related to the electric actuation, C and E depend on α_1, while K depends on the paramenters α_1, α_3 and N.

The spatial functions ϕ_i in (9) are picked up in the set of the linear undamped modal shapes. They are the solution of the eigenvalue problem given by Eq. (7) assuming an harmonic motion of the form $w_d(x,t) = \phi_n(x) e^{i\omega t}$ and neglecting the terms involving the forcing terms:

$$\phi_n^{iv} - \alpha_3 \phi_n^{vi} - N \phi_n'' = \omega_n^2 \phi_n \tag{11}$$

The eigenpair $\{\phi_n, \omega_n\}$ is the nth vibrating mode and its own natural (circular) frequency. Considering the undamped single-degree-of-freedom problem with $V_{ac} = 0$, Eq. (10) can be written in the simple form of:

$$\ddot{u} + a_1 u + a_2 u^2 + a_3 u^3 + \ldots + a_n u^n = 0 \tag{12}$$

where the a_i are linear combinations of the coefficients appearing in Eq. (10). For the sake of simplicity we use to indicate only with u, dropping the subscript one, the first dynamic response u_1.

1.2 H.A.M. homotopy analysis method

We briefly report the main features of the homotopy analysis method, that, however, can be found with more details in [11]. Defining a new independent variable $\tau = \omega t$, the Eq. (12) becomes:

$$\omega^2 \frac{d^2 u}{d\tau^2} + \sum_{i=1}^{n} a_i u^i = 0 \tag{13}$$

the problem is completed by the imposed initial conditions:

$$u(0) = A \quad \text{and} \quad \dot{u}(0) = 0 \tag{14}$$

According to [9] it can be constructed a two-parameter family of equations, called the zero-th order deformation equation, that read:

$$(1-q)\,\mathscr{L}\left[u(\tau;q) - u_0(\tau)\right] = q\hbar\mathscr{N}\left[u(\tau;q);\omega(q)\right] \tag{15}$$

with $q \in [0,1]$ and $\hbar$ respectively the embedding and the convergence-control parameter. By means of Eq. (15), varying q, the solution of the auxiliary problem $u(\tau;q)$, depending also on q, deforms from $u(\tau;0) = u_0(\tau)$, the initial guess, to $u(\tau;1) = u(\tau)$, the solution of ours nonlinear problem. $\mathscr{L}$ and $\mathscr{N}$ are respectively the associated linear and nonlinear auxiliary operator, defined as:

$$\mathscr{L}\left[u(\tau;q)\right] = \omega_0^2\left(\frac{\partial^2 u(\tau;q)}{\partial\tau^2} + u(\tau;q)\right), \quad \mathscr{N}\left[u(t;q),\omega(q)\right] = \left[\omega(q)\right]^2\frac{d^2u(t;q)}{d\tau^2} + \sum_{i=1}^{n} a_i\left[u(t;q)\right]^i \tag{16}$$

Since, as consequence of the way we defined the auxiliary operators, $u(\tau;q)$ and $\omega(q)$ depend on q, they can be expanded in Maclaurin series:

$$u(\tau;q) = u_0(\tau) + \sum_{m=1}^{\infty} u_m(\tau)q^m, \qquad \omega(q) = \omega_0 + \sum_{m=1}^{\infty}\omega_m q^m \tag{17}$$

Differentiating the zeroth-order deformation equation, Eq. (15), and computing for $q = 0$, we obtain the high-order deformation equation:

$$\mathscr{L}\left[u_m(\tau) - \chi_m u_{m-1}(\tau)\right] = \hbar R_m\left(u_1,...,u_{m-1},\omega_1,...,\omega_{m-1}\right) \tag{18}$$

with

$$\chi_m = \begin{cases} 0, & \text{if } m \le 0 \\ 1, & \text{if } m > 0 \end{cases} \tag{19}$$

and

$$R_m\left(u_1,...,u_{m-1},\omega_1,...,\omega_{m-1}\right) = \frac{1}{(m-1)!}\frac{\partial^{m-1}\mathscr{N}\left[u(t;q);\omega(q)\right]}{\partial q^{m-1}}\Bigg|_{q=0} \tag{20}$$

The secular term elimination requires that:

$$\frac{1}{\pi}\int_0^{2\pi}\hbar R_m\cos\tau d\tau = 0 \tag{21}$$

The imposition of secular term vanishing successively gives the solutions for ω_{m-1}. Furthermore the solutions of $u_m(\tau)$ are given from:

$$u_m(\tau) = \chi_m u_{m-1}(\tau) + \frac{\hbar}{\omega_0^2}\sum_{k=2}^{j(m)}\frac{b_{m,k}\cos(k\tau)}{(1-k^2)} + d_1\cos\tau + d_0 \tag{22}$$

with $j(m)$ an integer number depending on m, and d_0 and d_1 are constants calculate with the initial conditions (14).

2. Results and Conclusions

In this section we compare the analytical approximations of the HAM with the numerical results obtained by a Runge-Kutta integration scheme. The HAM is always used with a convergence parameter of $\hbar = -1$, it assures a wide range of convergence.

Figure 2 illustrates the amplitude of the dynamical response with respect to the nonlinear frequency. With the H.A. method we have a good approximation for the non-linear response for a quite large

amplitude; the agreement decreases with the the amplitude growth; this phenomenon progressively requires, because of the highly non-linear behaviour, an higher-order solution.

The number of terms retained in the HAM solution grows exponentially as the order of the approximation is increased and therefore, in equation (22), we truncated the approximate solution at $m = 3$. For larger values of m, the computational time becomes comparable to the computational time of a long-time numerical integration. In all the simulation, except where indicated, an $8th$-order Chebyshev approximation is used for the non-linear electric term.

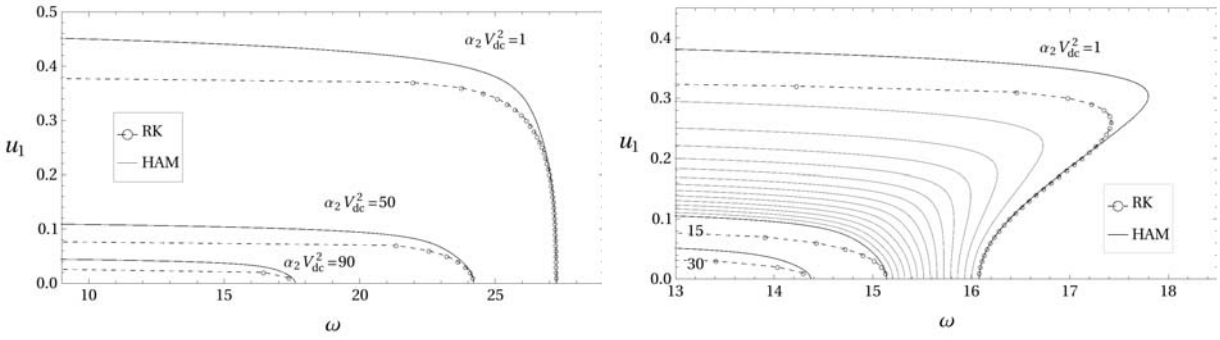

(a) $N = -20$, $\alpha_1 = 0$, $\alpha_3 = 10^{-7}$ (b) $N = 20$, $\alpha_1 = 10$, $\alpha_3 = 10^{-7}$

Figure 2. Amplitude of u_1 versus ω with a comparison between H.A.M. (solid line) and $4th$ order Runge-Kutta (circles), for different static working regimes.

In subfigure 2(a) a global softening response is shown; the dynamic instability phenomenon happens immediately near the static pull-in (lower curves), while, decreasing the static electric field, a larger value of the amplitude is needed so the instability occurs. Beside the same graphical arrangement of 2(a), where the analysis involves three different regimes, in subfigure $2(b)$ we also illustrate (lighter gray curves) the transition from the mechanical hardening effect, driven by the parameter α_1, to the soft response due to the electric field. Both subfigures 2(a) and 2(b) show, after a nonlinear transient, a sudden decreasing of the response frequency: the dynamic pull-in [15]. We finally investigate on the

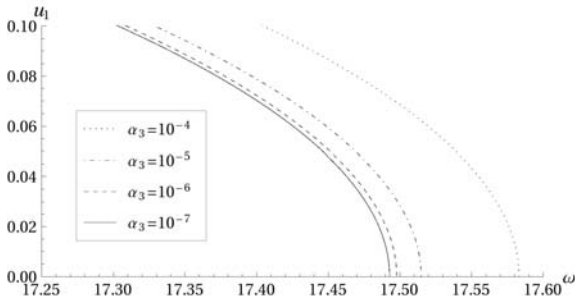

Figure 3. Variation of the nonlinear dynamic response for different values of α_3. Others parameters are $N = -10$, $\alpha_2 V_{dc}^2 = 25$, $\alpha_1 = 0$

influence of α_3, the parameter generated by the use of the strain-gradient elasticity theory in the beam modeling. In Fig. 3, several back-bone curves, obtained for different values of α_3, show the variation of the nonlinear frequency responses due to the high-order length scale parameters. An increasing value of α_3, progressively reduces the values of the nonlinear frequency for a fixed response amplitude. The homotopic approach, still given a very satisfactory uniform approximation, requires a too high-order solution. However, a low order H.A.M. solution can be successfully used for a low values of the electric field. The performed parametric analysis, simplified by the use of the analytical method, as shown the

double hardening/softening behaviours in competition between them, and the different approaches of the device towards the dynamic pull-in.

Acknowledgments

This work was partially supported by the Italian Ministry of Education, University and Research (MIUR) by the PRIN funded program 2010/11 N.2010MBJK5B "Dynamics, Stability and Control of Flexible Structures".

References

[1] Mestrom R.M.C., Fey R.H.B., van Beek J.T.M., Phan K.L., and Nijmeijer H. Modelling the dynamics of a mems resonator: Simulations and experiments. *Sensors and Actuators A: Physical*, Vol. 142, pp. 306–315, 2008.

[2] Li H., Preidikman S., Balachandran B., and Mote Jr C.D. Nonlinear free and forced oscillations of piezoelectric microresonators. *Journal of Micromechanics and Microengineering*, Vol. 16, pp. 356, 2006.

[3] Abdel Rahman E.M., Younis M.I., and Nayfeh A.H. Characterization of the mechanical behavior of an electrically actuated microbeam. *Journal of Micromechanics Microengineering*, Vol. 12, pp. 759–766, 2002.

[4] Kahrobaiyan M. H., Asghari M., Rahaeifard M., and Ahmadian M. T. A nonlinear strain gradient beam formulation. *International Journal of Engineering Science*, Vol. 49, pp. 1256–1267, 2011.

[5] Yang F., Chong A.C.M., Lam D.C.C., and Tong P. Couple stress based strain gradient theory for elasticity. *International Journal of Solids and Structures*, Vol. 39, pp. 2731–2743, 2002.

[6] Fleck N.A. and Hutchinson J.W. Strain gradient plasticity. volume 33 of *Advances in Applied Mechanics*, pp 295–361. Elsevier, 1997.

[7] Mindlin R.D. and Tiersten H.F. Effects of couple-stresses in linear elasticity. *Archive for Rational Mechanics and Analysis*, Vol. 11, pp. 415–448, 1962.

[8] Lam D.C.C., Yang F., Chong A.C.M., Wang J., and Tong P. Experiments and theory in strain gradient elasticity. *Journal of the Mechanics and Physics of Solids*, Vol. 51, pp. 1477–1508, 2003.

[9] Liao S. Notes on the homotopy analysis method: Some definitions and theorems. *Communications in Nonlinear Science and Numerical Simulation*, Vol. 14, pp. 983–997, 2009.

[10] Liao S. *Beyond Perturbation: Introduction to the Homotopy Analysis Method*. Chapman Hall/CRC, Boca Raton, 2003.

[11] Qian Y.H. , Ren D.X., Lai S.K., and Chen S.M. Analytical approximations to nonlinear vibration of an electrostatically actuated microbeam. *Communications in Nonlinear Science and Numerical Simulation*, Vol. 17, pp. 1947–1955, 2012.

[12] P. Belardinelli, S. Lenci, and M. Brocchini. Modeling and analysis of an electrically actuated microbeam based on non-classical beam theory. *Submitted to Journal of Computational and Nonlinear Dynamics*, 2013.

[13] Zhao J., Zhou S., Wang B., and Wang X. Nonlinear microbeam model based on strain gradient theory. *Applied Mathematical Modelling*, Vol. 36, pp. 2674–2686, 2012.

[14] Xie W.C., Lee H.P., and Lim S.P. Nonlinear dynamic analysis of mems switches by nonlinear modal analysis. *Nonlinear Dynamics*, Vol. 31, pp. 243–256, 2003.

[15] Nayfeh A.H., Younis M.I., and Abdel-Rahman E.M. Dynamic pull-in phenomenon in mems resonators. *Nonlinear Dynamics*, Vol. 48, pp. 153–163, 2007.

Proceedings of the 4th International Conference on Nonlinear Dynamics
ND-KhPI2013
June 19-22, 2013, Sevastopol, Ukraine

Large Amplitude Vibrations of Thin Hyperelastic Plates

Ivan Breslavsky*, Marco Amabili, Mathias Legrand

Abstract
Static and dynamic deflections under uniformly distributed pressure of a rectangular plate made of neo-Hookean rubber material is studied. A new method dedicated to the construction of local models which describe the behavior of the plate around a deformed configuration is proposed. This new method compares well with the exact solutions where available but is more versatile.

Keywords
physical and geometric nonlinearity, vibrations, plate theory

McGill University, Department of Mechanical Engineering
Macdonald Engineering Building, Room 270, 817 Sherbrooke Street West, Montreal, Quebec, Canada H3A 0C3
***Corresponding author**: ivan.breslavskyi@mcgill.ca

Introduction

The stress-strain relationships of rubbers and soft biological tissues are usually described through hyperelastic laws. In the context of large structural deflections and strains of structures made of hyperelastic materials, both geometrical and physical nonlinearities have to be accounted for [1, 2]. It is reported that the most commonly used hyperelastic material is of the incompressible neo-Hookean type which is implemented in the present work.

The finite displacements and corresponding deformations of a rectangular rubber plate under time-invariant external pressure are approximated through a truncated series of linear eigenmodes. The common simplification that consists of pre-assuming a shape for the deformed structure is not accounted for and the associated convergence analysis is undertaken. A method which systematically constructs a local model approximating the plate behavior around a deformed static configuration is proposed. Free and forced large-amplitude vibrations in the neighborhood of the previously calculated static equilibrium are analyzed with this method. The comparison with the geometrically nonlinear model is also performed to estimate the effect of physical nonlinearity. In contrast to the exact method, this method allows for the uncoupling of spatial and temporal components in the solution, which significantly simplifies the investigation of the plate behavior. This local model has the form of a system of ordinary differential equations with quadratic and cubic nonlinearities [3].

1. Description of Plate Behavior

The Lagrange framework to derive the governing equations is used to describe the static and dynamic behavior of a rectangular plate. The geometric nonlinearity is described by using the von Kármán nonlinear plate theory [3]. The physically nonlinear elasticity of natural rubber is described by neo-Hookean constitutive law [4, 5] through the following strain energy density:

$$W = \frac{E}{4(1+\nu)}(\bar{I}_1 - 3) + \frac{E}{6(1-2\nu)}(J-1)^2, \tag{1}$$

where $\bar{I}_1$ is the first invariant of the right Cauchy-Green deformation tensor $\mathbf{C}$ [4, 5]; J is the square root of the third invariant of the right Cauchy-Green deformation tensor; the pair E, ν stands for the Young's modulus and Poisson's ratio of the plate material, respectively. Since $\mathbf{C} = 2\mathbf{E} + \mathbf{I}$ [5], the two invariants

are expressed in terms of the Lagrange strain tensor $\mathbf{E}$ components as follows:

$$J^2 = (2\varepsilon_3+1)((2\varepsilon_1+1)(2\varepsilon_2+1)-\varepsilon_{12}^2); \tag{2}$$

$$\bar{I}_1 = \frac{2(\varepsilon_1+\varepsilon_2+\varepsilon_3)+3}{\sqrt[3]{(2\varepsilon_3+1)((2\varepsilon_1+1)(2\varepsilon_2+1)-\varepsilon_{12}^2)}}. \tag{3}$$

The displacements $u(x,y), v(x,y), w(x,y)$ along the directions x,y,z, respectively, are expanded into three distinct truncated series depending on the participations of the linear vibration eigenmodes of the underlying linearized system [3].

The von Kármán nonlinear plate theory provides the expressions the strain components $\varepsilon_1, \varepsilon_2, \varepsilon_{12}$ as functions of the displacements u, v, w , except for ε_3. Accordingly, this expression has to be explicitly derived. This is achieved by plugging the incompressibility condition $J = 1$ [4] into equation (2):

$$\varepsilon_3 = \frac{1}{2((2\varepsilon_1+1)(2\varepsilon_2+1)-\varepsilon_{12}^2)} - \frac{1}{2}. \tag{4}$$

At this stage, it is worth mentioning that the first terms of the expansion in the strain components of expression (1) after substituting Eq. (4) coincide with those found for a physically linear strain energy density [3]: in other words, in the small strains setting, both theories are identical.

2. Local Expansion of the Neo-Hookean Strain Energy Density

Expression (4) is not a polynomial in strains, which essentially complicates the investigation of the plate behavior. It is possible to obtain numerical approximations of the solutions of nonlinear systems deriving from non-polynomial potential energy but only for low-dimensional models. As a consequence, it is highly desirable to obtain the governing equations in the form of ordinary differential equations with polynomial nonlinearities of degree not higher than three. Due to higher-order terms in the expansion of (1), such a model will only capture the plate behavior in the vicinity of a given fixed-point. We assume that we know the configuration of slightly bent plate and we want to find the configuration of highly bent plate. The question how the initial configuration can be found is discussed in the next secion. This configuration (or the fixed-point) is identified by a vector of generalized coordinates $\mathbf{q}^{(0)} = \{q_i^{(0)}\}_{i=1,\dots,N}$. A new configuration $\mathbf{q} = \{q_i\}_{i=1,\dots,N}$, close to the configuration $\mathbf{q}^{(0)}$ can be expressed as $\mathbf{q} = \mathbf{q}^{(0)} + \alpha\mathbf{q}^{(1)}$ where $\alpha \ll 1$ is a small parameter. Corresponding strain components take the form:

$$\varepsilon_1 = \varepsilon_1^{(0)} + \alpha\varepsilon_1^{(1)} \quad ; \quad \varepsilon_2 = \varepsilon_2^{(0)} + \alpha\varepsilon_2^{(1)} \quad ; \quad \varepsilon_{12} = \varepsilon_{12}^{(0)} + \alpha\varepsilon_{12}^{(1)}. \tag{5}$$

In expressions (5), $\varepsilon_1^{(0)}$, $\varepsilon_2^{(0)}$, and $\varepsilon_{12}^{(0)}$ do not depend on the unknown generalized coordinate $\mathbf{q}^{(1)}$. Equation (1) is expanded into a series in the small parameter α up to the second power of α:

$$W(q^{(0)}) = \frac{E}{3}\left(\left[\varepsilon_1^{(0)} + \varepsilon_2^{(0)} + \frac{1}{2\Xi} - \frac{1}{2}\right] + \alpha\left(\varepsilon_1^{(1)} + \varepsilon_2^{(1)} + \frac{\kappa}{\Xi^2}\right) + \alpha^2\left(\frac{4\kappa^2 - (4\varepsilon_1^{(1)}\varepsilon_2^{(1)} - \varepsilon_{12}^{(1)2})\Xi}{2\Xi^3}\right)\right) \tag{6}$$

where

$$\Xi = (2\varepsilon_1^{(0)}+1)(2\varepsilon_2^{(0)}+1) - (\varepsilon_{12}^{(0)})^2 \quad ; \quad \kappa = \varepsilon_1^{(1)} + \varepsilon_2^{(1)} + 2\varepsilon_1^{(0)}\varepsilon_2^{(1)} + 2\varepsilon_2^{(0)}\varepsilon_1^{(1)} - \varepsilon_{12}^{(0)}\varepsilon_{12}^{(1)}. \tag{7}$$

The denominators in expression (6) do not depend on the unknown generalized coordinate $\mathbf{q}^{(1)}$ and equation (6) is thus polynomial in $\{q_i^{(1)}\}_{i=1,\dots,N}$. Once the spatial and temporal parts are separated, the Lagrange equations take the following form:

$$\ddot{q}_n^{(1)} + 2\zeta_n\Omega_n\dot{q}_n^{(1)} + \sum_{i=1}^{N} k_{ni}(\mathbf{q}^{(0)})q_i^{(1)} + \sum_{i,j=1}^{N} k_{nij}(\mathbf{q}^{(0)})q_i^{(1)}q_j^{(1)} + \sum_{i,j,l=1}^{N} k_{nijl}(\mathbf{q}^{(0)})q_i^{(1)}q_j^{(1)}q_l^{(1)} = Q_n \tag{8}$$

for $n = 1,\dots,N$. These equations represent the local model describing the behavior of the plate around the deformed configuration $\mathbf{q}^{(0)}$. The static counterpart of equations (8) can be recast in the usual compact form of a system of nonlinear algebraic equations $\mathbf{F}(\mathbf{q},\mathbf{Q}) = \mathbf{0}$ that can be solved with the Newton-Raphson technique.

3. Numerical Example

3.1 Problem of interest

As an example, a simply supported rectangular rubber plate defined on the domain:

$$V = \{x \in [0;a],\ y \in [0;b],\ z \in [-h/2;h/2]\}; \tag{9}$$

is considered with the following geometrical parameters $a = 0.1$ m, $b = 0.12$ m, $h = 0.0005$ m, and material characteristics $\nu = 0.5$, $E = 10^7$ Pa, $\rho = 1100$ kg/m^3. The plate is simply supported with immovable edges [3], that is:

$$w|_{\partial S} = M|_{\partial S} = u|_{\partial S} = v|_{\partial S} = 0, \tag{10}$$

where ∂S denotes the boundary of the plate; M is the bending moment per unit length.

Static and dynamic deflections under uniformly distributed constant pressure are investigated. Due to symmetry considerations on the geometry of the plate and the distribution of the external load, only the odd bending modes participate in the sought response if internal resonances are not activated:

$$w(x,y,t) = \sum_{n,m\in\mathbb{N}} w_{2n+1,2m+1}(t)\sin\Big(\frac{(2n+1)\pi x}{a}\Big)\sin\Big(\frac{(2m+1)\pi y}{b}\Big). \tag{11}$$

Similarly, respective in-plane modes have the form [3]:

$$\begin{aligned} u(x,y,t) &= \sum_{n,m\in\mathbb{N}} u_{2n,2m+1}(t)\sin\Big(\frac{2n\pi x}{a}\Big)\sin\Big(\frac{(2m+1)\pi y}{b}\Big); \\ v(x,y,t) &= \sum_{n,m\in\mathbb{N}} v_{2n+1,2m}(t)\sin\Big(\frac{(2n+1)\pi x}{a}\Big)\sin\Big(\frac{2m\pi y}{b}\Big). \end{aligned} \tag{12}$$

3.2 Static analysis

Convergence analysis shows that 12, 27 and 34 DOF models yield very similar results. This is true for model with physical and geometric nonlinearity as well as for the model with only geometric nonlinearity. The 12 DOF models with the generalized coordinates $w_{i,j}$, $i,j = 1,3$; $u_{i,j}$, $v_{j,i}$, $i = 2,\ 4$; $j = 1,\ 3$ are used in the remainder.

The deflection-pressure curves for the model with only geometric nonlinearity and exact solution for the 12 DOF system with both nonlinearities are compared in Fig. 1. It is shown that the difference within a range of deflection up to $30h$ is small since only a 6% maximal difference in deflection for a given pressure is observed in this range. The configuration with central deflection $25h$ obtained with the geometrically only nonlinear model is considered for the construction of local models.

Fig. 2 compares the corresponding results with both nonlinearities and an increasing number of DOF to the available exact solutions. As illustrated, the local model provides a sufficiently good approximation of the underlying plate behavior. At the same time, the local models are much more efficient in a computational sense. This figure shows that the 12 DOF model stands as a convincing compromise between prediction capabilities and computational cost. The maximal difference in deflection in the range $[0, 100h]$ is 2% with respect to the 34 DOF model.

3.3 Dynamic analysis

As at small strains, the effect of physical nonlinearities can be ignored, we study the free and forced vibrations around a pre-loaded state . The initial deformed configuration involves the principal generalized coordinate $w_{1,1} = 80h$. The comparison with the exact static solution shows that the local model around in a neighborhood of this deformed configuration is accurate for deflection up to $10h$ that will stand as the upper bound in the vibratory analysis. The vibrations are studied using the harmonic balance method and AUTO software [6].

Fig. 3 displays the backbone curves and frequency response for the free vibrations with frequencies close to the first natural frequency of the pre-loaded plate. Non-dimensional frequencies, normalized with respect to the natural frequency Ω_1 are shown on the horizontal axis.

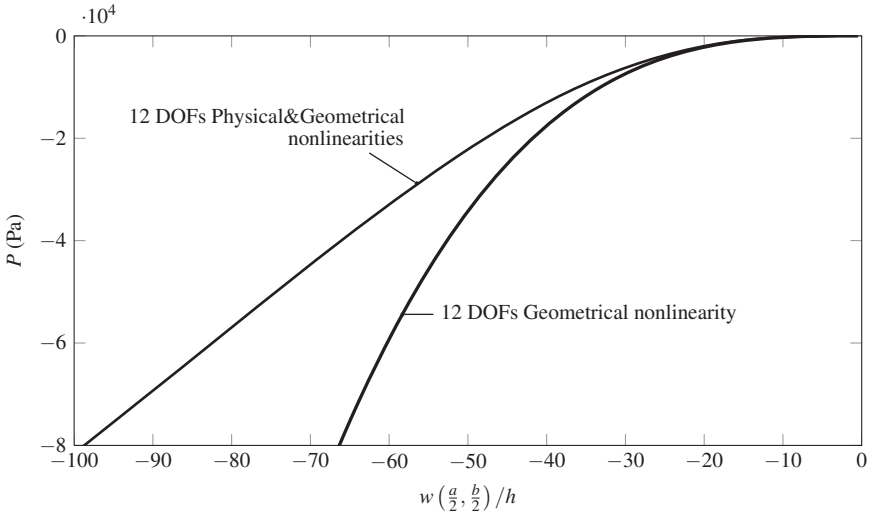

Figure 1. Comparison of the exact deflection-pressure curves for the model with only geometrical and both geometrical and physical nonlinearities; 12 DOFs.

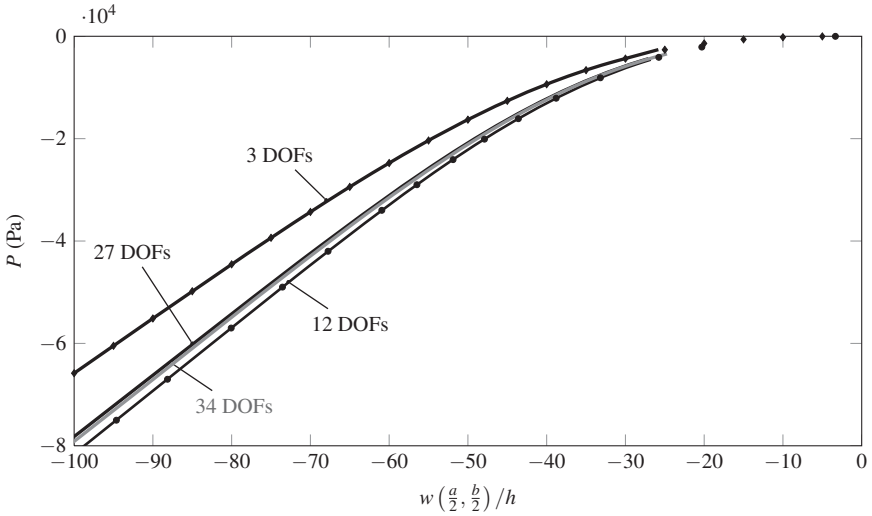

Figure 2. Deflection-pressure curves for models with physical and geometrical nonlinearities:—— , —— obtained with local models; ◆ 3 DOF exact solution; ● 12 DOF exact solution.

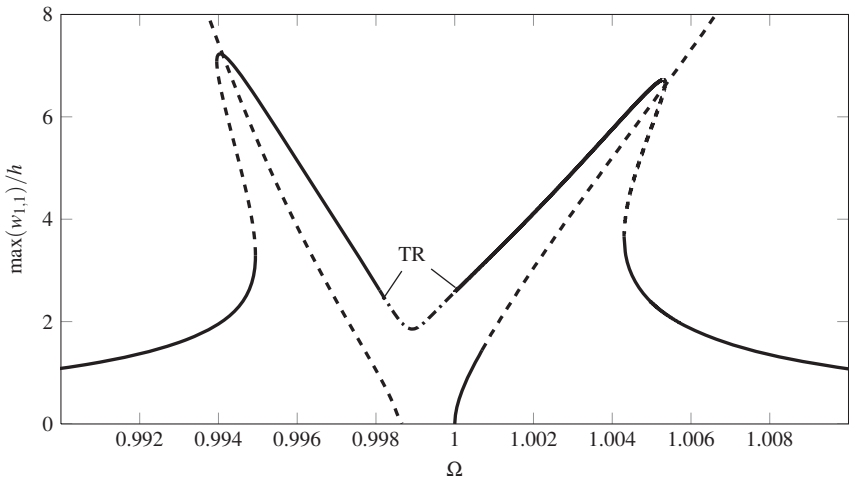

Figure 3. Frequency responses and backbone curves for principal bending mode $w_{1,1}$:—— stable motions;- - - unstable motions; —·— quasi-periodic motions; TR, Neimark-Sacker bifurcation.

As opposed to the vibrations of an unloaded initially flat plate [3], the explored pre-loaded plate exhibits a very weak nonlinear response. Similar effect of weaken nonlinearity in stretched membranes is reported in [2, 7]. Despite of the fairly minor deviation of the high-amplitude vibration frequency from the linear natural frequency, an internal resonance 2:1 with in-plane mode $v_{1,2}$ (softening branch in Fig. 3), is predicted. In the same vein, two Neimark-Sacker bifurcations and a quasi-periodic forced vibration response between them are found.

Conclusions

Large-amplitude vibrations of a rubber plate involving physical and geometrical nonlinearities are analyzed. The developed method transforms the Lagrange equations in space and time into a system of ordinary differential equations in time only. This facilitates the investigation of the vibrations around a deformed configuration taking into account both physical and geometrical nonlinearities. Both the static and the dynamic results show good agreement with the exact solution. While at small strains, the influence of the physical nonlinearity is weak, it becomes significant at finite strains. As opposed to the case of vibratory response of an undeformed plate, which exhibits strong amplitude-frequency dependence, the vibrations around a deformed plate configuration are nearly linear. However, some nonlinear effects like bifurcations and internal resonances are present in the system.

References

[1] Y.B. Fu and R.W. Ogden. *Nonlinear Elasticity: Theory and applications*. Cambridge University Press, Cambridge, 2001.

[2] P.B. Goncalves, R.M. Soares, and D. Pamplona. Nonlinear vibrations of a radially stretched circular hyperelastic membrane. *Journal of Sound and Vibration*, 327(1-2):231–248, 2009.

[3] M. Amabili. *Nonlinear vibrations and stability of shells and plates*. Cambridge University Press, New York, 2008.

[4] R.W. Ogden. *Non-Linear Elastic Deformations*. Dover Publications, New York, 1997.

[5] A. Bower. *Applied mechanics of solids*. CRC Press. Taylor and Francis Group, Boca Raton, 2010.

[6] E.J. Doedel, A.R. Champneys, T.F. Fairgrieve, Y.A. Kuznetsov, B. Sandstede, and X. Wang. *AUTO 97: Continuation and Bifurcation Software for Ordinary Differential Equations (with HomCont)*. Concordia University, Montreal, 1998.

[7] R.M. Soares and P.B. Goncalves. Nonlinear vibrations and instabilities of a stretched hyperelastic annular membrane. *International Journal of Solids and Structures*, 49(3-4):514–526, 2012.

Proceedings of the 4th International Conference on Nonlinear Dynamics
ND-KhPI2013
June 19-22, 2013, Sevastopol, Ukraine

Impact Failure Properties of Circular Glass and Composite Plates and Numerical Simulation of their Dynamical Behavior

D.Breslavsky[1]*, I.Naumov[1], V.Konkin[1], G.Lysachuk[1]

Abstract
Results of experimental and numerical investigations of impact loading of circular glass and composite aluminum plates are presented. Single for glass and repeated impact loading tests for aluminum plates were performed. The numbers of cycles to failure at the case of cyclic impacts were determined. The data of experimental investigations were used for numerical simulation of the deformation and long term strength of aluminum plates.

Keywords
Impact, circular plate, experimental investigations, numerical simulation, dynamical behaviour

[1]National Technical University 'Kharkiv Polytechnic Institute', Kharkiv, Ukraine
* **Corresponding author:** brdm@kpi.kharkov.ua

Introduction

Impact loading of thin-walled structural elements attracts attention of engineers more than one hundred years. There are many solved problems in this area, although the most well studied is ballistic impact with high speed velocity of projectiles [1, 2]. The case of low velocity impact today is studied predominantly for honeycomb composites [3, 4], where inner layer destroys due to its small strength.

However, the case of repeated impact action on a plate, when fracture occurs after several numbers of impacts, practically has not been studied. The presented paper deals with one example of such cyclic impact loading, which is realized in special hardware has been designed for preventing of unauthorized access to data stored on the hard disk of computer. Special striker jointly with electromagnetic device [5] is located into the casing of processor block and after receiving of appropriate command it switches on and punches the disk of hard drive.

Deformation and fracture of impact loaded thin glass and aluminum coated with iron alloy disks are studied experimentally and numerically using LS Dyna software. Impacts with low velocities which are equal to 10-15 m/s are investigated. Inductive dynamic engine (IDE) is used as an impact loading device in developed experimental unit. Impact tests have been done for different velocities which correspond to the cases of elastic, elastic- plastic deforming and punching. The repeated impact loading in which low cycle punching takes place in plates is investigated. Numerical simulation of impact deformation of circular plates is performed and results are compared with experimental ones.

1. Experimental investigations

Let us briefly present the experimental equipment and results. The special experimental unit was developed for impact tests on computer hard drive disks. The unit was made on the basis of designed device for preventing of unauthorized access to computer data [5]. The main parts of the unit are loading device built on IDE, equipment for plate's fixing (Fig. 1) and measurement hardware. The strain gauge sockets were pasted on the plate's surface, and data by use of analog-digital converter

ADA-1406 had been written into computer text files. In the case of plate's punching with large strains the measurements of deformed plate had been done.

A number of experiments directed to verification of results which can be obtained using developed experimental unit had been performed. Static loading of a plate, impact loading in elastic and elastic-plastic areas had been done. Fig. 2. presents the varying of strain components were

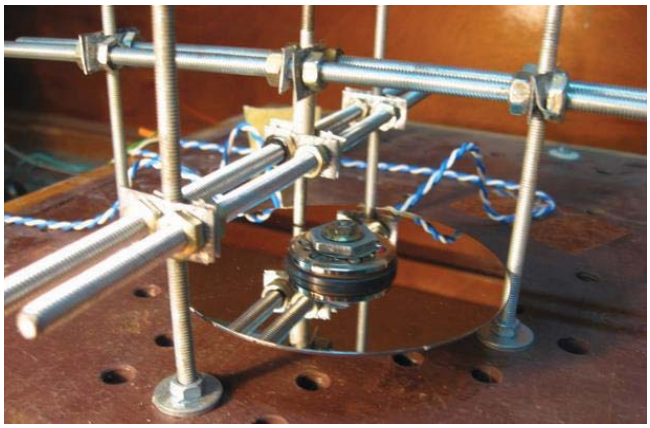

Figure. 1. Equipment for plate's fixing and loading

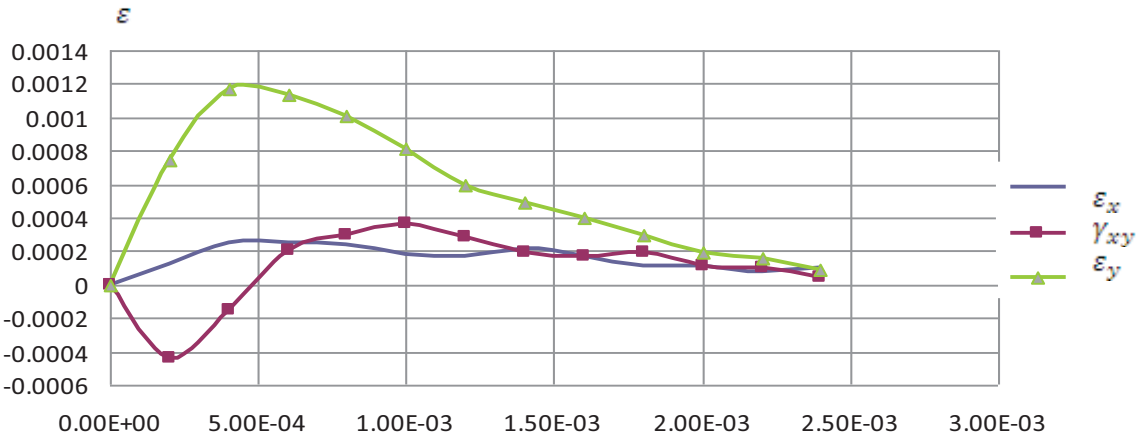

Figure 2. Variation of strain components

calculated by use of the measurement data for the case of elastic impact with velocity of 0.5 m/s in the strain gauge socket is placed near the striker.

Performed verification allowed us to move to impact tests in wide range of striker's velocities. For glass – based computer disks only cases of brittle fracture were studied. It was established that from the velocity value is equal to 0.5 m/s disk fracture occurs (Fig.3).

Figure 3. Glass disk after impact

Aluminum-based disks were tested at single and cyclic loading. For the case of single impact with the velocity is equal 10.3 m/s the deformation is characterized by large strains, the maximum value of the deflection is equal to 20.3 mm. In this case any substrate were placed under the disk.

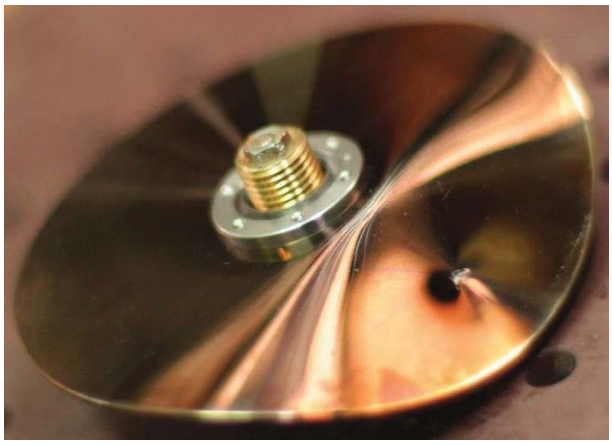

Figure 4. Disk after impact with velocity of 10.3m/s

Real working conditions of the disk are characterized by the presence of lower part of the hard disk drive shell, installed under the disk. Impacts with velocity in range 10-11 m/s cannot punch the disk from the first loading. So, the cyclic loading of a disk was studied. It was experimentally established that disk fracture occurs after 7 impacts (three tests got the value of 6, 7 and 8 impacts). Additionally the dependence between the velocity of striker and number of impact cycles to fracture was determined.

3. Numerical results

Numerical simulation of impact loading of a circular plates made from aluminum alloy had been done by use of LS Dyna software [6]. Mass and geometrical data of plates and striker, its velocity were determined in experimental part of a work and used in calculations. Brick finite elements with 8 nodes were used in simulation. Firstly elastic impact solutions were compared with experimental results. FE mesh contains 9500 nodes. Fig. 5 presents the comparison of experimental and numerical data for the case of impact with striker's velocity is equal to 0.55 m/s. The satisfactory agreement can be found.

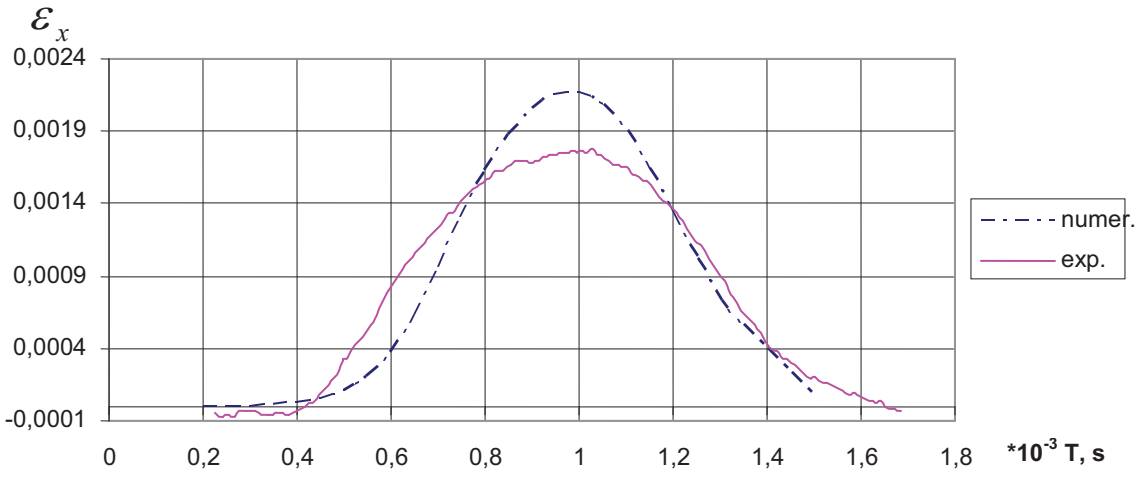

Figure 5. Radial strain component. Comparison of numerical and experimental data

The impact loading with the velocity of striker 10.3 m/s (experimental photo is presented on Fig.4) was numerically simulated. The results were compared with experimentally measured residual

deflections. Comparing Figs. 4 and 6, we can conclude, that numerical data qualitatively correct describe the residual shape of a disk after impact loading. Quantitatively we have a satisfactory agreement. For example, experimental value of maximal deflection is 20,3 mm, and numerical is equal to 20,19 mm. Maximum value of local displacement under the striker: experimental is equal to approximately 0,4 mm, numerical is equal to 0,6 mm, the difference in this comparison doesn't exceed 30%.

Low cycle deformation of a plate were studied numerically jointly with use of solving of kinetic equation for the damage parameter. Firstly the elastic-plastic stress-strain state were determined, after that by use of impact long term strength data the number of cycles to fracture was found. Its value was equal to 7.12, which practically coincides with experimental result.

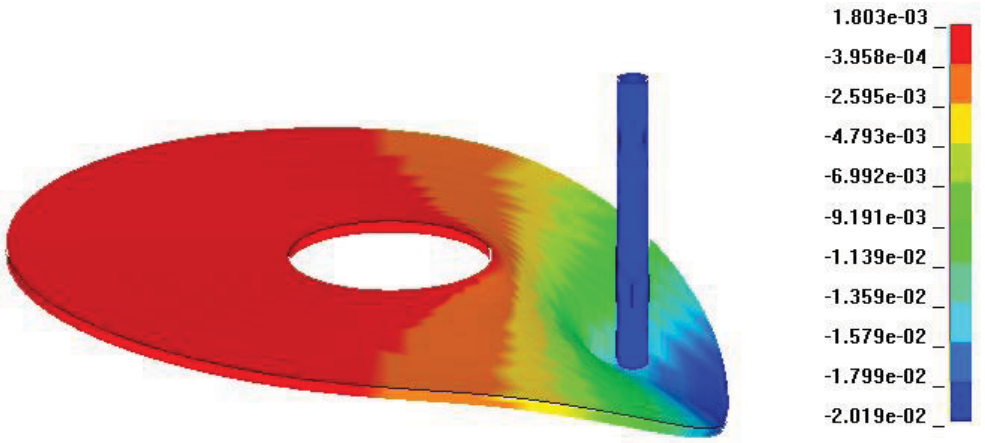

Figure 6. Deformed state of a disk, impact velocity 10.3 m/s

Conclusions

The paper contains the results of experimental and numerical investigations of deformation and cyclic long term strength of computer disks, which were simulated as a circular plates made from glass and aluminum alloy composite. The experimental technique allows to obtain the deflection distributions as well as the numbers of cycles to failure for studied disks. Comparison between experimental and numerical results confirms the right choice of FEM schemes and allows use them in selection of the best options of working conditions in hardware for preventing of unauthorized access to computer data.

References

[1] Ben-Dor G., Dubinsky A. and Elperin T. Ballistic Impact: Recent Advances in Analytical Modeling of Plate Penetration Dynamics–a Review *Applied Mechanics Reviews*, Vol. 58, pp. 355-371, 2005.

[2] Goldsmith W. Non-ideal projectile impact on targets *Int. J. Impact Eng.*, Vol. 22: 2-3, pp. 95-395, 1999

[3] Amaro A.M, M.S. de Moura M. F. and Reis P.N.B. Detection Of Low-velocity Impact Damage In Carbon-epoxy Plates Using NDT *Proc. of 16th European Conference of Fracture. Alexandroupolis, Greece, July 3-7*, 2006.

[4] Qixuan Zheng, Zhengneng Li, Di Wu. Damage Analysis of Honeycomb Core Composite Sandwich Plate Subjected Low Velocity Impact *Journal of Reinforced Plastics and Composites*, Vol. 19: 1, pp.58-68, 2000.

[5] Naumov I.V., Bolukh V.F., Breslavsky D.V. Deformation and fracture of plates under loading of cylindrical impactor *Mechanics and Machine Building*, Vol. 1, pp. 207-216, 2010. (In Russian).

[6] Hallquist J. *LS DYNA Theoretical Manual.* Livermore Software Technology Corporation, Livermore, USA, 2005.

Proceedings of the 4th International Conference on Nonlinear Dynamics
ND-KhPI2013
June 19-22, 2013, Sevastopol, Ukraine

Modeling the Dynamic Debonding Growth of Sandwich Plates

Vyacheslav N. Burlayenko[1*], Tomasz Sadowski[2]

Abstract
In this paper, the debonding growth of sandwich plate with foam core and composite sheets under dynamic loading is investigated by using the finite element method. The composite sheet is modeled by layered continuum shell elements considering first order shear effect, and the foam core is simulated by, in general, anisotropic solid elements, while for the bond line between the face sheet and the core is presented by applying a simple cohesive layer model with a bilinear constitutive relationship. The Quadratic Stress failure criterion defined the initiation of debonding, whereas the energy-based Benzeggagh-Kenane's fracture criterion is applied to tracing debonding growth at the mix mode conditions. By some numerical examples, the behavior of dynamic debonding growth of sandwich plates is investigated and discussed in detail.

Keywords
Sandwich plates, Debonding, Finite element analysis

[1] National Technical University 'KhPI', Kharkiv, Ukraine
[2] Lublin University of Technology, Lublin, Poland
* **Corresponding author:** burlayenko@yahoo.com

Introduction

Sandwich panels have become a popular structural element in many contemporary engineering applications over the two past decades. Because of their small weight and high stiffness and strength the sandwich panels are suitable in high performance applications of aerospace and automotive industries, where safety and durability demands are critical issues. Those structural members along with the advantages by exploiting the sandwich concept seem to be very prone to damaging. The most often damage is a partial detach along the skin-to-core interface layer, so-called debond [1]. Therefore, to ensure the reliability and safety of constructions made of sandwich panels, the knowledge on their mechanical behaviors taking into account a possible existing debond should be very well investigated at the design stage. In this respect, numerical methods are superior over expensive experimental approaches.

The finite element modeling of dynamic crack propagation has attracted a lot of attention over the last decades, e.g. papers [2, 3] among others. Within the discrete crack approach of fracture mechanics, the cohesive crack model describing the material behavior in the process zone in front of the crack tip is one of techniques in the finite element method. Such process zone appropriately accounts for the dissipative processes due to fracturing [4, 5]. Elices [6] gave a review of the main aspects of this model and relevant references. Sridharan and Li [7] simulated the interfacial damage in sandwich members under static and dynamic loading conditions. Two types of cohesive layer model with finite thickness and with zero initial thickness were utilized and compared. Han et al. [8] used cohesive element approach for simulating debonding propagation between a face sheet and a core in a honeycomb cored sandwich panel. The critical energy release rate and peak strength of the cohesive model were determined from Double Cantilever Beam (DCB) fracture tests and Flatwise Tension tests (FWT), respectively.

Most of the existing studies on strength of layered structures, in particular sandwich structural members, are focused on debonding/delaminition growth under static loading, while such investigations for the dynamic growth of this interfacial damage are limited. The present paper deals

with debonded sandwich plates subjected to dynamic loading and pays attention on the influence of loading rate and loading type upon dynamic debonding growth. Hence, outcomes of this research would form a useful contribution for a better understanding of the debonding growth under dynamic load of sandwich plates.

1. Statement of the problem

From the mathematical standpoint a sandwich panel with a debond subjected to dynamic loading fails into the large class of mechanical problems for which a discrete change in the stiffness are defined. Such systems usually are referred to impact-contact tasks, where contact and friction conditions should be assigned. On the other hand, to predict the propagation of debonding, damage initiation and damage evolution criteria are additionally required to be defined. Therefore, the system of governing equations involves the elastodynamics problem of a sandwich plate, contact and friction laws defined between surfaces in the debonded zone and fracture criteria at the skin-to-core interface. The statement of the elastodynamics problem of debonded sandwich plates accounting for contact and friction have been stated in [9], while the problem with fracturing conditions are considered herein.

1.1 Cohesive layer model

The modeling of fracture initiation and propagation in finite element analyses can be specified through a cohesive layer model. The cohesive layer model is implemented into a finite element mesh as interface (cohesive) elements, which are compatible with regular solid finite elements. In three dimension problems they consist of two surfaces separated by a thickness, as shown in Fig. 1a, where an 8-noded cohesive element with three displacement degrees of freedom per node is presented.

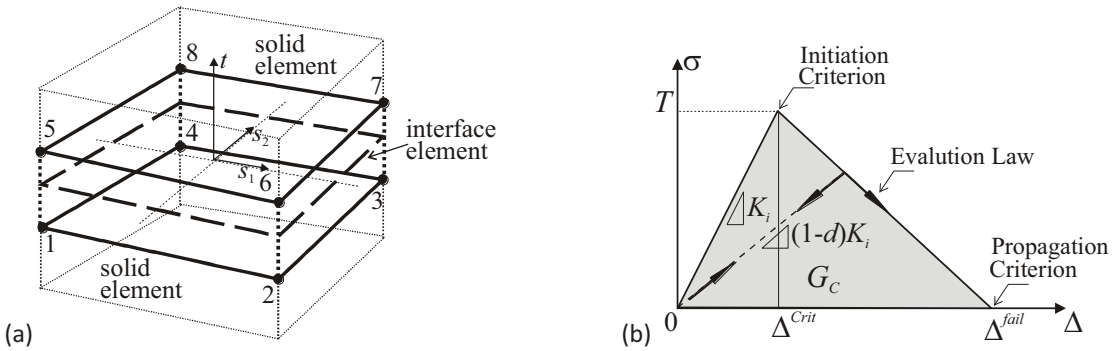

Figure 1. (a) An eight-node cohesive element; and (b) a typical bilinear cohesive law

The relative motion of the bottom and top parts of the cohesive element measured along the thickness direction represents opening or closing of the interface and it can be represented in the terms of nodal displacements of paired *I*-th node as follows:

$$\Delta_I = u_I^{top} - u_I^{bot} \tag{1}$$

Such relative motion of theses parts with respect to the element mid-plane is qualified as the transverse shear behavior of the cohesive element. The stretching and shearing of the element mid-plane are associated with membrane strains. The notion of strain is suspended and relative displacements of the nodes of the element are used to characterize the deformation and compute the nodal forces. Moreover, the cohesive element has zero initial thickness and is usually represented as a line in an undeformed state.

Then, the interface opening along the cohesive surface is interpolated from nodal relative displacement jumps (1) by using shape functions, e.g. the shape function N_I associated with the *I*-th node we can write down implying summation over repeated indices in the form:

$$\mathbf{\Delta}(\mathbf{x},t) = N_I(\mathbf{x})\mathbf{\Delta}_I(t) \tag{1}$$

Based on the approximated displacement field, the internal force vector and the tangent stiffness matrix of the cohesive element are given in (2), respectively, as the following:

$$\mathbf{f}_I^{coh} = \int_{\Gamma^e} \mathbf{B}_I^{coh} \mathbf{T}_I^{coh} dS \text{ and } \mathbf{K}_{IJ}^{coh} = \frac{\partial \mathbf{f}_I^{coh}}{\partial \mathbf{u}_J} = \int_{\Gamma^e} \left(\mathbf{B}_I^{coh}\right)^T \frac{\partial \mathbf{T}_I^{coh}}{\partial \mathbf{\Delta}_J} \mathbf{B}_I^{coh} dS \,, \tag{2}$$

where $\mathbf{B}_I^{coh}$ is a displacement separation relation matrix, $\mathbf{T}_I^{coh}$ is cohesive traction along the fractured interface within the cohesive surface Γ^e and $\mathbf{u}_I$ is a vector of nodal displacements.

Note that the vector $\mathbf{T}_I^{coh}$ can be obtained by the definition of cohesive layer constitutive (traction-separation) laws. In this respect, linear, bilinear, parabolic, exponential and etc. relationships can be used.

The constitutive response of the cohesive elements used in this investigation is defined by bilinear traction-separation law as shown in Fig. 1b, where T represents the interfacial strength, Δ^{Crit} is the critical separation, Δ^{Fail} is the separation at failure, and the area under σ-Δ curve, G_C, is the critical strain energy release rate (SERR) per unit area dissipated during the fracture process. Under mixed-mode fracture conditions, the properties required to be defined for the bilinear traction-separation law are the three critical fracture energies G_{IC}, G_{IIC}, G_{IIIC}, the penalty stiffnesses K_1, K_2, K_3, and the interfacial strengths T, S_1, S_2.

The identification of the material parameters of such model can be employed by various techniques; however, toughnesses are dependent on the values of peak stress T_i, i.e. $\{T, S_1, S_2\}$, and the work of separation per unit area G_i, i.e. $\{G_I, G_{II}, G_{III}\}$, but not the shape of the curve [4].

The initial response of the cohesive element is assumed to be linear until a damage initiation criterion is met. The penalty stiffness, K_i, of the bilinear traction-separation law is defined as

$$K_i = \left. T_i \right/ \Delta_i^{Crit} \,, \tag{3}$$

where Δ_i^{Crit} is the critical separation for damage initiation at each separation direction. In general, the penalty stiffness is no a material parameter and it should be assigned such that its value must be high enough to avoid interpenetration of the faces at the fractured interfaces and to prevent artificial compliance from being introduced into the model by the cohesive elements. However, an overly large value can lead to numerical problems [5].

Another critical issue affecting the accuracy of predictions with the cohesive elements is the number of the cohesive elements in the cohesive zone. In turn, the length of the cohesive zone is a material property. Several guidelines for choosing the penalty stiffnesses and mesh size at the cohesive zone are presented in [5] and according to which we follow those rules in this study.

Several damage criteria such as maximum stress, maximum, strain, quadratic stress and quadratic strain criterion exist to represent the onset of damage. The quadratic stress (QS) damage initiation criterion shown in (4) is used throughout this numerical study:

$$\left\{\frac{\langle \sigma_z \rangle}{T}\right\}^2 + \left\{\frac{\tau_{xz}}{S_1}\right\}^2 + \left\{\frac{\tau_{yz}}{S_2}\right\}^2 = 1 \,, \tag{4}$$

where the Macaulay bracket $\langle \bullet \rangle$ signifies that the compression stress does not contribute to damage initiation.

Once the damage initiation criterion of the cohesive element is met, the stiffness of the element is degraded. The softening response of the cohesive elements is represented by expression:

$$\sigma_i = (1-d) K_i \Delta_i \,, i = 1,2,3 \tag{5}$$

Here d is the damage variable, which has value $d = 0$ when the interface is undamaged, and the value $d = 1$ when the interface is completely fractured.

For analysis presented herein, we use the energy-based Benzeggagh-Kenane (B-K) damage evolution criterion shown in (6) as

$$G_C = G_{IC} + (G_{IIC} - G_{IC}) \left(\frac{G_{Shear}}{G_T}\right)^{\eta} \,, \tag{6}$$

where η is the B-K material parameter, $G_{Shear} = G_{II} + G_{III}$ and $G_T = G_I + G_{II} + G_{III}$.

The nonlinear contact and friction conditions are employed as the same in [9] to avoid the unphysical overlap between the detached face sheet and core under dynamic loading.

1.2 Explicit solution algorithm

The discretization of an elastic sandwich plate into finite elements and the assembly of all element contributions into global matrices and vectors lead to the following equation of motion:

$$\mathbf{M}\ddot{\mathbf{U}}(t) + \mathbf{C}\dot{\mathbf{U}}(t) + \mathbf{K}\mathbf{U}(t) = \mathbf{F}(\mathbf{U}(t)) - \mathbf{F}^{coh}(\mathbf{U}(t)) - \mathbf{F}^{cont}(\mathbf{U}(t)), \tag{7}$$

where **M** is the mass matrix, **K** is the stiffness matrix and **C** is the damping matrix presented by Rayleigh type as $\mathbf{C} = \alpha\mathbf{M} + \beta\mathbf{K}$. The vectors **F** and $\mathbf{F}^{coh}$ are the right-hand side vectors of the prescribed and cohesive nodal forces and $\mathbf{F}^{cont}$ is the nodal contact and friction forces. The vector $\mathbf{U} = \mathbf{U}(t)$ is the global vector of nodal displacements, and its time derivatives $\ddot{\mathbf{U}}(t)$ and $\dot{\mathbf{U}}(t)$ are nodal accelerations and velocities, respectively. Moreover, some initial conditions at $t = 0$ are given. For the numerical solution of this second order differential equation, we have to discretize the time interval in finite steps of size Δt and calculate the approximate solution on time $t_{i+1} = t_i + \Delta t_{i+1}$.

Explicit time-stepping algorithms determine the solution of equation like (7) without iterations and tangent stiffness matrix by explicitly advancing of the kinematical state known from a previous increment to the next one. To introduce the concept of the explicit algorithm, the central-difference formulation can be exploited. First, accelerations at the beginning of each increment Δt_{i+1} are calculated from the equation (7) rewritten in the form:

$$\ddot{\mathbf{U}}_i = \widetilde{\mathbf{M}}^{-1}(\mathbf{F}_i - \mathbf{I}_i) \tag{8}$$

where $\widetilde{\mathbf{M}}$ is the lumped mass matrix, extracted from the consistent mass matrix **M**, and $\mathbf{I}_i$ is the sum of internal nodal forces, which are updated during the previous increment Δt_i.

Thereafter, the central difference operator uses the accelerations calculated at t_i to advance the velocity solution to time $t_i + \frac{1}{2}\Delta t_{i+1}$ and the displacement solution to time $t_i + \Delta t_{i+1}$ as follows:

$$\dot{\mathbf{U}}_{i+\frac{1}{2}} = \dot{\mathbf{U}}_{i-\frac{1}{2}} + \frac{1}{2}(\Delta t_{i+1} + \Delta t_i)\ddot{\mathbf{U}}_i, \quad \mathbf{U}_{i+1} = \mathbf{U}_i + \Delta t_{i+1}\dot{\mathbf{U}}_{i+\frac{1}{2}} \tag{9}$$

Besides, a contact algorithm and a fracture analysis that generate contact and cohesive internal forces, respectively, are being performed within this global time stepping scheme.

2. Simulation results

To simulate debonding growth of a sandwich plate with a central penny-shaped debonded zone, we developed a three-dimensional tri-layer finite element model in ABAQUS [10] with a layer of 3-D cohesive elements COH3D8 for the interface between the face sheets and the core. In the model, the face sheets are discretized by layered shell continuum elements SC8R based on the Reissner-Mindlin's plate theory, whereas the core is simulated by solid continuum elements C3D8R.

Table 1. Mechanical properties of material

Material properties	GFRP face sheet	Foam core
Young's modulus, GPa E_{xx}, E_{yy}, E_{zz}	19.3, 3.48, 19.3	0.085
Shear modulus, GPa G_{xy}, G_{xz}, G_{yz}	1.65, 7.7, 1.65	0.030
Density, kg/m^3	1650	52

The surface-to-surface contact approach is used for discretizing the contacting surfaces at the damaged skin-to-core interface. The kinematic predictor/corrector contact algorithm available in

ABAQUS/Explicit is utilized to enforce contact and friction constraints defined by the hard pressure-penetration relationship and the Coulomb friction law, respectively. The contact search is carried out with the small-sliding assumptions in order to detect interacting surfaces both initially existing in the plate geometry and which are formed due to the debonding growth in the plate.

The relative displacements of the pair nodes accounting for contact and friction are used by ABAQUS to calculate a stress field in the debonded sandwich plate at each instant of time. If the stress state satisfies the QS damage initiation criterion defined within the cohesive element layer, the stiffness of the cohesive elements starts to degrade in accordance with the B-K law until the critical value of the SERR will be accomplished. At this moment the cohesive elements are fully fractured and newly-created detached surfaces appear within the sandwich plate.

One configuration of the sandwich plate is used throughout this study. A simply supported rectangular sandwich plate of 180 by 270 mm consisting of a 50 mm-thick WF51 foam core and 2.4 mm-thick GFRP face sheets and containing the penny-shaped debonded zone of a 39.3 mm radius at its center, as shown in Fig. 2a, is analyzed. Properties of the constituent materials are given in Table 1.

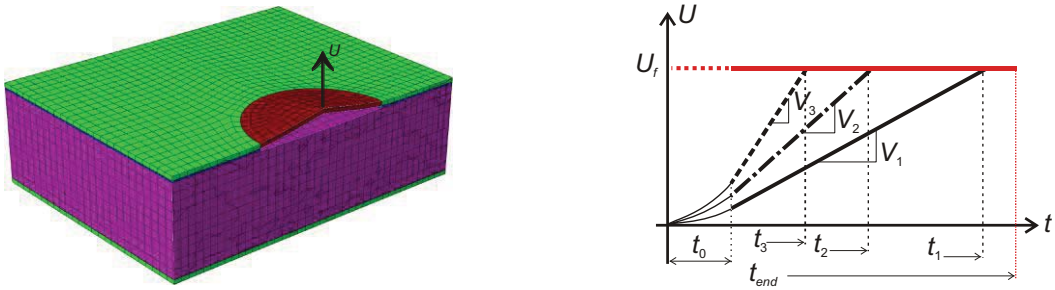

Figure 2. (a) A half of the finite element model; and (b) the displacement load

The debonded sandwich plate is loaded by a prescribed displacement U applied to the upper face sheet with various velocities V_i, while the bottom of the lower face sheet is fixed (see Fig. 2a).

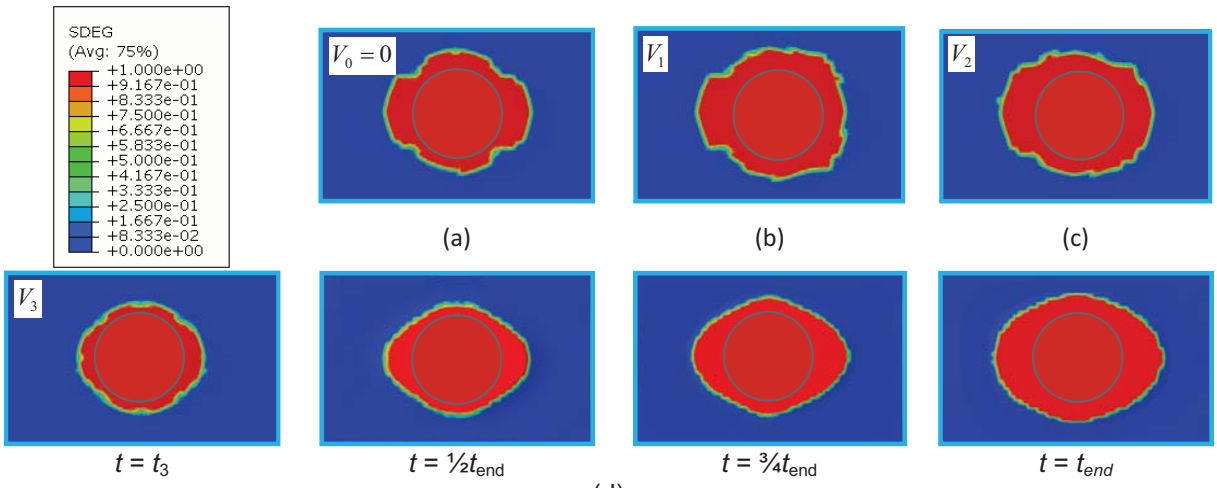

Figure 3. Debonding growth: (a) $V_0 = 0$, (b) $V_1 = 10^3$, (c) $V_2 = 10^4$ and (d) $V_3 = 10^5$ mm/s.

In numerical studies, the total opening displacement, U_f is the same for all cases and velocities are computed as a quotient of this displacement to a ramp time, during which this displacement could be achieved. The shorter is the ramp time, the more rapidly is the velocity of loading (see Fig. 2b). However, the velocities are chosen such that they not exceed the Rayleigh wave speed, which is 10^7 mm/s here. Thereby, the static critical SERRs can be used for predictions. In this study, $G_{IC} = 0.375$ N/mm, $G_{IIC} = G_{IIIC} = 2.125$ N/mm and $\eta = 1$ are accepted. The interfacial strengths are assigned as the following: $T = 3$ MPa and $S_1 = S_2 = 17.2$ MPa.

Fig. 3 shows the debonding growth under the applied displacement. One can see that the debonded area increases with increasing the loading rate. Moreover, as the speed of the displacement being applied has become relatively comparable with the Rayleigh wave speed, oscillations of the

sandwich plate produced by reflected stress waves take place. As a result, the debond continues to grow after the ramp time t_3 due to the dynamic stress field, which is enough high to advance it.

Considering the same sandwich plate with the skin-to-core interface circle debond, a dynamic harmonic concentrated load with amplitude 10 *N* and excitation frequency 1000 *Hz* was applied to the plate's bottom face sheet. Fig. 4 illustrates the debonding growth at the different moments of time. The debond propagates in the stick-slip manner, it jumps from one arrest position to another one in dependence on the dynamic stress state existing at the current instant of time.

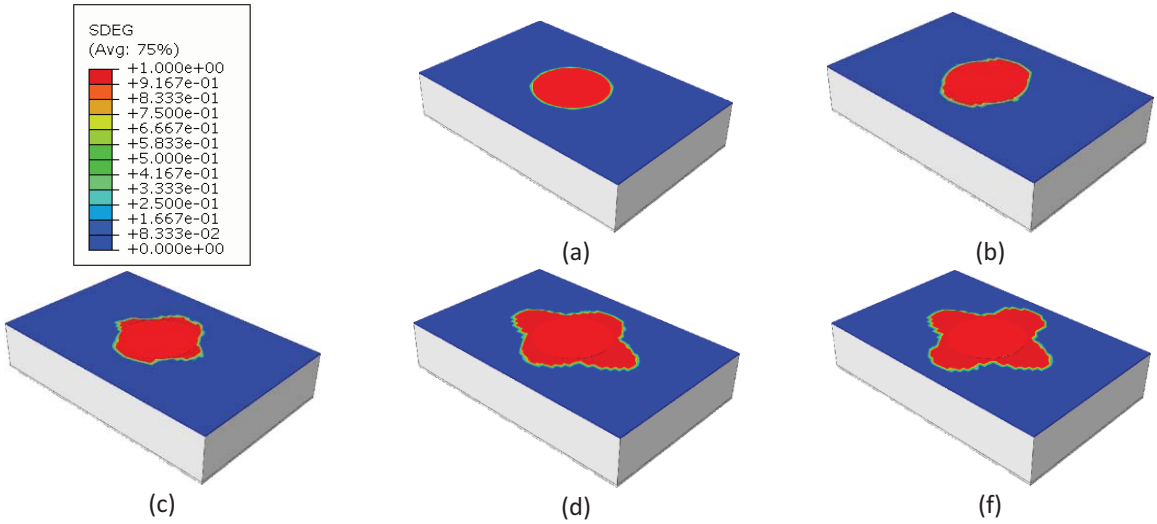

Figure 4. Debonding growth: (a) t = 1, (b) t = 3, (c) t = 5, (d) t = 7 and (f) t = 10 ms.

Conclusions

(1) The cohesive layer model and the dynamic debonding growth simulation method presented in the paper are effective for the debonding growth analysis of sandwich plate with skin-to-core debond. (2) The loading rate is essential for the debonding growth behavior of sandwich plate. (3) A harmonic loading causes the unstable debonding growth within the debonded zone of sandwich plates.

Acknowledgments

The research leading to these results has received funding from the European Union Seventh Framework Programme (FP7/2007-2013), FP7-REGPOT-2009-1, under grant agreement No. 245479.

References

[1] Carlsson L.A., Kardomateas G.A. *Structural and failure mechanics of sandwich composites*, Springer Science+Business Media, 2011.
[2] Nishioka T. Computational dynamic fracture mechanics, *International Journal of Fracture* Vol. 86, pp. 127-159, 1997.
[3] Song J.-H., Wang H. and Belytschko T. A comparative study on finite element methods for dynamic fracture, *Computational Mechanics*, Vol. 42, pp 239–250, 2008.
[4] Ortiz M. and Pandolfi A. A class of cohesive elements for the simulation of three-dimensional crack propagation. *International Journal for Numerical Methods in Engineering*, Vol. 44, pp. 1267–1282, 1999.
[5] Turon A., Davila C.G., Camanho P.P. and Costa J. An engineering solution for mesh size effects in the simulation of delamination using cohesive zone models, *Engineering Fracture Mechanics*, Vol. 74, pp. 1665-1682, 2007.
[6] Elices M., Guinea G.V., Gomez J. and Planas J. The cohesive zone model: advantages, limitations and challenges, *Engineering Fracture Mechanics*, Vol. 69, pp. 137-163, 2002.
[7] Sridharan S., Li Y. Static and dynamic delamination of foam core sandwich members, *AIAA Journal*, Vol. 44, pp. 2937-2948, 2006.
[8] Han T.-S., Ural A. and Chen Ch.-Sh. Delamination buckling and propagation analysis of honeycomb panels using a cohesive element approach, *International Journal of Solid and Structures*, Vol. 115, pp. 101-123, 2002.
[9] Burlayenko V.N. and Sadowski T. Finite Element Nonlinear Dynamic Analysis of Sandwich Plates with Partially Detached Facesheet and Core, *Finite Elements in Analysis & Design*, Vol. 62 pp. 49-64, 2012.
[10] ABAQUS. *Abaqus User's Manual*. Dassault Systèmes Simulia Corp. Providence, RI, USA, 2010.

Proceedings of the 4th International Conference on Nonlinear Dynamics
ND-KhPI2013
June 19-22, 2013, Sevastopol, Ukraine

Free Vibrations of Rockets Deflectors

M.V. Chernobryvko[1*], K.V. Avramov[1], T. Batutina[2], A.M. Tonkonogenko[2]

Abstract
Free vibrations of rockets deflections, which are described by parabolic shells, are considered. Kinetic and potential energies of the structure are derived to analyze free vibrations. The Rayleigh-Ritz method is used to analyze vibrations.

Keywords
Rocket deflection, parabolic shell, Rayleigh- Ritz method Rayleigh- Ritz method

[1] A.N. Podgorny Institute for Mechanical Engineering Problems, National Academy of Sciences of Ukraine, Kharkov, Ukraine
[2] M.K. Yangel "Yuzhnoye" State Design Office, Ukraine
* **Corresponding author:** chernobryvko@ipmach.kharkov.ua

Introduction

Elements of rockets perform intensive vibrations on flying. The vibrations take place due to aerodynamic loads, forces from engine operation. These vibrations can result in destruction of rockets elements on the first seconds of flying. Rocket deflector is a thin parabolic shell, which protect satellites during orbital injections. On flying, the aerodynamic loads, which result in intensive aeroelastic vibrations, act on deflectors. Deflectors are described by constant thickness parabolic shells. The Rayleigh- Ritz method is used to study the shell vibrations.

1. Problem Formulation

Construction diagram of the rocket deflector is shown in Fig.1. As follows from the analysis of the deflection geometry, it is described by parabolic shell with constant thickness. It is assumed, that amplitudes of the shell vibrations are significantly less then the shell thickness. Hooke's stress-strain relations are true. As the shell is thin, then shear and rotation inertia are not taken into account.

The displacements of the parabolic shell middle surface are projected on the tangents of the coordinates lines (Fig.2). As a result, the following three projections are obtained [1]: $u(\varphi,\theta,t)$, $v(\varphi,\theta,t)$, $w(\varphi,\theta,t)$. The angles φ,θ describe the location of the middle surface points.

2. The equations of the parabolic shell vibrations

The elastic potential energy of the shell takes the following form [2]:

$$\Pi = \frac{1}{2}\iiint_V \sigma_{11}\varepsilon_{11} + \sigma_{22}\varepsilon_{22} + \sigma_{12}\varepsilon_{12}\left(1+\frac{z}{R_\theta}\right)\left(1+\frac{z}{R_\varphi}\right)R_\theta R_\varphi \sin\theta d\theta\, d\varphi dz, \qquad (1)$$

where $\sigma_{11},\sigma_{12},\sigma_{22},\varepsilon_{11},\varepsilon_{12},\varepsilon_{22}$ are components of stresses and strains tensors; R_φ, R_θ are curvature radius of coordinate lines φ,θ.

The components of stress and strains tensors satisfy the Hooke's law:

$$\sigma_{11}=\frac{E}{1-\upsilon^2}\left(\varepsilon_{11}+\upsilon\varepsilon_{22}\right),\quad \sigma_{22}=\frac{E}{1-\upsilon^2}\left(\varepsilon_{22}+\upsilon\varepsilon_{11}\right),\quad \sigma_{12}=\frac{E}{1-\upsilon^2}\frac{1-\upsilon}{2}\varepsilon_{12}, \tag{2}$$

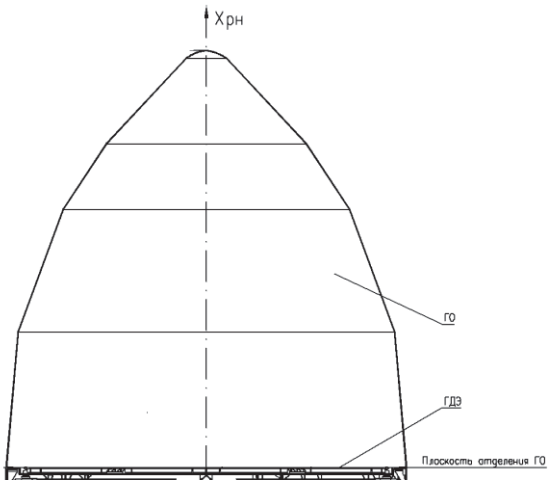

Figure 1. Design of rockets deflectors

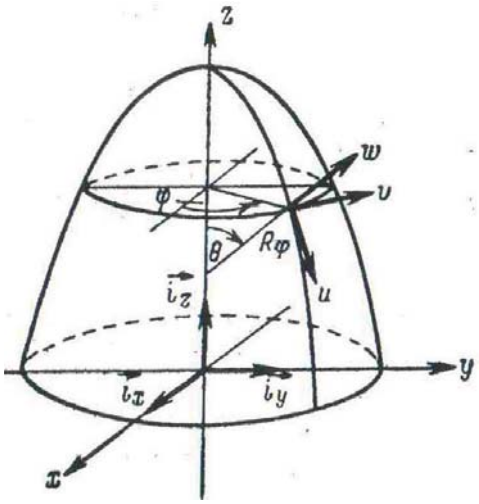

Figure 2. Middle surface of parabolic shell in Cartesian coordinates

and curvature radiuses are determined from the following relations:

$$R_\varphi=\frac{R_0}{\left(1+\chi\sin^2\theta\right)^{1/2}},\quad R_\theta=\frac{R_0}{\left(1+\chi\sin^2\theta\right)^{3/2}}. \tag{3}$$

The parameter χ determines the type of shell of revolution; for parabolic shell $\chi=-1$.

The top point of the shell $\theta=0$ is singular. Therefore, the hole with the diameter equal to the shell thickness is cut out close to the singular point to calculate the shell eigenfrequencies. This small hole slightly effects on the structure dynamics. Then taking into account (2), the potential energy of the shell is presented as

$$\Pi=\frac{1}{2}\int\limits_{-\frac{h}{2}}^{\frac{h}{2}}\int\limits_{0}^{2\pi}\int\limits_{h/R_0}^{\frac{\pi}{2}}\frac{E}{1-\upsilon^2}\left(\varepsilon_{11}^2+2\upsilon\varepsilon_{11}\varepsilon_{22}+\varepsilon_{22}^2+\frac{1-\upsilon}{2}\varepsilon_{12}^2\right)\times$$
$$\times\left(R_\theta R_\varphi\sin\theta+z\left(R_\varphi+R_\theta\right)\sin\theta+z^2\sin\theta\right)d\theta\,d\varphi dz, \tag{4}$$

where h is the shell thickness; R_0 is curvature radius in singular point $\theta=0$.

The elements of the strain tensor and displacements meet the following equations:

$$\varepsilon_{11}=\frac{1}{R_\theta}\left(\frac{\partial u}{\partial\theta}+w\right)+z\left[\frac{1}{R_\theta^2}\left(\frac{\partial u}{\partial\theta}-\frac{\partial^2 w}{\partial\theta^2}\right)+\frac{1}{R_\varphi^2\sin^2\theta}\left(\frac{\sin\varphi}{R_\theta}\frac{\partial v}{\partial\varphi}-\frac{1}{R_\theta}\frac{\partial w}{\partial\varphi}\right)\right],$$
$$\varepsilon_{22}=\frac{1}{R_\varphi\sin\theta}\left(\frac{\partial v}{\partial\varphi}+u\cos\theta+w\sin\theta\right)+z\left[\frac{1}{R_\varphi^2\sin^2\theta}\left(\frac{\partial v}{\partial\varphi}\sin\theta-\frac{\partial^2 w}{\partial\varphi^2}\right)+\right.$$
$$\left.+\frac{1}{R_\theta^2 tg\theta}\left(u-\frac{\partial w}{\partial\theta}\right)+\frac{1}{R_\theta^2}\left(\frac{\partial u}{\partial\theta}-\frac{\partial^2 w}{\partial\theta^2}\right)\right], \tag{5}$$
$$\varepsilon_{12}=\frac{1}{R_\varphi\sin\theta}\frac{\partial u}{\partial\varphi}-\frac{1}{R_\theta tg\theta}v+z\frac{1}{R_\theta R_\varphi tg\theta}v.$$

The kinetic energy of the shell takes the form:

$$T=\frac{\rho h}{2}\int_0^{\pi}\int_{h/R_0}^{\frac{\pi}{2}}\left(\left(\frac{\partial u}{\partial t}\right)^2+\left(\frac{\partial v}{\partial t}\right)^2+\left(\frac{\partial w}{\partial t}\right)^2\right)R_\theta R_\varphi\sin\theta d\theta\, d\varphi, \tag{6}$$

where ρ is density of the deflectors material.

The Rayleigh- Ritz method is used to calculate the eigenfrequencies and eigenmodes of the shell. The shell linear vibrations take the following form:

$$\begin{aligned}u(\theta,\varphi,t)&=\tilde{u}(\theta,\varphi)\cos(\omega t),\\ v(\theta,\varphi,t)&=\tilde{v}(\theta,\varphi)\cos(\omega t),\\ w(\theta,\varphi,t)&=\tilde{w}(\theta,\varphi)\cos(\omega t).\end{aligned} \tag{7}$$

Accounting to (7), the kinetic and potential energies of the shell take the following form:

$$T(\theta,\varphi,t)=\omega^2\sin^2\omega t\cdot\tilde{T}(\theta,\varphi); \tag{8}$$
$$\Pi(\theta,\varphi,t)=\cos^2\omega t\cdot\tilde{\Pi}(\theta,\varphi). \tag{9}$$

Now the shell displacements are considered. As the shell is closed, the shell displacements are expanded into the Fourier series. Then the shell eigenmodes take the following form:

$$\begin{aligned}\tilde{u}(\theta,\varphi)&=\sum_{i=1}^{N_1}\sum_{j=1}^{N_2}\psi_i^{(u)}(\theta)\left(A^{(1)}{}_{ij}\sin j\varphi+A^{(2)}{}_{ij}\cos j\varphi\right),\\ \tilde{v}(\theta,\varphi)&=\sum_{i=1}^{N_3}\sum_{j=1}^{N_4}\psi_i^{(v)}(\theta)\left(B^{(1)}{}_{ij}\sin j\varphi+B^{(2)}{}_{ij}\cos j\varphi\right),\\ \tilde{w}(\theta,\varphi)&=\sum_{i=1}^{N_5}\sum_{j=1}^{N_6}\psi_i^{(w)}(\theta)\left(C^{(1)}{}_{ij}\sin j\varphi+C^{(2)}{}_{ij}\cos j\varphi\right).\end{aligned} \tag{10}$$

where $A_{ij}^{(1)}, A_{ij}^{(2)},..., C_{ij}^{(2)}$ are unknown parameters; $\psi_i^{(u)}(\theta),\psi_i^{(v)}(\theta),\psi_i^{(w)}(\theta)$ are functions satisfying the shell boundary conditions.

The shell is clamped on the edge $\theta=\pi/2$ and it is free on the top (on the boundary of small cut). As the Rayleigh- Ritz method is used to determine the vibrations parameters, the boundary

conditions are not taken into account on the free edge of the shell. The boundary conditions on the clamped edge are the following:

$$\tilde{u}\Big|_{\theta=\frac{\pi}{2}} = \tilde{v}\Big|_{\theta=\frac{\pi}{2}} = \tilde{w}\Big|_{\theta=\frac{\pi}{2}} = \frac{\partial \tilde{w}}{\partial \theta}\Big|_{\theta=\frac{\pi}{2}} = 0. \tag{11}$$

The functions $\psi_i^{(u)}, \psi_i^{(v)}$ are eigenmodes of longitudinal vibrations of cantilever bar; the functions $\psi_i^{(w)}$ are eigenmodes of bending vibrations of cantilever beam. Accounting (11), these functions take the following form:

$$\begin{aligned}
&\psi_i^{(u)}(\theta) = \cos(2i-1)\theta, \\
&\psi_i^{(v)}(\theta) = \cos(2i-1)\theta, \\
&\psi_i^{(w)}(\theta) = \frac{1}{2}\left(\mathrm{ch}\left[k_i \left(\frac{\pi}{2} - \theta \right) \right] - \cos\left[k_i \left(\frac{\pi}{2} - \theta \right) \right] \right) - \\
&- \frac{\mathrm{sh}(k_i s) - \sin(k_i s)}{2\left(\mathrm{ch}(k_i s) - \cos(k_i s)\right)} \left(\mathrm{sh}\left[k_i \left(\frac{\pi}{2} - \theta \right) \right] - \sin\left[k_i \left(\frac{\pi}{2} - \theta \right) \right] \right)
\end{aligned} \tag{12}$$

The Hamilton variational principle is used to calculate eigenfrequencies and eigenmodes of the shell linear vibrations. The minimum of the following functional,

$$\int_0^{2\pi/\omega} \left(\Pi - T \right) dt = \frac{\pi}{\omega} \left\{ \tilde{\Pi}\left(A_{ij}^{(1)}, ..., C_{ij}^{(2)} \right) - \omega^2 \tilde{T}\left(A_{ij}^{(1)}, ..., C_{ij}^{(2)} \right) \right\}., \tag{13}$$

is determined on the set of parameters $A_{ij}^{(1)}, ..., C_{ij}^{(2)}$. From this minimum determination, the following eigenvalue problem is obtained:

$$Det\left[C - \omega^2 M \right] = 0, \tag{14}$$

where C is the stiffness matrix; M is the mass matrix.

Conclusions

The results, treated in this paper, can be used to analyze nonlinear aeroelastic vibrations of deflectors in subsonic and supersonic stream.

Acknowledgments

The authors express thanks to Professors V.I. Gulyaev and O.K. Morachkovski for useful discussions on the problems considered in this paper. This research is supported by grant of National Academy of Science of Ukraine II-67-13.

References

[1] Amabili M. *Nonlinear Vibrations and Stability of Shells and Plates,* New York: Cambridge University Press, 2008.
[2] Grigoluk E.I., Kabanov V.V. *Stability of Shells*, Moscow: Nauka, 1978 (in Russian).

Proceedings of the 4th International Conference on Nonlinear Dynamics
ND-KhPI2013
June 19-22, 2013, Sevastopol, Ukraine

The Probabilistic Solutions of Simply-Supported Plate with Large Deflection and Excited by Random Excitation Being Gaussian White Noise

Guo-Kang Er[1*], Vai Pan Iu[1]

Abstract
The random vibration of the von Kármán plate with moderately large deflection and excited by Gaussian white noise is analyzed. The equation of motion of the plate with moderately large deflection is a nonlinear partial differential equation in space and time. With Galerkin method, the nonlinear partial differential equation is reduced to a multi-degree-of-freedom nonlinear stochastic dynamical system which probabilistic solution is governed by Fokker-Planck-Kolmogorov equation. The state-space-split method is used to make the Fokker-Planck-Kolmogorov equation in high dimensions reduced to the Fokker-Planck-Kolmogorov equations in low dimensions. Then the exponential polynomial closure method is used to solve the reduced Fokker-Planck-Kolmogorov equations in low dimensions for the probability density function of the responses of the plate with moderately large deflection.

Keywords
Nonlinear stochastic dynamic system, Fokker-Planck-Kolmogorov equation, state-space-split, von Kármán plate

[1] Department of Civil and Environmental Engineering, University of Macau, Macau SAR, P.R. China.
* **Corresponding author:** gker@umac.mo

Introduction

Many problems in science and engineering can be modeled as nonlinear stochastic dynamical (NSD) systems with multi degrees of freedom (MDOF). It is known that the analysis on the probabilistic solutions of MDOF-NSD systems has been a challenge for almost a century, especially for the systems with strong nonlinearity. There are two methods for analyzing the MDOF-NSD systems. One is equivalent linearization (EQL) method and another is Monte Carlo simulation (MCS) method [1, 2]. It is well known that the EQL method is only suitable for the weakly nonlinear system. There are some challenges in using MCS method in analyzing strongly nonlinear stochastic dynamical systems, such as the problems of round-off error and numerical stability. Recently, a new method named state-space-split (SSS) method was proposed for the probabilistic solutions of large MDOF-NSD systems or solving the Fokker-Planck-Kolmogorov (FPK) equations in high dimensions [3-5]. The SSS method can make the problem of solving the FPK equation in high dimensions become the problem of solving some FPK equations in low dimensions or make the large NSD system decoupled into some small NSD systems. Therefore, the FPK equations in low dimensions can be solved with the exponential polynomial closure (EPC) method [6]. In this paper, the SSS-EPC method is further used to analyze the probabilistic solutions of the simply-supported von Kármán plate with moderate large deflection and excited by Gaussian white noise. The equation of motion of the plate is a nonlinear partial differential equation in time and space. With Galerkin method, the nonlinear partial differential equation is reduced to a MDOF-NSD system. The random vibration problems of many other plates with moderately large deflection can also be modeled with the similar MDOF-NSD systems. The results obtained with the SSS-EPC method are compared with those obtained with EQL

method and MCS to show the effectiveness of the SSS-EPC method in this case and the advantage of SSS-EPC method over EQL method and MCS in analyzing the resulted MDOF system with strong nonlinearity.

1. The MODF Systems for an Isotropic Plate with Moderately Large Deflection

Consider the random vibration problem of the isotropic plate with moderately large deflection governed by the following equations of motion or partial differential equations in space and time.

$$\begin{cases} \rho h\ddot{w}+c\dot{w}+D\nabla^4 w=[\rho h+M\delta(x)\delta(y)]W(t)+h(w_{,xx}F_{,yy}+w_{,yy}F_{,xx}-2w_{,xy}F_{,xy}) \\ \nabla^4 F=E(w_{,xy}^2-w_{,xx}w_{,yy}) \end{cases} \tag{1}$$

where $w(x,y,t)$ is the deflection of the plate, $F(x,y,t)$ is the Airy stress function, h is the thickness of the plate, E is modulus of elasticity of the isotropic plate, $D=\dfrac{Eh^3}{12(1-\nu^2)}$, ν is Poisson ratio, ρ is the mass density of the material, c reflects damping, M is lumped mass at the center of plate, $\delta(x)$ and $\delta(y)$ are Dirac functions, and $W(t)$ is Gaussian white noise with its power spectral density S. $W(t)$ can be used to describe the vertical ground acceleration caused by earthquake.

Consider the case that the four edges of a rectangular plate with length a and width b are all simply supported and free from boundary stresses. The boundary conditions for these edges can be written as follows when the origin of the coordinate system is at the center of the neutral plane of the plate, the x-axis is parallel to the length of the plate, and the y-axis is parallel to the width of the plate.

$$\begin{cases} w=w_{,xx}=F_{,yy}=F_{,xy}=0 & \text{at } x=\pm\dfrac{a}{2} \\ w=w_{,yy}=F_{,xx}=F_{,xy}=0 & \text{at y}=\pm\dfrac{\text{b}}{2} \end{cases} \tag{2}$$

The boundary conditions shown in Eq. (2) can be satisfied by the following expressions of $w(x,y,t)$ and $F(x,y,t)$.

$$\begin{cases} w(x,y,t)=\displaystyle\sum_{m=1,3,\ldots}^{N_x}\sum_{n=1,3,\ldots}^{N_y} w_{mn}(t)\cos\frac{m\pi x}{a}\cos\frac{n\pi y}{b} \\ F(x,y,t)=\displaystyle\sum_{p=1}^{M_x}\sum_{q=}^{M_y} F_{pq}(t)X_p(x)Y_q(y) \end{cases} \tag{3}$$

where $X_m(x)=\dfrac{\cosh\alpha_m x}{\cosh(0.5\alpha_m a)}-\dfrac{\cos\alpha_m x}{\cos(0.5\alpha_m a)}$ and $Y_m(y)=\dfrac{\cosh\beta_m y}{\cosh(0.5\beta_m b)}-\dfrac{\cos\beta_m y}{\cos(0.5\beta_m b)}$, $\alpha_m=2\lambda_m/a$, $\beta_m=2\lambda_m/b$, $\lambda_1=2.3650$, $\lambda_2=5.4978$, $\lambda_3=8.6394, \lambda_4=11.7810,$ and $\lambda_m=\pi(m-0.25)$ if $m>4$.

Substituting Eqs. (3) into Eqs. (1), the following equations governing w_{mn} and F_{ij} can be obtained by the Galerkin method [7].

$$\begin{aligned} \ddot{w}_{mn}+2\zeta\omega_{mn}\dot{w}_{mn}+\omega_{mn}^2 w_{mn}=&\frac{4q_{mn}W(t)}{\rho hab}-\frac{4\pi^2}{\rho ab}\sum_{p=1,3,\ldots}^{N_x}\sum_{q=1,3,\ldots}^{N_y}\sum_{r=1}^{M_x}\sum_{s=1}^{M_y} w_{pq}F_{rs} \\ &\left(\frac{p^2}{a^2}M_1^{rmp}N_2^{snq}+\frac{q^2}{b^2}M_2^{rmp}N_1^{snq}+2\frac{pq}{ab}M_3^{rpm}N_3^{sqn}\right) \qquad m,n=1,3,5,\ldots \end{aligned} \tag{4}$$

$$\left(\frac{b^2}{a^2}\lambda_i^4+\frac{a^2}{b^2}\lambda_j^4\right)F_{ij}+2\sum_{p=1}^{M_x}\sum_{1=}^{M_y}F_{pq}\lambda_p^2\lambda_q^2K_1^{ip}L_1^{jq}=\frac{\pi^4E}{16ab}\sum_{m=1,3,\ldots}^{N_x}\sum_{n=1,3,\ldots}^{N_y}\sum_{r=1,3,\ldots}^{N_x}\sum_{s=1,3,\ldots}^{N_y}w_{mn}w_{rs}$$
$$(mnrsM_4^{imr}N_4^{jns}-m^2s^2M_1^{imr}N_1^{jns}) \qquad i,j=1,2,3,\ldots \tag{5}$$

where $\omega_{mn}^2=\frac{D\pi^4}{\rho h}\left(\frac{m^2}{a^2}+\frac{n^2}{b^2}\right)^2$, $q_{mn}=\begin{cases}\frac{4ab\rho h}{mn\pi^2}\sin\frac{\mathrm{m}\pi}{2}\sin\frac{\mathrm{n}\pi}{2}+\mathrm{M} & m \text{ and } n=1,3,...\\ 0 & m \text{ or } n=2,4,...\end{cases}$,

$\frac{c}{\rho h}$ is replaced by $2\zeta\omega_{mn}$ in order to make the damping ratio consistent for each mode,

$K_1^{ip}=\frac{1}{a\alpha_p^2}\int_{-a/2}^{a/2}X_i(x)X_p^{"}dx$, $L_1^{jq}=\frac{1}{b\beta_q^2}\int_{-a/2}^{a/2}Y_j(y)Y_q^{"}dy$, $M_1^{rmp}=\int_{-a/2}^{a/2}X_r(x)\cos\frac{m\pi x}{a}\cos\frac{p\pi x}{a}dx$,

$M_2^{rmp}=\int_{-a/2}^{a/2}X_r^{"}(x)\cos\frac{m\pi x}{a}\cos\frac{p\pi x}{a}dx$, $M_3^{rpm}=\int_{-a/2}^{a/2}X_r^{'}(x)\sin\frac{p\pi x}{a}\cos\frac{m\pi x}{a}dx$, and

$M_4^{imr}=\int_{-a/2}^{a/2}X_i(x)\sin\frac{m\pi x}{a}\sin\frac{r\pi x}{a}dx$.

The constants N_1 to N_4 in Eqs. (4) and (5) are obtained by replacing M,X,x,a,m,p and r by $N,Y,y,b,n,q,$ and s, respectively, in the expressions of M_1 to M_4.

2. Dimension Deduction of FPK Equations with State-Space-Split Method

The governing equations for the random vibration of the above plate can be written in general as follows.

$$\ddot{Y}_i+h_i(\mathbf{Y},\dot{\mathbf{Y}})=\gamma_iW(t) \qquad i=1,2,\cdots,n_Y \tag{6}$$

where $Y_i\in R,(i=1,2,\cdots,n_Y)$, are components of the vector process $\mathbf{Y}\in R^{n_Y}$; $h_i:R^{n_Y}\times R^{n_Y}\to R$; $h_i(\mathbf{Y},\dot{\mathbf{Y}})$ are of polynomial type of nonlinearity and their functional forms are assumed to be deterministic; γ_i are constants, $W(t)$ is Gaussian white noise with power spectral density S.

Setting $Y_i=X_{2i-1}$, $\dot{Y}_i=X_{2i}$, $f_{2i-1}=X_{2i}$, $f_{2i}=-h_i$, $g_{2i-1}=0$, $g_{2i}=\gamma_i$, and $n_X=2n_Y$, then Eqs. (6) can be written by the following coupled Langevin equations or Ito differential equations:

$$\frac{d}{dt}X_i=f_i(\mathbf{X})+g_iW(t) \qquad i=1,2,\cdots,n_X \tag{7}$$

where the state vector $\mathbf{X}\in R^{n_X}$, $X_i\,(i=1,2,\ldots n_X)$ are components of the state vector process $\mathbf{X}$, and $f_i(\mathbf{X}):R^{n_X}\to R$. The state vector $\mathbf{X}$ is Markovian and the stationary PDF $p(\mathbf{x})$ of the Markovian vector is governed by the following FPK equation [8]:

$$\frac{\partial}{\partial x_j}[f_j(\mathbf{x})p(\mathbf{x})]-\frac{1}{2}\frac{\partial^2}{\partial x_i\partial x_j}[G_{ij}p(\mathbf{x})]=0 \tag{8}$$

where $\mathbf{x}$ is the deterministic state vector, $\mathbf{x}\in R^{n_X}$, and $G_{ij}=S_{ls}g_{il}g_{js}$. The summation convention is used in Eq. (8) and in the following discussions. It is assumed that $p(\mathbf{x})$ fulfils the following conditions:

$$\lim_{x_i\to\pm\infty}f_j(\mathbf{x})p(\mathbf{x})=0 \quad\text{and}\quad \lim_{\mathrm{x_i}\to\pm\infty}\frac{\partial p(\mathbf{x})}{\partial x_i}=0 \qquad i=1,2,\cdots,n_{X.} \tag{9}$$

If the joint PDF of $\{Y_i,\ \dot{Y}_i\}$ or $\{X_{2i-1},\ X_{2i}\}$ $(i=1,2,...,n_Y)$ are needed, separate the state vector $\mathbf{X}$ into two parts by $\mathbf{X}=\{\mathbf{X}_1,\mathbf{X}_2\}\in R^{n_X}=R^2\times R^{n_{X_2}}$ with $\mathbf{X}_1=\{X_{2i-1},\ X_{2i}\}\in R^2$, $\mathbf{X}_2\in R^{n_{X_2}}$, and $n_{x_2}=n_X-2$.

Denote the PDF of $\mathbf{X}_1$ as $p_1(\mathbf{x}_1)$. In order to obtain $p_1(\mathbf{x}_1)$, integrating Eq. (8) over $R^{n_{X_2}}$ gives

$$\int_{R^{n_{x_2}}}\frac{\partial}{\partial x_j}[f_j(\mathbf{x})p(\mathbf{x})]\mathrm{d}\mathbf{x}_2-\frac{1}{2}\int_{R^{n_{x_2}}}\frac{\partial^2}{\partial x_i\partial x_j}[G_{ij}p(\mathbf{x})]d\mathbf{x}_2=0 \tag{10}$$

Because of Eq. (9), we have

$$\int_{R^{n_{x_2}}}\frac{\partial}{\partial x_j}[f_j(\mathbf{x})p(\mathbf{x})]\mathrm{d}\mathbf{x}_2=0\quad\text{and}\quad\int_{R^{n_{x_2}}}\frac{\partial^2}{\partial x_i\partial x_j}[G_{ij}p(\mathbf{x})]d\mathbf{x}_2=0\qquad x_i\text{ or }x_j\in R^{n_{X_2}} \tag{11}$$

Eq. (10) can then be expressed as

$$\int_{R^{n_{x_2}}}\frac{\partial}{\partial x_j}[f_j(\mathbf{x})p(\mathbf{x})]\mathrm{d}\mathbf{x}_2-\frac{1}{2}\int_{R^{n_{x_2}}}\frac{\partial^2}{\partial x_i\partial x_j}[G_{ij}(\mathbf{x})p(\mathbf{x})]d\mathbf{x}_2=0\qquad x_i,x_j\in R^{n_{X_1}} \tag{12}$$

which can be further expressed as

$$\frac{\partial}{\partial x_j}\left[\int_{R^{n_{x_2}}}f_j(\mathbf{x})p(\mathbf{x})d\mathbf{x}_2\right]-\frac{1}{2}\frac{\partial^2}{\partial x_i\partial x_j}\left[\int_{R^{n_{x_2}}}G_{ij}p(\mathbf{x})d\mathbf{x}_2\right]=0\qquad x_i,x_j\in R^{n_{X_1}} \tag{13}$$

Separate $f_j(\mathbf{x})$ into two parts as

$$f_j(\mathbf{x})=f_j^{I}(\mathbf{x}_1)+f_j^{II}(\mathbf{x}) \tag{14}$$

Substituting Eq. (14) into Eq. (13) and noting $\int_{R^{n_{x_2}}}G_{ij}p(\mathbf{x})d\mathbf{x}_2=G_{ij}p_1(\mathbf{x})$ gives

$$\frac{\partial}{\partial x_j}\left[f_j^{I}(\mathbf{x}_1)p_1(\mathbf{x}_1)+\int_{R^{n_{x_2}}}f_j^{II}(\mathbf{x})p(\mathbf{x})d\mathbf{x}_2\right]-\frac{1}{2}\frac{\partial^2[G_{ij}p_1(\mathbf{x}_1)]}{\partial x_i\partial x_j}=0\qquad x_i,x_j\in R^{n_{X_1}} \tag{15}$$

For real systems, normally $f_j^{II}(\mathbf{x})$ are functions of only few state variables for given j. Express $f_j^{II}(\mathbf{x})$ by $f_j^{II}(\mathbf{x})=\sum_k f_{jk}^{II}(\mathbf{x}_1,\mathbf{z}_k)$ in which $\mathbf{z}_k\in R^{n_{Z_k}}\subset R^{n_{X_2}}$. n_{z_k} is the number of the state variables in $\mathbf{z}_k$. Then, Eq. (15) can be written as

$$\frac{\partial}{\partial x_j}\left[f_j^{I}(\mathbf{x}_1)p_1(\mathbf{x}_1)+\sum_k\int_{R^{n_{z_k}}}f_{jk}^{II}(\mathbf{x}_1,\mathbf{z}_k)p_k(\mathbf{x}_1,\mathbf{z}_k)d\mathbf{z}_\mathrm{k}\right]-\frac{1}{2}\frac{\partial^2[G_{ij}p_1(\mathbf{x}_1)]}{\partial x_i\partial x_j}=0\qquad x_i,x_j\in R^{n_{X_1}} \tag{16}$$

in which $p_k(\mathbf{x}_1,\mathbf{z}_k)$ denotes the joint PDF of $\{\mathbf{X}_1,\mathbf{Z}_k\}$. The summation convention not applies on the indexes k in Eq. (16) and in the following discussions.

From Eq. (16), it is seen that the coupling of $\mathbf{X}_1$ and $\mathbf{X}_2$ comes from $f_{jk}^{II}(\mathbf{x}_1,\mathbf{z}_k)p_k(\mathbf{x}_1,\mathbf{z}_k)$. Express $p_k(\mathbf{x}_1,\mathbf{z}_k)$ by

$$p_k(\mathbf{x}_1,\mathbf{z}_k)=p_1(\mathbf{x}_1)q_k(\mathbf{z}_k\mid\mathbf{x}_1) \tag{17}$$

where $q_k(\mathbf{z}_k\mid\mathbf{x}_1)$ is the conditional PDF of $\mathbf{Z}_k$ for given $\mathbf{X}_1=\mathbf{x}_1$. Substituting Eq. (17) into Eq. (16) gives

$$\frac{\partial}{\partial x_j}\left[f_j^I(\mathbf{x}_1)p_1(\mathbf{x}_1)+\sum_k\int_{R^{n_{z_k}}}f_{jk}^{II}(\mathbf{x}_1,\mathbf{z}_k)p_1(\mathbf{x}_1)q_k(\mathbf{z}_k\mid\mathbf{x}_1)d\mathbf{z}_k\right]-\frac{1}{2}\frac{\partial^2[G_{ij}p_1(\mathbf{x}_1)]}{\partial x_i\partial x_j}=0\qquad x_i,x_j\in R^{n_{X_1}}\quad(18)$$

Approximately replacing the conditional PDFs $q_k(\mathbf{z}_k\mid\mathbf{x}_1)$ by those obtained from equivalent linearization, Eq. (18) is written as

$$\frac{\partial}{\partial x_j}\left[f_j^I(\mathbf{x}_1)\widetilde{p}_1(\mathbf{x}_1)+\sum_k\int_{R^{n_{z_k}}}f_{jk}^{II}(\mathbf{x}_1,\mathbf{z}_k)\widetilde{p}_1(\mathbf{x}_1)\overline{q}_k(\mathbf{z}_k\mid\mathbf{x}_1)d\mathbf{z}_k\right]-\frac{1}{2}\frac{\partial^2[G_{ij}\widetilde{p}_1(\mathbf{x}_1)]}{\partial x_i\partial x_j}=0\qquad x_i,x_j\in R^{n_{X_1}}\quad(19)$$

where $\overline{q}_k(\mathbf{z}_k\mid\mathbf{x}_1)$ is the conditional PDF of $\mathbf{Z}_k$ obtained from EQL for given $\mathbf{X}_1=\mathbf{x}_1$ and $\widetilde{p}_1(\mathbf{x}_1)$ is the approximation of $p_1(\mathbf{x}_1)$. Denote

$$\widetilde{f}_j(\mathbf{x}_1)=f_j^I(\mathbf{x}_1)+\sum_k\int_{R^{n_{z_k}}}f_{jk}^{II}(\mathbf{x}_1,\mathbf{z}_k)\overline{q}_k(\mathbf{z}_k\mid\mathbf{x}_1)d\mathbf{z}_k\qquad(20)$$

Then Eq. (19) can be expressed as

$$\frac{\partial}{\partial x_j}\left[\widetilde{f}_j(\mathbf{x}_1)\widetilde{p}_1(\mathbf{x}_1)\right]-\frac{1}{2}\frac{\partial^2}{\partial x_i\partial x_j}\left[G_{ij}\widetilde{p}_1(\mathbf{x}_1)\right]=0\quad x_i,x_j\in R^{n_{X_1}}\qquad(21)$$

which is the approximate FPK equation for the joint PDF of the state variables $\mathbf{X}_1=\{X_{2i-1},\ X_{2i}\}\in R^2$. Because there are only two state variables in $\mathbf{X}_1$, the resulting FPK equations is in two dimensions and the EPC method can be employed to solve Eq. (21) [6].

3. Numerical Analysis

Consider the simply-supported rectangular von Kármán plate which edges are free from stresses. The material of the plate is reinforced concrete used in building design. The length a and width b of the plate equal 6m and 5m, respectively. The other parameters are given by $h=0.1\,m$, $E=2.55\times10^{10}N/m^2$, $\rho=2{,}000kg/m^3$, $\nu=0.316$, $M=20{,}000kg$, $\zeta=0.01$ for each mode, and $S=1$. The subspace $\mathbf{X}_1$ in the SSS procedure contains the deflection w and the velocity $\dot{w}$ at the center of the plate.

When the number of shape functions of deflection equals $N_x\times N_y=1\times1=1$ and the number of shape functions of Airy stress function equals $M_x\times M_y=1\times1=1$, the resulted equation of motion in term of deflection is a Duffing oscillator. The PDFs of the deflection at the center of the plate are obtained with the EPC method and EQL method. They are shown and compared in Fig. 1. The tails of the PDFs obtained with various methods are also compared in Fig. 2. In the figures, σ_w denotes the standard deviation of the deflection at the center of the plate. In this case, the exact solution of the probability density function of the deflection is obtainable for the resulted Duffing oscillator excited by Gaussian white noise. It is observed in Figs. 1 and 2 that the result obtained with EPC is the same as exact solution while the result corresponding to EQL deviates a lot from exact solution. Numerical experience shows that the results obtained with $N_x\times N_y=1\times1=1$ and $M_x\times M_y=2\times2=4$ are only slightly different from those corresponding to $N_x\times N_y=1\times1=1$ and $M_x\times M_y=1\times1=1$. In other words, increasing the number of shape functions in the Airy stress function can only influence the results slightly.

When the number of the shape functions of deflection equals $N_x\times N_y=3\times3=9$ and the number of shape functions of Airy stress function equals $M_x\times M_y=2\times2=4$, the equations of motion formulate a 9-DOF system. The PDFs of the deflection at the center of the plate are obtained with the SSS-EPC method, MCS, and EQL, respectively. They are shown and compared in Fig. 3.

The tails of the PDFs obtained with various methods are also compared in Fig. 4. The sample size in MCS is 10^7. The simulation about this 9-DOF system was conducted on the original 9-DOF system rather than on the SDOF system resulted from SSS deduction procedure.

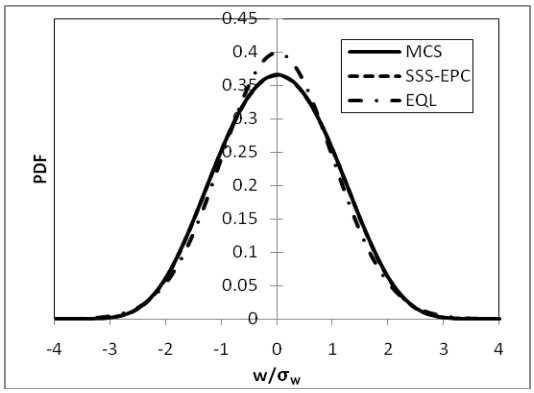

Figure 1. PDFs of deflection

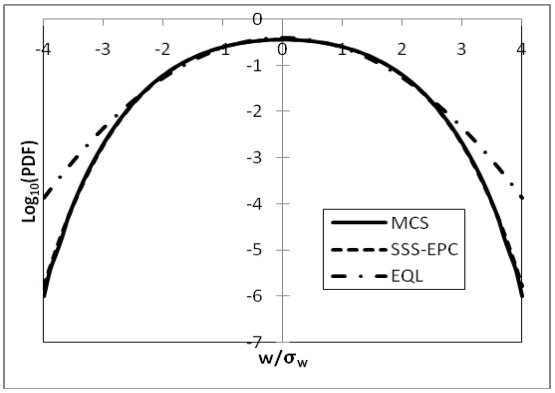

Figure 2. Logarithmic PDFs of deflection

It is observed in Figs. 3 and 4 that the result obtained with SSS-EPC is close to MCS while the result corresponding to EQL deviates a lot from MCS. Numerical experience showed that the results obtained with $N_x \times N_y = 3 \times 3 = 9$ are almost the same as those obtained with $N_x \times N_y = 4 \times 4 = 16$. Further increasing the number of $N_x, N_y, M_x,$ and M_y beyond $N_x \times N_y = 3 \times 3 = 9$ and $M_x \times M_y = 2 \times 2 = 4$ can not further increase the precision of the solution obviously. The results obtained with $N_x \times N_y = 4 \times 4 = 16$ and $M_x \times M_y = 2 \times 2 = 4$ are almost the same as those obtained with $N_x \times N_y = 3 \times 3 = 9$ and $M_x \times M_y = 2 \times 2 = 4$. The polynomial degree used in the EPC solution procedure is four.

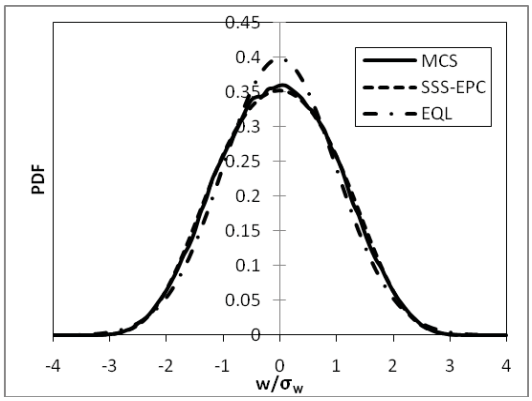

Figure 3. PDFs of deflection

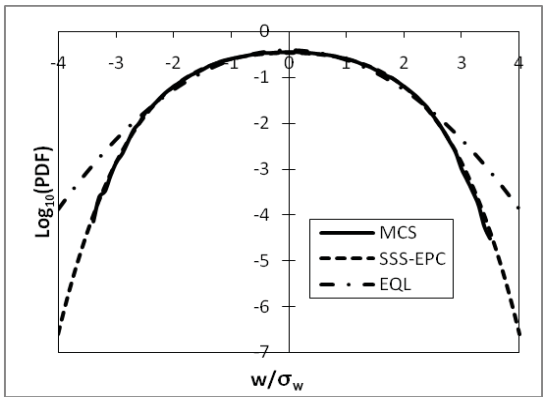

Figure 4. Logarithmic PDFs of deflection

Further increasing the number of samples in analyzing the 9-DOF system with MCS can make the computational effort huge and it can not make the results from MCS further improved due to the round-off error caused by the large sample size and large number of nonlinear terms in the system. Hence only part of the PDF of deflection can be obtained with MCS for this complex and strongly nonlinear system. It is one of the challenges inherent in MCS. Even so, the computational time needed by SSS-EPC method is in minutes mainly spent on the linearization procedure due to the large number of nonlinear terms while the computational time needed by MCS is in hours for this 9-DOF system in the same computer and same running environment.

From Fig. 2 and Fig. 4 we found that the PDF of the deflection obtained by modeling the system as a SDOF system is quite rough in comparison with the PDF of the deflection obtained by modeling the system as a 9-DOF system. The results obtained from SDOF system is about 1 to 5 times of the solution obtained from the 9-DOF system, as shown in Figs. 2 and 4. For either the SDOF system or the 9-DOF system, the result from EQL is far from being acceptable.

Conclusions

The solution procedure of the state-space-split method is used to make the MDOF systems governing the nonlinear random vibration of von Kármán plate decoupled or make the FPK equation that governing the PDF solution of von Kármán plate deducted to the FPK equations in low dimensions. Then the exponential polynomial closure method is used to solve the FPK equations in low dimensions. From numerical analysis it is observed that the SSS-EPC method works well for obtaining the PDF of the deflection of the plate though the nonlinearity is strong in the resulted MDOF system. It is found that the result obtained by modeling the problem as a SDOF oscillator is rough while the results obtained by modeling the problem as a 9-DOF system can be much improved by using three displacement mode functions and two Airy stress shape functions along each dimension of the rectangular plate. Further increasing the number of DOF can not make the solution further improved. It means that the solution obtained with this 9-DOF system can be considered as a converged solution in the sense of approximation with Galerkin method. It is also found that MCS can not make the PDF of deflection fully simulated because of the strong nonlinearity of the system, the limitation of acceptable computational effort, and the numerical stability in the simulation procedure. This problem can become more obvious when the system nonlinearity becomes stronger as the load increases or other system parameters change. The solution from EQL is far from being acceptable for this strongly nonlinear random vibration problem of plate.

Acknowledgments

This research is supported by the Research Committee of University of Macau (Grant No. MYRG138-FST11-EGK).

References

[1] Booton R.C. Nonlinear control systems with random inputs. *IRE Trans. on Circuit Theory* 1954; **CT-1**(1): 9-18.

[2] Kloeden P.E. and Platen E. *Numerical Solution of Stochastic Differential Equations*, Springer, Berlin, 1995.

[3] Er G.K. Methodology for the solutions of some reduced Fokker-Planck equations in high dimensions *Annalen der Physik*, **523**(3), pp.247-258, 2011.

[4] Er G.K. and Iu V.P. A new method for the probabilistic solutions of large-scale nonlinear stochastic dynamical systems, *Nonlinear Stochastic Dynamics and Control*, IUTAM Book Series 29, pp.25-34, Springer, Berlin, 2011.

[5] Er G.K. and Iu V.P. State-space-split method for some generalized Fokker-Planck-Kolmogorov equations in high dimensions *Physical Review E*, **85**, 067701, 2012.

[6] Er G.K. An improved closure method for analysis of nonlinear stochastic systems *Nonlinear Dynamics*, **17**(3), pp.285-297, 1998.

[7] Chia C.Y. *Nonlinear analysis of plates*, McGraw-Hill Inc., New York, 1980.

[8] Risken H. *The Fokker-Planck Equation, Methods of Solution and Applications*, Springer, Berlin, 1989.

Proceedings of the 4th International Conference on Nonlinear Dynamics
ND-KhPI2013
June 19-22, 2013, Sevastopol, Ukraine

Forced Nonlinear Vibrations of Turbine Blades Package with Pre-Stressed Detachable Shroud

Sergii O. Grytsan*, Oleksiy O. Larin

Abstract
Forced nonlinear vibrations of steam turbine two blades package with detachable bandage shroud has been considered. Static loads are taken into account. Numerical algorithm has been developed and nonlinear vibrations effects have been analyzed. Dynamic characteristics for the linearized and nonlinear pre-stressed finite element models of the blades package have been calculated. Investigation of the dynamic contact interaction together with the spectral analysis of stationary forced vibration regime have been performed.

Keywords
Dynamic contact, steam turbine blades, detachable shroud

National Technical University "Kharkiv Polytechnic Institute", Kharkiv, Ukraine
* **Corresponding author:** sergii.grytsan@gmail.com

Introduction

High levels of vibration are the most common cause of failures and breakdowns occurring during the operation of steam turbines. At that, the most dynamically loaded part is the blading of low pressure cylinder. These blades possess high bending-torsion flexibility due to complexity and variable cross section of the profile, large length of the blade and considerable angle of pre-twist. These properties of the blades may cause undesirably high levels of vibration.

In order to increase the stiffness of last stage bladings, the inter-blade detachable joints [1] are used. Strength and vibration characteristics of these blades sets are essentially dependent on the features of the contact interaction in the joints [1]. And due to the structural nonlinearity in the system, nonlinear vibrations occur under the influence of non-stationary loads. In the previous [1] studies of forced vibrations of blades packages the static loads were not taken into consideration. As a result, there were drawn conclusions on possibility of splitting of the joint. However, the influence of the static field of centrifugal force leads to a rather tight closure in the detachable bandage shroud. That has a considerable effect upon the dynamic behavior of the system.

Thus, there is a special practical importance of taking into consideration of the static pre-stress state in the analysis of forced nonlinear vibrations of the turbine bladings, since it can lead to more accurate results and conclusions.

1. Object of study

The free two blades package of fourth stage of low pressure cylinder of steam turbine has been considered. The chosen model is not fully reflects the behavior of blading, since the interaction of only two blades without influence of neighboring blades of assembly has been studied. However, firstly, this model enables to make some qualitative conclusions regarding effects that appear during forced vibrations. Secondly, due to thermal overloads [1], decomposition of the blading into separate packages is possible. And in this case the used model sufficiently reflects processes occurring, and has practical significance.

Blades are bounded by the one-tier integral detachable shroud, where contact occurs under technological preliminary penetration. The disc and the shank are omitted in simulation. It is considered that the root parts of the blades are rigid fixed.

For the numerical simulations the three-dimensional finite element (FE) model of two blades package (Fig. 1) has been used, at that the meshing of the blades was performed with isoparametric twenty-node finite elements. Contact interaction in the bandage shroud has been considered taking into account the dry friction (according to Coulomb's law) and simulated by finite elements of "surface-surface" type.

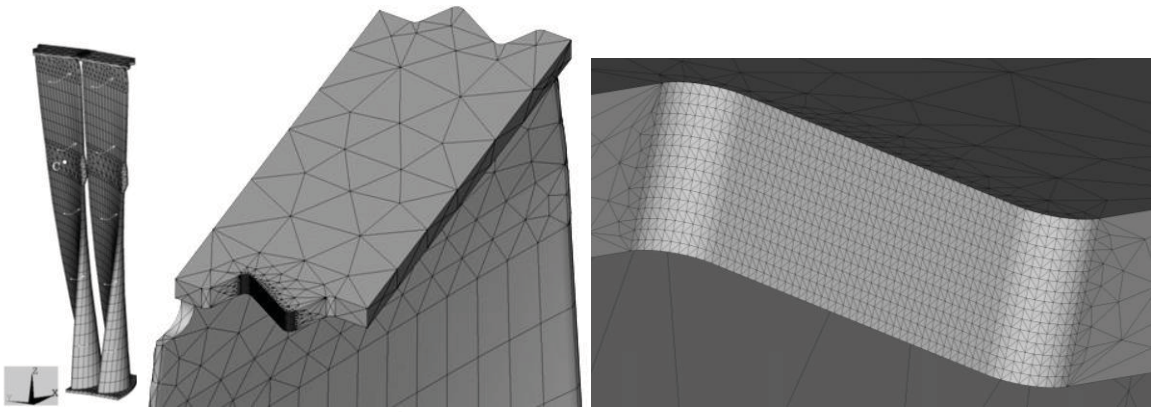

a b c

Figure 1. FE model of blades package: a – general view and steam load distribution; b – bandage shroud; c – contact area

The research is particularly focused on study of the contacting in the shroud of blades, since the secure tight closure of the joints is one of the most important conditions for the safe and stable operation of the last stage bladings of the low pressure cylinder.

2. Static analysis

In order to take the pre-stress into consideration in the forced vibrations of nonlinear system and for linearization, the static problem has been studied initially.

It is important to note that the results of solution of the contact interaction problems with dry friction depend on the loading history [2]. Because of this, the calculations should be carried out not in a single step, but rather large number of substeps. Thus, the process of speeding-up of the turbine rotor can be approximately simulated with gradual increase of the angular velocity and aerodynamic loads to their nominal values at the operating regime. With setting a large enough number (e. g., 1000) of load substeps in calculation, the problem becomes quasi-static.

Static displacement field (Fig. 2, a) has been obtained with the use of stated above approach, by solution of the static problem with the FE method. The contact interaction in the shroud under the influence of centrifugal and steam loads on the blades package has been considered. The results show that there is contact only on a small area of expected contact surface. The sliding contact area (Fig. 2, b) and the contact pressure (Fig. 2, c) are concentrated on the upper edge of the shroud prong. There is no area of sticking contact in the shroud joint.

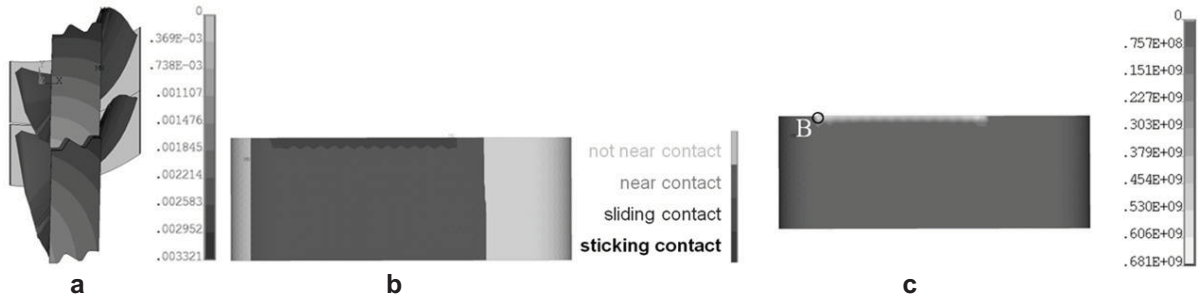

a b c

Figure 2. Results of the quasi-static solution: a – distribution of total displacements (m); b – contact status on the shroud prong; c – distribution of contact pressure (Pa)

3. Modal analysis of pre-stressed linearized models

In modern engineering practice the linearized FE models are used for determination of the dynamic characteristics of bladings. The contact conditions in such models are replaced by kinematic constraints. Particularly, the modal analysis results could give a range of variation of dynamic characteristics, within which the sought nonlinear process at various regimes of the forced vibrations is contained. The eigenfrequencies are taken as potential hazardous resonance frequencies, and eigenmodes – as approximations to the mode shapes that are realized by nonlinear moving of dynamic systems. In addition, it should be noted that at small oscillation amplitudes a nonlinear system approximates to the corresponding linear, which is an originative or the initial iteration in the solution's search. In this case the choice of a linearized model is of great importance, and it is urgent to develop scientifically grounded linearization procedures.

The following two variants of linearized dynamic models of the blades package have been developed for the modal analysis. The models possess a various stiffness level according to the types of the imposed kinematic constraints. At that the pre-stress from the obtained solution of the static problem is taken into consideration.

Variant 1: at the area of the sliding contact (dark area in Fig. 2, b) the coincidence condition for the perpendicular (to the contact surface) displacements of the nodes of the contact finite elements is applied.

Variant 2: at the area of the sliding contact (dark area in Fig. 2, b) the coincidence condition for all displacements of the nodes of the contact finite elements is applied.

The pre-stress has been taken into consideration for linear models with constraints by solution of the linear static problem with the same loads as in the contact interaction problem.

The pattern of total displacements distribution is shown in Fig. 3. It is evident that the deformed mode of the linearized model (Variant 1) qualitatively replicates the displacements distribution for the quasi-static contact interaction problem that is shown in Fig 2, a. While displacement field of the linearized model (Variant 2) has a better quantitative approximation to the previously considered equilibrium.

Due to giving the possibility of unlimited slide of the bandage shrouds, the linearized model (Variant 1) is subject to considerably greater displacements. Also there is possibility of the presence of such eigenmodes, where the relative shift of the bandage shrouds at a tangent to the contact surfaces occur.

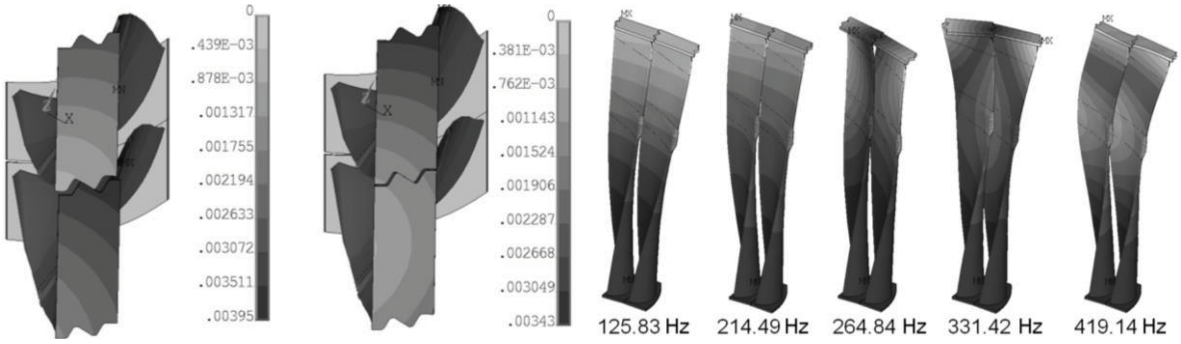

Figure 3. Distribution of static total displacements (m) in the linearized models:
a – Variant 1; b – Variant 2; c – eigenmodes for the pre-stressed linearized model (Variant 2)

Table 1. Eigenfrequencies of pre-stressed linearized models of the blades package

N	Frequency (Hz)	
	Variant 1	Variant 2
1	119.25	125.83
	128.08	
2	212.42	214.49
3	323.90	264.84
4		331.42
5	382.79	419.14

The obtained values of eigenfrequencies are given in Table 1. Spectra of the eigenfrequencies of developed linearized models have differences. The eigenfrequencies (for similar eigenmodes) may change for a few Hz, according to different ways of constraints imposition. This range of frequency variation has significant importance for practical calculations of securing against working in resonance regimes at operating frequencies (rotor rotation frequency and its 5 or 7 multiple frequencies). With the variation of the rotor rotation frequency from the nominal value for a few Hz, hazardous frequency ranges around multiple frequencies of rotor speed, in their turn, increase by greater values. The eigenmodes are given in Fig. 3, c, for the Variant 2 of linearization with constraints of higher stiffness. The first two and fifth eigenmodes correspond to in-phase deformation of the blades in package. Instead, the third and fourth eigenmodes relating to a mutual torsion of the blades correspond to antiphase deformation.

4. Simulation of forced nonlinear vibrations of pre-stressed blades package

A study of non-resonant nonlinear vibrations of the two blades package has been performed. The harmonic load caused by aerodynamic flow pulsation and static load (constant part of the steam pressure and centrifugal force due to the rotation of the turbine rotor) have been considered.

Within the numerical simulation the following algorithm for solving the problem has been developed:

– the first step of computation (steady-state analysis): quasi-static attainment of system to equilibrium at nominal loads;

– the second step of computation (full transient analysis): turning the inertia effects on, that leads to an initial-value problem and a necessity to define the appropriate initial condition. Initial displacements field is a solution of the first step of computation. Initial velocities are obtained automatically from the computational procedure which uses Newmark differential scheme. At this stage the dynamic loads are applying and the static loads remain unchanged.

Solving of the transient forced vibrations problem on the second step of computation within the FE method consists in finding solutions of matrix equations of motion of the blades package:

$$[M]\{\ddot{u}\}+\left([D_l]+\left[D_N\left(\{\dot{u}\}\right)\right]\right)\{\dot{u}\}+\left([K_l]+\left[K_N\left(\{u\}\right)\right]\right)\{u\}=\{F(t)\} \tag{1}$$

There are following designations introduced in the Eq. 1: $[M]$ – mass matrix; $[D_l]$, $[K_l]$ – linear components of damping and stiffness matrices; $[D_N]$, $[K_N]$ – nonlinear components of the matrices arising due to contact interaction in the joints of the bandage shrouds [3]; $\{\ddot{u}\}$, $\{\dot{u}\}$, $\{u\}$, $\{F(t)\}$ – vectors the nodal accelerations, velocities, displacements and stresses, respectively. Numerical simulation has been performed by software package that uses the direct integration of the full system of differential equations (1) based on the Newmark differential scheme. At each time step the nonlinear contact interaction problem is solving with augmented Lagrangian method [4]. According to the requirements of the computational algorithms, time step of the calculation should be from 2.5% to 5% of the expected period of the vibration process.

The case of in-phase applying of dynamic load has been considered. This type of load cannot lead to excitation of antiphase vibration modes (e. g., such as the third and fourth eigenmodes in Fig. 3). Also the probability of opening of contact joints and alternating wobble of the one blade's shroud prong about hollow of the other blade's shroud is reduced. These phenomena can occur by antiphase loading [1].

The mathematical model of computation of the forced vibrations of the blades package corresponds to Eq. (1), where the nodal loads vector $\{F(t)\}$ depends on time t as follows:

$$\{F(t)\}=\{F_0\}\cdot\sin(2\cdot\pi\cdot\omega\cdot t) \tag{2}$$

Here the amplitude $\{F_0\}$ of variable load is assumed to be 10% of the static component the steam pressure, ω=50 Hz – the turbine rotor rotation frequency. Damping ratio δ=0.007 has been taken according to recommendations for blades of this type [5]. Time interval of the forced vibrations study is to the establishment of the stationary vibration mode. Considering that the period of vibration is 0.02 s, time step of the calculation is 0.0005 seconds.

The resulting graph for time dependence of displacements in the X direction is shown in Fig. 4, a, for the point B, which corresponds to the point of maximum contact pressure on the shroud prong. Location of the point B is displayed on the distribution of contact pressure in Fig. 2, c. After a non-stationary process at the beginning of the computation time interval, the steady vibrations mode begins. It should be noted that the stationary motion occurs around a bit shifted equilibrium, as a result of dynamic loading effects. This phenomenon is a display of the nonlinearity of the system. In the phase trajectory, which is shown in Fig. 4, b, the process of transition from the equilibrium to the stable periodic motion mode for the point B is demonstrated.

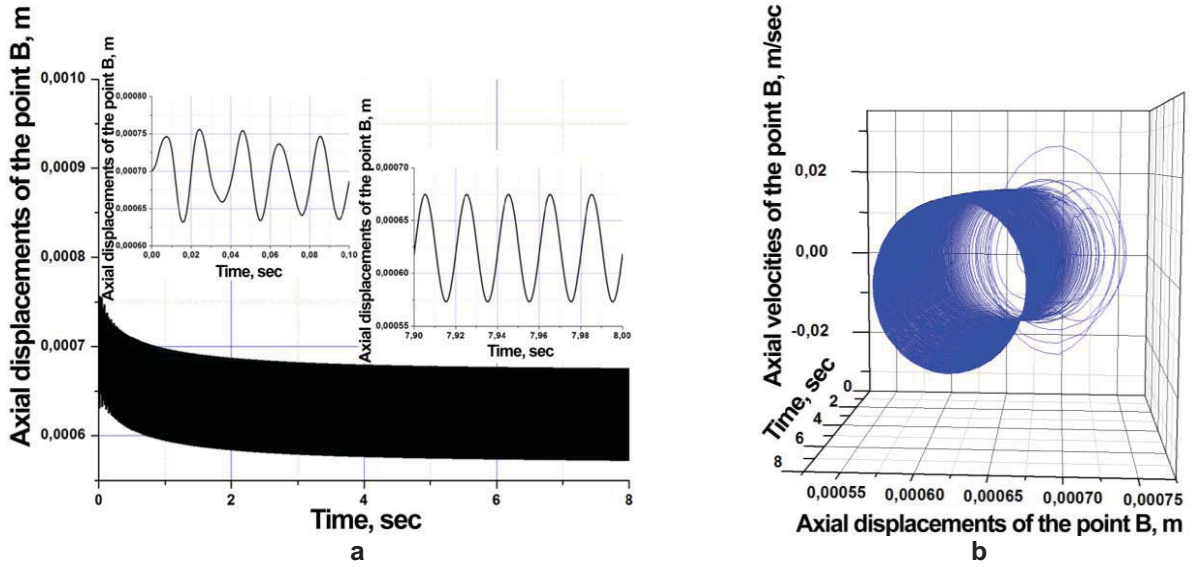

Figure 4. Dependence of displacements (a) and the phase trajectory (b) over time for the point B

The display of the nonlinearity of forced vibrations at stationary mode can be assessed by analyzing the relation between the axial displacements of the point B on the blade's shroud prong and the distant from the nonlinear contact interaction area point C in the center of the blade. Location of the point C is shown in Fig. 1. There is a linear relationship (Fig. 5, a) between the axial displacements of points B and C. So, only one mode of the forced vibrations is excited, which are mostly of harmonic nature. The phase trajectory has an elliptical form (Fig. 5, b), which is typical for the stationary linear harmonic vibrations. Thus, at the stationary regime of the forced vibrations there is a constant tight closure of the joint in the shroud, and there is a reliable contact between the blades.

For the stationary regime of forced vibrations the spectral analysis was performed according to the procedure of the fast Fourier transformation. The spectrum (Fig. 5, c) of the oscillation process presents the main characteristics for the point B: value of the displacement around which the oscillations occur (0.619 mm, which is less than the initial 0.7 mm – the result of the static computation; i. e. the vibrations have a relaxing effect upon the blades package); the vibration amplitude (0.05 mm) at the loading frequency 50 Hz. There is a slight excitation of frequencies that are multiples of the frequency of loading - superharmonics (100 and 150 Hz). But the cumulative contribution of their amplitudes is negligible and they do by no means affect the vibrations. For comparison, a study of the forced vibrations with taking static loads into consideration for the linearized model (Variant 2) has been performed. Mean values of displacements around which the oscillations occur are somewhat greater in the linear model than the corresponding values of the nonlinear model. The amplitudes of forced vibrations of the linear model are higher by 5-10%.

Study of the interaction in the contact joint at the forced vibrations has been performed for the points of the upper edge of the shroud prong (that is the contact zone by results of the quasi-static solution). Analysis of the nature of contacting for the stationary vibrations showed that the dynamic contact area does not change – the contact status is identical to illustrated in Fig. 2, b. But during the period of vibrations on the upper edge of the shroud prong the sticking contact area appears and disappears. Contact pressures in the studied locations have nearly harmonic vibration (with the frequency of loading – 50 Hz) component of small amplitude and a significant constant component around which oscillations occur. Graph of dependence of contact pressure over time for stationary forced vibrations for the point B is shown in Fig. 6.

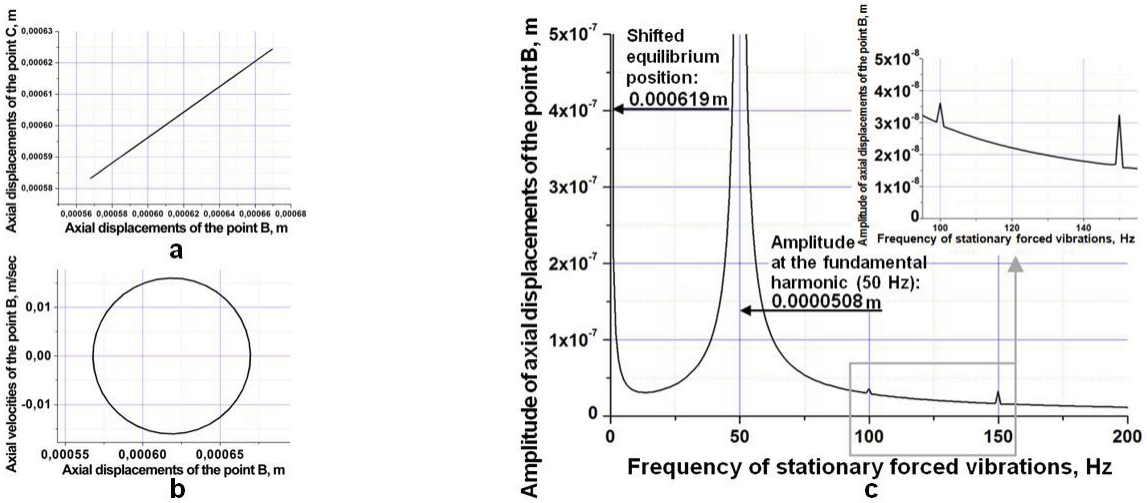

Figure 5. Characteristics of in-phase forced stationary vibrations of the blades package: a – relation between the displacements of the points B and C; b – phase trajectory at the point B; c – spectral response at the point B

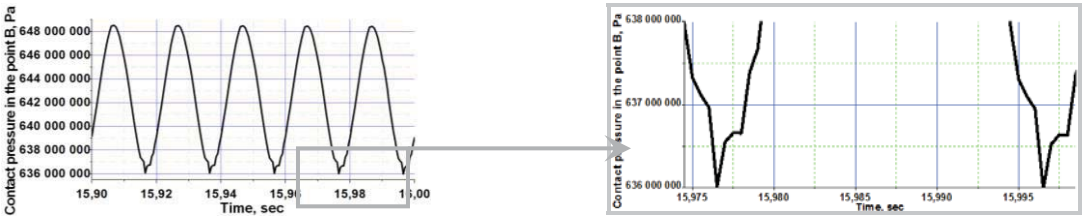

Figure 6. Dependence of the contact pressure over time at the point B at stationary forced vibrations

Conclusions

The numerical research algorithm for the forced nonlinear vibrations with consideration of pre-stress has been proposed and applied for the blades package with detachable peripheral shroud. Complex nonlinear phenomena [1], which have been obtained at neglecting the static stress state, were not revealed in present study: here the complete opening of contact is impossible, and there is no amplitude modulation at the fundamental harmonic due to negligible contribution of superharmonic amplitudes. However, the nonlinear effect of a significant shift of the equilibrium (mean value of oscillations) by the action of dynamic loadings has been found. The obtained amplitudes of the nonlinear forced vibrations are lower by 5-10% in comparison with amplitudes of the linear forced vibrations. It should be claimed that the correct modeling of static loadings in the structurally nonlinear systems is an important stage of creation of the linearized models or the solution of the forced vibrations problems with consideration of the pre-stress.

References

[1] Larin A. A. and Stepchenko A. S. Forced nonlinear vibrations of turbine blades with a dynamic contact in the detachable shroud *Vibrations in Engineering and Technology,* Vol. 3 (63), pp. 18-26, 2011 (in Russian).

[2] Lukashevich A. A. Solution of contact problems for elastic systems with unilateral constraints by method of the step analysis *Abstract of a Technical Sciences Doctoral Dissertation,* 05.23.17, Tomsk, 2011 (in Russian),

[3] Wriggers P. *Computational Contact Mechanics,* Springer, 2006.

[4] Kondrykova A. A. and Larin O. O. Modelling of contact interaction between pneumatic tire and rigid road taking into account the geometrical and physical nonlinearity of deformation *Bulletin of the NTU "KhPI", Thematic Issue "Dynamics and Strength of Machines.",* Vol. 52, pp. 94-101, 2011 (in Ukrainian).

[5] Rao J. S., Peraiah K. Ch. and Singh U. K. Estimation of dynamic stresses in last stage steam turbine blades under reverse flow conditions *Advances in Vibration Engineering, J. Vib. Inst. India,* Vol. 8 (1), pp. 71-78, 2009.

Proceedings of the 4th International Conference on Nonlinear Dynamics
ND-KhPi2013
June 19-22, 2013, Sevastopol, Ukraine

Nonholonomic Whirling Vibrations of Drill String Bits in Deep Boreholes

Valery Gulyayev*, Olena Borshch, Lyudmyla Shevchuk

Abstract
In the paper the problem of whirl vibrations of a rotating drill string bit under conditions of its contact interaction with the bore-hole bottom surface is formulated. The mechanism of the bit spinning and rolling without sliding on the rigid surface of the bore-hole bottom is analyzed. To study the whirl vibrations, the methods of nonholonomic mechanics are used. As examples, whirling of spherical and ellipsoidal bits are considered. The kinematic inducement of the rotating bit motion without sliding is shown to be the main cause of its stability loss. The detailed study of the bit whirling has revealed three types of its stable and unstable motions associated with direct and inverse rolling as well as pure spinning.
It is found that the most detectable influence on the system dynamics and its stability is exerted by the overall stiffness of the drill string tube which depends on parameters of compressive axial force and torque and diminishes as their critical values are approached. Essential effect of the bit's shape on the process stability is studied.

Keywords
Drill string1, drill bit whirling2, nonholonomic constraints3, direct rolling4, inverse rolling5, pure spinning6

National Transport University, Kiev, Ukraine
***Corresponding author:** valery@gulyayev.com.ua

Introduction

Nowadays, the depths of oil and gas deposits are more than 7000 m. The exploitation of these fields represents serious technological difficulties relating to deep drilling. One of the major problems is the risk of contingencies due to quasistatic-equilibrium critical states and vibrations of a drill string bottom hole assembly (BHA) [1,2]. They include critical flexural buckling of a drill string (DS) [3, 4] and its vibrations that may combine several vibration occurrences simultaneously [5–7], making it difficult to pick out each of them and to explain their mechanisms.

Considering the direction of the vibrating motion, there are three main types of vibrations of the drill string BHA: axial, torsional, and flexural. The DS axial (longitudinal) vibrations cause multiple interruptions of the drill bit contact with the well bottom (i.e., rebounds), alternating with the bit–rock impact contact interactions. Torsional vibrations arise through self-excitation during stalling-type frictional interaction between the drill bit and the wellbore wall [8]. Self-sustained vibrating systems usually feature two phases. During the first phase, the drill bit is seized by the wellbore wall and stays motionless (called "stuck" in the theory of self-excited vibrations). During the second phase, the drill bit detaches itself from the borehole wall and slips along the wall with an increased angular velocity.

However, the most complex mechanism are the flexural vibrations of the drill string BHA, which are induced by the action of time-variable normal and tangential forces of the contact and frictional interaction between the drill bit and borehole wall. In this case, the drill bit geometrical centre starts moving around the borehole axis, passing ahead or lagging behind the rotation of the drill string itself. Similar motions in a laundry washer of an old design are executed by its rotor due to gyroscopic and centrifuge inertia forces. In mechanics they are called the precession vibrations. In [5–7] it was stated that the drill bit motion as described above is of different nature. It was studied using rather simplified physical and mathematical models and was called whirling [9-12].

Note that in the theory of rotating shafts much attention is paid to shaft balancing and self-centring in order to prevent precession vibrations. However, in the theory of drilling less attention is paid to the problems of preventing whirl vibration. This is mostly due to the fact that the flexural motions of a drill bit and drill string BHA are limited by the borehole wall. On the one hand, this limitation stabilizes the system movement, while on the hand it makes the vibration nature more complicated and the problem statement more cumbersome. As demonstrated by experiments and full-scale tests, in some cases the drill bit centre starts moving along rather complex trajectories that look like a many-petalled flower, to produce a set of grooves on the borehole wall, which are not permitted by the drilling specification [5–7]. The present work is dedicated to the problem of computer modelling of the above effects and theoretical prediction thereof. The simulation is performed on the basis of the nonholonomic mechanics methods [13].

1. Equations of The Drill String

The whirl vibration of drill bit rotating with an angular velocity ω usually involves also the DS lower sections located between centralizers which serve as additional supports. Usually, no more than five supports are used and their spacing l_i ranges from 9 to 18 m. Since the most intensive flexural vibrations of a DS occur in the section directly adjacent to the drill bit, during the analysis of the mechanism of excitation of the drill bit whirl vibration we will disregard the influence of the DS upper sections and pick out a DS fragment of length l between two lower centring supports A and B by arbitrarily separating it from the DS upper section and the adjacent cantilevered section of length e with a drill bit on its end. The drill bit will be tentatively represented in the form of a body (Fig. 1).

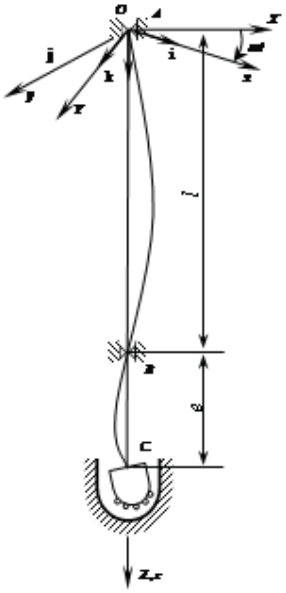

Figure 1. Schematic of the drill string segment separated for calculation

The DS tubular section picked out is pre-stressed by a torque M_z applied to the drill bit and by a longitudinal compressive force T equal to the reaction of support of the drill bit on the borehole bottom. Dynamics of this section will be modelled based on the theory of compressed–twisted rotating rods [3, 4]. For this purpose we specify a fixed coordinate system $OXYZ$ and a coordinate system $Oxyz$ which rotates jointly with the DS, both systems having a common origin O on the support A. The axes OZ and Oz coincide with the DS pipe axis. We take into account that a drilling fluid runs inside the DS pipe and during the vibrations it acts as additional mass.

Consider spatial flexural vibrations of the pipe. To analyze them equations of the moment balance for a tubular element dz with respect to axes Oy and Ox are used [9]:

$$EI\frac{\partial^4 u}{\partial z^4}-T\frac{\partial^2 u}{\partial z^2}-M_z\frac{\partial^3 v}{\partial z^3}-(\rho F+\rho_l F_l)\omega^2 u-2(\rho F+\rho_l F_l)\omega\frac{\partial v}{\partial t}+(\rho F+\rho_l F_l)\frac{\partial^2 u}{\partial t^2}=0,$$
$$EI\frac{\partial^4 v}{\partial z^4}-T\frac{\partial^2 v}{\partial z^2}+M_z\frac{\partial^3 u}{\partial z^3}-(\rho F+\rho_l F_l)\omega^2 v+2(\rho F+\rho_l F_l)\omega\frac{\partial u}{\partial t}+(\rho F+\rho_l F_l)\frac{\partial^2 v}{\partial t^2}=0, \quad (1)$$

Then, at this point the functions u and v, and their even derivatives are zero, which is equivalent to the bending moments M_x and M_y being zero. Hence, at the edge $z=0$ one has

$$u_A=v_A=0, \qquad \partial^2 u/\partial z^2\big|_A=\partial^2 v/\partial z^2\big|_A=0 \quad (2)$$

At the centralizer B $(z=l)$, the transverse displacements equal zero and slewing angles are continuous. So

$$u_B=v_B=0, \qquad \frac{\partial u}{\partial z}\Big|_{l-0}=\frac{\partial u}{\partial z}\Big|_{l+0}, \qquad \frac{\partial v}{\partial z}\Big|_{l-0}=\frac{\partial v}{\partial z}\Big|_{l+0} \quad (3)$$

To formulate boundary equations at point $z=l+e$, assume that the process of whirling excitation is at the commencing stage and the bit can move in a narrow clearance without touching the borehole side surface. As this takes place, the character of the bit rolling and the C boundary equations, resulting from it, are determined by the surface geometries of both the bit itself and the borehole bottom also. In a general case, they may have shapes of different rotary surfaces, which can be approximated by spheres or ellipsoids (Fig. 2). Consider the simplest case, when the both surfaces are spheres of radii a and R, correspondingly.

Figure 2. Geometrical shapes of the bits

To describe the bit slewing through the DS bending, introduce also the $Cx_1y_1z_1$ coordinate system rigidly bound to it. At the initial state, axes Cx_1, Cy_1 are parallel to axes Ox, Oy, correspondingly, and in elastic bending of the DS, they slew through angles – $v'\big|_C$ and $u'\big|_C$.

Rolling of bit surface on surface of the borehole bottom will be determined in the movable right-hand coordinate system $Gx_2y_2z_2$ with origin G located at the contact point of their surfaces. This system axis Gz_2 is an extension of the CG segment, while axis Gy_2 is normal to the plane containing axis OZ and segment CG, and is oriented along the rotation direction.

The condition of the bit rolling without sliding gives the possibility to formulate two groups of boundary equations at the C point. They include two kinematic equations determining the C point velocity and two dynamic ones expressing dynamic equilibrium of all moments relative to the G point.

Assume, that displacements u, v, and angles $u' = \partial u/\partial z$, $v' = \partial v/\partial z$ are small. To determine the velocity of the bit's center C, represent the absolute angular velocities of the introduced coordinate systems through the $\boldsymbol{\omega}$ angular velocity of the $Oxyz$ system, angles u', v' of elastic slewing of the bit and angular velocities $\dot{u}'$, $\dot{v}'$ of this slewing.

Using the methods of nonholonomic mechanics, one obtains the kinematic boundary equations

$$\begin{aligned} &\dot{u} - \omega v - a\sqrt{1 - \frac{u^2 + v^2}{(R-a)^2}}\left(-\dot{u}' - \omega v' + \frac{\omega v}{R-a}\right) = 0, \\ &\dot{v} + \omega u - a\sqrt{1 - \frac{u^2 + v^2}{(R-a)^2}}\left(-\dot{v}' + \omega u' - \frac{\omega u}{R-a}\right) = 0. \end{aligned} \tag{4}$$

They represent the nonholonomic constraints.

Dynamical boundary equations for the C point follow from the condition of dynamical equilibrium of the moments of elastic forces, inertia forces moments, and constraint reaction moments applied to the bit. In their derivation, selection of the polar point and orientations of the reference frame axes can have an essential effect on their structure and simplicity. It is usual to take the contact point as a polar one and to choose the coordinate axes ensuring invariability of axial inertia moments of the movable body as the reference frame [14]. The first condition leads to exclusion of the nonholonomic constraint reaction from consideration, while the second one permits to exclude the necessity to differentiate the inertia moments of the body with respect to time. In this connection, the G point is chosen as the pole and the $Gx_2y_2z_2$ coordinate system as the reference frame.

2. Results of Computer Simulation

Correlations (1)-(4) determine the three-point boundary value dynamic problem for the lower segment of the DS and the bit. They are also complemented by initial conditions prescribing initial perturbation of the system. Numerical solution of the stated problem is carried out by the finite difference method with application of an implicit scheme of integration with respect to time t. This scheme is stable for any value of the time increment Δt, but it provides satisfacfory precision only for its reasonably small values.

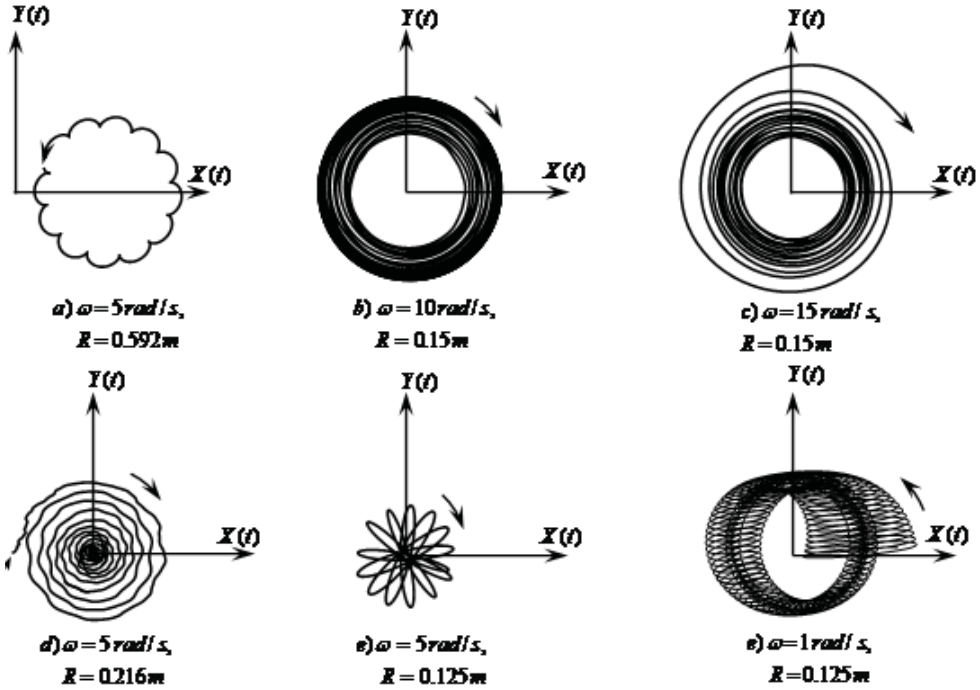

Figure 3. Trajectories of the bit's center motion for different values of ω and R

As a result, the rate of excitation of the self-induced vibrations and their modes has been found to depend on the DS rigidity, values of T and M_z, and the ratio a/R. In this connection, it can be inferred that choosing different values of these parameters one can stabilize or destabilize the dynamics of the whirl vibrations.

The calculation results for $a = 0.12m$, $EI = 4.066 \cdot 10^6\ Pa \cdot m^4$, $T = -1 \cdot 10^5\ N$, $M_z = -1 \cdot 10^4\ N \cdot m$ are shown in Fig. 3. The values of angular velocity ω and radius R of the borehole bottom surface were varied.

As the simplest example with spherical bodies illustrates, the bit whirling reveals three types of its motion associated with direct and inverse rolling as well as pure spinning (drilling).

The distinguishing feature of these processes is essential change of the modes of motion and their stability states with variation of the mechanical parameters, as often happens in nonholonjmic systems. For this reason, it is difficult to establish general regularities of their dynamics. Novertheless, it should be pointed out that the states of the motion certainly become unstable when the DS tube loses its stiffness.

It is known also that dynamics of contacting bodies depends on their shapes. Consequently, the performed analysis can be continued with ellipsoidal bits (oblate and oblong) which are commonly encountered in practice.

References

[1] Gulyayev V.I., Hudoly S.N., and Glovach L.V. The computer simulation of drill column dragging in inclined bore-holes with geometrical imperfections *Int. J. Solids Struct*, Vol. 48, pp. 110-118, 2011.

[2] Gulyayev V.I., Khudoliy S.N., and Andrusenko E.N. Sensitivity of resistance forces to localized geometrical imperfections in movement of drill strings in inclined bore-holes *Interaction and Multiscale Mechanics*, Vol.4(1), pp. 1-16, 2011.

[3] Gulyayev V.I., Gaidaichuk V.V., Solovjov I.L., and Gorbunovich I.V. The buckling of elongated rotating drill strings *J. Petr. Sci. Eng*., Vol. 67, pp. 140-148, 2009.

[4] Gulyayev V.I. and Glushakova O.V. Large-scale and small-scale self-excited torsional vibrations of homogeneous and sectional drill strings *Interaction and Multiscale Mechanics*, Vol. 4(4), pp. 291-311, 2011.

[5] Gulyayev V.I., Hudoliy S.N., and Glushakova O.V. Simulation of torsion relaxation auto-oscillations of drill string bit with viscous and Coulombic friction moment models *J. Multibody Dyn*., Vol. 225(1), pp.139-152, 2011.

[6] Gulyayev V.I. and Borshch O.I. Free vibrations of drill strings in hyper deep vertical bore-wells *J. Petr. Sci. Eng*., Vol. 78, pp. 759-764, 2011.

[7] Yigit A.S. and Christoforou A.P. Stick-slip and bit-bounce interaction in oil-well drillstrings *J. Energy Resources Techn.*, Vol. 128(4), pp. 268-274, 2006.

[8] Warren T.M., Brett J.F., and Sinor L.A. Development of a whirl-resistant bit *SPE Drilling Eng*., Vol. 5(4), pp. 267-275, 1990.

[9] Jansen J.D. Wirl and chaotic motion of stabilized drill collars *SPE Drilling Eng*., Vol. 7(2), pp.107-114, 1992.

[10] Leine R.I., Van Campen D. H., and Keulties W.J.G. Stick-slip whirl interaction in drillstring dynamics *J. Vibr. Acoustics*, Vol.124, April, pp. 209-220, 2002.

[11] Jellison M.J., Chandler R.B., Payne M.L., and Shepard J.S. Ultradeep drilling pushes drillingstring technology innovations *SPE Middle East Oil and Gas Show Conference,* March 2007, pp. 38-46, 2007.

[12] Germay C., Denoël V., and Detournay E. Multiple mode analysis of self-excited vibrations of rotary drilling systems *J. Sound Vibr.*, Vol.325(1), pp. 362-381, 2010.

[13] Neimark Ju.I. and Fufaev N. A. *Dynamics of Nonholonomic Systems*, Translation of mathematical monographs, 33, Amer. Math. Soc., Providence, RI, 1972.

[14] Goldstein H., Poole Ch., and Safko J. *Classical Mechanics*, San Francisco, Boston, New York, Capetown, Hong-Kong, London, Madrid, Mexico City, Montreal, Munich, Paris, Singapore, Sydney, Tokyo, Toronto, 2011.

Proceedings of the 4th International Conference on Nonlinear Dynamics
ND-KhPI2013
June 19-22, 2013, Sevastopol, Ukraine

Dynamics of Stationary Structures in a Parabolic Problem with the Reflection of the Spatial Variable

Yuliya Hazova[1*]

Abstract
Properties of the stationary structures in a nonlinear optical resonator with lateral inversions transformer in feedback are investigated. The mathematical description of optical structures is based on the scalar parabolic equation with inversion spatial arguments. We determine the forms of stationary structures and investigate its stability as the diffusion coefficient decrease.

Keywords
parabolic equation, bifurcation, stationary structure, stability, center manifold.

[1] Simferopol, Ukraine
*** Corresponding author:** hazova.yuliya@hotmail.com

INTRODUCTION

Extension of research in nonlinear optics is now caused by the intensive use of optical systems in information technology. Among the nonlinear optical systems the one of the most popular is a system consisting of a thin layer of the Kerr nonlinear medium and differently organized two-loop feedback. Nonlinear interferometer with a mirror image of the field in the feedback loop is one of the simplest optical systems that implement the non-local nature of the interaction of light fields. Experimental researches have shown a variety of types of optical structures arising in this case [3] - [6]. Following [7], we construct a hierarchy of its simplified models.

1. FORMULATION OF THE PROBLEM

Mathematical model is the next task

$$u_t + u = Du_{\varphi\varphi} + K(1+\gamma\cos u(\pi-\varphi,t)), t>0 \quad (1)$$

$$u(\varphi+2\pi,t) = u(\varphi,t) \quad (2)$$

The task (1), (2) models dynamics of phase modulation $u(\varphi,t)$, $\varphi\in(0,2\pi)$, $t>0$, the light wave which has passed a thin layer of the nonlinear medium of kerrovsky type with reflection transformation of coordinates in the feedback loop in one-dimensional approach. Designations: D is a diffusion coefficient of the nonlinear medium, a positive coefficient K is proportional to the intensity of the input field, γ is a visibility (contrast) of the interference pattern, $0<\gamma<1$.

In this paper we consider the existence, shape and stability of spatially non-uniform stationary solutions bifurcating from the spatially uniform stationary solutions, i.e. decisions $u(\varphi,t)=\omega$ defined by the equation

$$\omega = K(1+\gamma\cos\omega) \tag{3}$$

With the growing of K the number of co-existing roots of this equation increases indefinitely, so one fix a smooth branch of solutions, $\omega = \omega(K,\gamma)$, $1+K\gamma\sin\omega(K,\gamma)\neq 0$. After linearization of the equations (1), (2) by $\omega(K,\gamma)$ one obtains the equation

$$u_t + Lu = 0$$

where $Lu = u - Du_{\varphi\varphi} - \Lambda Qu$, $\Lambda = \Lambda(K,\gamma) = -K\gamma\sin\omega$, Q - the operator defined by the equality $Qu(\varphi,t) = u(\pi-\varphi,t)$.

Lemma 1. The operator L has a complete orthogonal system of eigenfunctions $1,\cos\varphi,\sin\varphi,\cos 2\varphi,\sin 2\varphi,\ldots$ related to the eigenvalues $\lambda_0 = 1-\Lambda$, $\lambda_1 = 1+D+\Lambda$, $\lambda_2 = 1+D-\Lambda$, $\lambda_3 = 1+4D+\Lambda$, $\lambda_4 = 1+4D-\Lambda$

Now we fix K such that the following condition is satisfied.

Condition 1. $\Lambda = \Lambda(K,\gamma) < -1$.

From a lemma 1 and conditions 1 follows that $\omega = \omega(K,\gamma)$ is the stable solution of the problem (1), (2). At reduction D and its passing through value $D_1 = -(1+\Lambda)$ ω loses stability. Instability index [8]; a solution ω at $\frac{D_1}{4} < D < D_1$ is equal 1. At reduction D and its passing through the values $\frac{D_1}{(k+1)^2}$, $k = 1,2,...$ each time the instability index of the solution ω increases by an order. One takes D as the bifurcation parameter. Replacement $u = v + \omega$ leads the equation (1) to the following:

$$\dot{v} + Lv = R(Qv) \tag{4}$$

where

$$R(Qv) = \Lambda\frac{1}{2!}ctg\,\omega\cdot Qv^2 - \Lambda\frac{1}{3!}\cdot Qv^3 + O(v^4) \tag{5}$$

Using designations $L = 1 - D\Delta - \Lambda Q$, $\Lambda = -K\gamma\sin\omega$, $Qv = v(\pi-\varphi,t)$, one obtains

$$v_t + v = D\Delta v + \Lambda Qv + \Lambda\frac{1}{2!}ctgw\cdot Qv^2 - \Lambda\frac{1}{3!}\cdot Qv^3 + O(v^4)$$

Find the solution of the problem (1), (2) by the method of the central manifold [9]

$$v = z\cos\varphi + \frac{1}{2!}\Omega_2(z,\varphi,D) + \frac{1}{3!}\Omega_3(z,\varphi,D) + \ldots, \tag{6}$$

where $\Omega_2(z,\varphi,D)$, $\Omega_3(z,\varphi,D),\ldots$ are forms of the second, third, ... degrees with respect to z. The equation (4) takes the form

$$\dot{z} = -\lambda_1(D)z + c_1(D)z^3 + \ldots \tag{7}$$

Find the coefficients of decomposition (6), (7). Substitute (6), (7) in (4) and equate the coefficients of the same degrees by z. Assuming $\Omega_2 = q_2 z^2$, one has at z^2 that

$(L-2!\lambda_1)q_2=\Lambda ctg\,\omega\cos^2\varphi$. By the lemma 1 $q_2=\frac{\Lambda}{2}ctg\,\omega\left((\lambda_0-2\lambda_1)^{-1}-(\lambda_3-2\lambda_1)^{-1}\cos 2\varphi\right)$.

Assuming $\Omega_3=q_3z^3$, we come to a conclusion that q_3 satisfies to the equation

$$\frac{1}{3!}(L-3\lambda_1)q_3+c_1(D)\cos\varphi=-\frac{1}{2}\Lambda ctg\,\omega\cos\varphi Qq_2+\Lambda\frac{1}{3!}\cos^3\varphi. \tag{8}$$

Condition of solvability of this equation in a class analytical on D and periodic on φ functions leads to unequivocal definition

$$c_1(D)=\frac{\Lambda}{8}-\frac{1}{4}(\Lambda ctg\,\omega)^2\left((\lambda_0-2\lambda_1)^{-1}+\frac{1}{2}(\lambda_3-2\lambda_1)^{-1}\right)<0$$

The equation (8) has a solution of the same type as its discontinuity:

$$q_3=(\lambda_5-3\lambda_1)^{-1}\left(\frac{\Lambda}{4}-\frac{3}{4}\Lambda^2ctg^2\omega(\lambda_3-2\lambda_1)^{-1}\right)\cos 3\varphi$$

The specified process will continue indefinitely. Under the condition 1 one has that $c_1(D_1)<0,\ \lambda_1(D_1)=0$. As $\lambda_1'(D_1)=1$ there is a supercritical bifurcation from the trivial singular point of (7) two exponentially stable points branch off,

$$z^{\pm}=\pm\left(\frac{D-D_1}{c_1(D_1)}\right)^{1/2}+O((D-D_1)). \tag{9}$$

Therefore, the family of (4) gives us the supercritical bifurcation of exponentially stable stationary solutions:

$$\begin{aligned}v^{\pm}(\varphi,D)\approx\pm\left(\frac{D-D_1}{c_1(D_1)}\right)^{1/2}\cos\varphi+\frac{1}{2!}\left(\frac{D-D_1}{c_1(D_1)}\right)\left(\frac{\Lambda}{2}ctg\,\omega(\lambda_0-2\lambda_1)^{-1}+(\lambda 2-2\lambda_1)^{-1}\cos 2\varphi\right)\pm\\ \pm\frac{1}{3!}\left(\frac{D-D_1}{c_1(D_1)}\right)^{3/2}(\lambda_5-3\lambda_1)^{-1}\left(\frac{\Lambda}{4}-\frac{3}{4}\Lambda^2ctg^2\omega(\lambda_3-2\lambda_1)^{-1}\right)\cos 3\varphi\end{aligned} \tag{10}$$

Theorem 1. Let the condition 1 is satisfied. Exists $\delta_0>0$ such that if $0<D_1-D<\delta_0$, the task (1), (2) has two solutions: $u^{\pm}(\varphi,D)=\omega+v^{\pm}(\varphi,D)$, where satisfies (10). The solution $u^{\pm}$ is stable.

Example 1. Let $K=4,\ \gamma=0{,}7$. Then the equation for the stationary solutions will be: $\omega=4(1+0{,}7\cos\omega)$. Solving this equation, we receive three values: ω: 2.24721 5.1264 6.63168

Check a condition 1: -2.18351 2.56344 -0.956161. Condition is satisfied if $\omega=2.24721$. Critical value D: D_1= 1.18351, then $c_1(D_1)=-0.562709<0$. Depending on value D different values $u(\varphi,D)=v(\varphi,D)+\omega$, $v(\varphi,D)=v^+(\varphi,D)$ are obtained

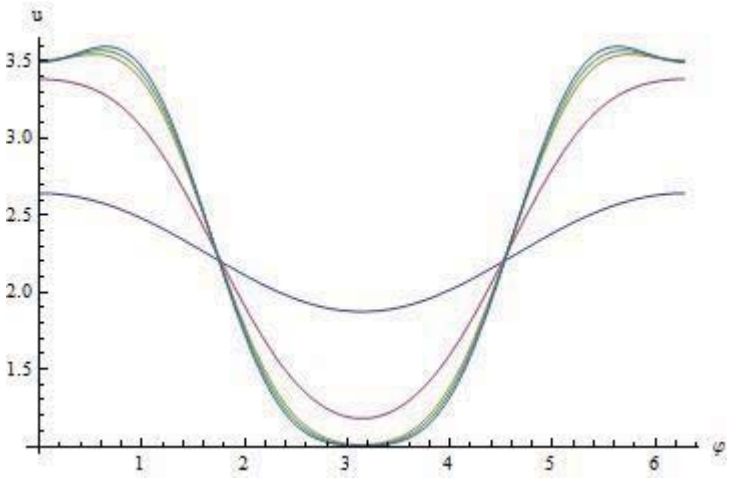

Figure 1. Function u at $D=1.1$, $D=0.44$, $D=0.08$, $D=0.04$, $D=0.007$.

Field of application of equality to describe spatially non-uniform stationary solutions of (4) is narrow. In this regard, we construct a two-mode approximation of the equation (4). We use the formalism of constructing the center manifold in combination with the Galerkin method. The approximate solution of equation (4) as

$$v = z_1 \cos\varphi + z_2 \sin(2\varphi) + \frac{1}{2!}\Omega_2(z,\varphi,D) + \frac{1}{3!}\Omega_3(z,\varphi,D) \tag{11}$$

where Ω_2, Ω_3 - forms second, third degree relatively z, $z=(z_1,z_2)$ - the system solution

$$\begin{cases} \dot{z}_1 = -\lambda_1 z_1 + g_1(z,D) \\ \dot{z}_2 = -\lambda_4 z_2 + g_2(z,D) \end{cases} \tag{12}$$

here g_1, g_2 are forms of the third degree with respect to z. Substitute (11), (12) in (4) and equate the form of the second and third degree. Using the algorithm described earlier, one determines Ω_2, Ω_3, g_1, g_2

$$\begin{cases} \dot{z}_1 = z_1\left(-\lambda_1 + C_{20}^1 z_1^2 + C_{11}^1 z_1 z_2 + C_{02}^1 z_2^2\right) \\ \dot{z}_2 = z_2\left(-\lambda_4 + C_{20}^2 z_1^2 + C_{11}^2 z_1 z_2 + C_{02}^2 z_2^2\right) \end{cases} \tag{13}$$

where

$$C_{20}^1 = -\left(\frac{\Lambda}{2} ctgw\right)^2 \left((\lambda_0 - 2\lambda_1)^{-1} + \frac{1}{2}(\lambda_3 - 2\lambda_1)^{-1}\right) + \frac{\Lambda}{8}$$

$$C_{02}^1 = -\left(\frac{\Lambda}{2} ctg\,\omega\right)^2 \left((\lambda_0 - 2\lambda_4)^{-1} + \frac{1}{2}(\lambda_2 - \lambda_1 - \lambda_4)^{-1} + \frac{1}{2}(\lambda_6 - \lambda_1 - \lambda_4)^{-1}\right) + \frac{\Lambda}{4}$$

$$C_{11}^1 = 0,\ C_{11}^2 = 0$$

$$C_{20}^2 = -\left(\frac{\Lambda}{2} ctg\,\omega\right)^2 \left((\lambda_0 - 2\lambda_1)^{-1} + \frac{1}{2}(\lambda_2 - \lambda_1 - \lambda_4)^{-1} + \frac{1}{2}(\lambda_6 - \lambda_1 - \lambda_4)^{-1}\right) + \frac{\Lambda}{4}$$

$$C_{02}^2 = -\left(\frac{\Lambda}{2} ctg\,\omega\right)^2 \left((\lambda_0 - 2\lambda_4)^{-1} + \frac{1}{2}(\lambda_7 - 2\lambda_4)^{-1}\right) + \frac{\Lambda}{8}$$

Note that the coefficients in (13) are analytic functions of D. Let $(x_1(D), x_2(D))$ - a continuous branch of stationary solutions of the system (13), branching off from the zero solution and such that $x_1(D) > 0$ at small $D_1 - D > 0$. Then, by (11), (13) approximate stationary solutions of the equation (4) are the following functions:

$$\nu^{\pm} = \pm(x_1(D)\cos\varphi + x_2(D)\sin 2\varphi) + \frac{\Lambda}{4} ctg\,\omega\Big(\Big[(\lambda_0 - 2\lambda_1)^{-1} + (\lambda_3 - 2\lambda_1)^{-1}\cos 2\varphi\Big]x_1^2(D) +$$
$$+\Big[(\lambda_0 - 2\lambda_4)^{-1} - (\lambda_7 - 2\lambda_4)^{-1}\cos 4\varphi\Big]x_2^2(D) +$$
$$+2\Big[(\lambda_2 - \lambda_1 - \lambda_4)^{-1}\sin\varphi + (\lambda_6 - \lambda_1 - \lambda_4)^{-1}\sin 3\varphi\Big]x_1(D)x_2(D)) +$$
$$+\frac{1}{6}\Big(\Big[(\lambda_5 - 3\lambda_1)^{-1}\Big(\frac{\Lambda}{4} - \frac{3}{4}(\lambda_3 - 2\lambda_1)^{-1}\Lambda^2 ctg^2\omega\Big)\cos 3\varphi\Big]x_1^3(D) +$$
$$+3x_1^2(D)x_2(D)\Big[(\lambda_8 - 2\lambda_1 - \lambda_4)^{-1}\Big(\frac{\Lambda}{4} - \frac{\Lambda^2}{4} ctg^2\omega(\lambda_3 - 2\lambda_1)^{-1} - \frac{\Lambda^2}{4} ctg^2\omega(\lambda_6 - \lambda_1 - \lambda_4)^{-1}\Big)\sin 4\varphi\Big] +$$

$$+3x_1(D)x_2^2(D)\Big[(\lambda_5 - \lambda_1 - 2\lambda_4)^{-1}\Big(-\frac{\Lambda}{4} + \frac{\Lambda^2}{4} ctg^2\omega(\lambda_7 - 2\lambda_4)^{-1} + \frac{\Lambda^2}{4} ctg^2 w(\lambda_2 - \lambda_1 - \lambda_4)^{-1}\Big)\cos 3\varphi\Big]$$
$$+(\lambda_9 - \lambda_1 - 2\lambda_4)^{-1}\Big(-\frac{\Lambda}{4} + \frac{\Lambda^2}{4} ctg^2\omega(\lambda_7 - 2\lambda_4)^{-1} + \frac{\Lambda^2}{4} ctg^2\omega(\lambda_6 - \lambda_1 - \lambda_4)^{-1}\Big)\cos 5\varphi] +$$
$$+x_2^3(D)\Big[(\lambda_{12} - 3\lambda_4)^{-1}\Big(-\frac{\Lambda}{4} + \frac{3}{4}\Lambda^2 ctg^2\omega(\lambda_7 - 2\lambda_4)^{-1}\Big)\sin 6\varphi\Big])$$

Note that denominators in (13) are positive on the next interval of the parameter D change: (D, D_1^1) Here $D_1^1 = \frac{-1-3\Lambda}{8}$ - equation's root $\lambda_0 - 2\lambda_4 = 0$. Coefficients of system (13) $C_{20}^1, C_{02}^1, C_{20}^2, C_{02}^2$ grow without bound as $D \to D_1^1 + 0$. Necessary defined at the appropriate point $D = D_1^1$.

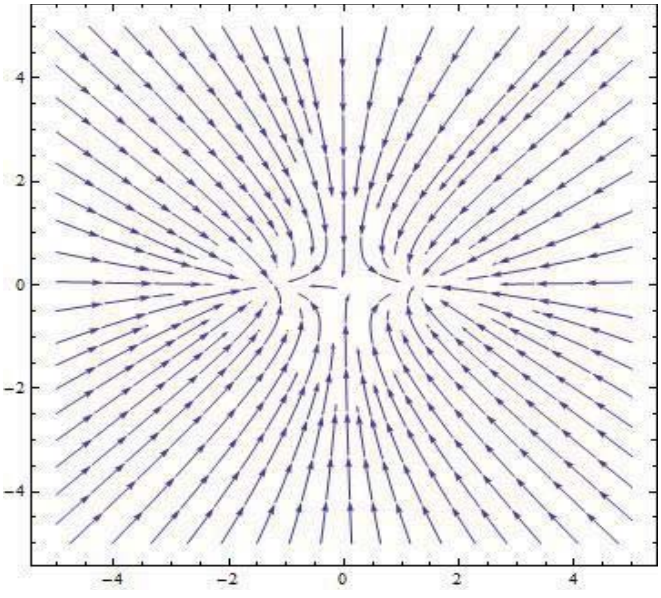

Figure 2. Stationary points of system (13)

Example 2. When passing through critical value $D = D_1 = 1.18351$ from the stationary solution of system (13) two stable spatially nonuniform solutions $(\pm x_1(D),0)$ are appeared, and the trivial solution loses stability.

One considers the interval $(D; D_1^1) = (1.18; 0.69)$. The following figure shows graphs of the solutions $(x_1(D) > 0;0)$.

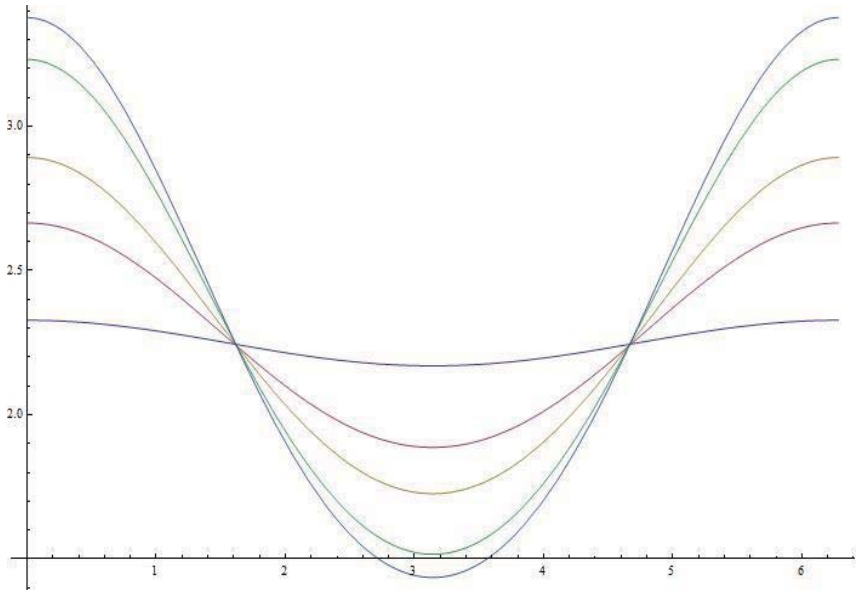

Figure 3. Function u at $D = 1.1$, $D = 0.44$, $D = 0.08$, $D = 0.04$, $D = 0.007$.

CONCLUSIONS

Theorems on existence and stability of stationary structures in a problem of nonlinear optical resonator with lateral inversions transformer in feedback, are proved under some general assumptions. At unlimited decrease of the diffusion coefficient the stationary structures evolve and pass to contrasting structures.

REFERENCES

[1] Razgulin A.V. *Non-linear Models of Optical Synergy*, M.: Section of Faculty VMiK, MSU, MAKS Press, 2008 (in Russian).
[2] Razgulin A.V. Self-oscillations in a nonlinear parabolic problem with transformed argument, *JFMMF*, №1, pp. 69-80, 1993 (in Russian).
[3] Vorontsov M.A., Zheleznykh N.I., Ivanov V.Yu. Transverse interaction in 2-D feedback non-linear optical systems, *Opt. and Quant. Electron*, V.22, pp. 501-515, 1988.
[4] Vorontsov M.A., Zheleznykh N.I. Transverse bistability and multistability in nonlinear optical systems with feedback, *Mat. Modeling*, Vol.2, №2, pp. 31-38, 1990 (in Russian).
[5] Zheleznykh N.I. *The study of nonlinear control systems with optical feedback,* PhD Thesis (Physics & Mathematics), 05.13.16, Moscow, 1991 (in Russian).
[6] Akhmanov S.A., Vorontsov M.A., Ivanov V.Yu. Controlling transverse-wave interactions in nonlinear optics generations of spatiotemporal structures, *J. Optical Soc. Amer. Ser. B*, V.9, №1, pp.78-90, 1992.
[7] Ahromeeva T.S., Kurdyumov S.P., Malineckaya G.G., Sanarskiy A.A. *Structure and chaos in nonlinear media,* M.:Fizmatlit, 2005 (in Russian).
[8] Babin A.B., Vishik M.I. *Attractors of evolution equations*, M.:Nauka, 1989 (in Russian).
[9] Marsden J., MacCraken M. *Bifurcation of the cycle and its applications,* M.:Mir, 1980.
[10] Belan E.P Dynamics of stationary structures in a parabolic problem with the reflection of the spatial variable, *Cybernetics and Systems Analysis*, Vol. 46, №5, pp. 99-111, 2010 (in Russian).

Proceedings of the 4th International Conference on Nonlinear Dynamics
ND-KhPI2013
June 19-22, 2013, Sevastopol, Ukraine

Nonlinear Stages of Kelvin-Helmholtz Instability Suppressed by Tangential Electric Field

Evgeny A. Kochurin[1*], Nikolay M. Zubarev[1]

Abstract
The problem of stabilization of Kelvin-Helmholtz instability of the interface between two deep dielectric fluids by the external tangential electric field is considered. Three regimes of fluids motion are revealed for which the nonlinear dynamics of interface can be described analytically. For the first one, the tangential discontinuity of the velocity field at the liquids interface is negligibly small, that is a destabilizing factor is absent. It is found that weakly nonlinear waves on the boundary can move without distortion in the direction and against the direction of the external electric field; the analytical expression that describes the interaction of counterpropagating nonlinear waves is obtained. In the second regime, the electrostatic pressure exerted by the external field completely compensates the hydrostatic pressure on the interface and, hence, the evolution of the system is only determined by nonlinearity. For this case, a class of exact solutions (with accuracy up to quadratic nonlinear terms) is obtained, which describes the propagation and interaction of structurally stable localized waves at the interface. In the third regime of fluids motion, the electrostatic pressure exceeds the hydrostatic one (a transitional regime between the first and second ones). In the general case, the profile of the nonlinear wave is distorted with time. We find the conditions under which this distortion does not occur, and nonlinear waves can propagate without dispersion in the direction or against the direction of the external electric field.

Keywords
Nonlinear waves, Kelvin-Helmholtz instability, tangential electric field

[1] Institute of Electrophysics, UB of RAS, Yekaterinburg, Russia
* **Corresponding author:** kochurin@iep.uran.ru

Introduction

The one of the most frequent types of hydrodynamic unsteadiness is the Kelvin–Helmholtz instability occurring when there is velocity shear in a single continuous fluid, or where there is a velocity difference across the interface between two fluids [1]. Meanwhile, it is well known that the external electric field directed tangentially to unperturbed fluids boundary has a stabilizing effect [2]. Thus, the stabilization of fluids interface undergoing such instabilities as the Kelvin-Helmholtz or the Rayleigh-Taylor instability can provide the electrostatic pressure exerted by tangential electric field. The features of nonlinear waves evolution on the interface in the presence of the horizontal (tangential) field and the Kelvin-Helmholtz instability have been analyzed in [3, 4]. In [5, 6] the problem of stabilization of Rayleigh-Taylor instability using the tangential electric field has been studied. As a rule the complexity of equations describing the evolution of the boundary requires the use of numerical methods. Nevertheless studies [7, 8] have shown that in some cases a significant progress can be attainable in analytical investigating of the interface dynamics. In the present work we generalize the approaches developed in [7, 8] to study the nonlinear stages of the interface Kelvin-Helmholtz instability suppressed by the external electric field. Three classes of analytical solutions corresponding to the different modes of fluids motion are obtained. These results demonstrate the stability of nonlinear waves and possibility of their propagation without shape distortion.

1. Boundary conditions and the weakly nonlinear model equations

Let us consider the dynamics of the interface between two deep perfect dielectric (nonconducting) fluids moving with different velocities in an external horizontal electric field. In the unperturbed state, the interface is a horizontal plane z=0. The electric field strength is directed along the axis x and in absolute value is equal to E. Let the deviation of the interface from the plane $z = 0$ be given by the function $\eta(x, t)$, that is the equation $z = \eta$ defines the shape of the boundary. We will consider the plane-symmetric waves, i.e. all values depend on two spatial variables (z, x), as shown in Figure 1. We assume that both fluids are inviscid and incompressible, and their flows are irrotational (potential). The velocity potentials for fluids $\Phi_{1,2}$, as well as the electric field potentials $\varphi_{1,2}$, satisfy the Laplace equations (here and below the subscripts "1" and "2" refer to the lower and upper fluids, respectively).

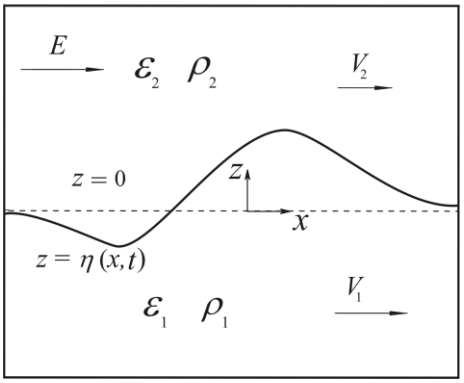

Figure 1. The geometry of the problem.

The normal components of the velocities are equal at the interface, i. e. $\partial_n\Phi_1 = \partial_n\Phi_2$, here ∂_n denotes the derivative along the normal to the boundary $z = \eta$. The tangential component of the electric field and the normal component of the electric displacement field are continuous at the interface. Thus, the electric field potentials obey the boundary conditions at the interface $\varphi_1 = \varphi_2$, $\varepsilon_1\partial_n\varphi_1 = \varepsilon_2\partial_n\varphi_2$, where $\varepsilon_{1,2}$ are the dielectric constants of the lower and upper fluids, respectively. At an infinite distance from the interfacial boundary the velocity field and the electric field are uniform $\Phi_{1,2}\to V_{1,2}x$, $\varphi_{1,2} \to Ex$.The Hamiltonian H coincides with the total energy of the system

$$H = \rho_1\int_{z\le\eta}\frac{(\nabla\Phi_1)^2 - V_1^2}{2}d^3r + \rho_2\int_{z\ge\eta}\frac{(\nabla\Phi_2)^2 - V_2^2}{2}d^3r$$
$$-\varepsilon_0\varepsilon_1\int_{z\le\eta}\frac{(\nabla\varphi_1)^2 - E^2}{2}d^3r - \varepsilon_0\varepsilon_2\int_{z\ge\eta}\frac{(\nabla\varphi_2)^2 - E^2}{2}d^3r \qquad (1)$$

where $\rho_{1,2}$ are the densities of fluids, ε_0 is the vacuum permittivity. For convenience of the further analysis, we switch to dimensionless notations (with dashes) as follows:

$$\Phi_{1,2}' \to \frac{\Phi_{1,2}}{V\lambda} \qquad \varphi_{1,2}' \to \frac{\varphi_{1,2}}{E_0\lambda} \qquad \psi' \to \frac{\psi}{V\lambda(\rho_1+\rho_2)} \qquad V_{1,2}' \to \frac{V_{1,2}}{V}$$
$$E' \to \frac{E}{E_0} \quad \boldsymbol{r}' \to \frac{\boldsymbol{r}}{\lambda} \quad t' \to t\frac{V}{\lambda} \quad E_0 = V\sqrt{\frac{\rho_1+\rho_2}{\varepsilon_0(\varepsilon_1+\varepsilon_2)}}$$

here V, λ are the characteristic velocity and the wave length, respectively. Let us introduce perturbations of the velocity potentials and the electric field potentials of liquids: $\Phi_{1,2}= \Phi'_{1,2} - V_{1,2}x$, $\varphi_{1,2}= \varphi'_{1,2}+Ex$. Further the dashes, in the notation of all dimensionless variables, are omitted. The equations describing the motion of the interface $z = \eta$ can be represented in the Hamiltonian form [9]:

$$\psi_t = -\frac{\delta H}{\delta\eta} \qquad \eta_t = \frac{\delta H}{\delta\psi}$$

where ψ is generalized momentum defined as $\psi(x,y,t) = \rho_1 \Phi_1\big|_{z=\eta} - \rho_2 \Phi_2\big|_{z=\eta}$.

Consider the dynamics of the interface in the approximation of small angles of inclination of the boundary, i.e. $|\nabla_\perp \eta| \sim \alpha \ll 1$, here α is a small parameter. To obtain the equations of the interface motion is necessary to express the Hamiltonian of system (1) in terms of the canonical variables η and ψ. We write the expression for Hamiltonian (with the accuracy up to the cubic terms in integrand) omitting the procedure details of the integrand expansion in the powers of η and ψ (for more details see [7,8])

$$H = -V_c \int \psi \eta_x dx - \frac{1}{2}\int \left(\psi \hat{H} \psi_x + A\eta \left[(\hat{H}\psi_x)^2 - \psi_x^2 \right] \right) dx - \frac{A_E^2 E^2}{2} \int \eta \left(\hat{H}\eta_x + A_E \left[(\hat{H}\eta_x)^2 - \eta_x^2 \right] \right) dx$$
$$+ \frac{(1-A^2)(V_1 - V_2)^2}{8} \int \eta \left(\hat{H}\eta_x - A \left[(\hat{H}\eta_x)^2 - \eta_x^2 \right] \right) dx + \frac{(1-A^2)(V_1 - V_2)}{2} \int \eta_x \left[\hat{H}(\eta\psi_x) - \eta \hat{H}\psi_x \right] dx$$

where $\hat{H}$ denotes the Hilbert integral transform, $A = (\rho_1 - \rho_2)/(\rho_1 + \rho_2)$ is the Atwood number and $A_E = (\varepsilon_1 - \varepsilon_2)/(\varepsilon_1 + \varepsilon_2)$ is an analogue of the Atwood number for dielectric constants, V_c is the velocity of fluids center mass, and without loss of generality, we can set it equals to zero, which corresponds to a transition in the center of mass of the fluids. Taking the variational derivatives of H, we obtain the desired equations of motion:

$$\psi_t - \left(A_E^2 E^2 - \frac{(1-A^2)(V_1 - V_2)^2}{4} \right) \hat{H}\eta_x = \frac{A}{2}\left((\hat{H}\psi_x)^2 - \psi_x^2 \right)$$
$$- \frac{(1-A^2)(V_1 - V_2)}{2} \left(\psi_x \hat{H}\eta_x + \eta_x \hat{H}\psi_x - (\eta \hat{H}\psi_x)_x + \hat{H}(\eta\psi_x)_x \right)$$
$$+ \left(A_E^3 E^2 + \frac{A(1-A^2)(V_1 - V_2)^2}{4} \right) \left(\frac{1}{2}\left((\hat{H}\eta_x)^2 - \eta_x^2 \right) + \hat{H}(\eta \hat{H}\eta_x)_x + (\eta\eta_x)_x \right) \qquad (2)$$

$$\eta_t + \hat{H}\psi_x = \frac{(1-A^2)(V_1 - V_2)}{2} \left(\hat{H}(\eta\eta_x)_x - (\eta \hat{H}\eta_x)_x \right) - A\left(\hat{H}(\eta \hat{H}\psi_x)_x + (\eta\psi_x)_x \right) \qquad (3)$$

As can be seen, these equations are a fairly complicated system of nonlinear integral-differential equations. Construction of the general solution of the system (2)-(3) is very hard problem; therefore we consider a number of special cases in which the system can be described analytically.

2. Nonlinear waves in the absence of velocity discontinuity

The first regime of motion discussed in the paper is realized when the following conditions are satisfied:

$$V_1 - V_2 = 0 \qquad A_E = A \Leftrightarrow \rho_1/\rho_2 = \varepsilon_1/\varepsilon_2 \qquad (4)$$

That is the interface velocity discontinuity is absent, and the ratio of fluids densities is equal to ratio of their dielectric constants. In this case the system of equations (2)-(3) has pair of exact solutions:

$$\eta(x,t) = f(x - AEt) \qquad \eta(x,t) = g(x + AEt) \qquad (5)$$

here $f(x-AEt)$ and $g(x+AEt)$ are arbitrary functions. In accordance with the expressions (5) the nonlinear waves of arbitrary shape propagate without distortion in the direction and against the direction of external electric field. Thus in the regime, the nonlinearity has not an influence on wave speed and does not lead to the singularity. The nonlinear effects should be considered only in the analysis of the interaction of counterpropagating waves. Let us consider the interaction of counterpropagating waves (5), in a situation where the condition (4) is satisfied. As in [8], we find the general solution of the equations (2)-(3)

$$\eta(x,t) = f(x - AEt) + g(x + AEt) + \frac{A}{2}\partial_x\left[\hat{H}\left(fg + \hat{H}f \cdot \hat{H}g\right) - \left(f\hat{H}g + g\hat{H}f\right)\right] \qquad (6)$$

This expression describes the nonlinear superposition of the counterpropagating nonlinear waves (5). From (6) we can see that the interacting waves are structurally stable.

3. Nonlinear waves in the neutral stability regime

The second motion regime corresponds to the situation for which the Kelvin-Helmholtz instability is completely stabilized by the external field, i.e. under the following condition $E^2 = E_c^2$, here E_c is the critical value of electric field strength

$$E_c^2 = \frac{(1-A^2)(V_1 - V_2)^2}{4A_E^2}$$

A significant progress in the study of the problem can be achieved in the case $\psi \equiv 0$ (this condition can be realized if $A_E = -A$, or that the same $\rho_1 / \rho_2 = \varepsilon_2 / \varepsilon_1$). Since applying the Hilbert transform to a function analytic in the upper half-plane reduces to its multiplication by the imaginary unit equation (5) can be rewritten in the complex form

$$\eta_t^+ = (1-A^2)(V_1 - V_2)i\hat{P}^+(\eta^+\eta_x^-)_x \qquad (7)$$

here $\hat{P}^+ = (1 - i\hat{H})/2$ is the projection-operator, that action on an arbitrary complex function defined as $\hat{P}^+\phi = \phi^+$, here ϕ^+ is an analytic function in the upper complex half-plane. This equation admits the exact solution in the form of structurally stable perturbation of the form

$$\eta^+(x,t) = \frac{iS/2}{x + b(t) + ia(t)} \quad \Leftrightarrow \quad \eta = 2\,\mathrm{Re}\,\eta^+ = \frac{Sa}{(x-b)^2 + a^2} \qquad (8)$$

here S is a real constant, (-b,-ia) are coordinates of the singular point (pole in the lower complex half-plane $a(t) > 0$). After substitution of the function $\eta^+(x,t)$ into equation (7) we obtain ordinary differential equations for the $a(t)$, $b(t)$

$$\frac{da}{dt} = 0 \qquad \frac{db}{dt} = \frac{S}{8a^2}(1-A^2)(V_1 - V_2) = V_s$$

It follows directly that $a = const$, $b(t) = x_0 + V_s t$, that is the localized perturbation of the form (8) propagates without shape distortion along the interface with the velocity V_s, which depends on parameters S and a. It should be noted that the equation (7) can be reduced to ODE system for the more general case, where the solution of system is a superposition of the perturbations (8)

$$\eta^+(x,t) = \sum_{n=1}^{N} \frac{iS_n/2}{x + p_n(\mathrm{t})}$$

here S_n are real constants, $p_n(t)$ are complex functions, that determine the locations of poles in the lower complex half-plane $\mathrm{Im}\, p_n(\mathrm{t}) > 0$. After substituting this expression into equation (7) we obtain the ODE system

$$\frac{dp_n}{dt} = -(1-A^2)(V_1 - V_2)\sum_{j=1}^{N} \frac{S_j/2}{(p_n - \bar{p}_j)^2}$$

The system of ODE describes the propagation and interaction of stable nonlinear waves of the form (8) along the interface between liquids.

4. Nonlinear waves in the regime of suppression of the Kelvin-Helmholtz instability

In this section we consider the situation in which the tangential velocity discontinuity at the boundary is not zero, and the electric field does not equal to the critical value. We suppose that $E>E_c$, i.e. the regime is intermediate between that discussed in Section 2 (which formally corresponds $E \gg E_c$), and that considered in Section 3 (for which $E = E_c$). The equations (2) and (3) can be rewritten using new variables

$$f = \frac{(V_0^{-1}\hat{H}\psi + \eta)}{2} \qquad g = \frac{(V_0^{-1}\hat{H}\psi - \eta)}{2}$$

where $V_0 > 0$ is the speed of linear wave

$$V_0 = \left(A_E^2 E^2 - \frac{(1-A^2)(V_1 - V_2)^2}{4} \right)^{1/2}$$

In the linear approximation, the equations (2) and (3) have the following form in terms of the new variables

$$f_t + V_0 f_x = 0 \qquad g_t - V_0 g_x = 0$$

Thus, the equations system (2)-(3) is divided into independent equations. The equation for f describes the propagation of linear wave to the left and the equation for g does to the right. The same way we can divide the system (2)-(3) in the framework of weakly nonlinear model. So the equations for the traveling waves have the following form

$$f_t + V_0 f_x = \frac{1}{2}\left(AV_0(\gamma - 1) + (1-A^2)(V_1 - V_2) \right)\left(\frac{1}{2}\hat{H}\left((\hat{H}f_x)^2 - f_x^2 \right) + \hat{H}(f f_x)_x - (f\hat{H}f_x)_x \right) \quad (9)$$

$$g_t - V_0 g_x = \frac{1}{2}\left(AV_0(\gamma - 1) - (1-A^2)(V_1 - V_2) \right)\left(\frac{1}{2}\hat{H}\left((\hat{H}g_x)^2 - g_x^2 \right) + \hat{H}(g g_x)_x - (g\hat{H}g_x)_x \right) \quad (10)$$

here we also introduced dimensionless parameter γ

$$\gamma = \left(A_E^2 E^2 \frac{A_E}{A} + \frac{(1-A^2)(V_1 - V_2)^2}{4} \right) \Big/ \left(A_E^2 E^2 - \frac{(1-A^2)(V_1 - V_2)^2}{4} \right)$$

It is not difficult to see that the case of dispersionless nonlinear wave propagation, discussed in the Section 2, corresponds to the value of the parameter $\gamma = 1$, and $A = A_E$, $V_1 - V_2 = 0$. Here, we should note the possibility of dispersionless wave propagation, if the following conditions are satisfied:

$$AV_0(\gamma - 1) \pm (1-A^2)(V_1 - V_2) = 0 \quad (11)$$

i.e. in this case either the right part of the equation (9) equals to zero or the right part of (10) equals to zero. The conditions (11) determine an implicit dependence of electric field on the physical parameters of the problem ($V_1 - V_2$, A, A_E). Herewith, the choice of sign in (11) corresponds to the different directions of dispersionless wave propagation; the plus for the left-traveling waves, and the minus for the right-traveling waves. That is the wave propagation without distortion is only possible in one direction, in contrast to the regime discussed in Section 2, in which waves can propagate

without dispersion in both directions. It should be noted that the conditions (11) do not contain a strict condition on A and A_E , whereas for the realization of above mentioned regimes the conditions were necessary: $A_E = \pm A$.

Conclusions

In the present work, the nonlinear dynamics of the interface of dielectric liquids in a horizontal electric field in the presence of velocity discontinuity at the interface have been studied. In the framework of Hamiltonian formalism the nonlinear integral-differential equations describing the propagation of quadratic nonlinear waves at the interface are obtained. It is shown that the external electric field can stabilize nonlinear stages of the Kelvin-Helmholtz instability. Three regimes of fluids motion are considered, for that the nonlinear surface waves propagate without distortion of their shape. It is important that for the obtained solutions the evolution of system does not lead to an increase of surface disturbances and singularities formation. As a consequence the angles of interface slope remain small and applicability conditions of the theory are not broken. It should be noted that the above results are applicable for the description of wave propagation at the interface between ferromagnetic liquids in a horizontal magnetic field at replacement the of electric field strength E on the magnetic field strength H and the dielectric constants $\varepsilon_{1,2}$ on the magnetic permeability $\mu_{1,2}$.

Acknowledgments

This study was supported by RFBR (11-08-00434) and the Presidium of the Ural Branch of the Russian Academy of Sciences in the framework of the Presidium of RAS program "Fundamental problems of nonlinear dynamics in the mathematical and physical sciences" (Project 12-П-2-1023) and the program for young scientists and postgraduate students (Project 13-2-НП-380), and the "Dynasty" foundation.

References

[1] Drazin, P. G. *Introduction to hydrodynamic stability*, Cambridge University Press, Cambridge Texts in Applied Mathematics, Cambridge, 2002.

[2] Melcher J.R. Electrohydrodynamic and magnetohydrodynamic surface waves and instabilities *Phys. Fluids*, Vol. 4 N.11, pp. 1348-1354, 1961.

[3] Grandison S., Papageorgiou D.T., Vanden-Broeck J.-M. Interfacial capillary waves in the presence of electric fields *European Journal of Mechanics B/Fluids,* Vol. 2, pp. 404-421, 2007.

[4] Papageorgiou D.T., Vanden-Broeck J.-M. Large-amplitude capillary waves in electrified fluid sheets *J. Fluid Mech,* Vol. 508, pp. 71-88, 2004.

[5] Barannyk L.L., Papageorgiou D. T., Petropoulos P.G. Suppression of Rayleigh-Taylor instability using electric fields *Math. Comput. Simul.*, Vol. 82, pp. 1008-1016, 2012.

[6] Korovin V.M. Effect of tangential electric field on the evolution of the Rayleigh-Taylor instability of a dielectric liquid film, *Technical Physics,* Vol. 56 N.10, pp. 1390-1397, 2011.

[7] Zubarev N.M. Nonlinear waves on the surface of a dielectric liquid in a strong tangential electric field *Phys. Lett. A,* Vol. 333, pp. 284-288, 2004.

[8] Zubarev N.M. Nonlinear waves on the surface of a dielectric liquid in a horizontal electric field in 3D geometry: Exact solutions *JETP Letters*, Vol. 89 N. 6, pp. 271-274, 2009.

[9] Kuznetsov E.A., Spector M.D., Zakharov V.E. Surface singularities of ideal fluid *Phys. Lett. A.*, Vol. 182, pp. 387-393, 1993.

Proceedings of the 4th International Conference on Nonlinear Dynamics
ND-KhPI2013
June 19-22, 2013, Sevastopol, Ukraine

Dynamics of Stationary Structures in a Parabolic Functional-Differential Equation

A. A. Kornuta

Abstract
We consider on a circle the scalar parabolic equation with a rotation of the spatial variable. Dynamics of its stationary structures is investigated provided that the diffusion coefficient aspires to zero. It is proved that the original problem possesses the orbitally exponentially stable one-parameter family of solutions of the type of internal shock layer for sufficiently small coefficient of diffusion.

Keywords
Bifurcation, parabolic equation,optical structure,orbitally stability, stability,internal shock layer,Galerkin method

Taurida National V.I.Vernadsky University, Simferol, Ukraine
*__Corresponding author__: korn_57@mail.ru

Introduction

Consider an equation in a circle $\mathbb{R}/2\pi\mathbb{Z}$ [1]

$$\begin{gathered}\partial_t u + u = \mu\partial_{xx}u + L\,\mathrm{T}_h u + (\mathrm{T}_h u)^3,\\ u(x+2\pi,t) = u(x,t),\\ u(x,0) = u_0(x),\ \ 0 < x < 2\pi,\end{gathered} \tag{1}$$

where $\mathrm{T}_h u = u(x+h,t)$, h is an angle of rotation of the field, and L, $\mu > 0$ are parameters. The original problem is obtained in the case of investigation of the optical structures in a nonlinear interferometer with transformation of rotation in the two-dimensional feedback as a result of a series of simplifying assumptions. In the present work, it is assumed that $h = \pi$. We note that stationary structures in Eq. (1) with transformation of rotation are investigated in [2-4].

For each value of the parameter μ, Eq. (1) generates a dynamical system in the Sobolev space $H^1(\mathbb{R}/2\pi\mathbb{Z})$ of $2\pi-$periodic functions. The solutions of Eq. (1) approach one of its stationary solutions as $t \to +\infty$. For $L < -1$, Eq. (1) possesses three stationary spatially homogeneous solutions: 0 and $\pm\sqrt{-1-L}$. For $\mu > -1-L$, the trivial solution is exponentially stable.

The transition of the parameter μ through the value

$$\mu_k^* = \frac{-L-1}{k^2}, \qquad k = 1,3,\ldots$$

leads to changes in the character of stability of the trivial solution. As μ passes through the value μ_1^*, one simple eigenvalue of the trivial solution passes through zero from the negative semiaxis to the positive semiaxis. As a result of this bifurcation, two stable and continuous (in μ) branches of spatially inhomogeneous stationary points $\pm\varphi_1(x,\mu)$ separate from the trivial solution.

By using the method of central manifolds, we arrive at the equality

$$\varphi_1(x,\mu) = \frac{2}{\sqrt{3}}\sqrt{-1-L-\mu}\cos x + O(-1-L-\mu).$$

As the parameter μ decreases and passes through the value μ_k^* for $k = 3,5,\ldots$, the instability index of the trivial solution increases each time by an order of magnitude. As a result, a couple of stationary points $\pm\varphi_k(x,\mu)$ with instability index $\dfrac{k-1}{2}$ separates from zero.

By applying the similarity principle

$$\varphi_k(x,\mu) = \varphi_1(kx; k^2\mu),$$

we get

$$\varphi_k(x,\mu) = \frac{2}{\sqrt{3}}\sqrt{-1-L-k^2\mu}\cos kx + O\left(-1-L-k^2\mu\right).$$

In the present work, to study the behavior of the stationary structures $\varphi_k(x,\mu)$ as the parameter μ moves from the corresponding bifurcation value, we construct a hierarchy of simplified models of Eq. (1).

1. Galerkin Approximation

We represent the solution of the original equation in the form

$$u = \sum_{k=0}^{N} z_k \cos kx \tag{2}$$

and substitute this expression in Eq. (1). In the equation obtained as a result, we equate the coefficients of $\cos kx$, $k = \overline{0,N}$, and arrive at the following gradient system of equations:

$$\dot{z}_k = -\frac{\partial G_N(z)}{\partial z_k}, \quad k = \overline{0,N}. \tag{3}$$

In system (3), the trivial stationary solution is stable for $\mu > -1-L$. As the parameter μ passes through $-1-L$, the trivial solution becomes unstable with instability index 1. As a result, two continuous branches of fixed points $\pm z_1(\mu,N) = \pm(z_{1,0}; z_{1,1}; \ldots; z_{1,N})$ separate from zero

$$z_{1,2s} = 0, \quad (-1)^s z_{1,2s+1} > 0, \quad s = 0,1,\ldots; \quad z_{1,1} > |z_{1,3}| > z_{1,5} > \ldots$$

Thus, we get the following approximare inequality:

$$\varphi_1(x,\mu) \approx \sum_{s=1}^{n} z_{1,2s-1}\cos(2s-1)x, \quad n = \begin{cases} \frac{N}{2}, & \text{is } N \text{ is even;} \\ \frac{N+1}{2}, & \text{if } N \text{ is odd.} \end{cases} \tag{4}$$

The numerical analysis is performed for the case $L = -\dfrac{3}{2}$. In the vicinity of the value of the parameter $\mu = -1-L$, the plot of the function has a quasiharmonic form with low amplitude. As the parameter μ decreases, the amplitude of the function $\varphi_1(x,\mu)$ increases. Moreover, the modulus of this function takes its maximal value at the points 0, π and 2π. As soon as the function $|\varphi_1(x,\mu)|$ attains its maximum value $\approx \sqrt{-1-L}$, the growth of its amplitude terminates. As the parameter μ decreases further, the intervals adjacent to $x = 0$, $x = \pi$, and $x = 2\pi$ in which the function takes constant values increase. As soon as μ attains a certain value depending on N, the function $\varphi_1(x,\mu)$ begins to oscillate, i.e., we observe a manifestation of the Gibbs phenomenon. As N increases, the amplitude of oscillations decreases and their frequency increases. For μ close to zero, $\varphi_1(x,\mu)$ has the form of a contrast structure with two transition points $\dfrac{\pi}{2}$ and $\dfrac{3\pi}{2}$. As an illustratioin, in Fig. 1, we present the plots of the function $\varphi_1(x,\mu)$ for $N = 21$ and the values $\mu = 0.4,\ 0.1,\ 0.01,\ 0.001,\ 0.00001$.

We now proceed to the analysis of stability of the function $\varphi_1(x,\mu)$. It has already been indicated that $\pm\varphi_1(x,\mu)$ are born stable. To this end, we consider the problem of stability of fixed points $\pm z_1(\mu,N)$. According to the results of numerical analysis performed for the values $N = \overline{5,21}$, these points are stable. All points of the spectrum $\lambda_k(\mu,N), k = \overline{0,N}$, of the stability matrix

$$-\frac{\partial^2 G_N(z,\mu)}{\partial z^2}\Big|_{z=z^1(\mu,N)}$$

lie on the negative semiaxis. As the parameter μ decreases, the points of the spectrum become closer. Thus, $\lambda_k(\mu,N), k = \overline{1,N}$, monotonically decrease in the interval $\left(0; \dfrac{1}{2}\right)$. The maximum point of the spectrum

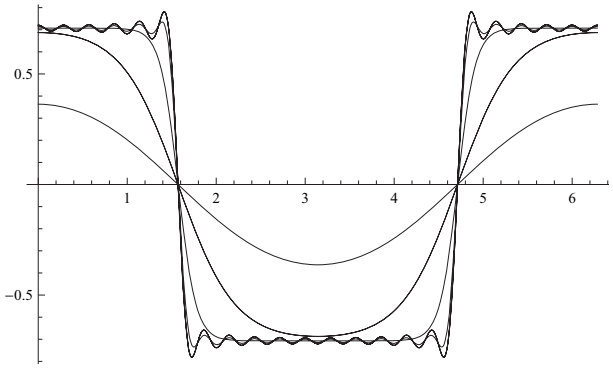

Figure 1. Plots of the function $\varphi_1(x,\mu)$

$\lambda_0(\mu,N)$ monotonically decreases in the interval $(0;0.011)$ and monotonically increases in the interval $\left(0.011;\frac{1}{2}\right)$. Moreover, for the values of the parameter μ close to zero, we have $\lambda_0(\mu,N)\approx -0.7$.

As the parameter μ decreases and passes through the value $\frac{-1-L}{9}$, the instability index of the trivial solution increases by 1. As a result, the second couple of stationary points $\pm z_3(\mu,N) = \pm(z_{3,0}, z_{3,1}, \dots z_{3,N})$ continuous in μ and such that

$$z_{3,k}=0,\ \ k\neq 3,9,\dots;\ \ (-1)^s z_{3,6s+3}>0,\ \ s=0,1,\dots;\ \ z_{3,3}>|z_{3,9}|>z_{3,15}>\dots.$$

separates from zero. In view of (2) and (3), we get the following approximate equality:

$$\varphi_3(x,\mu)\approx\sum_{s=1}^{n} z_{3,6s-3}\cos(6s-3)x,\quad n=\left[\frac{N-1}{9}\right]+1. \tag{5}$$

The function $\varphi_3(x,\mu)$ has six transition points $\frac{k\pi}{6}$, $k=1,3,...,11$ and its behavior is similar to the behavior of $\varphi_1(x,\mu)$. As an illustration, in Fig. 2, we present the plots of the function $\varphi_3(x,\mu)$ for $N=21$ and the values $\mu=0.05,\ 0.04,\ 0.01,\ 0.001,\ 0.00001$.

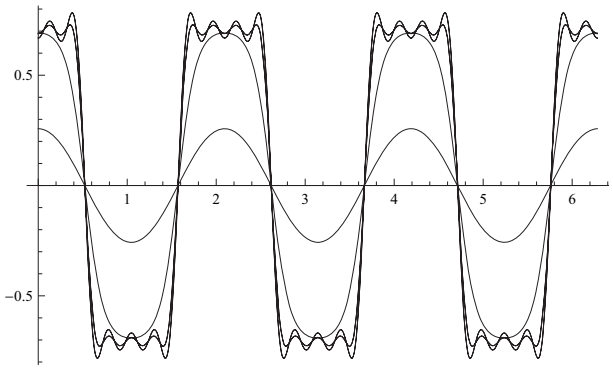

Figure 2. Plots of the function $\varphi_3(x,\mu)$

The solutions $\varphi_3(x,\mu)$ are born unstable with instability index 1. The points $z_3(\mu,N)$ are also born unstable with instability index 1. The analysis of the stability of $z_3(\mu,N)$ for $N=\overline{5,21}$ gives the following results:

For any N, the eigenvalues $\lambda_s(\mu,N)<0$, $s=\overline{1,N}$, in the interval $\left(0;\frac{-1-L}{9}\right)$.

For $N=5,6$, as the parameter μ decreases, the sole positive eigenvalue $\lambda_0(\mu,N)$ shifts to the negative semiaxis for $\mu\approx 0.02$ and remains negative as the parameter μ decreases further. Note that, for μ close to zero, $\lambda_0(\mu,N)$ is small, e.g., $\lambda_0(0.000001)\approx -0.00002$.

For $N = 7,8$, as the parameter μ decreases, the point of the spectrum $\lambda_0(\mu,N) > 0$ in the interval $\left(0; \frac{-1-L}{9}\right)$: the function $\lambda_0(\mu,N)$ monotonically increases as $(0;0.0194)$ and monotonically decreases as $\left(0.0194; \frac{-1-L}{9}\right)$.

For $N = 9,10$ as the parameter μ decreases, the positive eigenvalue $\lambda_0(\mu,N)$ shifts to the negative semiaxis for $\mu \approx 0.01804$. As the parameter decreases further, $\lambda_0(\mu,N)$ remains negative and moves from the origin.

For $N = 11,12,17,18$, the behavior of $\lambda_0(\mu,N)$ is similar to its behavior for $N = 5,6$ but, in this case, $\lambda_0(\mu,N)$ shifts to the left semiaxis for $\mu = 0.01333$ and $\mu = 0.00959$, respectively.

For $N = 13,14,19,20$, the positive eigenvalue $\lambda_0(\mu,N)$ remains on the right semiaxis as in the case $N = 7,8$.

For $N = 15,16,21$, the unstable stationary point z_3 becomes stable, as in the case $N = 9,10$, but for smaller value of the parameter μ.

The results presented above enable us to make the following conclusion: For small μ, the spectrum of the stationary point $\varphi_3(x,\mu)$ of the original problem contains 0. This means that, for small μ, $\varphi_3(\cdot,\mu)$ is a point of an orbitally exponentially stable one-parameter family of stationary points. This family is a one-parameter family of solutions of the type of internal shock layer [5]. Thus, the original problem has the following specific feature: If the parameter μ is located near the critical value, then there exists an isolated stationary solution $\varphi_3(x,\mu)$ monotonically decreasing in the interval $[0, \frac{\pi}{3}]$ and such that $\varphi_3(\frac{\pi}{6},\mu) = 0$. We note that $\varphi_3(0,\mu)$ increases as μ decreases.The growth of the function $\varphi_3(0,\mu)$ terminates as soon as it becomes equal to $\sqrt{-1-L}$. In this case, the function $\varphi_3(x,\mu)$ turns into a solution of the type of internal shock layer with transition point $\frac{k\pi}{6}$,$k = 1,3,...,11$. Than, we observe the loss of the isolated character of the stationary solution $\varphi_3(x,\mu)$. The problem of the character of bifurcation connected with the transition from the isolated solution to a one-parameter family of solutions of the shock type is of significant interest. To solve this problem, we consider simplified models (3) of the original problem.

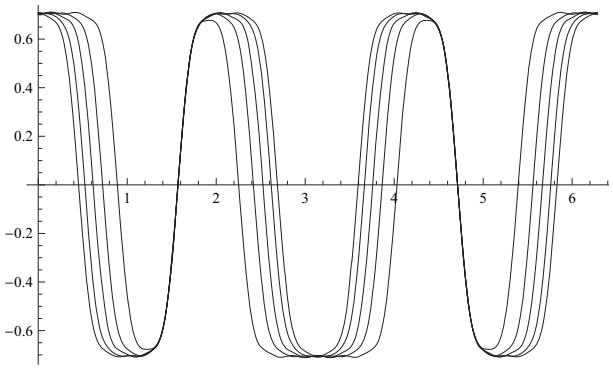

Figure 3. Plots of one-parameter family $\varphi_3(\cdot,\mu)$

The solutions of the shock type with different transition points are presented in Fig. 3. These approximate solutions correspond to the bifurcation values of the parameter $\mu = 0.005$ obtained for system (3) in which $N = 25$.

In the gradient systems (3), as the parameter μ decreases, we observe the realization of a great variety of saddle-node bifurcations. The bifurcations leading, by virtue of (2), to the solutions of the shock-layer type with three transition point are characterized by the following specific features: For fixed N, the bifurcation values of the parameter μ are close. The branches of stationary points born stable or unstable are defined for all positive values of the parameter μ lower than the corresponding bifurcation value. The character of their stability preserves as the parameter μ decreases. The spectra of stationary points of the indicated type almost coincide. As the parameter μ decreases, the highest points points of these spectra slowly move from zero. The stationary points in the branch slowly vary as the parameter μ decreases.

To illustrate these observations, we now present examples of saddle-node bifurcations for $N = 25$.

Thus,

$$\mu = 0.000920618,$$
$$(0.86968; -0.21197; 0.04326; 0.04397; 0.09327; 0.11702; -0.12182; -0.11302; -0.09561; ...),$$
$$\sigma_s = \{-2.53192; ...; -1.00413; -0.99984; -0.99814; -0.58296; -0.00011371\},$$
$$(0.86969; -0.21201; 0.04332; 0.04390; -0.09320; 0.11696; -0.12177; -0.11298; -0.09559; ...),$$
$$\sigma_u = \{-2.53204; ...; -1.00413; -0.99984; -0.99813; -0.58295; \quad 0.00011379\}.$$

$$\mu = 0.0001,$$
$$(0.86549; -0.20008; 0.02369; 0.07119; -0.12764; 0.15719; -0.16541; 0.15685; -0.13616; ...),$$
$$\sigma_s = \{-2.06130; ...; -0.96356; -0.93894; -0.93582; -0.89937; -0.16546\},$$
$$(0.88365; -0.25391; 0.10771; -0.03437; -0.01111; 0.04072; -0.05912; 0.06879; -0.07144; ...),$$
$$\sigma_u = \{-2.43375; ...; -0.92573; -0.90616; -0.89004; -0.65910; \quad 0.34249\}.$$

$$\mu = 0.000001,$$
$$(0.86584; -0.20139; 0.02565; 0.06919; -0.12629; 0.15712; -0.16702; 0.16021; -0.14095; ...),$$
$$\sigma_s = \{-2.0107; ...; -0.93763; -0.93505; -0.89991; -0.89287; -0.18034\},$$
$$(0.88434; -0.25614; 0.11132; -0.03897; -0.00602; 0.03568; -0.05468; 0.06537; -0.06934; ...),$$
$$\sigma_u = \{-2.43636; ...; -0.90020; -0.88279; -0.85259; -0.65068; \quad 0.36349\}.$$

It is clear that the next point of the spectrum after the maximal point along the negative semiaxis is located near -1.

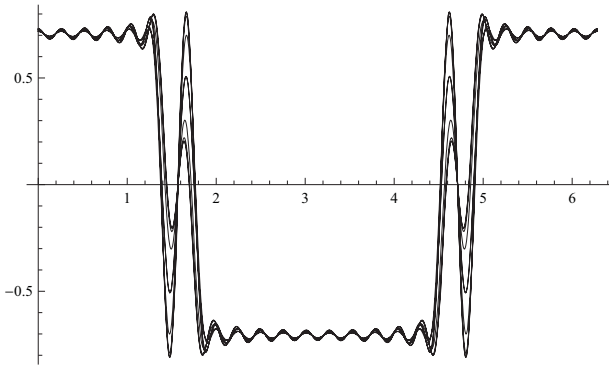

Figure 4. Plots of the function $\varphi_{s,u}(x,\mu)$

In Fig. 4, for $\mu = 0.000920618,\ 0.0001,\ 0.000001$, we present the plots of the corresponding structures.

We observe so saddle-node bifurcations leading, by virtue of (2), to the solutions with splash points.

There are serious reasons to believe that the results obtained in the present work remain true for $N > 25$.

Conclusions

Existence of an orbital asymptotically stable family of stationary solutions of the considered problem for sufficiently small coefficient of diffusion is shown in this article. Points of the family are stationary solutions of internal transition layer, which are constructed using the Galerkin method.

References

[1] Akhmanov S.A., Vorontsov M.A. and Ivanov V.Yu. Generation of structures in optical systems with two-dimensional feedback; On the way to the creation of nonlinear optical analogues of neural networks. In:*New physical principles of the optical information processing.* Nauka, Moscow, 1990.

[2] Kashcenko S.A. Asymptotic of spatially heterogeneous structures in coherent nonlinear optical systems, *Zh.Vichist. Mat.Fiz*, Vol. 3, pp. 467-473, 1994.

[3] Grigorieva E.V., Haken H., Kashchenko S.A., Pelster A. Travelling wave dynamics in a nonlinear interferometer with spatial field transformer in feedback , *Physika D*. Vol. 125, pp. 123-141, 1999.

[4] Belan E.P. Optical buffering in stationary structures, *Cybernetics and Systems Analysis*, Vol. 5, pp. 61-75, 2008.

[5] Vasil'eva A.B., Butuzov V.F. *Asymptotic methods in a singular perturbation theory*, Vyssh. Shkola, Moscow, 1990.

[6] Mishchenko E.F., Sadovnichy V.A., Kolesov A.Yu. and Rozov N.Kh. *Autowave processes in nonlinear media with diffusion*, Moscow, 2005.

Proceedings of the 4th International Conference on Nonlinear Dynamics
ND-KhPI2013
June 19-22, 2013, Sevastopol, Ukraine

Application of R-Functions Theory to Study Parametric Vibrations and Dynamical Stability of Laminated Plates

Lidiya Kurpa [1*], Olga Mazur[2], Igor Tsukanov[3]

Abstract
The problem of nonlinear parametric vibrations and stability analysis of the symmetric laminated plates is considered. The proposed method is based on multimode approximation of displacements and solving series auxiliary linear tasks. The main feature of the work is the application of the R-functions theory, which allows investigating parametric vibrations of plates with complex shape and different boundary conditions.

Keywords
R function method, laminated plates, parametric vibrations

[1] NTU "KhPI", Kharkiv, Ukraine
[2] NTU "KhPI", Kharkiv, Ukraine
[3] Florida International University, Miami, FL, USA
* **Corresponding author:** kurpa@kpi.kharkov.ua

Introduction

This work is devoted to a study of the nonlinear vibrations and stability of laminated plates with complex geometric shape that are subjected to a periodic in-plane load. The relevance of the problem is explained by wide adoption of composite materials in the industrial applications. A special attention has been paid to the vibrations of composite plates under various types of loading, and in particular, parametric vibrations. There are many publications on this subject, but the previous works considered mostly the plates of a canonical form with a homogeneous subcritical state. Currently, the computer simulation of the nonlinear dynamics of plates with complex geometric shape and inhomogeneous subcritical state are performed using the Finite Element Method (FEM) [5]. A different approach has been proposed in references [2,4]. It is based on the theory of R-functions and variational methods, and enables obtaining the meshless solutions to the plate and shell vibration problems. In this work the R-functions method (RFM) is extended to a new class of problems – nonlinear parametric vibrations and dynamical stability of laminated plates. In the proposed approach we will take into account the subcritical state.

1. Mathematical Statement

Let us consider the parametric vibrations of the laminated plates with symmetric structure. We assume that plate and all its layers have a constant thickness; and the plate is subjected to a periodic in-plane load $p = p_0 + p_t \cos\theta t$, where p_0 is a static component, p_t is an amplitude of a periodic part, and θ is a frequency of the load. We derive mathematical formulation of the problem using Kirchhoff's hypotheses. Accordingly, the strains acting in the midplane are expressed as follows:

$$\varepsilon_x = \frac{\partial u}{\partial x} + \frac{1}{2}\left(\frac{\partial w}{\partial x}\right)^2,\ \varepsilon_y = \frac{\partial v}{\partial y} + \frac{1}{2}\left(\frac{\partial w}{\partial y}\right)^2,\ \varepsilon_{xy} = \frac{\partial u}{\partial y} + \frac{\partial v}{\partial x} + \frac{\partial w}{\partial x}\frac{\partial w}{\partial y},$$

$$\chi_x = -\frac{\partial^2 w}{\partial x^2};\ \chi_{xy} = -2\frac{\partial^2 w}{\partial x \partial y};\ \chi_y = -\frac{\partial^2 w}{\partial y^2}.$$

In these expressions *u, v, w* are the displacements of the points in a midplane in the directions of the coordinate axes *Ox, Oy*, and *Oz*. Stress resultants N_x, N_y, N_{xy} and moments M_x, M_y, M_{xy} are presented as:

$$\{N\} = [\mathbf{C}] \cdot \{\varepsilon\},\quad \{M\} = [\mathbf{D}] \cdot \{\chi\},$$

where **C** and **D** are stiffness matrices:

$$\mathbf{C} = \begin{pmatrix} C_{11} & C_{12} & C_{16} \\ C_{12} & C_{22} & C_{26} \\ C_{16} & C_{26} & C_{66} \end{pmatrix},\ \mathbf{D} = \begin{pmatrix} D_{11} & D_{12} & D_{16} \\ D_{12} & D_{22} & D_{26} \\ D_{16} & D_{26} & D_{66} \end{pmatrix},$$

$\{\varepsilon\}, \{\chi\}, \{N\}, \{M\}$ are strain, stress and moment vectors:

$$\{\varepsilon\} = (\varepsilon_x, \varepsilon_y, \varepsilon_{xy})^T,\ \{\chi\} = (\chi_x, \chi_y, \chi_{xy})^T,$$
$$\{N\} = (N_x, N_y, N_{xy})^T,\ \{M\} = (M_x, M_y, M_{xy})^T.$$

The components C_{ij}, D_{ij} $(ij = 11,22,12,16,26,66)$ of stiffness matrices are defined as [1]:

$$(C_{ij}, D_{ij}) = \sum_{s=1}^{N} \int_{h_s}^{h_{s+1}} B_{ij}^{(s)} (1, z^2) dz,\ i, j = 1,2,6,$$

where $B_{ij}^{(s)}$ are the mechanical characteristics of the s-*th* layer. Ignoring the inertial terms, the motion equations, expressed in the displacements, can be written as follows [1]:

$$L_{11}u + L_{12}v = -Nl_1(w),\ L_{21}u + L_{22}v = -Nl_2(w) \tag{1}$$

$$L_{33}w = Nl_3(u,v,w) - \varepsilon m_1 \frac{\partial w}{\partial t} - m_1 \frac{\partial^2 w}{\partial t^2} \tag{2}$$

Differential operators L_{ij}, Nl_i $i, j = 1,2,3$ in the equations (1)-(2) are defined as

$$L_{11}w = C_{11}\frac{\partial^2}{\partial x^2} + 2C_{16}\frac{\partial^2}{\partial x \partial y} + C_{66}\frac{\partial^2}{\partial y^2},\ L_{22} = C_{66}\frac{\partial^2}{\partial x^2} + 2C_{26}\frac{\partial^2}{\partial x \partial y} + C_{22}\frac{\partial^2}{\partial y^2},$$

$$L_{12} = L_{21} = C_{16}\frac{\partial^2}{\partial x^2} + (C_{12} + C_{66})\frac{\partial^2}{\partial x \partial y} + C_{26}\frac{\partial^2}{\partial y^2},$$

$$L_{33} = D_{11}\frac{\partial^4}{\partial x^4} + 2(D_{12} + 2D_{66})\frac{\partial^4}{\partial x^2 \partial y^2} + 4D_{16}\frac{\partial^4}{\partial x^3 \partial y} + 4D_{26}\frac{\partial^4}{\partial x \partial y^3} + D_{22}\frac{\partial^4}{\partial y^4},$$

$$Nl_1 = \frac{\partial w}{\partial x}L_{11}w + \frac{\partial w}{\partial y}L_{12}w,\ Nl_2 = \frac{\partial w}{\partial x}L_{12}w + \frac{\partial w}{\partial y}L_{22}w,$$

$$Nl_3 = N_x\frac{\partial^2 w}{\partial x^2} + N_y\frac{\partial^2 w}{\partial y^2} + 2N_{xy}\frac{\partial^2 w}{\partial x \partial y},$$

where ε is a damping coefficient. System (1)-(2) is supplemented by the initial and boundary conditions. The load, specified at the traction portion of the plate's boundary, is specified by its normal and tangential components:

$$N_n = -p, T_n = 0.$$

The normal component N_n of the applied load can be expressed via the stress resultants N_x, N_y, N_{xy}

$$N_n = N_x l^2 + N_y m^2 + 2N_{xy} lm,\ T_n = N_{xy}\left(l^2 - m^2\right) + \left(N_y - N_x\right) lm,$$

where $l = \cos(n,Ox), m = \cos(n,Oy)$ are directional cosines of the normal vector n to the plate's boundary.

2. Investigation Method

The proposed method reduces solution of a nonlinear problem to a series of auxiliary linear problems. First, we need to determine the subcritical state and solve a linear vibration problem for the loaded plate in the midplane. Detailed description of the solution methods involved in this step as well as several numerical examples can be found in the reference [4]. Once eigenfunctions w_i of a linear vibration problem are determined, they can be utilized in a truncated series to represent the deflection w of the plate:

$$w(x,y,t) = \sum_{i=1}^{n} y_i(t) w_i(x,y). \tag{3}$$

To satisfy the motion equations (1) we propose to present the in-plane displacements as

$$u(x,y,t) = u_1(x,y)p + \sum_{i,j=1}^{n} y_i(t) y_j(t) u_{ij}(x,y),\quad v(x,y,t) = v_1(x,y)p + \sum_{i,j=1}^{n} y_i(t) y_j(t) v_{ij}(x,y). \tag{4}$$

In these expressions functions (u_1, v_1) are solution of system

$$L_{11}u_1 + L_{12}v_1 = 0,$$
$$L_{21}u_1 + L_{22}v_1 = 0,$$

supplemented by the following boundary conditions:

$$N_n^{(L)}(u_1,v_1) = -1,\ T_n^{(L)}(u_1,v_1) = 0,$$

on the loaded part of the domain's boundary $\partial\Omega_1$. Here $N_n^{(L)}$, $T_n^{(L)}$ are linear parts of N_n, T_n :

$$N_n = N_n^{(L)} + N_n^{(N)},\qquad T_n = T_n^{(L)} + T_n^{(N)},$$
$$N_n^{(L)} = \{P\}\cdot\{\varepsilon\}^{(L)},\ N_n^{(N)} = \{P\}\cdot\{\varepsilon\}^{(N)}\ T_n^{(L)} = \{Q\}\{\varepsilon\}^{(L)},\ T_n^{(N)} = \{Q\}\{\varepsilon\}^{(N)}.$$

Vectors $\{P\} = (P_1, P_2, P_3)$ and $\{Q\} = (Q_1, Q_2, Q_3)$ are defined as:

$$P_1 = C_{11}l^2 + C_{12}m^2 + 2C_{16}lm;\ P_2 = C_{12}l^2 + C_{22}m^2 + 2C_{26}lm;$$
$$P_3 = C_{16}l^2 + C_{26}m^2 + 2C_{66}lm;$$
$$Q_1 = C_{11}(l^2 - m^2) + (C_{12} - C_{11})lm;\ Q_2 = C_{26}(l^2 - m^2) + (C_{22} - C_{12})lm;$$
$$Q_3 = C_{66}(l^2 - m^2) + (C_{26} - C_{16})lm.$$

Functions (u_{ij}, v_{ij}) are solutions of the following inhomogeneous system:

$$\begin{aligned} L_{11}(u_{ij})+L_{12}(v_{ij}) &= -Nl_1^{(2)}(w_i, w_j), \\ L_{21}(u_{ij})+L_{22}(v_{ij}) &= -Nl_2^{(2)}(w_i, w_j), \end{aligned} \tag{5}$$

They satisfy the following boundary conditions:

$$N_n^{(L)}(u_{ij}, v_{ij}) = -N_n^{(N)}(w_i, w_j), \quad T_n^{(L)}(u_{ij}, v_{ij}) = -T_n^{(N)}(w_i, w_j). \tag{6}$$

Right hand side of the system (5) depends on the eigenfunctions w_i and can be written as follows:

$$\begin{aligned} Nl_1^{(2)}(w_i^{(c)}, w_j^{(c)}) &= w_{i,x}L_{11}w_j + w_{i,y}L_{12}w_j, \\ Nl_2^{(2)}(w_i^{(c)}, w_j^{(c)}) &= w_{i,x}L_{12}w_j + w_{i,y}L_{22}w_j. \end{aligned}$$

Functions in the right hand side of the boundary conditions (6) are defined as

$$N_n^{(N)}(w_i, w_j) = \frac{1}{2}\left(P_1 \frac{\partial w_i}{\partial x}\frac{\partial w_j}{\partial x} + P_2 \frac{\partial w_i}{\partial y}\frac{\partial w_j}{\partial y} + P_3\left(\frac{\partial w_i}{\partial y}\frac{\partial w_j}{\partial x} + \frac{\partial w_i}{\partial x}\frac{\partial w_j}{\partial y} \right) \right),$$

$$T_n^{(N)}(w_i, w_j) = \frac{1}{2}\left(Q_1 \frac{\partial w_i}{\partial x}\frac{\partial w_j}{\partial x} + Q_2 \frac{\partial w_i}{\partial y}\frac{\partial w_j}{\partial y} + Q_3\left(\frac{\partial w_i}{\partial y}\frac{\partial w_j}{\partial x} + \frac{\partial w_i}{\partial x}\frac{\partial w_j}{\partial y} \right) \right).$$

To determine the functions u_1, v_1, u_{ij}, v_{ij} we will use the R-function method (RFM).

Substituting expressions (3),(4) in equation (2) and applying Bubnov-Galerkin method to the resulting equation, we will obtain a system of ordinary differential equations (ODEs):

$$y_m''(t) + \varepsilon y_m'(t) + \Omega_m^2\left(y_m(t) + p_t \cos\theta t \sum_{k=1}^{n} \alpha_k^{(m)} y_k(t) + \sum_{i=1}^{n}\sum_{j=1}^{n}\sum_{k=1}^{n} \gamma_{ijk}^{(m)} y_i(t) y_j(t) y_k(t) \right) = 0, \tag{7}$$

where $m = \overline{(1,n)}$. The coefficients in this system of ODEs are defined by the formulas:

$$\alpha_k^{(m)} = -\frac{\iint_\Omega Nl_{31}(u_1, v_1, w_k) w_m d\Omega}{m_1 \Omega_m^2 \|w_m\|^2}, \quad \gamma_{ijk}^{(m)} = -\frac{\iint_\Omega Nl_{32}(u_{ij}, v_{ij}, w_k) w_m d\Omega}{m_1 \Omega_m^2 \|w_m\|^2},$$

where

$$Nl_{31}(u_1, v_1, w_k) = N_x^{(L)} \frac{\partial^2 w_k}{\partial x^2} + N_y^{(L)} \frac{\partial^2 w_k}{\partial y^2} + 2N_{xy}^{(L)} \frac{\partial^2 w_k}{\partial x \partial y},$$

$$Nl_{32}(u_{ij}, v_{ij}, w_k) = N_x \frac{\partial^2 w_k}{\partial x^2} + N_y \frac{\partial^2 w_k}{\partial y^2} + 2N_{xy} \frac{\partial^2 w_k}{\partial x \partial y}.$$

Let us consider in detail the one-mode approximation:

$$w(x,y,t) = y(t)\, w_1(x,y)$$

$$u(x,y,t) = p(t)u_1(x,y) + y^2(t)\cdot u_{11}(x,y), \quad v(x,y,t) = p(t)v_1(x,y) + y^2(t)\cdot v_{11}(x,y),$$

In this case the system of equations (7) is reduced to one equation

$$y''(t) + \varepsilon y'(t) + \Omega_L^2 (1 + \alpha p_t \cos\theta t + \gamma\, y^2(t)) y(t) = 0. \tag{8}$$

Equation (8) uses the following notations:

$$y(t)=y_1(t),\ \Omega_L=\Omega_1,\ \alpha=\alpha_1^{(1)},\ \gamma=\gamma_{1\,1\,1}^{(1)}.$$

Equation (8) can be transformed to the known form [3]:

$$y''(t)+2\varepsilon_1 y'(t)+\Omega_L^2((1-2k\cos\theta t)y(t)+\gamma y^3(t))=0, \tag{9}$$

where $\alpha\cdot p_t=-2k,\ \varepsilon_1=\varepsilon/2$.

The main task of investigation of parametric vibrations is finding instability areas and studying behavior of plate after loss of stability. To investigate the stability [3], it is enough to consider the linearized equation ($\gamma=0$): it is well-studied Mathieu equation and its main instability domain is situated near $\theta=2\Omega_L$ and bounded by curves [3]:

$$2\Omega_L\sqrt{1-\sqrt{k^2-\left(\frac{\Delta}{\pi}\right)^2}}\le\theta\le 2\Omega_L\sqrt{1+\sqrt{k^2-\left(\frac{\Delta}{\pi}\right)^2}},$$

where $\Delta=\dfrac{2\pi\varepsilon_1}{\Omega}$. The relation between the frequency ratio and the amplitude of nonlinear vibrations after the loss of stability, according to [3], has the form:

$$A=\frac{2}{\sqrt{3\gamma}}\sqrt{\left(\frac{\theta}{2\Omega_L}\right)^2-1\pm\sqrt{k^2-\left(\frac{\theta}{2\Omega_L}\right)^2\left(\frac{\Delta}{\pi}\right)^2}}.$$

3. Parametric vibrations of a plate with circular cutouts

Now we will use the proposed method to investigate parametric vibrations of a three-layered plate with circular cutouts that is shown in Fig.1. Plate is subjected to a load along the sides parallel to axis *OX*.

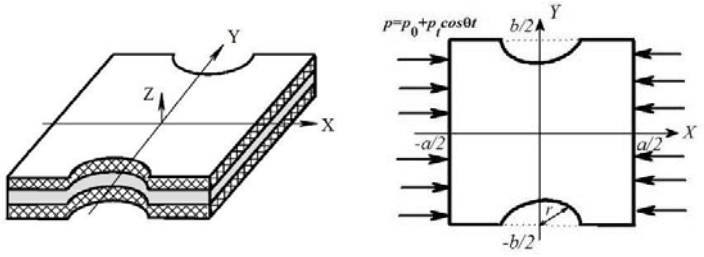

Figure 1

Numerical results are obtained for the following mechanical parameters (glass-epoxy $E_1/E_2=3,\ G/E_2=0.6,\ \nu_1=\nu_2E_1/E_2=0.25$) and geometric parameters ($b/a=1,\ 2r/a=0.5,\ h/a=0.01$). The boundary of the plate is simply supported.

Table 1 presents the values of the frequency and critical load parameters

$$\bar{\lambda}=\Omega_L a^2\sqrt{\frac{12(1-\mu_1\mu_2)}{E_2h^2}},\ \bar{p}_{kr}=a^2p_{kr}/E_2h^3.$$

Table 1. Frequency and critical load parameters

$\bar{p}_{kr}$	$\bar{\lambda}$		
	p_0/p_{kr}		
	0.25	0.5	0.75
9.45	46.68	38.33	27.29

Results of the influence analysis of static load component on the location of the instability domains and amplitude-frequency relations are presented in Fig. 2,3. The load increase results in the shift of domains to lower values of excitation frequency. The value of the static component of load affects the slope of the curves.

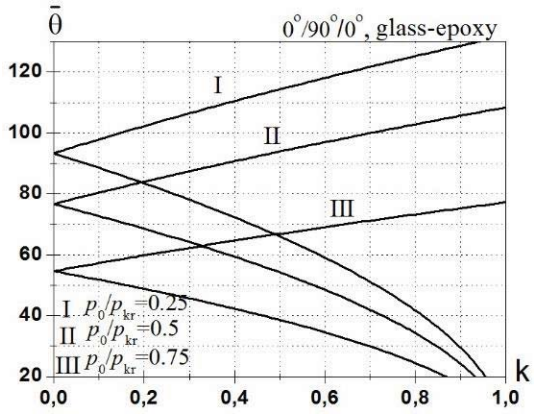

Figure 2

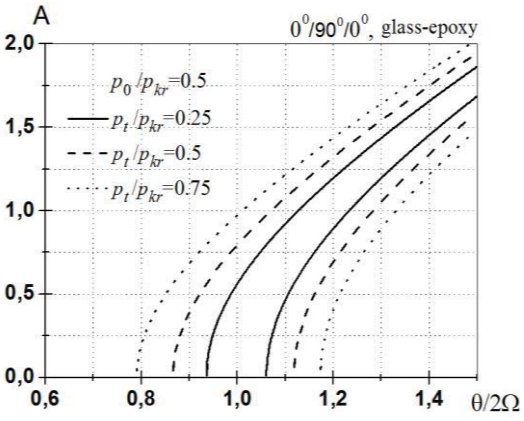

Figure 3

Conclusions

The paper presents an approach for studying the parametric vibrations of the laminated plates with symmetric structure and constant thickness. Applying multi-mode approximation enables investigating the parametric resonances of the plate near $\theta = 2\Omega_i, i = 1,2,..$ and mutual influence of the vibration modes. The method is based on the theory of R-functions, which makes this method useful for plates of complex geometric shape and various boundary conditions.

References

[1] Ambartsumyan S. A. *Theory of Anisotropic Plates: Strength, Stability, & Vibrations,* Taylor & Francis; 2nd edition, 1991.

[2] Awrejcewicz J., Kurpa L., Mazur O. On the parametric vibrations and meshless discretization of orthotropic plates with complex shape*, International Journal of Nonlinear Sciences and Numerical Simulation*, Vol. 11, Is. 5, pp. 371–386, 2010.

[3] Bolotin V.V. *The dynamic stability of elastic systems*, Holden-Day, 1964.

[4] Kurpa L.V. *R-functions Method for Solving Linear Problems of Bending and Vibrations of Shallow Shells*, Kharkiv NTU Press, Kharkiv, 2009.

[5] Sahu S. K., Datta P. K. Dynamic Stability of Laminated Composite Curved Panels with Cutouts*, Journal of Engineering mechanics*, Vol. 129(11), pp. 1245-1253, 2003.

Proceedings of the 4th International Conference on Nonlinear Dynamics
ND-KhPI2013
June 19-22, 2013, Sevastopol, Ukraine

Investigation of Geometrically Nonlinear Vibrations of Laminated Shallow Shells with Layers of Variable Thickness by Meshless Approach

Lidiya Kurpa[1]* ,Tatiana Shmatko[1]

Abstract
Geometrically nonlinear vibrations of laminated shallow shells with layers of variable thickness are studied. Nonlinear equations of motion for shells based on the first order shear deformation and classical shells theories are considered. In order to solve this problem we use the numerically-analytical method proposed in work [1]. Accordingly to this approach the initial problem is reduced to consequences of some linear problems including linear vibrations problem, special elasticity ones and nonlinear system of ordinary differential equations in time. The linear problems are solved by the variational Ritz' method and Bubnov-Galerkin procedure combined with the R-functions theory [2]. To construct the basic functions that satisfy all boundary conditions in case of simply-supported shells we propose new solutions structures. The proposed method is used to solve both test problems and new ones.

Keywords
R-functions method, laminated shallow shells, nonlinear vibration, variable thickness

[1] NTU "KhPI", Kharkiv, Ukraine ,
* **Corresponding author:** kurpa@kpi.kharkov.ua

Introduction

Extensive literature reviews on nonlinear vibrations of plates and open shallow shells have been given by many scientists [1-3]. A huge number of publications is devoted to this issue. But virtually no studies that have investigated multilayer shallow shells with layers of varying thickness. In this paper we attempt to develop an algorithm for solving this class of problems. Proposed algorithm applies meshless discretization. It is based on combination of the classical approaches and modern constructive tools of the R-functions theory [8]. Application of R-functions theory allows studying geometrically nonlinear dynamic response of the laminated shallow shells and plates with complex shape and different boundary conditions. We present also new types of structure formulas that allow to construct appropriate system of basic functions. These basic functions satisfy exactly all boundary conditions.

1. Mathematical Formulation

Laminated shallow shells of an arbitrary plan form with radii of curvature R_x, R_y which consist of M layers of the variable thickness $h_i(x, y)$ are considered. Assume that the plane of $x_1 \mathrm{O} x_2$ coincides with the mid-surface of the shallow shell. The shell theories used in the present

investigation are shear deformable theory (FSDT) and the classical shell theory (CST). According to these theories we assume that the tangent displacements are linear functions of coordinate z and the transverse displacement w is a constant along the thickness of the shell. Let us recall that the CST adopts Kirchhoff's hypothesis. But FSDT is based on hypothesis of straight line. This means that the normal to the mid-surface remains straight line after deformation, but not necessary normal to the mid surface. In the abbreviated form the nonlinear stress strain relations can be written as follows:

$$\{F\}=[A]\cdot\{\varepsilon\} \tag{1}$$

where

$$\{F\}=\{N_{11},N_{22},N_{12},M_{11},M_{22},M_{12},Q_x,Q_y\},\ [A]=\begin{bmatrix}[C] & [K] & 0\\ [K] & [D] & 0\\ 0 & 0 & [S]\end{bmatrix}$$

$$\{\varepsilon\}=\{\varepsilon_{11},\varepsilon_{22},\varepsilon_{12},\chi_{11},\chi_{22},\chi_{12},\varepsilon_{23},\varepsilon_{13}\},\ \varepsilon_{11}=u_{,x}+\frac{w}{R_x}+\frac{1}{2}w_{,x}^2,\ \varepsilon_{22}=v_{,y}+\frac{w}{R_y}+\frac{1}{2}w_{,y}^2$$

$$\varepsilon_{12}=u_{,y}+v_{,x}+w_{,x}\,w_{,y},\ \varepsilon_{13}=\delta\left(w_{,x}+\psi_x-\frac{u}{R_x}\right),\ \varepsilon_{23}=\delta\left(w_{,y}+\psi_y-\frac{v}{R_y}\right),$$

$$\chi_{11}=\delta\psi_{x,x}-(1-\delta)w_{,xx},\ \chi_{22}=\delta\psi_{y,y}-(1-\delta)w_{,yy},\ \chi_{12}=\delta(\psi_{x,y}+\psi_{y,x})-2(1-\delta)w_{,xy}$$

Here u, v and w are the displacements at the mid-surface, ψ_x and ψ_y are the rotations about the y- and x-axes respectively and N, M, Q are the stress, moment and the transverse shear resultants. Matrices $[C]$, $[D]$ and $[K]$ have the following form:

$$[C]=\begin{bmatrix}C_{11} & C_{12} & C_{16}\\ C_{12} & C_{22} & C_{26}\\ C_{16} & C_{26} & C_{66}\end{bmatrix},\ [D]=\begin{bmatrix}D_{11} & D_{12} & D_{16}\\ D_{12} & D_{22} & D_{26}\\ D_{16} & D_{26} & D_{66}\end{bmatrix}$$

$$[S]=\begin{bmatrix}S_{44} & S_{45}\\ S_{54} & S_{55}\end{bmatrix},\ [K]=\begin{bmatrix}K_{11} & K_{12} & K_{16}\\ K_{12} & K_{22} & K_{26}\\ K_{16} & K_{26} & K_{66}\end{bmatrix}$$

Since the laminate consists of a number of variable thickness lamina, the elements of the constitutive matrices $[A]$, $[C]$, $[K]$, $[D]$, $[S]$ are expressed as [2,7]:

$$\begin{aligned}&\left(C_{ij}(x,y),K_{ij}(x,y),D_{ij}(x,y)\right)=\sum_{m=1}^{M}\int_{h_m(x,y)}^{h_{m+1}(x,y)}B_{ij}^{(m)}\left(1,z,z^2\right)dz,\quad (i,j=1,2,6)\\ &S_{ij}(x,y)=k_i^2\sum_{m=1}^{M}\int_{h_m(x,y)}^{h_{m+1}(x,y)}B_{ij}^{(m)}dz,\quad (i,j=4,5)\end{aligned} \tag{2}$$

In the expressions (2) values $B_{ij}^{(m)}$ are stiffness coefficients of the m-th layer; k_i ($i=\overline{4,5}$) are shear correction factors. Further we assume that $k_4=k_5=5/6$, that is $S_{45}=S_{54}$. Indicator δ is the tracing constant which takes values 1 and 0 for the FSDT and CST respectively. It should be noted that problem about nonlinear vibrations of shallow shells with symmetric layers is essentially simple than relative problem for nonsymmetrical layers. This is explained by the fact that factors K_{ij} vanish and matrix A takes the form:

$$[A]=\begin{bmatrix}[C] & 0 & 0\\ 0 & [D] & 0\\ 0 & 0 & [S]\end{bmatrix}$$

In this paper we will only consider symmetric cross-ply and angle-ply laminated shallow shells.

2. Method of solution

We will apply the method proposed in works [7]. According to this approach the first step is study of linear problem in order to find the natural frequencies and eigenfunctions $\{U^{(c)}\}=\{u^{(c)},v^{(c)},w^{(c)},\psi_x^{(c)},\psi_y^{(c)}\}^T$ that satisfy the given boundary conditions. Solution of linear problems for laminated shells with variable thickness we will fulfill by RFM [8]. Note that we will not ignore inertia forces solving linear problem. Since linear vibrations are harmonic ones, then this problem may be reduced to variational problem about finding minimum of the following functional

$$J=\Pi_{\max}-T_{\max} \tag{3}$$

where $\Pi_{\max}$, $T_{\max}$ are strain and kinetic energies relatively. These energies are defined by the following expressions:

$$U_{\max}=\frac{1}{2}\iint\limits_{\Omega}\left[N_{11}\varepsilon_{11}+N_{22}\varepsilon_{22}+N_{12}\varepsilon_{12}+M_{11}\chi_{11}+M_{22}\chi_{22}+M_{12}\chi_{12}+\delta\left(Q_x\varepsilon_{13}+Q_y\varepsilon_{23}\right)\right]d\Omega$$

$$T_{\max}=\frac{\Omega_L^2}{2}\iint\limits_{\Omega}\left(\rho(x,y)\left(h(x,y)\left(u^2+v^2+w^2\right)+\delta\frac{h^3(x,y)}{12}\left(\psi_x^2+\psi_y^2\right)\right)\right)d\Omega$$

In order to find extreme of the functional (3) we will use method by Ritz. The system of basic functions we will build by R-functions theory. That is why first we construct the corresponding solutions structures [6-8], which satisfy the given boundary conditions.

3. Solutions structures for different boundary conditions

Below we present solutions structure for some boundary conditions for case of the classical theory.

Clamped edge. Solution structure is known for this case and may be found in references [6-8]. Solution structures have more bulky form for other boundary conditions. Below we present some of them.

Movable simply supported edge. Let us consider the following boundary conditions:

$$w=0,\quad M_n=0 \tag{4}$$

$$N_n=0,\quad T_n=0 \tag{5}$$

It is possible to prove that the following structures satisfy all boundary conditions (4-5):

$$v=\Phi_2-\omega D_1\Phi_2-\frac{\omega P}{P^2+\omega^2}\left[P_2^{(v)}T_1\Phi_2-P_1^{(v)}T_1\Phi_1\right]$$

$$u=\Phi_1-\omega D_1\Phi_1-\frac{\omega P}{P^2+\omega^2}\left[P_1^{(u)}T_1\Phi_1+P_2^{(u)}T_1\Phi_2\right]$$

$$w=\omega\Phi_3-\frac{\omega^2B_1}{2(B_1^2+\omega^2)}\left(B_1\left(2D_1\Phi_3+\Phi_3D_2\omega\right)+2B_2\left(\Phi_3D_1T_1\omega+T_1\Phi_3\right)+B_3\Phi_3T_2\omega\right)$$

Here

$$P_1^{(u)} = C_2P_3 - C_3P_2,\ P_2^{(u)} = C_4P_3 - C_3P_4$$

$$P_1^{(v)} = P_1C_2 - C_1P_2,\ P_2^{(v)} = C_1P_4 - C_4P_1,\ P = C_1P_3 - C_3P_1$$

$$C_1 = C_{11}(\partial_x\omega)^3 + 3C_{16}(\partial_x\omega)^2(\partial_y\omega) + (C_{12} + 2C_{66})(\partial_x\omega)(\partial_y\omega)^2 + C_{26}(\partial_y\omega)^3$$

$$C_2 = C_{16}(\partial_x\omega)^3 + (2C_{66} - C_{11})(\partial_x\omega)^2(\partial_y\omega) + (C_{26} - 2C_{16})(\partial_x\omega)(\partial_y\omega)^2 - C_{12}(\partial_y\omega)^3$$

$$C_3 = C_{16}(\partial_x\omega)^3 + (C_{12} + 2C_{66})(\partial_x\omega)^2(\partial_y\omega) + 3C_{26}(\partial_x\omega)(\partial_y\omega)^2 + C_{22}(\partial_y\omega)^3$$

$$C_4 = C_{12}(\partial_x\omega)^3 + (2C_{26} - C_{16})(\partial_x\omega)^2(\partial_y\omega) + (C_{12} - 2C_{66})(\partial_x\omega)(\partial_y\omega)^2 - C_{26}(\partial_y\omega)^3$$

$$P_1 = C_{16}(\partial_x\omega)^3 + (C_{11} + C_{66} - C_{12})(\partial_x\omega)^2(\partial_y\omega) - C_{26}(\partial_x\omega)(\partial_y\omega)^2 - C_{66}(\partial_y\omega)^3$$

$$P_2 = C_{66}(\partial_x\omega)^3 - C_{26}(\partial_x\omega)^2(\partial_y\omega) - (C_{11} + C_{66} - C_{12})(\partial_x\omega)(\partial_y\omega)^2 + C_{16}(\partial_y\omega)^3$$

$$P_3 = C_{66}(\partial_x\omega)^3 + C_{16}(\partial_x\omega)^2(\partial_y\omega) + (C_{12} - C_{22} - C_{66})(\partial_x\omega)(\partial_y\omega)^2 - C_{26}(\partial_y\omega)^3$$

$$P_4 = C_{26}(\partial_x\omega)^3 + (C_{12} - C_{22} - C_{66})(\partial_x\omega)^2(\partial_y\omega) - C_{16}(\partial_x\omega)(\partial_x\omega)^2 + C_{66}(\partial_x\omega)^3$$

$$B_1 = -D_{11}(\partial_x\omega)^4 - 4D_{16}(\partial_x\omega)^3(\partial_y\omega) - 2(D_{12} + 2D_{66})(\partial_x\omega)^2(\partial_y\omega)^2 -$$

$$- 4D_{26}(\partial_x\omega)(\partial_y\omega)^3 - D_{22}(\partial_y\omega)^4$$

$$B_2 = -D_{16}(\partial_x\omega)^4 + (D_{11} - D_{12} - 2D_{66})(\partial_x\omega)^3(\partial_y\omega) + 3(D_{16} - D_{26})(\partial_x\omega)^2(\partial_y\omega)^2 +$$

$$+ (D_{12} - D_{22} + 2D_{26})(\partial_x\omega)(\partial_y\omega)^3 + D_{26}(\partial_y\omega)^4$$

$$B_3 = -D_{12}(\partial_x\omega)^4 + 2(D_{16} - D_{26})(\partial_x\omega)^3(\partial_y\omega) - (D_{11} + D_{22} - 4D_{66})(\partial_x\omega)^2(\partial_y\omega)^2 -$$

$$- 2(D_{16} - D_{26})(\partial_x\omega)(\partial_y\omega)^3 - D_{12}(\partial_y\omega)^4$$

The function $\omega(x, y)$ satisfies the following conditions:

$$\omega(x,y) \succ 0, \forall (x,y) \in \Omega, \qquad \omega(x,y)\big|_{\partial\Omega} = 0$$

Hence $\omega(x,y) = 0$ is equation of the domain boundary. To build this function we will apply R-functions theory worked out by V.L.Rvachev [8].

The differential operators $D_m f(x,y), T_m f(x,y)$ are defined as [8]:

$$D_m f(x,y) = (\nabla\omega, \nabla)^m f = \left(\partial_x\omega \cdot \partial_x + \partial_y\omega \cdot \partial_y\right)^m f, \quad T_m f(x,y) = \left(\partial_x\omega \cdot \partial_y - \partial_y\omega \cdot \partial_x\right)^m f$$

Note that boundary condition will be satisfied at any choice of the indefinite components Φ_1, Φ_2, Φ_3.

Immovable simply supported edge. The boundary conditions of the immovable simply supported edge are described as

$$u = 0, \quad v = 0, \quad w = 0, \quad M_n = 0 \tag{6}$$

We can prove that the following structures of solution satisfy boundary conditions (6)

$$u = \omega\Phi_1, \qquad v = \omega\Phi_2,$$

$$w = \omega\Phi_3 - -\frac{\omega^2 B_1}{2(B_1^2 + \omega^2)}\left(B_1\left(2D_1\Phi_3 + \Phi_3 D_2\omega\right) + 2B_2\left(\Phi_3 D_1 T_1\omega + T_1\Phi_3\right) + B_3\Phi_3 T_2\omega\right)$$

In order to obtain the basic functions we will expand the indefinite components in series on some complete system of functions (power or trigonometric polynomial, splines or others).

Like previous case we can obtain appropriate structures for case of the first order of the shear deformable theory.

4. Method of solving nonlinear problem

Let us present unknown functions in the following form:

$$w=\sum_{i=1}^{n} y_i(t) w_i^{(c)}(x,y), \quad \psi_x=\delta\sum_{i=1}^{n} y_i(t)\psi_{xi}^{(c)}(x,y), \quad \psi_y=\delta\sum_{i=1}^{n} y_i(t)\psi_{yi}^{(c)}(x,y)$$

$$u=\sum_{i=1}^{n} y_i(t) u_i^{(c)}(x,y)+\sum_{i=1}^{n}\sum_{j=1}^{n} y_i y_j u_{ij}\ ,\ v=\sum_{i=1}^{n} y_i(t) v_i^{(c)}(x,y)+\sum_{i=1}^{n}\sum_{j=1}^{n} y_i y_j v_{ij} \tag{7}$$

where $y_k(t)$ are unknown functions in time, $w_i^{(c)}(x,y), u_i^{(c)}(x,y),\ v_i^{(c)}(x,y),\ \psi_{xi}^{(c)}(x,y),\ \psi_{yi}^{(c)}(x,y)$ are components of the *i*-th eigenfunctions of linear vibration problem. Functions u_{ij}, v_{ij} must be solutions of the following system [6-7]

$$\begin{cases} L_{11}u_{ij}+L_{12}v_{ij}=-Nl_1^{(2)}(w_i,w_j) \\ L_{21}u_{ij}+L_{22}v_{ij}=-Nl_2^{(2)}(w_i,w_j) \end{cases}$$

Obtained system is solved by RFM. Substituting the expressions (7) for functions u, v, w, ψ_x, ψ_y in initial system of equation of motion and applying procedure by Bubnov-Galerkin we get nonlinear system of ordinary differential equations in unknown functions $y_j(t)$:

$$y_j''(t)+\alpha_j y_j(t)+\sum_{i=1}^{n}\sum_{k=1}^{n}\beta_{jik} y_i(t) y_k(t)+\sum_{i=1}^{n}\sum_{k=1}^{n}\sum_{l=1}^{n}\gamma_{jikl} y_i(t) y_k(t) y_l(t)=\widetilde{F}\ \ \left(j=\overline{1,n}\right) \tag{8}$$

Expressions for coefficients $\alpha_j, \beta_{jik}, \gamma_{jikl}$ are found and expressed through double integrals of known functions. In order to solve the obtained system (8) we will apply method by Runge-Kutta.

5. Numerical results

The developed approach is validated on some tested problems and will be applied to solve new ones.

Problem. Consider three-layers clamped shallow shell with square planform of side *a* and thickness $h=0.01a$. Suppose that the face layers are isotropic, but middle layer is orthotropic with the following mechanical constants:

$$E_1/E_0=0.25,\ E_2/E_0=0.077,\ G_{12}/E_0=0.029,\ \nu_1=0.24.$$

Here E_0 is elastic modulus for isotropic layers, Poisson's ratio for isotropic layers $\nu_0=0.3$ and density of all layers is taken by the same $\rho=\rho_0$. As middle surface we take the plane $z=0$. Assume that thickness of layers varies linearly, but the general thickness is a constant and defined as:

$$\sum_{s=1}^{3} h_s=h.$$

Equations of surfaces which bound the inner layer maybe written as (Fig.1):

$$z=\frac{h}{2}\left(m+\frac{x}{a}(1-2m)\right),\quad z=-\frac{h}{2}\left(m+\frac{x}{a}(1-2m)\right)$$

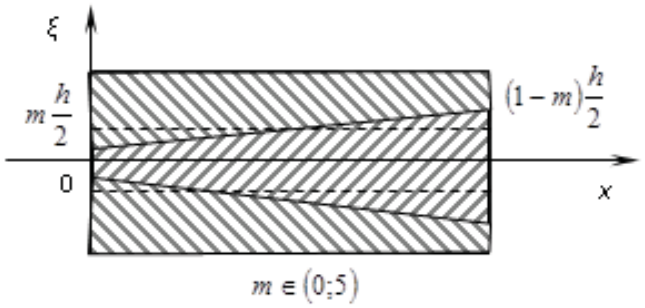

Figure 1. Surface bounding the inner layer

In the given case rigid coefficients are expressed by the following relations:

$$C_{ij}(x,y)=h\left(E_0+(E_1-E_0)\left(m+\frac{x}{a}(1-2m)\right)\right),$$

$$D_{ij}(x,y)=\frac{h^3}{12}\left(E_0+(E_1-E_0)\left(m+\frac{x}{a}(1-2m)\right)^3\right)$$

Table 1. Comparison of the values for three layers square clamped plate

λ_i	Meth.	$m=0$	$m=0.25$	$m=0.5$
λ_1	RFM	0.886	1.023	1.057
	[4]	0.88	1.02	1.06
λ_2	RFM	3.608	4.259	4.369
	[4]	3.60	4.25	4.35
λ_3	RFM	3.781	4.264	4.429
	[4]	3.80	4.26	4.40

The values of non-dimensional frequencies $\lambda_i=\omega_i^2a^2\rho_0/\left(E_oh^2\right),(i=1,2,3)$ obtained by proposed method are presented in the Table 1. In paper [4] the similar results were obtained for plates. Comparison of received results with available confirms the validation of proposed method. In the Tables 2 we present values of non-dimensional frequencies $\lambda_i=\omega_ia^2\sqrt{\rho_0/E_0h^2}$ for cylindrical and spherical shells with square planform.

Table2. Effect of parameter *m* on values of non-dimensional frequencies of the clamped cylindrical and spherical shells

	Cylindrical shells($k_1=0.25$, $k_2=0$)			Spherical shells ($k_1=0.25$, $k_2=0$ .25)		
λ_i	$m=0$	$m=0.25$	$m=0.5$	$m=0$	$m=0.25$	$m=0.5$
λ_1	18.2872	19.527	19.836	24.382	26.836	27.562
λ_2	20.633	22.042	22.392	26.941	28.918	28.992
λ_3	25.275	26.996	27.382	28.023	29.078	29.565
λ_4	30.983	32.813	33.269	34.422	36.524	37.027

The backbone curves were also obtained for clamped and simply supported spherical and cylindrical panels.

6. Conclusion

Numerically-analytical approach for investigation of nonlinear vibration of shallow shells with layers of variable thickness is developed. New solution structures satisfying all boundary conditions corresponding movable and immovable simply supported edge are proposed for shells with symmetrical layers. The present approach has advantage of being suitable for considering different types of the boundary conditions in domains of arbitrary shape.

7. References

[1] Amabili M. *Nonlinear Vibrations and Stability of Shells and Plates*, Cambridge: Cambridge University Press, 2008.
[2] Ambartsumyan S.A. *The general theory of anisotropic shells,* Moscow: Nauka, 1974.
[3] Awrejcewicz J., Kurpa L, Shmatko T. Large amplitude free vibration of orthotropic shallow shells of complex shapes with variable thickness. *Latin American Journal of Solds and Structure* (10): 147-160, 2013.
[4] Budak V.D., Grigorenko A.Ya., Puzyrev S.V. Free Vibrations of Rectangular Orthotropic Shallow Shells with Varying Thickness. *J. Int. Applied Mechanics* 43(6): 670-682, 2007.
[5] Kurpa L., Pilgun G., Amabili M. Nonlinear Vibrations of Shallow Shells with Complex Boundary:R-FunctionsMethod and Experiments. *J. Sound and Vibration* (306): 580-600, 2007.
[6] Kurpa L.V. *R-functions Method for Solving Linear Problems of Bending and Vibrations of Shallow Shells,* Kharkiv: Kharkiv NTU Press, 2009.
[7] Kurpa L.V. Nonlinear Free Vibrations of Multilayer Shallow Shells with a Symmetric Structure and Complicated Form of the Plan. *J. Mathem.Sciences* 162(1): 85-98, 2009.
[8] Rvachev, V.L. *Theory of R-functions and some of its Applications,* Kiev: NaukaDumka, 1982.

Proceedings of the 4th International Conference on Nonlinear Dynamics
ND-KhPI2013
June 19-22, 2013, Sevastopol, Ukraine

Forced Non-resonance Nonlinear Vibrations of Turbine Blades Package with Dynamic Contact in the Shroud

Oleksiy Larin*, Oleksandr Stepchenko

Abstract
The work deals with the investigation of the forced non-resonance vibrations of blades package of steam turbine. The non-linear model of the blades package, with taking into account the contact interaction in the shroud and linearized models have been developed. The package of coupled and free blades is introduced as two linear models. The modeling has been carried out in the framework of the finite element approach. The direct numerical simulation of the nonlinear forced vibration has been carried out. The wobble contact character in the blades shroud has been defined through the simulation of the non-linear vibrations of the blades package. The realization of the harmonics with natural frequencies of the coupled blades and independent blade shows a necessity to take into account both the linear systems spectra at the resonance detuning. In addition the presence of the super- harmonic component at the vibration process has been found. An adequacy of linearized models has also been analyzed.

Keywords
Dynamic contact, steam turbine blades, detachable shroud

National Technical University "Kharkiv Polytechnic Institute", Kharkiv, Ukraine
* **Corresponding author:** AlexeyA.Larin@gmail.com

Introduction

Failures caused by the increased vibrations are widespread at steam turbines operation. The blades assemblies of low-pressure cylinder are the most dynamically loaded elements of the steam turbines. Inter-blades detachable joints are used for blades stiffness magnification. Dynamic and strength characteristics of these designs essentially depend on the contact interacting peculiarities in such bandage [1-5]. Linearized finite-elements models where the contact conditions are replaced by the kinematic constrains are commonly developed for studying the vibrational characteristics in the modern engineering practice [2-8]. Thus, these constrains are applied to the areas which are set a priori [2, 8] or by results of the preliminary static solution of the contact interaction in the bandage under centrifugal forces [3-7]. It should be noted that results obtained on basis of linearized models often have significant difference with experimental data [2 and 8].

The series of reasons may lead to this particular situation.

At first, the blades assembling technology leads to deviations in the inter-blade joints that could be a cause of bladed disk assembly mistuning [5-7].

Secondly, it stands to mention that linearized procedures lead to the inter-blade joints stiffness overestimation. This leads to the development of the augmented linearization procedures as well as on the estimation of the linearized models usage possibilities.

At third, the dynamic changing of the contact in the bandage joints is realised under aerodynamic loading [5, 8, 9]. This has been proved via experimental observations. The wear marking [8], peening, the craters formation and material transfers are found sometimes in detachable joints of blades of the steam turbines low-pressure cylinder and in blades of gas-turbine engines.

Such situations occur at the long term operation of the bladed disk assemblies [10], or, for example, at the work of the turbine under the temperature overloading conditions (fig. 1). Vibrations

of the blades assembly become nonlinear under dynamic contact in the bandage [9-14] and can be accompanied by the great number of the various phenomena.

The work deals with the investigation of the forced non-linear vibrations of blades package of steam turbine, taking into account the contact interaction in the shroud.

1. The Object of the Research

An independent (free) package of two blades of the fourth stage of the low-pressure cylinder of the steam turbine is considered as an object of the research. The model does not represent the real blading because 2 blades without the influence of the neighbouring blades of assembly are observed only.

At the same time the model allows to make some qualitative conclusions about the realised phenomena in case of the non-linear vibrations, and also allows to estimate the degree of conformity of the linearized models and to formulate recommendations for their construction. It should be noted, that a decomposition of the shrouded blading on separate packages is possible as a result of temperature overloading (fig. 1). The model is adequately reflect the situation and has practical value in this special case.

Figure 1. The damaged detachable shrouds of the steam turbine blading after the 3 years of operation (the series of temperature overloading was missed in operation of the turbine)

The blades have a variable cross-section, considerable length (28 inch) and the angle of pre-twisting. They assembled on the package via shroud. The blade tail and disk has been neglected in the investigations. The rigid termination was applied to the root part of blades.

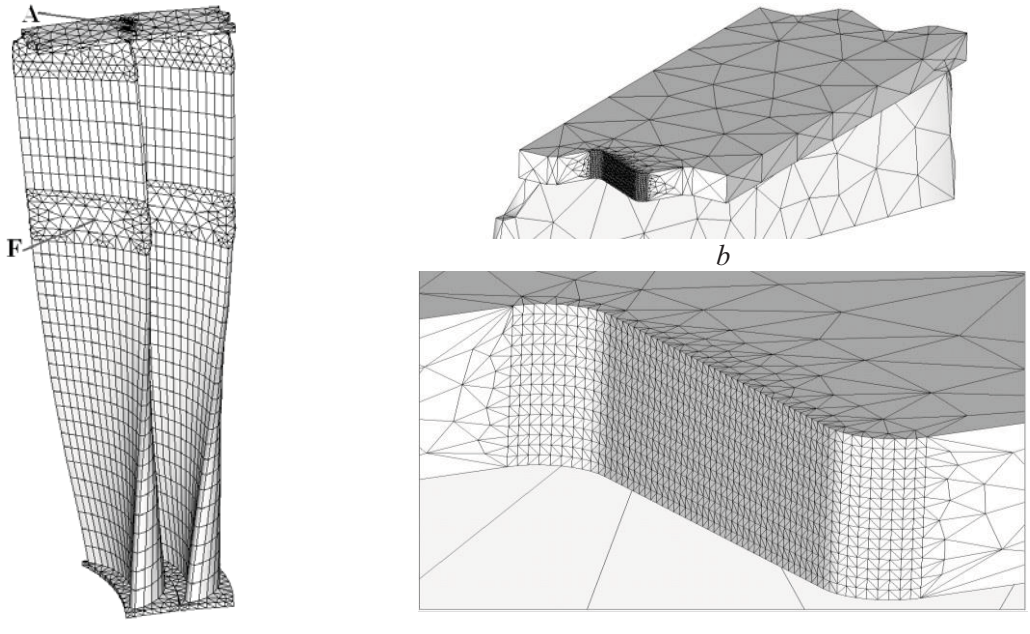

Figure 2. FE mesh of the blades package(*a* – general view, *b* – shroud, *c* - contact zone)

All researches were done on the basis of three-dimensional finite-element (FE) models of the package of two blades (fig. 2a) which has been developed in the commercial CAE software package. Isoparametric eight-node solid FE is used in the mesh. FE mesh of the blades is shown in the Fig.2.

2. Static and Linear Modal Analysis

An important phase of the analysis of system dynamics is the problems of static strength and modal analysis. The static deformation defines a system equilibrium position where vibration processes are observed, and initial stresses are capable of executing the work at the dynamic strains, consequently influencing the design stiffness.

In the work, preliminary the static structural analysis of a design has been carried out under the centrifugal and steam pressure loadings which are applied to the package of blades taking into account contact interaction in the shroud. Contact interaction was considered taking into account the dry friction Coulomb's law. Friction coefficient for the steel was set as 0.15 according to the data from the manufacturing company (OJSC "Turboatom"). The level and spatial distribution of the steam pressure on the blade was set by the manufacturing company.

The procedure of FE geometry updating has been carried out based on the obtained results:

$$\{R\} = \{R_0\} + \{u_{st}\}, \tag{1}$$

where $\{R\}$ is the vector of nodal coordinates of updated FE model, $\{R_0\}$ is the vector of nodal coordinates of initial FE model, $\{u_{st}\}$ is the vector of nodal displacements, defined in the static structural solution.

The updated geometry defines the equilibrium position of system and allows to carry out the analysis of its dynamic behaviour without applying the static loading (the centrifugal force and constant component of steam pressure loading). The pre-stress effect has not been taken into account in the linearized model for the simplification of the computational scheme of nonlinear system. Such assumption is a compulsory measure and, of course, distorts the results.

In addition, the modal analysis of the blades package has been carried out on the basis of the linearized model. Such model has been built basing on the results of static strength analysis. Thus, the total compatibility of displacements constrains have been applied to the nodes of finite elements in the places, where the contact status shows stick character.

The natural frequencies, which were calculated, are shown in the table 1. Single blade natural frequencies also are shown in the table.

Table 1 Natural frequencies

N	Natural frequency (Hz)	
	Single blade	Linearized model of a package from 2 blades
1	68.935	82.425
2	174.06	181.28
3	–	239.95
4	330.08	289.25

It is obvious, that not all the modes can be excited in the forced vibrations. Harmonic analysis has been carried out with the aim of definition of excited modes and their amplitudes in linearized statement. The amplitude of harmonic load (the value was set as 10 % from static pressure according to the data from the manufacturing company OJSC "Turboatom").

Two types of loading: in-phase and out-of-phase have been considered. The damping ratio was set to 0.7% according to recommendations [1]. The computed amplitude to frequency characteristics (AFCh) are shown in the Fig. 3 for the blades package under in-phase and out-of-phase loading. The results are presented in the point on the blades shroud (A) and in the point on the blade feather (F). The amplitude to frequency characteristics for the single blade is also shown in the same figures (blue line). In the graphics the variable U is used for summary displacement.

Only two first natural frequencies are excited at in-phase vibrations of the package and amplitude of vibrations in the shroud (point A) above the amplitude in the blade feather (point F).

The different excitation is observed at out-of-phase vibrations in a package for points A and F: in the shroud (point A) all natural frequencies are excited from a range with similar amplitudes; in the blade feather (point F) first and third natural frequencies are only excited, and amplitude of resonance on third natural frequency is considerably higher.

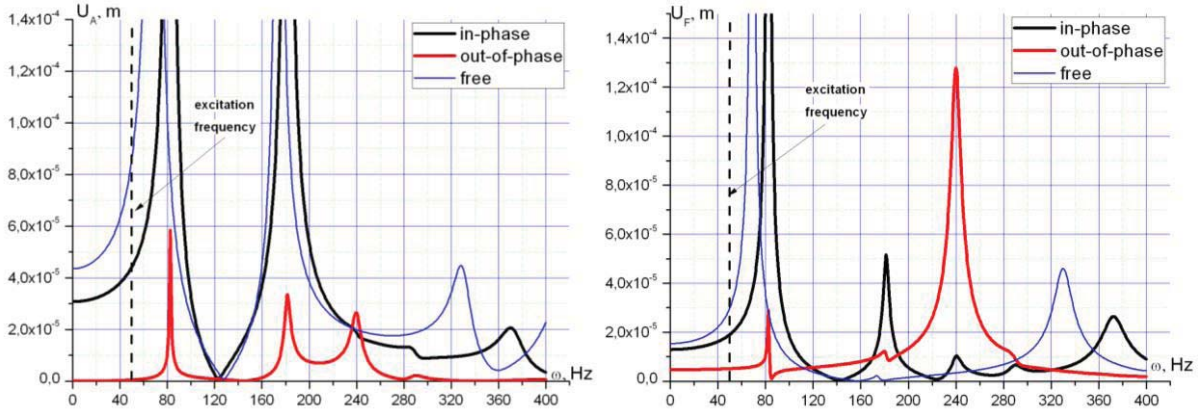

a *b*

Figure 3. AFCh in the points A and F on the shroud (*a*) and leaf (*b*) of the blade

3. A Non-Linear Vibrations Simulation of the Blades Package

Non-linear vibrations have been studied for a blades package under the influence of harmonic loading with the frequency of excitation according to the nominal angular velocity of the turbine rotor (50 Hz). Non-resonance vibrations are only dealt with in the work.

The matrix equation of the nonlinear vibrations of blades package of blades within the FEM framework is:

$$[M]\left\{\frac{d^2u}{dt^2}\right\}+\left([D_l]+\left[D_N\left(\left\{\frac{du}{dt}\right\}\right)\right]\right)\left\{\frac{du}{dt}\right\}+([K_l]+[K_N(\{u\})])\{u\}=\{F_{01}\}\cdot\sin(\omega\cdot t)\,, \qquad (2)$$

where $[M]$ is a matrix of mass, $[D_l],[K_l]$ are linear matrixes of a damping and stiffness, $[D_N],[K_N]$ are matrixes of nonlinear components of the damping and stiffness, which appears due to the contact interacting in the shroud. Contact interaction was considered taking into account the dry friction Coulomb's law. Friction coefficient for the steel was set as 0.15. A direct integration of full system of the differential equations on the basis of Newmark scheme, with the solution of a nonlinear algebraic problem by the Newton-Raphson method on each time step was used for the solution of the problem of non-linear vibrations of blades package. Up to the 70 periods of external loading have been studied through calculations. In the graphics the variable U is used for summary displacement and variable V is used for summary velocity.

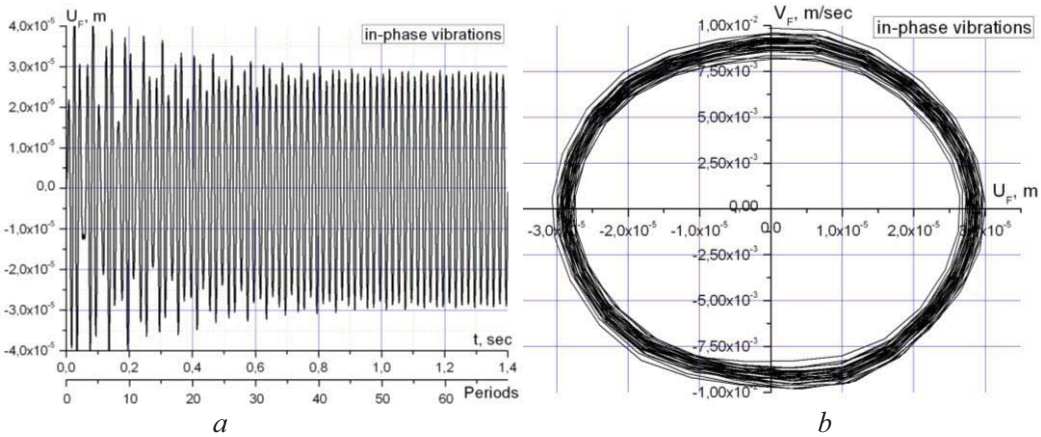

a *b*

Figure 4. Time dependence of displacements in the point F (*a*) and the phase path (*b*)

The results of non-linear vibrations calculations are shown in the Fig. 4 for the point on the blade feather (F) under the in-phase loading. The analysis of time dependencies (fig. 4) shows that non-stationary vibrations become steady approximately after 50 periods of a loading.

Quasi-periodic vibrations are observed in steady regimes. The small harmonic modulation of amplitude is also found in the results. The phase path has not elliptic character. It represents the combination of two ellipses with different curvatures. Such phase paths is the result of non-linearity realisation and are common for the system with gaps. This can account for the periodic contact opening in the shroud during vibrations.

Five points in the shroud contact zone have been monitored aiming at the contact interaction monitoring at the forced vibrations. The points are marked in the Fig. 5.

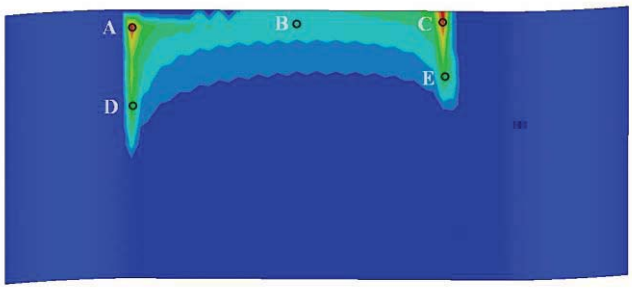

Figure 5. The points under control in the contact zone

The analysis has shown that the contact is observed only near the points A and C. Synchronous periodic breakings of contact in both points (fig. 6) occurred during vibrations. Time dependencies of displacements in the point A and of contact pressures in the points A and C are presented in the Fig. 6. Amplitudes of contact displacements and pressures have a harmonic modulation as well. In the graphics the variable *P* is used for normal contact pressure.

The spectral analysis (fast Fourier transformation) of received time dependencies has been done aiming at a deeper analysis of the results. Spectral characteristics of vibrational process in point F are shown in Fig. 7. The non-steady process (within the time range of up to 50 periods of influence) and steady process (within the time range from 50 to 70 periods of influence) have been separately studied basing on their spectral characteristics.

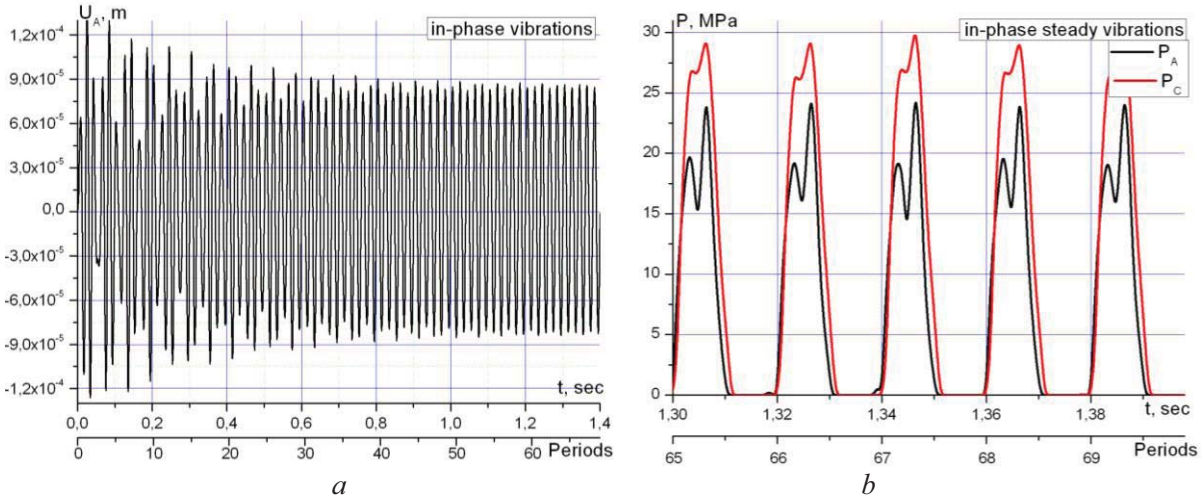

a *b*

Figure 6. Time dependences of displacements (*a*) and contact pressure (*b*) in the points A and C

The spectrum of non-steady vibrations (Fig. 7,*b*) shows that the natural frequencies of single blade are strongly excited together with the frequency of loading. It is necessary to note, that a two-fold harmonic of the excitation (super- harmonic) is also found in the spectrum. The presence of the super- harmonic represents the fundamental phenomena of nonlinearity.

Comparison with the spectrum of the steady vibrations (Fig. 7,*a*) shows the decay of the natural frequencies accompanying vibrations at the initial period of time. The presence of the super- harmonic in vibrations defines its amplitude modulation. The amplitude of a super- harmonic is less than 1%

from amplitude of basic harmonic. The small equilibrium position shifting is also possible to note in the results.

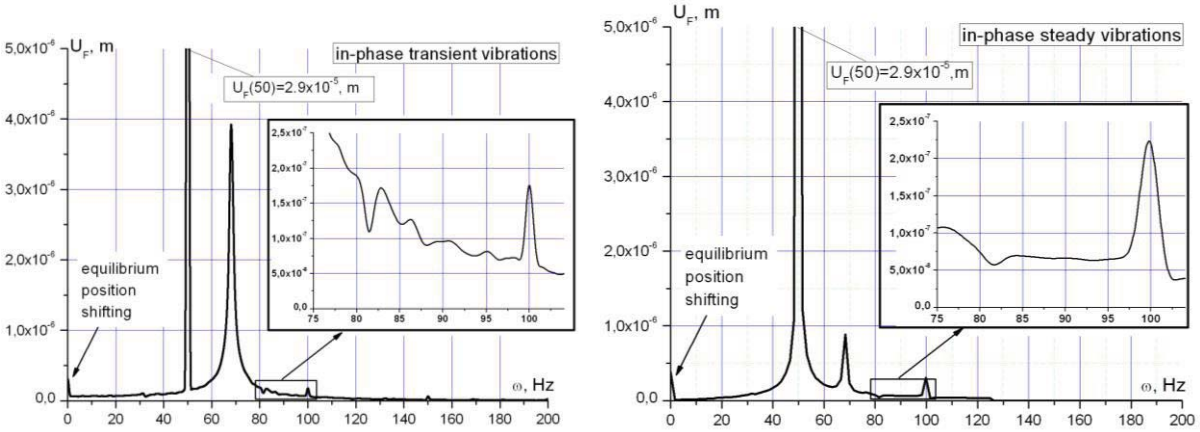

a *b*

Figure 7. Spectral characteristics of non-steady (*a*) and steady (*b*) vibrations in the point F

Thus, quasi-harmonic steady motions are observed at the in-phase loading. The maximum amplitude of the nonlinear steady vibrations of the package is more than 30% higher than the corresponding amplitude of linearized package (Fig. 3). This is because at the nonlinear vibrations the motions are accompanied by the periodic opening of shroud contact and the blades become independent. Therefore, the amplitude of the nonlinear steady vibrations of the package is close to the amplitude of free blades forced vibrations (less than 4%).

Analogous researches have been carried out at the out-of-phase loading. Results of these investigations are shown in the Figures 8 and 9. The analysis of time dependencies (fig. 8) shows that non-stationary vibrations become steady approximately after 15 periods of loading. Quasi-periodic vibrations are observed in steady regimes, as well as in the motions under in-phase loading.

Essential difference from the previous case is observed in the contact behaviour in the shroud. So, during the vibrations occurring under out-of-phase loading a nonsynchronous periodic contact opening in the points A and C is observed (Fig. 8). Thus, the point C is involved into the contact after the point A has got out of the contact. The wobble motion of the blades shroud cog relative to the next blade shroud cavity has been observed. The maximum value of contact pressure is higher than in the vibrations under the in-phase loading.

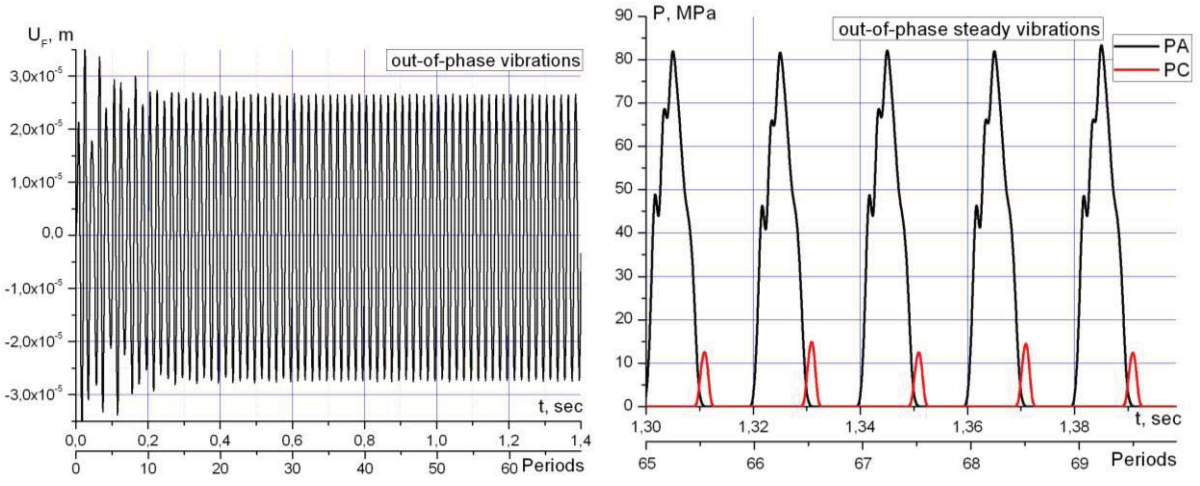

a *b*

Figure 8. Time dependences of displacements (*a*) and contact pressure (*b*) in the points A and C

Phase paths (Fig. 9) show the great irregularity of process of vibrations at the period of loading. Phase paths in the points A and F are very different.

The spectral analysis for all time dependencies has been done. The non-steady process and steady process have been separately tested for their spectral characteristics. The spectrum of non-

steady vibrations (Fig. 10) shows that the frequencies near the natural frequency of single blade and the super- harmonic are strongly excited together with the frequency of loading.

The basic and super- harmonics appears at the steady vibrations (fig. 10,*b*). The amplitude of a super- harmonic is about 4% of the amplitude of basic harmonic in the nonlinear vibrations under out-of-phase loading. The slight equilibrium position shift is also to be noted in the results

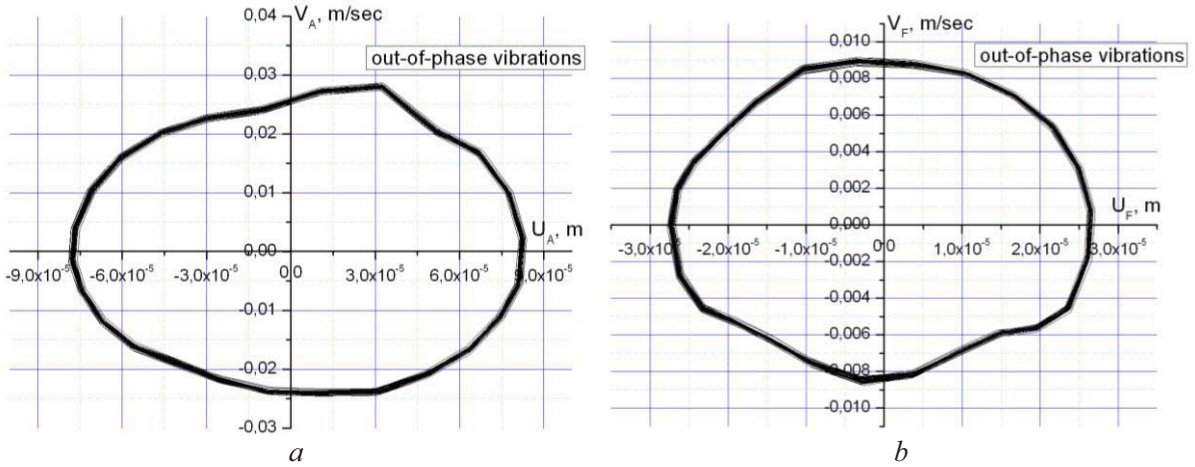

a *b*

Figure 9. Phase paths in a point A (*a*) and in point F (*b*)

Thus, quasi-harmonic steady motions are also observed at the out-of-phase loading.

The complex motions of the shroud occur at the nonlinear vibrations. The wobble contact appears between the edge points of shroud cog. Such kinematics is poorly described by the developed linearized models. The maximum amplitude of the nonlinear steady vibrations of the package is more than 20% higher than the matching amplitude of linearized package and more than 10% less than the matching amplitude of single blade vibrations (fig. 3, at the excitation frequency, 50 Hz).

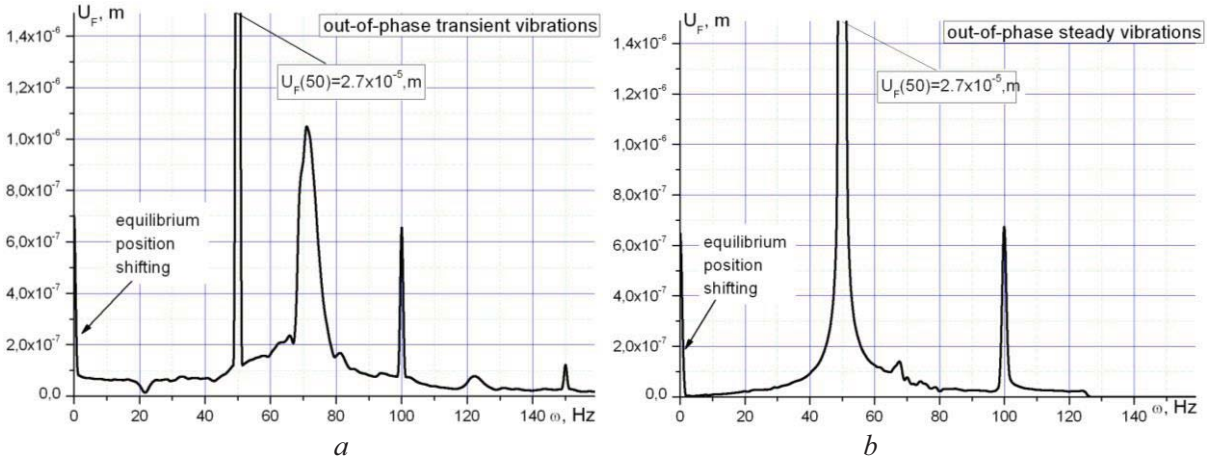

a *b*

Figure 10. Spectral characteristics of non-steady (*a*) and steady (*b*) vibrations in the point F

To kinematics peculiarities of the contact interaction at the vibrations under out-of-phase loading allow to offer another procedure of linearization. So, a linearization by constraining of the normal displacements in the point between the points A and C allows to realise the degree of freedom for the shroud twisting and will be more realistic for the description of the features of contact natures.

Conclusions

The wobble contact character between the points A and C of the blade shrouds cog has been defined through the simulation of the non-linear vibrations of the blades package.

The realization of the harmonics with natural frequencies of the coupled blades and independent blade shows the necessity to take into account both of the linear systems spectra at the resonance detuning. The super- harmonious component presence at vibration process, despite its

small-scale amplitude accounts for the possibility of the complex resonance regimes (super- and combines resonances). The linearized mode with rigid kinematic constrains in the shroud provides essentially underrated values of amplitudes of forced vibrations.

References

[1] Rao J.S., Peraiah K.Ch., Singh U.K. Estimation of Dynamic Stresses in Last Stage Steam Turbine Blades under Reverse Flow Conditions, *Advances in Vibration Engineering, J. Vib. Inst. India,* 8 (1), pp. 71-81, 2009

[2] Kaneko Y., Ohyama H. Analysis and measurements of damping characteristics of integral shroud blade for steam turbine, *Journal of System Design and Dynamics*, 2(1), pp. 311–322, 2008

[3] Stepchenko A.S., Larin A.A., Artomov S.L. An investigation of the dynamic characteristics of the blades assembly with double-leveled detachable bandaging, *Bulletin of the National Technical University "KhPI"*, Seria: Dynamics and Strength of Machines, Vol. 48, pp. 3-14, 2010 (in Russian)

[4] I. Fedorov, J. Szwedowicz, W. Kappis, I. Putchkov Reliable FE Modeling of Chord-Wise Blade Modes in Compressor Design Process, *Proceedings of the ASME Turbo Expo 2010, June 14-18, 2010, Glasgow, UK*, GT2010-22619, pp. 12, 2010

[5] Zhovdak V.A., Larin A.A., Stepchenko A.S., Demuz Ya.D., Solyannikiva Yu.V. An investigation of dynamic contact interaction in inter-bandage conjunctions of steam turbines blades packages *The Problems of the Computational Mechanic and Strength of Constructions*, Vol. 11, Dnipropetrovsk National University, pp. 53-62, 2007 (in Russian)

[6] Zhovdak V.A., Kabanov A.F., Larin A.A Statistical dynamics of turbomachine rotor wheels with a technological mistuning, *Strength of Materials*, 40(5), pp. 577-583, 2008

[7] Larin O.O. Forced vibrations of bladings with the random technological mistuning, *Proceedings of the ASME Turbo Expo 2010, June 14-18, 2010, Glasgow, UK*, GT2010-23099, pp. 667-672, 2010

[8] Kaneko Y., Tomii M., Ohyama H., Kurimura T. Analysis of Fretting Fatigue Strength of Internal Shroud Blade for Steam Turbine, *Journal of Power and Energy Systems*, 2(3), pp. 909–920, 2008

[9] Petrov E.P. A high-accuracy model reduction for analysis of nonlinear vibrations in structures with contact interfaces, *Proceedings of the ASME Turbo Expo 2010, June 14-18, 2010, Glasgow, UK*, GT2010-23295, pp. 13 2010

[10] V. Ya. Krivoshei, N. I. Glushchenko and S.S. Tripol'skii Effect of design factors on the life of shroud flanges of turbine rotors*, Strength of Materials*, 19(8) pp. 1110-1115, 1987

[11] Petrov E.P., Ewins, D.J. Analitical Formulation of Friction Interface Elements for Analysis of Nonlinear Multi-Harmonic Vibrations of Bladed Disks *Trans. of the ASME*, 125, pp. 364-371, 2003

[12] Ender Cigeroglu, H. Nevzat Ozguven Nonlinear vibration analysis of bladed disks with dry friction dampers, *Journal of Sound and Vibration*, 295, pp.1028-1043, 2006

[13] Ender Cigeroglu, Ning An, Chia-Hsiang Menq Forced Response Prediction of Constrained and Unconstrained Structures Coupled Through Frictional Contacts, *Journal of Engineering for Gas Turbines and Power*, 131, pp. 11, 2009

[14] Yang B.D., Menq C.H. Modeling of Friction Contact and Its Application to the Design of Shroud Contact, *Journal of Engineering for Gas Turbines and Power*, 119, pp. 958-963, 1997

Proceedings of the 4th International Conference on Nonlinear Dynamics
ND-KhPI2013
June 19-22, 2013, Sevastopol, Ukraine

Numerical Prediction of the Vibratory Response of Mechanical Systems Undergoing Unilateral Contact Conditions

Mathias Legrand[1]*, Christophe Pierre[2]

Abstract
The Harmonic Balance Method based on Fourier expansion is a common formulation to efficiently obtain the vibratory response of a mechanical structure. In the context of nonsmooth dynamics involving unilateral contact conditions, wavelet bases may be superior. This assumption is explored by means of an axially vibrating rod undergoing regularized inequality constraints on one tip. The introduced distributional formulation in time makes use of weak derivatives to efficiently capture the possible nonsmoothness and discontinuity possibly exibited by the displacement, velocity, and acceleration fields. The mixed wavelet Petrov-Galerkin solutions are found to yield better results than HBM.

Keywords
wavelet analysis, Petrov-Galerkin method, weak formulation, unilateral contact conditions, nonsmooth dynamics

[1]Assistant Professor, Department of Mechanical Engineering, McGill University, Macdonald Engineering Building, Room 270, 817 Sherbrooke Street West Montreal, QC H3A 0C3, Canada
[2]Professor, Department of Mechanical Science and Engineering, University of Illinois at Urbana-Champaign, Mechanical Engineering Building, 1206 W. Green St., Urbana, IL 61801, USA
*__Corresponding author__: mathias.legrand@mcgill.ca

Introduction

Efficiently predicting the vibratory responses of flexible structures which experience unilateral contact is becoming of high engineering importance where light materials and thin designs involving larger displacements together with tighter operating clearances between components are becoming common. In the time domain, structural displacements and velocities which satisfy these non-penetration Signorini conditions are known to respectively feature absolute continuity and bounded variation only [1]. This implies displacements are not necessarily differentiable everywhere in the defined domain and velocities may exhibit jumps; these types of problems are generally referred to as nonsmooth.

It is proposed to approach this class of unilateral problems in the framework of vibration theory. The original initial-value formulations are transformed into partial differential equations periodic in time [2]. They are subsequently solved through a weighted residual technique. This method involves approximating the solution using a set of time-dependent basis functions and enforcing the respective residual error to be orthogonal to a set of independent functions. The periodicity conditions satisfied by the targeted vibratory behavior are exactly enforced while the remaining unilateral contact constraints and governing local equations of motion are satisfied in a weak integral sense [3, 4]. The main goal of the current work is to explore relevant basis functions whose order of smoothness can be adapted to a particular system to attain accurate approximations and rapid convergence.

1. System of Interest

A schematic of a simple unilateral contact system showing a one-dimensional bar clamped on the left is depicted in Fig. 1. A gap g exists between the tip and a rigid foundation. When the tip displacement is sufficiently large, the bar comes into contact with the rigid foundation and unilateral contact conditions are activated. The existence of periodic solutions of period T are assumed where T is the period of

the external forcing $f(x,t)$ acting on the bar. The unknown displacement has to satisfy the following complementary boundary value problem:

1. local equation of motion

$$\rho S\ddot{u}(x,t) + ESu_{,xx}(x,t) = f(x,t), \quad \forall x \in]0,\ell[, \quad \forall t \tag{1}$$

2. conditions of periodicity in time

$$u(x,t+T) = u(x,t) \quad \text{and} \quad \dot{u}(x,t+T) = \dot{u}(x,t), \quad \forall x \in [0,\ell], \quad \forall t \tag{2}$$

3. boundary condition in displacement

$$u(0,t) = 0, \quad \forall t \tag{3}$$

4. unilateral contact conditions

$$g - u(\ell,t) \geq 0 \quad ; \quad \lambda(t) \geq 0 \quad ; \quad \lambda(t) \cdot \big(g - u(\ell,t)\big) = 0, \quad \forall t. \tag{4}$$

Here ρ signifies density, S cross-sectional area, and E elastic modulus. The dot superscript represents a temporal derivative, whereas the subscript x represents a spatial derivative. The periodicity conditions result in a final formulation derived on a circle in time. Without loss of generality, the basis functions are taken from an $L^2(\mathbb{S}^1)^N$ Hilbert space [5].

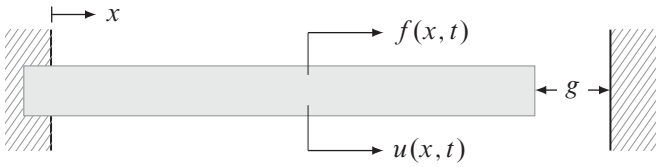

Figure 1. One-dimensional linear bar undergoing unilateral contact conditions

The quantity $\lambda(t)$, that mechanically is a contact force, stems from the enforced non-penetration condition $g - u(\ell,t) \geq 0$ and is necessarily positive. The complementarity condition $\lambda(t) \cdot \big(g - u(\ell,t)\big) = 0$ states that the contact force $\lambda(t)$ and the distance $g - u(\ell,t)$ separating the rod's end-tip from the rigid foundation may not be zero at the same time. These three conditions are such that the mathematical object pairing the contact force to the displacement is not a function in the usual sense. This motivates the derivation of numerical techniques capable of efficiently handling functional nonsmoothness. As a first approach, the unilateral contact inequalities (4) are replaced by a penalty function of the form:

$$f_{\mathrm{c}}(u(\ell,t)) = \max\big(a_{\mathrm{c}}(\mathrm{e}^{\alpha(u(\ell,t)-g_0)} - 1), 0\big). \tag{5}$$

to approximate the contact forces.

2. Weighted Residual Formulations in Time

The method of weighted residuals is a classic method of obtaining numerical solutions to boundary value problems by expanding the sought solution as a finite sequence of basis functions, also known as *trial functions* in a proper functional space. The subsequent residual is rendered orthogonal to a set a linearly independent functions of the same space, referred to as *weighting functions*. The Petrov-Galerkin suggests the selection of two independent bases in the construction of weighting and trial functions. The functional space into which the solution is sought is such that the boundary conditions in space and time are satisfied. To solve Eqs. (1), (2), (3), and (4), the unknown displacement is expanded into a truncated series of N functions separated in space and time:

$$u(x,t) = \sum_{i=1}^{N} \vartheta(x) u_i(t) \tag{6}$$

The standard Finite Element Method is implemented for the spatial variable using two-node linear rod elements [6]. This yields the following vector ordinary differential equation of size N:

$$\mathbf{M}\ddot{\mathbf{u}}(t) + \mathbf{C}\dot{\mathbf{u}}(t) + \mathbf{K}\mathbf{u}(t) = \mathbf{f}_{\mathrm{ext}}(\mathbf{u}(t),t) \tag{7}$$

together with the remaining periodicity conditions in time and the unilateral contact condition. Condition (3) is also enforced. Here $\mathbf{M}$ and $\mathbf{K}$ are the standard mass and stiffness matrices for a rod, and β-damping is enforced such that $\mathbf{C} = \beta\mathbf{K}$ to account for structural damping. The displacement vector $\mathbf{u}(t)$ in Eq. (7) stores the temporal unknowns $u_i(t)$, $i = 1,\dots,N$, where N is the number of spatial degrees-of-freedom. Similarly, $\mathbf{f}_{\text{ext}}(\mathbf{u}(t),t)$ stores the external forcing functions for each degree-of-freedom as well as the contact forces stemming from Eq. (5).

2.1 Strong integral form

The standard weighted residual formulation of a differential equation is commonly termed the strong form. Taking the inner product of Eq. (7) with a weighting function stored column-wise in $\mathbf{v}$ results in the strong integral form of the equation: find $\mathbf{u} \in H^2(\mathbb{S}^1)^N$ such that

$$\forall \mathbf{v} \in L^2(\mathbb{S}^1)^N, \quad \int_{\mathbb{S}^1} \left(\mathbf{v}^T\mathbf{M}\ddot{\mathbf{u}} + \mathbf{v}^T\mathbf{C}\dot{\mathbf{u}} + \mathbf{v}^T\mathbf{K}\mathbf{u} - \mathbf{v}^T\mathbf{f}_{\text{ext}}(\mathbf{u},t)\right) \mathrm{d}t = 0 \tag{8}$$

and the superscript T denotes a transpose. This strong form of the equation is not the best framework for obtaining a solution [6]; for this example, the solution must be at least H^2, limiting the permissible basis of trial functions.

2.2 Weak form

The respective weak form of the weighted residual statement can be obtained by performing one integration by parts over the domain $\mathbb{S}^1$ for all terms containing a double time derivative in Eq. (8). This results in: find $\mathbf{u} \in H^1(\mathbb{S}^1)^N$ such that

$$\forall \mathbf{v} \in H^1(\mathbb{S}^1)^N, \quad \int_{\mathbb{S}^1} \left(-\dot{\mathbf{v}}^T\mathbf{M}\dot{\mathbf{u}} + \mathbf{v}^T\mathbf{C}\dot{\mathbf{u}} + \mathbf{v}^T\mathbf{K}\mathbf{u} - \mathbf{v}^T\mathbf{f}_{\text{ext}}(\mathbf{u},t)\right) \mathrm{d}t = 0 \tag{9}$$

The integral form of the weak formulation offers the advantage of shifting a portion of the functional smoothness requirement from the trial functions onto the weighting functions. This allows the trial functions to be chosen from a wider permissible space [6].

2.3 Formulation in a distributional sense

A weaker formulation is proposed by integrating again the terms involving time derivatives of the trial functions. This formulation can be understood in the sense of distributions, also known as generalized functions, *ie*: find $\mathbf{u} \in L^2(\mathbb{S}^1)^N$ such that

$$\forall \mathbf{v} \in H^2(\mathbb{S}^1)^N, \quad \int_{\mathbb{S}^1} \left(\ddot{\mathbf{v}}^T\mathbf{M}\mathbf{u} - \dot{\mathbf{v}}^T\mathbf{C}\mathbf{u} + \mathbf{v}^T\mathbf{K}\mathbf{u} - \mathbf{v}^T\mathbf{f}_{\text{ext}}(\mathbf{u},t)\right) \mathrm{d}t = 0 \tag{10}$$

Here the double time differential on the field variable is transferred to the weighting function and the continuity requirement on the trial function is reduced. As discussed later, the desired displacement functions $\mathbf{u}$ can now be described using a series of constant piecewise functions for instance. Each of the strong, weak, and distributional formulations can now be discretized with proper basis functions.

3. Trial and weighting function bases

The selection of functional bases to be used in the above approaches is an important factor in approximation accuracy and computational efficiency [6]. In the current investigation two bases are investigated to compare the quality of approximation: Daubechies and Haar wavelets.

3.1 Discrete orthogonal wavelets

Discrete orthogonal wavelet families are composed of highly localized, oscillatory functions which provide a basis of $L^2(\mathbb{R})$ and can be adapted to the periodic domain $L^2(\mathbb{S}^1)$ [7]. These localized characteristics allow sparse representation of piecewise signals including transients and singularities. This makes them useful functions for use in the Galerkin approach when nonsmooth solutions are predicted [8]. Galerkin methods using appropriate discrete wavelet families as the trial functions have been shown to accurately approximate the solutions to differential equations [9]. The discrete wavelet family is built

from scaling functions $\phi(t)$ and wavelet functions $\psi(t)$ and the decomposition of a continuous time signal $y(t)$ can be written as:

$$y(t) = \sum_k g_k \phi_{J,k}(t) + \sum_{j=J}^{m} \sum_{\ell} h_{j,\ell} \psi_{j,\ell}(t) \tag{11}$$

with $\phi_{J,k}(t) = 2^{J/2}\phi(2^J t - k)$ and $\psi_{J,k}(t) = 2^{J/2}\psi(2^J t - k)$ where $J,k \in \mathbb{Z}$; J is the dilation parameter, k is the translation parameter, and m is the maximum resolution given by the sampling rate of the function $y(t)$. Standard wavelet definitions are commonly built on the real line. The functions can be adapted to periodic functions of $L^2(\mathbb{S}^1)$ by utilizing a standard periodization technique [10]. Let $\phi^{(p)}(t)$ be the periodized form of the scaling function $\phi(t)$ defined on $\mathbb{R}$

$$\phi_{J,k}^{(p)}(t) = \sum_{\ell \in \mathbb{Z}} \phi_{J,k}(t - \ell) \qquad 0 \leq k \leq 2^J - 1. \tag{12}$$

A number of periodic discrete wavelet families exist [7]. The investigation considers two families to determine how they perform in unilateral, nonsmooth contact problems: Daubechies and Haar.

3.2 Daubechies wavelets

The Daubechies wavelet family is defined by a set of L filter coefficients $\{p_\ell : \ell = 0, 1, \ldots, L-1\}$, where L is an even integer. The scaling function is defined by the fundamental two-scale equation [11]:

$$\phi(t) = \sum_{\ell=0}^{L-1} p_\ell \, \phi(2t - \ell) \tag{13}$$

which has support over the finite intervals $[0, L-1]$. This equation can be used to determine the value of the scaling function at dyadic points $t = n/2^J$, $n = 0, 1, \ldots$ [11]. The corresponding scaling functions are highly nonsmooth and fractal in nature. When Daubechies scaling functions are used in a Galerkin

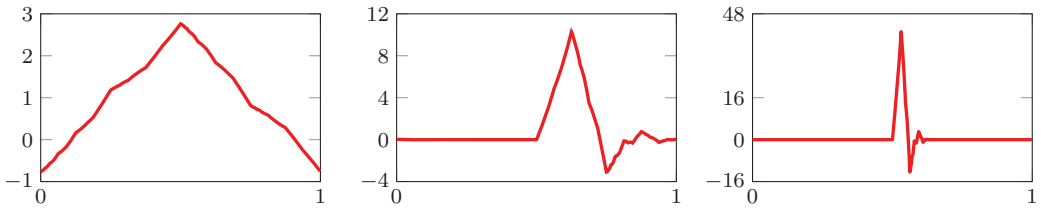

(a) $\phi_{1,1}$ (b) $\phi_{3,5}$ (c) $\phi_{5,17}$

Figure 2. Examples of periodized 6-coefficient Daubechies scaling functions (DB6)

approach, it is necessary to derive the inner products of the scaling function with itself or derivatives of itself. The exact solution to these inner products can be found by using the recursive nature of the fundamental equation on $L^2(\mathbb{R})$ [11]. Fig. 2 provides examples of the 1-periodized scaling functions.

3.3 Haar scaling functions

The simplest Daubechies wavelet family requires only two filter coefficients ($p_0 = p_1 = 1$) and is commonly known as the Haar wavelet family. The Haar scaling functions are rectangular tophat-type functions. Since the compact support of the father scaling function is $\mathbb{S}^1$, the periodized function is equivalent. Examples of normalized Haar scaling functions are shown in Fig. 3.

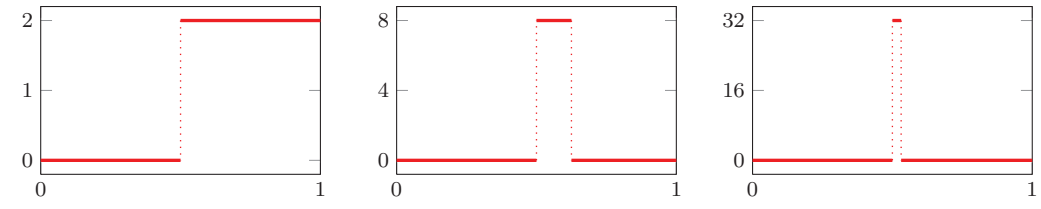

(a) $\phi_{1,1}$ (b) $\phi_{3,5}$ (c) $\phi_{5,17}$

Figure 3. Examples of periodized Haar scaling functions

4. Results

To act as a comparison solution, the unilateral contact finite-element equations detailed above are solved using a variable-order numerical differentiation formula time-stepping algorithm. It is indicated as a gray line in the coming figures. Three combinations of functions are employed to solve the nonlinear weighted residual formulation: Fourier:Fourier (HBM), Daubechies 6:Daubechies 6, and Haar:Fourier.

4.1 Tip displacement

Samples of the approximate tip displacement responses at 150 Hz using 64 basis functions are provided in Fig. 4. For this number of basis functions, HBM (Fourier:Fourier) as well as DB6:DB6 approximate

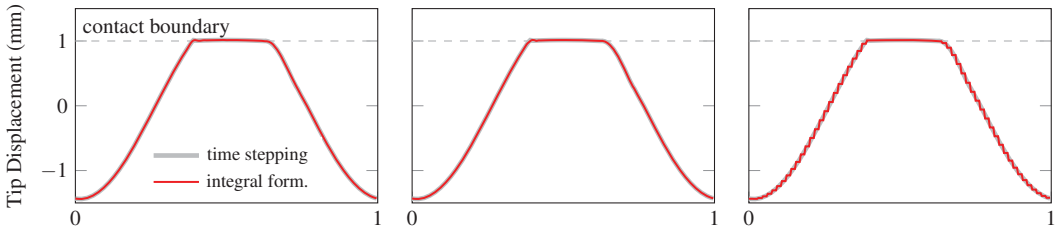

(a) Fourier:Fourier (b) DB6:DB6 (c) Haar:Fourier

Figure 4. Tip displacement versus normalized time t for Case 1

the tip displacements well compared to the time-stepping solution. However, close examination of the contact plateau for the 150 Hz case shows oscillations due to Gibbs phenomenon and rounding off of the sharp gradient changes. Alternatively, the Haar:Fourier combination appears to approximate the tip displacement outside the contact zone less well due to the blocky nature of the Haar scaling functions. However, the contact plateau is well represented by the constant Haar scaling functions.

4.2 Tip velocity

When the trial basis functions are sufficiently smooth, they are differentiated pointwise with respect to time to approximate velocities. Haar trial functions are piecewise constant functions and cannot be directly differentiated in the usual pointwise sense. Instead, their weak expression is used.

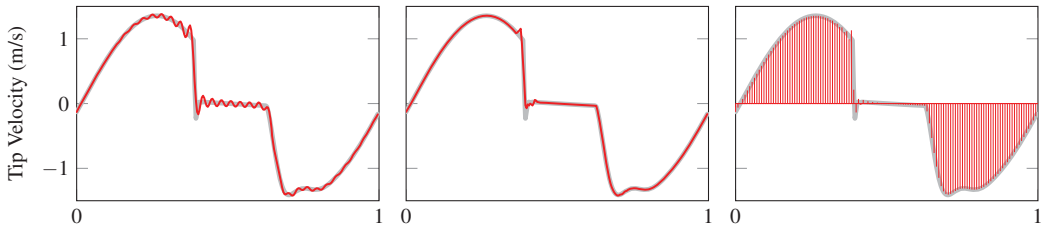

(a) Fourier:Fourier (b) DB6:DB6 (c) Haar:Fourier

Figure 5. Tip velocity versus normalized time t

The approximate tip velocity response at 150 Hz is plotted in Fig. 5. It is visible from these approximations that there is a sharp jump in velocity due to the contact condition. As expected, this results in ringing due to Gibbs phenomenon when the Fourier trial functions are used. The DB6 trial functions appear to do the best job of approximating the tip response. This is attributed to the compact support of the scaling functions allowing accurate representation of rapid changes in gradient. For Haar trial functions, the velocity function envelope is reasonably approximated by the weak representation.

4.3 Tip contact force

The tip contact force is calculated using the penalty function provided in Eq. (5) in conjunction with the predicted tip displacement and presented in Fig. 6. The effect of Gibbs phenomenon can be seen in the HBM. The cases where Haar trial functions are used approximate the contact force well. It is hypothesized that when a rigid contact law is enforced the Haar scaling functions will perform even better relative to the other functions. Again, the DB6 trial functions appear to most accurately approximate the contact forces compared to the other cases.

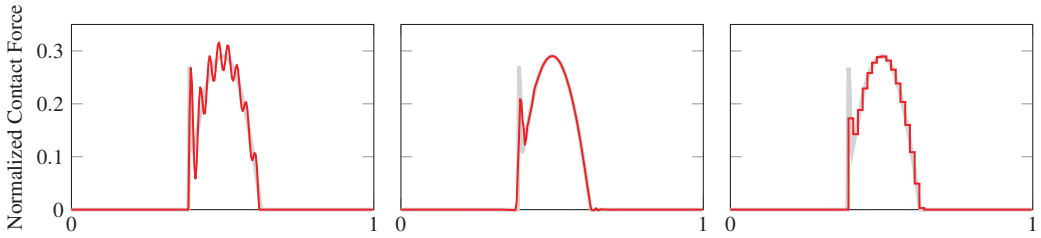

(a) Fourier:Fourier (b) DB6:DB6 (c) Haar:Fourier

Figure 6. Normalized contact force versus normalized time t

5. Conclusions

The method of weighted residuals for capturing the periodic responses of unilateral contact problems is investigated. The contact condition is simulated using an exponential penalty function approach. Weak and distributional formulations are introduced which transfer trial function continuity requirements to the weighting functions. This allowed piecewise constant Haar scaling functions to be used as a trial basis. Results show that a number of trial:weighting function combinations produce accurate solutions which rapidly converge as the size of the discrete spaces is increased. As expected, Fourier functions perform well as a trial basis, though nonsmooth functions such as Haar and Daubechies scaling functions are also attractive since they provide comparable prediction accuracy and even out perform the Fourier functions in some measures. It is also shown that all the basis combinations considered can be used in an arc-length continuation framework to capture the nonlinear frequency response of the unilateral contact problem.

References

[1] Thorsten Schindler and Vincent Acary. Timestepping schemes for nonsmooth dynamics based on discontinuous galerkin methods: Definition and outlook. *Mathematics and Computers in Simulation*, 2012.

[2] Denis Laxalde and Mathias Legrand. Nonlinear modal analysis of mechanical systems with frictionless contact interfaces. *Computational Mechanics*, 47(4):469–478, 2011.

[3] Yu Wang. Dynamics of unsymmetric piecewise-linear/non-linear systems using finite elements in time. *Journal of Sound and Vibration*, 185(1):155–170, 1995.

[4] David Demailly, Fabrice Thouverez, and Louis Jézéquel. Unbalance responses of rotor/stator systems with nonlinear bearings by the time finite element method. *International Journal of Rotating Machinery*, 10(3):155–162, 2004.

[5] Matthias Holschneider. Wavelet analysis on the circle. *Journal of Mathematical Physics*, 31(1):39–44, 1990.

[6] Gui Rong Liu and Siu Sin Quek. *Finite element method: a practical course*. Butterworth-Heinemann, Oxford, 2003.

[7] Stéphane Mallat. *A wavelet tour of signal processing*. Elsevier/Academic Press, Amsterdam, 3 edition, 2009.

[8] Gilbert Strang and Truong Nguyen. *Wavelets and filter banks*. Wellesley-Cambridge Press, Wellesley, 1996.

[9] Stéphane Pernot and Claude-Henri Lamarque. A wavelet-Galerkin procedure to investigate time-periodic systems: transient vibration and stability analysis. *Journal of Sound and Vibration*, 245(5):845–875, 2001.

[10] Yves Meyer. *Ondelettes*, volume 1. Hermann, Paris, 1990.

[11] Ming-Quayer Chen, Chyi Hwang, and Yen-Ping Shih. The computation of wavelet-Galerkin approximation on a bounded interval. *International Journal for Numerical Methods in Engineering*, 39(17):2921–2944, 1996.

Proceedings of the 4th International Conference on Nonlinear Dynamics
ND-KhPI2013
June 19-22, 2013, Sevastopol, Ukraine

FREE GEOMETRICALLY NONLINEAR VIBRATIONS OF COMPOSITE PLATES AND SHELLS

M.V. Marchuk[1*], V.S.Pakosh[1]

Abstract
Thin-walled composite plates and shells are among the most common support structural elements of buildings and facilities of various purposes. Under intensive dynamic performance loads (including cyclic ones) displacements of the elements are comparable with their thickness. This leads to geometric nonlinearity of their stress-strain state. To prevent resonances in the operating conditions it is needed to determine the spectrum of natural frequencies of such elements at the design stage. Using the classical theory by Karman, based on the Kirchhoff-Love theory, and the theory based on shear model by S.P. Timoshenko, it is developed analytical and numerical methods to determine the basic natural frequency for plates and a rather wide class of shells. However, the specified approach does not fully take into account the following features of deformation of thin-walled elements with modern composite materials reinforced polymer-based, as pliability to transverse shear and compression. Previously, the authors found a significant impact on the value of the basic natural frequency for geometrically nonlinear vibrations of composite plates. High density of a cyclic loads is requires defining a set of values of the spectrum of natural frequencies. Knowledge of a wide range of natural frequencies is needed to identify internal resonances of plates and shells.
To solve this problem the relations of refined theory of geometrically nonlinear dynamic deformation pliable to transversal shear and compression of orthotropic shells and plates, are obtained and justified. The problem of finding the spectrum of natural frequencies for geometrically nonlinear vibrations of plates, strips and elongated cylindrical panels is reduced to infinite system of integro-differential equations by time coordinates. Methods of determining the number of their first natural frequencies and amplitudes on the base of asymptotic method are developed. The influence of the parameters of pliability to transversal shear and compression on the associated amplitude-frequency dependence is investigated. Expressions for characteristics of longitudinal and shear vibration processes by generated transversal vibrations are obtained

Keywords
Thin-walled composite plates and shells, geometrically nonlinear vibrations

[1] Pidstryhach Institute for Applied Problems of Mechanics and Mathematics of NASU, Lviv, Ukraine *
Corresponding author:

Proceedings of the 4th International Conference on Nonlinear Dynamics
ND-KhPI2013
June 19-22, 2013, Sevastopol, Ukraine

Nonlinear Dynamics of a Thin Plate in a Nonstationary Electromagnetic Field of the Inductor

Oleg K. Morachkovsky[1], Denis V. Lavinsky[1*]

Abstract
The problems of the non-stationary deformation of a thin round plates in the electromagnetic field (EM-field) created by a massive inductor are considered. The finite element method is used for the analysis of spatial-temporal distribution of the electromagnetic field components and the parameters of the stress-strain state in the system of the «inductor-billet (plate)» with a consideration of the air layer. The data of measurements in experimental studies of vibrations of plates in pulsed EM-field are used to establish the frequency modes with the maximum values ponderomotive forces generated by an EM-field. The solution of the problem of plate vibrations was obtained. The temporal and spatial distribution of components of the electromagnetic field, displacements and stresses on the surface of the plate with the analytical solutions and experimental data are compared. Areas with the maximum displacements and stresses in the plate were installed for some «configuration» of electromagnetic field.

Keywords
Electromagnetic field, vibrations, deforming

[1] NTU "KhPI", Kharkov, Ukraine
* **Corresponding author:** lavinsky_d@mail.ru

Introduction

The interaction of electro-conductive bodies with the electromagnetic field (EM-field) leads to occurrence in them of the solenoidal currents, which in turn causes the appearance of ponderomotive forces leading to movement and deformation of the conductive bodies. Influence of intensive EM-fields is exposed to the elements of various technical devices: various converters of energy (generators, transformers), devices for the geological exploration with the help of pulsed EM-field, the system for processing of materials by EM-field forces. The energy created in the EM-field, can reach such values, in which the strength of structural elements is violated. In addition, the movement of structural elements in an EM-field (vibrations) can lead to the distortion of the distribution of EM-field components, which might disturb the normal mode of work of the device.

Thus, the problem of the analysis of component of the EM-field and the subsequent analysis of the stress-strain state (SSS) is relevant in the scientific and practical terms. It should be noted that a large number of scientists in different times focus special attention to problems of the analysis of the thermo-mechanics in presence of the EM-field. A significant contribution was made by S.A. Ambratcumyan, Ya.Yo. Burak, O.S. Wol'mir, A.R. Gachkevich, O.M. Guz', S.A. Kaloerov, Ya. S. Pidstryhach etc. However, basically these researches are focused on the analysis of elastic behavior of material, and the solutions are given for bodies of the canonical form. Thus, the problem for the creation of effective methods of calculation of magneto-elastic plasticity for a body of arbitrary shape in the present time is actual one.

The paper presents the analysis of the spatial-temporal distribution component of the EM-field in the system for electromagnetic forming (EMF) of materials and the subsequent analysis of deformation of the elements of this system. EMF is one of the progressive methods of processing of materials, based on the ability of metals to deform plastically under the action of ponderomotive

forces. In this case, the high levels of ponderomotive forces on the one hand positively influence on process of plastic deformation of the workpiece, on the other hand, they negatively affect the resistance of the inductor systems, because it may violate the strength of the inductor.

1. Problem Statement

Let's consider one variant of the inductors designed a deformation of thin-walled billets. In this case, it is a massive body of rotation of the complex form (fig.1). In the center of the inductor the bore (window) was made in the form of a truncated cone. It is necessary to analyze the distribution of the component of the EM-field in the system of the «inductor-billet», consider the vibration process in the system, to assess the SSS of the system.

Figure 1. The inductor with cone bore

The mathematical formulation of the problem in this case has the following form. The equations of motion:

$$\sigma_{ij,j} + F_{pi} = \rho \ddot{u}_1 , \ \vec{F}_p(x_i) = \rho \vec{E} + \mu_c \left[\vec{j} \times \vec{H} \right] \tag{1}$$

where u_i are components of the vector of displacements, σ_{ij} are components of the stress tensor, ρ is the mass density, F_{pi} are components of the vector of volumetric forces of Lorentz, $\vec{j}$ is the vector of current density , $\vec{E}$, $\vec{H}$ are vectors of the intensity of electric and magnetic fields, μ_c is the magnetic permeability. The electromagnetic field is determined by the system of the Maxwell's equations [1]:

$$rot\ \vec{H} = \varepsilon_c \frac{\partial \vec{E}}{\partial t} + \rho \omega \dot{\vec{u}} + \vec{j} , \ \ rot\ \vec{E} = -\mu_c \frac{\partial \vec{H}}{\partial t} , \ \ div\vec{H} = 0 , \ \varepsilon_c div\vec{E} = \rho \omega \tag{3}$$

where ω is the density of electrical charges, ε_c is the electrical permeability. Equations (1) and (3) are supplemented by physical relations:

$$\vec{D} = \varepsilon_c \vec{E} , \ \ \vec{B} = \mu_c \vec{H} , \ \vec{j} = \gamma_c \vec{E} + \gamma_c \left[\dot{\vec{u}} \times \vec{B} \right] , \ \ \varepsilon_{ij} = A^e_{ijkl} \sigma_{kl} \tag{4}$$

where $\vec{D}$, $\vec{B}$ are induction vectors of electric and magnetic fields, γ_c is an electrical conductivity of the material, ε_{ij} are the components of a tensor of strain, A^e_{ijkl} is the components of a tensor adopted for the description of the properties of the material, within the limits of linear elasticity of the material, the ratio meet the generalized Hook's law. For isotropic body the material constant tensor is defined as: $A^e_{ijkl} = \frac{1}{E}\left[(1+\nu)\delta_{ik}\delta_{jl} - \nu\delta_{ij}\delta_{kl}\right]$, where E, ν are the elastic modulus and Poisson's ratio. The relationship between deformations and displacements will be considered in the framework of the linear Cauchy relations:

$$\varepsilon_{ij} = 1/2\left(u_{j,i} + u_{i,j}\right) \tag{5}$$

The problem is supplemented by boundary conditions:

$$\vec{E}_\Gamma \times \vec{n} = 0, \quad \vec{D}_\Gamma \cdot \vec{n} = 0, \quad \vec{H}_\Gamma \times \vec{n} = 0, \quad \vec{B}_\Gamma \cdot \vec{n} = 0; \quad \vec{\sigma}_n = \vec{p}_n + \frac{\Xi}{2}\vec{E}_\Gamma + \frac{\mu_c}{2}\left(\Xi\dot{\vec{u}}_\tau + \vec{i}\right) \times \vec{H}_\Gamma \tag{6}$$

where $\vec{\sigma}_n = \sigma \cdot \vec{n}$ is the vector of mechanical stresses on the boundary with the normal $\vec{n}$, $\Xi, \vec{i}$ – density of surface charges and currents, $\dot{\vec{u}}_\tau$ are the projection of the velocity vector of a point on a plane tangent to the boundary of the body.

2. Solution and Analysis of the Results

2.1 The analysis of the distribution component of the EM-field in the system of the «inductor-billet»

Let us consider the distribution of components of the EM-field in the system of the «inductor-billet» with the help of the finite element method (FEM). In the first approximation inductor can be modeled as an axisymmetric body [2]. The calculation scheme of the problem of determination of space-time configuration of the EM-field is shown in figure 2. In this case, the system of Maxwell's equations in a cylindrical coordinate system relative to the component of the magnetic field intensity, in the mind of axial symmetry, is reduced to the form (8):

$$\begin{cases} rot\vec{H}(r,z,t) = \dfrac{\partial H_z}{\partial r} - \dfrac{\partial H_r}{\partial z} = 0; \\ div\vec{H}(r,z,t) = \dfrac{1}{r} \cdot \dfrac{\partial}{\partial r}\left(r \cdot H_r\right) + \dfrac{\partial H_z}{\partial z} = 0. \end{cases} \tag{8}$$

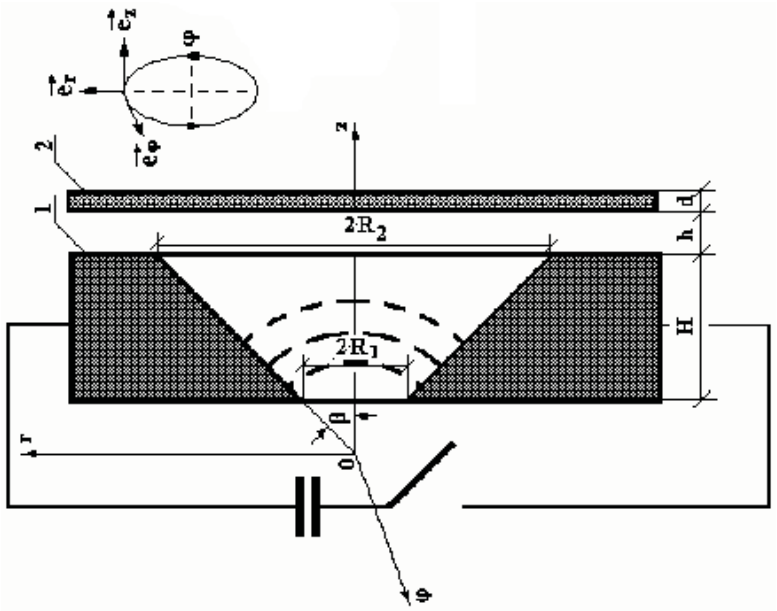

Figure 2. Calculation model of the analysis of the EMF in system of the «inductor-billet»

To solve this problem use a FEM that allows to largely avoiding the various simplifying assumptions. In addition, it is necessary to have in mind that the transfer of the current of the inductor for billet takes place through the intermediate environment – air, which is excluded from consideration in the analytical solution. Enter into a consideration the magnetic vector potential [3] – $\vec{A}(r,z,\varphi,t)$: $\vec{B} = rot\vec{A}$. In this case, the magnetic vector potential has only one non-zero component $A_\varphi = A$. Compare the obtained solution with the analytical and experimental data [2]. Figure 3 shows the distribution of the radial components of the intensity of electromagnetic field on the surface of the billet directly in the neighborhood of the window field. The solid line is the solution

obtained FEM, dashed line – analytical solution, points – experimental data [3]. From the figure it is shown a good agreement between the numerical and an analytical solution, which testifies to expediency of application of the FEM for the analysis of the distribution of EM-field in the systems similar to, considered one.

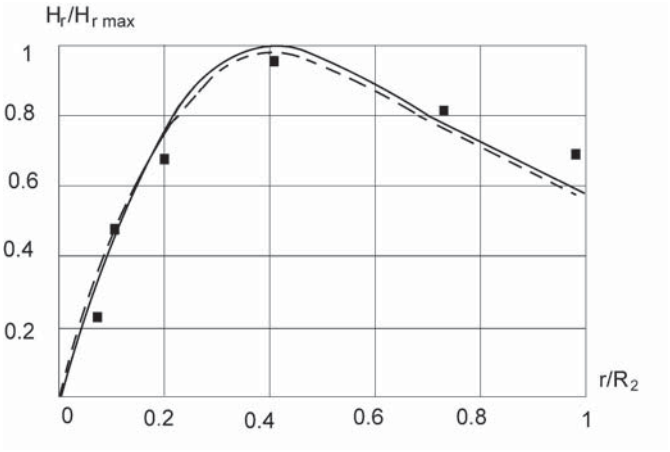

Figure 3. The comparison of the distribution of the radial component of magnetic field intensity on the surface of the billet

2.2 Analysis of vibrations of a round plate in a variable magnetic field

The variability in time of the EM-field components, obviously, leads to vibrations of elements of the «inductor-billet». Due to the fact, that the inductor is much more massive than the workpiece, the vibrations of the workpiece are most pronounced. For their modeling consider vibrations of a thin round plate in a variable magnetic field, which is a transverse to the surface of the plate – fig.4. In this case, for the analysis of bending vibrations of plates we can use the equation of the [4]:

$$D\nabla^4 w + 2\rho h\ddot{w} - h\frac{\partial}{\partial x}\left(\sigma_{zx}^{+} + \sigma_{zx}^{-}\right) - h\frac{\partial}{\partial y}\left(\sigma_{zy}^{+} + \sigma_{zy}^{-}\right) - \left(\sigma_{zz}^{+} + \sigma_{zz}^{-}\right) = \\ = \frac{\partial}{\partial x}\int_{-h}^{h} f_x z dz + \frac{\partial}{\partial y}\int_{-h}^{h} f_y z dz + \int_{-h}^{h} f_z dz \tag{9}$$

where $\sigma_{zx}^{+}, \sigma_{zx}^{-}, \sigma_{zy}^{+}, \sigma_{zy}^{-}, \sigma_{zz}^{+}, \sigma_{zz}^{-}$ – the stresses at the top and bottom of the outer boundaries of the plates, f_x, f_y, f_z – components of the Lorentz force, $D = \frac{2Eh^3}{3\left(1-\nu^2\right)}$ – the bending stiffness of the plate.

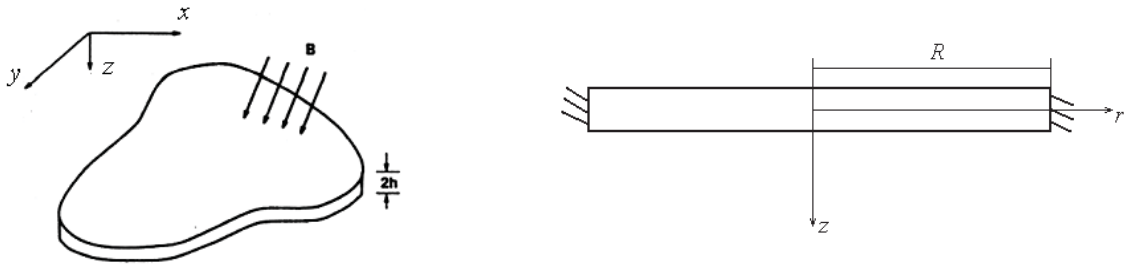

a) b)

Figure 4. Calculation model of the analysis of vibrations of a round plate in a variable magnetic field

We approximated the distribution of the functions of the bending of the plate along the radial coordinate of the function:

$$w = A(t)\left(R^2 - r^2\right)^2 \tag{10}$$

where $A(t)$ – the value of the bending in the center of the plate, t – the time. This function automatically satisfies the boundary conditions type of rigid fixation. Let us pass to dimensionless designations of variables and functions: $\bar{r} = \frac{r}{R}$; $\overline{A} = \frac{A}{h}$; $\overline{w} = \frac{w}{h}$. Then, taking into account dependencies (4) and (5), and taking into account the axial symmetry of the equation (9) is converted to the form:

$$D\nabla^4\overline{w} + \frac{2h}{\mu_0}\left(1 - \frac{\mu_0}{\mu}\right)B^2\nabla^2\overline{w} + 2\rho h\ddot{\overline{w}} = f_z + f_r \tag{11}$$

After substitution, we obtain:

$$64D\overline{A}R^4 + \frac{16h}{\mu_0}\left(1 - \frac{\mu_0}{\mu}\right)B^2\overline{A}R^4\left(2\bar{r}^2 - 1\right) + 2\rho h\ddot{\overline{A}}R^4\left(1 - \bar{r}^2\right)^2 = f_z + f_r \tag{12}$$

The components of the Lorentz force can be presented according to [5] in the form of:

$$f_z + f_r = e^{-\delta_0\omega t}\cos(\omega t)\left[\frac{2 + \bar{r}^2}{1 + \bar{r}^2}\right], \tag{13}$$

where ω is a frequency of current in pulse. Let us consider the solution of the tasks for the following data:

$h = 0{,}0005(\text{i})$, $R = 0.07(\text{m})$, $\delta_0 = 0{,}25$, $B = 40$, $\mu = 2$, $\mu_0 = 1{,}257 \cdot 10^{-6}$, $\omega = 17{,}9 \cdot 10^3\left(\text{s}^{-1}\right)$,

pulse duration – of 0.001(s). Fig. 5 shows the plot of the time-dependence of the bending of a centre of a plate. The graph shows that the pulse of the impact of the fixed plate makes damped oscillations, which are continuing in time longer than the current pulse. Also note that the first maximum displacement, attributable to the initial moment of time, is almost twice more than the second maximum. It is logical to assume that this is the first maximum corresponds to the occurrence of the maximum levels of stress, which can lead to the appearance of plastic deformations. Thus, in the analysis of deformation of systems for EMF, the task can be considered in the quasi-stationary set, which corresponds to, in fact, a review of the distribution of EM-field in the initial moment of time.

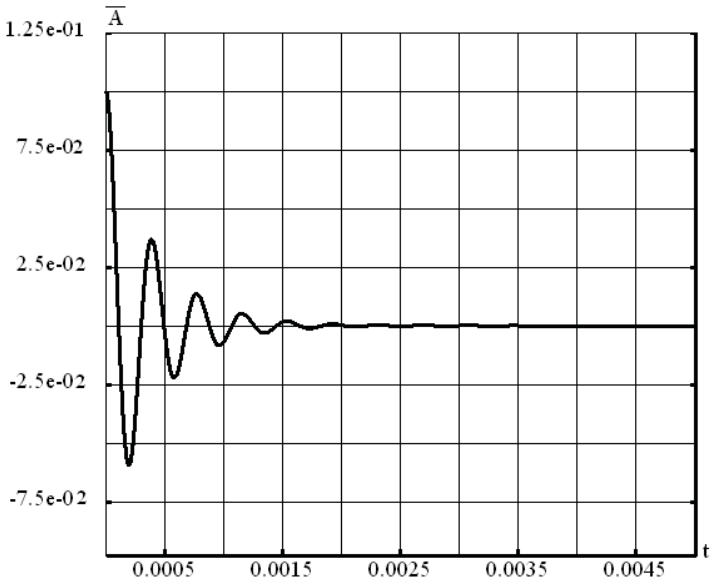

Figure 5. The time-dependence of the bending of a centre of a plate

2.3 The analysis of the SSS of the system «inductor-billet» in the case of quasi-stationary EM-field

The analysis of the SSS of the system «inductor-billet» was made with the help of FEM, means the software package (SP) ANSYS. Baseline data for the analysis of the SSS served as the distribution component of the EM-field. As is known, the ponderomotive forces can lead both to the repulsion and to the attraction of conducting bodies. It is experimentally shown [2] that the low-frequency current in pulse inductor mechanisms for attraction prevails over the mechanisms of repulsion. An ideal variant, in which the attraction is the impact of a constant current of great strength, but in reality to implement such a process, is not possible. At the same time calculated in the approximation of quasi-stationary process provides an opportunity to carry out qualitative assessments of the deformation of the elements of the system. It is in this setting, and the calculation was done. The picture of the deformed state of the system «inductor-billet» is presented in Fig. 6. Note that the most intensive process of deformation is directly opposite the cone of the window field. Also as results of the analysis of the SSS have been identified zones, in which the stress intensity reaches maximum values and it is in these areas should be expected of plastic deformations.

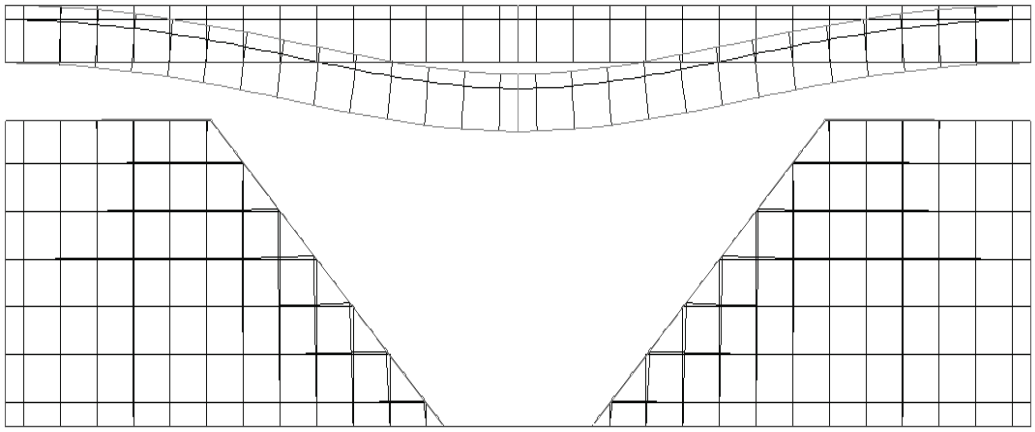

Figure 6. The deformed shape of the system «inductor-billet»

Conclusions

In the article the problems of the analysis of component of the EM-field for a system of interacting bodies and the subsequent analysis of deformation have been shown. The calculations on the example of the system of the «inductor-billet», which are used in the processes of EMF, have been made. The analysis of the distribution component of the EM-field and the subsequent analysis of deformation produced by FEM. Elements of the system «inductor-billet» are considered in the framework of the united calculation model. Vibrations of a thin conducting of the round plate in a variable magnetic field have been analyzed.

References

[1] Maxwell J.C. *A treatise on Electricity and Magnetism,* Clarendon Press, Oxford, 1873.
[2] Turenko A.N., Batygin Yu.V. and Gnatov A.V. *Pulse magnetic fields to progressive technologies*: *Theory and experiment of thin-walled metal attraction by pulsed magnetic field,* KhNADU, Kharkov, 2009 (in Russian).
[3] Tozoni O.V., Mayergoiz I.D. *Calculation of three-dimensional electromagnetic fields,* «Tekhnika», Moscow, 1974 (in Russian).
[4] Ambratcumyan S.A., Baghdasaryan G.E. and Belubekyan M.V. *Magneto elastic of thin shells and plates,* Nauka, Moscow, 1977 (in Russian).
[5] Batygin Yu.V., Gnatov A.V. and Shigoleva S.A. The direction of the forces acting on the sheet ferromagnetic, depending on the temporal characteristics of the PMFM, *Electrotehnika ta elektromechanika*, Vol. 3., pp.56-61, 2011 (in Russian).

Proceedings of the 4th International Conference on Nonlinear Dynamics
ND-KhPI2013
June 19-22, 2013, Sevastopol, Ukraine

Periodic solutions to a parabolic problem with the shift transformation space variable

Negrimovskaya Anastasia

Abstract
Transformation of the field in two-dimensional nonlinear optical feedback system leads to a rotating structures [1]. Such systems are used in modern computer technology and research of laser beams. In this paper it was shown that a traveling-wave solution branches off spatially homogeneous stationary solution by vibrational buckling. This solution is orbitally asymptotically stable.

Keywords
bifurcation, parabolic equation, asymptotically stable

[1] TNU, Simferopol, Ukraine
* **Corresponding author:** anastasiya.neg@gmail.com

Introduction

Transformation of the field in two-dimensional nonlinear optical feedback system leads to a rotating structures [1]. Such systems are used in modern computer technology and research of laser beams. Mathematical model of the system is a quasi-linear parabolic functional differential equation with the transformation of the spatial variables. The problem of self-oscillations in the equation for the case of a thin circular ring and a rotation transformation is considered in [2-5]. The papers [2,4, 6-8] are devoted to the small diffusion coefficient study.

1. The problem on bifurcation of periodic traveling-wave solutions of the spatially homogeneous steady state

On the circle $S^1 = R/2\pi Z$ let's consider the equation

$$\frac{\partial u}{\partial t} + u = \mu \frac{\partial^2 u}{\partial \theta^2} + K(1 + \gamma \cos Qu),\ Qu(\theta,t) = u(\theta + h,t), \tag{1}$$

where u is the phase of the light wave; $\mu > 0$ is the particle diffusion coefficient of the nonlinear medium; $0 < \gamma \le 1$ is the visibility of the interference pattern; $K > 0$ is a coefficient which is proportional to light intensity.

The problem of bifurcation of periodic traveling-wave solutions of the spatially homogeneous steady state is the following:

$$w = K(1 + \gamma \cos w) \tag{2}$$

In the study of bifurcation loop an interest is in a loss of stability of the stationary solutions, and approximate formulas for periodic solutions that are grown with small amplitude.

With the K growing number of co-existing roots of this equation increases indefinitely, and for $K \to \infty$ their composition is constantly updated: an appearance of the new state of equilibrium and a vanishing of the old.

In this regard, we fix some continuous branch of solutions

$$w = w(K),\ 1 + K\gamma \sin w(K) \neq 0 \tag{3}$$

of (2). Then we linearize the equation (1) near the state of equilibrium (3) and apply it to the S^1 resulting equation for

$$\frac{\partial u}{\partial t} = \mu \frac{\partial^2 u}{\partial \theta^2} - u + \Lambda(K)Qu$$

where $\Lambda(K) = -K\gamma \sin w(K)$, the Fourier method for system functions $\exp(im\theta),\ m = 0,\pm1,\pm2,\ldots$.

As a result, we can see that the range of stability of the equilibrium state under consideration is determined by the eigenvalues

$$\lambda_m = -1 - \mu m^2 + \Lambda(K)\exp(imh),\quad m = 0,\pm1,\pm2,\ldots \tag{4}$$

where $\Lambda(K) = -K\gamma \sin w(K)$. One considers the case $\Lambda(K) < -1$.

Next, we consider the following case. $h = \frac{2\pi}{3}$.

It is easy to verify the equality $\operatorname{Re}\lambda_1(\mu^*) = 0,\ \mu^* = -\Lambda \cdot \frac{\sqrt{3}}{2} - 1 > 0,\ \operatorname{Im}\lambda_1(\mu^*) = \Lambda(K)/2.$

Let's denote

$$\sigma_2(z,\bar{z},\theta) = -\frac{1}{2}(ctg\,w)\left(\frac{z^2 e^{i2(\theta+h)}}{2\lambda_1 - \lambda_2} + \frac{2z\bar{z}}{\lambda_1 + \bar{\lambda}_1 - \lambda_0} + \frac{\bar{z}^2 e^{-2i(\theta+h)}}{2\bar{\lambda}_1 - \lambda_{-2}}\right),$$

$$\sigma_3(z,\bar{z},\theta) = \frac{1}{3!}\Lambda z^3 e^{i3(\theta+h)} \cdot \frac{1}{3\lambda_1 - \lambda_3} + \frac{2}{4}(ctg w)^2 \Lambda^2 \cdot \left(\frac{z^3 e^{i3(\theta+2h)}}{3\lambda_1 - \lambda_3} + \frac{\bar{z}^3 e^{-i3(\theta+2h)}}{3\bar{\lambda}_1 - \bar{\lambda}_3}\right) + \frac{\frac{1}{3!}\Lambda z^3 e^{-i3(\theta+h)}}{3\bar{\lambda}_1 - \bar{\lambda}_3},$$

$$c_3 = \frac{1}{2}\Lambda \cdot e^{ih} + \frac{2}{4}(ctg\,\omega)^2 \Lambda^2 \left(2 \cdot \frac{e^{2ih}}{\lambda_1 + \bar{\lambda}_1 - \lambda_0} + \frac{e^{2ih}}{2\lambda_1 - \bar{\lambda}_2}\right).$$

Suppose that $\operatorname{Re} c_3 < 0$.

Theorem: Suppose that the above conditions. Then there is $\delta > 0$ that if $0 < \mu^* - \mu < \delta$ there are two periodic solutions (1) traveling wave

$$u^{\pm} = w(K) \pm \varphi(\omega(\mu)t \pm \theta, \mu) + O\left(\left|\mu^* - \mu\right|\right)^2,$$

where

$$\varphi(\omega(\mu)t + \theta, \mu) = \left(ze^{i\theta} + \bar{z}e^{-i\theta} + \sigma_2(z,\mu) + \sigma_3(z,\mu)\right)\Big|_{z(t,\mu)},$$

$$z(t,\mu) = \left(-\frac{\operatorname{Re}\lambda_1}{\operatorname{Re} c_3}\right)^{\frac{1}{2}} e^{i\omega t},\ \omega(\mu) = \operatorname{Im}\left(\lambda_1 + c_3 \cdot \frac{\operatorname{Re}\lambda_1}{-\operatorname{Re} c_3}\right).$$

Solutions $u^{\pm}$ - orbitaly asymptotically stable.

Conclusions

In this paper it was shown that a traveling-wave solution branches off spatially homogeneous stationary solution by vibrational buckling. This solution is orbitally asymptotically stable.

Acknowledgments

I express my deep appreciation and gratitude to my supervisor, Eugene Petrovich Belan for the help in preparing the material.

References

[1] Akhmanov S.A., Vorontsov M.A., Ivanov V.Yu. Generation of structures in optical systems with two-dimensional feedback: On the way to the creation of nonlinear optical analogues of neural networks *New Physical Principles of Optical Information Processing*, Nauka, Moscow, pp.263-325, 1990 (in Russian)

[2] Kashchenko S.A. Asymptotics of spatially inhomogeneous structures in coherent nonlinear-optical systems *J. of Computational Mathematics and Mathematical Physics*, V.31 (3), pp. 467-473, 1991 (in Russian).

[3] Razgulin A.V. Self-excited oscillations in the non-linear parabolic problem with transformed argument *J. of Computational Mathematics and Mathematical Physics*, V. 33 (1), pp. 69-80, 1993 (in Russian).

[4] Grigorieva E.V., Haken H., Kashchenko S. A., Pelster A Travelling wave dynamics in a nonlinear interferometer with spatial field transformer in feedback *Physika D,* V. 125 (1-2), pp. 123-141, 1999.

[5] Razgulin A.V. *Non-linear Models of Optical Synergy* Dept. Faculty Computational Mathematics and Cybernetics, MAKS Press, - p. 201. - 2008.

[6] Kolesov A.Yu, Rozov N. Kh, Optical Buffering and Mechanisms for Its Occurrence *Teoretical and Mathematical Physics*. V.140 (1), pp. 14–28, 2004.

[7] Mishchenko E.F., Sadovnichiy V.A., Kolesov A.Yu., Rozov N.Kh.. *Autowave Processes in Nonlinear Media with Diffusion,* M. Francis, London, 2005.

[8] Belan E.P. Dynamics of traveling waves in a parabolic equation with the transformation of the space variable shift *J. of Math. Physics, Analysis, Geometry,* 2005.

Proceedings of the 4th International Conference on Nonlinear Dynamics
ND-KhPI2013
June 19-22, 2013, Sevastopol, Ukraine

Three-dimensional Non-linear Models of the Dynamic Problems of the Elasticity and Plasticity Theory and Numerical Algorithms for their Implementation'

Sh.A. Nazirov[1]

Abstract
This work is devoted to the development of computational algorithms that implement three-dimensional mathematical models of dynamical problems of the elasticity and plasticity theory. Proposed algorithm is based on combination of the following methods: R-functions (Rvachev's functions) method, Bubnov–Galerkin and variational method and the method of successive approximations.

Keywords: Nonlinear mathematical model, variational principle, computational algorithm, three-dimensional body, R-functions method , successive approximation

[1] Tashkent University of Information Technology, Tashkent, Uzbekistan
* **Corresponding author**: shnazirov@mail.ru

Introduction

This work is devoted to derivation of the non-linear strain fields' models in the three-dimensional space. We also propose some algorithms for their realization. The mathematical model has been obtained by variational principle of Hamilton- Ostrogradskii [1-3]. The models are constructed in orthogonal curvilinear coordinates. This procedure we can call algorithmic because it is a common approach to the construct mathematical models of different processes.

1. Derivation of three-dimensional nonlinear mathematical models for dynamical problems of elasticity and plasticity theory

In the general theory of vibrations, displacements of the deformable bodies u_1, u_2 and u_3 are functions of four variables: the coordinates x_1, x_2 and x_3 and time t. Equation motion and boundary conditions are derived from Hamilton-Ostrogradskii's principle:

$$\delta\int_{t_1}^{t_2}(K-\Pi+A)dt=0, \tag{1}$$

where K, P are kinetic and potential energy relatively, and A is the work of external volume and surface forces. Variation of the kinetic energy is defined as follows [2]:

$$\int_{t_1}^{t_2}\delta K dt=-\int_{t_1}^{t_2}\int_{v}\rho\left[\frac{\partial u_1}{\partial t^2}\delta u_1+\frac{\partial^2 u_2}{\partial t^2}\delta u_2+\frac{\partial^2 u_3}{\partial t^2}\delta u_3\right]dVdt. \tag{2}$$

Let us introduce the notation σ_{11}, σ_{22}, σ_{33}, σ_{12}, σ_{23}, σ_{31} and ε_{11}, ε_{22}, ε_{33}, ε_{12}, ε_{23}, ε_{31} for the components of stress and strain.Then for the variation of potential energy, we have

$$\delta\Pi' = \int_{t_1}^{t_2} \delta\Pi dt = \int_{t_1}^{t_2}\int_{v} (\sigma_{11}\delta\varepsilon_{11} + \sigma_{22}\delta\varepsilon_{22} + \sigma_{33}\varepsilon_{33} + \sigma_{12}\delta\varepsilon_{12} + \sigma_{23}\delta\varepsilon_{23} + \sigma_{31}\delta\varepsilon_{31})dVdt. \tag{3}$$

Let us denote the linear strain component as $\varepsilon^{L}{}_{ij}$ and nonlinear one by $\varepsilon^{N}{}_{ij}$. Then strains may be presented as [4]

$$\varepsilon_{ij} = \varepsilon^{L}{}_{ij} + \varepsilon^{N}{}_{ij}$$

Here $\varepsilon^{L}{}_{ij} = e_{ij}$, $i = \overline{1,3}$ $j = \overline{1,3}$; $\varepsilon^{N}{}_{11} = \frac{1}{2}\left[e_{11}^2 + \left(\frac{1}{2}e_{12} + \omega_3\right)^2 + \left(\frac{1}{2}e_{13} - \omega_2\right)^2 \right]$,

$$\varepsilon^{N}{}_{22} = \frac{1}{2}\left[e_{22}^2 + \left(\frac{1}{2}e_{12} - \omega_3\right)^2 + \left(\frac{1}{2}e_{23} + \omega_1\right)^2 \right], \varepsilon^{N}{}_{33} = \frac{1}{2}\left[e_{33}^2 + \left(\frac{1}{2}e_{13} + \omega_2\right)^2 + \left(\frac{1}{2}e_{23} - \omega_1\right)^2 \right],$$

$$\varepsilon^{N}{}_{12} = e_{11}\left(\frac{1}{2}e_{12} - \omega_3\right) + e_{22}\left(\frac{1}{2}e_{12} + \omega_3\right) + \left(\frac{1}{2}e_{13} - \omega_2\right)\left(\frac{1}{2}e_{23} + \omega_1\right),$$

$$\varepsilon^{N}{}_{13} = e_{11}\left(\frac{1}{2}e_{13} + \omega_2\right) + e_{33}\left(\frac{1}{2}e_{13} - \omega_2\right) + \left(\frac{1}{2}e_{12} + \omega_3\right)\left(\frac{1}{2}e_{23} - \omega_1\right),$$

$$\varepsilon^{N}{}_{23} = e_{22}\left(\frac{1}{2}e_{23} - \omega_1\right) + e_{33}\left(\frac{1}{2}e_{23} + \omega_1\right) + \left(\frac{1}{2}e_{12} - \omega_3\right)\left(\frac{1}{2}e_{13} + \omega_2\right) \tag{4}$$

where

$$\left.\begin{aligned} &e_{11} = \frac{1}{H}\left(a_{11}\frac{\partial u_1}{\partial x_1} + \beta_{11}u_2 + \gamma_{11}u_3 \right), e_{22} = \frac{1}{H}\left(\alpha_{22}u_1 + a_{22}\frac{\partial u_2}{\partial x_2} + \gamma_{22}u_3 \right), \\ &e_{33} = \frac{1}{H}\left(\alpha_{33}u_1 + \beta_{33}u_2 + a_{33}\frac{\partial u_3}{\partial x_3} \right), e_{12} = \frac{1}{H}\left(a_{12}\frac{\partial u_1}{\partial x_2} + a_{21}\frac{\partial u_2}{\partial x_1} + \alpha_{12}u_1 + \beta_{12}u_2 \right) \\ &e_{23} = \frac{1}{H}\left(a_{23}\frac{\partial u_2}{\partial x_3} + a_{32}\frac{\partial u_3}{\partial x_2} + \beta_{23}u_2 + \gamma_{23}u_3 \right), e_{31} = \frac{1}{H}\left(a_{13}\frac{\partial u_1}{\partial x_3} + a_{31}\frac{\partial u_3}{\partial x_1} + \alpha_{13}u_1 + \gamma_{13}u_3 \right) \end{aligned}\right\}, \tag{5}$$

$$\frac{1}{2}e_{12} + \omega_3 = \frac{1}{H}\left(a_{11}\frac{\partial u_2}{\partial x_1} + \alpha_{12}u_1 \right), \frac{1}{2}e_{13} - \omega_2 = \frac{1}{H}\left(\alpha_{13}u_1 + a_{21}\frac{\partial u_3}{\partial x_1} \right), \frac{1}{2}e_{12} - \omega_3 = \frac{1}{H}\left(\beta_{12}u_2 + a_{22}\frac{\partial u_1}{\partial x_2} \right)$$

$$, \frac{1}{2}e_{13} + \omega_2 = \frac{1}{H}\left(a_{13}\frac{\partial u_1}{\partial x_3} + \gamma_{13}u_3 \right), \frac{1}{2}e_{23} + \omega_1 = \frac{1}{H}\left(a_{22}\frac{\partial u_3}{\partial x_2} + \beta_{23}u_2 \right), \frac{1}{2}e_{23} - \omega_1 = \frac{1}{H}\left(\gamma_{23}u_3 + a_{31}\frac{\partial u_2}{\partial x_3} \right),$$

$$\left.\begin{aligned} &a_{11} = H_2H_3, \beta_{11} = H_3\frac{\partial H_1}{\partial x_2}, \ \gamma_{11} = H_2\frac{\partial H_1}{\partial x_3}, \alpha_{22} = H_3\frac{\partial H_2}{\partial x_1}, \ a_{22} = H_1H_3, \ \gamma_{22} = H_1\frac{\partial H_2}{\partial x_3} \\ &\alpha_{33} = H_2\frac{\partial H_3}{\partial x_1}, \ \beta_{33} = H_1\frac{\partial H_3}{\partial x_2}, \ a_{33} = H_1H_2, a_{12} = H_1H_3, a_{21} = H_2H_3, \ \alpha_{12} = -H_3\frac{\partial H_1}{\partial x_2} \\ &\beta_{12} = -H_3\frac{\partial H_2}{\partial x_1}, a_{13} = H_1H_2, \ a_{31} = H_2H_3, \alpha_{13} = -H_2\frac{\partial H_1}{\partial x_3}, \ \gamma_{13} = -H_2\frac{\partial H_3}{\partial x_1}, \ a_{23} = H_1H_2 \\ &a_{32} = H_1H_3, \beta_{23} = -H_1\frac{\partial H_2}{\partial x_3}, \ \gamma_{23} = -H_1\frac{\partial H_3}{\partial x_2}, H = H_1H_2H_3 \end{aligned}\right\}, \tag{6}$$

We'll consider the linear and nonlinear part of the variation (3) separately. Then

$$\delta\varepsilon_{ij} = \delta\varepsilon_{ij}^{L} + \delta\varepsilon_{ij}^{N} \qquad (i, j = \overline{1,3}),$$

and the variation of the potential energy becomes

$$\delta\Pi = \delta\Pi^{L} + \delta\Pi^{N}$$

Here Π^{L} is linear and Π^{N} is nonlinear part of the potential energy

$$\delta\Pi^{L} = \int_{v} (\sigma_{11}\delta e_{11} + \sigma_{22}\delta e_{22} + e_{33}\delta e_{33} + \sigma_{12}\delta e_{12} + \sigma_{23}\delta e_{23} + e_{23}\delta_{23} + e_{31}\delta e_{31})dV$$

$$\delta\Pi^{N} = \int_{v} (\sigma_{11}\delta\varepsilon_{11}^{N} + \sigma_{22}\delta\varepsilon_{22}^{N} + \sigma_{33}\delta\varepsilon_{33}^{N} + \sigma_{12}\delta\varepsilon_{12}^{N} + \sigma_{23}\delta\varepsilon_{23}^{N} + \sigma_{23}\delta\varepsilon_{23}^{N})dV$$

Let us denote components of the volume forces as P_1, P_2, P_3 and components of the surface forces as q_1, q_2, q_3. Then the variation of the work of the external forces takes the form

$$\delta A = \int_{t_1}^{t_2}\int_{v}\{(P_1\delta u_1 + P_2\delta u_2 + P_3\delta u_3)dV + \int_{t_1}^{t_2}\int_{s}(q_1H_1n_1\delta u_1 + q_2H_2n_2\delta u_2 + q_3H_3n_3\delta u_3)ds \qquad (7)$$

After calculation of the variations $\delta\varepsilon_{11}^{N}$, $\delta\varepsilon_{22}^{N}$, $\delta\varepsilon_{33}^{N}$, $\delta\varepsilon_{12}^{N}$, $\delta\varepsilon_{23}^{N}$, $\delta\varepsilon_{23}^{N}$ and $\delta\Pi^{N}$ $\delta\Pi^{L}$ we can obtain the variational equation of nonlinear vibrations of elastic and elastic-plastic three-dimensional bodies. From this equation we get systems of differential equations of motion, the natural boundary and initial conditions. The obtained system is nonlinear system of differential equations with partial derivatives:

$$\begin{aligned}
&\left(\sum_{i=1}^{3}\frac{\partial(a_{1i}\sigma_{1i})}{\partial x_i} - \alpha_{22}\sigma_{22} - \alpha_{33}\sigma_{33} - \alpha_{12}\sigma_{12} - \alpha_{13}\sigma_{13}\right) + R_1 + H\left(-\rho\frac{\partial^2 u_1}{\partial t^2} + P_1\right) = 0,\\
&\sum_{i=1}^{3}\left(\frac{\partial(a_{2i}\sigma_{2i})}{\partial x_i} - \beta_{11}\sigma_{11} - \beta_{33}\sigma_{33} - \beta_{12}\sigma_{12} - \beta_{23}\sigma_{23}\right) + R_2 + H\left(-\rho\frac{\partial^2 u_2}{\partial t^2} + P_2\right) = 0, \qquad (8)\\
&\left(\sum_{i=1}^{3}\frac{\partial(a_{3i}\sigma_{3i})}{\partial x_i} - \gamma_{11}\sigma_{11} - \gamma_{22}\sigma_{22} - \gamma_{13}\sigma_{13} - \gamma_{23}\sigma_{23}\right) + R_3 + H\left(-\rho\frac{\partial^2 u_3}{\partial t^2} + P_3\right) = 0
\end{aligned}$$

Here $R_i(i = 1,2,3)$ are the nonlinear terms of the $\delta\varepsilon_{ij}^{N}$ equations, resulting from the variation, the essence and content are detailed in [5]. $H = H_1, H_2, H_3$ are Lame coefficients [1,4].

The natural boundary conditions is defined as

$$\left[\sum_{i=1}^{3}(\sigma_{si}H_in_i + q_sH_s) + G_s\right]_{\Gamma_s} = 0, s = 1..3, \qquad (9)$$

Here, G_s are the nonlinear terms of the boundary conditions, from the $\delta\varepsilon_{ij}^{N}$ resulting variation, substance and content are detailed in [5].

Next, we write down the initial conditions:

$$\mathrm{u}_i\big|_{t=t_0} = \mathrm{u}_{i0}, \dot{u}_i\Big|_{t=t_0} = \dot{u}_{i0}, \quad i = 1..3; \qquad (10)$$

where

$$\mathrm{u} = (\mathrm{u}_1, \mathrm{u}_2, \mathrm{u}_3).$$

Thus, we obtain a system of nonlinear partial differential equations (8), supplemented by boundary and initial conditions (9) and (10).

This system is nonlinear three-dimensional mathematical model of vibration problems for elastic and elastoplastic bodies. [5-6].

2. The computational algorithm for solving problem

In the system (8) expressions $R_i (i = \overline{1,3})$ and $\sigma_{ij} (i = \overline{1,3};\ j = \overline{1,3})$ contain nonlinear terms. That is why we present $\sigma_{ij} (i = \overline{1,3};\ j = \overline{1,3})$ in the following form

$$\sigma_{ij} = \sigma_{ij}^L + \sigma_{ij}^N, \quad i = \overline{1,3},\ j = \overline{1,3} \tag{11}$$

For clarity, the system (8) with the notation (6) and (11) can be rewritten as

$$\begin{cases} \rho H_1 H_2 H_3 \dfrac{\partial^2 u_1}{\partial t^2} - \dfrac{\partial}{\partial x_1}(H_2 H_3 \sigma_{11}^L) - \dfrac{\partial}{\partial x_2}(H_1 H_3 \sigma_{12}^L) - \dfrac{\partial}{\partial x_3}(H_1 H_2 \sigma_{13}^L) + \sigma_{22}^L H_3 \dfrac{\partial H_1}{\partial x_1} + \\ + \sigma_{33}^L H_2 \dfrac{\partial H_3}{\partial x_1} - \sigma_{12}^L H_3 \dfrac{\partial H_1}{\partial x_2} - \sigma_{13}^L H_2 \dfrac{\partial H_1}{\partial x_3} = P_1 + R_1^*, \\ \rho H_1 H_2 H_3 \dfrac{\partial^2 u_2}{\partial t^2} - \dfrac{\partial}{\partial x_1}(H_2 H_3 \sigma_{21}^L) - \dfrac{\partial}{\partial x_2}(H_3 H_1 \sigma_{22}^L) - \dfrac{\partial}{\partial x_3}(H_2 H_1 \sigma_{23}^L) + \sigma_{33}^L H_1 \dfrac{\partial H_3}{\partial x_2} + \\ + \sigma_{11}^L H_3 \dfrac{\partial H_1}{\partial x_2} - \sigma_{23}^L H_1 \dfrac{\partial H_2}{\partial x_3} - \sigma_{21}^L H_3 \dfrac{\partial H_2}{\partial x_1} = P_2 + R_2^*, \\ \rho H_1 H_2 H_3 \dfrac{\partial^2 u_3}{\partial t^2} - \dfrac{\partial}{\partial x_1}(H_2 H_3 \sigma_{31}^L) - \dfrac{\partial}{\partial x_2}(H_1 H_3 \sigma_{32}^L) - \dfrac{\partial}{\partial x_3}(H_1 H_2 \sigma_{33}^L) + \sigma_{11}^L H_2 \dfrac{\partial H_1}{\partial x_3} + \\ + \sigma_{22}^L H_1 \dfrac{\partial H_2}{\partial x_3} - \sigma_{13}^L H_2 \dfrac{\partial H_3}{\partial x_1} - \sigma_{23}^L H_1 \dfrac{\partial H_3}{\partial x_2} = P_3 + R_3^* \end{cases} \tag{12}$$

Here

$$R_1^* = R_1 + \frac{\partial}{\partial x_1}(H_2 H_3 \sigma_{11}^N) + \frac{\partial}{\partial x_2}(H_1 H_3 \sigma_{12}^N) + \frac{\partial}{\partial x_3}(H_1 H_2 \sigma_{13}^N) - \sigma_{22}^N H_3 \frac{\partial H_1}{\partial x_1} +$$
$$+ \sigma_{12}^N H_3 \frac{\partial H_1}{\partial x_2} + \sigma_{13}^N H_2 \frac{\partial H_1}{\partial x_3}, \quad R_2^* = R_2 + \frac{\partial}{\partial x_1}(H_2 H_3 \sigma_{21}^N) + \frac{\partial}{\partial x_2}(H_3 H_1 \sigma_{22}^N) +$$
$$\frac{\partial}{\partial x_3}(H_2 H_1 \sigma_{23}^N) - \sigma_{33}^N H_1 \frac{\partial H_3}{\partial x_2} - -\sigma_{11}^N H_3 \frac{\partial H_1}{\partial x_2} + \sigma_{23}^N H_1 \frac{\partial H_2}{\partial x_3} + \sigma_{12}^N H_3 \frac{\partial H_2}{\partial x_1},$$

$$R_3^* = R_3 + \frac{\partial}{\partial x_1}(H_2 H_3 \sigma_{21}^N) + \frac{\partial}{\partial x_2}(H_3 H_1 \sigma_{22}^N) + \frac{\partial}{\partial x_3}(H_2 H_1 \sigma_{23}^N) - \sigma_{33}^N H_1 \frac{\partial H_3}{\partial x_2} -$$
$$-\sigma_{11}^N H_3 \frac{\partial H_1}{\partial x_2} + \sigma_{23}^N H_1 \frac{\partial H_2}{\partial x_3} + \sigma_{12}^N H_3 \frac{\partial H_2}{\partial x_1}, R_3^* = R_3 + \frac{\partial}{\partial x_1}(H_2 H_3 \sigma_{31}^N) + \frac{\partial}{\partial x_2}(H_1 H_3 \sigma_{32}^N)$$
$$+ \frac{\partial}{\partial x_3}(H_1 H_2 \sigma_{33}^N) - \sigma_{11}^N H_2 \frac{\partial H_1}{\partial x_3} - -\sigma_{22}^N H_1 \frac{\partial H_2}{\partial x_3} + \sigma_{13}^N H_2 \frac{\partial H_3}{\partial x_1} + \sigma_{23}^N H_1 \frac{\partial H_3}{\partial x_2}$$

Solution algorithm is based on the method of successive approximations. In this case, the basic functions are constructed by R-functions method [6-7], i.e,

$$u_{1n} = \sum_{i=1}^{n} C_i^{(1)}(t)\varphi_i(x,y,z), \quad u_{2m} = \sum_{j=1}^{m} C_j^{(2)}(t)\psi_j(x,y,z), \quad u_{3\ell} = \sum_{k=1}^{\ell} C_k^{(3)}(t)\chi_k(x,y,z) \tag{13}$$

The essence of the method of successive approximations is following: First, we solve the linear equation, putting $R_1^*=0,\ R_2^*=0$ and $R_3^*=0$. For this purpose let us substitute (13) into (12) and (10) and apply the Bubnov-Galerkin procedure [9]. Taking into account that each σ_{ij} is the function of u_1,u_2,u_3, we finally obtain the following system of linear ordinary differential equations,

$$A\frac{d^2C}{dt^2}+BC=F \tag{14}$$

The system (14) can be solved upon special initial conditions

$$C\big|_{t=0}=C_0(x,y,z),\quad \dot{C}\Big|_{t=0}=\dot{C}_0(x,y,z) \tag{15}$$

Here

$$A=\begin{pmatrix}A_1&0&0\\0&A_2&0\\0&0&A_3\end{pmatrix},\quad B=\begin{pmatrix}B_1&0&0\\0&B_2&0\\0&0&B_3\end{pmatrix},\quad F=\begin{pmatrix}F_{1i}\\F_{2j}\\F_{3k}\end{pmatrix},\ C=\begin{pmatrix}C_{1i}\\C_{2i}\\C_{3i}\end{pmatrix},$$

$$A_1=\left(a_{ij}^{(1)}\right),\ a_{ij}^{(1)}=\left\{\iiint\limits_V \rho H_1H_2H_3\,u_{1i}u_{1j}dV\right\},\ i=\overline{1,n},\ j=\overline{1,n};$$

$$A_2=\left(a_{ij}^{(2)}\right),\ a_{ij}^{(2)}=\left\{\iiint\limits_V \rho H_1H_2H_3\,u_{2i}u_{2j}dV\right\},\ i=\overline{1,m},\ j=\overline{1,m};$$

$$A_3=\left(a_{ij}^{(3)}\right),\ a_{ij}^{(3)}=\left\{\iiint\limits_V \rho H_1H_2H_3\,u_{3i}u_{3j}dV\right\},\ i=\overline{1,\ell},\ j=\overline{1,\ell}.$$

$$B_1=\left\{b_{ij}^{(1)}\right\},B_2=\left\{b_{ij}^{(2)}\right\},B_3=\left\{b_{ij}^{(3)}\right\}$$

$$b_{ij}^{(1)}=\left\{\iiint\limits_V\left[-\frac{\partial}{\partial x_1}(H_2H_3\sigma_{11}^L(u_{1n},u_{2m},u_{3k}))-\frac{\partial}{\partial x_2}(H_1H_3\sigma_{12}^L(u_{1n},u_{2m},u_{3k}))-\right.\right.$$
$$-\frac{\partial}{\partial x_3}(H_1H_2\sigma_{13}^L(u_{1n},u_{2m},u_{3k}))+\sigma_{22}^L(u_{1n},u_{2m},u_{3k})H_3\frac{\partial H_1}{\partial x_1}+\sigma_{33}^L(u_{1n},u_{2m},u_{3k})H_2\frac{\partial H_3}{\partial x_1}-$$
$$\left.\left.-\sigma_{12}^L(u_{1n},u_{2m},u_{3k})H_3\frac{\partial H_1}{\partial x_2}-\sigma_{13}^L(u_{1n},u_{2m},u_{3k})H_2\frac{\partial H_1}{\partial x_3}\right]u_{1j}dV\right\},\quad i=1,2,...,n+m+k,\quad j=\overline{1,n}$$

$$b_{ij}^{(2)}=\left\{\iiint\limits_V\left[-\frac{\partial}{\partial x_1}(H_2H_3\sigma_{21}^L(u_{1n},u_{2m},u_{3k}))-\frac{\partial}{\partial x_2}(H_3H_1\sigma_{22}^L(u_{1n},u_{2m},u_{3k}))-\right.\right.$$
$$-\frac{\partial}{\partial x_3}(H_2H_1\sigma_{23}^L(u_{1n},u_{2m},u_{3k}))+\sigma_{33}^L(u_{1n},u_{2m},u_{3k})H_1\frac{\partial H_3}{\partial x_2}+\sigma_{11}^L(u_{1n},u_{2m},u_{3k})H_3\frac{\partial H_1}{\partial x_2}$$
$$\left.\left.-\sigma_{23}^L(u_{1n},u_{2m},u_{3k})H_1\frac{\partial H_2}{\partial x_3}-\sigma_{21}^L(u_{1n},u_{2m},u_{3k})H_3\frac{\partial H_2}{\partial x_1}\right]u_{2j}dV\right\},\quad i=1,2,...,n+m+k,\quad j=\overline{1,m}$$

$$b_{ij}^{(3)}=\left\{\iiint\limits_V\left[-\frac{\partial}{\partial x_1}(H_2H_3\sigma_{31}^L(u_{1n},u_{2m},u_{3k}))-\frac{\partial}{\partial x_2}(H_1H_3\sigma_{32}^L(u_{1n},u_{2m},u_{3k}))-\right.\right.$$

$$-\frac{\partial}{\partial x_3}(H_1H_2\sigma_{33}^L(u_{1n},u_{2m},u_{3k}))+\sigma_{11}^L(u_{1n},u_{2m},u_{3k})H_2\frac{\partial H_1}{\partial x_3}+\sigma_{22}^L(u_{1n},u_{2m},u_{3k})H_1\frac{\partial H_2}{\partial x_3}-$$

$$\left.\left.-\sigma_{13}^L(u_{1n},u_{2m},u_{3k})H_2\frac{\partial H_3}{\partial x_1}-\sigma_{23}^L(u_{1n},u_{2m},u_{3k})H_1\frac{\partial H_3}{\partial x_2}\right]u_{3j}dV\right\},\quad i=1,2,...,n+m+k,\quad j=\overline{1,k}$$

$$F_{1i}=\left\{\iiint\limits_V P_1\ u_{1i}dV\right\},\quad i=\overline{1,n},F_{2j}=\left\{\iiint\limits_V P_2\ u_{2j}dV\right\},\quad j=\overline{1,m},F_{3k}=\left\{\iiint\limits_V P_3\ u_{3k}dV\right\},\quad k=\overline{1,\ell}.$$

$$C_{si0}=T_{s0}^{-1}U_{s0},\quad T_{10}=\left\{\iiint\limits_V u_{1i}u_{1j}dV\right\},\quad U_{s0}=\left\{\iiint\limits_V u_{s0}u_{si}dV\right\},\quad s=1:i=\overline{1,n},\quad j=\overline{1,n};$$

$$s=2:i=\overline{1,m},\quad j=\overline{1,m};s=1:i=\overline{1,l},\quad j=\overline{1,l};$$

$$\dot{C}_{si0}=\dot{T}_{s0}^{-1}\dot{U}_{s0},\quad \dot{T}_{s0}=\left\{\iiint\limits_V \dot{u}_{si}u_{sj}dV\right\},\quad \dot{U}_{s0}=\left\{\iiint\limits_V \dot{u}_{s0}u_{si}dV\right\},s=1:i=\overline{1,n},\quad j=\overline{1,n};$$

$$s=2:i=\overline{1,m},\quad j=\overline{1,m};s=1:i=\overline{1,l},\quad j=\overline{1,l};$$

$$\dim(B_1)=(n+m+\ell)\times n,\ \ \dim(B_2)=(n+m+\ell)\times m,\ \ \dim(B_3)=(n+m+\ell)\times \ell,$$
$$\dim(A_1)=n\times n,\quad \dim(A_2)=m\times m,\quad \dim(A_3)=\ell\times\ell,$$
$$\dim(F_{1i})=1\times n,\quad \dim(F_{2j})=1\times m,\quad \dim(F_{3k})=1\times\ell.$$

Hence, we obtain the vector C of unknown functions. Knowing values C we can calculate values $(u_{1n}^{(0)},u_{2m}^{(0)},u_{3k}^{(0)})$ by formulas (13) and hence the values $u_{1n}^{(0)}$, $u_{2m}^{(0)}$ and $u_{3k}^{(0)}$.and the values $R_1^*(u_{1n}^{(0)},u_{2m}^{(0)},u_{3k}^{(0)})$, $R_2^*(u_{1n}^{(0)},u_{2m}^{(0)},u_{3k}^{(0)})$, $R_3^*(u_{1n}^{(0)},u_{2m}^{(0)},u_{3k}^{(0)})$. These values and values $R_i^*(i=\overline{1,3})$ are substituted into (12). Applying the Bubnov-Galerkin procedure we obtain the following system of ordinary linear differential equations:

$$A\frac{d^2C^{(1)}}{dt^2}+BC^{(1)}=F+R^*\left(u_{1n}^{(0)},\ u_{2m}^{(0)},\ u_{3\ell}^{(0)}\right),\tag{16}$$

which are supplemented by condition (15).

Here

$$R^*=\begin{pmatrix}R_1^*\left(u_{1n}^{(0)},u_{2m}^{(0)},u_{3k}^{(0)}\right)\\ R_2^*\left(u_{1n}^{(0)},u_{2m}^{(0)},u_{3k}^{(0)}\right)\\ R_3^*\left(u_{1n}^{(0)},u_{2m}^{(0)},u_{3k}^{(0)}\right)\end{pmatrix}$$

On the following step we determine the unknown function $C^{(1)}$ and hence the values $u_{1n}^{(1)},u_{2m}^{(1)},u_{3k}^{(1)}$. This process continues until an acceptable solution is found. When we have *i*-th iteration step, the equation (16) takes the form

$$A\frac{d^2C^{(i)}}{dt^2}+BC^{(i)}=F+R^*\left(u_{1n}^{(i-1)},\,u_{2m}^{(i-1)},\,u_{3\ell}^{(i-1)}\right) \qquad (17)$$

The rate of convergence of simple iterations is directly related to the choice of initial approximation. Therefore, in order to improve the convergence rate we use extrapolation method described in reference [7].

Conclusion

Thus, we have constructed a mathematical model of nonlinear vibrations problem for three-dimensional elastic and elastoplastic bodies and suggested algorithms of its implementation on the base of the method of successive approximations. The proposed approach may be used for solving both static and dynamic nonlinear problems for three-dimensional bodies with a complex shape.

REFERENCES

[1] Kabulov V.K. *Algorithmic in elasticity and the deformation theory of plasticity*, Tashkent, Fan, 1966 (in Russian).
[2] Kabulov V.K Faizullaev O.Kh., Nazirov S.A. *AlKhorezm,algorithm,algorithmic*, Tashkent, Fan, 2006.
[3] Vasidzu K. *Variational methods in elasticity and plasticity*, Academic Press, 1987.
[4] Novozhilov V.V. *Fundamentals of nonlinear elasticity*, Leningrad, GITTL, 1948 (in Russian).
[5] Nazirov S.A. A three-dimensional mathematical model of deformable solid bodies's mechanics *Problems of Computational and Applied Mathematics*, Issue 128, Tashkent, 2012, pp.14-46, 2012.
[6] Nazirov S.A. A three-dimensional model of the theory of elasticity and plasticity *Proc. of the Int. Conference "Actual Problems of Applied Mathematics and Information Technology, Al-Khwarizmi 2012"*, Vol. 2, Tashkent., pp. 70-76, 2012.
[7] Rvachev V.L. *Theory of R-functions and some of its applications*, Kiev, Naukova Dumka, 1981 (in Russian).
[8] Rvachev V.L, Kurpa L.V. *R-functions in the theory of plates*, Kiev, Naukova Dumka, 1987 (in Russian).
[9] Mikhlin S.G. *Variational methods in mathematical physics* Moscow, Nauka, 1970 (in Russian).

Proceedings of the 4th International Conference on Nonlinear Dynamics
ND-KhPI2013
June 19-22, 2013, Sevastopol, Ukraine

Mathematical Models of Nonlinear Vibrations of Thin Shells and Plates in a Magnetic Field

Nazirov Sh.A.[1*], Nuraliev F.M.[1]

Abstract
Basic equations of the magnetoelastic theory of thin shells and plates are derived.. To construct specific models we apply principle by Hamilton-Ostrogradskiy, Kirchhoff-Love theory of thin shells and plates, geometrically nonlinear Cauchy relations and physical relationships in the reverse form to Hooke's law. The ponderomotive force of the electromagnetic field is expressed by Lorentz presentation.

Keywords
Mathematical model, magneto-elasticity, thin shell and plate

[1]Tashkent University of Information Technologies, Tashkent, Uzbekistan
[*]**Scorresponding author:** shnazirov@mail.ru

1. Total Governing equations

In order to obtain the movement equations of magneto-elasticity theory of thin shells and plates we apply the classical approach based on variational principle of Hamilton-Ostrogradskiy [1]. Assume that Kirchhoff-Law hypothesis for thin shells and plates, geometrical Cauchy relations and physical correlation in inverse form to Hooke's law are fulfilled. Representation of ponderomotive forces of electromagnetic field is carried out by Lorentz expressions. [2]. Cartesian system of coordinates is used to obtain movement equations. Then it is possible to show that equations of motion for shells and boundary conditions have the following form:

$$
\begin{aligned}
&-\rho h\frac{\partial^2 U}{\partial t^2}+\frac{\partial N_{11}}{\partial x}+\frac{\partial N_{12}}{\partial y}+N_x+R_x+q_x+T_{zx}=0,\\
&-\rho h\frac{\partial^2 V}{\partial t^2}+\frac{\partial N_{12}}{\partial x}+\frac{\partial N_{22}}{\partial y}+N_y+R_y+q_y+T_{zy}=0,\\
&-\rho h\frac{\partial^2 W}{dt^2}+\frac{\partial^2 M_{11}}{dx^2}+\frac{\partial^2 M_{12}}{dxdy}+\frac{\partial^2 M_{22}}{\partial y^2}+N_{11}\frac{\partial^2 w}{\partial x^2}+N_{22}\frac{\partial^2 w}{\partial y^2}+2N_{12}\frac{\partial^2 w}{\partial x\partial y}+Q_z+R_z-\frac{\partial}{\partial x}(M_x+M_{Rx})-\\
&-\frac{\partial}{\partial y}(M_y+M_{Ry})+q_z+T_{zz}+\frac{\partial}{\partial x}(M^+_{qx}+M^-_{qx}+M^+_{Tzx}+M^-_{Tzx})+\frac{\partial}{\partial y}(M^+_{qy}+M^-_{qy}+M^+_{Tzy}+M^-_{Tzy})=0,
\end{aligned}
\tag{1}
$$

Natural boundary conditions are:

$$
\begin{aligned}
&(-N_{11}+N_{Px}+N_{Txx})\delta U\big|_x=0,(-N_{12}+N_{Py}+N_{Txy})\delta V\big|_x=0,\\
&(-\frac{h^3}{12}\frac{\partial^2 W}{\partial x dt}-\frac{\partial M_{11}}{\partial x}-\frac{\partial M_{12}}{\partial y}+Q_{Pz}+Q_{Txz}-M^-_{qx}-M^-_{qx}-M^+_{Tzx}-M^-_{Tzx})\delta W\big|_x=0,\\
&(M_{11}-M_{Px}-M_{Txx})\delta\frac{\partial W}{\partial x}\big|_x=0,\ (-M_{12}-M_{Py}-M_{Txy})\delta\frac{\partial W}{\partial y}\big|_x=0,
\end{aligned}
\tag{2}
$$

$$(-M_{12}-M_{Py}-M_{Txy})\delta\frac{\partial W}{\partial y}\Big|_x=0,\ (-N_{12}+N_{Fx}+N_{Tyx})\delta U\Big|_y=0,$$

$$(-N_{22}+N_{Fy}+N_{Tyy})\delta V\Big|_y=0,$$

$$(-\frac{h^3}{12}\frac{\partial^2 W}{\partial y\partial x}-\frac{\partial M_{12}}{\partial x}-\frac{\partial M_{22}}{\partial y}+Q_{Fz}+Q_{Tyz}-M_{qy}^{+}-M_{qy}^{-}-M_{Tzy}^{+}-M_{Tzy}^{-})\delta W\Big|_y=0,$$

$$(M_{12}-M_{Fx}-M_{Tyx})\delta\frac{\partial W}{\partial x}\Big|_y=0,\ (M_{22}-M_{Fy}-M_{Tyy})\delta\frac{\partial W}{\partial y}\Big|_y=0,$$

where

$$N_{11}=\int_z\sigma_{11}dz,\ M_{11}=\int_z z\sigma_{11}dz,\ N_{12}=\int_z\sigma_{12}dz,\ M_{12}=\int_z z\sigma_{12}dz,\ N_{22}=\int_z\sigma_{22}dz,$$

$$M_{22}=\int_z z\sigma_{22}dz,$$

$$N_x=\int_z Xdz,\ M_x=\int_z zXdz,\ N_y=\int_z Ydz,\ M_y=\int_z zYdz,\ Q_z=\int_z Zdz,\ R_x=\int_z\rho K_x dz,$$

$$M_{Rx}=\int_z z\rho K_x dz,\ R_y=\int_z\rho K_y dz,\ M_{Ry}=\int_z z\rho K_y dz,\ R_z=\int_z\rho K_z dz,$$

$$M_{qx}^{+}=q_x^{+}(\frac{h}{2}),\ \boldsymbol{M_{qx}^{-}=q_x^{-}(-\frac{h}{2})},\ M_{qy}^{+}=q_y^{+}(\frac{h}{2}),\ M_{qy}^{-}=q_y^{-}(-\frac{h}{2}),$$

$$M_{Tzx}^{+}=T_{zx}^{+}(\frac{h}{2}),\ M_{Tzx}^{-}=T_{zx}^{-}(-\frac{h}{2}),\ M_{Tzy}^{+}=T_{zy}^{+}(\frac{h}{2}),\ M_{Tzy}^{-}=T_{zy}^{-}(-\frac{h}{2}),$$

$$N_{Px}=\int_z P_x dz,\ M_{Px}=\int_z zP_x dz,\ N_{Py}=\int_z P_y dz,\ M_{Py}=\int_z P_y dz,\ Q_{Pz}=\int_z P_z dz,\ N_{Txx}=\int_z T_{xx}dz,$$

$$M_{Txx}=\int_z zT_{xx}dz,\ N_{Txy}=\int_z T_{xy}dz,\ M_{Txy}=\int_z zT_{xy}dz,\ Q_{Txz}=\int_z T_{xz}dz,\ N_{Fx}=\int_z F_x dz,\ M_{Fx}=\int_z zF_x dz,$$

$$N_{Fy}=\int_z F_y dz,\ M_{Fy}=\int_z zF_y dz,\ Q_{Fz}=\int_z F_z dz,\ N_{Tyx}=\int_z T_{yx}dz,\ M_{Tyx}=\int_z zT_{yx}dz,\ N_{Tyy}=\int_z T_{yy}dz,$$

$$M_{Tyy}=\int_z zT_{yy}dz,\ Q_{Tyz}=\int_z T_{yz}dz.$$

The body forces of electromagnetic origin are included into the total volume forces [5,6], in the form

$$f=\rho\mathrm{K}=\frac{1}{4\pi}(\mathrm{rot}(\,\mathrm{rot}\,(\mathrm{UxH})))\mathrm{xH}, \tag{3}$$

where *H (Hx, Hy, Hz)* is the magnetic field vector.

In order to complete the derivation we should add surface and contour forces described by Maxwell electromagnetic stress tensors [2, 5, 6]

$$T_{ik}=\frac{1}{4\pi}\left[H_i h_k+h_i H_k\right]-\frac{б_{ik}}{4\pi}\vec{h}\vec{H},\ T_{ik}^{e}=\frac{1}{4\mu\pi}\left[H_i^e h_k^e+h_i^e H_k^e\right]-\frac{б_{ik}}{4\pi}\vec{h}^{e}\vec{H}^{e}. \tag{4}$$

Here $б_{ik}=\begin{cases}0, i\neq k,\\ 1, i=k.\end{cases}$

2. Mathematical models of magneto-elasticity of thin plates

As a particular case we can obtain mathematical models of vibration problem for isotropic plate made of a material with finite electrical conductivity provided that an external magnetic field has given intensity. These equations are

$$\begin{aligned}
&\rho_0 \frac{\partial^2 u}{\partial t^2} - \frac{\partial N_x}{\partial x} + \frac{\partial N_{xy}}{\partial y} + P_x + q_x = 0 \\
&\rho_0 \frac{\partial^2 v}{\partial t^2} - \frac{\partial N_{xy}}{\partial x} + \frac{\partial N_y}{\partial y} + P_y + q_y = 0 \\
&\rho_0 \frac{\partial^2 w}{\partial t^2} + D\nabla^4 w - \frac{\partial m_x}{\partial x} - \frac{\partial m_y}{\partial y} + N_x \frac{\partial^2 w}{\partial x^2} + N_y \frac{\partial^2 w}{\partial y^2} + 2N_{xy} \frac{\partial^2 w}{\partial x \partial y} + P_z + q_z = 0
\end{aligned} \tag{5}$$

where

$$P_x = \int_{-d}^{d} f_x dz, \quad P_y = \int_{-d}^{d} f_y dz, \quad P_z = \int_{-d}^{d} f_z dz, \quad m_x = \int f_x z dz, \quad m_y = \int f_y z dz$$

3. Mathematical models magneto-elasticity of thin shells

Similarly we can obtain nonlinear motion equations for thin shallow shells.

By relation (6) the components of body forces of electromagnetic origin and their moments are as follows:

$$P_x := \frac{h}{4\pi}\left(\left(\left(k_1 \frac{\partial u}{\partial y} - \frac{1}{A_1}\frac{\partial^2 w}{\partial y \partial x}\right)H_y - \left(k_2 \frac{\partial v}{\partial y} - \frac{1}{A_2}\frac{\partial^2 w}{\partial y^2}\right)H_x - \frac{\partial^2 w}{\partial x^2}H_x + \frac{\partial^2 u}{\partial x^2}H_z + \frac{\partial^2 v}{\partial x \partial y}H_z - \frac{\partial^2 w}{\partial y \partial x}H_y\right)H_z - \right.$$
$$\left. - \left(\left(k_2 \frac{\partial v}{\partial x} - \frac{1}{A_2}\frac{\partial^2 w}{\partial y \partial x}\right)H_z - \frac{\partial^2 u}{\partial x^2}H_y + \frac{\partial^2 v}{\partial x^2}H_x - \frac{\partial^2 u}{\partial y^2}H_y + \frac{\partial^2 v}{\partial y^2}H_x - \left(k_1 \frac{\partial u}{\partial y} - \frac{1}{A_1}\frac{\partial^2 w}{\partial y \partial x}\right)H_z\right)H_y\right)$$

$$P_y := \frac{h}{4\pi}\left(\left(\left(k_2 \frac{\partial v}{\partial x} - \frac{1}{A_2}\frac{\partial^2 w}{\partial y \partial x}\right)H_z - \frac{\partial^2 u}{\partial x^2}H_y + \frac{\partial^2 v}{\partial x^2}H_x - \frac{\partial^2 u}{\partial x^2}H_y + \frac{\partial^2 w}{\partial y^2}H_x - \left(k_1 \frac{\partial u}{\partial y} - \frac{1}{A_1}\frac{\partial^2 w}{\partial y \partial x}\right)H_z\right)H_x - \right.$$
$$\left. - \left(\frac{\partial^2 w}{\partial x \partial y}H_x - \frac{\partial^2 w}{\partial y \partial x}H_z + \left(k_1 \frac{\partial u}{\partial x} - \frac{1}{A_1}\frac{\partial^2 w}{\partial y \partial x}\right)H_y - \frac{\partial^2 v}{\partial y^2}H_z + \frac{\partial^2 w}{\partial y^2}H_y - \left(k_2 \frac{\partial v}{\partial x} - \frac{1}{A_2}\frac{\partial^2 w}{\partial y \partial x}\right)H_x\right)H_x\right)$$

$$P_z := \frac{h}{4\pi}\left(\left(\left(k_2 \frac{\partial v}{\partial x} - \frac{1}{A_2}\frac{\partial^2 w}{\partial y \partial x}\right)H_z - \frac{\partial^2 u}{\partial x^2}H_y + \frac{\partial^2 v}{\partial x^2}H_x - \frac{\partial^2 u}{\partial y^2}H_y + \frac{\partial^2 v}{\partial y^2}H_x - \left(k_1 \frac{\partial u}{\partial y} - \frac{1}{A_1}\frac{\partial^2 w}{\partial x \partial y}\right)H_z\right)H_x - \right.$$
$$\left. - \left(\frac{\partial^2 w}{\partial x \partial y}H_x - \frac{\partial^2 u}{\partial y \partial x}H_z + \left(k_2 \frac{\partial u}{\partial x} - \frac{1}{A_1}\frac{\partial^2 w}{\partial x^2}\right)H_y - \frac{\partial^2 v}{\partial y^2}H_z + \frac{\partial^2 w}{\partial y^2}H_y - \left(k_2 \frac{\partial v}{\partial x} - \frac{1}{A_2}\frac{\partial^2 w}{\partial y \partial x}\right)H_x\right)H_z\right)$$

$$m_x := \frac{h^3}{48\pi}\left(\left(\left(k_1 \frac{\partial^2 u}{\partial x^2} - \frac{1}{A_1}\frac{\partial^3 w}{\partial x^3}\right)H_z - \left(k_2 \frac{\partial^2 v}{\partial y \partial x} - \frac{1}{A_2}\frac{\partial^3 w}{\partial y^2 \partial x}\right)H_z\right)H_z - \right.$$
$$\left. - \left(\left(k_1 \frac{\partial^2 u}{\partial x^2} - \frac{1}{A_1}\frac{\partial^3 w}{\partial x^3}\right)H_y + \left(k_2 \frac{\partial^2 v}{\partial x^2} - \frac{1}{A_2}\frac{\partial^3 w}{\partial y \partial x^2}\right)H_x - \left(k_1 \frac{\partial^2 u}{\partial y^2} - \frac{1}{A_1}\frac{\partial^3 w}{\partial y^2 \partial x}\right)H_y + \left(k_2 \frac{\partial^2 v}{\partial y^2} - \frac{1}{A_2}\frac{\partial^3 w}{\partial y^3}\right)H_x\right)H_y\right)$$

$$m_y := \frac{h^3}{48\pi}\left(\left(-\left(k_1 \frac{\partial^2 u}{\partial x^2} - \frac{1}{A_1}\frac{\partial^3 w}{\partial x^3}\right)H_y + \left(k_2 \frac{\partial^2 v}{\partial x^2} - \frac{1}{A_2}\frac{\partial^3 w}{\partial y \partial x^2}\right)H_x - \left(k_1 \frac{\partial^2 u}{\partial y^2} - \frac{1}{A_1}\frac{\partial^3 w}{\partial y^2 \partial x}\right)H_y + \left(k_2 \frac{\partial^2 v}{\partial y^2} - \frac{1}{A_2}\frac{\partial^3 w}{\partial y^3}\right)H_x\right)H_x - \right.$$
$$\left. - \left(-\left(k_2 \frac{\partial^2 v}{\partial y^2} - \frac{1}{A_2}\frac{\partial^3 w}{\partial x^3}\right)H_z + \left(k_1 \frac{\partial^2 u}{\partial x \partial y} - \frac{1}{A_1}\frac{\partial^3 w}{\partial y \partial x^2}\right)H_z\right)H_z\right)$$

Substituting these expressions into equations (1) we get non-linear system of differential equations of the motion for magneto - elastic thin shallow shells. The system supplemented by boundary and initial conditions. To solve the resulting problems iterative algorithm is developed. This

algorithm is based on combined application of the method by Bubnov-Galerkin and structure method of R-functions [8-10]. We will develop corresponding software to implement proposed approach.

References

[1] Kabulov V.K. *An Algorithmic Theory of Elasticity and the Deformation Theory of Plasticity* Tashkent, Fan, 1979 (in Russian).
[2] Tamm I.E. *Fundamentals of the Theory of Electricity* Moscow, Nauka, 1966 (in Russian).
[3] Leibenzon L.S. *Course in the Theory of Elasticity* Moscow, GITTL, 1947 (in Russian).
[4] Volmir A.S. *Nonlinear Dynamics of Plates and Shells* Moscow, Nauka, 1972 (in Russian).
[5] Rakhmatulin K.A., ShkenevY.S. *Interaction Environments and Fields* Tashkent, Fan, 1985 (in Russian).
[6] Ambartsumian S.A., Bagdasarian G.E.,Belubekyan M.V. *Magneto-Elasticity of the Thin Shells and Plates* Moscow, Nauka, 1977 (in Russian).
[7] Harness V.M. Mathematical and computer modeling of nonlinear free vibration of elastic thin shells step-variable thickness. *Civil Engineering Journal,* N1, 2010, pp. 38-49.
[8] Rvachev V.L. *Theory of R-function and some its Applications* Kiev, NaukovaDumka, 1987 (in Russian).
[9] Kurpa L.V. *R-functions Method for Solving Linear and Bending Vibrations of Thin Shells* Kharkov, NTU "KPI", 2009 (in Russian).
[10] Kurpa L.V. Nonlinear free vibrations of thin shells symmetric multilayer structure with a complex shape plan *Mat. Methodical Fiz.-Mech. Field, V.* 51 (2), pp. 75-85, 2008 (in Russian).

Proceedings of the 4th International Conference on Nonlinear Dynamics
ND-KhPI2013
June 19-22, 2013, Sevastopol, Ukraine

Using 2-D Padé Approximants in Nonlinear Dynamics of Shells

Victor I. Olevs'kyy[1*], Igor V. Andrianov[2]

Abstract
We discuss a use of two-dimensional Padé approximants for meromorphic continuation of approximate solutions obtained by the method of artificial parameter for the nonlinear oscillations of shells. Method simplifies the determination of the period of oscillation for nonlinear structures.

Keywords
Padé approximants, artificial parameter, shell, nonlinear dynamics

[1] Ukrainian state chemistry and technology university, Dnipropetrovs'k, Ukraine
[2] RWTH Aachen University, Germany
* **Corresponding author:** volevnew@gmail.com

Introduction

Wide usage of lightweight constructions requires new complex calculation schemes for extremely thin walled shells. Their behavior is nonlinear, mostly, and thus development of new calculation methods is topical. Analytic solution of shells dynamics equations leads to expressions in form of power series. The problem of convergence of such series, especially in a case of artificial parameter, is often solved by means of general summation. One of the most efficient methods of general summation is the method of Padé approximants [1]. There is shown earlier [2], that the best results are produced by special kind of perturbation of equations and boundary conditions combining with 2-D Padé approximants in form by V. Vavilov. This form of the modified method of continuation by parameter (MMCP) provides an existence and convergence for meromorphic continuation of approximate solutions.

Theory of dynamics of shells is usually applied for technical purposes. There are some technical parameters, which are usually used for analysis of vibrations: frequency, period, amplitude, etc. They are the result of usage of methods based on representation of approximate solutions by means of trigonometric functions. Such representation is a common and occurs from classical form of solution for linear vibrations with small amplitude [1]. Classical perturbation approaches, such as the Lindstedt – Poincaré, van der Pol, Krylov – Bogolyubov methods are based on the use of small parameter. Contrary to the classical methods, MMCP leads to power series both by time and artificial parameter and is not restricted by the smallness of them [2]. In this paper we demonstrate that parameters of vibration can be found easy and accurately using even first few terms of MMCP without of any additional methods.

1. Model Example

Let's consider Duffing equation as a model example. This equation with initial conditions can be written in the following form

$$\begin{aligned} &\ddot{u} + u + \varepsilon u^3 = 0 \\ &u(0) = a \quad \dot{u}(0) = 0 \end{aligned} \tag{1}$$

Oscillations in this case are not isochronous [1]. Using of classic perturbation procedure leads to isochronous solution with secular terms. It is not appropriate on the whole time axe. For small nonlinearity and amplitude it can be used the Lindstedt - Poincaré method to construct appropriate approximate solution in term of trigonometric series in the form

$$u = a\cos(\omega t) + \frac{\varepsilon a^2}{32}\cos(3\omega t) + O\left(\varepsilon^2\right) \tag{2}$$

where circle frequency is found in the form

$$\omega = 1 + \frac{3}{8}\varepsilon a^2 - \frac{51}{256}\left(\varepsilon a^2\right)^2 + O\left(\varepsilon^3\right) \tag{3}$$

Thus period of oscillation T is

$$T \approx \frac{2\pi}{1 + \frac{3}{8}\varepsilon a^2 - \frac{51}{256}\left(\varepsilon a^2\right)^2} \tag{4}$$

The same result can be found using methods of stretched coordinates or averaging [1]. Everyone can see that it is not so easy to implement those methods even for so simple example. Moreover, initial conditions in (1) are satisfied approximately only: $u(0) = a + \varepsilon a^2/32 + O\left(\varepsilon^2\right)$.

On the other hand, MMPC solves this problem in the direct way. Let's involve artificial parameter ε_1 in form

$$\begin{gathered} \ddot{u} + \varepsilon_1\left(u + \varepsilon u^3\right) = 0 \quad u = \sum_{i=0}^{\infty} u_i \varepsilon_1^i \\ u_0(0) = a \;\; \dot{u}_0(0) = u_i(0) = \dot{u}_i(0) = 0 \quad i = \overline{1,\infty} \end{gathered} \tag{5}$$

We can get approximation in form

$$u \approx a - a\frac{\left(1 + \varepsilon a^2\right)}{2}\varepsilon_1 t^2 + a\frac{\left(1 + \varepsilon a^2\right)\left(1 + 3\varepsilon a^2\right)}{24}\varepsilon_1^2 t^4 \tag{6}$$

2-D Padé when $\varepsilon_1 = 1$ give us such approximation, exactly satisfied initial conditions

$$u \approx a\frac{12 - \left(5 + 3\varepsilon a^2\right)t^2}{12 + \left(1 + 3\varepsilon a^2\right)t^2} \tag{7}$$

Let's find quarter of period as first zero of this approximation

$$\frac{T}{4} \approx \frac{2\sqrt{3}}{\sqrt{5 + 3\varepsilon a^2}} \tag{8}$$

Behavior of corresponding approximations for measureless ratio of movements (3) (solid curves) and (7) (dashed curves) to initial amplitude $\bar{u}$ is shown on fig. 1. The numbers near curves correspond to values of parameter εa^2. Comparison between find periods according to (4) (solid curve) and (8) (dashed curve) is shown on fig. 2. They demonstrate good agreement in whole domain

under consideration. It worse mentioned, that near $\varepsilon a^2 \approx 1.4889$ additional terms in (3) are equal to the circle frequency of linear pendulum and so can't be treated as "small".

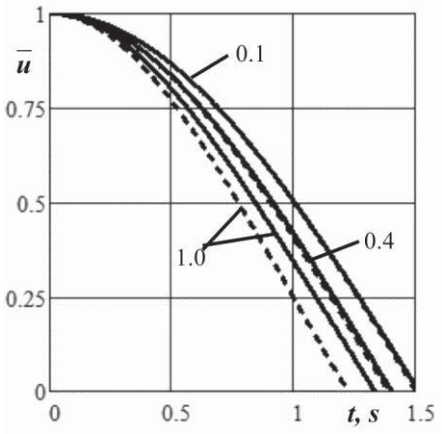

Figure 1. The movement response

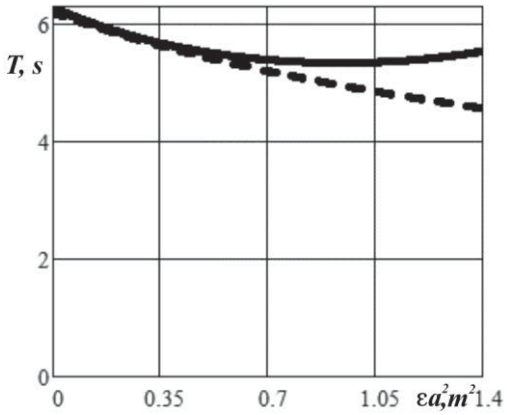

Figure 2. The period response

2. Free Nonlinear Vibration of Stringer Shell

Let's consider free vibration of a flexible elastic circular cylindrical shell of radius *R,* thickness *h* and length *L,* reinforced by a set of uniformly distributed stringers having a simple support at the ends (fig. 3). Shell is considered as the structurally-orthotropic one [1].

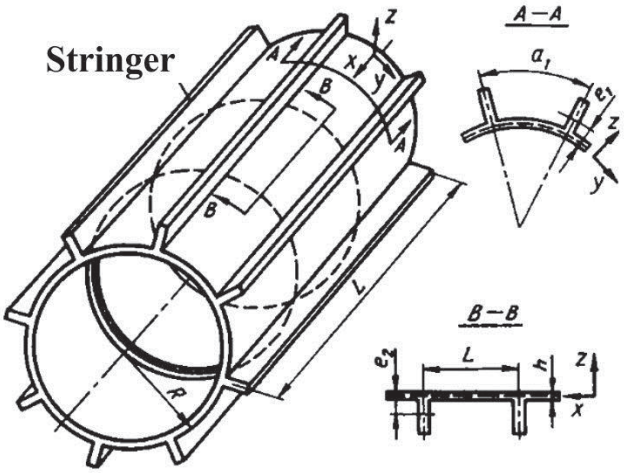

Figure 3. Scheme of the stringer shell

The calculation is based on mixed dynamical equations of the theory of shells after splitting them in powers of natural small parameters [3]. The shape of radial deflection w satisfies the boundary conditions given in the form

$$w = f_1(t)\sin(s_1 x_1)\cos(s_2 x_2) + f_2(t)\sin^2(s_1 x_1) \tag{9}$$

Here functions f_1 and $f_2 = 0,25R^{-1}s_2^2 f_1^2$ are related by the condition of continuity of displacements, the parameters $s_1 = \pi m l^{-1}$ and $s_2 = n$ are characterizing the wave generation along the generator and directrix, respectively.

The governing equations can be reduced by the Bubnov – Galerkin method to the Cauchy problem with respect to $\xi = f_1 / R$ on $t_1 = t\sqrt{B_1 / \rho R^2}$ (all symbols are taken in accordance with [3])

$$\begin{gathered} \ddot{\xi} + \alpha\xi\left[\left(\dot{\xi}\right)^2 + \xi\ddot{\xi}\right] + A_1\xi + A_2\xi^3 + A_3\xi^5 = 0 \\ \xi(0) = f\ \dot{\xi}(0) = 0 \end{gathered} \tag{10}$$

The application of the proposed method of parameter continuation to the Cauchy problem (10) gives approximation of the second order for the artificial parameter for frequency Ω of nonlinear oscillations in the form

$$\Omega = \sqrt{\left(1 + f^2(A_2 / A_1) + f^4(A_3 / A_1)\right) / (1 + \alpha f)} \tag{11}$$

and represented on fig. 4 ($\overline{f}$ – normalized amplitude, 1 – according the proposed method, 2 – Lindstedt - Poincaré method [3]).

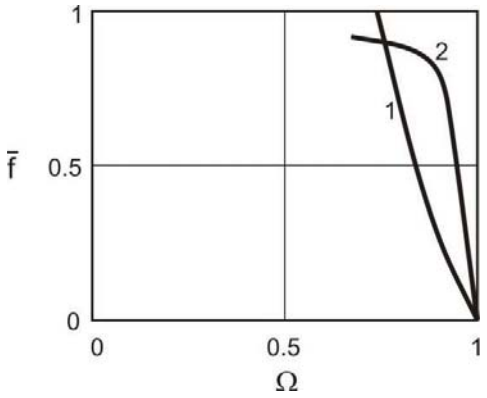

Figure 4. The frequency response

Conclusions

MMCP based on 2-D Padé approximations is an efficient method for recognizing of parameters of nonlinear shell vibrations.

References

[1] Obraztsov I.F., Nerubaylo B.V., Andrianov I.V. *Asymptotic Methods in the Structural Mechanics of Thin-Walled Structures,* Mashinostroyenie, Moscow, 1991 (in Russian).

[2] Andrianov I.V., Olevs'kyy V.I. Critical re-examination of Adomian's decomposition and homotopy perturbation methods in nonlinear mechanics. *Proceedings of the 3-rd International Conference on Nonlinear Dynamics ND-KhPI2010*, Kharkov, Ukraine, pp. 15-20, 2010.

[3] Andrianov I.V., Kholod E.G., Olevsky V.I. Approximate non-linear boundary value problems of reinforced shell dynamics. *J. Sound Vibr.*, 194(3), pp. 369-387, 1996.

Proceedings of the 4th International Conference on Nonlinear Dynamics
ND-KhPI2013
June 19-22, 2013, Sevastopol, Ukraine

Complex Dynamics of Circular Shells

Francesco Pellicano[1]

Abstract
This work analyses some complicated dynamic phenomena that take place when circular shells are excited along the axial direction with an excitation which cannot be considered as an infinite energy source. The interaction between the vibrating system, the shell, and the energy source, the shaker, has shown a surprisingly complex response. A circular cylindrical shells is excited from the bottom and a rigid disk is clamped on the top, allowing a rigid body-like motion. When the excitation is harmonic and resonant with the first axial-symmetric mode a violent resonant phenomenon is experimentally observed and theoretically reproduced, using a nonlinear model for the shell dynamics combined with a model of the electro-mechanic machine used in vibrating the shell base.
The shell model is based on the Sanders-Koiter theory and takes into account geometric nonlinearities and imperfections. An energy approach based on the Lagrange equations combines shell and shaker equations, giving rise to a large set of ODEs, which is solved numerically using high performance time integration algorithms, in order to be able to reproduce both stationary and nonstationary responses.
It is numerically proven that, in some frequency bands, when a sufficient energy is provided, periodic responses do not exist, even though the excitation is harmonic.

Keywords
Nonlinear vibration, Shell

[1] Dept. of Engineering "Enzo Ferrari", Univ. Modena and Reggio Emilia
* **Corresponding author:** francesco.pellicano@unimore.it

Introduction

Several commercial software allow to carry out static, stability and vibration analyses; however, regarding the shell dynamics, such kind of analyses are generally reliable in the linear filed, i.e. very small deformations. Problems like global stability, post-critical behaviours and nonlinear vibrations cannot yet be accurately analysed with commercial software; on such fields there is need of further development of computational models.

Readers interested to deepen the literature are suggested to read Refs.[1-6]: some topics of extreme importance need further investigations: dynamic stability, post-critical behavior, sensitivity to imperfections, nonlinear vibrations and fluid structure interaction.
Kubenko and Koval'chuk [7] published an interesting review on nonlinear problems of shells, where several results were reported about parametric vibrations; in such review the limitations of reduced order models were pointed out.

In Ref. [8] a new method, based on the nonlinear Sanders Koiter theory, suitable for handling complex boundary conditions of circular cylindrical shells and large amplitude of vibrations. The method was based on a mixed expansions considering orthogonal polynomials and harmonic functions. Among the others, the method showed good accuracy also in the case of a shell connected with a rigid body; this method is the starting point for the model developed in the present research.
Mallon et. al [9] studied circular cylindrical shells made of orthotropic material, the Donnell's nonlinear shallow shell theory was used with a multimode expansion for discretization (PDE to ODE). The theoretical model considered also the shaker-shell interaction; such work is strictly related to the present paper for which concern theory and experiments; here a further step toward improved modelling and complete understanding of complex dynamic phenomena is attempted, in addition here experiments show great coherence with theoretical results.

In the present paper, experiments are carried out on a circular cylindrical shell, made of a polymeric material (P.E.T.) and clamped at the base by gluing its bottom to a rigid support. The axis of the cylinder is vertical and a rigid disk is connected to the shell top end.

Nonlinear phenomena are investigated by exciting the shell using a shaking table and a sine excitation. Shaking the shell from the bottom induces a vertical motion of the top disk that causes axial loads due to inertia forces. Such axial loads generally give rise to axial-symmetric deformations; however, in some conditions it is observed experimentally that a violent resonant phenomenon takes place, with a strong energy transfer from low to high frequencies and huge amplitude of vibration. Moreover, an interesting saturation phenomenon is observed: the response of the top disk was completely flat as the excitation frequency was changed around the first axisymmetric mode resonance.

A semi-analytical approach is proposed for reproducing experimental results and giving a deeper interpretation of the observed phenomena. The shell is modelled using the nonlinear Sanders Koiter shell theory; in modelling the system the effect of the top disk was accounted for applying suitable boundary conditions and considering its inertial contribution; moreover, the interaction between the shell-disk and the electro-dynamic shaking table was included in the modelling. The shell displacement fields are represented by means of a mixed series (harmonic functions and orthogonal polynomials), which are able to respect exactly geometric boundary conditions; an energy approach, based on the Lagrangian equations, is used to obtain a set of ODE that represents the original system with good accuracy.

Comparisons between experiments and numerical results show a good behaviour of the model, numerical analyses furnish useful explanations about the instability phenomena that are observed experimentally.

1.1 Experimental setup and results

In the present section the problem under investigation is described by means of experimental results. The description follows the history of the present research, which started from experimental observations that led the author in developing the theoretical model.

1.1.1 The setup

The system under investigation is described in Figures 1 and 2; a circular cylindrical shell, made of a polymeric material (P.E.T.), is clamped at the base by gluing its bottom to a rigid support ("fixture"); the connection is on the lateral surface of the shell, in order to increase the gluing surface, see Figure 1; on the top, the shell is connected to a disk made of aluminium alloy, such disk is not externally constrained; therefore, it induces a rigid body motion to the top shell end.

The system data are the following: $=1366\frac{\text{kg}}{\text{m}^3}$, $=0.4$, $E=46\ \ 10^8\text{N/m}^2$; mass of the top disk 0.82kg. The geometry is: radius R=43.88 10^{-3}m, length L=96 10^{-3}m thickness h=0.25 10^{-3}m.

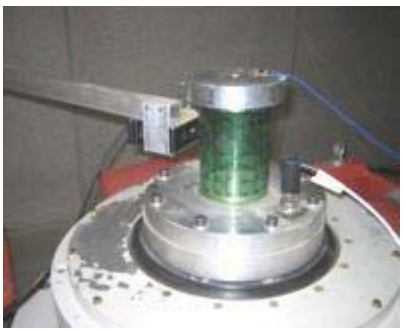

Figure 1. Experimental setup

The fixture is bolted to a high power shaker (LDS V806, 13000N peak force, 100g, 1-3000Hz band frequency).

When the base of the shell is excited by the shaker, a fluctuating vertical move is determined, such base movement results in a seismic-like excitation for the shell; the rigid body motion generates big inertia forces on the top disk that cause an axial shell loading. In particular, the vertical excitation can cause the resonance of the first axisymmetric mode of the shell, Figure 3; therefore, the base excitation can be amplified inducing large axial stresses on the shell.

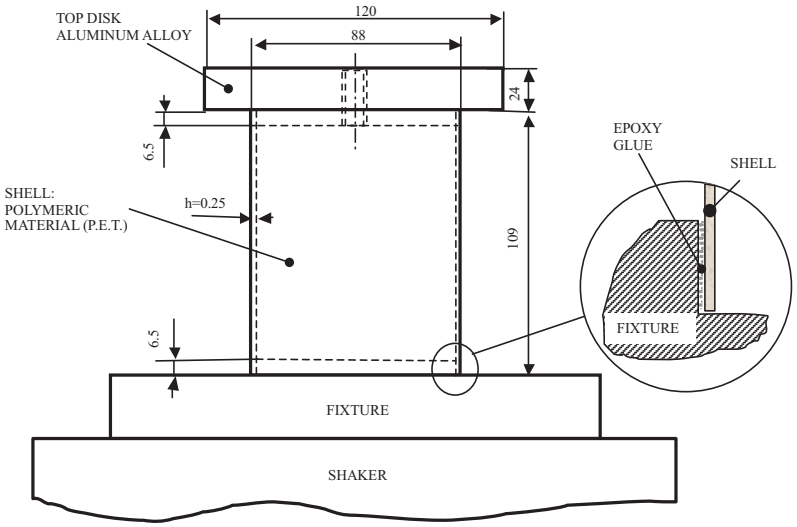

Figure 2. System geometry

1.1.2 Experimental results

Initially, an experimental modal analysis is carried out (about 80 points are considered) in order to extract (identify) natural frequencies, modal damping and mode shapes from experimental data.

The natural frequencies of the system are reported in Table 1, the corresponding mode shapes are represented in Figure 3.

Table 1. Natural frequencies and mode shape description [8].

Mode		Natural frequencies [Hz]				
		Experimental frequency	Theory		Finite elements	
k	n		Frequency	Error %	Frequency	Error%
first beam like mode *n*=1		95	96	1.1	93	2.1
1	0	314	322	2.5	314	0
second beam like mode *n*=1		438	432	2.5	424	3.2
1	6	791	797	0.8	782	1.1
1	7	816	802	1.7	802	1.7
1	5	890	888	0.2	885	0.6
1	8	950	926	2.5	918	3.4
1	9	1069	1016	5.0	1103	3.2

The first three modes of Table 1 present a shape that includes the top disk motion; the second mode (first axisymmetric mode) shows a simple translational motion of the top disk, see Figure 3; shell like modes (modes after the third of Table 1) behave like clamped-clamped shell modes, i.e. the top disk does not move. For the linear theory, shell like modes of a perfect shell are not directly excited by a translational base motion on the shell axis, because the top disk motion cannot pump energy in such modes. The only prediction that could be done using linear models is to consider the time varying axial forces caused by the top mass acceleration, this will lead to a time varying linear system, which could undergo to parametric instabilities of Mathieu type; therefore, linear theories could be able to analyze the instability boundaries only.

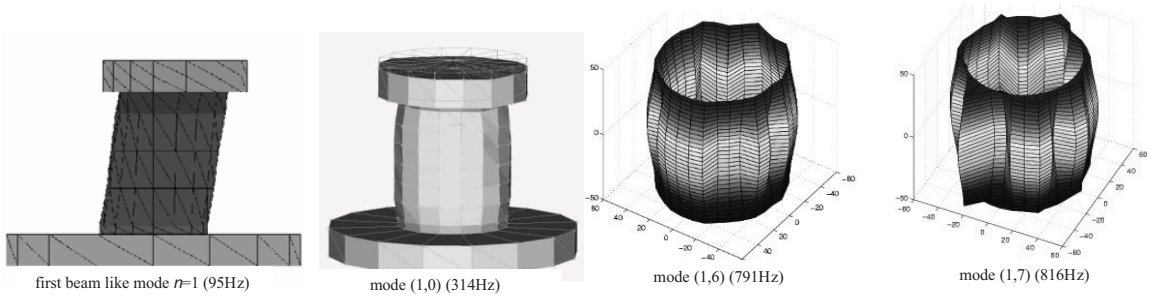

Figure 3. Experimental mode shapes [8].

Experiments proved that, when the shell is excited harmonically from the base, with an excitation frequency close to the first axisymmetric mode, complex dynamic scenarios appear and the energy pumped in the system at low frequency spreads over a wide range of the spectrum.

Tests are carried out using a seismic sine excitation, close to the resonance of the first axisymmetric mode (m=1, n=0).

The complexity and violence of vibrations due to nonlinear phenomena gave several problems to closed loop controllers of the shaking table; therefore, an open loop approach was chosen.
The accelerations of the base, the top, and the displacement of the shell lateral surface are measured.

Figures 4a-e represent the amplitudes of vibration in terms of acceleration (base and top disk vibration) or displacement (measured on the lateral surface of the shell, the vertical position is on the middle): during experiments the input voltage was sinusoidal ($v(t)=v_0\sin(2\pi f t)$, v_0=0.07V) and the frequency was moved step by step (stepped sine approach with a frequency step of 0.3Hz) starting from high frequency, 340Hz, and reducing up to 290Hz; the sampling frequency was about 6400Hz.

Figure 4a shows that the maximum excitation (base motion) is between 8 and 14 g; there is a strong interaction between the shaker and the shell-disk.

The top disk vibration (Figure b) increases as the first axisymmetric mode resonance is approached, from 340 to 333Hz the top disk response follows the usual behaviour expected by a linear resonance. The top disk vibration amplitude remains flat from 322 to 295 Hz.

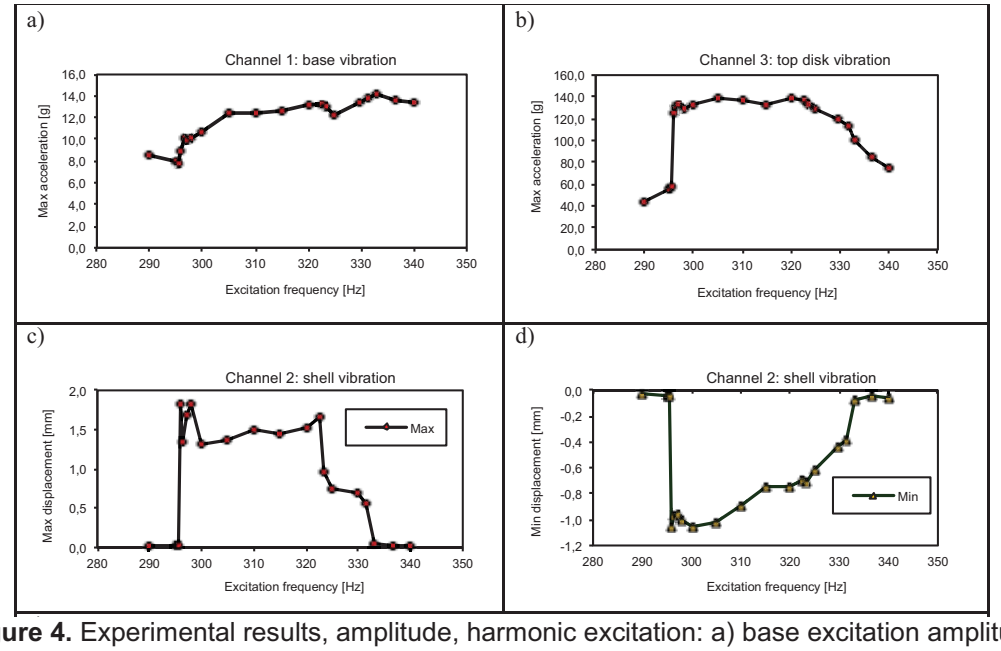

Figure 4. Experimental results, amplitude, harmonic excitation: a) base excitation amplitude (acceleration [g]), b) top disk amplitude (acceleration [g]), c) response on the shell mid-span (displacement [mm], positive inward), d) minimum response of the shell mid-span (displacement [mm], negative outward).

For frequencies higher than 333Hz the shell vibration is small, about 0.04 mm (about 16% with respect to the shell thickness, 0.25mm), Figure 4c; reducing the excitation frequency below 333Hz, the shell vibration amplitude suddenly grows up, at 331.5 Hz the amplitude is 0.57 mm, the increment is 1325%; such huge increment takes place in a narrow frequency band, i.e. from 333 Hz to 331.4 Hz

(about 0.5% frequency variation). Another jump in the shell response is observed from 325 Hz (0.75 mm amplitude) to 320 Hz (1.53 mm), i.e. 104% increment in terms of amplitude in 5 Hz. The response remains almost flat from 300 to 296Hz, the amplitude oscillates around 1.5 mm; then at 295 Hz the phenomenon suddenly disappears (0.022mm amplitude).

2.1 Modelling

The shaker used in the present experiments is an electromechanic machine, the main body is suspended on the ground by means of very soft gas suspensions, which have the task of reducing forces transmitted to the ground. The power supply is given by an amplifier that furnishes the current both to the field coil and the armature coil; the amplifier input $E_0(t)$ is a low power and voltage signal (up to 1V), it is generated by an external device.

In the present work the nonlinear Sanders-Koiter theory is considered, this is a theory based on the Love's first approximation

Details are omitted for the sake of brevity.

2.1.1 Numerical Analysis

Numerical analyses are carried out after a deep convergence analysis, details are omitted for the sake of brevity.

Results presented in Figure 5 are referred to a simulation carried out considering a sine excitation of the shaker with input voltage equal to 0.09V, this value is larger than the excitation used during the experiments (0.07V); however, below such value the numerical model did not detect any dynamic instability. Simulations are carried out by decreasing the excitation frequency. The issue about the voltage level is not really significant; indeed, the need of a voltage slightly larger than experiments is probably due to an underestimation of the amplifier gain: this quantity could be influenced by the operating conditions of the amplifier-shaker system.

The instability phenomenon is captured, i.e. the instability region is close to the experiments.

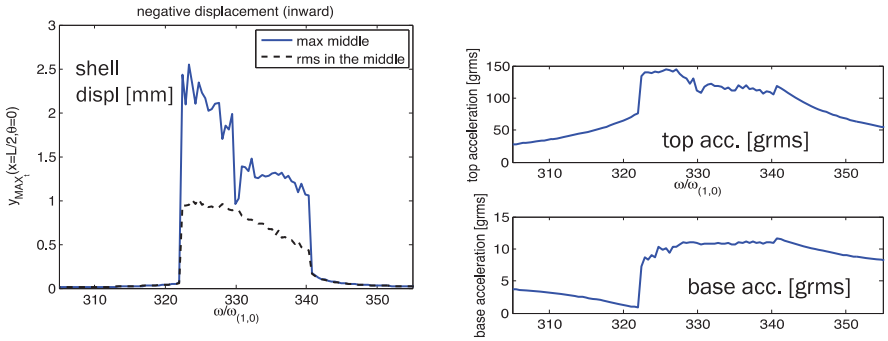

Figure 5. Amplitude frequency diagrams, numerical simulations, companion mode participation, backward frequency sweep, shell vibration (mm). a) inward displacement and RMS(*w*); b) outward (positive) displacement. Excitation source: 0.09V.

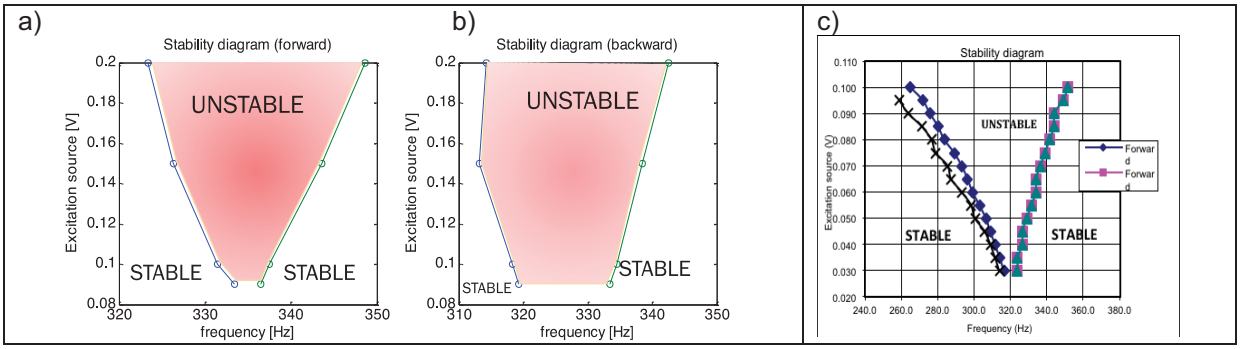

Figure 6. Stability boundaries. a,b) theory, c) experiments

Figure 6 shows the stability boundaries obtained numerically by varying both the excitation source voltage and frequency; the boundaries are coherent with experiments and similar to the Ince-Strutt diagrams referred to the Mathieu equation, this is a further confirmation that the instability is

due to a parametric resonance. The boundaries, obtained by increasing the excitation frequency (forward), are quite similar to the experimental boundaries; numerical boundaries are moved up with respect to the experiments, i.e. for the same excitation voltage the experimental instability region is wider. Backward boundaries present a wider instability region for low voltage; moreover, left and right curves do not match at the bottom, this indicates that the boundaries search could be improved by using a more sophisticated search, which is however beyond the purposes of the present work.

Conclusions

In this paper an experimental investigation on the nonlinear dynamics of circular cylindrical shells excited by a base excitation is presented. A nonlinear model of the shell considering also the shell shaker interaction is developed.

Experiments clearly show a strong nonlinear phenomenon appearing when the first axisymmetric mode is excited: the phenomenon leads to large amplitude of vibrations in a wide range of frequencies, it appears extremely dangerous as it can lead to the collapse of the shell; moreover, it appears suddenly both increasing and decreasing the excitation frequency and is extremely violent. By observing experimentally a strong transfer of energy from low to high frequency a conjecture can be made about the nonlinear interaction among axisymmetric (directly excited) and asymmetric modes. A saturation phenomenon regarding the vibration of the top disk is observed, this is associated with the violent shell vibration; the shell behaves like an energy sink, absorbing part of the disk energy.

The theoretical model shows satisfactory agreement with experiments and clarifies the energy transfer mechanism from low frequency axisymmetric modes and high frequency asymmetric modes, confirming the conjecture arising by the experimental data analysis.

It is now clear that, in order to safely predict the response of a thin walled shell carrying a mass on the top, i.e. the typical aerospace problem for launchers, a nonlinear shell model is needed, but it is not enough: a further modeling regarding the shell mass interaction and the interaction between shell and excitation source is needed.

References

[1] Leissa A.W., *Vibration of Shells*, NASA SP-288. Washington, DC: Government Printing Office. Now available from The Acoustical Society of America, 1993.

[2] Babcock C.D., Shell Stability. *Journal of Applied Mechanics*, Vol. 50, pp. 935-940, 1983.

[3] Calladine C.R., Understanding Imperfection-Sensitivity in the Buckling of Thin-Walled Shells. *Thin-Walled Structures*, Vol. 23, pp. 215-235, 1995.

[4] Teng J.G., Buckling of thin shells: Recent advances and trends. *Applied Mechanics Reviews*, Vol. 49(4), pp. 263-274, 1996.

[5] Amabili M., Païdoussis M.P., Review of studies on geometrically nonlinear vibrations and dynamics of circular cylindrical shells and panels, with and without fluid-structure interaction. *Applied Mechanics Reviews,* Vol. 56, pp. 349-381, 2003.

[6] Amabili M., *Nonlinear Vibrations and Stability of Shells and Plates*, Cambridge University Press, Cambridge, 2008.

[7] Kubenko V.D., Koval'chuk P.S., Nonlinear problems of the vibration of thin shells (review). *International Applied Mechanics,* Vol. 34, pp. 703- 728, 1998.

[8] Pellicano F., Vibrations of circular cylindrical shells: theory and experiments. *J. of Sound and Vibration*, Vol. 303, pp.154–170, 2007.

[9] Mallon N.J., Fey R.H.B., Nijmeijer H., Dynamic stability of a base-excited thin orthotropic cylindrical shell with top mass: Simulations and experiments. *J. of Sound and Vibration*, Vol. 329, pp. 3149-3170, 2010.

[10] F. Pellicano, Dynamic instability of a circular cylindrical shell carrying a top mass under seismic excitation: experiments and theory, *Int. J. of Solids and Structures*, Vol. 48, pp. 408-427, 2011.

Proceedings of the 4th International Conference on Nonlinear Dynamics
ND-KhPI2013
June 19-22, 2013, Sevastopol, Ukraine

Nonlinear Dispersive Waves in Elastic Wedges

Elena S. Sokolova [1,2*], Pavel D. Pupyrev [2,3], Alexey M. Lomonosov [3], Andreas P. Mayer [2], Alexander S. Kovalev [1]

Abstract
Nonlinear dynamics of acoustic wedge waves was investigated. For the theoretical analysis of this problem the displacement field was presented in the form of a double series of Laguerre functions. A nonlinear evolution equation for wedge waves in anisotropic elastic media, including weak dispersion, was derived. Dispersion laws were obtained for the cases of a surface coated by a thin film and modification of the wedge tip. A numerical solution, corresponding to a solitary pulse, was found.

Keywords
wedge waves, dispersion, anisotropy

[1] B.Verkin Institute for Low Temperature Physics and Engineering, NAS of Ukraine, Kharkiv, Ukraine
[2] Fakultät B+W, HS Offenburg - University of Applied Sciences, Gengenbach, Germany
[3] General Physics Institute, RAS, Moscow, Russian Federation

***Corresponding author:** es_sokolova@yahoo.com

Introduction

Edge acoustic waves are guided waves with associated displacement field decaying exponentially away from the tip in the plane normal to the edge [1]. Recently, these one-dimensional guided modes have attracted renewed interest [2-5], partly because of various potential applications including non-destructive testing, sensors, ultrasonic motors, and aquatic propulsion.

Theoretical investigations and numerical calculations of the characteristics of acoustic waves guided by wedges were carried out on the basis the finite element method [6] and of the Laguerre function approach [7,8]. In the following, we apply the latter.

Because of translational invariance along the apex direction (x-direction), the displacement field may be set up in the form $u_\alpha(x,y,z,t) = \exp\left[i(kx-\omega t)\right] w_\alpha(ky,kz)$, and for rectangular wedges, $w_\alpha(ky,kz) = \sum_{m,n} a^\alpha_{m,n} \Phi_m(ky)\Phi_n(kz)$, where $\Phi_m(\xi) = \exp(-\xi/2)\left[L_m(\xi)/m!\right]$ and $L_m(\xi)$ is the m-th Laguerre polynomial. In the case of sharp-angle wedges, a conformal transformation first maps the two faces of the wedge to the (x,y) and (x,z) planes.

1 Evolution Equation

We consider elastic nonlinearity that arises in the expansion of the Piola-Kirchhoff stress tensor in powers of the displacement gradients $u_{\alpha,\beta}$,

$$T_{\alpha\beta} = C_{\alpha\beta\,\gamma\delta} u_{\gamma,\delta} + \tfrac{1}{2} S_{\alpha\beta\,\gamma\delta\,\varepsilon\zeta}\, u_{\gamma,\delta} u_{\varepsilon,\zeta} + O(u^3_{\ldots,\ldots}) \tag{1}$$

Here, the components of the sixth-rank tensor (S) are linear combinations of 3rd-order and 2nd-order elastic moduli. Summation over repeated indices is implied.

The displacement field is written as an expansion in powers of a typical strain ε,

$$u_\alpha = \varepsilon u_\alpha^{(1)} + \varepsilon^2 u_\alpha^{(2)} + O(\varepsilon^3) \tag{2}$$

This expansion is inserted in the equations of motion in the elastic medium and boundary conditions at its surfaces,

$$\rho \ddot{u}_\alpha = \frac{\partial}{\partial x_\beta} T_{\alpha\beta}, \qquad N_\beta T_{\alpha\beta} = 0 \tag{3}$$

with stress tensor (1), and N_β are the Cartesian components of a unit vector normal to the surface.

These equations and conditions are required to be satisfied at each order of the expansion parameter ε. Consequently, the first-order field $u_\alpha^{(1)}$ may be set up as a superposition of linear wedge waves in the form

$$u_\alpha^{(1)}(x,y,z,t) = \int_0^\infty w_\alpha(ky,kz)\, \exp\left[ik(x - v_W t)\right] \frac{1}{ik} B(k,\tau)\, \frac{dk}{2\pi} + c.c. \tag{4}$$

where $v_W = \omega / k$ is the velocity of linear wedge waves and *c.c.* stands for the conjugate complex. $B(k,\tau)$ is a displacement gradient amplitude that depends on wave number k and on a "stretched" time coordinate $\tau = \varepsilon t$.

From a compatibility condition for the inhomogeneous linear boundary value problem obtained at second order of ε, the desired evolution equation for the strain amplitudes is obtained in the form [9]:

$$i \frac{\partial}{\partial \tau} B(k) = v_w k \left\{ \int_0^k G(k'/k) B(k') B(k-k') \frac{dk'}{2\pi} + 2 \int_k^\infty (k/k')^2 \left[G(k/k')\right]^* B(k') B^*(k'-k) \frac{dk'}{2\pi} \right\} \tag{5}$$

The dimensionless kernel function $G(X)$ may be expressed as an overlap integral over products of modal functions and their derivatives in the following way:

$$G(X) = \frac{i}{N_0} S_{\alpha\beta\mu\nu\varsigma\xi}\ \widetilde{G}_{\alpha\beta\mu\nu\varsigma\xi}(X) \tag{6}$$

where

$$N_0 = 4\rho v_w^2 \iint w_\alpha^*(\eta,\vartheta) w_\alpha(\eta,\vartheta) d\eta d\vartheta \tag{7}$$

$$\begin{aligned} \widetilde{G}_{\alpha\beta\mu\nu\varsigma\xi}(X) &= -\frac{1}{X(1-X)} \\ &\times \iint \left[D_\beta(1) w_\alpha(\eta,\vartheta)\right]^* \left[D_\nu(1) w_\mu(X\eta, X\vartheta)\right] \left[D_\xi(1-X) w_\varsigma((1-X)\eta,(1-X)\vartheta)\right] d\eta d\vartheta \end{aligned} \tag{8}$$

where we have defined the operator $\hat{D}(X) = (iX, \partial/\partial\eta, \partial/\partial\vartheta)$.

The double integrals in (7) and (8) with dimensionless integration variables η, ϑ run over the cross section of the wedge.

The function $G(X)$ is defined for real arguments $0 \le X \le 1$ and has the symmetry property $G(X) = G(1-X)$. Numerical calculations of $G(X)$ for different materials and wedge angles were done in framework of the Laguerre function method [10].

2 Dispersion

The existence of stationary nonlinear excitations like solitary waves is caused by a competition of two factors: nonlinearity of the system and dispersion (see corresponding predictions for wedge waves in [11] and [12]) of propagating waves. A necessary condition for dispersion of acoustic waves is the presence of a length scale in the system. In case of a perfect wedge, dispersion can only be due to discreteness of the crystalline lattice, which is beyond continuum theory and may be neglected for sufficiently long wavelengths. Numerous modifications of the ideal homogeneous wedge give rise to dispersion of wedge waves. Some of them have been discussed in [13] and references given there. For two of these modifications, namely coating of one of the wedge's surfaces by a thin film and a small deviation of the material properties near the apex from those in the rest of the wedge, we demonstrate here that they can be incorporated in the nonlinear evolution equation in a straightforward way, referring to our earlier work on dispersion of linear acoustic wedge waves [13].

Coating of the surface perpendicular to the z axis can be taken into account by an effective boundary condition of the form

$$T_{\alpha 3} = \varepsilon d\left\{\rho' \ddot{u}_\alpha - \frac{\partial}{\partial x_\Phi} \overline{C'}_{\alpha\Phi\mu\Theta} \frac{\partial u_\mu}{\partial x_\Theta}\right\} \tag{9}$$

where εd is the film thickness, scaled to be of first order in the expansion parameter ε introduced in section 1, ρ' is the density and $\overline{C'}_{\alpha\Phi\mu\Theta}$ are effective elastic moduli of the film material [13], which may be functions of the coordinates y and z. Capital Greek indices run over 1 and 2, only.

The deviation $\varepsilon\Delta\rho$ of the density and the deviations $\varepsilon\Delta C_{\alpha\beta\mu\nu}$ of the elastic moduli near the tip of the wedge from their values in the rest of the wedge are also scaled to be of first order of ε.

Extending the derivation of the nonlinear evolution equation described in section 1, it now takes the form

$$\begin{aligned} &i\frac{\partial}{\partial\tau}B(k) + v_w k\left[kdF_1 + 0.5F_3(ka)\right]B(k) = \\ &= v_w k\left\{\int_0^k G(k'/k)B(k')B(k-k')\frac{dk'}{2\pi} + 2\int_k^\infty (k/k')^2\left[G(k/k')\right]^* B(k')B^*(k'-k)\frac{dk'}{2\pi}\right\} \end{aligned} \tag{10}$$

The coefficient F_1 and the function F_3 were introduced in [13]. F_1 is determined by the acoustic mismatch between film and substrate. The function F_3 depends on the deviation of material constants near the apex of the wedge, a is a length characterizing the size of the modified part of the wedge's cross sectional area. In the linear limit, the following dispersion law is obtained: $\omega(k) - v_W k = \varepsilon\,\Omega(k),\ \Omega(k) = -v_W k(kdF_1 + 0.5F_3(ka))$. In the long-wavelength limit, $F_3(ka) \propto (ka)^2$. The coefficients F_1 and the function F_3 are strongly dependent on elastic moduli of the materials involved.

3 Numerical Results

All calculations have been done for waves propagating in the (-1-12) direction (x direction) of cubic elastic media. The other coordinate axes are y along (-110) and z along (-1-1-1). One surface of the wedge is always the xy plane with inner normal pointing into the (-1-1-1) direction (z direction).

The shift of the wedge wave velocity due to small modifications of material properties near the apex was calculated for wedges that consist of $GaAs$ in the spatial region $z > (a - y)/\tan(\theta/2)$

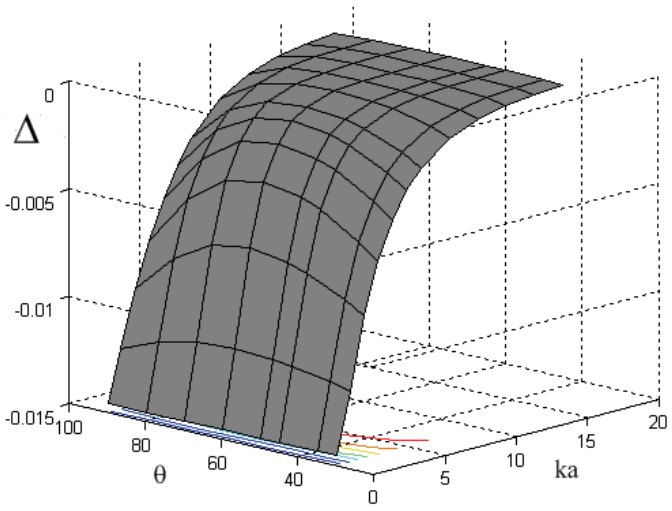

Figure 1. Shift of velocity of acoustic waves $\Delta = \frac{v_w^l - v_w^u}{v_w^u} + \left(\frac{\Delta v_w}{v_w^l}\right)\frac{v_w^l}{v_w^u}$ guided by the apex of an edge of angle θ consisting of on $GaAs$ in its lower part and of $Al_{0.1}Ga_{0.9}As$ in its upper part

(lower part) and of $Al_{0.1}Ga_{0.9}As$ in the region $z < (a - y)/\tan(\theta/2)$ (upper part) (Fig.1), where a is a given length. In the limiting cases $ka \to 0$ and $ka \to \infty$, the wedge wave velocity tends to the v_w^l and v_w^u which are velocities of acoustic waves guided by the tip of an edge purely made of $GaAs$ (lower material) and purely made of $Al_{0.1}Ga_{0.9}As$ (upper material), respectively.

Table 1. Numerical values for kernel function *G*(*X*) at two different arguments, computed with 2nd-order and 3rd-order elastic moduli for Si [15] and for CaF2 and SrF2 [16].

θ	X	Si	CaF2	SrF2
90	0.5	-0.126+0.134i	-0.071+0.041i	-0.082-0.015i
	0.01	0.030+0.045i	-0.028+0.032i	-0.006+0.006i
60	0.5	0.003-0.022i	-0.041+0.020i	-0.022+0.004i
	0.01	-0.006+0.008i	-0.001-0.002i	0.000-0.003i
45	0.5	0.040-0.012i	-0.028+0.012i	-0.010+0.003i
	0.01	0.005+0.006i	-0.004-0.007i	-0.002-0.004i
30	0.5	0.053+0.006i	0.034+0.001i	0.015+0.000i
	0.01	0.01+0.01i	-0.01-0.01i	-0.01-0.00i

The calculated kernel function $G(X)$ for various anisotropic materials and wedge angles and for the normalisation $w_3(0,0)=1$ is presented in Table 1. Silicon shows the strongest nonlinearity (the largest absolute value of the kernel function in the nonlinear evolution equation). The data in the table have been computed with a representation of the modal functions as a linear combination of products of the lowest 11 Laguerre functions. The quantity $|G(0.5)|$ for silicon and wedge angle 90°, calculated with the lowest 6 Laguerre functions, deviates from $|G(0.5)|$, calculated with the lowest 9 Laguerre functions, by less than 0.3% [13]. For smaller wedge angles, we used a convergence factor introduced in [14].

A stationary solution of the evolution equation (10) for F_3=0 was determined numerically in the form of a periodic pulse train consisting of spatially well-separated pulses. In Fig. 2 and Fig. 3 the surface elevation profile associated with a solitary pulse is presented for both of the two surfaces forming the edge (the (1 1 1) and (1 -1 0) surfaces). A half-period of the periodic pulse train is shown. The spatial extension of the pulse in the *y*-direction (normal to the edge) is similar to that in the *x* direction (along the edge).

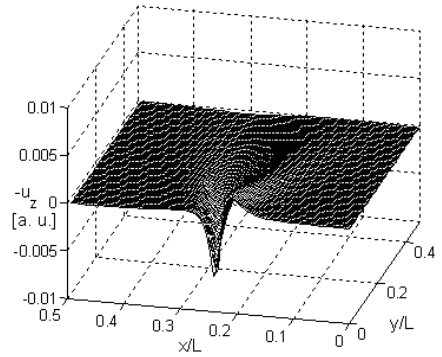

Figure 2. Surface elevation profile $-u_3$ of the (1 1 1) surface of a rectangular silicon wedge, corresponding to a solitary pulse train with periodicity *L* (with x axis along (-1 -1 2) and z axis along (-1-1-1) directions) [12]

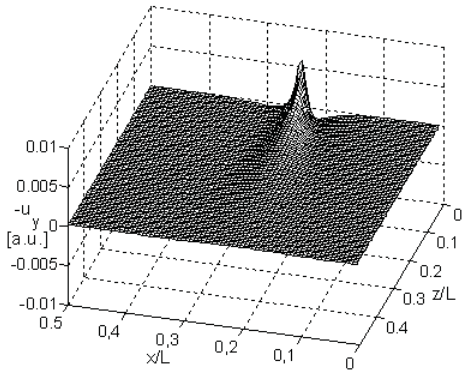

Figure 3. Surface elevation profile $-u_2$ of the (1 -1 0) surface of a rectangular silicon wedge, corresponding to a solitary pulse train with periodicity *L* (with x axis along (-1 -1 2) and z axis along (-1-1-1) directions)

Conclusions

We demonstrated that the propagation of acoustic waves guided by the apex of an anisotropic wedge is influenced by second-order nonlinearity. It has been shown how the kernel function in the

nonlinear evolution equation for wedge acoustic waves can be computed for wedge angles equal to or smaller than 90°.

Two mechanisms of generation of weak dispersion were considered: film covering of the wedge and spatial inhomogeneity of the elastic properties of the wedge material. For these cases dispersion laws were obtained.

These results form a basis for simulations of nonlinear stationary waves and pulse evolution. They should be useful also for finding wedge systems with high nonlinearity or to minimize nonlinear effects in technical applications where such effects are undesired.

Acknowledgments

The authors would like to thank Peter Hess for helpful discussions. Financial support by the Deutsche Forschungsgemeinschaft (Grant No. MA 1074-11) is gratefully acknowledged.

References

[1] Krylov V.V. Wedge acoustic waves: New theoretical and experimental results *Proc. of the II International Symposium on Surface Waves in Solids and Layered Structures and Acoustoelectronics '89, Borissov M., Spassov L., Georgiev Z. and Avramov I, Eds.*, World Scientific, Singapore, pp. 174-189, 1990.

[2] Liu I. H. and Yang C.-H. An investigation on wedge waves and the interaction with a defect using a quantitative laser ultrasound visualization system *Proc. 2010 IEEE Ultrasonics Symp*., pp. 817-820, 2010.

[3] Tung P.-H. and Yang C.-H. Application of anti-symmetrical flexural modes for the detection of moisture, *Proc. 31st Symp. Ultrasonic Electronics, Tokyo, 6-8 Dec.*, pp. 489-490, 2010.

[4] Yu T.-H., Yang S.-Y., Lee C.-L. and Yin C.-C. Bi-dimensional finite element analysis for modal separation of a circular cylindrical WW-USM *Finite Elements in Analysis and Design*, vol. 47, pp. 635–642, 2011.

[5] Krylov V.V. and Pritchard G.V. Experimental investigation of the aquatic propulsion caused by localized flexural wave propagation in immersed wedges and plates *Applied Acoustics,* vol. 68, pp. 97-113, 2007.

[6] Lagasse P.E. Analysis of dispersionfree guide for elastic waves *Electron. Lett.,* vol. 8, pp. 372-373, 1972.

[7] Moss S L., Maradudin A.A., Cunningham S L. Vibrational edge modes for wedges with arbitrary interior angles *Phys. Rev. B*, vol. 8, pp. 2999-3008, 1973.

[8] Datta S. and Hunsinger B.J. Analysis of line acoustical waves in general piezoelectric crystals *Phys. Rev. B*, vol. 16, pp. 4224-4229,1977.

[9] Krylov V.V., and Parker D.F., unpublished.

[10] Sokolova E.S., Kovalev A.S. and Mayer A.P. Second-order nonlinearity of wedge acoustic waves in anisotropic media *Wave Motion*, vol. 50(2), pp.246-252, 2013.

[11] Andersen D.R., Datta S. and Gunshor R.L. A coupled mode approach to modulational instability and envelope solitons *J. Appl. Phys*., vol. 54, pp.5608-5612, 1983.

[12] Mayer A.P., Lomonosov A.M. and Hess P. Nonlinear acoustic waves localized at crystal edges *Proc. 2009 IEEE Ultrasonics Symp*., pp. 1088-1091, 2009

[13] Sokolova E.S., Kovalev A.S., Timler R. and Mayer A.P. On the Dispersion of Wedge Acoustic Waves *Wave Motion*, vol. 50(2) pp.233-245, 2013.

[14] Sharon T.M., Maradudin A.A. and Cunningham S.L. Vibrational edge modes for small-angle wedges *Phys. Rev. B*, vol. 8, pp. 6024-6026, 1973.

[15] Hall J.J. Electronic effects in the elastic constants of n-type silicon, *Phys. Rev*., vol. 161, pp. 756-761, 1967.

[16] Landolt-Bornstein *Numerical Data and Functional Relationships in Science and Technology*, Vol. III/11, Hellwege K.-H., Ed., Springer, Heidelberg, 1979; and Vol. III/18, Hellwege K.-H. and Madelung O., Eds., Springer, Heidelberg, 1984.

Proceedings of the 4th International Conference on Nonlinear Dynamics
ND-KhPI2013
June 19-22, 2013, Sevastopol, Ukraine

Nonlinear Vibrations and Energy Distribution of Single-Walled Carbon Nanotubes

Matteo Strozzi[1*], Leonid I. Manevitch[2], Francesco Pellicano[1]

Abstract
The nonlinear vibrations of Single-Walled Carbon Nanotubes are analysed. The Sanders-Koiter elastic shell theory is applied in order to obtain the elastic strain energy and kinetic energy. The carbon nanotube deformation is described in terms of longitudinal, circumferential and radial displacement fields. The theory considers geometric nonlinearities due to large amplitude of vibration. The displacement fields are expanded by means of a double series based on harmonic functions for the circumferential variable and Chebyshev polynomials for the longitudinal variable. The Rayleigh-Ritz method is applied in order to obtain approximate natural frequencies and mode shapes. Free boundary conditions are considered. In the nonlinear analysis, the three displacement fields are re-expanded by using approximate eigenfunctions. An energy approach based on the Lagrange equations is considered in order to obtain a set of nonlinear ordinary differential equations. The energy distribution of the system is studied by considering combinations of different vibration modes. The effect of the conjugate modes participation on the energy distribution is analysed.

Keywords
Nonlinear vibrations, energy distribution, carbon nanotubes

[1] Department of Engineering "Enzo Ferrari", University of Modena and Reggio Emilia, Modena, Italy
[2] N.N. Semenov Institute of Chemical Physics, Russian Academy of Sciences RAS, Moscow, Russia
* **Corresponding author:** matteo.strozzi@unimore.it

Introduction

Carbon Nanotubes were discovered in 1991 by Iijima [1], who first analysed the synthesis of molecular carbon structures in the form of fullerenes and then reported the preparation of a new type of finite carbon structure, the carbon nanotubes, described as helical microtubules of graphitic carbon.

Rao et al. [2] studied the vibrations of SWNTs by using Raman scattering experimental techniques with laser excitation wavelengths in the range of the nanometers. They observed numerous Raman peaks, which correspond to vibrational modes of the nanotubes.

Gupta et al. [3] simulated the mechanical behaviour of SWNTs with free edges by using the molecular dynamics potential. They considered the effect of the chirality and geometry on the natural frequencies of the longitudinal, torsional and inextensional modes of vibration.

Arghavan and Singh [4] carried out a numerical study on the free and forced vibrations of SWNTs by considering the FE method. They analysed different boundary conditions, obtaining the natural frequencies and mode shapes, time histories and spectra of axial, bending and torsional modes.

Wang et al. [5] examined the applicability and limitations of different simplified models of elastic cylindrical shells for general cases of static buckling and free vibrations of carbon nanotubes. They considered the Flugge, Donnell thin shell and Donnell shallow shell models.

Strozzi et al. [6] analysed the linear vibrations of SWNTs for various boundary conditions in the framework of the Sanders-Koiter thin shell theory. They analysed several types of nanotubes by varying aspect ratio and chirality in a wide range of the natural frequency spectrum.

In the present paper, the nonlinear vibrations of SWNTs are analysed. The Sanders-Koiter thin shell theory is applied. The displacement fields are expanded by means of a double series based on harmonic functions for the circumferential variable and Chebyshev polynomials for the longitudinal variable. The Rayleigh-Ritz method is applied to obtain approximate natural frequencies and mode

shapes. Free boundary conditions are considered. In the nonlinear analysis, the three displacement fields are re-expanded by using approximate eigenfunctions. The Lagrange equations are considered to obtain a set of nonlinear ordinary differential equations. The total energy distribution is studied by considering different combined modes. The effect of the conjugate modes participation is analysed.

1. Elastic strain energy

The nondimensional elastic strain energy $\tilde{U}$ of a cylindrical shell, by neglecting the transverse normal stress σ_z (plane stress hypothesis) and the transverse shear strains γ_{xz}, $\gamma_{\theta z}$, is written as

$$\begin{aligned}\tilde{U} = &\frac{1}{2}\int_0^1\int_0^{2\pi}\left(\tilde{\varepsilon}_{x,0}^2+\tilde{\varepsilon}_{\theta,0}^2+2\nu\tilde{\varepsilon}_{x,0}\tilde{\varepsilon}_{\theta,0}+\frac{(1-\nu)}{2}\tilde{\gamma}_{x\theta,0}^2\right)d\theta d\eta \\ &+\frac{1}{2}\frac{\beta^2}{12}\int_0^1\int_0^{2\pi}\left(\tilde{k}_x^2+\tilde{k}_\theta^2+2\nu\tilde{k}_x\tilde{k}_\theta+\frac{(1-\nu)}{2}\tilde{k}_{x\theta}^2\right)d\theta d\eta\end{aligned} \tag{1}$$

where $(\tilde{\varepsilon}_{x,0}, \tilde{\varepsilon}_{\theta,0}, \tilde{\gamma}_{x\theta,0})$ are the nondimensional middle surface strains, $(\tilde{k}_x, \tilde{k}_\theta, \tilde{k}_{x\theta})$ represent the nondimensional middle surface changes in curvature and torsion, with ($\eta = x / L$) and ($\beta = h / L$).

2. Kinetic energy

The nondimensional kinetic energy $\tilde{T}$ of a cylindrical shell (rotary inertia neglected) is given by

$$\tilde{T}=\frac{1}{2}\int_0^1\int_0^{2\pi}(\tilde{u}'^2+\tilde{v}'^2+\tilde{w}'^2)d\theta d\eta=\frac{1}{2}\int_0^1\int_0^{2\pi}\left[\left(\frac{d\tilde{u}}{d\tau}\right)^2+\left(\frac{d\tilde{v}}{d\tau}\right)^2+\left(\frac{d\tilde{w}}{d\tau}\right)^2\right]d\theta d\eta \tag{2}$$

where $(\tilde{u}, \tilde{v}, \tilde{w})$ are the nondimensional displacement fields, $(\tilde{u}', \tilde{v}', \tilde{w}')$ denote the nondimensional velocity fields and τ is the nondimensional time variable obtained by introducing a reference natural frequency ω_0.

2. Linear vibration analysis

A modal vibration can be written in the form

$$\tilde{u}(\eta,\theta,\tau)=\tilde{U}(\eta,\theta)\varphi(\tau)\qquad \tilde{v}(\eta,\theta,\tau)=\tilde{V}(\eta,\theta)\varphi(\tau)\qquad \tilde{w}(\eta,\theta,\tau)=\tilde{W}(\eta,\theta)\varphi(\tau) \tag{3}$$

where $\tilde{U}(\eta,\theta)$, $\tilde{V}(\eta,\theta)$, $\tilde{W}(\eta,\theta)$ describe the mode shape and $\varphi(\tau)$ is the nondimensional time law.

The mode shape is expanded by means of a double series in terms Chebyshev polynomials $T_m^*(\eta)$ in the axial direction and harmonic functions (cos $n\theta$, sin $n\theta$) in the circumferential direction

$$\tilde{U}(\eta,\theta)=\sum_{m=0}^{M_u}\sum_{n=0}^{N}\tilde{U}_{m,n}T_m^*(\eta)\cos n\theta \tag{4}$$

$$\tilde{V}(\eta,\theta)=\sum_{m=0}^{M_v}\sum_{n=0}^{N}\tilde{V}_{m,n}T_m^*(\eta)\sin n\theta \tag{5}$$

$$\tilde{W}(\eta,\theta)=\sum_{m=0}^{M_w}\sum_{n=0}^{N}\tilde{W}_{m,n}T_m^*(\eta)\cos n\theta \tag{6}$$

where $T_m^* = T_m(2\eta - 1)$, m is the polynomials degree and n denotes the number of nodal diameters.

3. Nonlinear vibration analysis

The displacement fields $\tilde{u}(\eta,\theta,\tau)$, $\tilde{v}(\eta,\theta,\tau)$, $\tilde{w}(\eta,\theta,\tau)$ are expanded by using both the linear mode shapes $\tilde{U}(\eta,\theta)$, $\tilde{V}(\eta,\theta)$, $\tilde{W}(\eta,\theta)$ obtained in the previous linear analysis and the conjugate mode shapes $\tilde{U}_c(\eta,\theta)$, $\tilde{V}_c(\eta,\theta)$, $\tilde{W}_c(\eta,\theta)$ in the following form

$$\begin{aligned}
\tilde{u}(\eta,\theta,\tau) &= \sum_{j=1}^{N_u}\sum_{n=1}^{N}\left[\tilde{U}^{(j,n)}(\eta,\theta)\varphi_{u,j,n}(\tau) + \tilde{U}_c^{(j,n)}(\eta,\theta)\varphi_{u,j,n,c}(\tau)\right] \\
\tilde{v}(\eta,\theta,\tau) &= \sum_{j=1}^{N_v}\sum_{n=1}^{N}\left[\tilde{V}^{(j,n)}(\eta,\theta)\varphi_{v,j,n}(\tau) + \tilde{V}_c^{(j,n)}(\eta,\theta)\varphi_{v,j,n,c}(\tau)\right] \\
\tilde{w}(\eta,\theta,\tau) &= \sum_{j=1}^{N_w}\sum_{n=1}^{N}\left[\tilde{W}^{(j,n)}(\eta,\theta)\varphi_{w,j,n}(\tau) + \tilde{W}_c^{(j,n)}(\eta,\theta)\varphi_{w,j,n,c}(\tau)\right]
\end{aligned} \tag{7}$$

The Lagrange equations of motion for free vibrations are expressed in the following form

$$\frac{d}{d\tau}\left(\frac{\partial \tilde{L}}{\partial \dot{\tilde{q}}_i}\right) - \frac{\partial \tilde{L}}{\partial \tilde{q}_i} = 0 \qquad i \in [1, N_{\max}] \qquad (\tilde{L} = \tilde{T} - \tilde{U}) \tag{8}$$

where the nondimensional modal coordinates $\tilde{q}_i$ are ordered in a vector $\tilde{q}(\tau)$ = [..., $\varphi_{u,j,n}$, $\varphi_{u,j,n,c}$, $\varphi_{v,j,n}$, $\varphi_{v,j,n,c}$, $\varphi_{w,j,n}$, $\varphi_{w,j,n,c}$, ...] and the maximum number of degrees of freedom N_{max} depends on the number of modes considered in expansions (7).

Using the Lagrange equations (8), a set of nonlinear ordinary differential equations is obtained; such system is then solved by using numerical methods.

4. Numeric results

In order to analyse the discrete molecular carbon nanotube as a continuum thin shell, equivalent mechanical parameters (Young's modulus, Poisson's ratio, mass density, wall thickness) must be considered. These parameters are not dependent from the CNT diameter (no size effect). The carbon nanotube described in Table 1 is considered for the following computations.

Table 1. Effective and equivalent parameters of the Single-Walled Carbon Nanotube

Effective thickness h_0 (nm)	0.10 ÷ 0.15
Equivalent thickness h (nm)	0.066
Effective Young's modulus E_0 (TPa)	1.0 ÷ 2.0
Equivalent Young's modulus E (TPa)	5.5
Effective Poisson's ratio ν_0	0.12 ÷ 0.28
Equivalent Poisson's ratio ν	0.19
Surface density of graphite σ (kg/m^2)	7.718×10^{-7}
Equivalent mass density ρ (kg/m^3)	11700

The present model is validated with molecular dynamics data available in the literature [3]; the results reported in Table 2 show that the model is accurate and the equivalent parameters are correct.

Table 2. Natural frequencies of the radial breathing mode ($j = 0$, $n = 0$): comparisons between the Sanders-Koiter theory (SKT) and the Molecular Dynamics Simulations (MDS).

Natural frequency (THz)			**Difference %**
(r, s)	SKT - Present model	MDS - Ref. [3]	
(10, 0)	8.966	8.718	2.84
(6, 6)	8.636	8.348	3.45
(12, 0)	7.478	7.272	2.83
(7, 7)	7.399	7.166	3.25
(8, 8)	6.473	6.275	3.15
(14, 0)	6.414	6.235	2.87
(16, 0)	5.606	5.455	2.77
(10, 10)	5.184	5.026	3.14
(18, 0)	4.985	4.850	2.78
(20, 0)	4.489	4.364	2.86

In Figures 1(a-f), three mode shapes of a free-free carbon nanotube are presented, such modes are considered for the development of the semi-analytic nonlinear model of the carbon nanotube in the re-expansion of Equation (7). In Figures 2-4, the total vibration energy distribution is represented, where the nanotube is unwrapped on a plane in order to allow the energy representation. The damping is not considered here, so the total energy is constant (the integral of the density over the surface).

The sequence of Figures 2(a-f) shows the distribution of the total energy density [Jm^{-2}] in the linear field during a time period corresponding to the natural frequency of the fundamental mode. The analysis of the total energy distribution over the shell shows a periodicity along the circumferential direction. This is expected as in this preliminary linear analysis no conjugate modes are present. The energy is distributed symmetrically along the longitudinal direction because we are combining the two symmetric modes (0,2) and (2,2).

The sequence of Figures 3(a-f) shows the distribution of the total energy density [Jm^{-2}] in the nonlinear field for the two combined modes (0,2) and (2,2). Comparing linear and nonlinear analyses (with same initial conditions) we obtain that, due to the nonlinearity, the energy distribution changes dramatically evolving in a complex pattern with absence of periodicity.

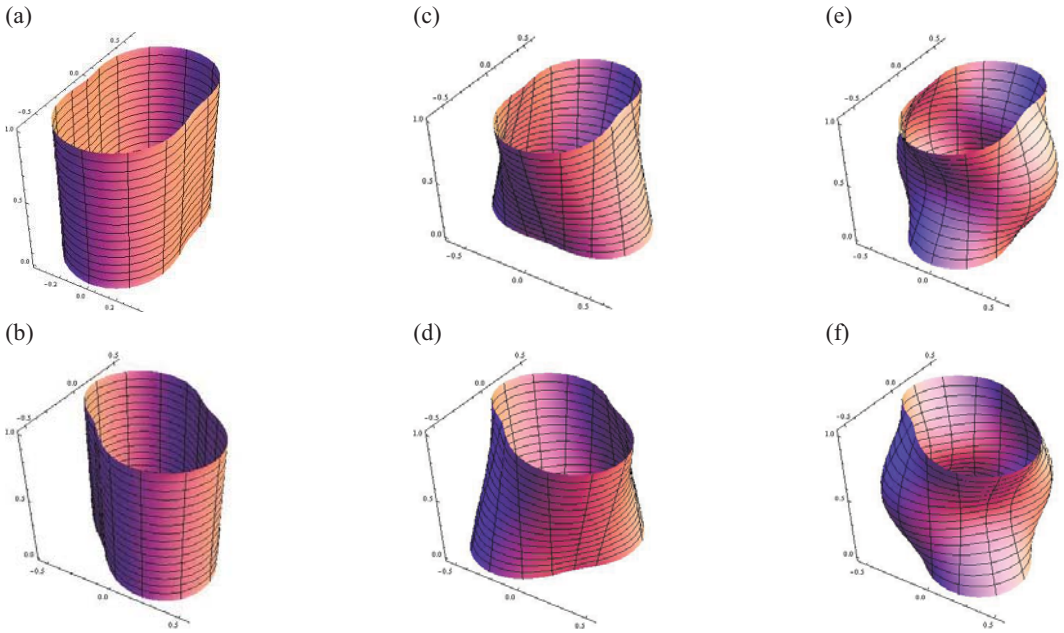

Figure 1. Mode shapes of the SWNT ($r = 10$, $s = 0$, $L = 10.0$ nm). Equivalent parameters of Table 1. (a),(b) Conjugate modes (0,2). (c),(d) Conjugate modes (1,2). (e),(f) Conjugate modes (2,2).

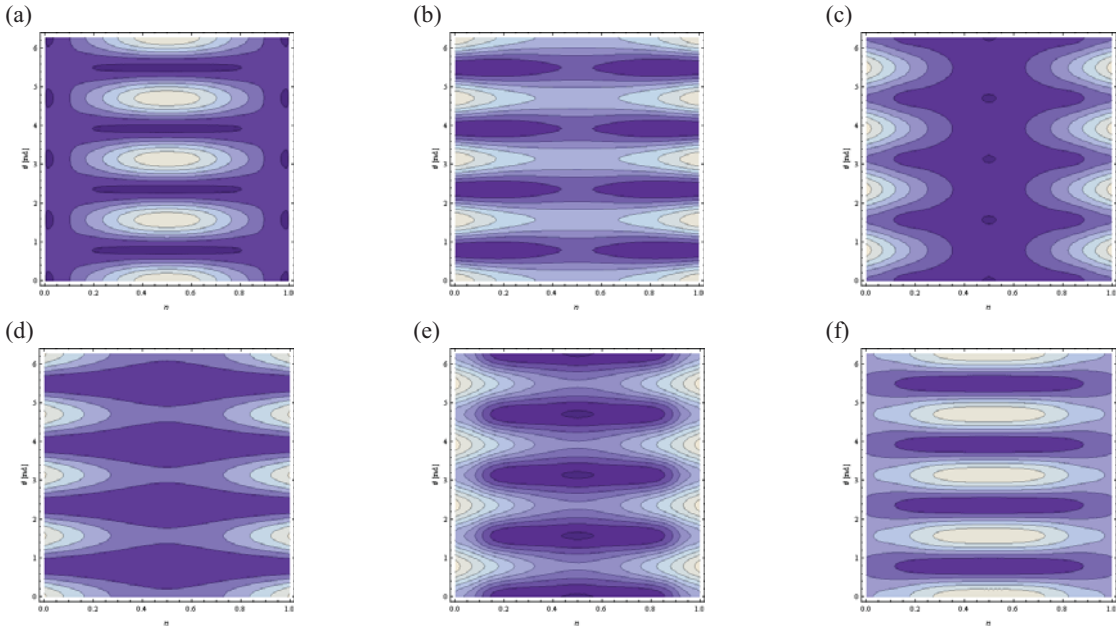

Figure 2. Contour plots of the total energy distribution $\tilde{E}(\eta, \theta, \tau)$. Linear vibration analysis. Combined modes (0,2) and (2,2). (a) τ = 4.90. (b) τ = 6.40. (c) τ = 7.60. (d) τ = 8.20. (e) τ = 9.40. (f) τ = 10.60.

The sequence of Figures 4(a-f) shows the total energy density [Jm^{-2}] in the nonlinear field for the two conjugate modes (1,2). The periodicity along the circumferential direction is now lost due to the presence of the conjugate modes and the nonlinearity. The participation of both conjugate modes gives rise to a travelling wave moving circumferentially around the shell. The initial conditions on the conjugate modes are different, one of them is activated and the second one is slightly perturbed, i.e., an infinitesimal initial energy is provided; after a suitably long time period the conjugate mode having infinitesimal initial energy is activated and it vibrates with large amplitude, this is due to an internal transfer of energy probably due to the internal resonance (1:1). The activation of the second conjugate mode implies that the energy distribution on the shell surface is completely different with respect to the linear model.

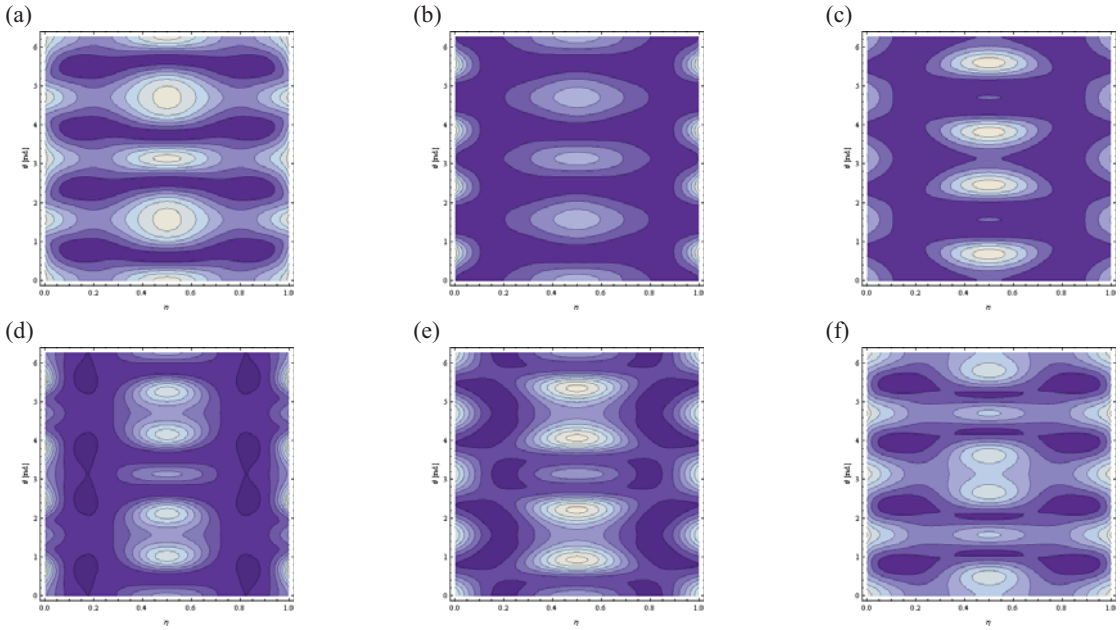

Figure 3. Contour plots of the total energy distribution $\tilde{E}(\eta, \theta, \tau)$. Nonlinear analysis. Combined modes (0,2), (2,2). (a) τ = 10.88. (b) τ = 10.91. (c) τ = 11.00. (d) τ = 11.15. (e) τ = 11.39. (f) τ = 11.54.

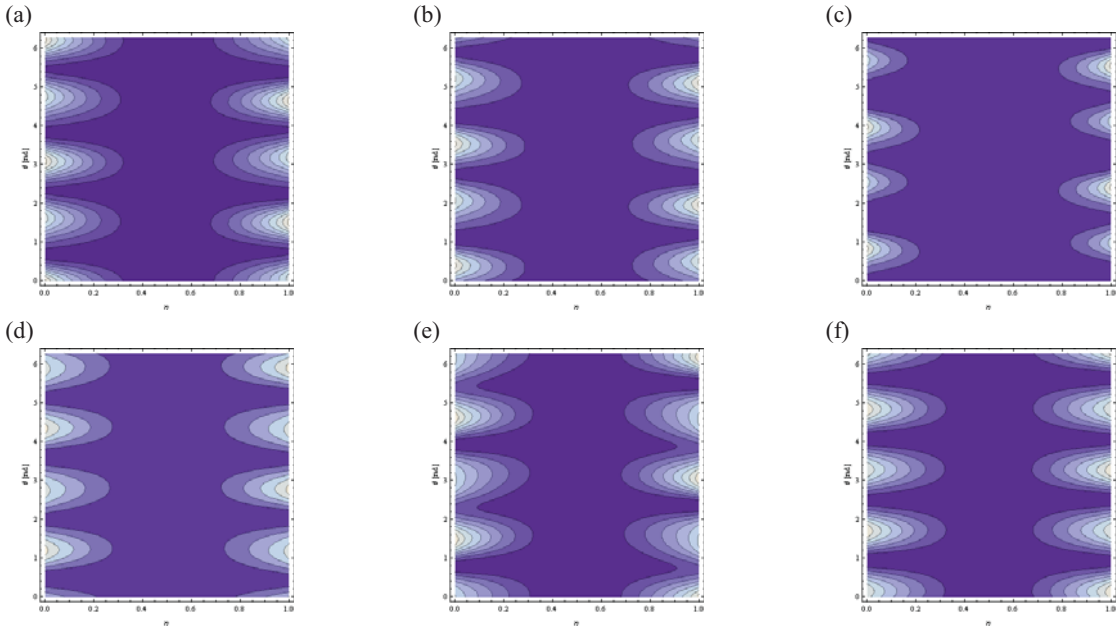

Figure 4. Contour plots of the total energy distribution $\tilde{E}(\eta, \theta, \tau)$. Nonlinear analysis. Conjugate modes (1,2). (a) τ = 7.68. (b) τ = 7.72. (c) τ = 7.76. (d) τ = 7.92. (e) τ = 8.06. (f) τ = 8.08.

Conclusions

The nonlinear vibrations of SWNTs are studied. Equivalent parameters, which allow to analyse the discrete carbon nanotube as a continuum thin shell, are considered. The Sanders-Koiter elastic shell theory is applied in order to obtain the elastic strain energy and kinetic energy. The Rayleigh-Ritz method is applied in order to obtain approximate natural frequencies and mode shapes. The present model is validated in linear field with molecular dynamics data available in the literature. An energy approach based on the Lagrange equations is considered in order to obtain a set of nonlinear ordinary differential equations. The total energy distribution is analysed, where the nanotube is unwrapped on a plane in order to allow the energy representation. The energy distribution in linear and nonlinear field with the same initial conditions is compared. The nonlinear energy distribution changes dramatically evolving in a complex pattern with absence of periodicity. The participation of conjugate modes gives rise to an energy transfer between the two conjugate modes and nonstationary response.

References

[1] Iijima S. Helical microtubules of graphitic carbon. *Nature*, 354, pp. 56-58, 1991.
[2] Rao AM, Richter E, Bandow S, Chase B, Eklund PC, Williams KA, Fang S, Subbaswamy KR, Menon M, Thess A, Smalley RE, Dresselhaus G and Dresselhaus MS. Diameter-Selective Raman Scattering from Vibrational Modes in Carbon Nanotubes. *Science*, 275, pp. 187-191, 1997.
[3] Gupta SS, Bosco FG and Batra RC. Wall thickness and elastic moduli of single-walled carbon nanotubes from frequencies of axial, torsional and inextensional modes of vibration. *Computational Materials Science*, 47, pp. 1049-1059, 2012.
[4] Arghavan S and Singh AV. On the vibrations of single-walled carbon nanotubes. *Journal of Sound and Vibration*, 330, pp. 3102-3122, 2011.
[5] Wang CY, Ru CQ and Mioduchowski A. Applicability and Limitations of Simplified Elastic Shell Equations for Carbon Nanotubes. *Journal of Applied Mechanics*, 71, pp. 622-631, 2004.
[6] Strozzi M, Manevitch LI, Pellicano F, Smirnov VV and Shepelev DS. Low-frequency linear vibrations of Single-Walled Carbon Nanotubes: analytical and numerical models. *Journal of Sound and Vibration* (paper submitted).

Proceedings of the 4th International Conference on Nonlinear Dynamics
ND-KhPI2013
June 19-22, 2013, Sevastopol, Ukraine

Nonlinear Vibrations of Functionally Graded Shells Subjected to Harmonic External Load

Matteo Strozzi*[1], Francesco Pellicano[1]

Abstract
The nonlinear vibrations of functionally graded (FGM) circular cylindrical shells are analysed. The Sanders-Koiter theory is applied in order to model the nonlinear dynamics of the system. The shell deformation is described in terms of longitudinal, circumferential and radial displacement fields. Simply supported boundary conditions are considered. The displacement fields are expanded by means of a double mixed series based on Chebyshev polynomials for the longitudinal variable and harmonic functions for the circumferential variable. Both driven and companion modes are considered. Numerical analyses are carried out in order to characterize the nonlinear response when the shell is subjected to a harmonic external load. A convergence analysis is carried out to obtain the correct number of axisymmetric and asymmetric modes describing the actual nonlinear behaviour. The influence of the material distribution on the nonlinear response is analysed considering different configurations and volume fractions of the constituent materials. The effect of the companion mode participation on the nonlinear response of the shell is analysed.

Keywords
Nonlinear vibrations, functionally graded materials, circular cylindrical shells

[1] Department of Engineering "Enzo Ferrari", University of Modena and Reggio Emilia, Modena, Italy
* **Corresponding author:** matteo.strozzi@unimore.it

Introduction

Functionally graded materials (FGMs) are composite materials obtained by combining two or more different constituent materials, which are distributed along the thickness in accordance with a volume fraction law.

The idea of FGMs was first introduced in 1984/87 by a group of Japanese material scientists [1]. They studied many different physical aspects such as temperature and thermal stress distributions, static and dynamic responses.

Loy et al. [2] analysed the vibrations of the cylindrical shells made of FGM, considering simply supported boundary conditions. They found that the natural frequencies are affected by the constituent volume fractions and configurations of the constituent materials.

Pradhan et al. [3] studied the vibration characteristics of FGM circular cylindrical shells made of stainless steel and zirconia, under different boundary conditions. They found that the natural frequencies depend on the material distributions and boundary conditions.

Amabili [4] analysed the nonlinear vibrations and stability of isotropic and FGM shells. He carried out a comparison of thin shells theories for large-amplitude vibrations of circular cylindrical shells and analysed the effect of the companion mode participation on the nonlinear response.

Pellicano [5] studied the dynamic instability of a cylindrical shell carrying a top mass under base excitation. He investigated the shell response with a resonant harmonic forcing applied taking into account geometric nonlinearities, electrodynamic shaker equations and shell-shaker interaction.

The method of solution used in the present work was developed by Strozzi et al. in Ref. [6].

In this paper, the nonlinear vibrations of FGM cylindrical shells are analysed. The Sanders-Koiter theory is applied to model the nonlinear dynamics of the system. Simply supported boundary conditions are studied. Both driven and companion modes are considered allowing for the travelling-wave response in the circumferential direction. The model is validated in the linear field by means of

data present in the literature. Numerical analyses are carried out in order to characterize the nonlinear response when the shell is subjected to a harmonic external load. A convergence analysis is carried out by considering different axisymmetric and asymmetric modes. The present study is focused on determining the nonlinear character of the shell dynamics as the material distribution varies.

1. Functionally graded materials

A general material property P_{fgm} of an FGM depends on the material properties and the volume fractions of the constituent materials, and it is expressed in the form

$$P_{fgm}(T,z)=\sum_{i=1}^{k}\tilde{P}_i(T)V_{fi}(z) \tag{1}$$

where $\tilde{P}_i$ and V_{fi} are the material property and the volume fraction of the constituent material i.

For an FGM thin cylindrical shell made of two different constituent materials, the Young's modulus E, the Poisson's ratio ν and the mass density ρ are expressed as

$$E_{fgm}(T,z)=\left(E_2(T)-E_1(T)\right)\left(\frac{z+h/2}{h}\right)^p+E_1(T) \tag{2}$$

$$\nu_{fgm}(T,z)=\left(\nu_2(T)-\nu_1(T)\right)\left(\frac{z+h/2}{h}\right)^p+\nu_1(T) \tag{3}$$

$$\rho_{fgm}(T,z)=\left(\rho_2(T)-\rho_1(T)\right)\left(\frac{z+h/2}{h}\right)^p+\rho_1(T) \tag{4}$$

where the power-law exponent p is a positive real number, ($0 \le p \le \infty$), and z describes the radial distance measured from the middle surface of the shell, ($-h/2 \le z \le h/2$).

2. Sanders-Koiter nonlinear theory of cylindrical shells

The elastic strain energy U_s of a cylindrical shell (plane stress hypothesis $\sigma_z = 0$) is given by

$$U_s=\frac{1}{2}LR\int_0^1\int_0^{2\pi}\int_{-h/2}^{h/2}(\sigma_x\varepsilon_x+\sigma_\theta\varepsilon_\theta+\tau_{x\theta}\gamma_{x\theta})d\eta d\theta dz \tag{5}$$

The kinetic energy T_s of a cylindrical shell (rotary inertia neglected) is given by

$$T_s=\frac{1}{2}LR\int_0^1\int_0^{2\pi}\int_{-h/2}^{h/2}\rho(z)(\dot{u}^2+\dot{v}^2+\dot{w}^2)d\eta d\theta dz \tag{6}$$

The virtual work W done by the external forces (q_x, q_θ, q_z) distributed per unit area is written as

$$W=LR\int_0^1\int_0^{2\pi}(q_x u+q_\theta v+q_z w)d\eta d\theta \tag{7}$$

The Rayleigh's dissipation function (viscous damping coefficient c) is written as

$$F = \frac{1}{2} cLR \int_0^{2\pi} \int_0^1 (\dot{u}^2 + \dot{v}^2 + \dot{w}^2) d\eta d\theta \tag{8}$$

3. Linear analysis

A modal vibration can be written in the form

$$u(\eta,\theta,t) = U(\eta,\theta) f(t) \qquad v(\eta,\theta,t) = V(\eta,\theta) f(t) \qquad w(\eta,\theta,t) = W(\eta,\theta) f(t) \tag{9}$$

where $U(\eta,\theta)$, $V(\eta,\theta)$, $W(\eta,\theta)$ describe the mode shape and $f(t)$ is the time law.

The mode shape is expanded by means of a double series in terms Chebyshev polynomials $T_m^*(\eta)$ in the axial direction and harmonic functions (cos $n\theta$, sin $n\theta$) in the circumferential direction

$$U(\eta,\theta) = \sum_{m=0}^{M_u} \sum_{n=0}^{N} \tilde{U}_{m,n} T_m^*(\eta) \cos n\theta \tag{10}$$

$$V(\eta,\theta) = \sum_{m=0}^{M_v} \sum_{n=0}^{N} \tilde{V}_{m,n} T_m^*(\eta) \sin n\theta \tag{11}$$

$$W(\eta,\theta) = \sum_{m=0}^{M_w} \sum_{n=0}^{N} \tilde{W}_{m,n} T_m^*(\eta) \cos n\theta \tag{12}$$

where $T_m^* = T_m(2\eta - 1)$, m is the polynomials degree and n denotes the number of nodal diameters.

4. Nonlinear analysis

The displacement fields $u(\eta,\theta,t)$, $v(\eta,\theta,t)$, $w(\eta,\theta,t)$ are expanded by using the linear mode shapes $U(\eta,\theta)$, $V(\eta,\theta)$, $W(\eta,\theta)$ and the conjugate mode shapes $U_c(\eta,\theta)$, $V_c(\eta,\theta)$, $W_c(\eta,\theta)$

$$u(\eta,\theta,t) = \sum_{j=1}^{N_u} \sum_{n=1}^{N} \left[U^{(j,n)}(\eta,\theta) f_{u,j,n}(t) + U_c^{(j,n)}(\eta,\theta) f_{u,j,n,c}(t) \right] \tag{13}$$

$$v(\eta,\theta,t) = \sum_{j=1}^{N_v} \sum_{n=1}^{N} \left[V^{(j,n)}(\eta,\theta) f_{v,j,n}(t) + V_c^{(j,n)}(\eta,\theta) f_{v,j,n,c}(t) \right] \tag{14}$$

$$w(\eta,\theta,t) = \sum_{j=1}^{N_w} \sum_{n=1}^{N} \left[W^{(j,n)}(\eta,\theta) f_{w,j,n}(t) + W_c^{(j,n)}(\eta,\theta) f_{w,j,n,c}(t) \right] \tag{15}$$

The Lagrange equations of motion for forced vibrations are expressed in the following form

$$\frac{d}{dt}\left(\frac{\partial L}{\partial \dot{q}_i} \right) - \frac{\partial L}{\partial q_i} = Q_i \qquad i \in [1, N_{\max}] \qquad (L = T_s - U_s) \tag{16}$$

The generalized forces Q_i are obtained by the differentiation of the Rayleigh's dissipation function F (8) and of the virtual work done by the external forces W (7), in the form

$$Q_i = -\frac{\partial F}{\partial \dot{q}_i} + \frac{\partial W}{\partial q_i} \tag{17}$$

Using the Lagrange equations (16) a set of nonlinear ordinary differential equations is obtained; such system is then solved by using numerical methods.

5. Numerical results

The present study is carried out on an FGM made of stainless steel and nickel; its properties are graded in the thickness direction according to a volume fraction distribution, where p is the power-law exponent. The material properties, reported in Table 1, have been extracted from Ref. [2].

Table 1. Properties of stainless steel and nickel vs. coefficients of temperature (300 K)

	Stainless steel			**Nickel**		
	E	ν	ρ	E	ν	ρ
P_0	2.01×10^{11} Nm^{-2}	0.326	8166 kgm^{-3}	2.24×10^{11} Nm^{-2}	0.3100	8900 kgm^{-3}
P_{-1}	0 K	0 K	0 K	0 K	0 K	0 K
P_1	3.08×10^{-4} K^{-1}	-2.002×10^{-4} K^{-1}	0 K^{-1}	-2.79×10^{-4} K^{-1}	0 K^{-1}	0 K^{-1}
P_2	-6.53×10^{-7} K^{-2}	3.797×10^{-7} K^{-2}	0 K^{-2}	-3.99×10^{-9} K^{-2}	0 K^{-2}	0 K^{-2}
P_3	0 K^{-3}	0 K^{-3}	0 K^{-3}	0 K^{-3}	0 K^{-3}	0 K^{-3}
P	2.08×10^{11} Nm^{-2}	0.318	8166 kgm^{-3}	2.05×10^{11} Nm^{-2}	0.3100	8900 kgm^{-3}

In order to validate the present method, the natural frequencies of simply supported FGM shells are compared with those of Loy et al. [2], see Table 2. The comparison shows that the present method gives results quite close to Ref. [2], the differences being less than 1%.

Table 2. Comparisons for a simply supported FGM shell (h/R = 0.002, L/R = 20, p = 1)

Natural frequency (Hz)				**Difference** %
m	n	Present model	Ref. [2]	
1	3	4.1562	4.1569	0.02
1	2	4.4794	4.4800	0.01
1	4	7.0379	7.0384	0.01
1	5	11.241	11.241	0.00
1	1	13.211	13.211	0.00
1	6	16.455	16.455	0.00

The shell is excited by an external modally distributed radial force $q_z = f_{1,6} \sin\eta \cos 6\theta \cos \Omega t$; the amplitude of excitation is $f_{1,6} = 0.0012\, h^2\, \rho\, \omega_{1,6}{}^2$ and the frequency of excitation is $\Omega \approx \omega_{1,6}$. The external forcing $f_{1,6}$ is normalized with respect to the mass, acceleration and thickness; the damping ratio is equal to $\xi_{1,6} = 0.0005$.

Table 3. Nonlinear convergence analysis. Modes selected for the expansions (13-15).

(j,n)	(1,6)	(1,12)	(1,18)	(3,6)	(3,12)	(3,18)	(1,0)	(3,0)	(5,0)	(7,0)
6 dof	u, v, w	v	–	–	–	–	u, w	–	–	–
9 dof	u, v, w	v	–	–	v	–	u, w	u, w	–	–
12 dof	u, v, w	v	–	u, v, w	v	–	u, w	u, w	–	–
15 dof	u, v, w	v	v	u, v, w	v	–	u, w	u, w	u, w	–
18 dof	u, v, w	v	v	u, v, w	v	v	u, w	u, w	u, w	u, w

In Figure 1, a moderately thick and long shell is analysed (h/R = 0.025, L/R = 20, p = 1), the amplitude-frequency curves are obtained with the expansions of Table 3. The 6 dof model, with an insufficient number of axisymmetric modes, is clearly inaccurate; indeed, for this kind of shell the

correct behaviour is softening. From the convergence analysis, one can claim that the 9 dof model gives satisfactory results with the minimal computational effort; therefore, in the following the 9 dof model of Table 3 will be used.

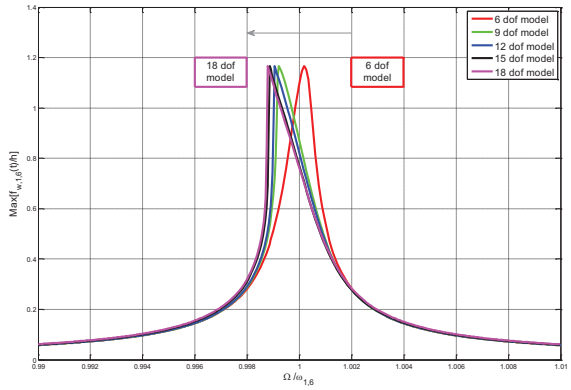

Figure 1. Convergence analysis, amplitude-frequency curves (h/R = 0.025, L/R = 20, p = 1). "–", 6 dof model; "–", 9 dof model; "–", 12 dof model; "–", 15 dof model; "–", 18 dof model.

The effect of the material distribution on the nonlinear response is analysed by considering two different FGM shells, Type I (nickel on the inner surface and stainless steel on the outer surface) and Type II (stainless steel on the inner surface and nickel on the outer surface).

In Figures 2(a-b), the behaviour of the natural frequency $\omega_{1,6}$ and the nonlinear character vs. the exponent p (equations (2-4)) is shown for the FGM shell (h/R = 0.025, L/R = 20) having a softening nonlinear character identified by means of the following indicator

$$NL_b = \frac{\omega_{1,6\ nonlin} - \omega_{1,6\ lin}}{\omega_{1,6\ lin}} \times 1000 \tag{18}$$

where the nonlinear character is hardening when $NL_b > 0$, softening when $NL_b < 0$.

When the stiffer material is outside (Type I FGM, Figure 2(a)), an increment of the exponent p leads to a predominance of the material with a smaller Young's modulus (nickel) and this implies a decreasing of the natural frequencies, while an increase in the predominance of the weaker material produces a decrease of the nonlinearity of the system. In the case of FGM with stiffer material inside (Type II FGM, Figure 2(b)), the increment of the exponent p magnifies the presence of stainless steel, increasing the natural frequencies and the nonlinearity.

(a)

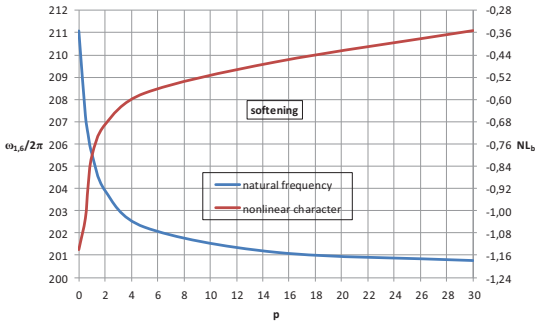

(b)

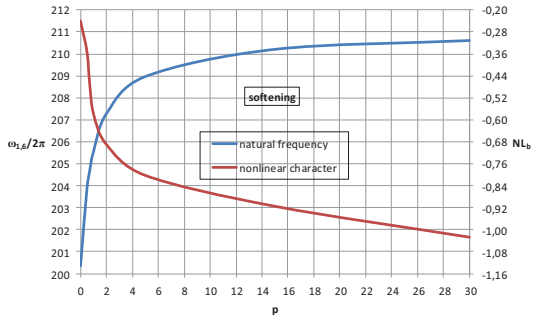

Figure 2. Natural frequency $\omega_{1,6}$ and nonlinear character NL_b vs. exponent parameter p for the cylindrical shell (h/R = 0.025, L/R = 20). (a) Type I FGM. (b) Type II FGM.

The effect of the companion mode participation on the nonlinear response is analysed. In Figures 3(a-b), the amplitude-frequency curve with the companion mode participation is presented ($h/R = 0.025$, $L/R = 20$, $p = 1$, mode (1,6)). The response $f_{w,1,6}(t)$ with companion mode participation, solid blue line of Figure 3(a), is very similar to the response without companion mode participation, dashed black line, see Figure 1. The companion mode, Figure 3(b), produces a variation in the small region close to the resonance ($0.9996 < \Omega/\omega_{1,6} < 0.9999$), where the companion mode is excited by means of a 1:1 internal resonance which induces an energy transfer between the two conjugate modes.

(a) (b)

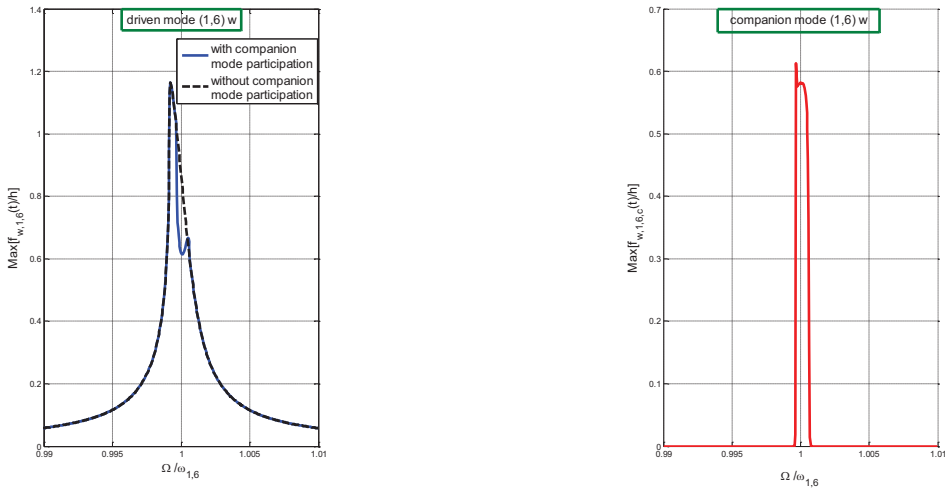

Figure 3. Amplitude-frequency curves of the FGM shell ($h/R = 0.025$, $L/R = 20$, $p = 1$). 14 dof model. (a) "– –", driven mode (1,6) w without companion mode participation; "–", driven mode (1,6) w with companion mode participation. (b) Companion mode (1,6) w.

6. Numerical results

The nonlinear vibrations of FGM cylindrical shells are analysed. The Sanders-Koiter theory is applied to model the nonlinear dynamics of the system in the case of finite amplitude of vibration.

A convergence analysis is carried out. The fundamental role of the axisymmetric and higher-order asymmetric modes is clarified in order to obtain the actual nonlinearity.

The effect of the material distribution is analysed. The relationships between the power-law exponent, the corresponding natural frequency and nonlinearity are studied.

The effect of the companion mode participation on the nonlinear response is analysed. Both driven and companion modes are considered. Nonlinear amplitude-frequency curves are obtained.

References

[1] Report from Technology Agency of Japanese Government "*Research on the Basic Technology for the Development of Functionally Gradient Materials for Relaxation of Thermal-stress*", 1987.

[2] Loy CT, Lam KY, Reddy JN. Vibration of functionally graded cylindrical shells, *International Journal of Mechanical Sciences*, 41, pp. 309-324, 1999.

[3] Pradhan SC, Loy CT, Lam KY, Reddy JN. Vibration characteristics of functionally graded cylindrical shells under various boundary conditions, *Applied Acoustics*, 61, pp. 111-129, 2000.

[4] Amabili M. *Nonlinear Vibrations and Stability of Shells and Plates*, Cambridge University Press, New York, 2008.

[5] Pellicano F. Dynamic instability of a cylindrical shell carrying a top mass under base excitation: Experiments and theory. *International Journal of Solids and Structures*, 48, pp. 408-427, 2011.

[6] Strozzi M, Pellicano F. Nonlinear vibrations of functionally graded cylindrical shells, *Thin-Walled Structures*, 67, pp. 63-77, 2013.

Proceedings of the 4th International Conference on Nonlinear Dynamics
ND-KhPI2013
June 19-22, 2013, Sevastopol, Ukraine

Geometrically Nonlinear Vibrations of Laminated Shallow Shells with Mixed Boundary Conditions

G.N. Timchenko[1*], N.A. Budnikov[1]

Abstract
The presented paper is devoted to the numerical study of the dynamic behavior of shallow shells with complex form of the plan and the mixed boundary conditions. For the calculation the method proposed earlier in [1,2] have been used. This method uses essentially the R-functions theory, the variational Ritz, Bubnov-Galerkin and Runge-Kutta methods. For the considered three-layer spherical shell with mixed boundary conditions (combinations of clamped and simply supported conditions) amplitude-frequency characteristics for different types of material are produced and the natural frequencies and mode shapes are presented.

Keywords
Nonlinear vibrations, laminated shallow shells, R-functions theory

[1] NTU "KhPI", Kharkov, Ukraine
* **Corresponding author:** GNTimchenko@mail.ru

Introduction

Elements of many modern constructions are designed with the help of composite laminated shallow shells. The attention of many researchers is drawn to the construction methods of investigation laminated shallow shells and plates. Refs. [3–5] are the most complete reviews of studies on nonlinear vibrations of shallow shells. As can be seen from the review, one of the most the most widely used method for solving this class of problems is the finite element method (FEM). In [1,2, etc.] an alternative numerical-analytical approach based on the theory of R-functions is proposed. This method allows us to investigate geometrically non-linear vibrations of laminated shallow shells with complex form of the plan and mixed boundary conditions.

1. Formulation

To describe the dynamic behavior of thin shallow shells the mathematical formulation is carried out in the framework of the classical geometrically nonlinear theory by Donnell-Mushtari-Vlasov, which is based on the Kirchhoff-Love hypotheses adopted for the whole package of layers of the shell as a whole [6]. In matrix form, the system of equations of motion of the shell is:

$$[L]\{U\} = \{NL\} + m_1 \partial_{tt}\{U\}, \tag{1}$$

where $[L] = [L_{ij}]_{i,j=\overline{1,3}}$ is a matrix of linear operators, $\{NL\}$ is a vector of nonlinear operators, $\{U\} = \{u, v, w\}^T$ is a vector of displacements. The system (1) in expanded form is represented in [1]. The system is supplemented by the boundary and initial conditions. In this paper we consider the combination of the following types of boundary conditions:

Clamped edge:

$$u = 0, \quad v = 0, \quad w = 0, \quad \partial_n w = 0 \tag{2}$$

Immovable simply supported:

$$u = 0, \quad v = 0, \quad w = 0, \quad M_n = 0 \tag{3}$$

Here $M_n = M_{11}l^2 + M_{22}m^2 + 2M_{12}lm$, expressions $l = \cos\alpha$, $l = \cos\beta = \sin\alpha$ are the direction cosines of the normal vector to the boundary of shell.

The initial conditions were adopted in the form of:

$$w\big|_{t=0} = w_{\max}, \; \partial_t w\big|_{t=0} = 0. \tag{4}$$

2 Method of solution

According to the method proposed in [1,2], we represent solutions of the system (1) as follows:

$$\begin{cases} u(x,y,t) = \sum\limits_{i=1}^{n} y_i(t) \cdot u_i^{(c)}(x,y) + \sum\limits_{i=1}^{n}\sum\limits_{j=i}^{n} y_i(t) \cdot y_j(t) \cdot u_{ij}(x,y), \\ v(x,y,t) = \sum\limits_{i=1}^{n} y_i(t) \cdot v_i^{(c)}(x,y) + \sum\limits_{i=1}^{n}\sum\limits_{j=i}^{n} y_i(t) \cdot y_j(t) \cdot v_{ij}(x,y), \\ w(x,y,t) = \sum\limits_{i=1}^{n} y_i(t) \cdot w_i^{(c)}(x,y), \end{cases} \tag{5}$$

where $y_i(t)$ are unknown functions, depending on the time, $u_i^{(c)}(x,y)$, $v_i^{(c)}(x,y)$ and $w_i^{(c)}(x,y)$ are eigenfunctions of the linear vibrations of the shell. Functions $u_{ij}(x,y)$ and $v_{ij}(x,y)$ are solutions of the following system:

$$\begin{cases} L_{11}u_{ij} + L_{12}v_{ij} = -Nl_1^{(2)}\left(w_i^{(c)}, w_j^{(c)}\right), \\ L_{12}u_{ij} + L_{22}v_{ij} = -Nl_2^{(2)}\left(w_i^{(c)}, w_j^{(c)}\right), \end{cases} \tag{6}$$

where L_{pm}, $p,m = \overline{1,2}$ are the linear operators of the system (1), $Nl_1^{(2)}$ and $Nl_2^{(2)}$ are nonlinear operators that depend on the partial derivatives of the eigenfunctions $w_i^{(c)}$ [1,2].

The system (6) is supplemented by appropriate boundary conditions. For cases considered in this work they have the form:

$$u_{ij}(x,y) = 0, \quad v_{ij}(x,y) = 0, \quad \forall(x,y) \in \partial\Omega \tag{7}$$

The sequence of tasks (6) – (7) and the linear problem of free vibrations of the shell are solved by the R-functions method (RFM).

Let us substitute the relations (5) into equations (1). Then the first two equations of (1) are satisfied identically. Applying the Bubnov-Galerkin procedure to the third equation of system (1), we obtain a system of ordinary differential equations, which have been described in [1]. Solutions of the system of ordinary differential equations are sought for by the Runge-Kutta method of order 7-8.

3 Numerical results

We investigate nonlinear free vibrations of three-layered shells with the form of the plan shown in Fig. 1. Table 1 shows values of the dimensionless mechanical properties of materials, which are considered in this paper.

The solution structure [7] for this problem is:

$$w = \omega_1^2\omega_2\Phi_1, \quad u = \omega\Phi_2, \quad v = \omega\Phi_3, \tag{8}$$

where $\omega(x,y)=0$ is the equation of domain boundary, $\omega_1(x,y)=0$ is the equation of clamped part of the domain, $\omega_2(x,y)=0$ is the equation of immovable simply supported part of the domain:

$$\omega(x,y)=(f_1\wedge_0 f_2\wedge_0 f_3)\wedge_0(f_4\vee_0 f_5)\wedge_0(f_4\vee_0 f_6),$$
$$\omega_1(x,y)=f_1,\quad \omega_2(x,y)=(f_2\wedge_0 f_3)\wedge_0(f_4\vee_0 f_5)\wedge_0(f_4\vee_0 f_6),$$

Table 1. Mechanical characteristics of shells

Material	E1/E2	G12/E2	v1
Glass-epoxy	3	0.5	0.25
Boron-epoxy	10	0.33333	0.3
Graphite-epoxy	40	0.6	0.25

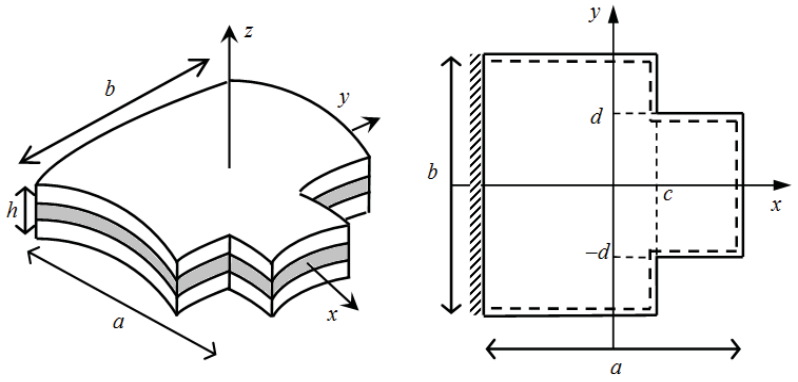

Figure 1. Plan form of the shell

where

$$f_1=\left\{\sigma_1=\frac{1}{\sqrt{2}}\left(\frac{a}{2}+x\right)\ge 0\right\},\ f_2=\left\{\sigma_2=\frac{1}{b}\left(\left(\frac{b}{2}\right)^2-y^2\right)\ge 0\right\},\ f_3=\left\{\sigma_3=\frac{1}{\sqrt{2}}\left(\frac{a}{2}-x\right)\ge 0\right\},$$
$$f_4=\left\{\sigma_4=\frac{1}{\sqrt{2}}(c-x)\ge 0\right\},\ f_5=\left\{\sigma_5=\frac{1}{\sqrt{2}}(d+y)\ge 0\right\},\ f_6=\left\{\sigma_6=\frac{1}{\sqrt{2}}(d-y)\ge 0\right\},$$

$\wedge_0$ is the R-conjunction symbol, $\vee_0$ is the R-dizjunction symbol [7].

The geometrical parameters of the shell are following: $b/a=1$, $h/a=0.01$, $c/a=0.2$, $d/a=0.3$. Table 2 shows the values of the dimensionless linear frequencies $\Omega_i=\omega_{Li}b^2\sqrt{\rho/E_1h^2}$ and forms of vibrations of three-layered spherical cross-ply (0º/90º/0º) shells which is made of a Boron-epoxy.

Table 2. Non-dimensional linear frequencies and forms of vibration

Linear frequencies	Ω1 = 11.28	Ω2 = 13.66	Ω3 = 16.13
Forms of vibration	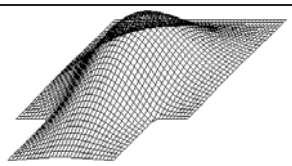	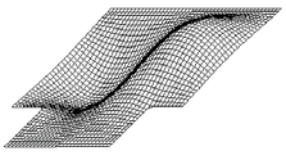	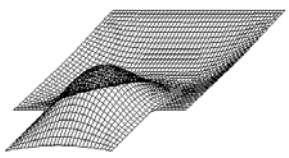

The amplitude-frequency curves of vibrations of cross-ply (0º/90º/0º) shallow spherical shells ($R_x/a=R_y/a=0.1$) which are made of different materials are presented in Figure 2a. Futher the results are presented for shells made of Boron-epoxy. Effect case of the way of stacking of layers on amplitude–frequency curves is shown in Figure 2b. Figure 2c shows a comparison of the amplitude-

frequency curves of cross-ply cylindrical, spherical shells and panels of double curvature. As shown in Figure 2c, the amplitude-frequency curves for panels of double curvature are curves of the rigid type, and in the other cases (for cylindrical and spherical shells) they are curves of the soft type.

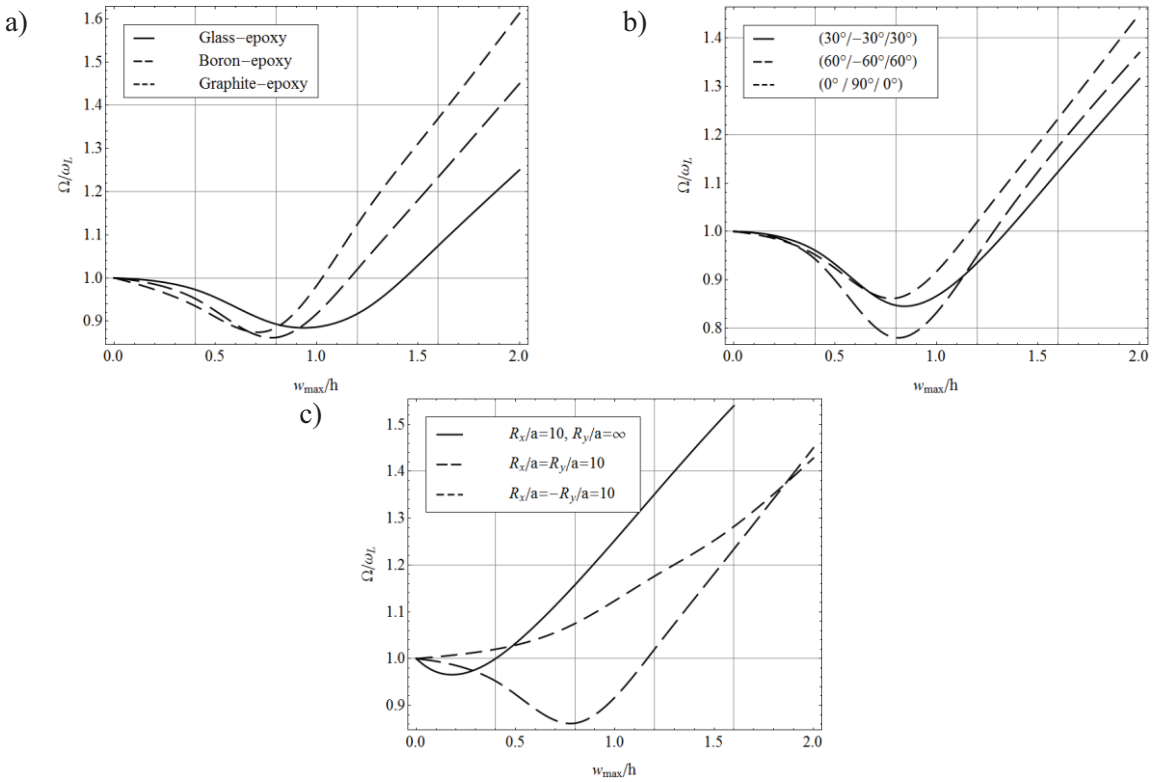

Figure 2. The amplitude-frequency response of shells

Conclusions

A numerical-analytically approach proposed in [1,2] is used to research free vibration problems for laminated shallow shells with complex planform. Three-layered shells made of different materials with various ways of stacking and curvature ratios are considered. Form of the plan of the considered shells includes two rectangular cutouts, the domain partially clamped and partially immovable simply supported. The amplitude-frequency curves of vibrations of considered shells have been constructed using the first-mode approximation.

References

[1] Kurpa L.V., Budnikov N.A. Investigation of forced nonlinear vibrations of laminated shallow shells with multimodal approximation. *Bulletin of the Donetsk National University, Series A. Natural Sciences*, № 1, pp. 55–60, 2013.

[2] Kurpa L.V., Budnikov N.A. Investigation of forced geometrically nonlinear vibrations of the laminated shallow shells with antisymmetrical structure, *Problems of the Computational Mechanics and Strength of Structures* (editors A.P. Dziuba and al.), Dnipropetrovsk, Lear, Vol. 20, pp. 208–216, 2012 (in Russian).

[3] Amabili M. *Nonlinear Vibrations and Stability of Shells and Plates*, Cambridge, Cambridge University Press, 2008.

[4] Zhang Y.X., Yang C.H. Recent developments in finite element analysis for laminated composite plates, *Composite Structures,* Vol. 88, pp 147–157, 2009.

[5] Sharma A.K., Mittal N.D. Review on Stress and Vibration Analysis of Composite Plates, *J. of Applied Sciences,* V. 10 (23), pp. 3156–3166, 2010.

[6] Ambartsumyan S.A. *The General Theory of Anisotropic Shells,* Moscow, Nauka, 1974 (in Russian).

[7] Rvachev V.L. *The R-Functions Theory and some its Application,* Kiev, Naukova Dumka, 1982 (in Russian).

Proceedings of the 4th International Conference on Nonlinear Dynamics
ND-KhPI2013
June 19-22, 2013, Sevastopol, Ukraine

Nonlinear deformations of structures cylindrical element under local shock

Y.S. Vorobiov[1*], L. Kruszka[2] , N.Y. Ovcharova[1]

Abstract
High rate deformations of structures cylindrical elements are considered 3D formulation. Elastic-plastic finite deformations and dynamic properties of material take into account. The problem is geometrically and physically nonlinear, and the finite element method is used. The numerical analysis of dynamics stress-strain state of real structures elements is executed.

Keywords
Local impact, high rate deformations, 3D FEM models.

[1]A.N. Podgorny Institute of Mechanical Engineering Problems NAS, Ukraine, Kharkov
[2]Military University of Technology, Warsaw, Poland
* **Corresponding author:** Vorobiev@ipmash.kharkov.ua

Introduction

Cylindrical elements of many structures are subjected by local shock. For example, it may be the elements of the cases and the input and output devices in gas turbine engines, equipment cases of many industries, technological chambers and other. While such structural elements often possess axial symmetry, the problem is not axial-symmetric because of the peculiarities of local load, which is attached to a limited area. These cylindrical elements can not also be consider as thin, as in a limited area of impact develop three-dimensional elastoplastic deformation. Therefore, the problem is considered in three-dimensional formulation. Speed deformation of structural elements at impact occurs in the elastoplastic stage. In these cases it is necessary take into account the dynamic properties of materials. With intensive shock loads may arise finite displacements and deformations [1 - 3]. Cylindrical elements of modern structures can be performed from metal, polymer and composite materials.

1. Problem Statement

Cylindrical structures elements are considered in three-dimensional formulation [1, 2], taking into account the relations of the dynamic theory of plastic deformation.

$$\begin{aligned}
(\lambda+\mu)\frac{\partial \varepsilon_0}{\partial r}-\mu\left(\frac{u}{r^2}+\frac{2}{r^2}\frac{\partial v}{\partial \varphi}\right)+\mu\Delta u=\rho\frac{\partial^2 u}{\partial t^2}\\
(\lambda+\mu)\frac{\partial \varepsilon_0}{\partial \varphi}-\mu\left(\frac{u}{r^2}+\frac{2}{r^2}\frac{\partial u}{\partial \varphi}\right)+\mu\Delta v=\rho\frac{\partial^2 v}{\partial t^2}\\
(\lambda+\mu)\frac{\partial \varepsilon_0}{\partial z}+\mu\Delta w=\rho\frac{\partial^2 w}{\partial t^2}
\end{aligned} \qquad (1)$$

where λ,μ – Lame parameter, ρ – density of material, $U(u,w,v)$ – displacement vector, $\varepsilon_0 = divU$ – relative volume expansion , which is given by

$$\varepsilon_0 = \varepsilon_r + \varepsilon_\varphi + \varepsilon_z = \frac{\partial u}{\partial r} + \frac{\partial v}{r\partial \varphi} + \frac{u}{r} + \frac{\partial w}{\partial z} \tag{2}$$

Nonlinear deformation is

$$\begin{gathered}
\varepsilon_r = \frac{\partial u}{\partial r} + \frac{1}{2}\left(\left(\frac{\partial u}{\partial r}\right)^2 + \left(\frac{\partial v}{\partial r} - \frac{v}{r}\right)^2 + \left(\frac{\partial w}{\partial r}\right)^2\right) \\
\varepsilon_\varphi = \frac{\partial v}{r\partial \varphi} + \frac{u}{r} + \frac{1}{2}\left(\left(\frac{\partial v}{r\partial \varphi} + \frac{u}{r}\right)^2 + \left(\frac{\partial u}{r\partial \varphi}\right)^2 + \left(\frac{\partial w}{r\partial \varphi}\right)^2\right) \\
\varepsilon_z = \frac{\partial w}{\partial z} + \frac{1}{2}\left(\left(\frac{\partial u}{\partial z}\right)^2 + \left(\frac{\partial v}{\partial z}\right)^2 + \left(\frac{\partial w}{\partial z}\right)^2\right) \\
\gamma_{r\varphi} = \frac{\partial u}{r\partial \varphi} + \frac{\partial v}{\partial r} - \frac{v}{r} + \frac{1}{2}\left(\frac{\partial u}{r\partial \varphi}\frac{\partial u}{\partial r} + \left(\frac{\partial v}{r\partial \varphi} + \frac{u}{r}\right)\left(\frac{\partial v}{\partial r} - \frac{v}{r}\right) + \frac{\partial w}{r\partial \varphi}\frac{\partial w}{\partial r}\right) \\
\gamma_{z\varphi} = \frac{\partial v}{\partial z} + \frac{\partial w}{r\partial \varphi} + \frac{1}{2}\left(\frac{\partial v}{\partial z}\left(\frac{\partial v}{r\partial \varphi} + \frac{u}{r}\right) + \left(\frac{\partial u}{\partial z}\frac{\partial u}{r\partial \varphi}\right) + \frac{\partial w}{\partial z}\frac{\partial w}{r\partial \varphi}\right) \\
\gamma_{zr} = \frac{\partial u}{\partial z} + \frac{\partial w}{\partial r} + \frac{1}{2}\left(\frac{\partial u}{\partial z}\frac{\partial u}{\partial r} + \frac{\partial u}{\partial z}\left(\frac{\partial v}{\partial r} - \frac{v}{r}\right) + \frac{\partial w}{\partial z}\frac{\partial w}{\partial r}\right)
\end{gathered} \tag{3}$$

The relations between stresses and strains in a cylindrical coordinate system x, r, φ is given by

$$\begin{aligned}
\sigma_r - \sigma &= \frac{1}{\psi}\left(\varepsilon_r - \frac{1}{3}\varepsilon\right) & \tau_{r\varphi} &= \frac{1}{\psi}\gamma_{r\varphi} \\
\sigma_\varphi - \sigma &= \frac{1}{\psi}\left(\varepsilon_\varphi - \frac{1}{3}\varepsilon\right) & \tau_{\varphi z} &= \frac{1}{\psi}\gamma_{\varphi z} \\
\sigma_z - \sigma &= \frac{1}{\psi}\left(\varepsilon_z - \frac{1}{3}\varepsilon\right) & \tau_{rz} &= \frac{1}{\psi}\gamma_{rz} \\
\sigma &= \frac{1}{3}(\sigma_r + \sigma_\varphi + \sigma_z) & \varepsilon &= \varepsilon_r + \varepsilon_\varphi + \varepsilon_z
\end{aligned} \tag{4}$$

where - $\sigma_r, \sigma_\varphi, \sigma_z$ the components of the stress; $\varepsilon_r, \varepsilon_\varphi, \varepsilon_z$ - strain components

In the case of elastic deformation $\psi = \frac{1}{2\mu}$, where μ - Lame parameter. Then the relations (4) become the expression of Hooke's law. When plastic deformation factor ψ has the form

$$\psi = \frac{3}{2}\frac{\varepsilon_i}{\sigma_i} \tag{5}$$

Formula (2) contains relation between the intensities of the stress σ_i and of intensities strain ε_i, and strain rate $\dot{\varepsilon}_i$.

$$\sigma_i = \sigma_i\left(\varepsilon_i, \dot{\varepsilon}_i\right) \tag{6}$$

There are a series of empirical relations of the form (6) [1 - 3]. The investigation uses the relation of the Pezhiny type [3].

$$\sigma_i = \left[1 + \left(\frac{\dot{\varepsilon}_i^{\,pl}}{\gamma}\right)^m\right] E\varepsilon_i \tag{7}$$

where E is the elastic modulus;

m and r are coefficients of sensitivity to strain rate;

$\dot{\varepsilon}_i^{\,pl}$ is the rate of deformation in the plastic phase.

The problem is nonlinear and requires special modifications to the finite element method.

Cylindrical structures of metal and composite material are considered. The layer thickness is variable $h(x)$. The finite element model of the system takes into account of the elastoplastic high rate deformation, the dynamic properties of the material and the finite displacements and deformations.

The zone of intense stress at impact is very limited. Stress decrease rapidly in time and at a distance of about five - ten times the size of the zone of load application [4, 5]. Therefore, as a result of the numerical analysis of stress intensity zone is found, there is an allocation of the structural element area of interest. In this area can be used over a dense grid.

2. Analysis of the Numerical Results

The finite-element models of cylindrical elements of different materials are considered. The numerical analysis of the dynamic stress-strain state in the region under impact loading on the inner surface of a series of cylindrical elements. The projectile hade mass = 0.1 kg and speeds of impact was different.

It is present the results of analysis of impact of the projectile on the inner surface of the element made of composite material. It is considered the element with internal diameter of 800 mm., thickness 30 mm. Material of element has density ρ = 1300 kg/m^3, modulus of elasticity E = 2660 MPa, Poisson's ratio ν = 0,45. For these element when impact speed is 400 m/s maximum displacement were $0.167 \cdot 10^{-2}$ m, and maximum stress intensity up to 54 MPa. In these case the plastic strains is occur in a small area.

Fig. 1 shows the distribution of displacement intensities on the inner surface of the cylindrical element made of composite material. Fig. 2 shows the distribution of stresses intensities in the cross section over the thickness of the element in the impact zone.

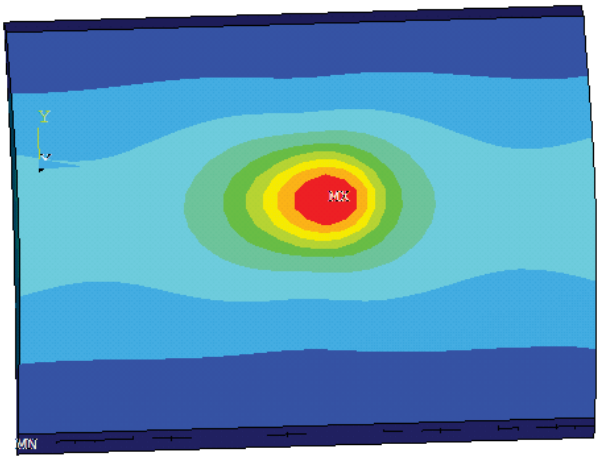

Figure 1. Field of displacements intensities on the inner surface of the cylindrical element under impact with speed 400 m/s

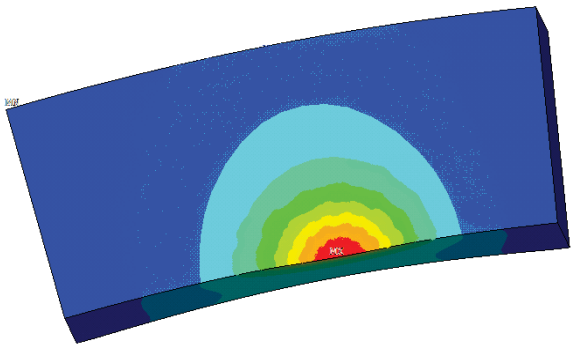

Figure 2. Fields of the stresses intensities in the cross section of the cylindrical element under impact with speed 400 m/s

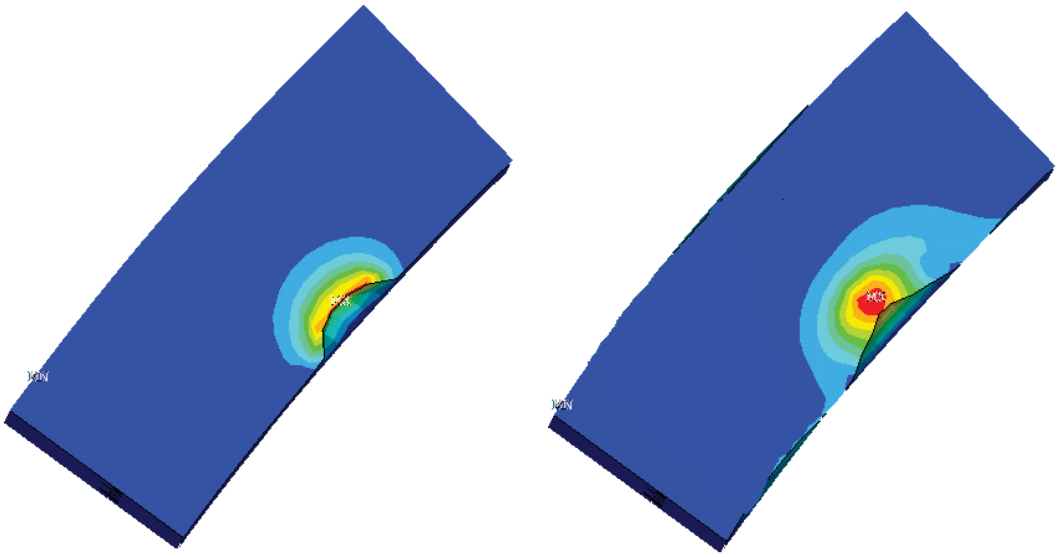

Figure 3. Fields of the stresses intensities in the cross section of the cylindrical element under impact with speed over 1000 m/s

If the impact speeds over 1000 m/s are observed plastic deformation and further penetration element (Fig. 3).

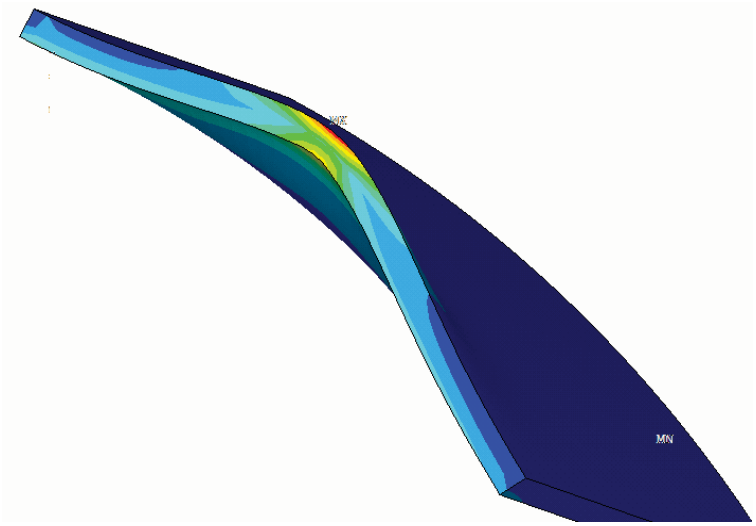

Figure 4. Fields of the stresses intensities in the cross section of the cylindrical element under impact with speed over 400 m/s (the moment of impact)

For example, the results of the analysis of the dynamic stress strain state of a steel cylindrical element are showed. It is considered element of steel with inner diameter of 400 mm and the thickness h_1 = 1,4 mm and h_2 = 2 mm. When the impact speed is 400 m/s the stress in one-layer element intensity reaches 123 MPa in the zone of impact (Fig. 4) and reduced to 1 MPa after unloading (Fig.5). It is elastic deformations for these impact speed. The maximum intensity of the displacements make $0.26 \cdot 10^{-3}$ m and $0.13 \cdot 10^{-13}$ m after unloading. When the impact speeds are more than 1000 m/s there is significant plastic deformation and further penetration of the element.

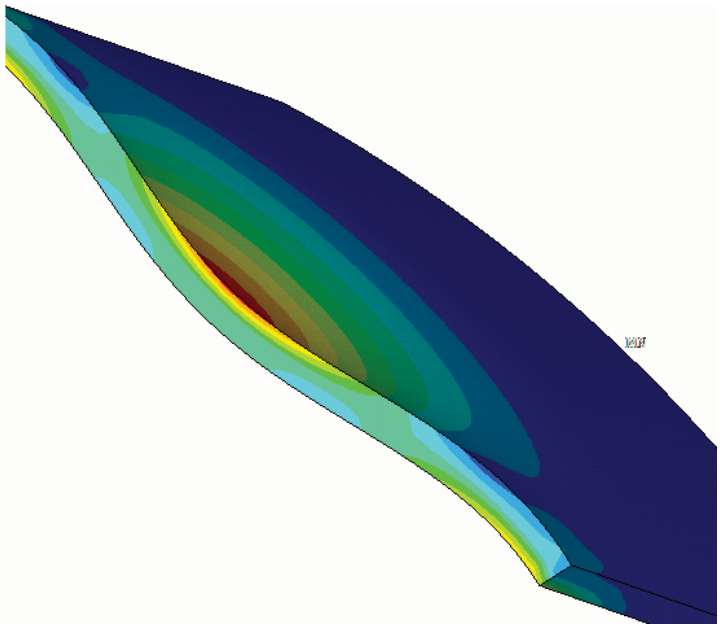

Figure 5. Fields of the stresses intensities in the cross section of the cylindrical element under impact with speed over 400 m/s (after unloading)

Fig. 6 show fields of the displacements and stress intensity in the two- layer cylindrical element under impact with speed over 1000 m/s.

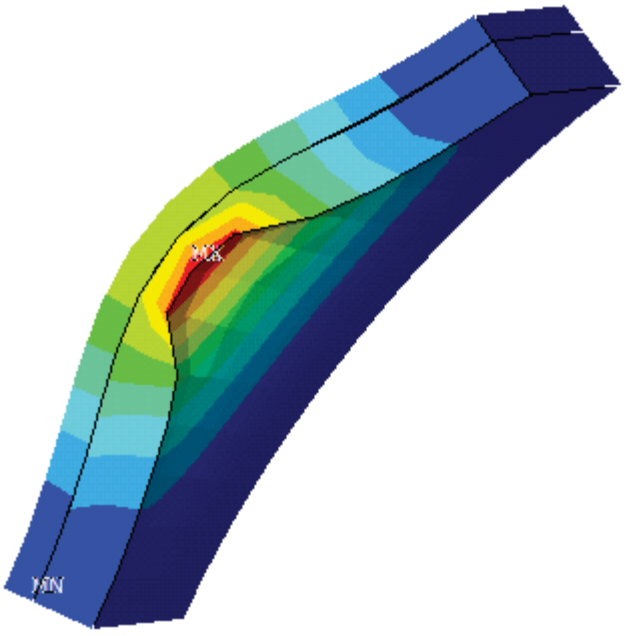

Figure 6. Fields of the displacements and stress intensity in the two- layer cylindrical element under impact with speed over 1000 m/s in local zone with a dense grid

The analysis of the stress-strain state of structural elements under local shock confirmed that zone of intensive displacement, strains and stresses is very limited. It should be noted the wave propagation of stresses and displacements

The results of these investigations were used to analysis the dynamic strength of the elements of real structures. In particular, the dynamic strength of cases of gas turbine engines and power transmission are considered

Conclusions

Three-dimensional dynamic stress-strain state development in structural element under local shock is considered. There for it is necessary to used three-dimensional models taking into account finite elastic-plastic deformations and dynamics properties of material.

Under an action of the local shock loadings with speeds 300 m/s in the cylindrical elements of corps the dynamic stress-strain state takes place, as a rule, in the elastic stage.

At the increase of speed of projective the elastic-plastic process takes place and after unloading there are remaining deformations.

References

[1] Troshchenko V.T., Lebedev, A,A,, Strizhalo V.A.. *Mechanical Behavior of Materials under Different Types of Loading*, Logos, Kiev, 2000 (in Russian).

[2] Vorobiov Y.S., Kolodyazhny A.V., Sevryukov V.I., Yanyutin E.G. *High-speed Deformation of Structure Elements*, Naukova Dumka, Kiev, 1989 (in Russian).

[3] Meyers M.A. *Dynamics Behavior of Materials*, Wiley, New York, 1994.

[4] Vorobiov Y.S., Chernobryvko M.V., Yaryzhko A.V., Stepanchenko D.I., Evchenko N.Y., Problems of analysis of high rate deformation of structural elements under impulse loading *Aerospace Technical and Technology*, № 11(47)., pp. 35 – 43, 2007.

[5] Vorobiov Y., Chernobryvko M., Kruszka L. Strain rate deformation and damage of structural elements under local impulse loadings *Military University of Technology*, pp. 679 – 687, Warsaw 2010.

Proceedings of the 4th International Conference on Nonlinear Dynamics
ND-KhPI2013
June 19-22, 2013, Sevastopol, Ukraine

Circular Cylindrical Shells Under Combined Axial Loads: an Experimental Study

Antonio Zippo[1]*, Marco Barbieri[1],Francesco Pellicano[1]

Abstract
Thin shells structures have an important role in engineering; several important examples can be found in Structural Engineering, Mechanical Engineering and Aerospace: water tanks, containment shells of nuclear power plants, concrete arch domes, piping systems, pressure vessels, aircrafts, missiles, rockets, ships. Even though many researchers have extensively studied nonlinear vibrations of cylindrical shells, experimental studies are rather limited in number; in particular, rare experimental reports have been published about shells loaded with in-plane . In this paper the response of a circular cylindrical shells subjected to axial compressive and periodic loads has been experimentally investigated. The experimental setup is explained and deeply described along with the analysis of preliminary results. The linear shell behavior is investigated by means of a finite element model in order to enhance the comprehension of experimental results in the linear field. The main goal is to investigate the nonlinear phenomena associated with a combined effect of compressive static and a periodic axial loads, the investigation have been carried out for different combinations of loads. Several interesting nonlinear phenomena have been observed such as softening-type non-linearity and non stationary response when the periodic axial load is resonant with one of the shell modes.

Keywords
vibration, shells, nonlinear dynamics

[1]Università di Modena e Reggio Emilia, Modena, Italy
*__Corresponding author__: antonio.zippo@unimore.it

Introduction

In the present paper, circular cylindrical shells subjected to axial loads having static (compressive) and harmonic components are investigated. Difficulties in developing accurate models for shell structures were the motivations of a large scientific production [1, 2, 3, 4, 5, 6, 7, 8, 9, 10], withal there are few experimental studies about dynamic instabilities and the comparisons between theory and experiments are not yet satisfactory.

1. Experiments

This section provides informations about the experimental setup developed to test thin shell structures under constant axial load and periodical excitation. In Figure 1 a schematic representation of the setup is shown. A shaker is rigidly inserted in a frame designed for the application of the preload. Connections to the system for data acquisition are shown.

1.1 Description

The system under investigation consists of a circular cylindrical shell, made of aluminum alloy, clamped both base and top sides by means of two worm gear clamps at two rigid supports. The bottom support is an aluminum alloy circular disk rigidly bolted to the shaker. The top disk is connected to the frame by means of a dynamic load cell, a stinger, and a static load cell. The stinger is introduced in order to reduce the effects of misalignments. A laser vibrometer is used to measure the velocity of the side of the shell and its output is routed both to the spectrum analyzer and to the LDS controller. The control system is open-loop in order to avoid control instabilities induced by nonlinear behavior of the tested structures.

The characteristics of the shell are the following: length $L = 0.137m$, thickness $h = 0.1 \times 10^{-3}m$, mean radius $R = 32.9 \times 10^{-3}m$, density $\rho = 2796\frac{kg}{m^3}$, Young's modulus $E = 71.020 \times 10^9 \frac{N}{m^2}$, Poisson's

ratio$\nu = 0.31$ and static preload $P_0 = 0 - 250N$.

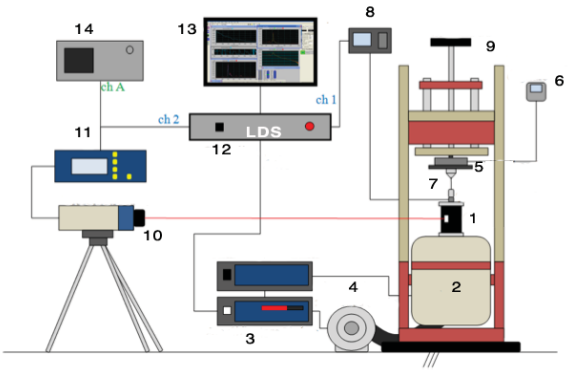

Figure 1. System setup: (1) structure under test (2) shaker (3) shaker amplifier (4) air cool system (5) static load cell (6) digital load gauge (7) force transducer “pcb m231b” (8) force transducer amplifier (9) press system to apply static preload (10) laser vibrometer (11)laser controller (12) lds dactron laser usb shaker control system (13) pc (14) spectrum analyzer “ono-sokki cf-5220”.

The press system has been suitably designed for this research. A screw can move up or down a plate which applies the desired preload to the shell, both compressive and tractive. A static load cell “AEP transducers TC8 10KN” is interfaced with a digital load gauge that displays the exact preload applied to the shell. The Shaker “LDS V530” is integrated rigidly in the press system structure, is powered independently and equipped with a system of air cooling.

The laser vibrometer is targeted on the shell surface and plays a significant role as it measures velocity data acquisition on the shell side without interfering with it. This point is very significant for thin structures, because the use of a standard accelerometer would introduce an undesired extra mass, thus altering the symmetry of the structure. The signal coming from the laser is splitted and directed both to the spectrum analyzer, used to detect the regions of instability, and to the LDS controller.

1.2 Data presentation

In this section all tests carried out on the shell are described. Formerly few tests were done to calibrate the devices properly, then several combination were investigated for different preloads. The experimental analysis was carried out by sweeping frequencies from 700Hz to 2500Hz, with a step rate of 7.5 Hz per second, starting from the highest frequency (2500Hz) towards the lower frequency (700Hz) and backwards, each time varying the magnitude of the oscillations generated from the shaker, from 0.1 V with regular steps of 0.1 V up to the maximum value of 1.0 V. These sweeps were repeated, not only by varying the power supplied to the shaker, but also by imposing an increasing axial static compressive load P_0. The static axial load is increased from $0N$ up to $250N$ (safety limit to avoid shaker damage). Results are presented for preload values of $0N$, $100N$ and $250N$ and for voltage levels of $0.5V$ and $0.8V$. In Figures 2 and 3, d and u represent the decreasing frequency sweep (d, down) and the increasing frequency sweep (u, up).

1.2.1 External load amplitude of 0.5 volt

In Figure 2 the dynamic axial load vs frequency is plotted whereas in figure 3 the amplitude of vibration of the shell (in terms of velocity) vs.-frequency are shown.

Dynamic load-frequency diagrams show a reduction in terms of resonance frequency for increasing preloads. The amplitude of the resonance peak has a peculiar behavior: it has a maximum value of 350N for the mid value of preload (100N), see Figure 2b. This point needs further investigations. The same behavior can be observed in terms of velocity amplitude at the target point, see Figure 3. The maximum velocity, i.e. the maximum amplitude of vibration, is seen for $P_0 = 100N$. The velocity frequency diagram shows another resonance between 1300 and 1350 Hz. For this resonance, the amplitude of vibration is minimum for $P_0 = 100N$.

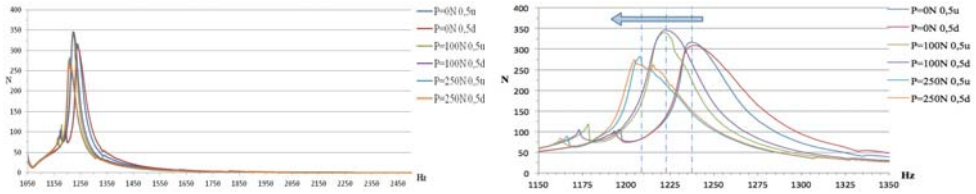

Figure 2. Dynamic load-frequency diagram for different preloads at 0.5 volt.

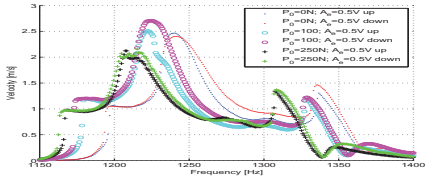

Figure 3. Amplitude-frequency diagram for different preloads at 0.5 volt.

1.2.2 External load amplitude of 0.8 volt

Figure 4 and 5 present the corresponding experimental results for 0.8V excitation amplitude. From Figure 4a and 4b it is noted that increasing the static load P_0, the maximum peak in dynamic load is reduced. The system presents the opposite behavior with respect to the case of 0.5V excitation. Moreover, Figure 5 shows again the frequency reduction due to the preload.

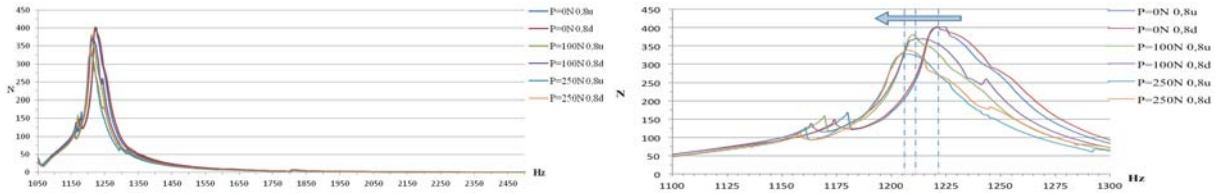

Figure 4. Dynamic load-frequency diagram for different preloads at 0.8 volt.

2. Measured Non-linear Phenomena

The behavior of the structure close to the mode (1,4) is investigated. Numerical and experimental analyses show that this mode is close to 1623 Hz and it is quite far from other modes. The amplitude-frequency diagram for such resonance is shown in Figure 6. In order to describe the nonlinear behavior close to the resonance, it is useful to introduce the following dimensionless values:

1. $\omega_x = \omega_n/\omega_{0,1}$, is the ratio between the frequency corresponding to the maximum amplitude for the n-th excitation amplitude and the frequency at which the maximum occurs for the reference case (0.1 V);

2. $v_x = v_n/v_{0,1}$, is the ratio between the corresponding maximum velocities.

In terms of dimensionless variables, the backbone can be drawn by interpolating the maxima, Figure 6 it results that the shell presents a softening behavior. The backbone curve moves to the left with respect to the vertical line through the resonance frequency.

Figure 7 shows dependence of the non linear behavior on the different values of the preload. The preload of $100N$ produces a less softening resonance, with respect to the non preloaded case and the case of $250N$ preload.

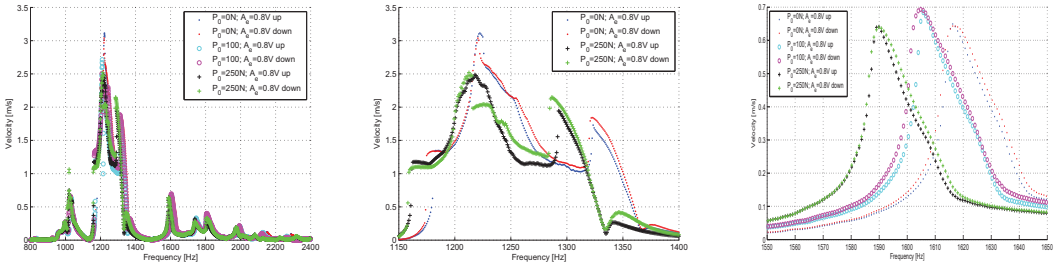

Figure 5. Amplitude-frequency diagram for different preloads at 0.8 volt.

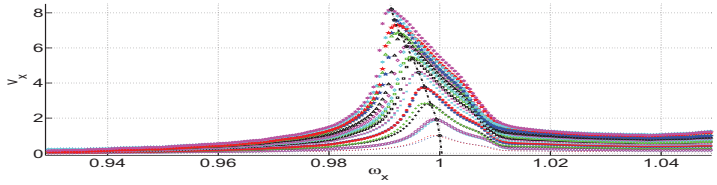

Figure 6. Amplitude-frequency diagram. mode (1,4); $P_0 = 100N$; voltage levels 0.1-1V

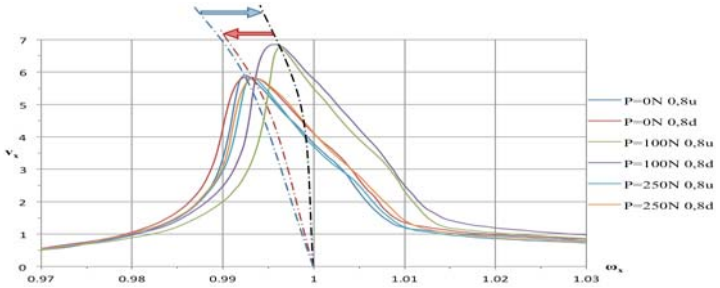

Figure 7. Amplitude-frequency diagram comparison of mode (1,4) with different preloads (0N, 100N and 250N) at 0.8 volt

3. Nonstationary Response

Tests performed on the shell structure pointed out the existence of certain frequency intervals characterized by high amplitude of vibration and complex dynamics; in the following we will call them ”instability regions”, this gives the clear idea that the periodic orbit has lost stability. Table 1 summarizes the instability ranges found during experiments and Figures 8 - 11 shows the time histories and spectra of the lateral shell vibration at different forcing loads and with a static compression of $100N$.

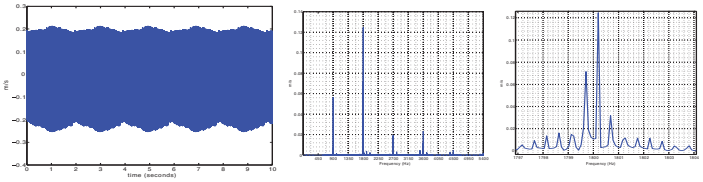

Figure 8. Time history and Spectrum at 900 Hz forcing load

In Figure 8 the dynamic scenario is represented, the excitation frequency is $900Hz$. The response is quasi-periodic, i.e. there is an amplitude modulation that presents two time scales: i) a slow time scale with period of 2s (see $0.5Hz$ sidebands); ii) intermediate time scale with period of 10-2s (see $100Hz$

Table 1. Frequency ranges of instability regions with different preload.

P_0 (N)	Voltage level (V)	Instability range (Hz)
100	0.8	1210.01 - 1217.92
	0.9	1205.61 - 1218.80
	1.0	1201.22 - 1225.84
150	0.7	1208.25 - 1210.01
	0.8	1202.97 - 1212.53
	0.9	1199.46 - 1215.29
	1.0	1196.82 - 1221.44
200	0.7	1209.13 - 1211.77
	0.8	1207.37 - 1213.53
	0.9	1195.06 - 1215.29
	1.0	1191.54 - 1218.80
250	0.5	1208.25 - 1215.29
	0.6	1204.73 - 1221.44
	0.7	1202.92 - 1234.63
	0.8	1198.53 - 1236.39
	0.9	1194.18 - 1238.42
	1.0	1189.78 - 1242.42

sidebands). The response is dominated by the second main spectral harmonics ($1800Hz$), suggesting an important role of quadratic nonlinearities; this role is also confirmed by the loosing of symmetry in the time response ($max = 0.2m/s$, $min = -0.25m/s$).

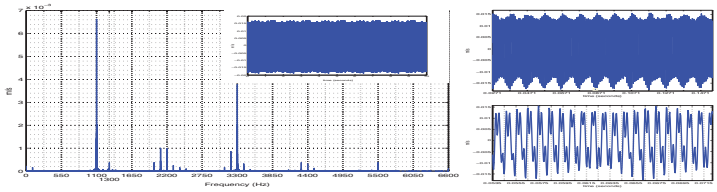

Figure 9. Time history and Spectrum at 1100 Hz forcing load

At $1100Hz$ (Figure 9) the scenario changes; here the energy in frequency domain is mainly concentrated at 1100 and $3300Hz$. This means that here the linear and cubic behaviors are dominant; note that this is confirmed by the symmetry in the time history.

At $1182Hz$ (Figure 10) an interesting phenomenon takes place, the response is quasi-periodic but something interesting happens in the "periodicity". The main spikes in the spectrum are spaced of about $590Hz$, i.e. one half the excitation frequency. This means that the periodic part of the response presents a fundamental frequency of $590Hz$. The straightforward consideration is that the response is one

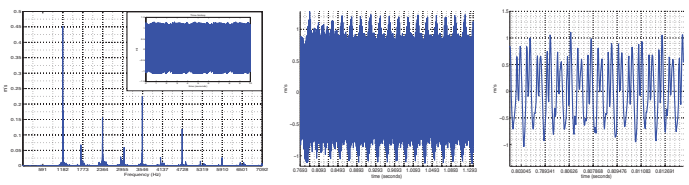

Figure 10. Time history and Spectrum at 1182 Hz forcing load

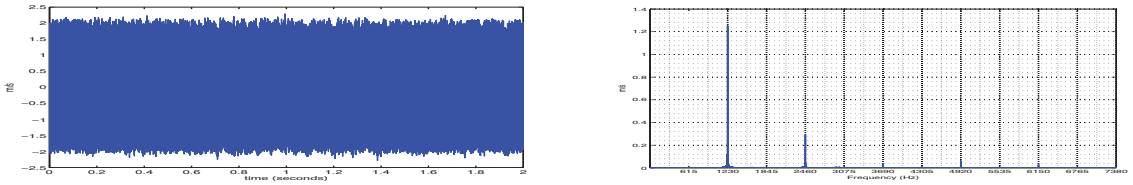

Figure 11. Time history and Spectrum at 1230 Hz forcing load

half sub-harmonic; this is partially contradicted by the spectrum that does not present spikes at $590Hz$. However, if one zooms around $590Hz$, then will disclose an extremely small peak. Our conjecture is that the response is sub-harmonic and the amplitude of the fundamental harmonic is negligible.

4. Conclusions

The dynamic behavior of a thin cylindrical shell under static axial preload and harmonic external axial load has been characterized. An *ad hoc* setup has been developed in order to measure both the dynamic load and the amplitude of vibration on the shell surface. Tests performed at different preload values and different amplitudes of the external excitation pointed out the existence of non linear behavior in certain instability ranges. Nonstationary response is found close to 1230 Hz and a very well defined softening behavior can be observed close to the mode (1,4). Non linear dependence of the response on the preload parameter is observed. Further experiments and correlation with numerical and theoretical models need to be performed in order to fully understand the observed phenomena.

References

[1] Von Kármán T. and Tsien H.S. The buckling of thin cylindrical shells under axial compression. *Journal of the Aeronautical Sciences*, 8(8):303–312, 1941.

[2] Catellani G., Pellicano F., Dall'Asta D., and Amabili M. Parametric instability of a circular cylindrical shell with geometric imperfections. *Computers & Structures*, 82(31–32):2635 – 2645, 2004.

[3] Vijayaraghavan A. and Evan-Iwanowski R. M. Parametric instability of circular cylindrical shells. *Journal of Applied Mechanics*, 34(4):985–990, 1967.

[4] Amabili M. *Nonlinear Vibrations and Stability of Shells and Plates*. Cambridge University Press, 2008.

[5] Gonçalves P. B., Del Prado, and Zenón J.G.N. Nonlinear oscillations and stability of parametrically excited cylindrical shells. *Meccanica*, 37:569–597, 2002.

[6] Pellicano F. Vibrations of circular cylindrical shells: Theory and experiments. *Journal of Sound and Vibration*, 303(1–2):154 – 170, 2007.

[7] Pellicano F. and Avramov K.V. Linear and nonlinear dynamics of a circular cylindrical shell connected to a rigid disk. *Communications in Nonlinear Science and Numerical Simulation*, 12(4):496 – 518, 2007.

[8] Pellicano F. Dynamic instability of a circular cylindrical shell carrying a top mass under base excitation: Experiments and theory. *International Journal of Solids and Structures*, 48(3–4):408 – 427, 2011.

[9] Kubenko V. and Koval'chuk P. Experimental studies of the vibrations and dynamic stability of laminated composite shells. *International Applied Mechanics*, 45:514–533, 2009. 10.1007/s10778-009-0209-4.

[10] Fey R. H. B., Mallon N. J., Kraaij C.S., and Nijmeijer H. Dynamic stability of two harmonically excited thin-walled structures carrying a top mass. In *11th European Conference on Spacecraft Structures, Materials Mechanical Testing*, pages 1–7, 2009.

MINI-SYMPOSIUM
“CREEP AND PLASTICITY AT CYCLIC LOADING”

Proceedings of the 4th International Conference on Nonlinear Dynamics
ND-KhPI2013
June 19-22, 2013, Sevastopol, Ukraine

Cyclic Loading of Oxide Nanopowders

G.Sh. Boltachev[1*], N.B. Volkov[1], E.A. Kochurin[1], K.E. Lukyashin[1]

Abstract
Quasistatic processes of multi-cyclic compaction of oxide nanopowders have been studied by the granular dynamics method in 3D. Uniaxial and isotropic compaction processes have been simulated. Elastic forces of repulsion, tangential forces of "friction" (Cattaneo - Mindlin), and dispersion forces of attraction (Van der Waals – Hamaker) have been taken into account. During cyclic process a system is subjected to multiple increase of outside pressure up to a predetermined level, followed by a complete unloading the pressure. The dependence of the unloading density of powders on the number (*N*) of "loading–unloading" cycles has been studied and asymptotic density values in the limit of large *N* have been estimated. It is shown that under certain conditions, the multi-cyclic compaction allow achieving large densities, which are near the density of hexagonal close packing.

Keywords
Nanopowder, cyclic loading, granular dynamics

[1] Institute of Electrophysics, Ural Branch of RAS, Ekaterinburg, Russia
* **Corresponding author:** grey@iep.uran.ru

Introduction

Compression of nanopowders is a necessary step in many processing routes of nanostructured materials manufactured by powder metallurgy [1]. Strong ceramics can be obtained by this way if the initial blanks have been compacted up to high densities. However, it has been known from experiments that nanopowder pressing is characterized by the so-called size effect, i.e., the smaller the particle size, the greater the pressure necessary to reach a preset density [2, 3]. Thus, studying the features of different processes of nanopowder compactions and searching for methods to raise the efficiency of these processes have presently a high priority.

In this work we present the theoretical results of an investigation on oxide nanopowder compaction processes by the granular dynamics method [3]. The high sphericity and the non-deformability (the strength) of oxide nanopowder particles make the granular dynamics method particularly attractive and promising tool of the theoretical analysis. Simulations have been performed in 3D for mono-sized systems, whose particle diameter is in the range of 10–100 nm. Interactions of powder particles involve elastic forces of repulsion (modified Hertz law), tangential forces of "friction" (Cattaneo – Mindlin law), as well as dispersion forces of attraction (van der Waals – Hamaker forces). Taking into account the dispersion forces allows correct describing the properties of nanosized powders and, in particular, simulating the size effect in compaction processes [2, 3].

As a candidate for a highly effective method of nanopowder compaction the multi-cyclic processes have been studied. During these processes a powder system is subjected to multiple quasi-static increase of outside pressure to the predetermined level, followed by a complete unloading the pressure. In practice the maximum level of the outside pressure is determined by the mechanical properties of the experimental setup, as a rule. The high efficiency of such processes has been revealed in previous simulations of 2D structures [2]. In the present study the multi-cyclic compaction has been tested with a more realistic 3D model. Free parameters of the model have been determined by experimental data on uniaxial compaction of alumina based nanopowders.

1. Theoretical model

In the first stage of a compaction process simulation a model cell is filled by an initial structure with given number (8000) of particles. Periodic boundary conditions are imposed at sides of the model cell. An original algorithm developed makes it possible to create rather isotropic and uniform distributions of particles, which form a connected cluster. Properties of structures are controlled by the analysis of such characteristics as the radial distribution function, the angular distribution of interparticle forces and contacts, and the coordination numbers of particles. For all simulations the minimum size of model cells (even after compression) exceeds 18*d*, where *d* is the diameter of powder particles. As test simulations have showed, this value (18*d*) exceeds the correlation radius of particles arrangement more than double in the whole range of densities studied.

A compression step of a model cell implements by a simultaneous reduction of the cell size (all sizes when simulating the isotropic compaction; the cell height when simulating the uniaxial compaction) by 0.1 percent of the current value and the proportional resizing of coordinates of all particles. New equilibrium positions of all particles are determined after each compression step. A particle moving is determined by the interaction of it with other particles.

The elastic force f_e of repulsion of particles when compressing is calculated on the basis of the modified Hertz law [4]

$$\frac{f_e}{Ed^2} = \frac{1}{3}\frac{(h/d)^{3/2}}{1-\nu^2} - \frac{\pi}{4}\frac{1-\nu}{(1-2\nu)(1+\nu)}\left[\frac{h}{d} + \ln\left(1-\frac{h}{d}\right)\right], \qquad (1)$$

where E and ν are the Young modulus and the Poisson's ratio of particle material, $h = d - r$ is the displacement of particles after coming into contact (at the moment of $r = d$, where r is the center distance of the particles). The law of Eq. (1), on the one hand, does not contrary to the classical Hertz law in the limit of infinitesimal particle deformations ($h \ll d$) and, on the other hand, increases significantly the repulsion of particles at large deformations, where Hertz law becomes already invalid. The interparticle force of "friction" f_t when the tangential displacement δ with respect to the contact plane taking place is described by the linearized Cattaneo – Mindlin law

$$f_t(\delta) = \min\left\{\frac{4Ea\delta}{(2-\nu)(1+\nu)};\ \mu f_e\right\}, \qquad (2)$$

where $a = \sqrt{hd}/2$ is the radius of the contact spot, μ is the friction coefficient. The dispersion force of attraction f_a is determined by modified Hamaker formula [3],

$$f_a(r) = \frac{\pi^2}{3}\frac{(nd_0^3)^2 \varepsilon d^6}{(r+\alpha d_0)^3[(r+\alpha d_0)^2 - d^2]}, \qquad (3)$$

where d_0 and ε are the size and energy parameters of intermolecular interactions. The α-phase of aluminium oxide is intended as the particle material, and simulation parameters are: $E = 382$ GPa, $\nu = 0.25$, $nd_0^3 = \sqrt{2}$, $\alpha = 0.24$, $d_0 = 0.392$ nm [3]. The value of ε, in contrast to Ref. [3], is set equal to $1224\, k_B$. At that the maximal value of dispersion force $f_a(d)$ is in accord with the adhesive force of DMT model ($\pi\gamma d$), where the surfave energy $\gamma = 1$ J m^{-2} that representes typical covalent/ionic ceramic material [5].

2. Comparison with experimental data

To verify the theoretical model the natural and numerical experiments on uniaxial and isotropic compactions of nanopowders have been performed. The natural experiments have been performed with Al_2O_3 nanopowders (alumina based powders) and Y_2O_3 nanopowders (yttrium oxide doped with 1% neodymium). The powders is obtained in the Institute of Electrophysics (Ural Branch of RAS) by target evaporation with a pulse-periodic CO_2 laser. Size distributions of the powders is adequately fitted by a log-normal distribution. In the case of Al_2O_3 powder the half-width of the size distribution

is about 15 nm and the typical size of particles, where the maximum of distribution function takes place, is equal to $d \cong 10.4$ nm. The Y_2O_3 nanopowder is characterized by close values of the parameters. During natural experiments the powders were subjected to pressures of 100, 150 and 200 MPa. The closed-die compaction (i.e., uniaxial compaction) was performed in a hydraulic decimal press DP-36. Here the powder was placed into the cylindrical hole of metal mould, and the external pressure p_z was applied to the upper movable punch. The isotropic pressing was performed by an original izostate based on the hydraulic machine NGR-2000. Fig. 1 presents the experimental results in the coordinates of "density vs uniaxial pressure p_z".

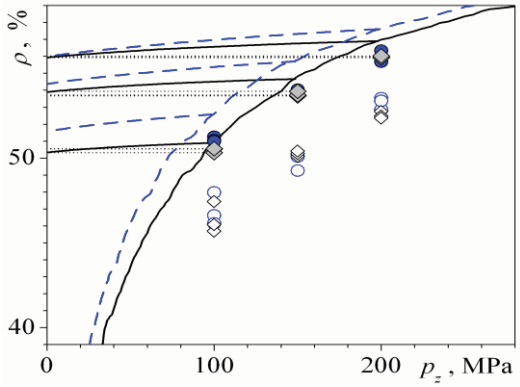

Figure 1. The powder density depending on the pressure applied. Symbols are the natural experimental data on the uniaxial (diamonds) and the isotropic (circles) compaction of Al_2O_3 (solid) and Y_2O_3 (open) nanopowders. Lines show the simulation results on the uniaxial (solid) and the isotropic (dashed) compaction of Al_2O_3 nanopowder. The curve of monotonic loading and the curves of elastic unloading from the levels of $p_z = 100$, 150, and 200 MPa are shown. Simulation parameters are d = 10.4 nm, μ = 0.13, α = 0.37.

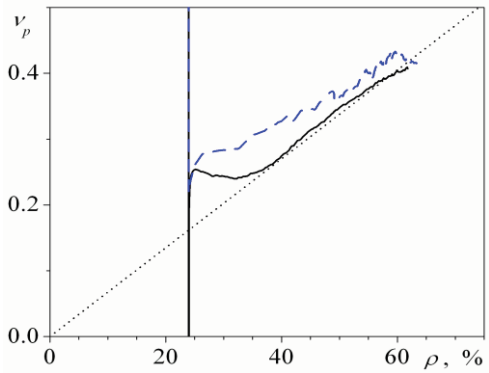

Figure 2. The "Poisson's ratio" of the powder body calculated from the ratio of lateral pressure to axial one during the uniaxial compaction of model systems with d = 10 nm (solid line) and 100 nm (dashed line). The dotted line shows the approximation of Eq. (5).

The friction coefficient μ and the value of α parameter were playing the role of free parameters of the theoretical model. The values of these parameters can depend strongly on the state of the surface of powder particles. A value of α determines the minimal separation between particles ($h = \alpha d_0$), which is considered as a touch of the particles. Note that the value of $\alpha = 0.24$ was obtained in Ref. [3] with reference to the clean surfaces of particles, when nothing prevented them coming together. In this study, to keep a low powder agglomeration we have not performed powder annealing, during of which cleaning the surfaces of particles from the volatile matter takes place. As a consequence, the increased content of adsorbates should increase the separation between particles in contact, i.e., the value of α.

The best description of the experimental data has been obtained with the following parameters: $\mu = 0.13$ and $\alpha = 0.37$, see Fig. 1. In addition to the monotonic loading curve the lines of elastic unloading have been presented, where the outside axial pressure p_z is decreased from the values of

100, 150, and 200 MPa to zero. It is the powder density, which is realized after the pressure release (the unloading density), which should be compared with experimental data, since the latter are also obtained from the analysis of unloaded compacts. Fig. 1 shows that the theoretical model can reproduce the experimental data with high accuracy, the error in the density is less than the scatter of the experimental points. Note that all theoretical curves in the figure have been constructed by averaging over 10 independent simulations.

The theoretical model with the fixed parameters μ and α has been used to study the powders compaction in other geometry of outside load, i.e., the isotropic (or isostatic) loading. A joint analysis of the experimental data and the simulation curves in Fig. 1 shows a complete consent of them. It turns out that the density of the oxide nanopowder dependents very weakly on the geometry of the outside load. Both the simulation and the natural experiments reveal a little difference (less than 1 percent) between the unloading densities of the compacts after isostatic or uniaxial compaction with pressure $p_z = 100$ MPa. When the maximal pressure p_z is raised up to 200 MPa, these differences wholly disappear.

It should be noted that the observed insensitivity of oxide nanopowders to the geometry of outside loads is very surprising. Traditional continuum theories (see, for example, Ref. [1]) predict an apreciable influence of the loading geometry on the final porosity of compacts. For example, in the pressure range investigated the theory of plastically hardening porous body of [1] predicts the difference in density between the isotropic and the uniaxial compaction processes of about 10 percent that corresponds exactly to the behaviour of coarce powders [6]. Contrary to this predictions the oxide nanopowders studied show a qualitatively different behavior, namely, they display the extremely low sensitivity to the geometry of outside loads. On the one hand, it is evidence of the inapplicability of traditional continuum theories to describe the mechanical properties of these powders. On the other hand, it emphasizes the high reliability of the simulations within the theoretical model developed, which makes it possible to reproduce this specific behavior of oxide nanopowders to high precision.

The insensitivity of powder density with respect to geometry of loading, as it would seem, brings their behavior to the fluid one. However, in contrast to fluids in the powder systems studied there is no evenning the stresses in different directions in the course of uniaxial loading. In support of this, Fig. 2 demonstrates the "Poisson's ratio" ν_p of powder systems, which determines the ratio of lateral ($p_x = p_y$) to axial (p_z) pressures when uniaxial compacting.

$$\frac{p_x}{p_z} = \frac{\nu_p}{1-\nu_p}. \tag{4}$$

The figure shows that, first, the value of ν_p for the systems studied is significantly lower than 0.5 (the value for fluids) and, secondly, the density dependence is nearly linear. In the case of the system with d = 10 nm, for example, with the exception of starting density range (the density of initial structures is equal to 24 percent) this dependence is well fitted by the expression,

$$\nu_p = \frac{3}{\pi\sqrt{2}}\rho, \tag{5}$$

which gives the value $\nu_p = 0.5$ at the density of hexagonal close packing $\rho_{hcp} = \pi\sqrt{2}/6$.

3. Simulations of cyclic compaction processes

During multi-cyclic compactions a powder system is subjected to multiple quasi-static increase of outside pressure to the predetermined level, followed by a complete unloading the pressure. The high efficiency of such processes has been revealed in previous simulations of 2D structures [2]. The theoretical approach presented above allows studying the cyclic loading with more realistic powder model: 3D geometry, accordance with natural experimental data. Fig. 3 demonstrates a typical shape of simulation curves.

The figure does show a noticeable rise of the unloading density of the powder when a number of "loading-unloading" cycles increasing. However, it should be noted that this effect is about twice lower than in the case of 2D structures of Ref. [2]. For example, when unloading run from the level of 100 MPa the increase of the unloading density ρ_u in 2D geometry is about 3 percent, whereas in 3D we have less than 1.5 percent at similar conditions. Fig. 4 displays another difference from the case of 2D geometry. Here the dependence of ρ_u on a number of "loading-unloading" cycles performed has been presented. If in 2D geometry the unloading density ρ_u is proportional to the number of cycles with exponent equal to $-1/2$ then now the same exponent is $-1/3$. Fig. 4 shows that starting with $N_{cyc} = 4$ the results of simulations are surely fitted by a linear dependence in the coordinates of "ρ_u vs $N_{cyc}^{-1/3}$". This fact makes it possible to extrapolate easily the results obtained to the region of large values of N_{cyc}, right up to the limit $N_{cyc} \to \infty$. Of course, the large values of N_{cyc} can be realized within the real setup on conditions only that it is completely automated. This condition, in particular, is not in existence for our experimental equipment.

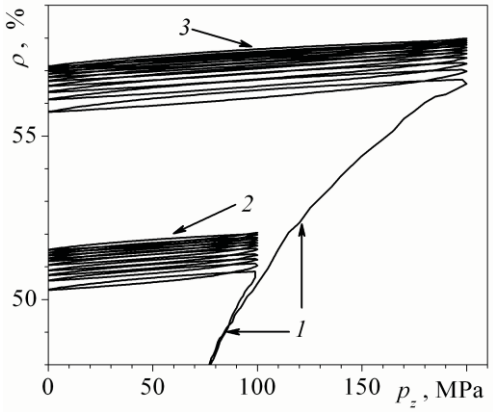

Figure 3. The powder density depending on the pressure p_z when uniaxial loading. Ten cycles of "loading-unloading" at the levels of p_z = 100 MPa /2/ and 200 MPa /3/ are shown. The first cycle includes the curve of primary loading from the initial density ρ_0 = 24 percent /1/

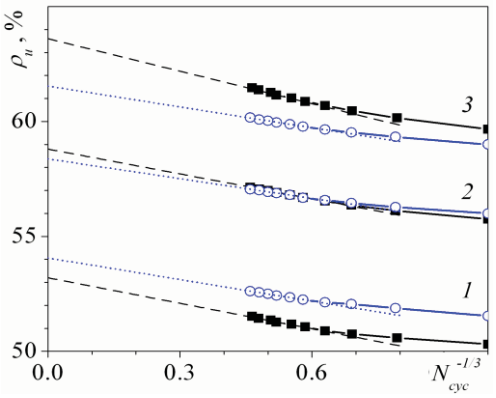

Figure 4. The unloading density of the powder system depending on the number N_{cyc} of "loading-unloading" cycles when uniaxial compacting (solid squares) and isotropic compacting (open circles) with maximal pressure p_z = 100 MPa /1/, 200 MPa /2/, and 500 Mpa /3/. In addition to the simulation results the extrapolations to the region of large values of N_{cyc} have been shown: dashed lines are the uniaxial process, dotted lines are the isotropic pressing

Fig. 5 presentes the powder density, reached in the limit of infinite number of "loading-unloading" cycles performed, in comparison with density, reached after single cycle. Simulation results for the levels of maximal pressures $p_z = 100$, 200, and 500 Mpa have been fitted by dependences in the form of $\rho_u = \rho_{\max} + k\, p_z^{-m}$, where $\rho_{\max}$, k, and m are the adjusting parameters. These approximation functions, shown by the curves in Fig. 5, make it possible to get a theoretical prognosis (of course, it is an overbold prognosis) for the region of large levels of pressures p_z, which exceed appreciably an ability of our experimental equipment. According to this prognosis, the rise of the pressure p_z value results in a noticeable increase in the efficiency of the multi-cyclic process in the case of the uniaxial compaction. For example, the value of $\rho_{\max}$ parameter, which gives the maximal density reached in the hypothetical limit of $p_z \to \infty$, is equal to 71 percent in the case of uniaxial compaction process. It is close to the density of hexagonal close packing of spheres ($\rho_{hcp} \cong 74$ percent). While, the density, which is reached by a single cycle, tends to the value of 64 percent in the same limit, i.e., the density increase resulted from the multi-cyclicity amounts to 7 percent. In the case of the isotropic compaction the efficiency of multi-cyclic process is noticeably smaller. Here, according to the

theoretical prognosis, the density increase does not exceed 3.5 percent in the whole range of pressures and the maximal compact density is about 65 percent.

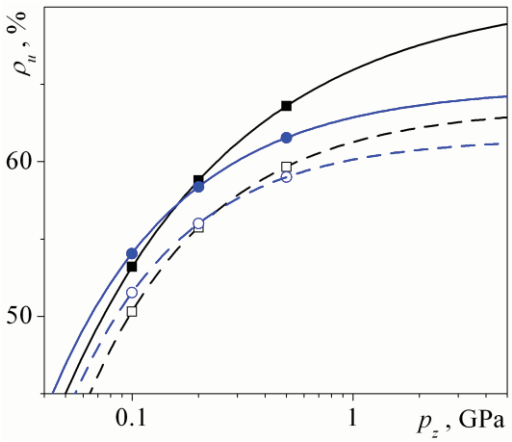

Figure 5. The unloading density of the powder system after single process of loading and unloading (open symbols, dashed lines) and in the limit of infinite number of "loading-unloading" cycles performed (solid symbols, solid lines) depending on the level of maximal pressures: squares are the uniaxial compaction, circles are the isotropic compaction.

Conclusions

A discrete theoretical model of oxide nanosized powders has been presented. Free parameters of the model have been determined by the experimental data on the uniaxial compaction of alumina based nanopowders. The processes of uniaxial and isotropic compaction have been studied both experimentally and theoretically (within the model developed). Contrary to the predictions of traditional phenomenological theories, both numerical and natural experiments have revealed a low sensitivity of nanosized powders to the geometry of outside loading. Processes of multi-cyclic compaction, when a system is many times subjected to the outside pressure increase up to the predetermined level, followed by a complete unloading, have been simulated. A high efficiency of such processes in the case of the uniaxial compaction has been revealed. Here, in the hypothetical limit of an infinite number of "loading-unloading" cycles and large pressures the powder densities can be reached, which are close to the density of closest packing of spheres in space. In the case of isotropic compaction the efficiency of the multi-cyclic process is noticeably smaller: the total increase in density due to additional "loading-unloading" cycles does not exceed 3 percent.

Acknowledgments

The work is supported by the RFBR (projects 12-08-00298 and 11-08-00005) and the Presidium of the Ural Branch of RAS (projects 12-P-2-1023 and 12-C-2-1018).

References

[1] Shtern M.B., Serdyuk G.G., Maksimenko L.A., Truhan Yu.V., and Shulyakov Yu.M. *Phenomenological Theories of Powder Pressing*, Naukova Dumka, Kiev, 1982 (in Russian).
[2] Boltachev G.Sh., Volkov N.B., Kaygorodov A.S., and Loznukho V.P. The Peculiarities of Uniaxial Quasistatic Compaction of Oxide Nanopowders *Nanotechnologies in Russia*, Vol. 6: 9-10, pp. 639-646, 2011.
[3] Boltachev G.Sh. and Volkov N.B. Simulation of Nanopowder Compaction in Terms of Granular Dynamics *Technical Physics*. Vol. 56: 7, pp. 919-930, 2011.
[4] Boltachev G.Sh., Volkov N.B. and Zubarev N.M. Tangential interaction of elastic spherical particles in contact. *Int. J. Solids Struct*. Vol. 49: 15-16, pp. 2107-2114, 2012.
[5] Balakrishnan A., Pizette P., Martin C.L., Joshi S.V. and Saha B.P. Effect of particle size in aggregated and agglomerated ceramic powders *Acta Materialia*. Vol. 58, pp. 802-812, 2010.
[6] Kiparisov S.S. and Libenson G.A. *Powder metallurgy*, "Metallurgia", Moscow, 1980 (in Russian).

Proceedings of the 4th International Conference on Nonlinear Dynamics
ND-KhPI2013
June 19-22, 2013, Sevastopol, Ukraine

Ratcheting Simulation under Nonproportional Loading within the Scope of Endochronic Theory of Plasticity

M. V.Borodii[1]*, V. O. Stryzhalo[1], M. P. Adamchuk[1]

Abstract
In this paper, the analysis of the possibility of describing the cyclic creep effect is performed using a system of equations of the endochronic theory of plasticity. It is shown that the introduction of the dependence of the kinematic hardening on the maximum stresses reached on the previous portion of loading has made it possible to avoid the closure of the elastic-plastic hysteresis loop, and the improved model is capable of predicting the ratcheting under non-proportional loading.

Keywords
Non-proportional loading, ratcheting, kinematic hardening.

[1] G.S.Pisarenko Institute for Problems of Strength NAS of Ukraine, Kiev, Ukraine
* **Corresponding author:** bor@ipp.kiev.ua

Introduction

A special feature in the use of a number of currently available machines and units is their operation under multiaxial asymmetrical loading. Such loading is peculiar to power engineering and chemical engineering structures and structures of transportation engineering. Here, the presence of the asymmetry of loading with stress control results in the accumulation of plastic strains, which can lead to unacceptable displacements. This phenomenon got the name "cyclic creep, or ratcheting."

At present, experimental and theoretical investigations on the effect of cyclic creep under non-proportional loading are urgent. Numerous investigations on this subject matter are known in the literature, however, they still have significant differences in the experimental and theoretical data. It should be noted that the available models for predicting the kinetics of the stress-strain state are rather complicated in use and require a large number of basic experiments to be performed in order to determine the necessary calculation parameters. In view of the above said, it can be concluded that the problem of constructing a simple model for engineering calculations is still urgent.

1. Development of the model of cyclic plasticity to describe the ratcheting effect

When constructing the cyclic plasticity model, we will analyze the case with biaxial loading of thin-walled tubular specimens of 316 stainless steel from the square paths in the deviatoric stress space under the combined action of the axial force and torque. Consider a random portion of this path, for example, AB. Let the intrinsic time value z_2 correspond to the point *A,* and z_3 to the point B. Then, for the given stage of loading, $z_2 \le z \le z_3$, the following equation for a straight line can be written:

$$\sigma = k \cdot \sqrt{3}\tau + \bar{\sigma}, \tag{1}$$

where k is the slope of the straight line AB; $\bar{\sigma}$ is the coordinate of the intersection of the straight line AB with the ε axis, Fig. 1. Since the straight line AB is parallel to this axis, then, in order to avoid the

indeterminacy $K=\infty$, there is no need to strictly fulfill the parallelism conditions. In this case, the accuracy will remain the same if we introduce a very small slope different from 0.

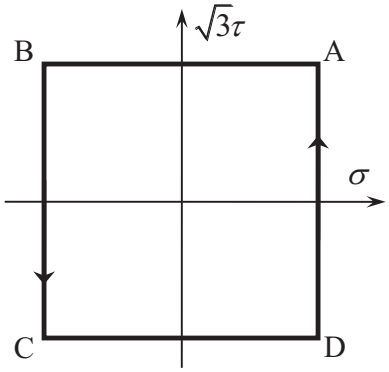

Figure 1. The non-proportional loading path

Since the initial model based on the constitutive relations of the Valanis endochronic theory of plasticity [1] is unable to predict correctly the ratcheting evolution, we employ a simple model of cyclic plasticity proposed previously to describe the asymmetrical uniaxial low-cycle loading.

To describe the cyclic creep effect, in Refs [2, 3, 4] the constitutive equations of the endochronic theory of plasticity were refined by using a more complex definition of the hereditary function, namely:

$$E(z,\delta)=E_1e^{-\alpha z}+E_2(\delta). \tag{2}$$

That is, the model was constructed from the assumption that the kinematic hardening defined by the hereditary function E depends not only on the measure of the deformation process – the intrinsic time z - but also on the level of stresses reached in the previous loading half-cycle. The latter assertion admits the dependence of the hereditary function E on the characteristic distance in the stress space δ proposed in Ref. [5] to improve the kinematic hardening rule of the plastic flow theory. Such improvement has made it possible to solve the problem of the elastic-plastic hysteresis loop closure that was the cause of the impossibility of describing the effect of cyclic creep when simulating the asymmetrical cyclic loading according to the classical model.

In view of the above said, for the case of biaxial loading, the hereditary function can be written in the following way:

$$E\left(z,\,\delta_\sigma,\delta_\tau\right)=E_1e^{-\alpha\, z}+E_2\left(\delta_\sigma,\delta_\tau\right), \tag{3}$$

i.e., we can say that the values of this function in some equations of the endochronic theory of plasticity [1] will take the values different from one another, that is:

$$E\left(z,\,\delta_\sigma\right)=E_1e^{-\alpha\, z}+E_2\left(\delta_\sigma\right),$$
$$E\left(z,\,\delta_\tau\right)=E_1e^{-\alpha\, z}+E_2\left(\delta_\tau\right).$$

Thus, the output set of constitutive equations of the endochronic theory of plasticity [1] can be re-written in the following way:

$$\sigma_x=\sigma_y\frac{d\varepsilon^p}{dz}+\int_0^z E_1e^{-\alpha\,(z-z')}\frac{d\varepsilon^p}{dz'}dz'+\int_0^z E_2\left(\delta_\sigma\right)\frac{d\varepsilon^p}{dz'}dz', \tag{4}$$

$$\sqrt{3}\tau_{xy}=\sigma_y\frac{d\gamma^p}{\sqrt{3}dz}+\int_0^z E_1e^{-\alpha\,(z-z')}\frac{d\gamma^p}{\sqrt{3}dz'}dz'+\int_0^z E_2\left(\delta_\tau\right)\frac{d\gamma^p}{\sqrt{3}dz'}dz', \tag{5}$$

$$\sigma_x=k\cdot\sqrt{3}\tau_{xy}+\bar{\sigma}, \tag{6}$$

$$F^2(z)=\left(\frac{d\varepsilon^p}{dz}\right)^2+\frac{1}{3}\left(\frac{d\gamma^p}{dz}\right)^2, \tag{7}$$

where σ_y is the yield strength, z is the intrinsic time, $F(z)$ is the hardening function:

$$F(z)=C-(C-1)e^{-\beta z}. \tag{8}$$

After the corresponding transformations, a non-linear system of differential equations of different orders was obtained describing the stress-strain state of the material on the n-th $(z_n \le z \le z_{n+1})$ portion of the piecewise polygonal path in the stress space:

$$\begin{aligned}
&\ddot{\varepsilon}_n + A_{\varepsilon_n}\dot{\varepsilon}_n + B_{\varepsilon_n}\varepsilon_n + C_{\varepsilon_n} = \alpha\sigma_n + \dot{\sigma}_n,\\
&\ddot{\gamma}_n + A_{\gamma_n}\dot{\gamma}_n + B_{\gamma_n}\gamma_n + C_{\gamma_n} = \alpha\tau_n + \dot{\tau}_n,\\
&\sigma = k_n\cdot\tau + s_n,\\
&F^2(z)=(\dot{\varepsilon})^2+(\dot{\gamma})^2,
\end{aligned} \tag{9}$$

where $A_{\varepsilon_n}=\alpha+\frac{E_1}{\sigma_y}+\frac{E_2(\delta_\sigma)_n}{\sigma_y}$; $\quad B_{\varepsilon_n}=\alpha a_{2_n}$;

$A_{\gamma_n}=\alpha+\frac{E_1}{\sigma_y}+\frac{E_2(\delta_\tau)_n}{\sigma_y}$; $\quad B_{\gamma_n}=\alpha a_{3_n}$;

$$C_{\varepsilon_n}=\alpha\sum_{i=0}^{n-1}\frac{E_2(\delta_\sigma)_i}{\sigma_y}\left(\varepsilon(z_{i+1})-\varepsilon(z_i)\right)-\alpha\frac{E_2(\delta_\sigma)_n}{\sigma_y}\varepsilon(z_n);$$

$$C_{\gamma_n}=\alpha\sum_{i=0}^{n-1}\frac{E_2(\delta_\tau)_i}{\sigma_y}\left(\gamma(z_{i+1})-\gamma(z_i)\right)-\alpha\frac{E_2(\delta_\tau)_n}{\sigma_y}\gamma(z_n);$$

$$s_n=\frac{\bar{\sigma}_n}{\sigma_y}.$$

The system of equations (9) has no analytical solution, and therefore it was solved numerically using the Runge-Kutta method. For the numerical implementation of this method, an appropriate calculation program was compiled. The transition to the next step occurred only when the obtained stresses reached the required value with a certain accuracy. During this transition, a change occurred in the constants describing the loading path, and the corresponding stress and strain values were taken as initial conditions from the previous portion. As a first approximation to the unknown strain increments on new portions, these increments were determined from the equations of the initial model [6]:

$$\frac{d\varepsilon^p}{dz}=\frac{1}{k^2+1}\left[\Phi'(z)\pm k\sqrt{F^2(z,...)\left(k^2+1\right)-\left(\Phi'(z)\right)^2}\right];$$

$$\frac{d\gamma^p}{\sqrt{3}dz}=\frac{1}{k^2+1}\left[-k\Phi'(z)\pm\sqrt{F^2(z,...)\left(k^2+1\right)-\left(\Phi'(z)\right)^2}\right].$$

To evaluate the possibility of the given model to describe the process of the accumulation of ratcheting irreversible strains, the test problem on the representation of the stress-strain state for the square path shown in Fig. 1 was solved.

The calculations for the simulation of the square loading path for the peak values of stresses $\sigma_a = 200\ MPa$ and the mean stress $\sigma_m = 50\ MPa$ were carried out with the parameter values as listed in Table 1. Figure 2 shows the stress-strain diagram for stainless 304L steel obtained during the

simulation according to the improved procedure and the use of the conventional values of the hereditary kernel. It is evident that the introduction of the dependence of the kinematic hardening on the maximum stresses reached on the previous portion of loading has made it possible to avoid the elastic-plastic hysteresis loop closure, and the improved model is capable of predicting the ratcheting. At the same time, a slight discrepancy (a turn) in the calculated strain field distribution with respect to the experimental one is observed. This can be caused by the following reasons, namely: the insufficient accuracy of determining the material constants, such as the modulus of elasticity E_0 which was taken from the analysis of the static diagram; a small deviation of the calculated strain path from the experimental one to avoid the singularity of the equations; the influence of the path bend points, etc.

Table 1. Parameters of the computational model

$\sigma_т$, MPa	E_1, MPa	E_2, MPa	E_0, MPa	α	C	β	p
140	172	4280	178202	2300	1,33	32	1

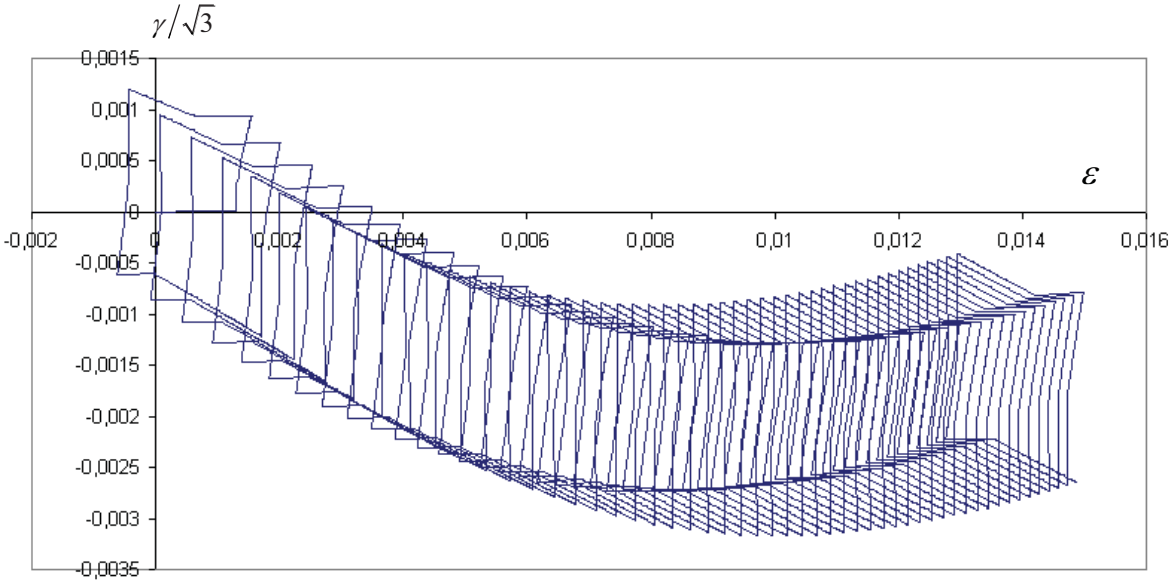

Figure 2. Simulation of strain for the 304L stainless steel with the modified model

Besides, to test for the correctness of calculations according to the developed numerical procedure, the analysis of the stress-strain state kinetics under asymmetrical uniaxial tension-compression was performed, and the results obtained were compared with those obtained for the calculation according to the uniaxial model [4].

As a test example, we selected the loading of 1020 carbon steel with the following cycle parameters: maximum stress $\sigma_{\max} = 402{,}5\,MPa$, minimum stress $\sigma_{\min} = -281{,}2\,MPa$. The other parameters of the endochronic model used in the prediction are given in Table 2.

Table 2. Parameters of the computational model for steel CS 1020

E, MPa	$\sigma_т$, MPa	E_1, MPa	$E_2(0)$, MPa	α	C	β_2
$1{,}73\cdot10^5$	275	$1{,}74\cdot10^5$	11850	965	0,78	30

In addition, the hereditary function form defined earlier [7] was also used in the calculation:

$$E_2(\delta) = E_2(0) - 6{,}3\cdot10^{-7}\cdot\delta^6\cdot\left(\frac{\sigma_a-\sigma_s}{\sigma_a^{bas}-\sigma_s}\right)^8, \qquad (10)$$

where σ_a is the stress amplitude, σ_a^{bas} is the stress amplitude in the basic experiment; σ_s is the plasticity surface radius in a stabilized state.

Figure 3 illustrates the calculated ratcheting curves for CS 1020 steel under conditions of the above-mentioned loading. The curves with points correspond to the calculation results according to the uniaxial model presented in [4]; the solid lines correspond to results of the calculation according to the approach proposed in this paper. It is obvious that the developed numerical procedure is completely correct, and the approximate selection of the initial conditions does not introduce considerable error.

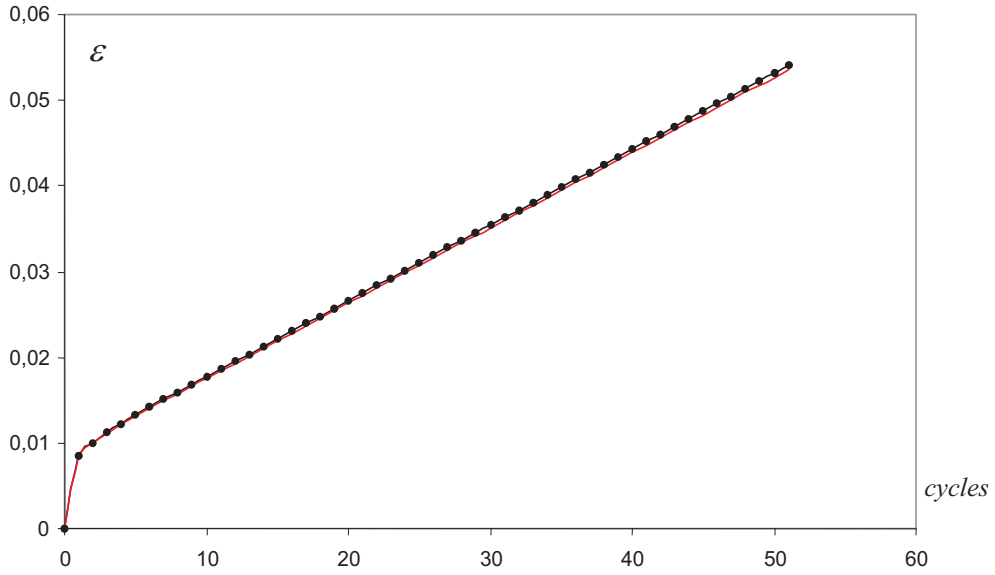

Figure 3. Calculated cyclic creep curves for CS 1020 steel

Conclusions

The constitutive relations of the endochronic theory of plasticity were modified by introducing the dependence of the kinematic hardening on the maximum stresses reached during the previous portion of loading. An appropriate numerical procedure was developed, and the calculation of the test problem in the square path loading of the material in the stress space was performed. It was shown that the given model has made it possible to eliminate the closure of the elastic-plastic hysteresis loop and is capable of predicting the ratcheting under non-proportional loading.

References

[1] Valanis K.C. Fundamental consequences of new intrinsic time measure plasticity as a limit of the endochronic theory *Archives of Mechanics,* Vol. 32, pp. 171-191, 1980.
[2] Borodii M.V. Model of plasticity aimed at the prediction of cyclic creep *Strength of Materials,* Vol. 30, pp. 611–615, 1998 (in Russian).
[3] Borodii M.V. Modeling of the asymmetric low-cycle loading in the space of stresses *Strength of Materials,* Vol. 30, pp. 472–480, 1998 (in Russian).
[4] Borodii M. V. and Adamchuk M. P. Numerical simulation cyclic creep effect according to uniaxial loading programs *Strength of Materials,* Vol. 42., pp 711-716, 2010 (in Russian).
[5] Hassan T., Kyriakides S. Ratcheting in cyclic plasticity, part I: uniaxial behavior *International Journal of Plasticity*, Vol 8, pp. 91–116, 1992.
[6] Borodii M. V. Application of endochronic theory of plasticity for modeling nonproportional repetitive-variable hard loading *Strength of Materials,* Vol. 26, pp 321-327, 1994 (in Russian).

Proceedings of the 4th International Conference on Nonlinear Dynamics
ND-KhPI2013
June 19-22, 2013, Sevastopol, Ukraine

Analysis of Beam Flexural Oscillations Considering High Temperature Creep of its Material

D.Breslavsky[1]*, O. Galas[1]

Abstract
The paper contains the equations of steel beam flexural oscillations which were obtained considering creep strains. Approximated solution had been obtained by use of Galerkin method, solution for reduced model had been found by numerical integration. Numerical data are discussed.

Keywords
Beam, high temperature, creep, forced flexural oscillations, Galerkin method.

[1]National Technical University 'Kharkiv Polytechnic Institute', Kharkiv, Ukraine
* **Corresponding author:** brdm@kpi.kharkov.ua

Introduction

Cyclic loading of structural elements which work at elevated temperatures can be accompanied by arising of creep irreversible strains. This case of nonlinear deformation is well-known for polymers [1], and much worse for metals. Dynamic loading which leads to forced oscillations in creep conditions causes the phenomenon which is called as 'dynamic creep' [2]. Calculations of stress-strain components in structural elements in dynamic creep conditions can be carried by use of methods of two time scales and averaging in period [3]. This approach allows us to obtain the averaging dependences of stresses and strains from the time reflecting the influence of cyclic loading, which is the acceleration of displacement and strain growth. Otherwise, several solutions can be obtained directly. The paper contains one of similar problem, formulated for the beam flexural oscillations when creep irreversible strains are developed in a beam material.

1. Equations of the flexural oscillations

Let us regard the long isotropic steel beam which is heated to such elevated temperature when creep irreversible strains are developed it material. We suppose, that total strain can be presented as a sum of elastic e and creep component c :

$$\varepsilon = e + c, \tag{1}$$

Let us use Bailey-Norton power law [1] for creep strain rate

$$\dot{c} = B\sigma^n, \quad c = B\sigma^n t, \tag{2}$$

where B and n are the material constants, t is the time. To be definite, let us regard the beam material as a high-temperature steel CIS grade 45X14P14B2M at 873 K. For this steel $B=2\ 10^{-10}$ $(MPa)^{-n}$, $n=3$.

Following [4] we use traditional way for obtaining the equation of motion. Let us present the bending moment:

$$dM = Fdx. \tag{3}$$

Let us use the linear geometrical equations, considering small strains and displacements. After classical transformation for elastic part and bracketing it as a multiplier we obtain:

$$F(x,t)=\frac{\partial M}{\partial x}=-EI\frac{\partial^3 y(x,t)}{\partial x^3}\left[1+n\left(\frac{\partial^2 y(x,t)}{\partial x^2}\right)^{n-1}B\cdot t\cdot\Phi(y)\right], \tag{4}$$

where *y(x,t)* is the beam deflection, $\Phi(y)=\left.\frac{y^{n-2}}{\frac{n+1}{3}}\right|_{-h/2}^{h/2}$, E is the Young modulus, I is inertia moment of beam with rectangular cross-section *hxh*. For *dF* we have:

$$dF=\frac{\partial F}{\partial x}dx=-EI\frac{\partial^4 y}{\partial x^4}\left[1+n\left[\frac{\partial^4 y}{\partial x^4}\left(\frac{\partial^2 y}{\partial x^2}\right)^{n-1}+\left(\frac{\partial^3 y}{\partial x^3}\right)^2(n-1)\left(\frac{\partial^2 y}{\partial x^2}\right)^{n-1}\right]\right].$$

Let us use the d'Alembert principle. The inertia force has the following form:

$$dF_{in}=\rho S\frac{\partial^2 y}{\partial t^2}dx\,.$$

Here *S* is a square of the beam cross-section, ρ is the density of beam's material. Finally we have:

$$\frac{\partial^2 y(x,t)}{\partial t^2}+a^2\frac{\partial^4 y(x,t)}{\partial x^4}+$$
$$+a^{2n}\left[\frac{\partial^4 y(x,t)}{\partial x^4}\left(\frac{\partial^2 y(x,t)}{\partial x^2}\right)^{n-1}+\left(\frac{\partial^3 y(x,t)}{\partial x^3}\right)^2(n-1)\left(\frac{\partial^2 y(x,t)}{\partial x^2}\right)^{n-2}\right]\cdot b\cdot t\cdot\Phi(y)=f(x,t), \tag{5}$$

Here $a^2=\frac{EI}{\rho S}$, *f(x,t)* is an internal force which is considered as $f=A\sin(\omega t)$. The console beam is considered.

2. Method of solution

Obtained equation (5) is solved by method of weighted discrepancies in Galerkin's form. Beam deflection is presented in the standard form of product of functions depends upon time and co-ordinate:

$$y(x,t)=q(t)\varphi(x), \tag{6}$$

where *q(t)* – is the generalized co-ordinate, *φ(x)* –is the first eigen form of beam oscillations. Following approach of S.P.Timoshenko it is presented in simplified form:

$$\varphi(x)=2\left(1-\cos\frac{\pi x}{2l}\right), \tag{7}$$

where l is a beam length. Let us substitute the expression (6) into equation (5). The result of substitution designates as operator $L[y(x,t)]$. Due to approach of the method of weighted discrepancies $L[y(x,t)]$ is multiplying on function (7) and integrating over a beam's length:

$$\int_0^L L[y(x,t)]\cdot\varphi(x)\,dx = 0. \tag{8}$$

After transformations and calculations of integrals we obtain the ordinary differential equation, which describes the physically non-linear forced oscillations of a beam:

$$A_1\,\ddot{q} + a^2 A_2 q + a^{2n}\left(A_3 q^n + A_4 q^n\right)\cdot b\cdot t\cdot\frac{3}{n+1}h^{n-2} = f(x,t). \tag{9}$$

Here cumbersome coefficients $A_i, i=\overline{1,4}$ are omitted.

3. Numerical results

Differential equation (9) is integrated numerically by Runge-Kutta method. Some steps were used for convergence analysis, and finally calculations had been done with the time step 0.01s.

Let as take the following values of beam parameters: cross-section with *h = 1mm,* Young modulus: $E = 1.67\cdot 10^5\ MPa$, steel density: $\rho = 7.8\cdot 10^3\ \frac{kg}{m^3}$, beam's length *l = 50 mm*. The force amplitude is *A*=0.1H.The time of a process was selected as 1200s.

Results are presented in figures 1-2. The growth of amplitude due to irreversible creep is presented in Fig.1.

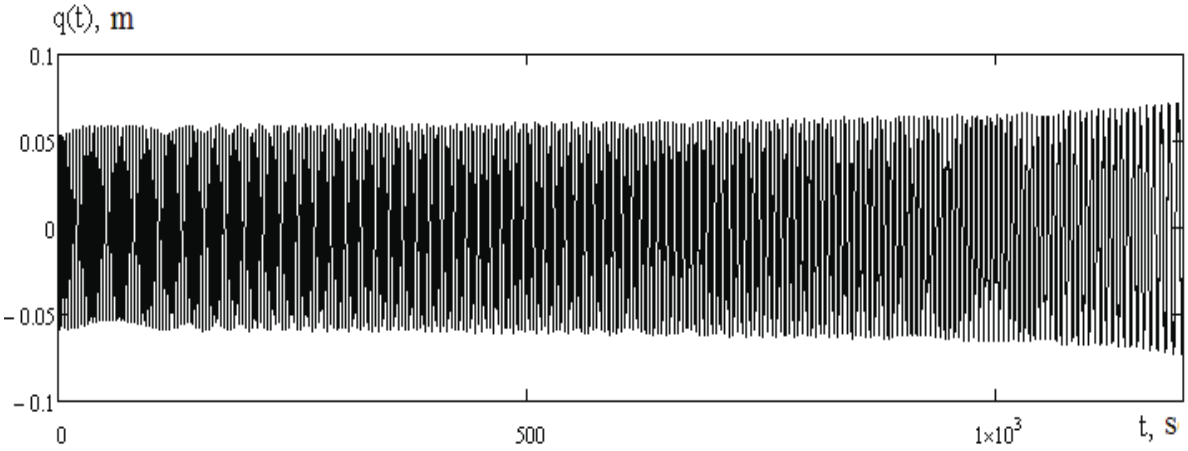

Figure 1. Beam deflection versus time

More detailed the varying of the maximum deflection in a cycle of loading through time is presented on Fig. 2. It can be seen that the maximum amplitude value at the moment t=1200s is equal to 1.3 sm. Such result can be regarded as only qualitative because the displacement is more greater than beam cross-section height. So, the geometrical nonlinear equations have to be used for satisfactory description of the creep-forced oscillations process.

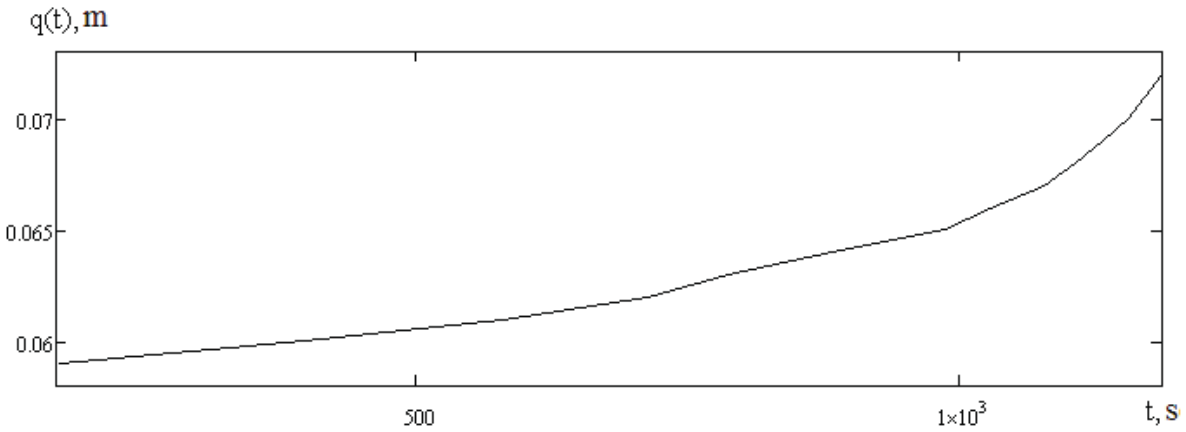

Figure 2. Maximum beam amplitude versus time

Conclusions

The paper contains the new approach for the beam flexural oscillations with considerations of essential creep of its material. The equation was derived, reduced to simplified model and numerically solved. Physically non- controversial result of cyclic amplitude growth had been obtained.

References

[1] Rabotnov Yu. N. *Elements of Hereditary Solid Mechanics*, Mir, Moscow, 1980 (in Russian).
[2] Taira S. and Ohtani R. *Theory of High Temperature Strength of Materials*, Metallurgia, Moscow, 1986 (in Russian).
[3] Breslavsky D. and Morachkovsky O. A new model of nonlinear dynamic creep *IUTAM Symposium on Anisotropy, Inhomogenity and Nonlinearity in Solid Mechanics, Dordrecht*, pp. 161-166, 1995.
[4] Warburton G.B. *The dynamical behaviour of structures,* Oxford, Pergamon Press, 1976.

Proceedings of the 4th International Conference on Nonlinear Dynamics
ND-KhPI2013
June 19-22, 2013, Sevastopol, Ukraine

Numerical Calculations of Creep Damage at Cyclic Loading by Use of Tensor Damage Parameter Model

D.Breslavsky[1*], Yu. Korytko[1], V.Mietielov[1], O.Morachkovsky[1], O.Tatarinova[1]

Abstract
Creep of cyclically loaded bodies and their fracture due to creep mechanisms are studied. Creep damage equations are built by use of tensor parameter for titanium alloy. Similar equations were derived for stress cyclic varying using the method of asymptotic expansions and averaging in a period. 2d plane stress problems were solved by FEM and fields of stress, strain, displacement, damage parameter components as well as time to rupture values were obtained

Keywords
Creep, damage, cyclic loading, tensor damage parameter, FEM, plane stress, numerical simulation

[1] National Technical University 'Kharkiv Polytechnic Institute', Kharkiv, Ukraine
* **Corresponding author:** brdm@kpi.kharkov.ua

Introduction

New structural materials like light weight alloys and metallic composites are widely used in industrial applications. Their creep-damage behavior is strongly anisotropic which demands using of tensor models for description of creep strain rate as well as damage accumulation. Such models had been suggested by Murakami [1], Cordebois-Sidoroff [2], O.Morachkovsky [3] and others. In recent years these approaches were used for the case of static loading.

Otherwise, very often structural elements are loaded by joint action of static and cyclic loading from their forced vibrations. As it is known [4], in this case so-called 'dynamic creep' processes are developed in the material. They are characterized by essential acceleration of creep strain rate as well as of damage accumulation which leads to decreasing of time to rupture values in comparison with pure static loading.

Constitutive equations for description of dynamic creep-damage processes as well mathematical procedures for their adequate numerical simulation were suggested by D.Breslavsky and O.Morachkovsky [5, 6]. In this paper these approaches were applied for tensor creep-damage model [3].

1. Anisotropic creep-damage laws

Let us regard creep-damage laws for anisotropic materials which correspond to general linear tensor dependences for principal axes of symmetry of creep and damage properties of anisotropic material. Damage accumulation in this case will be described by tensor of second rank ϖ_{ij}.

Let as accept that damage tensor ϖ_{ij}, as an internal parameter, corresponds to the associated with it tensor of thermodynamic stresses in damaged media R_{ij}. For materials with initial anisotropy equivalent stress σ_V is determined by mutual invariants of stress tensor σ_{ij} with material creep properties tensors a_{ij}, b_{ijkl}, as well as equivalent stress R_V is determined by mutual invariants of tensor R_{ij} with material damage properties g_{ij}, d_{ijkl}:

$$\sigma_V = \sigma_1 + \sigma_2,\ \ \sigma_1 = a_{ij}\sigma_{ij},\ \ \sigma_2 = \sqrt{b_{ijkl}\sigma_{ij}\sigma_{kl}};\ \ R_V = R_1 + R_2,\ \ R_1 = g_{ij}R_{ij},\ \ R_2 = \sqrt{d_{ijkl}R_{ij}R_{kl}}.$$

Using above mentioned suggestions let us present the dissipation potentials for creep strain and damage parameter's rates in the following forms:

$$\dot{D} = \dot{D}(\sigma_V; \varpi, T) = \sigma_{ij}\dot{c}_{ij}, \quad \dot{\Omega} = \dot{\Omega}(R_V; \varpi, T) = R_{ij}\dot{\varpi}_{ij}. \tag{1}$$

Thereat the flow rule and damage equations can be presented using the gradiental law as follows:

$$\dot{c}_{ij} = \dot{\lambda}\frac{\partial \dot{D}}{\partial \sigma_{ij}}, \quad \dot{\varpi}_{ij} = \dot{\lambda}_*\frac{\partial \dot{\Omega}}{\partial R_{ij}},$$

where scalar multipliers $\dot{\lambda}, \dot{\lambda}_*$ are determined from eqs (1) after specification of the form of each potential.

For the establishing of failure criterion in invariant scalar form let us consider in a some material point the dissipation's part which is responsible for creep damage, as well as its limit value in the rupture time moment:

$$\Omega(t) = \int_0^t \dot{\Omega}dt, \qquad \Omega_* = \int_0^{t_*} \dot{\Omega}dt.$$

Let us suppose that limit value of creep damage dissipation of the material Ω_* is completely definite material characteristic. In this case, assuming as the scalar damage measure the value of $\omega(t) = \Omega(t)/\Omega_*$, the failure criterion can be written in the following form: $\omega(t_*) = 1$, where t_* is the value of failure time.

By use of thermodynamic assumptions for materials with initial creep anisotropy we obtain the constitutive equations:

$$\dot{c}_{ij} = \frac{\dot{D}}{\sigma_V}\left(a_{ij} + \frac{b_{ijkl}\sigma_{kl}}{\sigma_2}\right),\ \ \dot{\varpi}_{ij} = \frac{\dot{\omega}}{R_V}\left(g_{ij} + \frac{d_{ijkl}R_{kl}}{R_2}\right), \tag{2}$$

where c_{ij}, ϖ_{ij} are symmetric tensors of irreversible creep strains and damage; $\dot{D} = \sigma_{ij}\dot{c}_{ij}$ is dissipation due to creep: $\dot{\omega} = R_{ij}\dot{\varpi}_{ij}$ is the dissipation due to creep damage, which is referred for its limit value Ω_* at failure moment $(0 \le \omega \le 1)$.

By using of the principle of strain equivalence the influence of damage tensor on effective stress is considered from the following equation: $R_{ij} = \sigma_{ij}/(1-\omega)$, and besides $\dot{\omega} = R_{ij}\dot{\varpi}_{ij}$, $(0 \le \omega \le 1)$, $\omega(t_*) = 1$. Keeping of the demands of basic thermodynamic inequality $\dot{D} + \dot{\Omega} \ge 0$ dissipation potentials (1) can be rewritten in the following form:

$$\dot{D}(\sigma_V; \omega, T) = \dot{D}(R_V), \quad \dot{\Omega}(\sigma_{*V}; \omega, T) = \dot{\Omega}(R_{*V}), \tag{3}$$

where $R_V = \sigma_V/(1-\omega)$, $\sigma_V = \sigma_1 + \sigma_2$, $\sigma_1 = a_{ij}\sigma_{ij}$, $\sigma_2 = \sqrt{b_{ijkl}\sigma_{ij}\sigma_{kl}}$; $R_{*V} = \sigma_{*V}/(1-\omega)$, $\sigma_{*V} = \sigma_{*1} + \sigma_{*2}$, $\sigma_{*1} = g_{ij}\sigma_{ij}$, $\sigma_{*2} = \sqrt{d_{ijkl}\sigma_{ij}\sigma_{kl}}$ are effective stress invariants.

Within the supposed assumptions the principal directions of the material anisotropy are considered constant directly to failure, as well as surfaces of the dissipation potentials in the stress space are expanded in time proportionally to one parameter, which is connected with damage measure $0 \le \omega \le 1$.

Let us regard further constitutive equations (2) for materials with creep transversally isotropy.

Dissipation potentials (3) are chosen as power functions from stress invariants:

$$\dot{D} = R_V^N, \;\; \dot{\omega} = R_{*V}^k / (1-\omega)^S, \tag{4}$$

where N, k, S are the constants.

Equations (2) are regarded as constitutive ones for materials with initial anisotropy and creep-damage properties asymmetry, in particular for tension and compression. If these effects are absent, then $a_{ij} = g_{ij} = 0$. In this case creep-damage equations for materials with creep transversally isotropy can be written in the following form:

$$\underline{\dot{c}} = b_{1111}^{(N+1)/2} \frac{\overline{\sigma}_2^{N-1}}{(1-\omega)^N} [B]\underline{\sigma}, \;\; \underline{\dot{\varpi}} = d_{1111}^{k/2} \frac{\sigma_{*2}^{k-2}}{(1-\omega)^{k+S-1}} [D]\underline{\sigma}, \tag{5}$$

$$\dot{\omega} = d_{1111}^{k/2} \frac{\sigma_{*2}^k}{(1-\omega)^{k+S}}, \;\; \omega(0) = 0, \;\; \omega(t_*) = 1, \tag{6}$$

where $\underline{\dot{c}} = (\dot{c}_{11}, \dot{c}_{22}, 2\dot{c}_{12})^T$, $\underline{\sigma} = (\sigma_{11}, \sigma_{22}, \sigma_{12})^T$, $\underline{\dot{\varpi}} = (\dot{\varpi}_{11}, \dot{\varpi}_{22}, 2\dot{\varpi}_{12})^T$ are the vectors of creep strain rates, stresses and damage rates $\overline{\sigma}_2^2 = \underline{\sigma}^T [B]\underline{\sigma}$, $\sigma_{*2}^2 = \underline{\sigma}^T [D]\underline{\sigma}$ are the stress invariants;

$$[B] = \begin{vmatrix} 1 & \beta_{12} & 0 \\ \beta_{21} & \beta_{22} & 0 \\ 0 & 0 & 4\beta \end{vmatrix}, \;\; \beta_{12} = -\frac{1}{2} b_{1111}, \beta_{22} = \frac{b_{2222}}{b_{1111}}, 4\beta = \frac{b_{1212}}{b_{1111}},$$

$$[D] = \begin{vmatrix} 1 & \delta_{12} & 0 \\ \delta_{21} & \delta_{22} & 0 \\ 0 & 0 & 4\delta \end{vmatrix}, \;\; \delta_{12} = -\frac{1}{2} d_{1111}, \delta_{22} = \frac{d_{2222}}{d_{1111}}, 4\delta = \frac{d_{1212}}{d_{1111}}.$$

Further let us regard the cyclic loading, where stress tensor consists from pure static part σ_0 and fast varying part σ_1 : $\sigma = \sigma_0 + \sigma_1$. The frequency f is the frequency of forced oscillations: $\sigma_1 = \sigma^a \sin(2\pi f t)$, where σ^a is amplitude stress. Such process is referred as dynamic creep-damage process [4]. It had been mathematically described in [6] for scalar damage parameter by use of method of asymptotic expansions jointly with averaging in a period technique.

Let us use this approach for eqs (5)-(6). After introducing the small parameter $\mu = T/t_*$ we present processes in two time scales (slow t and fast $\xi = \tau/T$, where $\tau = t/\mu$,) in the following form of expansions:

$$c \cong c^0(t) + \mu c^1(\xi), \;\; \omega \cong \omega^0(t) + \mu \omega^1(\xi), \tag{7}$$

where $c^0(t)$, $\omega^0(t)$, $c^1(\xi)$, $\omega^1(t,\xi)$ are the functions which coincide to basic creep-damage process in slow (0) and fast (1) time scales.

Considering the dependence of creep strain and damage parameters only from 'slow' time [5], after averaging we have:

$$\left\langle c^0(\xi) \right\rangle = \int_0^1 c^0(t) d\xi \cong c^0(t), \quad \left\langle c^1(\xi) \right\rangle = \int_0^1 c^1(\xi) d\xi \cong 0, \qquad \left\langle \omega^0(\xi) \right\rangle = \int_0^1 \omega^0(t) d\xi \cong \omega^0(t),$$

$$\left\langle \omega^1(\xi) \right\rangle = \int_0^1 \omega^1(\xi) d\xi \cong 0, \quad \left\langle \varpi^0(\xi) \right\rangle = \int_0^1 \varpi^0(t) d\xi \cong \varpi^0(t), \qquad \left\langle \varpi^1(\xi) \right\rangle = \int_0^1 \varpi^1(\xi) d\xi \cong 0.$$

So, by use of asymptotic expansions methods with subsequent averaging in a period of cyclic load, after transition to the case of multi-axial stress state, we obtain constitutive equations for dynamic creep-damage processes in alloys with orthotropic creep-damage properties:

$$\dot{\underline{c}} = b_{1111}^{(N+1)/2} K(A_n) \frac{\overline{\sigma}_2^{N-1}}{(1-\omega)^N} [B]\underline{\sigma}, \quad \dot{\underline{\varpi}} = d_{1111}^{k/2} H_1(A_k) \frac{\sigma_{*2}^{k-2}}{(1-\omega)^{k+S-1}} [D]\underline{\sigma}, \tag{8}$$

$$\dot{\omega} = d_{1111}^{k/2} H_2(A_k) \frac{\sigma_{*2}^k}{(1-\omega)^{k+S}}, \quad \omega(0) = 0, \quad \omega(t_*) = 1, \tag{9}$$

where $K(A_n) = \int_0^1 (1 + A_n \sin(2\pi\xi))^n d\xi$, $A_n = \frac{\overline{\sigma}_2^a}{\overline{\sigma}_2}$, $H_1(A_k) = \int_0^1 (1 + A_k \sin(2\pi\xi))^{k-1} d\xi$, $H_2(A_k) = \int_0^1 (1 + A_k \sin(2\pi\xi))^k d\xi$, $A_r = \frac{\sigma_{*2}^a}{\sigma_{*2}}$. $(\overline{\sigma}_2^a)^2 = (\underline{\sigma}^a)^T [B] \underline{\sigma}^a$, $(\sigma_{*2}^a)^2 = (\underline{\sigma}^a)^T [D] \underline{\sigma}^a$ are the invariants of cyclic stresses.

2. FEM solution for plane stress problem

Let us regard the problem statement for structural element, made from material with anisotropic creep-damage properties, which is in plane stress state. The volume V is fixed in a surface part S_1 and is loaded by traction p $\{p_1, p_2\}$ on another surface part S_2. In co-ordinate system OX_1X_2 the motion of material points under the creep conditions is described by use of Lagrange approach. The vectors of displacements $u=\{u_1, u_2\}^T$ and their rates $v=\{v_1, v_2\}^T$ are introduced. In these assumptions creep problem for the case of small displacements and strains is described by following boundary – initial value problem:

$$\sigma_{ij,j} + f_i = \rho \dot{v}_j, \quad (i,j=1,2) \quad x_1, x_2 \in V; \quad \sigma_{ij} n_j = p_i + p_i^a \sin 2\pi f t, \quad x_1, x_2 \in S_2. \tag{10}$$

$$v_1 = du_1/dt = \dot{u}_1; \quad v_2 = du_2/dt = \dot{u}_2 \tag{11}$$

$$\varepsilon_{11} = \frac{\partial u_1}{\partial x_1}, \quad \varepsilon_{22} = \frac{\partial u_2}{\partial x_2}, \quad \varepsilon_{12} = \frac{1}{2}\left(\frac{\partial u_1}{\partial x_2} + \frac{\partial u_2}{\partial x_1}\right), \tag{12}$$

The level of stresses which don't exceed yield limit will be considered. Let us accept, that elastic e_{ij} and creep c_{ij} strain components as well as their rates are additive:

$$\dot{\varepsilon}_{ij} = \dot{e}_{ij} + \dot{c}_{ij}, \tag{13}$$

Obtained system (10-13) has to be solved jointly with constitutive equations (8-9). Boundary conditions on surface parts $S_1 : \dot{u}_i = \dot{u}_i^*$ and S_2: $\dot{\sigma}_{ij} n_j = \dot{p}_i$ as well initial ones at t=0 considering the elastic strain-stress distribution have to be added. Constitutive equations (8-9) are added to above system.

The system (8-13) is solved by use of two time scales method jointly with averaging in a period of forced vibration *1/f*. Full description of the procedure can be found in [5,6]. The problem derives to the simplified one which is similar to problem of static loading, but with constitutive equations (8-9).

Anisotropic creep-damage behavior is simulated by FEM software had been developed in NTU 'KhPI'. Triangular linear element is used. The problem which is formulated in rates is solved:

$$[K]\dot{\underline{\delta}} = \dot{\underline{F}} + \dot{\underline{F}}_c, \tag{14}$$

where $[K] = \sum_e \int_{V^e} [B]^T [D][B] dV$ is global stiffness matrix; $\dot{\underline{F}} = \sum_e \int_{\Sigma_2^e} [N]^T \dot{\underline{p}} d\Sigma$, $\dot{\underline{F}}_c = \sum_e \int_{V^e} [B]^T \underline{\sigma}^* dV$ are the loading vectors from traction and forces which determined by creep strains.

3. Anisotropic creep-damage in titanium plates

Developed method and software were used for creep-damage modeling in titanium plates made from BT1-0 alloy which is similar to IMI125 or T40 grades. The properties of creep and long term strength of the specimens made from the plane billet in three directions were experimentally obtained for temperature T=773K by O.Morachkovsky and V.Konkin [7]. The constants values which had been obtained after data processing are the following: $b_{1111}=2{,}303\cdot10^{-4}$, $b_{1122}=-1{,}151\cdot10^{-4}$, $b_{2222}=1{,}924\cdot10^{-4}$, $b_{1212}=2{,}058\cdot10^{-4}$, $(\text{MPa})^{-2N/N+1}/\text{h}^{2/N+1}$; $d_{1122}=-1{,}771\cdot10^{-5}$, $d_{2222}=3{,}324\cdot10^{-5}$, $d_{1212}=3{,}127\cdot10^{-5}$, $(\text{MPa})^{-2}/(\text{h})^{2/k}$; $k=N=5$, $s=1$. Comparison between experimental data at static loading for specimens had been cut in different directions with numerical simulations of rectangular plates in tension simulating the above test data were done at first in order to verify numerical method. A satisfactory agreement which doesn't exceed 25-32% had been obtained for time variation of strains and time to rupture values. Table 1 contains some examples of these comparisons for time to rupture values for net stress 60 MPa.

Table 1. Comparison of time to rupture values for static loading

Orientation of anisotropy axes, ϑ°	Stress, MPa	Experimental value of time to rupture t_*, h	Numerical value of time to rupture t_*, h
0	60	24	25.9
45	60	19	20.5
90	60	28.7	19.7

Further the static and dynamic creep of titanium plate (0.8mx0.8m) with a central hole (radius is equal to 0.1m) were numerically simulated. One quarter of a plate was considered and stress-strain state and damage redistribution on time were analyzed. Fig.1 contains the distribution of damage measure ω for the case of pure static loading by net stress 10MPa at the moment t=220h which is nearest to the failure moment t_*=221h. Essential stress concentration near the hole leads to failure in this area. The creep –damage behavior of the plate is strongly non-linear: increasing of the traction from 10 to 13MPa leads to decreasing of time to failure from 221h to 68.5h.

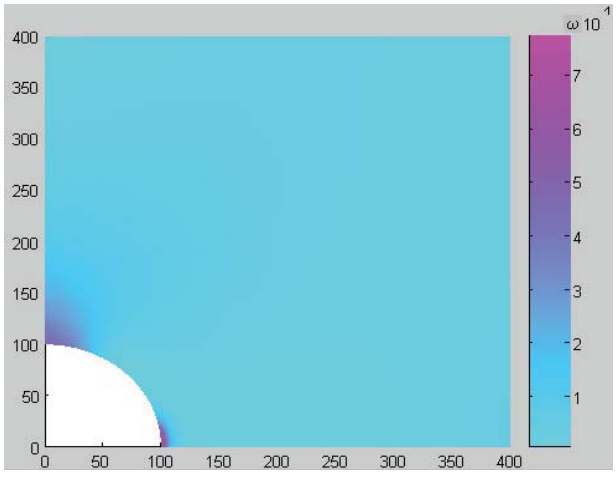

Figure 1. Damage parameter at t=220h

Let us present the results of dynamic creep simulation of the similar plate. The axial loading in this case consists from static part p_0=16.9MPa and the cyclic one which is varying due to sine law with frequency 10Hz. Let us introduce the loading parameter $L=p_0/p_a$, where p_a is amplitude value of the loading. The varying of L from 0 to 0.3 was analyzed.

The time to failure values in this loading program decreases with increasing of L from 0.166 h for L=0 to 0.122h for L=0.3. It happens for material with anisotropic creep-damage properties just the same in dynamic creep processes of elements with isotropic ones [6]. The character of stress and damage redistribution is similar for the static case, but both processes are run faster.

However, for smaller values of net stress, and, respectively, for smaller stress values in a plate, character of a process differs from above analyzed one. Dynamic loading accelerates the stress relaxation in area near the hole as well as in conventional dynamic creep [6], wherein the obtained stress level became so small, that rate of damage accumulation decrease significantly. For example, for p_0=13MPa the value of time to failure for L=0 is equal to t_*=68.5 h, but adding of small cyclic part (L=0.05) leads to it's increasing and t_*=72.6 h. Subsequent increasing of L leads to similar growth of time to failure values due to fast dynamic relaxation at first time of a process: for L=0.1 t_*=120.1 h.

Conclusions

An approach for the effective mathematical modeling of dynamic creep-damage processes in structural elements made from the titanium alloy with anisotropic properties is presented. The use of two time scale method with asymptotical expansions on the small parameter and subsequent averaging in a period allows us to avoid the direct integration through a cycle and simulate only static problems with flow rule and damage equation of special form. Effects of essential acceleration of strain and damage rate growth as well as stress relaxation due to dynamic creep had been established for plate with a hole made from material with anisotropic creep-damage properties.

References

[1] Murakami S. Notion of Continuum Damage Mechanics and Its Application to Anisotropic Creep Damage Theory *J. Engng. Mater. Techn,* Vol. 105, pp. 99-105, 1983.

[2] Cordebois J.P., Sidoroff F. Damage Induced Elastic Anisotropy *Mechanical Behaviour of Anisotropic Solids (*J. P. Boehler, editor), Colloque Euromech 115, Villard-de-Lans, June 19-22, Martinus Nijhoff Publishers, pp. 761- 774, 1979.

[3] Morachkovsky O.K., Pasynok M.A. Investigation of the influence of the obtained anisotropy due to precurcive creep on the creep of materials *Proc. KhSPU* , KhSPU, Kharkiv, Vol. 27, pp. 197-203, 1998 (in Russian).

[4] Taira S., Ohtani R. *Theory of High Temperature Strength of Materials,* Metallurgia, Moscow, 1986. (in Russian, translated from Japan).

[5] Breslavsky D., Morachkovsky O. A new model of nonlinear dynamic creep. *IUTAM Symposium on Anisotropy, Inhomogenity and Nonlinearity in Solid Mechanics*, Kluwer Academic Publishers, Dordrecht, pp. 161-166, 1995.

[6] Breslavsky D., Morachkovsky O. Dynamic creep continuum damage mechanics: FEM-based design analysis. *Computational Plasticity: Fundamentals and Applications. Proc. of the Fifth International Conference on Computational Plasticity held in Barselona, Spain, 17-20 March 1997*, IMNE, Barselona IMNE, Part 1, pp.1071-1076, 1997.

[7] Konkin V.N., Morachkovsky O.K. Creep and long term strength of light weight alloys with anisotropic properties. *Problems of Strength*, Vol. 5, pp. 38-42, 1987. (in Russian)

Proceedings of the 4th International Conference on Nonlinear Dynamics
ND-KhPI2013
June 19-22, 2013, Sevastopol, Ukraine

Loading Sequence Effect of Notched Specimens under Biaxial Loading

Maksym Gladskyi[1*], Sergiy Shukayev[1]

Abstract
Notch effects on uniaxial and torsion fatigue behavior of low-carbon steel are investigated in this study. Constant and variable amplitude axial and torsion both load and strain-controlled tests were conducted on smooth and notched tubular specimens. Maximum principal stress theory was chosen as driving parameter for experimental program. Torsion loading resulted in significantly shorter lives and fatigue data could not be correlated by the maximum principal stress theory for smooth specimens. However, considering fatigue notch factor for notched tubes the maximum principal stress theory gives acceptable results. Linear rule, Glinka's rule, Neuber's rule as well as FE analysis were used to estimate local strain at the notch root. Similar results were found for Neuber's rule and FEA simulation due to plane stress condition. However, strain energy density rule correlates data better. The Fatemi-Socie (FS) critical plane parameter was found to correlate constant amplitude data of both specimen geometries very well. Maximum principal stress and the linear cumulative damage rule were also employed for fatigue life prediction of notched specimens under block loadings with different contribution of axial and torsion cycling.

Keywords
Notch effects, uniaxial and torsion fatigue, low-carbon steel

[1] National Technical University of Ukraine "KPI", Kyiv, Ukraine
* **Corresponding author:** gladsky@gmail.com

Proceedings of the 4th International Conference on Nonlinear Dynamics
ND-KhPI2013
June 19-22, 2013, Sevastopol, Ukraine

Damage Indicators During Fatigue of Metal Matrix Composites

Zbigniew L. Kowalewski[1*], Tadeusz Szymczak[1],
Katarzyna Makowska[2], Krystyna Pietrzak[2]

Abstract
Selected damage measures applied for degradation description of engineering materials subjected to fatigue loading conditions are presented. In addition to well-known measures the new concepts of fatigue damage development are discussed using known mechanisms of cyclic plasticity and ratcheting. Their usefulness was studied on the basis of experimental results for modern metal matrix composites commonly applied in many branches of the industry.

Keywords
Damage, fatigue, composites

[1]Institute of Fundamental Technological Research, Warsaw, Poland
[2]Motor Transport Institute, Warsaw, Poland
[*]**Corresponding author: zkowalew@ippt.gov.pl**

Introduction

First investigations aimed to clarify the phenomenon of fatigue were already carried out in the first half of the nineteenth century. The tests in this area were conducted by Albert in 1838. The first experimental programme important from the scientific point of view was executed for selected metals by A. Wöhler in 1860. From that moment, intensifying progress of material testing under fatigue conditions can be observed and it is continued to this day. Especially in recent years there has been an increased interest in the problems of fatigue and at the same time enormous progress in this field. This is mainly because of an increase either in the level of loading or degree of loading complexity in the number of operating units. As typical examples one can indicated aviation where aircraft speed and weight increase or energetics with rapid temperature increase of devices producing energy. The observed technical progress enforces a development of fatigue testing methods, because the safety of people depends many times on the results of these tests. Modern passenger aircrafts may be operated, if parallel simulation fatigue tests are carrying out, the results of which allow for the safe exploitation of machines being currently in use. Among fatigue tests one can distinguish two basic directions:

- investigations conducted by physicists and metallurgists focusing on trying to learn the mechanisms governing the process of fatigue,
- theoretical and experimental investigations in order to create a phenomenological theory to allow quantitative description of the phenomenon.

Both of these trends are currently developing parallelly [e.g. 1-6].

1. Experimental evaluation of fatigue damage

In order to assess damage degree due to fatigue of the material in the as-received state and after exploitation the Wöhler diagrams may be elaborated that represent the number of cycles required for failure under selected stress amplitude. The results of such approach are illustrated in Fig.1 for the 13HMF steel. As you can see, the Wöhler diagrams depending on the state of material differ themselves, thus identifying the fatigue strength reduction due to the applied loading history.

Unfortunately, such method of degradation assessment of the material undergoing fatigue suffers on very high cost and additionally it is time consumable.

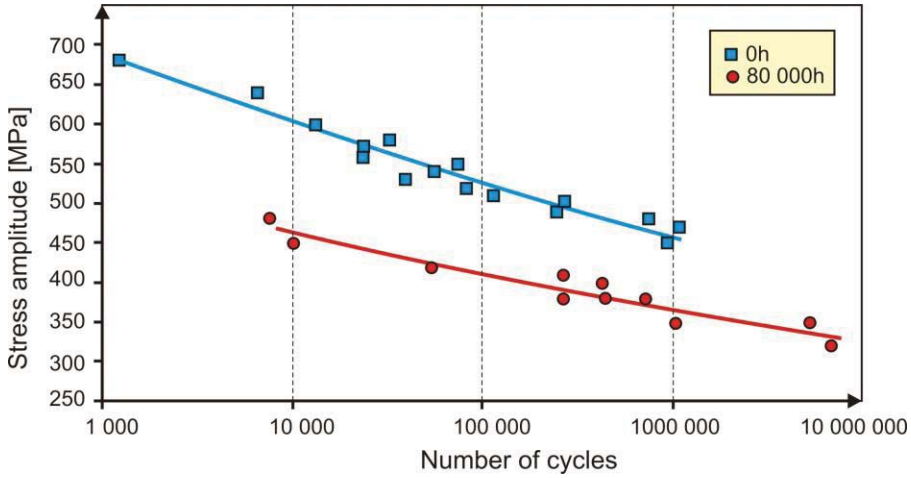

Figure1. Wöhlers diagram for the 13HMF steel before (0h) and after exploitation (80 000h) [7]

Therefore, searches are conducted continuously for new solutions that would provide a better assessment of the fatigue damage development. To obtain this effect, an adequate damage parameter must be defined on the basis of the measurable indicators of its development. Selected proposals are discussed in the next section of this paper.

2. Indicators and measures of fatigue damage

The essence of fatigue are changes in the structure of a material due to operational stresses, movement of lattice defects (slip dislocations, vacancies migration), the concentration of these defects in areas where they face further obstacles to movement (grain boundaries, inclusions), forming the so-called persistent slip bands, and other processes, such as stress/temperature-induced phase transformations, and diffusion processes. The net effect of these phenomena is the nucleation and growth of microcracks, and in the final stage of damage development formation of the dominant crack in the material. Such crack develops subsequently in the element of structure until it reaches a critical size. After that the service loading applied can cause its uncontrolled growth leading to structural failure.

The fatigue damage development is associated with nucleation and growth of micro-cracks. In the theoretical papers concerning fatigue damage a size of the micro-cracks located in the material was assumed as the fatigue damage measure. The most common idea of damage measure is the surface density of micro-cracks in the representative unit volume of a material (Kachanov, 1958 [8]). In this case the damage parameter is no scalar, since it depends on the direction. Such a concept has been developed further by other researchers, and as a consequence, in 1981 Murakami [9] introduced the second order tensor as a measure of damage. This form of damage parameter is still often used by a number of researchers. The disadvantage of such defined parameter, however, is that it cannot be measured in a period prior to the formation of a dominant crack in the material by any of the currently known methods. Nevertheless, experimental study of a damage measure changes in material during construction operation or laboratory tests is a necessary condition for fatigue life prediction and assessment of the risks associated with further safe operation of the structure. Therefore, intensive searches are still ongoing in order to find measurable parameter representing fatigue damage of structural materials.

The behaviour of materials under high cycle fatigue (HCF) for stress amplitude of levels below the yield point can be divided into two basic types according to their mechanisms of damage development.

The behaviour of the first group may be described by cyclic plasticity generated by dislocation movement at the level of local grains and slip bands. In this case a non-elastic strain is the damage indicator characterized by the width of the hysteresis loop at total unloading of the material, equation (1), Figs. 2a, 3.

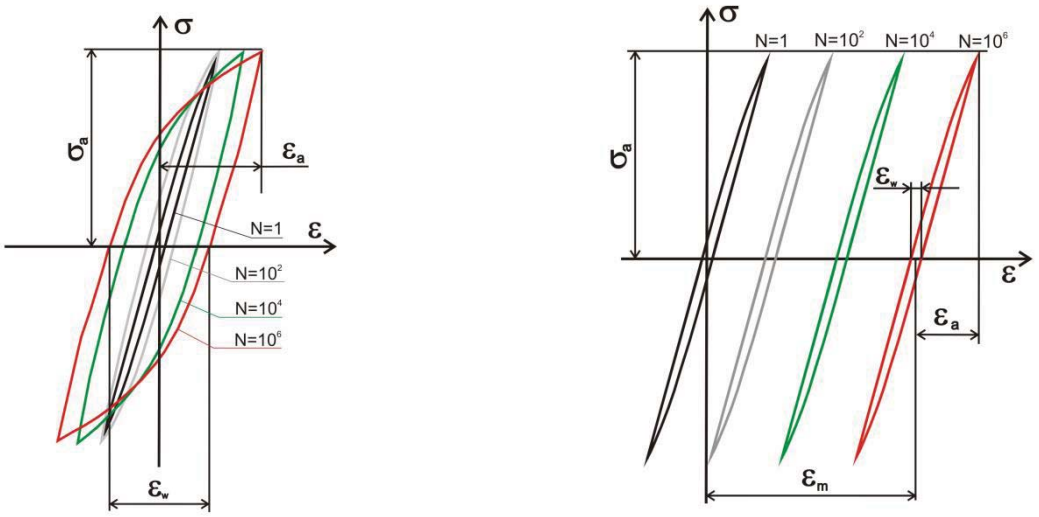

a) b)

Figure 2. Hysteresis loops depending on the damage mechanism: (a) cyclic plasticity, (b) ratcheting

$$\varepsilon_a^{in} = \frac{\varepsilon_{\max}(F=0) - \varepsilon_{\min}(F=0)}{2}. \tag{1}$$

Fatigue damage measure can be defined in such a case by the following relationship:

$$\varphi_N(\varepsilon_a^{in}) = \sum_1^N \left|\varepsilon_a^{in}\right|. \tag{2}$$

Using equation (2) a damage parameter taking values varying within <0;1> can be written in the following way:

$$\mathrm{D} = \frac{\varphi_N - (\varphi_N)_{\min}}{(\varphi_N)_{\max} - (\varphi_N)_{\min}}, \tag{3}$$

where φ_N – accumulated strain up to the current loading cycle; $(\varphi_N)_{\min}$ - accumulated strain at the first cycle; $(\varphi_N)_{\max}$ - accumulated total strain calculated for all cycles.

The behaviour of the second group of materials subjected to cyclic loading is described by ratcheting generated by local deformation around the voids, inclusions and other defects of the microstructure. In this case the damage indicator is atributted to the mean inelastic strain describing a shift of the hysteresis loop under unloaded state. It can be defined by the following expression,

$$\varepsilon_m^{in} = \frac{\varepsilon_{\max}(F=0) + \varepsilon_{\min}(F=0)}{2}. \tag{4}$$

Its graphical interpretation is shown in Fig.2b.

Applying damage indicator in the form of equation (4) the damage measure can be defined as:

$$\varphi_N(\varepsilon_m^{in}) = \sum_1^N \left|\varepsilon_m^{in}\right| \tag{5}$$

and thus damage parameter taking values varying within <0;1> can be expressed by the relationship of the structure of equation (3). The sign of absolute value at relationships (2) and (5) results from the fact, that the hysteresis loops of the subsequent cycles may move either in the positive or negative direction of the strain axis, Fig. 4.

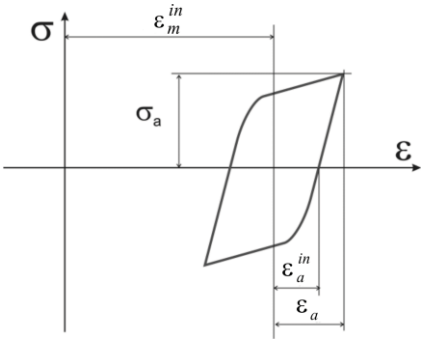

Figure 3. Ilustration of strain damage indicators during fatigue conditions

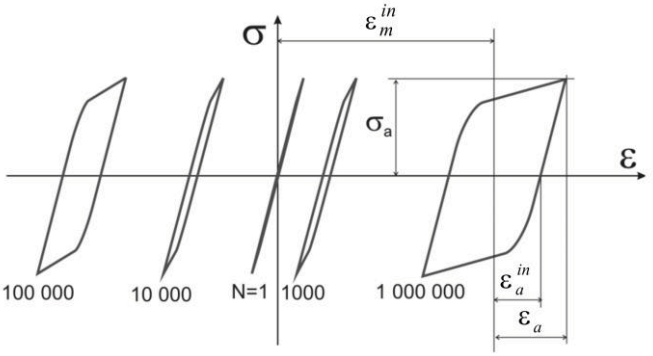

Figure 4. Variants the hysteresis loops movement

In both cases, changes of strain taken for the entire measuring volume of the specimen is the sum of local deformation developing around defects in the form of nonmetallic inclusions and voids for the first group of materials or developing slides at the consecutive grains in the case of the second one. Evolution of the hysteresis loop depending on the damage mechanism for the loads corresponding to stress levels below the yield point is shown in Fig. 2.

In many cases the process of fatigue damage is controlled by more than one mechanism. The fatigue tests carried out on metal matrix composites have shown that the damage process occurred due to combination of cyclic plasticity and ratcheting mechanisms. Therefore, using damage indicators determined on the basis of formulas (1) and (4), damage measure can be defined by the following relationship:

$$\varphi_N(\varepsilon_a^{in}, \varepsilon_m^{in}) = \sum_1^N \left|\varepsilon_a^{in}\right| + \sum_1^N \left|\varepsilon_m^{in}\right| . \tag{6}$$

Hence, a definition of damage parameter takes the form of equation (3), in which damage measure is included in the form of equation (6). The results published so far [e.g. 1, 10, 11] confirm the correctness of the adopted methodology for damage analysis of the materials after service loads, that taking into account parameters responsible for cyclic plasticity and ratcheting.

3. Application of damage parameters for fatigue tests analysis of MMC

Damage analysis presented in section 2 and confirmed for the conventional materials [1] was applied in this research for the metal matrix composite. The Al/SiC composite was prepared from a commercial Al powder with a purity of 99.7% and an average particle size of 6.74 μm (delivered by the Bend-Lutz Co) and the reinforcing phase was made of the SiC powder of 99.8% purity and an average particle size of 0.42 μm (Alfa Aesar Co). The technological process included several stages. In the first stage of process the powders were mixed so as to obtain (Al+x vol.% + SiC) mixtures, where x ranged from 0% to 10% and was changed at an increment of 2.5. The mixtures were homogenized, for 6h, in a polyethylene vessel using a suspension of isopropyl alcohol and Al_2O_3 balls, then dried and granulized at room temperature on a sieve with the mesh size of #0.25 mm. In the next stage, the powder mixtures were subjected to isostatic consolidation at the pressure p = 245 MPa. The samples thus obtained were machined to give them the desired shape (cylindrical) and dimensions (radius r=40 ± 1 mm, length ~50 mm). The final stage of the technological process included direct extrusion of the prepared samples in the KOBO 100T horizontal hydraulic press, equipped with a reversely rotating die whose movement was transmitted onto the extruded material so that its deformation path varied.

Force controlled high cycle fatigue tests (20 Hz frequency) were carried out on the servo-hydraulic testing machine MTS 858. During the tests, sine shape symmetric tension-compression

cycles were applied to keep constant stress amplitude equal to 65 and 70 MPa. Tests were performed at ambient temperature. Each cylindrical specimen manufactured from the Al/SiC rod was subjected to cyclic loading until fracture. A movement of the subsequent hysteresis loops along the strain axis was observed with an increasing number of cycle (Fig. 5). Simultaneously, a width of the subsequent hysteresis loops became almost unchanged. Such behaviour identifies the ratcheting effect. Only insignificant increase of inelastic strain amplitude was observed (Fig. 6).

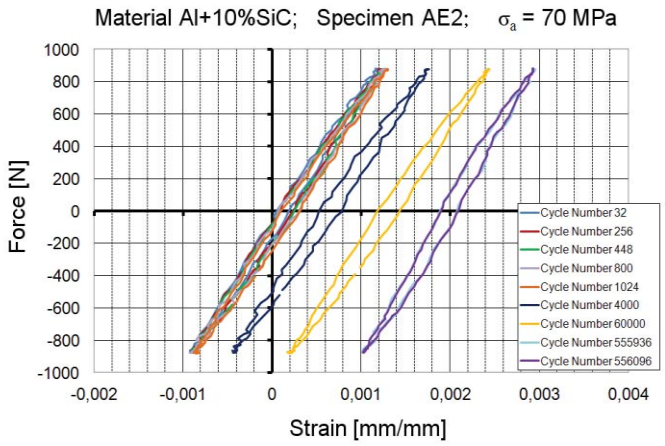

Figure 5. Hysteresis loops for selected cycles

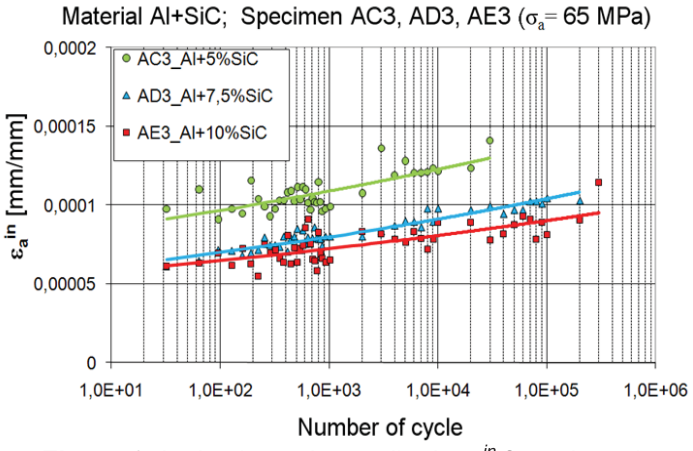

Figure 6. Inelastic strain amplitude ε_a^{in} for selected cycles

Since ratcheting is the dominant mechanism of the composite deformation, the mean strain was taken into account during a damage parameter calculation in the stable growth period. Hence, the damage parameter can be defined using equation (3). It is worth to notice that the rate of damage is relatively high at the beginning of the period. Afterwards, it becomes slower (Fig. 7).

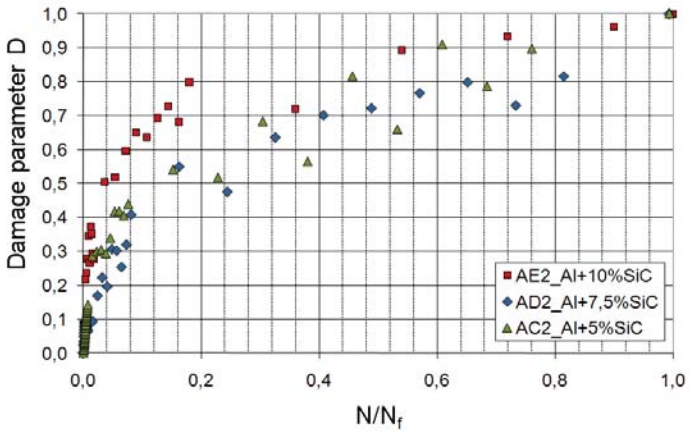

Figure 7. An influence of SiC content on damage parameter variation (stress amplitude 70MPa)

Such a phenomenon indicates that the linear damage accumulation rule cannot be applied for the Al/SiC MMC. Moreover, it can be seen that the rate of damage parameter at the initial stage of fatigue increases with an increase of the SiC particle content.

Conclusions

The paper presents an alternative method for damage evaluation of materials subjected to fatigue loads. Studies in which a width the hysteresis loop variation and its movement were recorded for cycles under fixed constant stress amplitude have demonstrated that this procedure gives a possibility to assess safe operation period for composites in question and there is no need to perform so many experiments, as is required for the Wöhler diagram determination. The proposed method of assessing fatigue damage evolution makes it possible to determine the damage, determine the damage indicators, assessment of fatigue and stress levels to find ranges in which the accumulation of damage can be described by a linear law.

An increase of the SiC content improved the fatigue resistance, and moreover, it increased the rate of hardening during monotonic tensile tests. Hence, it can be concluded generally that the SiC reinforcement led to the material properties improvement. However, it has to be mentioned that a larger content of the SiC particles may lead to generation of their clusters, which often include incoherent particles. Since is well known that the main part of the specimen loading is carrying out by reinforcements, such type of clusters do not contribute to tensile load transfer, and therefore, they can be treated as voids in the structure of a material.

Acknowledgments

The results have been obtained within the project KomCerMet (project No POIG.01.03.01-00-013/08 with the Polish Ministry of Science and Higher Education) in the framework of the Operational Programme Innovative Economy 2007-2013. The material was produced by team of prof. A. Olszyna (Warsaw University of Technology).

References

[1] Socha G. Experimental Investigations of Fatigue Cracks Nucleation, Growth and Coalescence in Structural Steel *International Journal of Fatigue*, Vol. 25/2, pp. 139-147, 2003.
[2] Morrow J.D. Internal Friction, Damping and Cyclic Plasticity: Cyclic Plastic Strain Energy and Fatigue of Metals *ASTM STP*, Vol. 378, pp. 45-84, 1965.
[3] Manson S.S. Behavior of Materials under Conditions of Thermal Stress *NASA TN-2933*, 1953.
[4] Coffin L.F., Jr. A Study of the Effects of Cyclic Thermal Stresses on a Ductile Metal *Trans. ASME*, Vol. 76, pp. 931-950, 1954.
[5] Lemaitre J., *A Course on Damage Mechanics,* Springer-Verlag, Berlin, 1996.
[6] Yang L. and Fatemi A. Cumulative Fatigue Damage Mechanisms and Quantifying Parameters: A Literature Review, *J. Testing and Evaluation*, Vol. 26: 2, pp. 89-100, 1998.
[7] Dietrich L., Grzywna P. and Kukla D. Material Damage Prediction in Cast Aluminum Alloy Using Elektronic Speckle Pattern Interferometry, *Proc. of 27 Danubia-Adria Symposium on Advances in Experimental Mechanics*, Wrocław, Poland, 2010.
[8] Kachanov L.M. *The theory of creep* (English translation edited by Kennedy A.J.), Boston Spa, National Lending Library, 1958.
[9] Murakami S. and Ohno E.T. A continuum theory of creep and creep damage, *Creep in Structures, Proc. of 3rd IUTAM Symp*., Leicester, 1980, Eds: A.R.S. Ponter, D.R. Hayhurst, Springer-Verlag, Berlin, pp. 422-444, 1981.
[10] Rutecka A., Kowalewski Z.L., Pietrzak K., Dietrich L. and Rehm W. Creep and low cycle fatigue investigations of light aluminium Alloys for Engine Cylinder Heads, *Strain – An International Journal of Experimental Mechanics*, Vol. 47, pp. 374-381, 2011.
[11] Szymczak T., Kowalewski Z.L. and Dietrich L. Experimental Analysis of Creep and Fatigue of Light Multifunctional Aluminium Alloys, *Materials Research Innovations*, Vol. 6, No 6, 2010.

Proceedings of the 4th International Conference on Nonlinear Dynamics
ND-KhPI2013
June 19-22, 2013, Sevastopol, Ukraine

Links between Phenomenology and Microstructure in a Ni-based Single Crystal Superalloy

Serge Kruch[1*], J.-B. le Graverend[1], J. Cormier[1], F. Gallerneau[1], J. Mendez[1]

Abstract
This paper is devoted to the presentation of a phenomenological model recently developed to reproduce effects of the microstructure on the overall behavior of a Ni-based single crystal superalloy. This one is used in aircraft engine blades for the very good mechanical properties at elevated temperatures and loads. It takes these interesting properties from the precipitation of high volume fraction (close to 70%) of long range L12 ordered γ' phase which appears as cubes coherently embedded in fcc solid solution γ matrix. However, the accumulation of temperatures and high stresses in fatigue with dwell times leads to important evolutions of the microstructure (directional coarsening, rafting) having a strong influence on the mechanical behavior. The proposed macroscopic model, based on a previous crystal plasticity one, must be able to take into account all these evolutions of the microstructure experimentally observed from thermo-mechanical tests detailed in the paper.
On each slip system, the yield criterion involves several terms including a classical Orowan stress which depends on the thickness of the γ channels, a non-linear isotropic hardening which describes the cyclic hardening effect, the age hardening and the recovery processes and a non-linear kinematic hardening which describes temperature aging effects like dissolution/precipitation of γ' precipitates . The internal variables governing the evolution of the isotropic and kinematic hardenings depend on the volume fraction of secondary and tertiary precipitates which evolve as a function of the cumulative plastic strain.
Also, in order to be able to describe the damage evolution during the secondary and tertiary creep stages, an isotropic damage variable, based on the classical Rabotnov-Kachanov-Hauyhurst concept, is coupled to the model using the effective stress approach. After the identification of the material parameters performed with complex thermo-mechanical tests and microstructure observations, the phenomenological model is applied to describe the behavior of a double notched specimen subjected to a non-isothermal complex creep load. The model is able to predict the strong multiaxial stress state and its influence on the evolution of the microstructure.

Keywords
Microstructure, crystal superalloy, phenomenological model

[1] ONERA / DMSM, Chatillon, France
*** Corresponding author:** serge.kruch@onera.fr

Proceedings of the 4th International Conference on Nonlinear Dynamics
ND-KhPI2013
June 19-22, 2013, Sevastopol, Ukraine

A Probability Approach to the Prediction of the High-Cycle Fatigue Lifetime Considering Aging Degradation of the Material

Oleksiy Larin[1*], Oleksii Vodka[1]

Abstract
The paper deals with the development of a new approach for high-cycle fatigue lifetime prediction, which is made in the stochastic framework and allows to take into account the natural degradation of the material properties. Mathematical expectation, correlation function and variance of the continuum damage function have been obtained.

Keywords
continuum damage, lifetime, high-cycle fatigue, natural degradation of the material properties

[1]National Technical University "Kharkov Polytechnic Institute", Kharkov, Ukraine
* **Corresponding author:** AlexeyA.Larin@gmail.com

Introduction

The reliability analysis for the most of engineering structures is performed on the basis of static and dynamic stress-strain states that are realized in the nominal operating conditions. Strength safety factors which are commonly applied when designing also provide a high level of reliability of the mechanical engineering systems on these operating regimes. In this regard, the life-time of such systems is determined by their work not on the nominal but on dangerous regimes, i.e. stress peaks and outbreaks at the start and stop of their usage or during any other harsh changes in operating conditions. Naturally, the life-time depends on the transient states rate which is determined by the usage conditions, and therefore can be changed during the operation so that frequency of loading is a random value for these systems.

Due to the relatively low incidence of the transient regimes and taking into account availability of strength safety factors, the lifetime of such engineering designs becomes comparable with the period of initiation of natural degradation processes in materials, i.e. aging. Degradation influences mechanical properties and especially strength characteristics of material because of irreversible microstructural changes as well as physical and chemical changes in materials. The study of these processes is performed experimentally. The information on the changes of characteristics is very limited, and the data obtained differs considerably. This determines the necessity for probabilistic approaches when modeling degradation of the mechanical properties of materials.

Thus, the actual problem is to develop models and approaches towards the reliability analysis and predicting the life-time of engineering design in the stochastic framework taking into account material degradation and the random time variation of the load frequency.

1. A problem statement

This paper deals with the life-time prediction of engineering designs under high-cycle fatigue. The life-time is determined by the non-localized damage accumulation rate. For this class of problems the hypothesis that the linear (Miner's) accumulation of fatigue resulting from stress cycling with a fixed level of amplitude and random frequency is introduced. Degradation of properties has been modeled as a process of the reduction of fatigue (endurance) limit in time.

Kinetics of damage accumulation is introduced in the framework of effective stress concept and could be described by the following equation [1]:

$$\frac{d}{dt}D(t)=\left(\frac{\sigma_a}{1-D(t)}\right)^m\cdot\frac{\omega(t)}{N_0\cdot\sigma_e^m(t)\cdot(m+1)}, \tag{1}$$

where $D(t)$ is a damage function, $\omega(t)$ is a variable in time frequency of the loading, N_0 is the base number of cycles before failure, m is the Wöhler (S-N) curve parameter (in the paper $m = 4$), σ_a is an amplitude of stress cycle, $\sigma_e(t)$ is the fatigue (endurance) limit, t is a time. In the paper, we assume that $\omega(t)$ and $\sigma_{-1}(t)$ are statistically independent random functions of time.

2. Characteristics of loading

This paper deals with the designs which are under the influence of cyclic loads with a fixed level of deterministic amplitude and random frequency. Such a situation can be realized in the systems for which the most dangerous regimes of operation are well-known and studied, but there is uncertainty as to the occurrence of these regimes. For example, these are the regimes of start, stop, etc.

We assume that the frequency of these regimes is a stationary random process, i.e., probabilistic characteristics of the process are independent of the starting time. Probabilistic characteristics of the process should be determined on the basis of the statistics of the operation of the design or its prototype. Expectation, variance, and correlation function of frequency can be known. Determination of the valid characteristics of the frequency requires a large number of statistical data, which often leads to considerable difficulties. Therefore, in practice it makes sense to postulate a priori a form of the correlation function, and to only define its parameters.

In this paper, approximation by the exponential law is used [2]. The parameters of approximation are variance (σ_ω^2) and intensity (λ_ω) of the appearance of dangerous regimes

$$K_\omega(t_1,t_2)=\sigma_\omega^2\cdot\exp\left(-\lambda_\omega\cdot|t_2-t_1|\right). \tag{2}$$

The intensity parameter is determined on the basis of correlation time, i.e. the period of time necessary for the expected statistical influence of frequency of a dangerous regime within time t_1 on the frequency of this mode within time t_2 to vanish. The correlation time can be found on the basis of the operation conditions and also can be calculated using the following equation [3]:

$$\tau_{\omega k}=\frac{1}{\sigma_\omega^2}\cdot\int_0^\infty K(\tau)d\tau, \quad \tau=t_2-t_1 \tag{3}$$

The intensity of the frequency of occurrence of the dangerous regime is defined as $\lambda_\omega=1/\tau_\omega$ taking into consideration the accepted form of the correlation function and a priori determined correlation time for the frequency of occurrence of dangerous regimes.

The intensity was assumed to be equal to 1 for the computation of test examples in this paper. Such assumption does not reduce the generality of the results due to the arbitrariness of the time scale.

3. Modeling the degradation as a gradual reduction fatigue limit in time

There are papers dealing with the experimental study of the natural aging processes of different materials [3-7].

The most detailed studies of the degradation processes are carried out in in elastomers, due to the relatively short time of noticeable changing of their mechanical and strength properties. For example, in [3,4], the results are represented for the rubber-like material used in the tire industry. In this case, it was found out that the natural aging of rubber during the 4 years leads to a decrease in its static and fatigue strength in more than 3 times. In [3] a hyperbolic dependence of the strength, decreasing was observed and described.

The works [5-8] deal with the study of aging of metals and alloys. In this case, it is determined that the natural aging of the metal has little effect on its static strength and elastic characteristics, but significantly changes the long-term strength (resistance to fatigue). Thus, in [5] for 45 steel it was found out that natural aging of the material for 50 years results in a change of static strength properties only within 5%, but reduces the fatigue limit by 44%. In the article it is argued that the fields of dispersion of the experimental data for non-aged and aged specimens do not overlap. A more detailed analysis of the samples allowed the authors to identify the fundamental structural changes in the processes of nucleation of fatigue micro- and macro- cracks in the material. Similar results were obtained in [6] for 20 steel – thus, it was determined that the aging during 15 years reduces the fatigue limit by 38%.

Summarizing the data from the literature on the degradation processes in this article we suggest the process of reducing the limit of fatigue to be considered as a hyperbolic dependence of the form:

$$\sigma_e(t) = \sigma_e^* \cdot \left[\beta_1 - \frac{\beta_1}{\beta_2 + \beta_3 \cdot t^p} \right] = \sigma_e^* \cdot \varphi(t), \tag{4}$$

where β_i and p – approximation parameters, σ_e^* – fatigue limit for non-degraded material.

The approximation parameter p determines the character of the decrease of the fatigue limit. The value of parameter p equals to 1 is used for polymer materials and $p = 2$ relevant for metals. Typical curve ($p = 2$), which describes the degradation of the fatigue limit is shown in Fig. 1. As the input data the results presented in [5] are used.

It should be noted that there is the necessity to consider variations in the values of the fatigue limit. Obviously, during the aging process of the material this uncertainty persists or even increases. Therefore, we assume that the fatigue limit is the product of the normalized to a unit function $\varphi(t)$ and the values of the fatigue limit at the initial time is a random variable, which (as recommended in [9,10]) follows the log-normal probability density function:

$$f_1(\sigma_e^*) = \frac{1}{\sigma_e^* s \sqrt{2\pi}} \exp\left(-\left[\frac{\ln(\sigma_e^*) - \mu}{2s} \right]^2 \right), \tag{5}$$

where s and μ are distribution parameters, which are determined from the values of mean and variance (or coefficient of variation) of the fatigue limit.

$$\left\langle \sigma_e^* \right\rangle = \exp\left(\mu + \frac{s^2}{2} \right),$$

$$Var[\sigma_e^*] = \left[\exp(s^2) - 1 \right] \cdot \left\langle \sigma_e^* \right\rangle^2, \quad V_{\sigma_e^*} = \frac{\sqrt{Var[\sigma_e^*]}}{\left\langle \sigma_e^* \right\rangle} = \left[\exp(s^2) - 1 \right]^{1/2}. \tag{6}$$

The notation <...> for mathematical expectation operator and *Var*[...] for the operator of the variance are introduced in the formulas (7); $V_{\sigma_e^*}$ is a variation factor.

Thus, the variation of the fatigue limit is a random non-stationary process. Its one-dimensional probability density function could be obtained from the linear transformation of the random variable σ_e^* (5) and has the form:

$$f(\sigma_e, t) = \frac{1}{\sigma_e s \sqrt{2\pi}} \exp\left(-\left[\frac{\ln(\sigma_e) - \mu - \ln \varphi(t)}{2s} \right]^2 \right). \tag{7}$$

Figure 2 graphically shows the one-dimensional probability density function of the random process of the decreasing in time of the fatigue limit. Graphs are built for the approximation with $p = 2$.

It is useful to normalize the fatigue limit by its mean value. Let us introduce a change of variables:

$$\sigma_e^* = \left\langle \sigma_e^* \right\rangle \cdot \chi \,, \tag{8}$$

where χ is a random variable that obeys the log-normal distribution, and has a unity mean value and variance equal to the variation factor of the fatigue limit in non-aged state

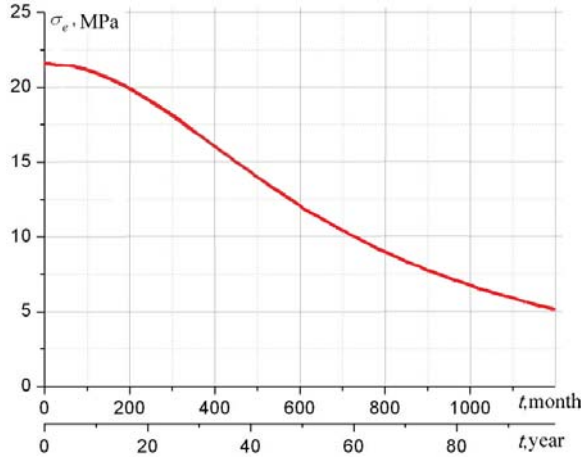

Figure 1. Approximations of the decreasing of fatigue limit due to natural aging (approximation is built for 45 steel according to data given in [5])

$$\langle \chi \rangle = 1 \,, \quad Var[\chi] = V^2_{\sigma_e^*} \,. \tag{9}$$

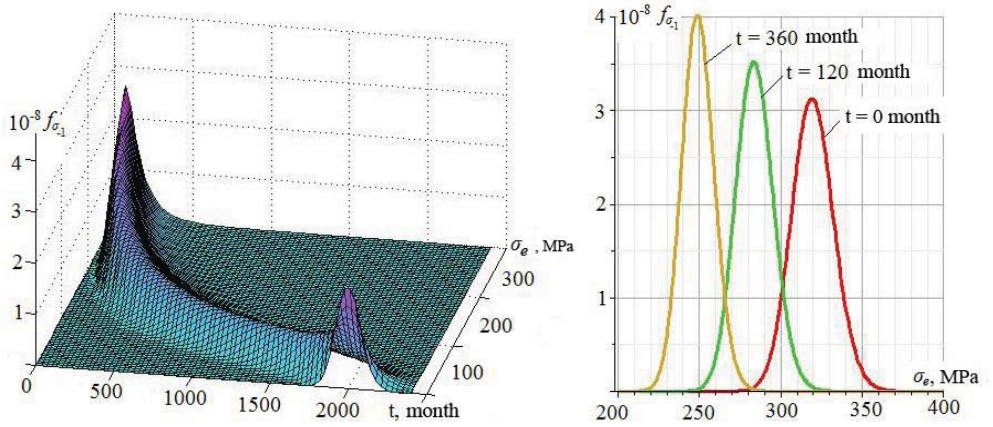

Figure 2. One dimensional probability density of the random process of the limit of fatigue strength falling over time as a result of degradation of the material

4. Probability characteristics of the process damage accumulation

The process of damage accumulation is described by the equation (1). It is a nonlinear differential equation due to the power dependence of the damage parameter and presence of the variable in time function of material degradation $\varphi(t)$. The equation (1) can be represented in quadrature

$$(m+1)\int_0^{D(t)} \left[1-D(t)\right]^m dD(t) = \frac{\sigma_a^m}{N_0} \cdot \int_0^t \frac{\omega(t')}{\sigma_{-1}^m(t')} dt' \,. \tag{10}$$

It is useful to simplify (11) substituting the variables which leads to the reduction to a linear relation. Let $U(t)$ be a new function which equals to:

$$U(t) = (m+1)\int_0^{D(t)} \left[1-D(t)\right]^m dD(t) = 1-\left[1-D(t)\right]^{m+1} \tag{11}$$

Under the notations (9) and (12) one can obtain:

$$U(t)=\psi\cdot\int_0^t\frac{\omega(t')}{\chi^m\cdot\varphi^m(t')}dt',\quad \psi=\frac{\sigma_a^m}{N_0\cdot\left\langle\sigma_{-1}^*\right\rangle^m}=const\ . \tag{12}$$

The mean value of the function *U(t)* is easily found by the averaging procedure taking into account the hypothesis of statistical independence of the loading and degradation processes:

$$\left\langle U(t)\right\rangle=\psi\cdot\left\langle\omega\right\rangle\cdot\left\langle\chi^{-m}\right\rangle\cdot\int_0^t\varphi^{-m}(t')dt'\ . \tag{13}$$

The correlation function of *U(t)* which is expressed through the second initial moment is used to determine the variance

$$K_U(t_1,t_2)=\left\langle U(t_1)\cdot U(t_2)\right\rangle-\left\langle U(t_1)\right\rangle\cdot\left\langle U(t_2)\right\rangle\ . \tag{14}$$

Using the integral representation of the function $U(t)$ (13) and the hypothesis of independence of the processes of loading and degradation, one obtains the following expressions:

$$\left\langle U(t_1)\cdot U(t_2)\right\rangle=\psi^2\left\langle\chi^{-2m}\right\rangle\cdot\int_0^{t_1}\int_0^{t_2}\frac{\left\langle\omega(t')\cdot\omega(t'')\right\rangle}{\varphi^m(t')\cdot\varphi^m(t'')}dt'dt''\ , \tag{15}$$

where

$$\left\langle\chi^{-2m}\right\rangle=\int_0^\infty\chi^{-2m}\cdot f_\chi(\chi)d\chi\ , \tag{16}$$

$f_\chi(\chi)$ is the log-normal probability density function with mean and variance, which are determined by the expression (10).

The second initial moment of a random frequency is expressed in terms of its correlation function and its squared mean value, which is a constant due to the assumption of stationary of processes.

$$K_\omega(t_1,t_2)=\left\langle\omega(t_1)\cdot\omega(t_2)\right\rangle-\left\langle\omega\right\rangle^2 \tag{17}$$

$$K_U(t_1,t_2)=\psi^2\cdot\int_0^{t_1}\int_0^{t_2}\frac{\left\langle\chi^{-2m}\right\rangle\left(K_\omega(t',t'')+\left\langle\omega\right\rangle^2\right)-\left\langle\omega\right\rangle^2\left\langle\chi^{-m}\right\rangle^2}{\varphi^m(t')\cdot\varphi^m(t'')}dt'dt''\ , \tag{18}$$

The variance of the function $U(t)$ is calculated from its correlation function

$$Var\left[U(t)\right]=K_U(t_1=t,t_2=t). \tag{19}$$

Due to the additivity of the process of accumulation of the function $U(t)$ it can be assumed that it satisfies the conditions of the central limit theorem, starting from a certain period of time. Then the probability density function of $U(t)$ has the form of a normal Gaussian distribution with the characteristics (14) and (21).

Using the relationship between the process $U(t)$ and damage (10) the probability density function of damage can be written in the form (23)

$$f_D(D,t)=f_U(U,t)\left|\frac{dU}{dD}\right| \tag{20}$$

$$f_D(D,t)=\frac{(m+1)(1-D)^m}{\sqrt{2\pi Var[U(t)]}}\exp\left(-\frac{1-(1-D)^m-\left\langle U(t)\right\rangle}{Var[U(t)]}\right) \tag{21}$$

Then the mean and variance of damage can be determined by the equation (24)

$$\langle D(t)\rangle = \int_{-\infty}^{\infty} D \cdot f_D(D,t)dD$$
$$Var[D(t)] = \int_{-\infty}^{\infty} \left[D - \langle D(t)\rangle\right]^2 f_D(D,t)dD \tag{22}$$

The spread of damage parameter values can be defined as a confidence interval with a set level of the confident probability α:

$$\frac{1-\alpha}{2} = \int_{-\infty}^{S_l(t)} f_D(D,t)dD \qquad \frac{1+\alpha}{2} = \int_{S_r(t)}^{\infty} f_D(D,t)dD \tag{23}$$

where α = 0,9973 which corresponds to the area under the normal law, obtained by the three sigma rule; $S_l(t)$ and $S_r(t)$ – left and right border of the damage spread (confidence interval).

Reliability function can be found from (27), and the density of the probability of failure is determined from (28). The mean and variance of time to failure are determined from (29) and (30).

$$P(t) = \Pr\left[D(t) \in [0;1]\right] = \int_0^1 f_D(D,t)dD\,, \qquad q(t) = -\frac{d}{dt}P(t) \tag{24}$$

$$\langle T_r\rangle = \int_0^{\infty} tq(t)dt \qquad Var[T_r] = \int_0^{\infty} \left(t - \langle T_r\rangle\right)^2 q(t)dt \tag{25}$$

5. Performing test calculations

Based on the proposed approach to the determination of the probability parameters of fatigue damage accumulation with the natural degradation of the material properties was carried out a series of test calculations. We assume that at the dangerous modes stress amplitude than the normal value of fatigue limit by 2 times, the intensity of the frequency of dangerous regimes λ_ω = 1, and the average frequency <ω> = 30. The variation of frequency is 0.5, i.e., standard deviation of the frequency is 1/2 of its average value. Degradation is modeled according to the data given in [5], i.e., it was thought that for 50 years the fatigue decreased by 44%. Random variations in the fatigue limit at a time to be fixed with a coefficient of variation of 0.05. The results of the calculations are shown in Figures 3 and 4. Predicted life-time parameters are listed in Table. 1

Table 1. Predicted life-time parameters

subject to degradation			without degradation		
$<T_r>$	Var[T_r]	V_T	$<T_r>$	Var[T_r]	V_T
732.66	896.79	0.040	3963.97	478611.1	0.175

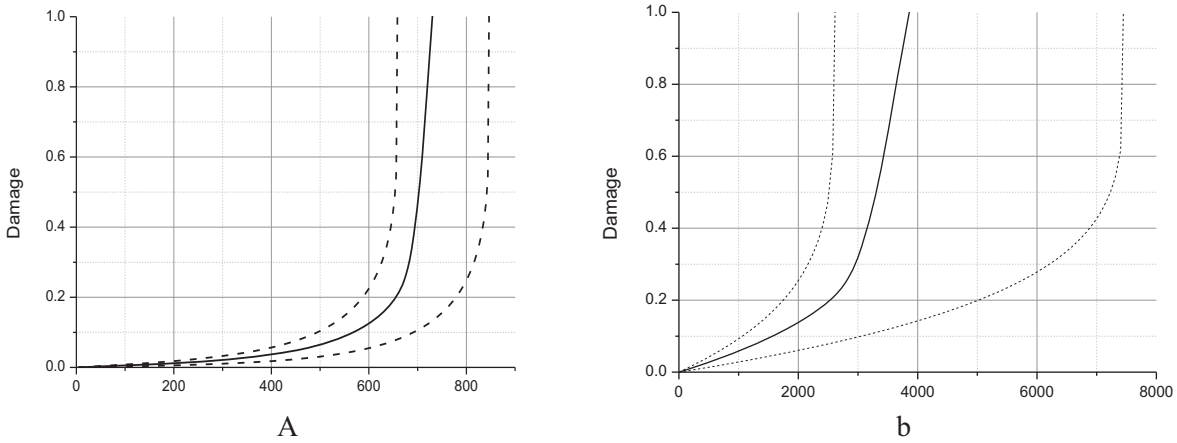

Figure 3. The accumulation of damage to time with the degradation of (a) and without (b)

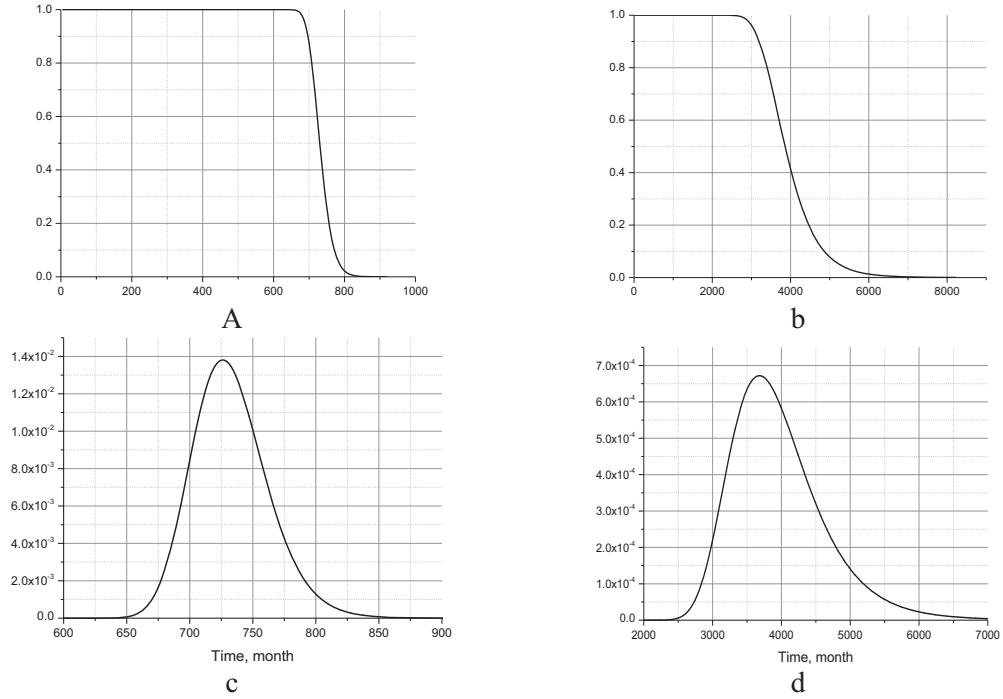

Figure 4. Reliability function and the probability density of failure: a,c - subject to degradation of b, d - without degradation

Conclusions

In this paper a new approach to predicting life-time under high-cycle fatigue, which is made in the stochastic way and allows taking into account the natural degradation of the material properties have been proposed. Resolving equations to determine the mathematical expectation and the variance of the correlation function of damage accumulation function have been obtained. The proposed approach allows for the analysis of reliability and life prediction of structures designed for long service life, the accumulation of damage to which only occurs when the realization of dangerous regimes, the occurrence of which is random.

References

[1] Zhovdak V.A., Tarasova L.F. *Predicting the Reliability of Mechanical Systems*, NTU «KhPI», Kharkov, 2007, Pp. 108 (in Russian).
[2] Sveshnikov A. *Applied Methods of the Theory of Random Functions*, Nauka, Moscow, 1968 (in Russian).
[3] Baldwin J. M., Bauer D. R., Ellwood K. R. Rubber aging in tires. Part 1: Field results, *Polymer Degradation and Stability*. Vol. 92, pp. 104-109, 2007
[4] Mott P.H., Roland C. M. Aging of natural rubber in air and seawater, Vol. 74, pp. 79-88, 2007.
[5] Botvina L. R. et al. Effect of long-term aging on fatigue characteristics of steel 45, *Zavodskaya Laboratoria. Diagnostika Materialov*. Vol. 77 (1), pp. 58-61, 2011 (in Russian).
[6] Botvina L. R., Petrova I. M., Gadolina I. V. High-cycle fatigue failure of low-carbon steel after long-term aging, *Inorganic Materials*. Vol. 46 (14), pp. 134–141, 2010.
[7] Zaletelj H. et al. High cycle fatigue of welded joints with aging influence, *Materials and Design*, No. 45, pp. 190–197, 2013.
[8] Singh S., Goel B. Influence of thermomechanical aging on fatigue behaviour of 2014 Al-alloy, *Bulletin of Materials Science*, Vol. 28 (2), pp. 91-96, 2005.
[9] Gusev A.S. *Fatigue Resistance and Durability of Structures under Random Loads*. Mashinostroenie, Moscow, 1989 (in Russian)
[10] Kogaev V.P. *Strength Calculations for Time-varying Stresses*, Mashinostroenie, Moscow, 1977 (in Russian).
[11] Larin A.A. *Prediction and Analysis of Reliability of Engineering Structures*, NTU KhPI, Kharkov, 2011, pp. 128 (in Russian).

Proceedings of the 4th International Conference on Nonlinear Dynamics
ND-KhPI2013
June 19-22, 2013, Sevastopol, Ukraine

Micro-macro analysis of creep and damage behavior of multi-pass welds

Ivan Lvov[1*], Konstantin Naumenko[1] and Holm Altenbach[1]

Abstract
Different zones of welded joints are subjected to different temperature fields during the process of welding. Furthermore, in multi-pass welding heating and cooling cycles, which occur due to the overlap of the pass beads, form a complex microstructure. In this paper a method of evaluating the creep response of the multi-pass weld based on the micro-macro mechanics approach is introduced. Multi-pass weld microstructure that consists of columnar, coarse-grained, and fine-grained zones is considered. The materials of these constituents assumed to be isotropic. Weld metal properties of inelastic behaviour have general type of symmetry and are described by an anisotropic creep constitutive model.
To model the microstructure of the multi-pass weld metal the representative volume elements (RVE's) with different number of passes are created and analyzed with FEA software ABAQUS. Numerical tests on uniform loading of the RVE's are performed. Creep material properties for equivalent weld material are found for welds with different number of passes.

Keywords
Multipass weld, anisotropic creep, micro-macro, homogenization

[1] Otto-von-Guericke University, Magdeburg, Germany
*** Corresponding author:** ivan.lvov@ovgu.de

Introduction

Quite often welded constructions are found damaged before the predicted lifetime of components [1]. One of the reasons for that is mismatch in creep deformation properties between the weld and the parent metal, non-favorable weld shapes, which result in stress concentrations developed within the weldment. This combined with the fact that creep produces damage in the form of voids and micro-cracks leads to material failure. A typical weld in a component consists of parent material, heat affected zone and a weld metal. The two parent materials joined by the weld may be made from same one or different. The weld and parent material can have the same or different composition. But even for welds joined by the weld metals with the same composition as the parent materials, the creep properties in parent, heat-affected zone and weld materials will be different [2]. Thus, the weldments are highly complex heterogeneous structures. Moreover, in the case of multi-pass welds, the weld material is also inhomogeneous. It consists of overlapping weld beads that will create specific heat affected zones within the weld metal because of cooling and heating from the next pass. A single weld bead generally consists of a columnar solidification structure. However in multi-pass weld when the further bead is laid over the previous one, part of it will be recrystallized and this will create coarse and fine grained structure [3]. It should be noted that the design rules of weldments under pressure are based only on the long term fracture properties of weldable material at uniaxial tension. However in reality such constructions operate at multi-axial stress state conditions. All of these factors make it important to take anisotropy into account in modeling creep behaviour of the multi-pass weld.

1. Constitutive Equations of Anisotropic Creep

The strain rate – stress relations for creep of anisotropic materials are based on the assumption of the existence of the creep potential. The creep potential hypothesis is widely used for continuum

mechanics modeling of isotropic and anisotropic creep [4]. During the secondary creep stage strain rate is defined by the scalar valued potential W($\boldsymbol{\sigma}$) and the flow rule:

$$\dot{\boldsymbol{\varepsilon}} = \frac{\partial W}{\partial \boldsymbol{\sigma}}. \tag{1}$$

For simple determination of creep potential on basis of uni-axial creep tests, the equivalent stress $\boldsymbol{\sigma}_{eq}$ is introduced as intermediate scalar argument W($\boldsymbol{\sigma}_{eq}(\boldsymbol{\sigma})$). The Norton-Bailey's power law is assumed here for the approximation of the strain rate-stress relations.

$$W = \frac{K}{n+1}\boldsymbol{\sigma}_{eq}^{n+1}, \tag{2}$$

where the material parameters K, n depend on the temperature.

The form of equivalent stress depends on the symmetry type of material. Materials of columnar, coarse and fine grained zones assumed to be isotropic. In case of isotropic creep, equivalent stress is suggested as von Mises type. For the Norton-Bailey type potential the flow rule results in:

$$\dot{\boldsymbol{\varepsilon}} = \frac{3}{2} K \boldsymbol{\sigma}_{eq}^{n-1} \boldsymbol{S}. \tag{3}$$

The macroscopic creep properties of equivalent continuum are anisotropic in general case. The symmetry type of equivalent media is determined by geometric structure of multi-pass weld and the creep properties of the microstructure components [5]. For modeling anisotropic creep behaviour the equivalent stress is assumed in the general quadratic form:

$$\boldsymbol{\sigma}_{eq}^2 = \boldsymbol{\sigma} \cdot\cdot {}^{(4)}\boldsymbol{B} \cdot\cdot \boldsymbol{\sigma}, \tag{4}$$

where ${}^{(4)}\boldsymbol{B}$ is the symmetric positively definite fourth rank tensor. The number of independent tensor components depends on symmetry class of equivalent continuum. For most multi-pass weld geometric structure RVE allows to consider equivalent continuum as an orthotropic solid. In this case tensor ${}^{(4)}\boldsymbol{B}$ can be presented in the base of orthonormal vectors $\boldsymbol{n}_1$, $\boldsymbol{n}_2$, $\boldsymbol{n}_3$, which are perpendicular to symmetry planes of orthotropic solid:

$${}^{(4)}\boldsymbol{B} = b_{ijkl}\boldsymbol{n}_i \otimes \boldsymbol{n}_j \otimes \boldsymbol{n}_k \otimes \boldsymbol{n}_l. \tag{5}$$

In this case tensor ${}^{(4)}\boldsymbol{B}$ includes 9 nonzero independent components b_{ijkl} (including K in Norton-Bailey's law). With equivalent stress (4) the secondary creep equations for orthotropic solid can be written as follows:

$$\dot{\boldsymbol{\varepsilon}} = K \boldsymbol{\sigma}_{eq}^{n-1} {}^{(4)}\boldsymbol{B} \cdot\cdot \boldsymbol{\sigma}. \tag{6}$$

Creep law for all microstructure zones of weld reflects the incompressibility of materials. Therefore it is assumed that the creep deformation does not produce a change in volume of equivalent continuum. The spherical part of the creep rate tensor is set to zero:

$$tr\dot{\boldsymbol{\varepsilon}} = K \boldsymbol{\sigma}_{eq}^{n-1} tr\left[{}^{(4)}\boldsymbol{B} \cdot\cdot \boldsymbol{\sigma} \right] = 0. \tag{7}$$

The volume constancy assumption reduces number of independent components of tensor B to 6. Identification of independent material constants in the equivalent stress and the creep potential for

homogeneous solid carried out experimentally. Only for secondary creep stage 6 independent stress states should be implemented in order to identify 6 constants of equivalent stress. In addition, for identification of the parameter n in the power law (6) a few uni-axial creep tests for different constant stress values should be executed. Theoretical determination of effective properties of multiphase periodical materials has many advantages with comparison to experimental investigation. The analytical or numerical homogenization technique for periodical media enables to find effective creep properties for many variants of multiphase structures. In this paper FEM is used for the determination of the averaged parameters of the creep law of the multi-pass weld.

2. Numerical Procedure of homogenization for multi-pass welds

2.1 Analysis of anisotropic creep

To model the anisotropic creep of multi-pass welding the representative volume element RVE is created as prismatic body with the transversal section shown on the Figure 1. This section is considered as the repeated unit cell periodically distributed in the plane OXY. The axis Z is directed along the weld seam. Material properties of weld metal grain size zones are assumed to be isotropic. To describe the creep behaviour of weld metal zones, the Norton creep law is used (3).

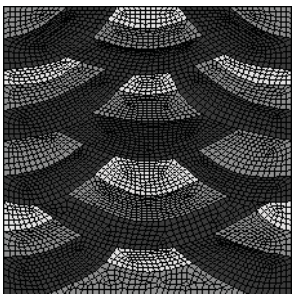

Figure 1. Finite element model of Representative Volume Element

Material parameters used for (3) are taken from [6] and are presented in Table 1. It should be noted that it is impossible to make the specimens directly from fine and coarse grained zones independently, that is why for this heat affected zones, material properties in them are assumed equal.

Table 1. Parameters of Norton law for weld metal zones

Zone type	K, $\frac{\text{MPa}^{-\text{n}}}{\text{sec}}$	n
Columnar	$2{,}74\cdot10^{-21}$	7,86
Coarse grained	$1{,}37\cdot10^{-20}$	7,86
Fine grained	$1{,}37\cdot10^{-20}$	7,86

The creep law for the homogenised continuum is presented by the averaged components in the volume V of the unit cell.

$$\dot{\boldsymbol{\varepsilon}}_{ij} = K\boldsymbol{\sigma}_{eq}{}^{n-1} b_{ijkl}\boldsymbol{\sigma}_{kl}, \tag{8}$$

$$\boldsymbol{\sigma}_{eq} = \left(\boldsymbol{\sigma}\cdot\cdot\mathbf{B}\cdot\cdot\boldsymbol{\sigma}\right)^{\frac{1}{2}}, \tag{9}$$

where $\dot{\boldsymbol{\varepsilon}}_{ij}$ and $\boldsymbol{\sigma}_{kl}$ are the averaged creep strain rates and stresses, which correspond to uniform macroscopic strain rate and stress:

$$\dot{\boldsymbol{\varepsilon}}_{ij} = \frac{1}{V}\int_V \dot{\boldsymbol{\varepsilon}}_{ij}\, dv; \tag{10}$$

$$\boldsymbol{\sigma}_{ij} = \frac{1}{V}\int_V \boldsymbol{\sigma}_{ij} dv;$$

For identification of 6 material constants in (8) 6 independent numerical tests should be executed. Since the structure of the weld material with a sufficiently large number of passes can be assumed periodical, three types of representative volume are created - a reference one (8 passes), the realization with twice more passes and realization with a half of the number of passes. Due to the fact that in different zones on microscale level creep behaviour is described by the different relations numerical experiments should be carried out to define the possibility to how equation (8) approximates the creep behaviour on the macroscopic level.

Series of creep analysis of RVE are performed under the constant uniform stresses for different time levels. From the results of numerical experiments one can extract the set of strain rate values for the different time moments $t_i \left(i = 1 \ldots N\right)$. For example, let us consider the numerical experiment on tension in 11 direction. To derive the exponent in creep law, set of numerical experiments under different macro-stress $\boldsymbol{\sigma}_{11}$ levels are made. Result of this series of M experiments is the set of $\dot{\boldsymbol{\varepsilon}}_{11}$ for different stress values $\boldsymbol{\sigma}_{11i}$, ($i = 1 \ldots M$).

To process the results of numerical experiments, simplified relation (8) is presented in logarithmic coordinates:

$$\ln \dot{\boldsymbol{\varepsilon}}_{11} = \ln K + n \cdot \ln \boldsymbol{\sigma}_{11} \ . \tag{11}$$

Material constants for creep law of homogenised material are defined by processing results of numerical experiments using the least squares method:

$$n = \frac{\sum_{i=1}^{M} \ln \boldsymbol{\sigma}_{11i} \cdot \ln \dot{\boldsymbol{\varepsilon}}_{11} - N \sum_{i=1}^{M} \ln \boldsymbol{\sigma}_{11i} \cdot \ln \dot{\boldsymbol{\varepsilon}}_{11}}{\left(\sum_{i=1}^{N} \ln \boldsymbol{\sigma}_{11i}\right)^2 - N\left(\sum_{i=1}^{N} \ln \boldsymbol{\sigma}_{11i}\right)^2}; \tag{12}$$

$$\ln K = \frac{1}{N}\left(\sum_{i=1}^{M} \ln \dot{\boldsymbol{\varepsilon}}_{11} - n \sum_{i=1}^{M} \ln \boldsymbol{\sigma}_{11i}\right). \tag{13}$$

The other components of the tensor ${}^{(4)}\boldsymbol{B}$ can be defined by processing the results of numerical experiments of uniaxial macroscopic stress state of other types.

Table 2. Parameters of tensor B multiplied by K, $\frac{\mathrm{MPa}^{-\mathrm{n}}}{\mathrm{sec}}$

-	8 – pass	16 – pass	4 – pass
$\boldsymbol{b}_{1111}$	$1.64 \cdot 10^{-n}$	$1.61 \cdot 10^{-n}$	$1.66 \cdot 10^{-5.25}$
$\boldsymbol{b}_{2222}$	$1.51 \cdot 10^{-n}$	$1.58 \cdot 10^{-n}$	$1.49 \cdot 10^{-n}$
$\boldsymbol{b}_{3333}$	$1.16 \cdot 10^{-n}$	$1.18 \cdot 10^{-n}$	$1.2 \cdot 10^{-n}$
$\boldsymbol{b}_{1212}$	$1.33 \cdot 10^{-n}$	$1.36 \cdot 10^{-n}$	$1.35 \cdot 10^{-n}$
$\boldsymbol{b}_{1313}$	$1.26 \cdot 10^{-n}$	$1.27 \cdot 10^{-n}$	$1.27 \cdot 10^{-n}$

2.2 Damage analysis

Thermal loading and melting-solidification cycles are not the only issue that influences material properties of the weld metal and HAZ in case of the multi-pass welds. Welding process itself creates structural imperfections and cracks on the weld metal. This phenomenon combined with voids and micro-cracks which nucleate during creep process may lead to the failure of the welded components

earlier than predicted during pure creep analysis. That is why it is necessary to include damage into account in modeling of the weldings behavior.

As we assumed previously, weld metal constituents are isotropic so to implement damage in modeling behaviour of the weld metal during creep, Kachanov-Rabotnov isotropic creep damage model is used. In this model, the creep rate depends on the damage parameter that can be referred to fraction of the voids and micro-cracks in the cross-section of the uniaxial specimen during the damage process

$$\dot{\varepsilon}_{cr} = \dot{\varepsilon}_{cr}\left(\sigma, \omega\right), \tag{14}$$

$$\omega = \frac{A_D}{A_0}, \tag{15}$$

where A_0 is the initial cross-section area, and A_D is the area of the voids and micro-cracks caused by damage. Damage process in this case can be formulated with the evolution equation

$$\dot{\omega} = \dot{\omega}\left(\sigma, \omega\right), \tag{16}$$

Assuming power laws for creep and damage the constitutive equations for isotropic materials can be written as follows

$$\dot{\varepsilon}_{vM}^{cr} = C\frac{\left|\sigma_I\right|^n}{\left(1-\omega\right)^m}, \tag{17}$$

$$\dot{\omega} = D\frac{\left|\sigma_I\right|^k}{\left(1-\omega\right)^l}, \tag{18}$$

$$\omega_{|t=0} = 0, \qquad \omega_{|t=t^*} = 1, \tag{19}$$

where t^* is the time to rupture value. Similar to pure creep analysis, it is not possible to define parameters C, D, n, m, k and l for all weld metal zones. However to perform qualitative evaluation of the influence from the inhomogeneity of the weld metal, we can take creep curves (Fig. 3) of the columnar zone and fine-grained zone in HAZ of the base metal from [7], and assume that the relation between time to rupture would be the same as for the columnar and HAZ of the weld metal.

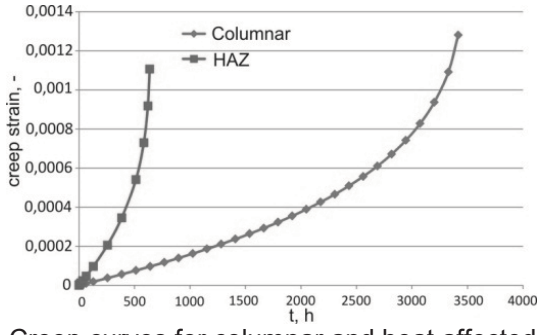

Figure 3. Creep curves for columnar and heat affected zones [7]

Processing the data from the creep curves and assuming that $n = m$, and $k = l$, relation between time to rupture of the weld metal constituents $t_h^* / t_c^* = 2.5$, where indexes h and c are for HAZ and columnar zone respectively. Power indexes are set $n = 3, k = 4$ for both materials.

To model the creep damage behavior of the equivalent homogenous material for weld metal, RVE from the previous analysis is used and the same set of numerical experiments is performed. As results of this numerical experiments damage parameter evolution during time is obtained.

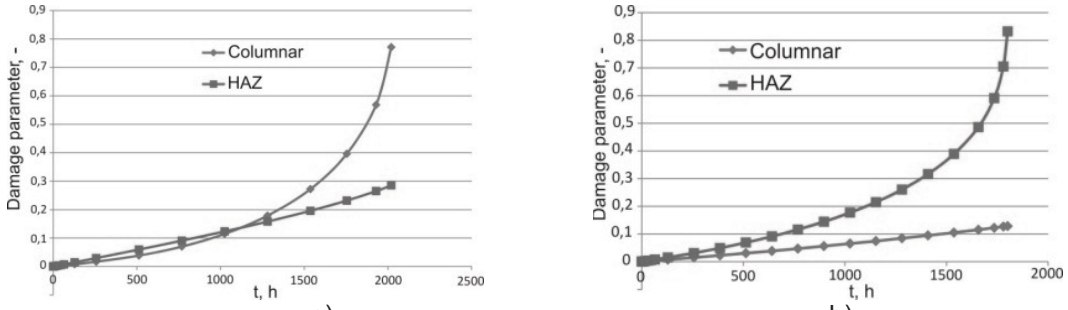

Figure 4. Damage parameter evolutions for a) longitudinal and b) transverse direction

On Fig. 4 one can see the difference in the damage parameter evolution between a) longitudinal tension test and b) test transverse direction. In case of the longitudinal direction damage parameter increases faster on the columnar zone, despite the fact that HAZ is more prone to damage according to the material parameters. This happens because of the stress redistribution due to creep in the longitudinal tension test. Obtained results show that stress during this numerical experiment concentrates in the columnar zone, and in some time points the equivalent stress in columnar zone may reach twice the value compared to HAZ. On the other hand, in numerical experiments on tension in one of the cross-section directions, stress redistributes between the zones not so dramatically, however still been higher in columnar zone. This is why damage parameter in these tests reflects material parameters better, and increases faster in more damage prone zone – HAZ.

Conclusions

Multi-pass weld joint as complex heterogeneous object was considered. As a result of finite element analysis on one-component loadings of a representative volume equivalent total strains are obtained and by processing them using averaging procedure the material constants for constitutive equation of the equivalent material were found. Influence of damage processes on a life period of the welded elements was analysed.

References

[1] Segle P. Numerical simulation of weldment creep response. *PhD thesis, Stockholm, Sweden, Royal Institute of Technology,* 2002.

[2] Hyde T.H., Sun W. and Williams J.A. Assessment of creep behaviour of a narrow gap. *International Journal of Pressure Vessels and Piping*, Vol. 76: 8, pp. 515–525, 1999.

[3] Segle P., Tu S.-T., Storesund J. and Samuelson L.A. Some issues in life assessment of longitudinal seam welds based on creep tests with cross-weld specimens. *Journal of Pressure Vessels and Piping*, Vol. 66: 1–3, pp. 199–222, 1996.

[4] Naumenko K. and Altenbach H. *Modeling of Creep for Structural Analysis.* Springer, Berlin, 2007.

[5] Altenbach H. and Naumenko K. A phenomenological model for anisotropic creep in a multi-pass weld metal. *Archive of Applied Mechanics*, pp. 808–819, 2005.

[6] Hyde T.H., Sun W. and Williams J.A. Creep analysis of pressurized circumferential pipe weldments. *Journal of Strain Analysis*, Vol. 38, pp. 62–91, 2003.

[7] Yongkui L. Study on creep damage in thick welded joint of modified 9Cr1Mo steel alloy. *PhD thesis, Kochi University of Technology,* Kochi, Japan, 2009.

Proceedings of the 4th International Conference on Nonlinear Dynamics
ND-KhPI2013
June 19-22, 2013, Sevastopol, Ukraine

Optimal Autofrettage of Thick-Walled Pipes

Gennadiy Lvov[1], Volodymyr Okorokov[1*]

Abstract
The paper presents the analysis of autofrettage process for thick-walled pipe in the case of plane strain. Relationships which describe elastoplastic behavior with material damage evolution are presented. The boundary problem in cylindrical coordinates is formulated and methods of its solving are given. Results of solving for the autofrettage problem are shown.

Keywords
Autofrettage, thick-walled pipe, damage

[1] NTU "Kharkiv Polytechnic Institute", Kharkiv, Ukraine
* **Corresponding author:** okorvol10@gmail.com

Introduction

This paper is devoted to the analysis of material damage influence on the autofrettage process and determination of optimal conditions of autofrettage for thick-walled pipes.

The issue of improvement of thick-walled pipes is important in many fields of heavy industry. It is especially important in military industry, because continuous improvement of armament requires an increase of strength characteristics of weapons. To give greater initial velocity for projectile it is necessary to increase pressure of explosion of powder gases in the barrel. However, the value of ultimate pressure is limited by material strength of a gun.

To improve strength properties of thick-walled pipes loaded with internal pressure, as well as a low-cycle fatigue lifetime the process of autofrettage is often used.

Such phenomenon as the Bauschinger effect may occur during unloading of a pipe. It is manifested by appearance of secondary plastic strains when a pipe is unloaded, and thus it leads to reduction of favorable residual stress. Therefore, for solving of autofrettage problems it is necessary to apply plasticity theory which allows considering the Bauschinger effect It's influence on the autofrettage process has been investigated in papers [1, 2].

The autofrettage process is based on formation of significant plastic strains. Therefore, the material damage can occur. A pipe can withstand the pressure increase for some time before failure, in spite of the fact that the damage appears on the internal layers of a pipe in the place of maximum plastic strains. Continuum damage mechanics is used for modeling this behavior of material.

As well as the Bauschinger effect, the damage of material leads to a decrease of residual hoop stress, therefore finding optimal conditions of the autofrettage has great practical importance.

1. Coupled plastic-damage governing equations

In order to simulate effect of softening at significant plastic strains occurring during the process of autofrettage the theory of damage mechanics in the case of isotropic damage is applied. Phenomenological models of damage growth based on thermodynamics of irreversible processes, and also methods of measurement and identification of parameters for damage evolution are considered in [3, 4, 5, and 6].

According to the principle of equivalence of strains postulated in [3] any constitutive equation for a damaged material can be replaced by the same for an undamaged material by introducing effective stress tensor. Effective stress tensor is introduced in accordance with effective stress concept [7]:

$$\widetilde{\sigma}_{ij} = \frac{\sigma_{ij}}{1-D}. \tag{1}$$

In order to obtain law of elasticity with damage, and also law of plasticity it is necessary to build a thermodynamic potential in form of the Helmholtz free energy. If we assume that damage does not depend on plasticity, and regard it only as the degradation of elastic properties the thermodynamic potential of its state variables in case of isothermal process will be written as:

$$\psi = \psi^e\left(\varepsilon_{ij}^e, D\right) + \psi^p\left(r\right). \tag{2}$$

In order to describe elasticity behavior of damaged material Chaboche [5] proposed to write ψ^e referring to the strain equivalence principle and effective stress conception in the following form:

$$\psi^e = \frac{(1-D)}{2\rho}\varepsilon_{ij}^e E_{ijkl}\varepsilon_{kl}^e. \tag{3}$$

Cauchy stress tensor and the thermodynamic force Y associated with the damage parameter:

$$\sigma_{ij} = \rho\frac{\partial\psi^e}{\partial\varepsilon_{ij}^e} = (1-D)E_{ijkl}\varepsilon_{kl}^e, \qquad Y = \rho\frac{\partial\psi^e}{\partial D} = -\frac{1}{2}E_{ijkl}\varepsilon_{ij}^e\varepsilon_{kl}^e. \tag{4}$$

Depending on the choice of the second part of the thermodynamic potential (2) we can obtain different models for plastic behavior of the material. We used the model with linear isotropic hardening:

$$\psi^p\left(r\right) = \frac{1}{2\rho}cr^2, \qquad R = \rho\frac{\partial\psi^p}{\partial r} = cr. \tag{5}$$

The second law of thermodynamics imposed positive intrinsic dissipation implies an existence of the potential of dissipation which is a scalar convex function of the dual variables and state variables acting as parameters:

$$F = F^p\left(\sigma_{ij}, R; D, \varepsilon_{ij}, r\right) + F^d\left(Y; D, r\right). \tag{6}$$

The first part of the potential F^p is a plastic potential. To obtain associate plasticity theories F^p is chosen equal to the loading function f. Using von Mises yield criterion the loading function takes the following form:

$$f = \frac{1}{1-D}\sqrt{\frac{3}{2}\sigma_{ij}^D\sigma_{ij}^D} - R - \sigma_T = 0. \tag{7}$$

It gives the constitutive equations for the evolution of dissipative variables. These laws of plasticity are derived from the plastic potential by means of a scalar multiplier which is always positive. This provides the normality condition of yielding for plasticity. For the chosen potential of plasticity the constitutive equations are defined as:

$$\dot{\varepsilon}_{ij}^{p} = \dot{\lambda}\frac{\partial f}{\partial \sigma_{ij}} = \frac{3}{2}\frac{\dot{\lambda}}{(1-D)}\frac{\sigma_{ij}^{D}}{\sigma_i}, \qquad \dot{r} = -\dot{\lambda}\frac{\partial f}{\partial R} = \dot{\lambda}. \tag{8}$$

Here σ_{ij}^{D} and σ_i are stress deviator and stress intensity respectively.

We can write the plastic multiplier $\dot{\lambda}$ through accumulated plastic strain rate $\dot{p}$ in the following way:

$$\dot{\lambda} = \dot{p}(1-D). \tag{9}$$

Accumulated plastic strain rate is defined as:

$$\dot{p} = \sqrt{\frac{2}{3}\dot{\varepsilon}_{ij}^{p}\dot{\varepsilon}_{ij}^{p}}. \tag{10}$$

The second term F^d is a part of the potential (6) from which the kinetic law of damage evolution is derived. In [3] Lemaitre offered following form of the potential for ductile damage and respectively following form of the kinetic law for damage evolution:

$$F^d = \frac{Y^2}{2S(1-D)}, \qquad \dot{D} = \dot{\lambda}\frac{\partial F^d}{\partial Y} = \frac{Y}{S}\dot{p}. \tag{11}$$

The plastic multiplier $\dot{\lambda}$ is determined from the consistency condition $\dot{f} = 0$. The paper [8] presents the way of obtaining of the plastic multiplier and also relations between strain rate and stress rate built by means of fourth-order tensor which is defined by current stress state, constants of elasticity, values characterizing plastic behavior and damage evolution of material. An incremental constitutive relations have been offered in the following form:

$$\dot{\varepsilon}_{ij} = B_{ijkl}\dot{\sigma}_{kl}. \tag{12}$$

Here B_{ijkl} is the fourth-order tensor known as the elastic-plastic-damage tangent operator which is defined in [8] as:

$$B_{ijkl} = \frac{1}{1-D}C_{ijkl}^{-1} + \left[\frac{2}{3}c\sigma_i(1-D)^2 - \frac{\sigma_i^2}{1-D}\frac{Y}{S}\right]^{-1}\left[\frac{3}{2\sigma_i}\sigma_{ij}^{D} + \frac{Y}{S(1-D)}\varepsilon_{ij}^{e}\right]\sigma_{kl}^{D}. \tag{13}$$

Here C_{ijkl} is the fourth order Hooke's elastic tensor.

Relation (12) can be written in invertible form:

$$\dot{\sigma}_{ij} = H_{ijkl}\dot{\varepsilon}_{kl} \tag{14}$$

2. Solving of the problem of autofrettage for thick-walled pipes

Modeling of autofrettage process consists in following: at the first stage we solve the problem of loading of the pipe subjected to internal pressure, and at the second stage pressure is removed, and we solve the problem of unloading. After unloading of the pipe there is residual stress state which we have to investigate .

Thick-walled pipe was considered under the assumption of plain strain. In this case relations between stress rate and strain rate according to (14) in cylindrical coordinate system are written in the following form:

$$\dot{\sigma}_r = H_{11}\dot{\varepsilon}_r + H_{12}\dot{\varepsilon}_\theta;$$
$$\dot{\sigma}_\theta = H_{21}\dot{\varepsilon}_r + H_{22}\dot{\varepsilon}_\theta. \tag{15}$$

For small deformation analysis relationships between strain and displacement are obtained:

$$\dot{\varepsilon}_r = \frac{d\dot{u}}{dr}, \qquad \dot{\varepsilon}_\theta = \frac{\dot{u}}{r}. \tag{16}$$

Differential equations of equilibrium:

$$\frac{d\dot{\sigma}_r}{dr} + \frac{\dot{\sigma}_r - \dot{\sigma}_\theta}{r} = 0. \tag{17}$$

The set of equation (15) - (17) can be reduced to one resolving equation for displacement rate:

$$H_{11}\frac{d^2\dot{u}}{dr^2} + \left[\frac{dH_{11}}{dr} + \frac{1}{r}(H_{12} - H_{21} + H_{11})\right]\frac{d\dot{u}}{dr} + \left[\frac{1}{r}\frac{dH_{12}}{dr} - \frac{H_{22}}{r^2}\right]\dot{u} = 0. \tag{18}$$

The second order differential equation should be complemented by boundary conditions at inner and outer radius. For displacement rate boundary conditions will be written as:

$$H_{11}\frac{d\dot{u}}{dr}(r_a) + \frac{H_{12}}{r_a}\dot{u}(r_a) = -\dot{P},$$
$$H_{11}\frac{d\dot{u}}{dr}(r_b) + \frac{H_{12}}{r_b}\dot{u}(r_b) = 0. \tag{19}$$

For solving the nonlinear elastoplastic problems we used iterative Newton-Raphson method which is based on sequential approximations of linear problems. In order to determinate the plastic multiplier on each equilibrium iteration the implicit radial return integration scheme was applied. Damage parameters were defined by means of explicit scheme. Detailed description of these methods is given in [9, 10]. Boundary problem was solved using the finite difference method. In this way the differentiation operator in the equation (18) was replaced by the finite differences. Arising set of linear equation was solved by the sweep method [11]. We have developed the solving algorithm which was implemented by using software Microsoft Visual Studio 2008 and programming language Visual C#.

3. Analysis of results

For the calculation we take the following parameters: inner radius $a = 0.05$ m; outer radius $b = 0.09$ m; Young's modulus $E = 2 \cdot 10^5$ MPa; Poisson's ratio $\nu = 0.32$; yield stress $\sigma_T = 260$MPa; tangent modulus $E_T = 6 \cdot 10^3$ MPa; energy strength of damage $S = 7$ MPa; damage threshold $p_D = 0.05$.

Figure 1 shows the distribution of residual hoop stress over pipe thickness for different values of autofrettage pressure. An increase of this pressure leads to a growth of the residual hoop stress until effects of material damage at significant plastic strains will not prevail. In order to obtain the optimal autofrettage pressure at which residual hoop stress on inner wall of the pipe has maximum value we carried out the calculations with different values of pressure. When autofrettage pressure reaches value equal to $P = 604$MPa the residual hoop stress have a maximum in absolute value. The damage parameter is then equal to $D = 0.125$. Figure 2 shows distribution of residual hoop stress under the pressure equal to $P = 604$MPa taking into account the material damage and excluding the damage effects. You can see that residual hoop stress significantly less if we take into account the material damage. Figure 3 shows the distribution of the damage parameter for different values of autofrettage

pressure. The damage is accumulated on inner bore of the pipe in a place where the level of accumulated plastic strains reaches its maximum value.

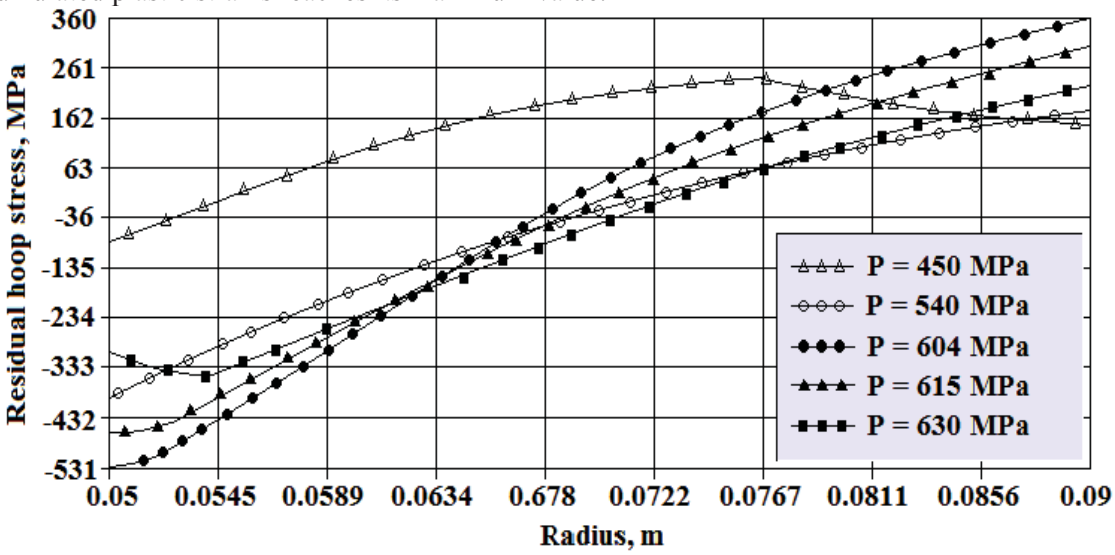

Figure 1. Distribution of the residual hoop stresses

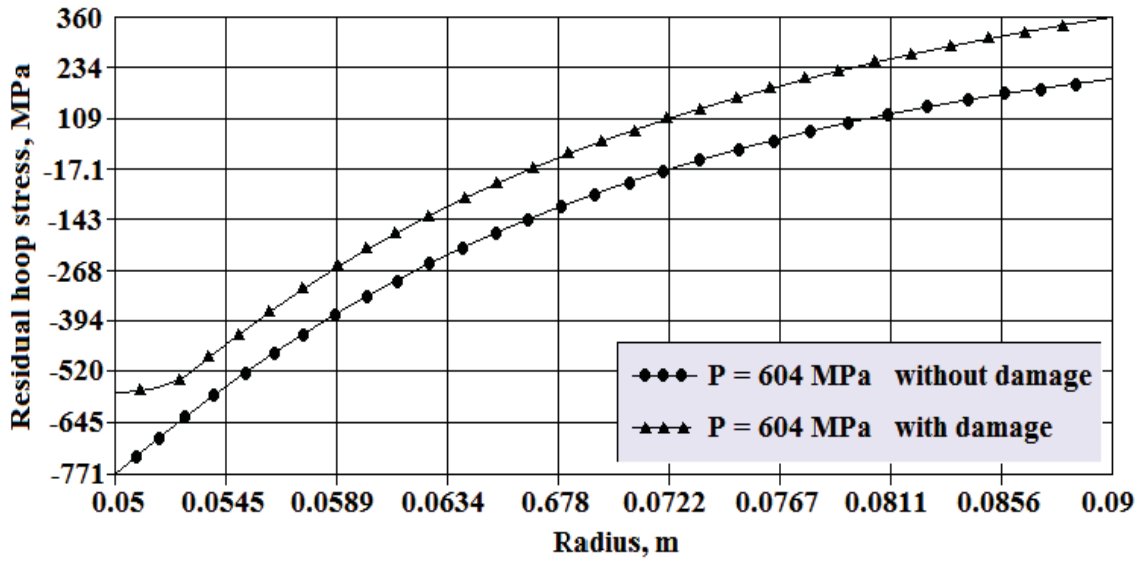

Figure 2. Distribution of the residual hoop stresses

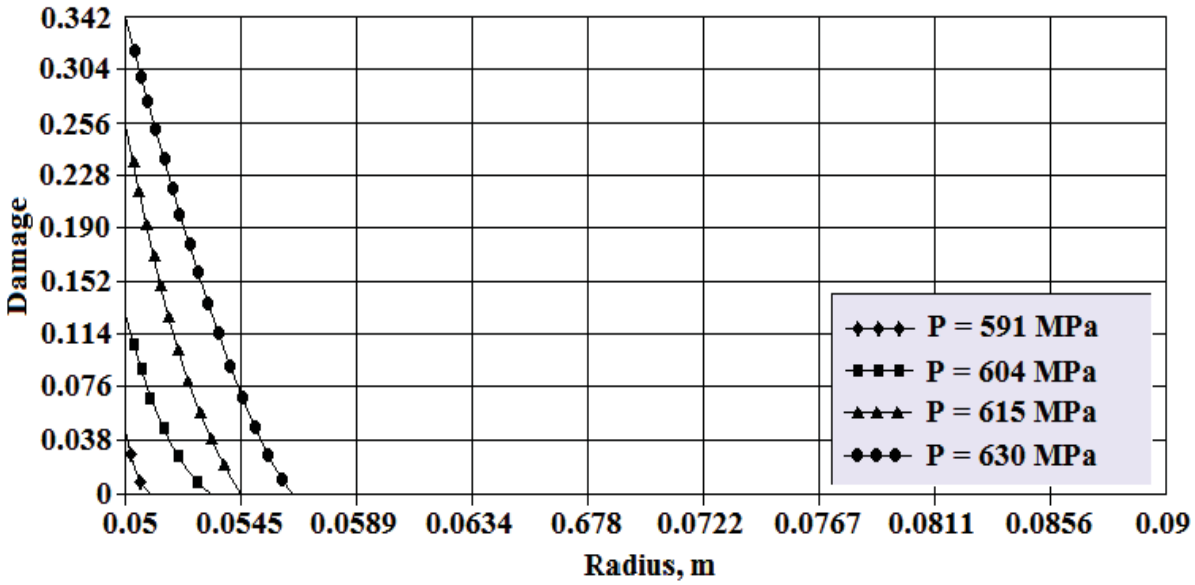

Figure 3. Distribution of the damage parameter

Conclusions

The analysis of the material damage influence on efficiency of the autofrettage process has been performed. Elasto-plastic constitutive equation with strain hardening and material damage has been introduced to the model of material behavior. The proposed material model is derived using rigorous and consistent thermodynamic formulation. The additive decomposition of the Helmholtz free energy concept is used to define the thermodynamic conjugate forces associated with the internal state variables, including the damage thermodynamic conjugate force (damage energy release rate). The energy dissipation mechanisms are formulated to satisfy the first inequality of thermodynamics, and to postulate the plastic and damage dissipation functions.

Continuous increase of autofrettage pressure proved not to lead to a growth of residual hoop stresses. As well as the Bauschinger effect the damage of material reduces favorable residual hoop stress. The optimal value of autofrettage pressure at which residual hoop stress has a maximum value has been found. Also comparison of the results obtained taking into account the material damage and excluding influence of the damage showed that residual hoop stress with damage significantly less than without the damage effect.

Once the technological process of the autofrettage is completed it is necessary the subsequent mechanical treatment of a pipe. It consists in removing material on inner bore of the pipe. Therefore, a zone occupied by the material damage formed in a place of maximum plastic strains can be removed. Also it will lead to reduction of the residual hoop stress. Therefore, further interest is investigation of residual stress-strain state of thick-walled pipes after the removal of material.

References

[1] Parker A.P., Underwood J.H., Kendall D.P. Bauschinger effect design procedures for autofrettaged tubes including material removal and Sachs' method *Journal of Pressure Vessel Technology*, Vol. 123, pp. 430-437, 1999.

[2] Parker A.P. Bauschinger effect design procedures for compound tubes containing an autofrettaged layer *Journal of Pressure Vessel Technology*, Vol. 74, pp. 203-206, 2001.

[3] Lemaitre J. A. *A Course on Damage Mechanics*, Springer, Berlin, 1996.

[4] Lemaitre J. A. and Desmorat R. *Engineering Damage Mechanics*, Springer, New York, 2005.

[5] Chaboche J.-L. Continuum Damage Mechanics *Journal of Applied Mechanics*, Vol. 55, pp. 60-63, 1999.

[6] Voyiadjis G.Z., Ju J.-W. and Chaboche J.-L. *Damage Mechanics in Engineering Materials*, Elsevier, Oxford, 1998.

[7] Rabotnov Yu.N. *Introduction to Fracture Mechanics*, Nauka, Moscow, 1987. (in Russian)

[8] Lvov G.I. and Okorokov V.O. Influence of material damage on autofrettage of thick-walled pipes *Proc of the National Technical University "KhPI"*, Vol. 55, pp. 108-114, 2012. (In Russian)

[9] Huang J. and Griffiths D. V. Return Mapping Algorithms and Stress Predictors for Failure Analysis in Geomechanics *Journal of Engineering Mechanics*, Vol. 135, pp. 286-284, 2012.

[10] Simo J. C. *Numerical analysis of classical plasticity*, Elsevier, Amsterdam, 1998.

[11] Samarskij A.A. and Nikolaev E.S. *Methods of solving difference equations*, Nauka, Moscow, 1978. (In Russian)

Proceedings of the 4th International Conference on Nonlinear Dynamics
ND-KhPI2013
June 19-22, 2013, Sevastopol, Ukraine

Effects of Cumulative Fatigue Damage under Tensional Cyclic Loading on the Constitutive Relation of AISI 1045 Steel

Wojciech Moćko[1*, 2]

Abstract
The paper presents results of the influence of initial fatigue loadings on the tensile stress-strain curves of AISI 1045 steel. Tensile characteristics were determined using servo-hydraulic testing machine at wide range of strain rates. It was found that the cumulative fatigue damage introduced into material may significantly affect the mechanical behavior of AISI 1045 steel. Lower CFD values, i.e. 25% and 50% induce the increase in the flow stress value, whereas further increase of CFD to 75% results the softening in the material due to fatigue damage. Higher pre-strain stress amplitude enhances influence of fatigue on the stress-strain curves. Strain rate sensitivity may be also modified by pre-fatigue loadings.

Keywords
Fatigue, constitutive equation, AISI 1045 steel

[1] Motor Transport Institute, Warsaw, Poland
[2] Institute of Fundamental Technological Research PAS, Warsaw, Poland
*** Corresponding author:** wojciech.mocko@its.waw.pl

Introduction

Development of the reliable method of the cumulative fatigue damage (CFD) assessment is major engineering challenge. Many structural effects related to the fatigue loadings still requires further research despite the fact that first works of Palmgren [1] and Miner [2] concerning the linear rule of fatigue damage growth were presented almost one hundred years ago. The investigations which have been carried out until nowadays were focused mainly on prediction of the structure lifetime on the basis of stress or strain magnitude and number of cycles [3-5]. Very comprehensive review of various methods of CFD estimation may be found in another paper [6].

On the contrary, instead of lifetime prediction, in this work attention has been focused on analysis of the effect of fatigue damage growth on the constitutive relation describing mechanical properties of AISI 1045 steel. The presented approach may be very important for the purposes of numerical simulation of structures behavior under extreme loading conditions i.e. energy absorbing structures [7]. Currently, FEM analysis are usually carried out applying viscoplastic material properties determined for the as-received material state [8]. Therefore, the influence of operational loads applied to the structure in normal use are not taken into account. This kind of simplification may lead to discrepancy between the simulation results and real behavior of the structure. Incorporating into calculation of the cyclic loadings influence on the evolution of elastoplastic material behavior may lead to increase accuracy of FEM modeling.

The number of papers concerning influence of the fatigue loadings on the visco-plastic material properties is very narrow despite practical importance of this phenomenon. According to the researches that have been carried out [9] the influence of fatigue loadings on the evolution of stress-strain characteristics may be different depending on the material microstructure. For the 6061-T6 aluminium alloy the influence of cyclic loadings on the characteristics determined at quasi-static and dynamic loading conditions may be neglected whereas the test carried out under the same loading conditions for AISI 4140T steel shows clearly visible effects of flow stress lowering.

Similar analysis has been done for 2017A-T3 and 5454-O aluminium alloys [10]. The specimens pre-strained under the high cycle fatigue loading conditions were subsequently subjected to tensile loadings at high strain rate equal to $300s^{-1}$. For the 2XXX series alloy a very significant drop of tensile force has been found, whereas the second alloy was insensitive to initial fatigue. The authors conclude that tensile curve is determined by microstructure of a given material since the pre-strain loading parameters has no results on the tensile curve.

In order to estimate the influence of the localization of Ti-6Al-4V alloy micro damages on the tensile characteristic the research composed of two stages has been carried out [11]. At the first phase the pre-fatigued specimens were subjected to tensile test. Subsequently, in the phase two, material after the same initial loadings like for the phase one was machined in order to remove surface layer. Afterwards the machined specimens were tested at tensile conditions. On the basis of comparison between tensile test carried out in the phases one and two, the authors conclude that the surface layer has a crucial importance in the phenomenon of mechanical properties degradation.

This work presents the results of analysis of the influence of initial tensile cyclic loadings on the constitutive relation estimated on the basis of stress-strain curves obtained at strain rates within the range from $10^{-4}s^{-1}$ to $10^{0}s^{-1}$. Proposed methodology of hybrid loadings was applied on the example of AISI 1045 steel. The chemical composition of the tested material is presented in Table 1. The specimens were fabricated by machining from a drawn rod of 1045 AISI steel. The shape of specimens was cylindrical with tangentially blending fillets between the test section and the ends. The gauge length and diameter were equal to 12 mm and 4 mm respectively. The surface was polished after machining.

Table 1. Chemical composition of AISI 1045 steel

C	Mn	Si	P	S	Cr	Ni	Cu	Mo
0.43	0.71	0.25	0.015	0.017	0.07	0.08	0.22	0.018

The research procedure consists of the following stages:

- determining of the stress-strain curves of AISI 1045 steel in the as-received state at wide range of strain rates;
- estimation of Wöhler chart of steel under cyclic tensile loading conditions;
- introducing initial fatigue damage into specimens;
- determining the stress-strain curves of pre-fatigued material;
- calibration of coefficients of the Johnson-Cook's constitutive equation on the basis of stress-strain curves [12].

1. Tensile test of AISI 1045 steel at wide range of strain rates

The tensile stress-strain curves of AISI 1045 steel in the as-received state were determined using the Instron servohydraulic testing machine. The strain of specimen was measured using electro-mechanical extensometer with a length of 10 mm. In order to obtain the true stress and strain values the axial strain was recalculated using the final diameter of the neck near the fragmentation zone. The characteristics obtained at three various strain rates equal to$10^{-4}s^{-1}$, $10^{-2}s^{-1}$ and $10^{0}s^{-1}$ are presented in Fig.1a. The strain rate sensitivity chart of AISI 1045 steel is shown in Fig. 1b. The tested material shows clearly visible effects of work hardening and strain rate hardening as well.

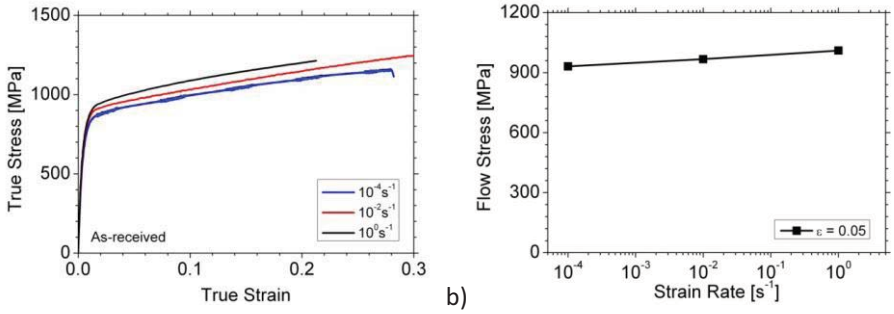

Figure 1. Mechanical properties of 1045 steel in the as-received state a) stress-strain curves; b) strain rate sensitivity chart

2. Fatigue tests

The next stage of analysis has been made in order to determine the S-N curve of AISI 1045 steel. The fatigue tests were carried out under the tensile loading conditions (R=0) at various stress amplitudes σ_a within the range from 550MPa to 750MPa. Obtained characteristic is presented in Fig. 2. Subsequently, initial fatigue loadings of two selected amplitudes i.e. 550MPa and 750 MPa have been introduced into specimens. Using the following formula:

$$CFD = \sum_{i=1}^{k} \frac{n_i}{N_i} \tag{1}$$

the number of cycles was selected in order to obtain CFD value, estimated using Miner's linear rule equal to 25%, 50% and 75%. The number of cycles was equal to 98 000, 196 000 and 294 000 for fatigue stress amplitude equal to 550MPa and 10 750, 21 500 and 32 250 for fatigue stress amplitude equal to 750 MPa.

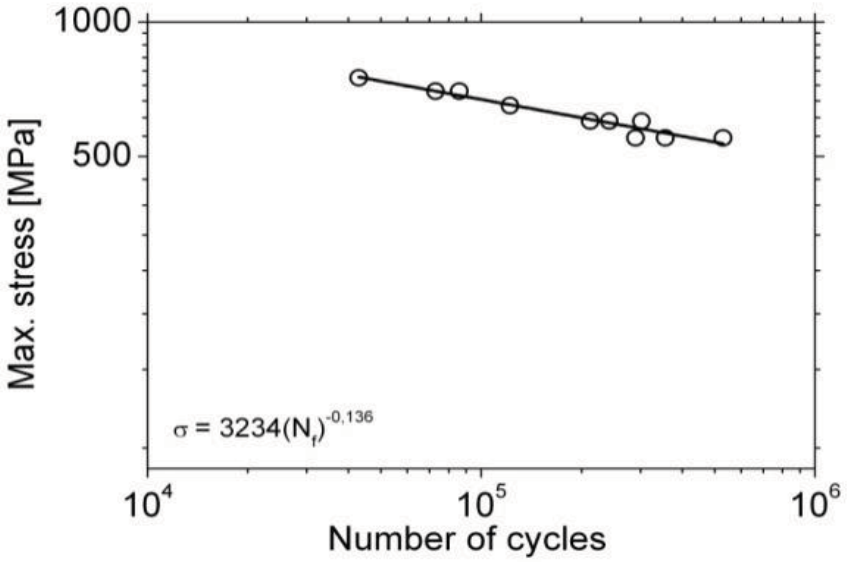

Figure 2. S-N curve of the 1045 steel

3. Tensile tests of pre-fatigued specimens

The tensile stress-strain curves recalculated to true values are presented in Fig. 3 and Fig. 4 for pre-fatigue amplitude equal to 550MPa and 750 MPa, respectively.

The tests were carried out at various strain rates. The limited material softening effect may be observed at CFD equal to 75% for specimens pre-strained at amplitude equal to 550MPa. The effect of material softening at the same CFD value is stronger at pre-strain amplitude equal to 750MPa. Moreover, after the initial hardening at CFD equal to 25% and 50% the clearly visible lowering of the flow stress due to fatigue damage growth may be observed.

The increase in work hardening modulus at strain rate equal to $10^0 s^{-1}$ may be found for both pre-fatigue stress amplitudes. The effect is clearly visible at CFD=25% and 50%. The further increase of initial fatigue cycles to CFD=75% reduces the effect, however it still may be observed.

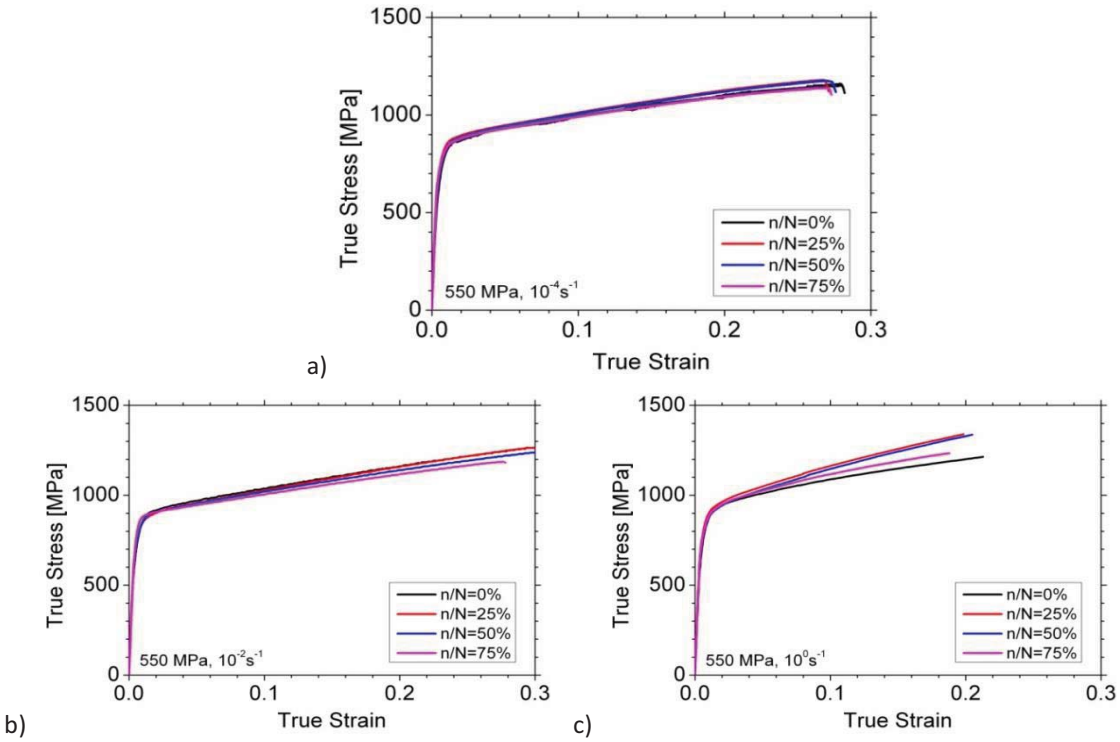

Figure 3. Stress strain curves of 1045 steel, after given number of pre-fatigue loadings cycles of magnitude equal to 550 MPa; a) $\dot{\varepsilon} = 10^{-4}\, s^{-1}$; b) $\dot{\varepsilon} = 10^{-2}\, s^{-1}$; c) $\dot{\varepsilon} = 10^{0}\, s^{-1}$.

The strain rate sensitivity chart is presented in Fig. 5. For the pre-fatigue stress amplitude equal to 550 MPa the effect of flow stress lowering may be found at strain rate equal $10^{-2}s^{-1}$ whereas at strain rate equal to $10^{0}s^{-1}$ flow stress has higher value in comparison to as received material. The phenomenon influence of CFD on the strain rate sensitivity disappears for pre-strain amplitude equal to 750 MPa.

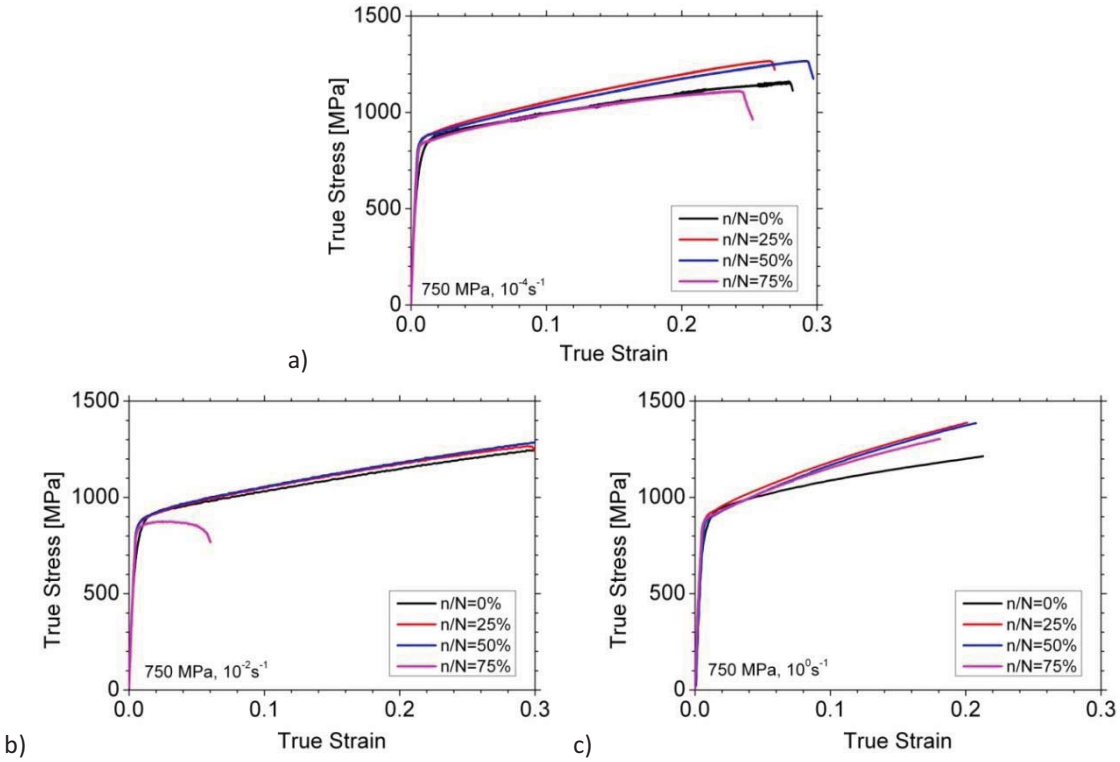

Figure 4. Stress strain curves of 1045 steel, after given number of pre-fatigue loadings cycles of magnitude equal to 750 MPa; a) $\dot{\varepsilon} = 10^{-4}\, s^{-1}$; b) $\dot{\varepsilon} = 10^{-2}\, s^{-1}$; c) $\dot{\varepsilon} = 10^{0}\, s^{-1}$.

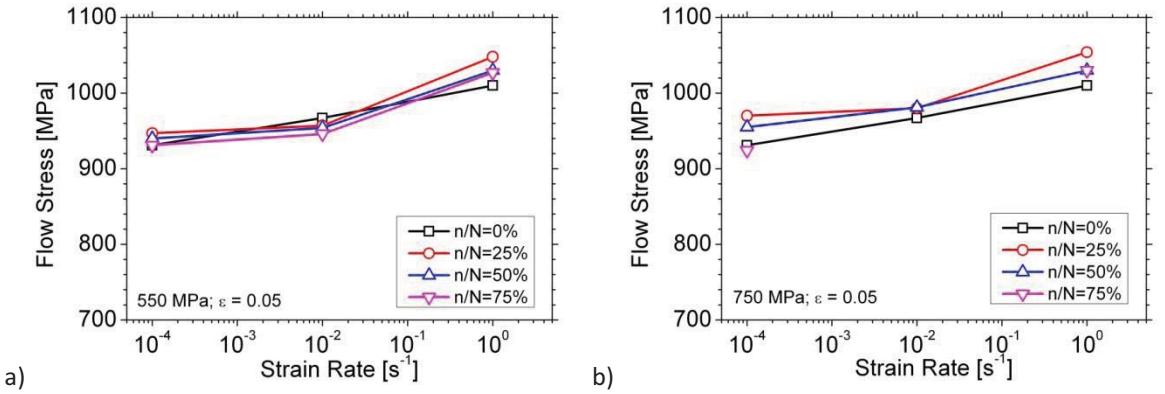

Figure 5. Strain rate sensitivity of 1045 steel after given number of pre-fatigue loadings cycles of magnitude equal to a) 550 MPa; b) 750 MPa

4. Constitutive modeling using Johnson-Cook's equation

Coefficient A, B and n of the Johnson-Cook's constitutive model of ASISI 1045 steel were calibrated on the basis of tensile curves determined at quasi-static loading conditions i.e. strain rate equal to $10^{-4}s^{-1}$. The analyses were carried out for as-received and pre-strained material. The comparison between measured and calculated stress-strain characteristics presented in shown in Fig. 6. A good agreement between experimental and model based curves has been achieved. The influence of strain rate on the flow stress is presented in Fig. 6. It may be stated that pre-fatigue introduces a large discrepancy between experimental and numerical predictions, especially for the case of pre-fatigue stress amplitude equal to 550 MPa.

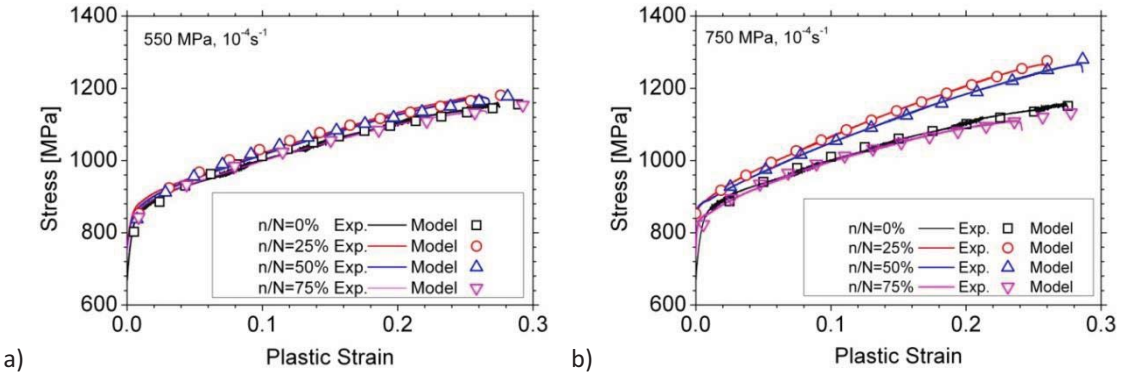

Figure 6. Quasi static stress-strain curves of 1045 steel calculated using JC model after given number of pre-fatigue loadings cycles of magnitude equal to a) 550 MPa; b) 750 MPa

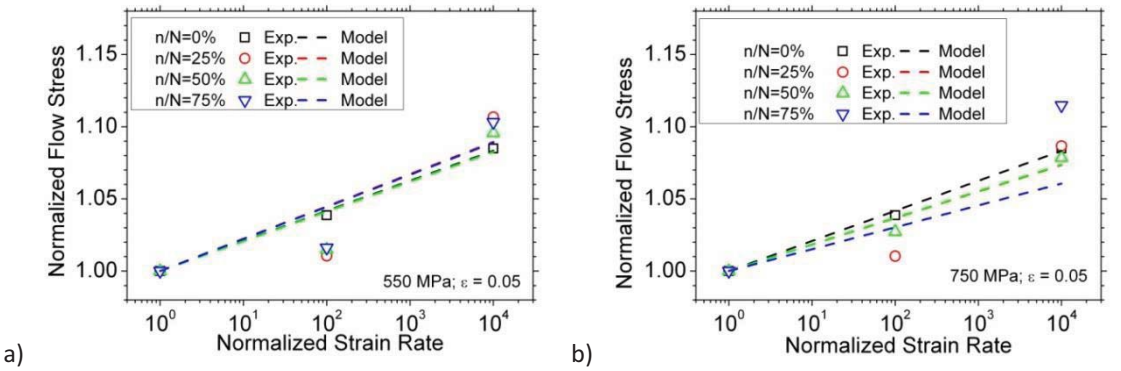

Figure 7. JC model of 1045 steel after given number of pre-fatigue loadings cycles of magnitude equal to a) 550 MPa; b) 750 MPa

Table 2. JC Coefficients

Max. Stress [MPa]	CFD [%]	JC coefficients			
		A	B	n	C
As-received material	0	679	723	0.33	0.009
550	25	750	734	0.41	0.010
	50	735	736	0.40	0.009
	75	750	673	0.41	0.009
750	25	852	1102	0.70	0.008
	50	860	1085	0.43	0.007
	75	738	652	0.39	0.006

Conclusions

The tensile fatigue loadings influence on the stress strain characteristics of AISI 1045 steel. Therefore the coefficients of constitutive equation describing mechanical properties of the material are also affected.

For both pre-fatigue stress amplitudes for CFD equal to 25% and 50% the increase of flow stress in comparison to as-received material may be found. The further increase in the number of cycles up to CFD=75% induces opposite effect i.e. material softening due to fatigue damage growth. Comparable effect may be found in both pre-fatigue cases, however for the initial stress amplitude equal to 750 MPa the phenomenon is much more intensive.

Some changes in the strain rate hardening curves may be also found for the material pre-fatigued by stress amplitude equal to 550 MPa. In comparison to as-received material, the initial loadings results in lowering of flow stress at a strain rate equal to $10^{-2}s^{-1}$, and increase of the flow stress a strain rate equals to $10^{0}s^{-1}$. The comparable phenomenon, however diminished, may be observed for the specimens, which are initially loaded at amplitude is equal to 750 MPa.

References

[1] Palmgren A. Die Lebensdauer von Kugellagern *Verfahrenstechnik,* Vol. 68, pp. 339–41, 1924.
[2] Miner M. A. Cumulative damage in fatigue *J. Appl. Mech.,* Vol. 67A, pp. 159–164, 1945.
[3] Socha G. Experimental investigations of fatigue cracks nucleation, growth and coalescence in structural steel *International Journal of Fatigue,* Vol. 25, pp. 139–147, 2003.
[4] Socha G. Prediction of the fatigue life on the basis of damage progress rate curves *International Journal of Fatigue,* Vol. 26, pp. 339–347, 2004.
[5] Dietrich L. and Radziejewska J. The fatigue damage development in a cast Al–Si–Cu alloy *Materials and Design,* Vol. 32, pp. 322-329, 2011.
[6] Fatemi A. and Yang L. Cumulative fatigue damage and life prediction theories: a survey of the state of art for homogeneous materials *Int J Fatigue,* Vol. 20, pp. 9-34, 1998.
[7] Moćko W. Application of Austenitic Steels in Energy Absorbing Structures *Journal of Kones,* Vol. 19: 3, pp. 305-310, 2012.
[8] Moćko W. and Kowalewski Z. L. Application of selected constitutive equations to mechanical behaviour description of VP159 high-nitrogen steel *Modelowanie inżynierskie,* Vol. 42, pp. 203-210, 2012.
[9] Sánchez-Santana U., Rubio-González C., Mesmacque G., Amrouche A. and Decoopman X. Effect of fatigue damage induced by cyclic plasticity on the dynamic tensile behavior of materials *International Journal of Fatigue,* Vol. 30, pp. 1708–1719, 2008.
[10] Froustey C. and Lataillade J. L. Influence of the microstructure of aluminium alloys on their residual impact properties after a fatigue loading program *Materials Science and Engineering A,* Vol. A500, pp. 155–163, 2009.

[11] Galán López J., Verleysen P., De Baere I. and Degrieck J. Tensile properties of thin-sheet metals after cyclic damage *Procedia Engineering,* Vol. 10, pp. 1961–1966, 2011.
[12] Johnson G. R. and Cook W. H. A constitutive model and data for metals subjected to large strains, high strain rates and high temperatures *Proceedings of Seventh International Symposium on Ballistics, The Hague, The Netherlands* ,pp. 541–547, 1983.
[13] Moćko W. and Kowalewski Z. L. Dynamic Compression Tests – Current Achievements and Future Development *Engineering Transactions,* Vol. 59, pp. 235-248, 2011.
[14] Moćko W., Rodriguez-Martinez J. A., Kowalewski Z. L. and Rusinek A. Compressive Viscoplastic Response of 6082-T6 and 7075-T6 Aluminium Alloys Under Wide Range of Strain Rate at Room Temperature *Experiments and Modelling Strain,* Vol. 48, pp.498-509, 2012.

Proceedings of the 4th International Conference on Nonlinear Dynamics
ND-KhPI2013
June 19-22, 2013, Sevastopol, Ukraine

Grain Boundary Sliding during creep in a polycrystalline material

Oksana Ozhoga-Maslovskaja , Holm Altenbach, Konstantin Naumenko, Oleksandr Prygorniev

Abstract
A polycrystal unit cell is simulated and investigated under creep conditions within the framework of continuum micromechanics. Geometrical 3D model of a polycrystalline microstructure is represented as a unit cell with grains of random crystallographical orientation and shape. Thickness of the planes, separating neighboring grains in the unit cell, has non-zero value. Obtained geometry assigns a special zone in the vicinity of grain boundaries, possessing unordered crystalline structure and used to represent grain boundary sliding. Within the grain interior crystalline structure is ordered, what prescribes cubic symmetry of a material. According to this the anisotropic material model with the cubic symmetry is implemented in ABAQUS and used to assign elastic and creep behavior of a grain interior. Material parameters are identified from creep tests for single crystals copper. Material behavior of the grain boundary region allows sliding within the grain boundary plane and disables deformation in the normal direction. Overall behavior of the unit cell with the grain boundary region is analyzed and verified according to the experiments under the polycrystalline copper.

Keywords
Creep, polycrystalline, copper, unit cell

Insitute of Mechanics, Otto von Guericke University Magdeburg, Germany

*__Corresponding author__: oksana.ozhoga-maslovskaja@ovgu.de

Introduction

The main mechanisms leading to the creep fracture are found to be dislocation creep within the grain, diffusion transport of matter from the grain boundaries or interior and grain boundary sliding (GBS). A lot of constitutive models exist, which enable good description of overall inelastic deformation of a polycrystal. But they are not able to account processes occurring on the level of grain boundaries, such as sliding or cavitation, which influence significantly macroproperties of material. The current work is dedicated to the detailed simulation of a polycrystalline geometry and its mechanical behavior during primary and secondary creep stages.

For the geometrical representation of polycrystalline material Voronoi tessellations [1] are widely used, which allow to generate the geometry of a random grain microstructure. Elastic analysis of a 3D Voronoi unit cell with a periodic mesh is performed in [2]. As one of the results isotropic elastic constants for polycrystalline copper, gold and nickel are evaluated from the statistical analysis of the unit cells with different number of grains. The 3D polycrystalline representation with detailed simulation of grain boundaries is done in [3]. The grain boundaries are represented by additional layer of cohesive finite elements which reproduce cracking. The layer of grain boundary elements is used to describe grain boundary sliding and opening due to corrosion processes. In the current work grain boundaries as separate geometrical objects are introduced. The mechanical behavior of this objects is assumed to describe sliding. The cavitation model implementation is planned in future.

The grain boundary sliding in a polycrystalline material is not an independent process and does not occur in the pollycrystalline material instantly after applying of loading. It occurs owing to the intergranular deformation and in this way contributes to the total creep strain. Hence grain boundary sliding can be caused by diffusion [4] or dislocation creep [5] deformation within the grains or by interaction of both these mechanisms. Different grain boundary sliding models are presented in the literature [6].

Dislocation based creep leads to the so called Rachinger type of sliding [7], which is characterized by increase of the grains number along the specimen, but mostly does not influence the grain shape. The slip within the grain interior leads to accumulation of dislocations on the grain boundaries. And the sliding occurs because the continuity between the mutual grains should be held. As a consequence the high–angle boundaries have a higher tendency to sliding, because the dislocations within low–angle boundaries can freely slide under applied stress, not causing the displacement of grain boundaries.
Widely used way of a polycrystalline geometry representation is a 2 dimensional massive of equal size hexagons. Such geometry is used, for example, in [8] in order to simulate grain boundary sliding. The problem is solved with assumptions of a plane strain under applied shear stress. Grain elements are prescribed to deform inelastically by the power law. The grains are connected by the thin layer of grain boundary elements, which are prescribed to shear in a Newtonian viscous manner. The different ways of viscosity coefficient are proposed depending on the grain boundary geometry. The similar approach is used in the current work.

1. CAE model of a polycrystal

The microstructure of many polycrystalline materials can be presented by the Voronoi tessellation with a random distribution of grain cores. An example of the grained unit cell constructed with the help of the Voronoi tessellation is described in [2]. Within the current work the Python script is developed, which allows us to design an analogous unit cell in ABAQUS. In the developed model the following input parameters are defined: number of grains, average grain size, material properties, and grain boundary thickness. The grain boundary thickness corresponds to the thickness of a plane, separating the neighboring grains. The unit cell consisting of 50 grains with zero grain boundary thickness is depicted in Fig. 1(a). As it known from the literature [9] grain boundaries are not planes, but nonplanar regions which

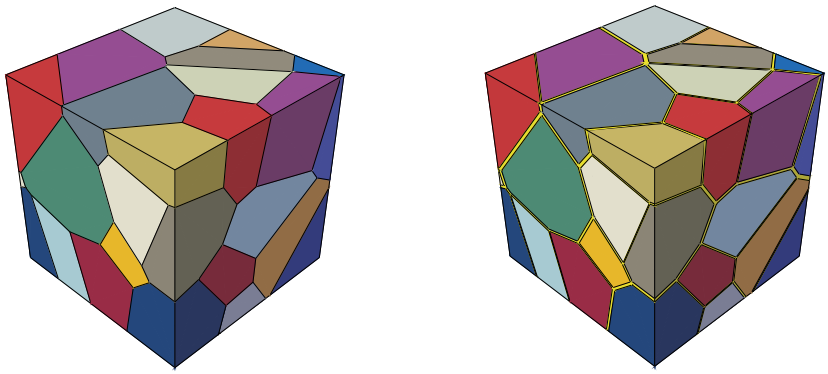

Figure 1. Polycrystal unit cell models with zero grain boundary thickness (a) and non-zero grain boundary thickness (b)

in contrast to grains possess an unordered crystalline structure. Origins of such structure are the lattices incompatibilities of neighboring grains, accumulated defects, obstacles, etc. Therefore it is necessary to determine special material behavior for the grain boundary. For this purpose the unit cell with grain boundary region is constructed, as it presented in Fig. 1(b). An important step in the simulation of the polycrystalline body is the set of material orientations. For this purpose local coordinate systems are used. In every grain the local coordinate system is specified, which is rotated by random angles relatively to the global coordinate system of the unit cell. With this random crystallographical orientation is reflected, which is observed in a polycrystal. For the grain boundary sliding representation one should distinguish between the shear and the normal deformation of the grain boundary. Therefore an individual local coordinate system is determined for every plane region of the grain boundary region. An example of such coordinate system one can see in Fig. 2. In this case the direction $\boldsymbol{g}_3$ is set as a normal to the grain boundary and other two directions $\boldsymbol{g}_1$ and $\boldsymbol{g}_2$ lie in the grain boundary plane. In the regions of

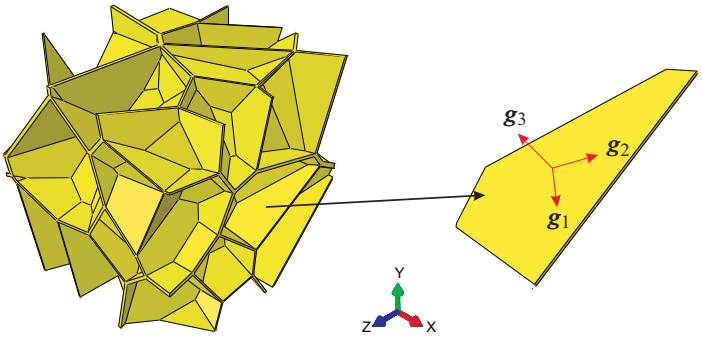

Figure 2. Grain boundary region with discrete material orientation.

grain boundaries junction the smooth transition from one coordinate system to another is automatically performed by ABAQUS.

2. Constitutive model

The developed unit cell possesses two types of material: grain interior and grain boundary region. These materials have different symmetry types and should represent different material response for elasticity and creep. Material of the grain interior possesses ordered crystalline structure, which in the case of phenomenological modeling is represented by the material with the cubic symmetry. In the vicinity of a grain boundary crystal lattice is distorted and symmetry type of this region is determined not by physical structure, but by its mechanical behavior. In the current model this region should allow sliding. With respect to the directions given in Fig. 2 the sliding shear strains are: ε_{13}, ε_{23}. The strain in the normal direction to the grain boundary ε_{33} should be neglected. For this purpose constitutive equations for the material with orthotropic symmetry are formulated, which allow to distinguish between normal and shear strain tensor components. Thus, orthotropic material model describes both faces: orthotropic grain boundary region and after appropriate parameters set grain interior with cubic symmetry type.

2.1 Elasticity

In the case of elasticity the dependence between stresses and elastic strains for both regions is represented through the material with orthotropic symmetry:

$$\begin{aligned}\boldsymbol{\sigma} &= (\alpha_1\varepsilon_{11}+\alpha_2\varepsilon_{22}+\alpha_3\varepsilon_{33})(\alpha_1\boldsymbol{g}_1\boldsymbol{g}_1+\alpha_2\boldsymbol{g}_2\boldsymbol{g}_2+\alpha_3\boldsymbol{g}_3\boldsymbol{g}_3)\\ &+ [\beta_1(\varepsilon_{11}-\varepsilon_{22})+\beta_2(\varepsilon_{11}-\varepsilon_{33})]\boldsymbol{g}_1\boldsymbol{g}_1+[\beta_1(\varepsilon_{22}-\varepsilon_{11})+\beta_3(\varepsilon_{22}-\varepsilon_{33})]\boldsymbol{g}_2\boldsymbol{g}_2\\ &+ [\beta_2(\varepsilon_{33}-\varepsilon_{11})+\beta_3(\varepsilon_{33}-\varepsilon_{22})]\boldsymbol{g}_3\boldsymbol{g}_3\\ &+ 2\beta_{12}\varepsilon_{12}(\boldsymbol{g}_1\boldsymbol{g}_2+\boldsymbol{g}_2\boldsymbol{g}_1)+2\beta_{13}\varepsilon_{13}(\boldsymbol{g}_1\boldsymbol{g}_3+\boldsymbol{g}_3\boldsymbol{g}_1)+2\beta_{23}\varepsilon_{23}(\boldsymbol{g}_2\boldsymbol{g}_3+\boldsymbol{g}_3\boldsymbol{g}_2).\end{aligned}$$

One can see in above formula 9 independent material parameters. With the following material parameters set we transit to the material with the cubic symmetry, which characterizes the grain interior:

$$\alpha_1^2=\alpha_2^2=\alpha_3^2=353.3\text{ MPa},\ \beta_1=\beta_2=\beta_3=12333\text{ MPa},\ \beta_{12}=\beta_{13}=\beta_{23}=62300\text{ MPa}.$$

The values are taken from the tests under single crystal copper [10]. The physical meaning of every coefficient is explained in details in the previous work [11]. For the grain boundary region the elastic parameters are assumed to be the same except the relation $\alpha_1^2=\alpha_2^2=\alpha_3^2=600$ MPa, which allows us to reduce the value of the bulk deformation.

2.2 Creep

In the case of plasticity crystal slip occurs on the crystallographical planes, which have the most preferable orientation to the applied load. Under high temperatures and activation of the viscous processes in the material one can observe a switching of one slip system to another, and also simultaneous operation

of several systems. A well known approach for the description of the creep behavior of a crystalline body is the crystal creep theory, which directly express the total creep strain rate through the shear rates on different slip systems [12, 13]. Such approach leads to the determination of a big number of material microparameters. In order to avoid this problem and receive the first estimation of the creep for the polycrystal unit cell an Odqvist–von Mises type anisotropic creep model based on the existence of the creep potential is applied [14]. The creep strain rate tensor for the incompressible material with orthotropic symmetry has the following form:

$$\begin{aligned}\dot{\boldsymbol{\varepsilon}}^{\mathrm{c}} &= \frac{1}{2}a\sigma_{eq}^{n-1}\Big\{(\mu_1(\sigma_{11}-\sigma_{22})+\mu_3(\sigma_{11}-\sigma_{33}))(\boldsymbol{g}_1\boldsymbol{g}_1-\frac{1}{3}\boldsymbol{I})\\ &+ (\mu_2(\sigma_{22}-\sigma_{33})+\mu_1(\sigma_{22}-\sigma_{11}))(\boldsymbol{g}_2\boldsymbol{g}_2-\frac{1}{3}\boldsymbol{I})\\ &+ (\mu_3(\sigma_{33}-\sigma_{11})+\mu_2(\sigma_{33}-\sigma_{22}))(\boldsymbol{g}_3\boldsymbol{g}_3-\frac{1}{3}\boldsymbol{I})\\ &+ 6\left[\mu_{12}\tau_{12}(\boldsymbol{g}_1\boldsymbol{g}_2+\boldsymbol{g}_2\boldsymbol{g}_1)+\mu_{13}\tau_{13}(\boldsymbol{g}_1\boldsymbol{g}_3+\boldsymbol{g}_3\boldsymbol{g}_1)+\mu_{23}\tau_{23}(\boldsymbol{g}_2\boldsymbol{g}_3+\boldsymbol{g}_3\boldsymbol{g}_2)\right]\Big\}.\end{aligned}$$

where the expression for the equivalent stress is:

$$\sigma_{eq}^2=\frac{1}{2}\left[\mu_1(\sigma_{11}-\sigma_{22})^2+\mu_2(\sigma_{22}-\sigma_{33})^2+\mu_3(\sigma_{33}-\sigma_{11})^2\right]+3\left[\mu_{12}\tau_{12}^2+\mu_{23}\tau_{23}^2+\mu_{13}\tau_{13}^2\right].$$

Material parameters for the grain interior are evaluated from the creep tests under crystalline copper at 800 K [1] and they are:

$$a=8.96\cdot10^{-15}(\mathrm{MPa})^{-n}/\mathrm{h},\ \ n=9.4,\ \ \mu_{12}=\mu_{13}=\mu_{23}=0.026.$$

$\mu_1=\mu_2=\mu_3=1$ are taken due to the assumption of the cubic symmetry of the grain material.
The shear strains in the grain boundary region are assumed to develop by the power law. The creep exponent $n^{gb}=4$ is reported in the literature [15]. Parameters $\mu_1^{gb}=\mu_2^{gb}=\mu_3^{gb}=1\cdot10^{-7}$ are taken close to zero in order to reduce the deformation in the normal direction. Other parameters should be obtained from the numerical tests and comparison with the experimental data of the grain boundary sliding in a polycrystalline copper with the average grain size 210 μm [16].

3. Results

The creep response of the unit cell varies depending on the number of grains and the thickness of the grain boundary layer. With the less number of grains averaged stiffness of the unit cell decreases. This occurs due to the fact, that deformation of an individual grain as a crystalline solid becomes more essential. Also stress concentrations on the grain boundaries are significant. At the same time when the number of grains increases, individual grains becomes constrained by others, possessing different orientation. This leads to the stress redistribution and more homogeneous deformation of the unit cell.
Within the current work unit cells are tested with the same boundary conditions. Symmetric boundary conditions are applied on three side faces of the cube in order to decrease boundary effects and to avoid artificial displacements in the corners. On the forth face a uniform tensile stress is applied. Other two faces are left free. Unit cells with 40, 80 and 120 grains and grain size 210 μm are tested under tensile pressure of 40 MPa. The thickness of the grain boundary layer is set as a fraction of the grain size. The fractions 0 (corresponds to the unit cell without grain boundary layer), 5 and 10 % are investigated. The average creep curves in the loading direction are presented in Fig. 3. If to compare the creep curves of the unit cells with 80 and 120 grains and equal grain boundary layer thickness, one can see that they almost coincide in contrast to the creep curve of the unit cell with 40 grains, which lies much higher. That means that the average stiffness of the unit cell has tendency to converge to a certain value with the

[1] Experimental data are furnished by courtesy of Dr.-Ing. Frederik Otto from Institute of Materials, Ruhr-University Bochum

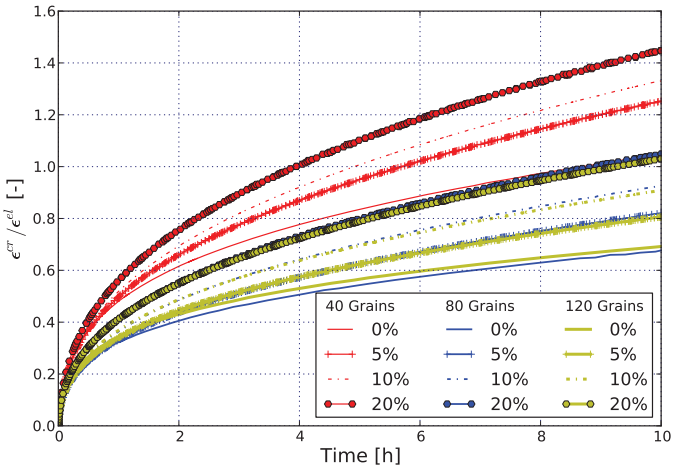

Figure 3. Normalized averaged creep strain.

increase of number of grains.

So far as we would like to introduce the grain boundary sliding through the shear deformation of the grain boundary region, the overall creep response of the unit cell is assumed to be more compliant in contrast to the unit cell, where grains are glued. Therefore, unit cells with bigger volume of the grain boundary region will exhibit higher creep rates.

In the real polycrystal there is no visible borders between grain boundary and grain interior. This region can be described as a zone influenced by the lattices mismatch and accumulation of vacancies or inclusions. Hereupon the thickness of the grain boundary region cannot be measured exactly. In the current work we assume, that this value should be as less as possible and at the same time be numerically admissible - too small value will lead to element's distortion and a divergence of analysis.

In the experiment on the grain boundary sliding the vertical offset of the grains on the specimen surface after creep loading is measured. From averaged value of the offsets the sliding strain is obtained, which contributes to the total creep strain around 10 %. In order to reproduce this numerically, the unit cells consist of 80 grains with the the average grain size 210 μm are constructed with and without grain boundary layer. They are tested under constant tension with the stress magnitude of 40 MPa until the averaged creep strain reaches the level 1.5 times higher than the averaged elastic strain. The sliding strain is obtained as a difference of the average creep strain of the unit cell with the grain boundary layer and without it. With the following model material parameters grain boundary sliding strain reached value of 10% from the total strain, predicted by experiments:

$$a^{gb} = 4 \cdot 10^{-8} (\mathrm{MPa})^{-n^{gb}}/\mathrm{h}, \;\; n^{gb} = 4, \;\; \mu_{12}^{gb} = \mu_{13}^{gb} = \mu_{23}^{gb} = 0.2$$

The influence of the grain boundary region on the stress state of the unit cell is investigated. The grains start to slide relatively to each other in that regions, where resulting shear stress is high enough. The stress state within the grains is almost not affected by the presence of grain boundary region. However high stresses within the grain boundary region are observed, especially in triple points and junctions of grains. After loading positive normal stresses in the grain boundary region are 2.5 times greater than averaged stresses in the grain interior. this can be explained by that fact, that the regions, where shear stress is moderate, do not slide and thereby constrain sliding of neighboring grain boundaries and produce stresses increase. This normal stress concentrators will be used as driving forces for the creep cavity radius growth as it discussed in [17].

4. Conclusions and Outlook

In this study the creep behavior of the polycrystalline material is investigated. The phenomenological power law creep model is used to assign grains material behavior within the unit cell. The assumption

is made for the interaction between grains by introducing the grain boundary region. The constitutive model within this region characterizes grain boundary sliding. The values of the elastic and creep model parameters for the grain material are identified for copper from available experimental data. An approach to determine material parameters for the grain boundary region is proposed. It is based on the numerical testing and validation with the experimental data. Unit cells with and without grain boundary region are analyzed. The unit cell with the 80 grains is assumed to be representative. From the numerical considerations grain boundary thickness should be set to 5 % of the grain size. The local analysis of an individual unit cell with recommended number of grains and thickness of boundary layer shows within it stress concentrations in the normal direction. These stresses will be used as driving forces in future simulation of the creep cavitation.

References

[1] C. H. Rycroft. *Multiscale modeling in granular flow*. PhD thesis, Massachusetts Institute of Technology, Cambridge (MA), 2007.

[2] F. Fritzen, T. Böhlke, and E. Schnack. Periodic three-dimensional mesh generation for crystalline aggregates based on Voronoi tessellation. *Comput. Mech.*, 43:701 – 713, 2009.

[3] I. Simonovski and L. Cizelj. Towards modeling intergranular stress corrosion cracks on grain size scales. *Nucl. Eng. Des.*, 246:107 – 114, 2012.

[4] R. Raj and M. F. Ashby. On grain boundary sliding and diffusional creep. *Metall. Trans.*, 2:1113–1127, 1971.

[5] R. C. Gifkins. Grain-boundary sliding and its accommodation during creep and superplasticity. *Metall. Trans. A*, 7A:1225–1232, 1976.

[6] R. L. Bell and T. G. Langdon. An investigation of grain–boundary sliding during creep. *J. Mater. Sci.*, 2:313–323, 1967.

[7] W.A. Rachinger. Relative grain translations in the plastic flow of aluminium. *J. I. Met.*, 81:33 – 41, 1952.

[8] F. W. Crossman and M. F. Ashby. The non-niform flow of polycrystals by grain-boundary sliding accommodated by power-law creep. *Acta Metall. Mater.*, 23:425–440, 1975.

[9] T. Norbygaard. *Studies of grain boundaries in materials subjected to diffusional creep*. PhD thesis, Riso National Laboratory, Roskilde, 2002.

[10] Y. A. Chang and L. Himmel. Temperature dependence of the elastic constants of Cu, Ag, and Au above room temperature. *J. Appl. Phys.*, 37:3567 – 3572, 1966.

[11] O. Ozhoga-Maslovskaja, H. Altenbach, K. Naumenko, O. Prygorniev, and O. Vodka. Micromechanical creep model for pure copper. *PAMM*, 11(1):419–420, 2011.

[12] N. Ohno, T. Mizuno, H. Kawaji, and I. Okada. Multiaxial creep of a nickel-base directionally solidified alloy: anisotropy and simulation. *Acta Metall. Mater.*, 40:559 – 567, 1992.

[13] L. Meric, P. Poubanne, and G. Cailletaud. Single crystal modeling for structural calculations: Part 1 – model presentation. *J. Engng. Mat. Technol.*, 113:162 – 170, 1991.

[14] F. K. G. Odquist. *Mathematical Theory of Creep and Creep Rupture*. Oxford university press, Oxford, 1974.

[15] T. G. Langdon. Grain boundary sliding revisited: Developments in sliding over four decades. *J. Mater. Sci.*, 41:597 – 609, 2006.

[16] A. Ayensu and T. Langdon. The inter–relationship between grain boundary sliding and cavitation during creep of polycrystalline Copper. *Metall. Mater. Trans. A*, 27A:901 – 907, 1996.

[17] E. van der Giessen, M. W. D. van der Burg, A. Needleman, and V. Tvergaard. Void growth due to creep and grain boundary diffusion at high triaxialities. *J. Mech. Phys. Solids*, 43:123 – 165, 1995.

Proceedings of the 4th International Conference on Nonlinear Dynamics
ND-KhPI2013
June 19-22, 2013, Sevastopol, Ukraine

Modeling of Cyclic Loading of Metal Products Using Crystal Plasticity Model

Alexey I. Shveykin[1*], Petr V. Trusov[1], Pavel S. Volegov[1]

Abstract
Two-level models of different polycrystalline metal's inelastic deformation based on crystal plasticity and describing viscoplastic intragranular dislocations slip, grain boundary sliding, twinning (for HCP metals), lattice rotation with an explicit consider of dislocation slip incompatibility in neighboring grains, and fragmentation of crystallites are developed. The homogenization of constitutive equations at various scale levels is used, which allows to connect the same type of characteristics of different scale levels and leads to an unambiguous description of geometric nonlinearity on the macro level by specifying the form of corotation derivative of Cauchy stress tensor. An algorithm for solving boundary value problems in FEM package Abaqus with using proposed models to describe the behavior of the material is developed, corresponding computational modules is created. Numerical investigation of cyclic loading of samples from various polycrystalline metals with a description of the evolving internal structure is done.

Keywords
crystal plasticity, multilevel model, homogenization of constitutive equations, geometric nonlinearity

[1] Perm National Research Polytechnic University, Perm, Russian Federation
* **Corresponding author:** alexsh59@bk.ru

Introduction

Numerous theoretical and experimental studies show that the performance of the internal material structure determines the behavior of the material at the macro level and its performance characteristics. During intensive plastic deformation the internal structure of the material is significantly restructured: the grain and dislocation structures are changing, crystallites lattice is rotated; it is widely used to produce materials with unique properties: submicrocrystalline, nanocrystalline, textured materials and materials, which are capable of superplastic deformation.

At the time, the construction of models capable of describing the change of the internal structure of polycrystalline materials, a growing acceptance of the approach based on an explicit introduction to the structure of the constitutive relations parameters reflecting the state and evolution of meso- and microstructure evolution and the kinetic equations for these parameters (so-called internal variables) [1]. In particular, recent decades, a very wide development of crystal plasticity based models, which built in the framework of this approach and explicitly describing the material structure and the mechanisms of inelastic deformation at the crystallite level, is observed; this models allows a natural way to describe the structure evolution at deep plastic strain.

Based on the crystal plasticity models can be divided into three classes [2,3]: statistics, self-consistent and direct. Models of the last two classes require inaccessible currently computing resources, so for modeling of real processes statistical constitutive model are more popular.

The article briefly discusses the general structure of the two-level models of polycrystalline metals inelastic deformation developed by the authors, explains how to homogenize the constitutive equations on different levels of scale, describes the algorithm for applying models of the material in the boundary value problems solution and obtaines the results.

1. The structure of two-level model of polycrystalline metals

In the simulation of polycrystalline metal's inelastic deformation scale levels hierarchy can be defined as follows: the macro level – meso level (the level of crystallite – grains, subgrains, fragment) – micro level (the dislocation structure) (Fig. 1). Currently, the two-level models (macro-meso) are most commonly used for the analysis of polycrystalline metals deformation.

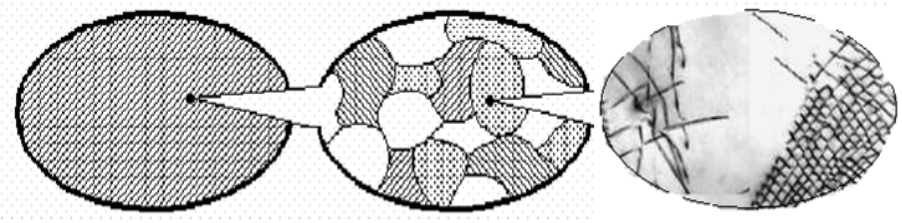

Figure 1. Schematic representation of the scale levels hierarchy in the simulation of polycrystalline metals (from left to right: the macro-level, meso, micro)

A representative volume of a polycrystalline metal, consisting of a set of crystallites (meso-level elements) is considered at the macro level . The constitutive equations system at the macro level is [1]:

$$\begin{cases} \boldsymbol{\Sigma}^{\mathrm{r}} \equiv \dot{\boldsymbol{\Sigma}} + \boldsymbol{\Omega}^{\mathrm{T}} \cdot \boldsymbol{\Sigma} + \boldsymbol{\Sigma} \cdot \boldsymbol{\Omega} = \mathbf{C} : \mathbf{D}^{\mathrm{e}} = \mathbf{C} : (\mathbf{D} - \mathbf{D}^{\mathrm{in}}) \\ \boldsymbol{\Omega} = \boldsymbol{\Omega}\left(\mathbf{w}_{(i)}, \mathbf{c}_{(i)}\right), i = 1,...,N \\ \mathbf{C} = \mathbf{C}(\mathbf{c}_{(i)}), i = 1,...,N \\ \mathbf{D}^{\mathrm{in}} = \mathbf{D}^{\mathrm{in}}(\mathbf{d}^{\mathrm{in}}_{(i)},\ \mathbf{c}_{(i)}), i = 1,...,N \end{cases} \tag{1}$$

where $\boldsymbol{\Sigma}$ is the Cauchy stress tensor, $\mathbf{C}$ is the elastic properties 4[th]-range tensor, $\mathbf{D}$, $\mathbf{D}^{\mathrm{e}}$, $\mathbf{D}^{\mathrm{in}}$ are the strain rate, its elastic and inelastic parts, the index «r» means derivative independent of the choice of reference system, $\boldsymbol{\Omega}$ is the tensor describing the motion of the moving coordinate system, which defines itself in relation to deformational movement [4] on the macro level. To determine $\boldsymbol{\Omega}$ the homogenization condition for constitutive equations on different scale levels is proposed. Thus, the inelastic strain rate $\mathbf{D}^{\mathrm{in}}$, the effective anisotropic elastic properties $\mathbf{C}$ and describing the motion of the moving frame tensor $\boldsymbol{\Omega}$ are explicit internal variables in the macro-level model, at any moment depends on the structure at the lower scale levels (and through it depends on the loading history) and determined by meso-level model, used for each crystallite (number of meso level items N should be sufficient for a statistical description of a representative volume at the macro level).

At the meso level the system uses the following relations (for the description of each crystallite, the index number of the crystallite is omitted):

$$\begin{cases} \boldsymbol{\sigma}^{\mathrm{r}} \equiv \dot{\boldsymbol{\sigma}} - \boldsymbol{\omega} \cdot \boldsymbol{\sigma} + \boldsymbol{\sigma} \cdot \boldsymbol{\omega} = \mathbf{c} : \mathbf{d}^{\mathrm{e}} = \mathbf{c} : (\mathbf{d} - \mathbf{d}^{\mathrm{in}}) \\ \mathbf{d}^{in} = \sum_{i=1}^{K} \dot{\gamma}^i \mathbf{m}^i \\ \dot{\gamma}^i = \dot{\gamma}_0 \left| \dfrac{\tau^i}{\tau_{\tilde{N}}{}^i} \right|^{1/n} H(\tau^i - \tau_{\tilde{N}}{}^i),\ i = 1,...,K \\ \dot{\tau}^i_C = f(\gamma^j, \dot{\gamma}^j),\ i,j = 1,...,K \\ \text{relations to determine } \boldsymbol{\omega}, \quad \dot{\mathbf{o}} \cdot \mathbf{o}^{\mathrm{T}} = \boldsymbol{\omega} \\ \mathbf{d} = \mathbf{D} \end{cases} \tag{2}$$

where $\boldsymbol{\sigma}$ is the Cauchy stress tensor, $\mathbf{c}$ is the fourth-rank elastic properties tensor of the crystallite, $\mathbf{d}, \mathbf{d}^{\mathrm{e}}, \mathbf{d}^{\mathrm{in}}$ are the strain rate, the elastic and inelastic strain rate, γ^i, τ^i_C are accumulated slip and the

critical shear stress on the *i*-th slip system, $\mathbf{m}^i$ is the orientation tensor of *i*-th slip system, $\mathbf{m}^i = 1/2(\mathbf{b}^i\mathbf{n}^i + \mathbf{n}^i\mathbf{b}^i)$, $\mathbf{b}^i, \mathbf{n}^i$ is the unit vectors in the direction of the Burgers vector and the normal to the sliping plane; bedding planes and orientation of the Burgers vector along the translational motion (slip) of edge dislocations are known, they are the most densely packed planes and directions, so, in fcc metals sliding edge dislocations are in the planes of $\{111\}$ in directions <110>, $\dot{\gamma}_0, n$ are the constants of the material: the characteristic shear rate and strain rate sensitivity of the material [1], τ^i is the shear stress in the *i*-th slip systemиe, $\tau^i = \mathbf{b}^i\mathbf{n}^i : \boldsymbol{\sigma}$, $H(\cdot)$ is the Heaviside function, K is the number of slip systems for considered type lattice, $\mathbf{o}$ is the tensor current orientation of the crystallographic coordinate system relative to the fixed grain laboratory system.

As constitutive relation at the meso level Hooke's law in the rate form is used (2_1), the geometric nonlinearity is takes into account: quasi-solid movement [4] associated with the rotation of the lattice (in crystallographic coordinates); spin tensor $\boldsymbol{\omega}$ in corotation derivative Cauchy stress tensor $\boldsymbol{\sigma}^{\mathrm{r}}$ characterizes the crystal lattice rotation. Thus, stress is characterized the elastic bonds in grain and determined by lattice distortions.

Equation (2_2) is kinematic equation, according to which the inelastic deformation of the crystallite is define by sliding to slip systems. If other intragranular deformation mechanisms, such as grain boundary sliding or twinning in the (2_2) to the modes of intragrain dislocation glide mechanisms are added to the appropriate mode for shear rates that determine the kinetic equations.

To determine inelastic deformation rate of polycrystalline metals can be used [2,3]: elastoplastic model based on the Lin model [5], or the elastoviscoplastic model used here (2_3), where $\mathbf{d}^{\mathrm{in}}$ (and $\boldsymbol{\omega}$) associated with implicit internal meso-level variables characterizing dislocation slip – shear rates on slip systems $\dot{\gamma}^i$, the critical stress τ_C^i, tensor $\mathbf{o}$ of the crystallographic orientation of the current coordinate system of grain relative to a fixed laboratory system coordinates. Specification of equation (2_4), describing the evolution of the critical shear stress on the slip system, is in the paper [6].

Taylor's hypothesis is applied for scale transition implemented at the macro level to the lowest levels in the scale model $\mathbf{d} = \mathbf{D}$.

Relations (2_5) for the determination of the spin system the following ratio are used:

$$\begin{cases} \boldsymbol{\omega} = \boldsymbol{\omega}_1 + \boldsymbol{\omega}_2 \\ \boldsymbol{\omega}_1 = \dfrac{1}{2}(\hat{\nabla}\mathbf{v}^{\mathrm{T}} - \hat{\nabla}\mathbf{v}) - \displaystyle\sum_{i=1}^{K} \frac{1}{2}\dot{\gamma}^i(\mathbf{b}^i\mathbf{n}^i - \mathbf{n}^i\mathbf{b}^i) - (\mathbf{B}:\boldsymbol{\sigma})\cdot\mathbf{D}^{in} + \mathbf{D}^{in}\cdot(\mathbf{B}:\boldsymbol{\sigma}) \\ \boldsymbol{\omega}_2 = \begin{cases} \dfrac{1}{\mathrm{A}}\boldsymbol{\mu}^r + \dfrac{1}{\mathrm{H}}\boldsymbol{\mu}, \ \text{ï ðè } \|\boldsymbol{\mu}\| = \mu_c \ \text{è } \boldsymbol{\mu}:\boldsymbol{\mu}^r > 0 \\ \dfrac{1}{\mathrm{A}}\boldsymbol{\mu}^r, \ \text{otherwise} \end{cases} \\ \boldsymbol{\mu}^r = \displaystyle\sum_{m=1}^{M}(\boldsymbol{\mu}^r)^m \\ \mathbf{m}^r = \mu\,\mathbf{N}\times\left[\displaystyle\sum_i^K \dot{\gamma}^i\mathbf{n}^i\mathbf{b}^i - \sum_j^K \dot{\gamma}^{j(m)}\mathbf{n}^{j(m)}\mathbf{b}^{j(m)}\right]\cdot\mathbf{N}, \ \text{for each neighboring grain } m \end{cases} \tag{3}$$

The first component $\boldsymbol{\omega}_1$ describes the rotation of the lattice with the grain material during the imposed kinematic effects (material associated with the orthogonal rotation tensor accompanying elastic deformation). The second component $\boldsymbol{\omega}_2$ describes the rotation of the actual crystallite lattice due to the interaction with the environment. To do this, the model (3) introduced the couple stresses $\boldsymbol{\mu}$ acting on the crystal, the critical moment stress μ_C and set the normal to the crystallite $\mathbf{q}^m, m = 1,...,M$ (M - number of neighboring crystallites). Additivity of the velocity moments of interaction with all neighboring grains is assumed in (3_4). The evolution of the vector-momentum

associated with the couple stress tensor and determines from the analysis of the incompatibility of dislocation motion on the boundary of the crystallites by equation (3_5). Based on the input of the couple stresses may be used for description of fragmentation [7].

2. The homogenization procedure of constitutive equations for scale transition

One of the keynote questions in the multilevel models construction is the issue of constitutive equations homogenization at various scale levels. The logical understanding of the problem is follows: macro level equations should be defining from meso level constitutive equations with a priori relations of the macro- and meso level parameters [1]; specific type of relations associated with the aggregation hypothesis (combining elements of meso level to the macro level element). For statistical crystal plasticity models a priori relation is the equality of velocity gradient, stresses and the effective elastic properties tensor at the macro level average the corresponding meso level characteristics (for the velocity gradient this conditions are automatically done due Taylor's hypothesis).

The constitutive equations homogenization procedure for the proposed model are as the following:

1) represent the quantities in the description of the stress-strain state at meso-level as the sum of average representative volume of macro-level variables and deviations from these averages;

2) substitute this representation in the meso-level of the defining equation (2_1), the obtained relations are averaged;

3) finding the form obtained in step 2 averaged meso-level constitutive equation running the macro-level (1_1), defining the necessary connections.

For the proposed models the connections are

$$\mathbf{\Omega} = <\boldsymbol{\omega}>, \quad \mathbf{D}^{in} = <\mathbf{d}^{in}> + \mathbf{C}^{-1} : <\mathbf{c}' : \mathbf{d}^{in\prime}> - \mathbf{C}^{-1} : (<\boldsymbol{\omega}' \cdot \boldsymbol{\sigma}'> - <\boldsymbol{\sigma}' \cdot \boldsymbol{\omega}'>) \quad (5)$$

Thus, the proposed approach results in more focused form of the defining relations on the macro level (and in particular – the type of independent of the reference system choice derivative). Proposed method is easy to apply for other forms of constitutive relations for meso- and macro-levels for a wide range of constitutive models with internal variables.

3. Algorithm for solving boundary value problems using constitutive model and the simulation results

The algorithm to use developed model for solving boundary value problems in FEM package ABAQUS is made. To do this, we use standard package – implementation of the proposed models in the custom procedure UMAT, including the integration of the constitutive equations of the model (determination of the stresses and internal variables at the end of step in the UMAT) and the definition of the current cutting modulus matrix $[\mathbf{C}^{ep}] = \dfrac{\partial\{\Delta\mathbf{\Sigma}\}}{\partial\{\Delta\mathbf{E}\}}$, where $\Delta\mathbf{\Sigma}$ is the increment of stress on the step, $\Delta\mathbf{E}$ is the increment deformation step. The analysis was carried out, resulting in an analytical expression for $\mathbf{C}^{ep}$ connecting it with the internal meso-scale variables.

It should be note that many existing models [2,3] are not considered in the explicit level the constitutive equations at the macro level, but at numerical implementation in FEM-package Abaqus is the (implicity) introduction is macro-scale level is done, there are Jauman derivative of Cauchy stress tensor is used in Abaqus, which violates the consistency of the two-level constitutive model. It is shown that this approach can lead to physically incorrect.

Using the developed software (other than computational module the post-processor for the analysis of results characterizing the changing internal structure was created) simulated for cyclic loading of samples from various polycrystalline metals is done. Figure 2 shows the characteristic pole figures for the [110]-direction under cyclic compression-tension. This one can note the good agreement between the results (for the parts of the sample away from the fixed boundaries) with experimental data.

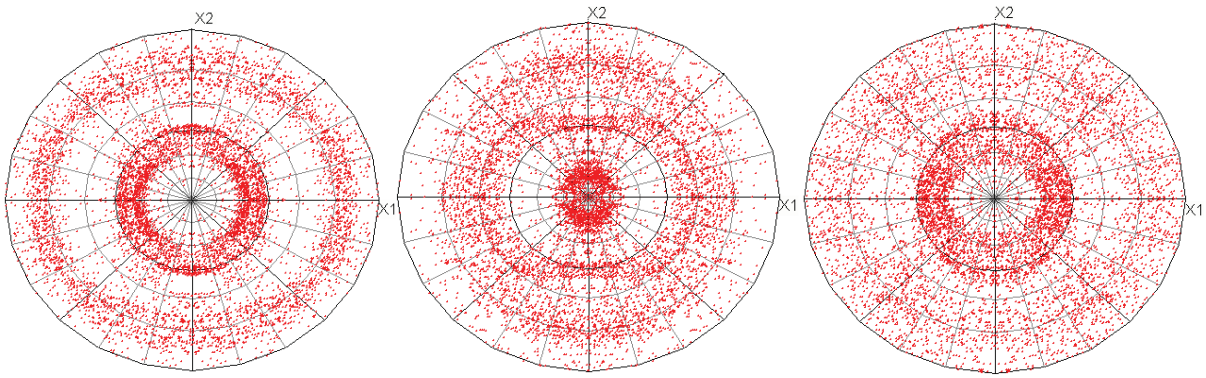

Figure 2. Pole figures for the [111]-direction, projecting from OX3, from left to right: when $\varepsilon_{33} = -1$ (after compression), $\varepsilon_{33} = 1$ (after tension), $\varepsilon_{33} = -1$ (after re-compression)

Conclusions

To describe the deformation processes of polycrystalline materials with the evolution of its meso-structure two-level constitutive model based on the crystal plasticity is developed. Approach to the homogenization of constitutive relations at different scale levels, allowing precise constitutive relations form ratio at the macro level (and in particular independent of the choice of the reference system derivative of stress tensor), proposed and applied.

An algorithm for solving boundary value problems using the Finite Element Method was implemented in the Abaqus package. With the use of modeling software system obtained results during cyclic loading of samples from various polycrystalline metals, including the evolution of the internal structure: the shape, size and orientation of the crystallographic axes of the structural elements of the polycrystalline aggregates (grains, subgrains, fragments), effective macroscopic elastic and plastic properties of polycrystalline materials, the results are in good agreement with experimental data.

Acknowledgments

This work was supported by RFBR (grants №12-08-01052-a, №12-08-33082-mol_a_ved, №12-01-31094-mol_a), the President Grants №МК-3989.2012.1, № МК-390.2013.1, Federal Target Program "Scientific and scientific-pedagogical personnel of innovative Russia in 2009 - 2013 years" (activity 1.2.2, Agreement 14.B37.21.0382).

References

[1] Trusov P.V., Shveykin A.I., Nechaeva E.S. and Volegov P.S. Multilevel models of inelastic deformation of materials and their application for description of internal structure evolution *Physical Mesomechanics*, Vol. 15: 3-4, pp. 155-175, 2012.

[2] Trusov P.V. and Shveykin A.I. Multilevel crystal plasticity models of single and polycrystals. Statistical models *Physical Mesomechanics*, Vol. 16:1, pp. 23-33, 2013.

[3] Trusov P.V. and Shveykin A.I. Multilevel crystal plasticity models of single and polycrystals. Direct models *Physical Mesomechanics*, Vol. 14: 5, pp. 5-30, 2011. (In Russian)

[4] Pozdeev A.A., Trusov P.V. and Nyashin Yu.I. *Large Elastoplastic Strains: Theory, Algorithms, Applications*, Nauka, Moscow, 1986. (In Russian)

[5] Kondratev N.S. and Trusov P.V. A mathematical model for bcc crystall deformation taking into consideration the twinning mechanism *Computational Continuum Mechanics*, Vol. 4:4, pp. 20-33, 2011. (in Russian)

[6] Trusov P.V., Volegov P.S. and Yanz A. Yu. Description of intragrain and grain-boundary hardening of mono-and polycrystals *Scientific and Technical Statements of St.Petersburg State Polytechnical University. Physics and Mathematics*, Vol. 2 (98), pp.110-119, 2010. (in Russian)

[7] Trusov P.V., Volegov P.S. and Yants A.Yu. Asymmetric crystal plasticity theory for the evolution of polycrystal microstructures. *Physical Mesomechanics*, Vol. 15: 1-2, pp. 35-45, 2012.

Proceedings of the 4th International Conference on Nonlinear Dynamics
ND-KhPI2013
June 19-22, 2013, Sevastopol, Ukraine

Two-level Polycrystal Models and Investigation Influence of Hardening Laws on the Macro Effects of Complex and Cyclic Loading

Pavel S. Volegov[1]*, Peter V. Trusov[1], Anton Yu. Yanz[1], Alexey I. Shveykin[1]

Abstract
The problem of constructing a physically based hardening laws of mono- and polycrystalline samples in multi-level theories using crystal plasticity is considered. These hardening laws should allow describing the process of the defect structure evolution of the material due to the intensive inelastic strains. It is also should be applicable to the description of complex and cyclic loading. An approach to the construction of a general and a particular form of hardening law is proposed, which takes into account the interaction of full and split dislocations with each other, forming and destruction of dislocation barriers, annihilation of dislocations during reverse loading, the interaction of intragranular and grain boundary dislocations. Using the obtained hardening law, the known experimental effects of complex and cyclic loading are described.

Keywords
Crystal plasticity, polycrystals, complex cyclic loading, dislocation slipping, hardening, grain boundaries, mechanisms of inelastic deformation.

[1] Perm National Research Polytechnic University, Perm, Russian Federation
* **Corresponding author:** crocinc@mail.ru

Introduction

Changes in the physical and mechanical properties of the specimen during deformation by complex cyclic path is a consequence of a substantial restructuring of the micro- and mesostructure of the material, mainly a consequence of a significant evolution of the dislocation (wider - defective) structure of the material [1]. Describing of such processes without studying and establishing the appropriate mathematical models that explicitly take into account the physical root causes of the material's microstructure evolution at large strains is practically impossible. Directly into the structure of crystal plasticity relations description of the microstructure evolution is introduced through specific relationships that determine the change of the critical shear stress on the slip systems on a set of parameters defined on the basis of physical analysis (shears, temperature, stacking fault energy etc.), which are commonly called hardening law [2-4]. The above explains the considerable attention in crystal plasticity theories, which is paid to the modification of hardening law, in particular in connection with the new experimental data obtained with the use of high-resolution equipment (in particular an electron microscope) [4].

The aim is to study the effects produced by polycrystalline representative macro volume of material under complex and cyclic loading (and the transition from one to another type of loading) as a consequence of changes occurring at the level of the dislocation structure in the process of loading, and attempt to modify the laws hardening so way that they can physically transparently describe these changes and effects. In particular, the unresolved issue is to justify and describe the known experimental effects, such as the dependence of additional cyclic hardening of the degree of disproportionality of loading, cyclic softening the transition from non-proportional to proportional loading, transverse reinforcement, which manifests itself when, after proportional loading in one direction is followed by proportional loading in the other direction.

1. Two-level constitutive model for inelastic defprmation of polycrystals

This paper uses a model based on the developed by a team of the Department of mathematical modeling of systems and processes PNRPU two-level approach to the consideration of inelastic deformation of polycrystalline metals [1]. As a top (macro-) level, we consider representative volume of the material, and the lower level means the level of the individual crystallites. Next, to simplify the upper level (macro-representative) will be called the macro level, and the lower (separate single crystals with ideal crystal lattice) will be called as meso level.

The constitutive model of the macro-level is the following set of equations (hereinafter macro-parameters are indicated in capital letters, the similar meso parameters – in lower case):

$$\begin{cases} \boldsymbol{\Sigma}^{\mathrm{R}} \equiv \dot{\boldsymbol{\Sigma}} + \boldsymbol{\Omega}^{\mathrm{T}} \cdot \boldsymbol{\Sigma} + \boldsymbol{\Sigma} \cdot \boldsymbol{\Omega} = \boldsymbol{\Pi} : \mathbf{D}^{\mathrm{e}} = \boldsymbol{\Pi} : (\mathbf{D} - \mathbf{D}^{\mathrm{in}}), \\ \boldsymbol{\Omega} = \boldsymbol{\Omega}\left(\boldsymbol{\omega}_{(i)}, \boldsymbol{\pi}_{(i)}, \boldsymbol{\sigma}_{(i)}\right), i = 1,...,N, \\ \boldsymbol{\Pi} = \boldsymbol{\Pi}(\boldsymbol{\pi}_{(i)}, \mathbf{o}_{(i)}), i = 1,...,N, \\ \mathbf{D}^{\mathrm{in}} = \mathbf{D}^{\mathrm{in}}(\mathbf{d}^{\mathrm{in}}_{(i)}, \boldsymbol{\pi}_{(i)}, \boldsymbol{\omega}_{(i)}), i = 1,...,N, \end{cases} \tag{1}$$

here $\boldsymbol{\Sigma}$ is the Cauchy stress tensor, $\boldsymbol{\Pi}$ is the elastic moduli tensor, $\mathbf{D}$, $\mathbf{D}^{\mathrm{e}}$, $\mathbf{D}^{\mathrm{in}}$ are strain rate tensor, its elastic and inelastic parts, index «R» means independent of reference system choice derivative [1], $\boldsymbol{\Omega}$ is the tensor describing the motion of the moving coordinate system with respect to which the strain is determined at the macro-level; $\boldsymbol{\pi}_{(i)}, \boldsymbol{\sigma}_{(i)}, \mathbf{d}^{\mathrm{in}}_{(i)}, \boldsymbol{\omega}_{(i)}, \mathbf{o}_{(i)}$ are elastic constant tensor, stress tensor, elastic and inelastic parts of strain rate tensor, spin and the orientation of *i*-crystallite, N is the number of crystallites forming a representative macro-level.

At the meso level (the level of the crystallite) in the two-level model using the following system of relations (crystallite number is omitted):

$$\begin{cases} \boldsymbol{\sigma}^{\mathrm{r}} \equiv \dot{\boldsymbol{\sigma}} - \boldsymbol{\omega} \cdot \boldsymbol{\sigma} + \boldsymbol{\sigma} \cdot \boldsymbol{\omega} = \boldsymbol{\pi} : \mathbf{d}^{\mathrm{e}} = \boldsymbol{\pi} : (\mathbf{d} - \mathbf{d}^{\mathrm{in}}), \\ \mathbf{d}^{\mathrm{in}} = \sum_{i=1}^{K} \dot{\gamma}^{(i)} \mathbf{m}^{(i)}_{(S)}, \\ \dot{\gamma}^{(i)} = \dot{\gamma}_0 \left| \dfrac{\tau^{(i)}}{\tau^{(i)}_c} \right|^{1/n} H(\tau^{(i)} - \tau^{(i)}_c), \ i = 1,...,K, \\ \dot{\tau}^{(i)}_c = f(\gamma^{(j)}, \dot{\gamma}^{(j)}), \ i, j = 1,...,K, \\ \text{relations for } \boldsymbol{\omega}, \\ \text{for which from the equation } \dot{\mathbf{o}} \cdot \mathbf{o}^{\mathrm{T}} = \boldsymbol{\omega} \\ \text{the orientation tensor } \mathbf{o} \text{ is defined,} \\ \hat{\nabla}\mathbf{v} = \hat{\nabla}\mathbf{V}, \end{cases} \tag{2}$$

where $\boldsymbol{\sigma}$ is the Cauchy stress tensor, $\boldsymbol{\pi}$ is the crystallite elastic moduli tensor, $\mathbf{d}, \mathbf{d}^{\mathrm{e}}, \mathbf{d}^{\mathrm{in}}$ are strain rate tensor, its elastic and inelastic parts, $\gamma^{(i)}, \tau^{(i)}_c$ are the accumulated shear and the critical shear stress on the *i*-th slip system, $\mathbf{m}^{(i)}_{(S)}$ is the symmetric part of the orientation tensor of the *i*-th slip system, $\mathbf{m}^{(i)}_{(S)} = 1/2(\mathbf{b}^{(i)}\mathbf{n}^{(i)} + \mathbf{n}^{(i)}\mathbf{b}^{(i)})$, $\mathbf{b}^{(i)}, \mathbf{n}^{(i)}$ are unit vectors in the direction of the Burgers vector and the normal to the slip plane; $\dot{\gamma}_0, n$ are material constants: the characteristic shear rate and rate sensitivity of the material, $\tau^{(i)}$ is the acting slip system shear stress, $\tau^{(i)} = \mathbf{b}^{(i)}\mathbf{n}^{(i)} : \boldsymbol{\sigma}$, $H(\cdot)$ is the Heaviside function, K is the number of slip systems for this type of crystal lattice, **o is** tensor of the current orientation of the crystallographic coordinate system to the fixed laboratory system.

As the defining relation (equation of state) at the mesolevel plays rate form of Hooke's law (2_1), taking into account the geometric nonlinearity: quasi-solid movement on the mesolevel is associated

with the rotation of the lattice (crystallographic coordinate system); in the corotation derivative of the Cauchy stress tensor appears spin tensor, characterizes the crystal lattice rotation rate.

For scale transition we used generalized Voigt hypothesis, according to which the velocity gradient of movement for each crystallite is equal to the macro-velocity gradient $\hat{\nabla}\mathbf{v} = \hat{\nabla}\mathbf{V}$.

In [1], the problem of different scale levels defining relations homogenization in the two-level model of inelastic deformation is considered, one of making results is to determine the quasi-solid movement on the macro level $\boldsymbol{\Omega}$ and the inelastic part of the strain rate tensor at the macro level $\mathbf{D}^{in}$ to ensure homogenization conditions:

$$\boldsymbol{\Pi} = <\boldsymbol{\pi}>, \boldsymbol{\Sigma} = <\boldsymbol{\sigma}>, \mathbf{D} = <\mathbf{d}>. \tag{3}$$

It is shown that for (3) in conjunction with the systems of equations (1) and (2) the spin $\boldsymbol{\Omega}$ and inelastic strain rate tensor $\mathbf{D}^{\text{in}}$ should be determined by the relations

$$\boldsymbol{\Omega} = <\boldsymbol{\omega}>, \tag{4}$$

$$\mathbf{D}^{in} = <\mathbf{d}^{in}> + \boldsymbol{\Pi}^{-1} : <\boldsymbol{\pi}' : \mathbf{d}^{in\prime}> - \boldsymbol{\Pi}^{-1} : (<\boldsymbol{\omega}' \cdot \boldsymbol{\sigma}'> - <\boldsymbol{\sigma}' \cdot \boldsymbol{\omega}'>), \tag{5}$$

where the prime denotes the deviation of the corresponding values from their average values at representative macto-volume.

In the numerical implementation of the mathematical model (1) - (5) is proposed to use the Adams-Moulton scheme ("predictor-corrector"), which can significantly improve the accuracy of the calculations without significantly increasing computing time [5].

2. Hardening description

The correct description of hardening, which is an essential mechanism of the plastic deformation, allows obtain the dependence between the numerical experiments with corresponding experiments, on the other hand, in the hardening laws it is inherent the description of the microstructure of the material and the laws of its evolution.

Hardening is divided into "non-oriented" and "oriented". The first describes the hardening regardless of the direction of deformation (under this definition, processes such as the formation of the intersection of dislocations, plaits, braids, dislocation barriers), and a hardening increases the critical shear stress at once on many slip systems (or even all at once). The second is related to the accumulation of elastic energy to "pursed dislocations" (at different barrier) and this energy may be released (fully or partially) at the change the direction of deformation. The second type, in general, can be described by the kinematic hardening, or due to simultaneous changes in the critical shear stress on the opposite slip systems.

By using the formalism of constitutive models with internal variables and two-level mathematical model of polycrystals inelastic deformation, based on the crystal elastoviscoplastic model at meso level, we received both general and particular form of hardening laws of mono- and polycrystalline, allows to describe the formation and destruction of dislocation barriers, the annihilation of dislocations (and so describes Bauschinger effect), and additional hardening, resulting from the interaction of intragranular and grain boundary dislocations [1].

As the basic law a power hardening law is considered in type of:

$$\dot{\tau}_{c\,b}^{(k)} = f^{(k)}\left(\gamma^{(i)}, \dot{\gamma}^{(i)}\right) = \psi E \left(\sum_{i=1}^{24} a_i^{(k)} \left(\frac{\gamma^{(i)}}{\sum_{j=1}^{24} \gamma^{(j)}} \right)^{\psi-1} \dot{\gamma}^{(i)} \right), \; k = \overline{1,24}, \;\; \psi > 1, \; \gamma^{(i)} \geq 0, \tag{6}$$

$$\tau_{c\,b}^{(k)}(0) = \tau_{c\,b0}^{(k)},$$

which takes into account the interaction of forest dislocations and modified to reflect the complexity of the previous loading.

Assuming additivity of the critical shear stress rates on the slip system due to different mechanisms of hardening, the power law (6) is supplemented by terms that take into account the basic mechanisms of obstacles during plastic deformation, left out the first (power) term:

$$\dot{\tau}_c^{(k)} = f^{(k)}\left(\gamma^{(i)}, \dot{\gamma}^{(i)}\right) + f_{bar}^{(k)}\left(\gamma^{(i)}, \dot{\gamma}^{(i)}; \alpha_1^{(i)}, \alpha_2^{(i)}, \ldots, \alpha_n^{(i)}\right) + f_{annih}^{(k)}\left(\gamma^{(i)}, \dot{\gamma}^{(i)}; \beta_1^{(i)}, \beta_2^{(i)}, \ldots, \beta_m^{(i)}\right), \; i,k = \overline{1,24}, \quad (7)$$

here $\alpha_1^{(i)}, \alpha_2^{(i)}, \ldots, \alpha_n^{(i)}$; $\beta_1^{(i)}, \beta_2^{(i)}, \ldots, \beta_m^{(i)}$ – sets of internal variables describing appropriate mechanisms (in general, its may different values at each moment of deformation for different slip systems) [6]; here the term describes additional hardening due to reactions to the split dislocations, and $f_{annih}^{(k)}\left(\gamma^{(i)}, \dot{\gamma}^{(i)}; \beta_1^{(i)}, \beta_2^{(i)}, \ldots, \beta_m^{(i)}\right)$ allows to consider a decrease of the critical shear stress for reverse slip through dislocation annihilation.

An additional hardening function $f_{bar}^{(i)}$ is taken in the form of:

$$f_{bar}^{(i)}\left(\gamma_{SFE}, \dot{\gamma}^{(i)}, \gamma^{(j)}\right) = \sum_{k=1}^{6} \xi_{ik} \tau_c^{(i)} \left(1 - \frac{\gamma_{SFE}}{\gamma^*_{SFE}}\right) \mathrm{H}\left(1 - \frac{\gamma_{SFE}}{\gamma^*_{SFE}}\right) \left(\int_0^t f_{bar}^{(i)} d\tau + f_0^{(i)}\right)^{-1} \times$$
$$\times \dot{\gamma}^{(i)} \left(\sum_{j \neq i}^{N^*} \gamma^{(j)} + \gamma_0^b\right) \mathrm{H}\left(\int_0^t f_{bar}^{(i)} d\tau - \tau_{c\,fr}^{(i)}\right), \quad (8)$$

where γ_{SFE} is the stacking fault energy (SFE) of the material, γ^*_{SFE} is critical SFE, beyond which this mechanism relies insignificant for this material, N^* is the number of slip systems, coupled to given, $\tau_c^{(i)}$ is current (full) critical stress, $\tau_{c\,fr}^{(i)}$ is critical stress for barrier destruction, γ_0^b is the small constant, ξ_{ik} are the material constants, taking into account the strength of each of the six types of barriers. Equation (8) is explicitly take into account the differences in the known types of dislocation barriers and different energies of destruction (or bypass) of these barriers (with the optional parameter $\tau_{c\,fr}^{(i)}$).

Oriented hardening, which is realized by "pursed" by obstacles dislocation annihilation, due to the changing the deformation direction is also considered; detail the physics of the annihilation process and factors affecting the decrease of the critical shear stress on the slip systems as a result of the annihilation of dislocations is considered [7]. To account for the released elastic energy in relation for $f_{annih}^{(i)}$ puts an additional factor that takes into consideration the complexity of the loading on all of the slip systems (here is an example for the for fcc lattice):

$$f_{annih}^{(i)}\left(\beta_1, \beta_2, \ldots, \beta_m\right) = \frac{d\tau_{annih}^{(i)}}{dt} = -\xi_2 \tau_{annih}^{(i)} \frac{\gamma^{(i)}}{\sum_j \gamma^{(j)}} \dot{\gamma}^{(i)} \left(\gamma^{(i+12)} + \gamma_0^a\right), \; \tau_{annih}^{(i)}\Big|_{t=0} = \tau_{c0}^{(i)}, \quad (9)$$

where γ_0^a is a small constant, ξ_2 is the material constant.

3. Numerical results

The diagram of the cyclic uniaxial loading of polycrystalline aggregate using modified relations (6) – (9) is shown in Fig. 1. The physical and mechanical parameters of the model correspond to the technically pure copper. Nonlinear effects associated with the formation and destruction of dislocation barriers, there do not appear in the smallness of strains; clearly visible out on the stationary trajectory of deformation.

It is noticeable that the hardening law of in the form (6) can only describe the effects of hardening associated with linear (or weakly nonlinear, depending on the ψ value) interaction of

dislocations (in the first time the interaction of individual dislocations with various point obstacles, as well as the interaction of dislocations each own elastic stress fields). Mathematically it is possible to determine the parameters of the law (6) considering a substantially nonlinear form of the loading curve, but such description cannot be considered physically correct if we try to base model on the physical separation of hardening mechanisms.

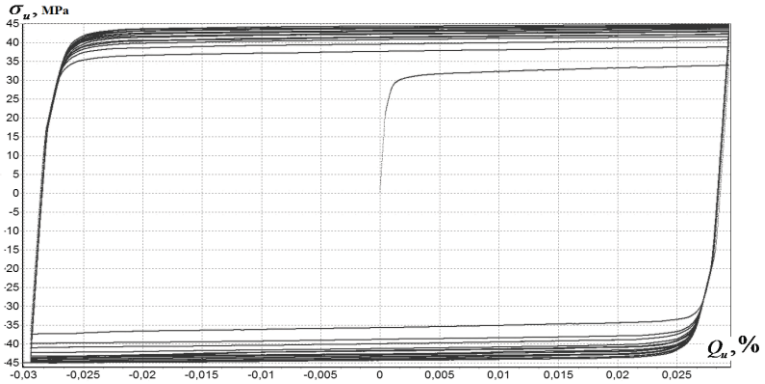

Fugure 1. The stress - strain diagram during cyclic deformation of polycrystalline aggregate, 20 cycles total

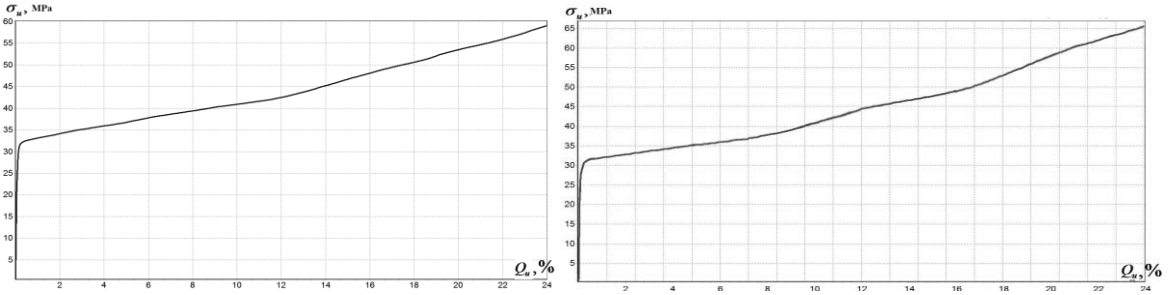

a) b)

Figure 2. The stress – strain diagram under uniaxial compression of polycrystalline aggregate, a) $f_0^{(i)} = 1{,}05$, $\gamma_0^b = 5 \cdot 10^{-5}$, b) $f_0^{(i)} = 1{,}02$, $\gamma_0^b = 2{,}5 \cdot 10^{-5}$

Fig. 2 shows the dependence of various stress-strain diagram for polycrystalline aggregate for the case of using the additional term in the form (8) in the hardening law, with the values specified in the caption. Clearly visible nonlinearities appearing in the diagram due to the effect of "blocking" slip systems by sessile dislocation when accumulated to a certain critical value, and accordingly releasing these systems from the deformation process. As long as there is a slip system (or set of slip systems), where the dislocation slip activate criteria is fulfilled, the material during plastic deformation will be forced to use a smaller number of slip systems than it is necessary in order to complete choose the prescribed deformation. So, in the moments of one system closing and before the activation of another systems the share of elastic deformation in full deformation rises, resulting in a steep increase in stress on the diagram.

In addition, interesting question is the consideration of the term, which reflects the formation of sessile dislocations, depending on the concrete slip system. Figure 3, on the left, shows a typical dependence of the critical additional stress due to (8), at all slip systems randomly selected grain, on the intensity of deformation. It may be noted very different from other systems rate of accumulation of barriers on two slip systems, which are symmetrically oriented with respect to the loading direction, in addition, a noticeable phenomenon connected associated deactivate and activate of slip systems process. Sharp bend at the diagram for some systems due not so much the shear rates in these systems as the accumulation of split dislocations in a pair of conjugated systems with the highest increase of additional stresses. When activating these systems, even small shear rate on them leads to an abrupt increase in the critical stress due to the large accumulated shift in their conjugate systems. In turn, such a high increase in the critical stress leads to a rapid shutdown of the system from the plastic deformation, and the process repeats.

Figure 3, on the right, shows stress-strain diagram for polycrystalline aggregate when the term (9) is considered, which describes the decreasing of the critical stress on the slip system, due to the annihilation of dislocations during pursed reverse loading. The calculations were performed for two cycles in tension-compression. Clearly visible reduction of the yield strength when the sign change of deformation: from 32 MPa initially to 28 MPa after the first change of deformation direction, and from 34 MPa to 30 MPa in the second cycle.

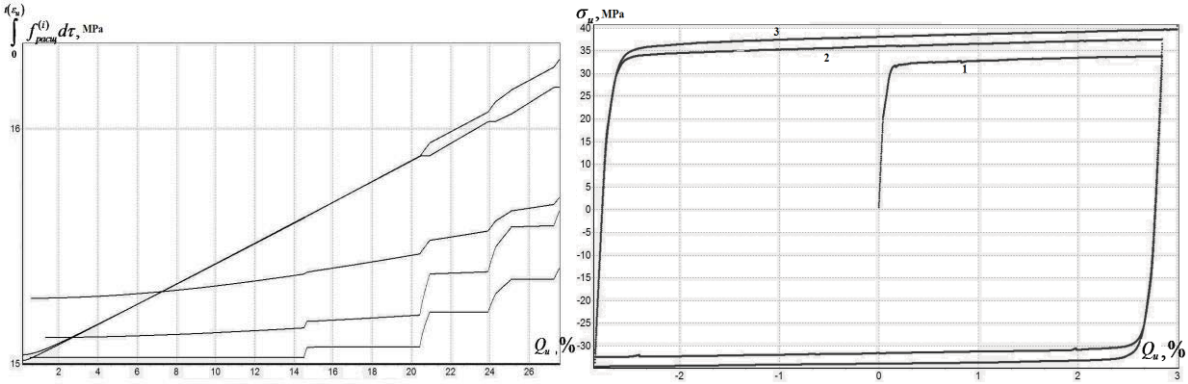

Figure 3. Left: typical dependence of the critical additional stress due to (8) for the slip systems of any grain; Right: the stress - strain diagram for cyclic deformation of polycrystalline aggregate with terms (8) and (9)

Conclusions

Thus, in the paper a general and a particular form of hardening law for mono-and polycrystalline were proposed, allowing describing the formation and destruction of dislocation barriers, and the annihilation of dislocations. The analysis of the possible mechanisms of interaction between carriers and the plastic deformation of the crystal lattice defects is executed; hardening laws which discovers a good agreement with experimental data are proposed. The study also attempted to justify and describe the known experimental effects, such as the dependence of additional cyclic hardening of the degree of disproportionality of loading, cyclic softening the transition from non-proportional to proportional loading, transverse reinforcement. The results of these studies are currently in the process of being published in scientific periodicals.

Acknowledgments

This work was supported by RFBR (grants №12-08-01052-a, №12-08-33082-mol_a_ved, №12-01-31094-mol_a, №13-01-96005-r_ural_a), the President Grants №МК-3989.2012.1, №МК-390.2013.1, Federal Target Program "Scientific and scientific-pedagogical personnel of innovative Russia in 2009 - 2013 years" (activity 1.2.2, Agreement 14.B37.21.0382).

References

[1] Trusov P.V., Shveykin A.I., Nechaeva E.S. and Volegov P.S. Multilevel models of inelastic deformation of materials and their application for description of internal structure evolution *Physical Mesomechanics*, Vol. 15: 3-4, pp. 155-175, 2012.

[2] Trusov P.V. and Volegov P.S. Crystal plasticity: theory and applications to the description of inelastic deformation of materials. Part 1: Rigid-plastic and elasto-plastic models *Vestnik PNIPU. Mehanika*, Vol.1, pp.5-45, 2011 (in Russian).

[3] Trusov P.V. and Volegov P.S. Crystal plasticity: theory and applications to the description of inelastic deformation of materials. Part 2: Viscoplastic and elastoviscoplastic models *Vestnik PNIPU. Mehanika*, Vol. 2, pp.101-131, 2011 (in Russian).

[4] Trusov P.V. and Volegov P.S. Crystal plasticity: theory and applications to the description of inelastic deformation of materials. Part 3: Hardening theories, gradient theories *Vestnik PNIPU. Mechanika*, Vol.3, pp.146-197, 2011 (in Russian).

[5] Volegov P.S. and Yanz A.Yu. Asymmetric crystal plasticity theory for FCC polycrystals: peculiarities of numerical implementation of some schemes of loading *Vestnik PNIPU. Mehanika*, Vol.1, pp.121-137, 2011 (in Russian).
[6] Trusov P.V. and Volegov P.S. Physical plasticity theories and its applications to describing policrystalline hardening *Tambov University Reports Natural and Technical Sciences*, Vol. 15: 3(1), pp. 983-984, 2010 (in Russian).
[7] Trusov P.V., Volegov P.S. and Yanz A. Yu. Description of intragrain and grain-boundary hardening of mono-and polycrystals *Scientific and Technical Statements of St.Petersburg State Polytechnical University. Physics and mathematics*, Vol. 2 (98), pp.110-119, 2010 *(*in Russian).

Proceedings of the 4th International Conference on Nonlinear Dynamics
ND-KhPI2013
June 19-22, 2013, Sevastopol, Ukraine

Active vibration control of seismic excitation

Marco Barbieri[1]*, Fabio Cinque[1], Sinniah Ilanko[2], Francesco Pellicano[1]

Abstract
Seismic wave control is very important both in civil and mechanical engineering. Common passive methods for isolating a building or a device include Base Isolators (BI) and Tuned Mass Dampers (TMD). In the present paper, a time varying controllable spring is considered as a vibration isolator for a linear mechanical system. The controller works as follows: when the seismic movement is active, the velocity of the moving mass is monitored as the reference velocity. When such reference velocity is positive, the stiffness is reduced; when it is negative, the stiffness is increased. Numerical investigations show that the controller is capable to filter seismic excitation close to the natural frequency of the controlled system, and to reduce the total seismic energy transfer up to 5 times. The role played by the gravity in the active vibration filtering is pointed out by showing that no filtering action can be observed in gravity-free simulations. Even though the controlled system is linear, the controller presents a non-smooth fluctuation of the stiffness, so that a limit cycle occur within the system.

Keywords
Active control, Seismic wave isolation

[1]Department of Engineering "Enzo Ferrari", University of Modena, Italy
[2]Department of Engineering, School of Science & Engineering, University of Waikato, New Zealand
***Corresponding author**: mark@unimore.it

Introduction

The problem of seismic wave isolation has been faced by many authors, both using passive and active control methods [1]. Seismic waves act on a building as a transient external forcing, so that they can be very dangerous if the harmonic content of the seismic forcing matches one of the system natural frequencies [2]. Passive isolation methods include Base Isolators (BI) [3], which are low-pass filters designed in order to cut out the frequencies containing most of the seismic energy. Another approach is to reduce the amplitude of oscillations in the structure by means of Tuned Mass Damper (TMD). The archetype of TMD has been described by Den Hartog [4] and is capable to cancel a resonance of the system. More recently, Non-linear Energy Sinks (NES) [5] and Tuned Liquid Dampers (TLD) [6] have been proposed as passive as passive seismic energy absorbers. Mohtat et al. [7] developed an active Tuned Mass Damper for controlling a seismically excited beam.

The recent literature include many papers about active isolation methods. In 2011, Fujita et al. [8] proposed a method for activating an air bearing isolating support upon earthquake occurrence. Recently, some works [9, 10] have shown, by numerical simulations, the effectiveness of an active switch of the stiffness of the base in seismic isolation. In the present paper, the active stiffness control of a system under seismic excitation is investigated.

1. Dynamic model

In the present work, a simple 2 dof model is considered, see Figure 1(a). The model consists of a mass m_1, which represents the base of the building, and of a suspended mass m_2, connected to the base by a spring having constant stiffness k_2, and by a viscous damper c_2. The base is connected to the ground by means of a spring having time varying stiffness k_1 and a viscous damper c_1. The maximum value of the varying stiffness is $\bar{k}_1$. The system is under the effect of the weight force, and of the seismic base forcing y_1. The motion equations are the following:

$$\begin{cases} m_1\ddot{x}_1 + k_1(x_1 - y_1) + k_2(x_1 - x_2) + c_1(\dot{x}_1 - \dot{y}_1) + c_2(\dot{x}_1 - \dot{x}_2) = -m_1 g \\ m_2\ddot{x}_2 + k_2(x_2 - x_1) + c_2(\dot{x}_2 - \dot{x}_1) = -m_2 g \end{cases} \tag{1}$$

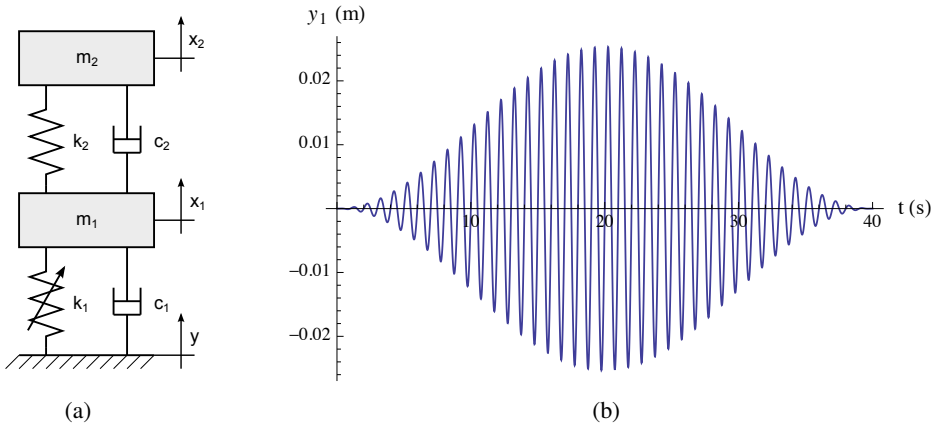

Figure 1. (a) Model of the two dof system; (b) external forcing y_1

The forcing displacement y_1 is a sine function of frequency f and maximum acceleration amplitude ag enveloped by a half sine wave having duration T, see eq. (2).

$$y_1(t) = \frac{a\,g \sin(2\pi f t) \sin\left(\frac{\pi t}{T}\right)}{(2\pi f)^2} \tag{2}$$

The simple model proposed can simulate the dynamic behavior of a building or an equipment or a shipping container. In these three cases, the model parameters and the exciting base vibration are different. In the present paper, simulations are performed referring to a seismic loading of a building: Table 1 collects the equivalent parameters used in numerical computations.

$m_1(kg)$	$m_2(kg)$	$\bar{k}_1(\frac{N}{m})$	$k_2(\frac{N}{m})$	$T(s)$	$a(g)$	$f_c(Hz)$
$8.0 \cdot 10^3$	$8.0 \cdot 10^3$	$1.05 \cdot 10^9$	$1.05 \cdot 10^9$	30	0.2	100

Table 1. Parameters used in the numerical simulations

k_1 is time varying due to the control activation: it changes during the simulation according to the following control strategy:

1. the control is activated if the overall base vibration (*i.e.* maximum base acceleration within a period of the exciting oscillation) exceeds a certain fraction of $1g$, namely ψ
2. when the control is activated, base velocity is checked at control frequency f_c: if the system base has positive velocity at the $k-th$ control instant $t_{c,k}$, then the stiffness $\bar{k}_1$ is reduced of a fraction ϕ.

Provided that the first condition is matched, at the $k-th$ control instant, k_1 is switched as follows:

$$\text{for} \quad t_{c,k} < t \leq t \quad k_1 = \begin{cases} \varphi \bar{k}_1 & \text{if} \quad \dot{x}_1(t_{c,k}) > 0 \\ \bar{k}_1 & \text{otherwise} \end{cases} \tag{3}$$

2. Results and Discussion

2.1 Control effectiveness

In order to show how the proposed method can be effective in controlling seismic vibrations, Figure 2(a) displays the results of a run without control (case A) along with a run having velocity control activated (case B). In both cases, the external forcing frequency f matches the fundamental frequency of the system f_1. The control parameters are $\varphi = 0.5$ and $\psi = 0.01$, *i.e.* stiffness is reduced by one half for positive base velocity and the control works only if the overall vibration exceeds $0.01g$. The control is capable to reduce by 88% the maximum acceleration of the suspended mass m_2: from $1.9g$ to $0.2g$. In the same picture, case D represents the solution obtained using the same control parameters, but for a system which

is not loaded by any weight force ($g = 0$ in eq. (1)). For case D, the maximum acceleration is cut by 44% only, thus suggesting that an important role in the proposed active control method is played by the weight force. Indeed, reducing the stiffness when the the base is going upwards (positive $\dot{x}_1$) means having a longer stroke for the weight force, when it is doing negative work over the system.

Figure 2(b) shows what happens if no check of the overall vibration is performed (case C, $\psi = 0$). The static equilibrium position is unstable, and the controlled system presents a limit cycle in the aftershock, oscillating around a new equilibrium position. In order to overcome such limit cycle arising, numerical simulations have proven that $\psi = 0.01$ is sufficient; moreover, an higher value of ψ would introduce higher vibrations when the control activates, due to the abrupt change in the system when it is already oscillating.

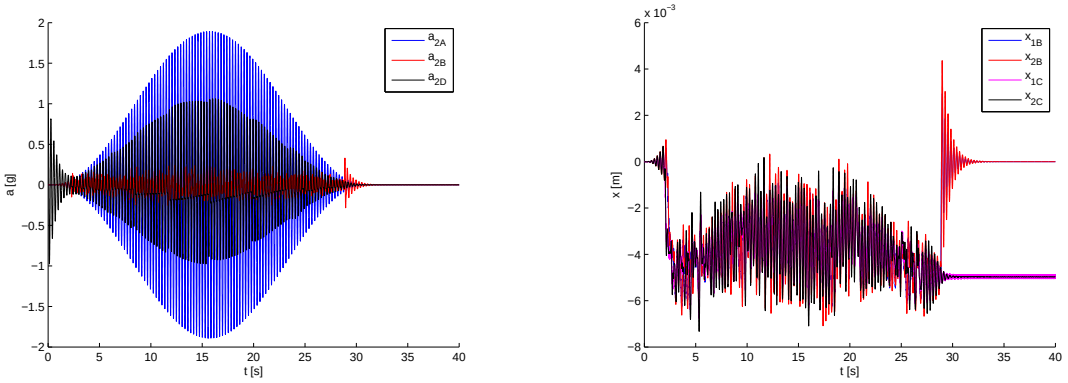

(a) (b)

Figure 2. Effectiveness of the control: (a) A – no control, B – controlled, D – controlled without gravity; (b) A – no control; C – control with $\psi = 0$

2.2 Optimal parameters

In this section, a parametric analysis is performed: the maximum acceleration of the top mass a_2 is chosen as the objective function, and its relationship with the forcing frequency f and the stiffness parameter φ is investigated (Figure 3). If the stiffness k_1 is reduced by a small amount, the acceleration is still high; if k_1 is reduced a lot, than the varying stiffness excites the system more than the seismic load itself. The best value for φ is 0.5: for such value the proposed control strategy is effective broadband, both below and over the fundamental frequency of the system.

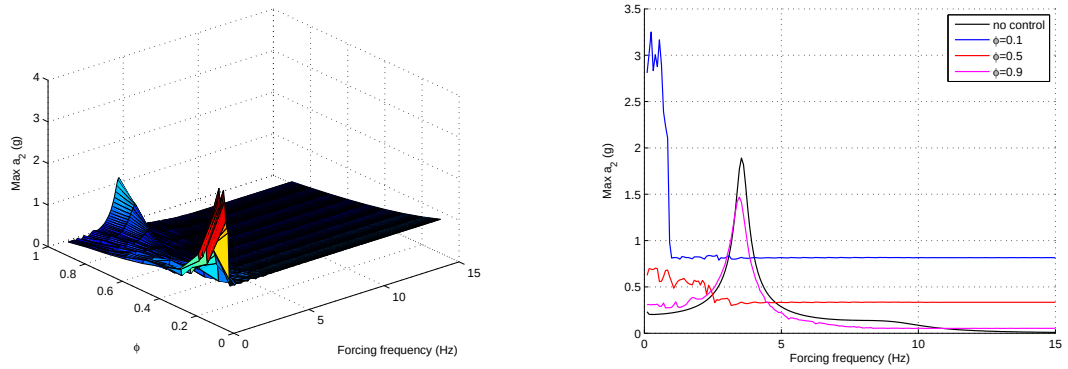

(a) (b)

Figure 3. Maximum top mass acceleration for varying control parameters

Figures 4 and 5 clarify the behavior of the system with/without control. Control activation changes the center around which the system oscillates: this is due to the reduced average stiffness. In terms of

acceleration, when the control is active the top mass acceleration is much lower than in the no control case, nonetheless the base presents a certain acceleration for all the seismic duration. Figure 5(b) clarifies this feature: each time the velocity v_1 reaches a zero, the corresponding acceleration a_2 has a jump, which is due to the sudden stiffness variation. The energy for this change, which cannot be instantaneous in the real application, must be provided by the control actuator. Figure 6(b) shows the isolation effect due to the control: the total energy of the system has a maximum of $4700J$ without control, $1040J$ with optimal control.

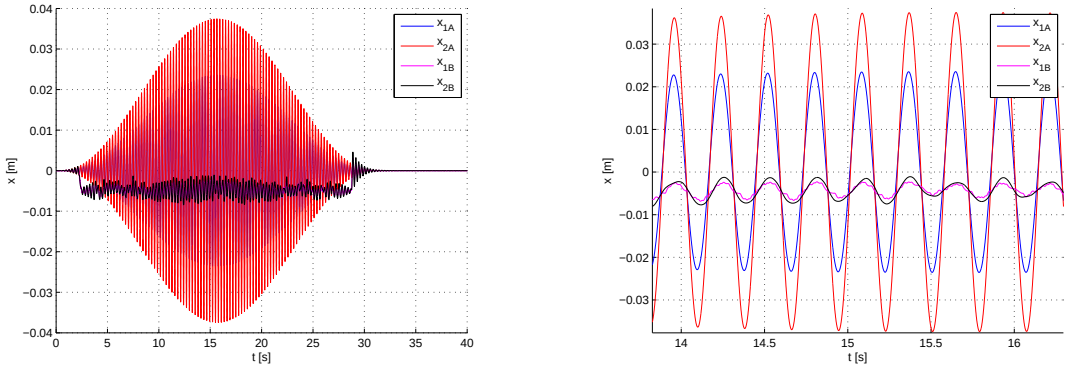

(a) (b)

Figure 4. Positions of the oscillating masses: case A – without control, case B – with $\varphi = 0.5$

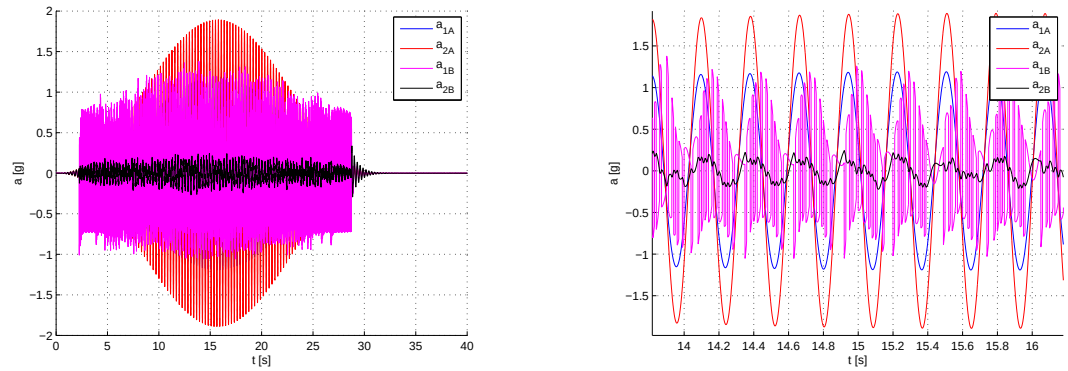

(a) (b)

Figure 5. Accelerations of the oscillating masses: case A – without control, case B – with $\varphi = 0.5$

3. Conclusions

A control method for seismic isolation of buildings or equipments has been theoretically investigated. The control consists in changing the stiffness of the building base when its velocity has opposite sign with respect to the weight force. The role of the weight force has been pointed out by means of numerical simulations, as well as the importance of setting a further control condition in terms of the overall acceleration, so that instabilities are prevented. A parametrical study has shown that the best control for all the forcing frequencies can be obtained for a base stiffness reduction of one half. For such value, the top mass acceleration is cut by 88% with respect to the uncontrolled case, nonetheless the base vibrates at constant amplitude for a longer time, due to effect of the actuator.

References

[1] B. Palazzo and L. Petti. Combined control strategy: base isolation and tuned mass damping. *ISET Journal of Earthquake Technology*, 36-395:121–137, 1999.

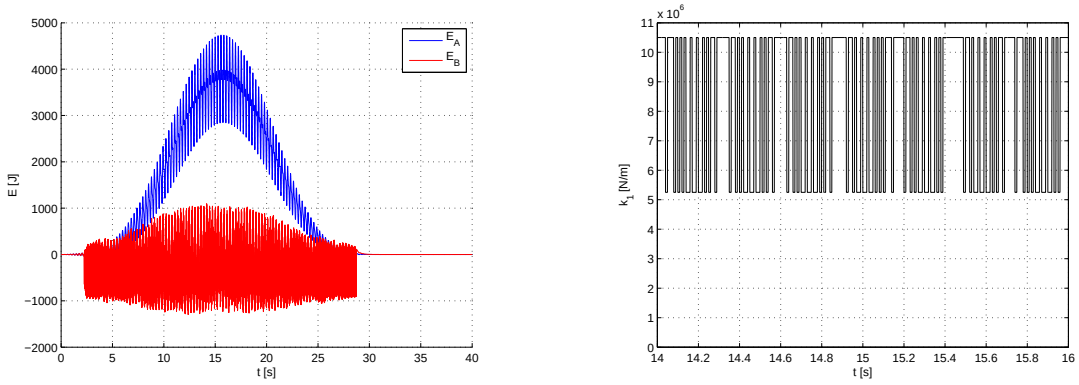

(a) (b)

Figure 6. (a) Total energy: case A $-$ no control, case B $-$ with $\varphi = 0.5$; stiffness fluctuation during seismic control

[2] J. Flores, O. Novaro, and T. H. Seligman. Possible resonance effect in the distribution of earthquake damage in Mexico City. *Nature*, 326:783 – 785, 1987.

[3] J.M. Kelly. Base isolation: Linear theory and design. *Earthquake Spectra*, 6-2, 1990.

[4] J.P. Den Hartog. *Mechanical Vibrations*. McGraw-Hill, New York, U.S.A., 1956.

[5] F. Nucera, F. Lo Iacono, D.M. McFarland, L.A. Bergman, and A.F. Vakakis. Application of broadband nonlinear targeted energy transfers for seismic mitigation of a shear frame: Experimental results. *Journal of Sound and Vibration*, 313(1):57 – 76, 2008.

[6] J.S. Love and M.J. Tait. Non-linear multimodal model for tuned liquid dampers of arbitrary tank geometry. *International Journal of Non-Linear Mechanics*, 46(8):1065 – 1075, 2011.

[7] A. Mohtat, A. Yousefi-Koma, and E. Dehghan-Niri. Active vibration control of seismically excited structures by atmds: stability and performance robustness perspective. *International Journal of Structural Stability and Dynamics*, 10, 2010.

[8] Fujita S., Minagawa K., Tanaka G., and Shimosaka H. Intelligent seismic isolation system using air bearings and earthquake early warning. *Soil Dynamics and Earthquake Engineering*, 31(2):223 – 230, 2011.

[9] A. Ramaratnam and Jalili N. A switched stiffness approach for structural vibration control: theory and real-time implementation. *Journal of Sound and Vibration*, 291:258–274, 2006.

[10] Ledezma-Ramirez D.F., Ferguson N.S., and Brennan M.J. Shock isolation using an isolator with switchable stiffness. *Journal of Sound and Vibration*, 330(5):868 – 882, 2011.

ALPHABETICAL INDEX

НАУКОВЕ ВИДАННЯ

The Fourth International Conference «Nonlinear Dynamics – 2013» Proceedings.

Упорядники: Ю. В.Міхлін, М. В. Перепелкін

Відповідальний секретар: О. О. Водка

Оформлювання оригінал-макету: О. О. Водка

Дизайн обкладинки Г. В. Руднєва.

Матеріали збірника публікуються
в авторському варіанті без редагування.

Підписано до друку 03.06.2013 р.
Формат 60x84/16. Папір офсетний. Гарнітура Times New Roman.
Цифровий друк. Ум. д. арк.. 25,575.
Наклад 100 екз. Замовлення № 128/83

ТОЧКА ВИДАВНИЦТВО TOCHKAPRINT.COM.UA

Видавництво «Точка»
61024, м. Харків, вул. Ольмінського, 11, оф. 5
Тел.: (057) 764-03-79
Свідотство суб'єкта видавничої діяльності:
серія ДК, №1790 від 19.05.2004 р.

МАДРИД ДРУКАРНЯ WWW.MADRID.IN.UA

Віддруковано в ООО «ДРУКАРНЯ МАДРИД»
61024, м. Харків, вул. Ольмінського, 11
Тел.: (057) 756-53-25
www.madrid.in.ua
e-mail: info@madrid.in.ua

ISBN 978-617-669-100-6

9 786176 691006